

Advances in Civil Engineering

Geohazard Risk Reduction Technologies in Geotechnical Engineering

Lead Guest Editor: Young-Suk Song

Guest Editors: Hajime Nakagawa, Tae-Hyung Kim, and Seongwon Hong





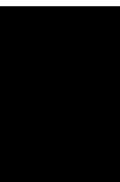
Geohazard Risk Reduction Technologies in Geotechnical Engineering

Advances in Civil Engineering

Geohazard Risk Reduction Technologies in Geotechnical Engineering

Lead Guest Editor: Young-Suk Song

Guest Editors: Hajime Nakagawa, Tae-Hyung Kim,
and Seongwon Hong



Copyright © 2020 Hindawi Limited. All rights reserved.

This is a special issue published in "Advances in Civil Engineering." All articles are open access articles distributed under the Creative Commons Attribution License, which permits unrestricted use, distribution, and reproduction in any medium, provided the original work is properly cited.






Chief Editor

Cumaraswamy Vipulanandan, USA










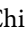



Associate Editors

Chiara Bedon , Italy
Constantin Chalioris , Greece
Ghassan Chehab , Lebanon
Ottavia Corbi, Italy
Mohamed ElGawady , USA
Husnain Haider , Saudi Arabia
Jian Ji , China
Jiang Jin , China
Shazim A. Memon , Kazakhstan
Hossein Moayedi , Vietnam
Sanjay Nimbalkar, Australia
Giuseppe Oliveto , Italy
Alessandro Palmeri , United Kingdom
Arnaud Perrot , France
Hugo Rodrigues , Portugal
Victor Yepes , Spain
Xianbo Zhao , Australia

Academic Editors

José A.F.O. Correia, Portugal
Glenda Abate, Italy
Khalid Abdel-Rahman , Germany
Ali Mardani Aghabaglou, Turkey
José Aguiar , Portugal
Afaq Ahmad , Pakistan
Muhammad Riaz Ahmad , Hong Kong
Hashim M.N. Al-Madani , Bahrain
Luigi Aldieri , Italy
Angelo Aloisio , Italy
Maria Cruz Alonso, Spain
Filipe Amarante dos Santos , Portugal
Serji N. Amirkhania, USA
Eleftherios K. Anastasiou , Greece
Panagiotis Ch. Anastasopoulos , USA
Mohamed Moafak Arbili , Iraq
Farhad Aslani , Australia
Siva Avudaiappan , Chile
Ozgur BASKAN , Turkey
Adewumi Babafemi, Nigeria
Morteza Bagherpour, Turkey
Qingsheng Bai , Germany
Nicola Baldo , Italy
Daniele Baraldi , Italy

Eva Barreira , Portugal
Emilio Bastidas-Arteaga , France
Rita Bento, Portugal
Rafael Bergillos , Spain
Han-bing Bian , China
Xia Bian , China
Huseyin Bilgin , Albania
Giovanni Biondi , Italy
Hugo C. Biscaia , Portugal
Rahul Biswas , India
Edén Bojórquez , Mexico
Giosuè Boscato , Italy
Melina Bosco , Italy
Jorge Branco , Portugal
Bruno Briseghella , China
Brian M. Broderick, Ireland
Emanuele Brunesi , Italy
Quoc-Bao Bui , Vietnam
Tan-Trung Bui , France
Nicola Buratti, Italy
Gaochuang Cai, France
Gladis Camarini , Brazil
Alberto Campisano , Italy
Qi Cao, China
Qixin Cao, China
Iacopo Carnacina , Italy
Alessio Cascardi, Italy
Paolo Castaldo , Italy
Nicola Cavalagli , Italy
Liborio Cavaleri , Italy
Anush Chandrappa , United Kingdom
Wen-Shao Chang , United Kingdom
Muhammad Tariq Amin Chaudhary, Kuwait
Po-Han Chen , Taiwan
Qian Chen , China
Wei Tong Chen , Taiwan
Qixiu Cheng, Hong Kong
Zhanbo Cheng, United Kingdom
Nicholas Chileshe, Australia
Prinya Chindaprasirt , Thailand
Corrado Chisari , United Kingdom
Se Jin Choi , Republic of Korea
Heap-Yih Chong , Australia
S.H. Chu , USA
Ting-Xiang Chu , China

Zhaofei Chu , China
Wonseok Chung , Republic of Korea
Donato Ciampa , Italy
Gian Paolo Cimellaro, Italy
Francesco Colangelo, Italy
Romulus Costache , Romania
Liviu-Adrian Cotfas , Romania
Antonio Maria D'Altri, Italy
Bruno Dal Lago , Italy
Amos Darko , Hong Kong
Arka Jyoti Das , India
Dario De Domenico , Italy
Gianmarco De Felice , Italy
Stefano De Miranda , Italy
Maria T. De Risi , Italy
Tayfun Dede, Turkey
Sadik O. Degertekin , Turkey
Camelia Delcea , Romania
Cristoforo Demartino, China
Giuseppe Di Filippo , Italy
Luigi Di Sarno, Italy
Fabio Di Trapani , Italy
Aboelkasim Diab , Egypt
Thi My Dung Do, Vietnam
Giulio Dondi , Italy
Jiangfeng Dong , China
Chao Dou , China
Mario D'Aniello , Italy
Jingtao Du , China
Ahmed Elghazouli, United Kingdom
Francesco Fabbrocino , Italy
Flora Faleschini , Italy
Dingqiang Fan, Hong Kong
Xueping Fan, China
Qian Fang , China
Salar Farahmand-Tabar , Iran
Ilenia Farina, Italy
Roberto Fedele, Italy
Guang-Liang Feng , China
Luigi Fenu , Italy
Tiago Ferreira , Portugal
Marco Filippo Ferrotto, Italy
Antonio Formisano , Italy
Guoyang Fu, Australia
Stefano Galassi , Italy

Junfeng Gao , China
Meng Gao , China
Giovanni Garcea , Italy
Enrique García-Macías, Spain
Emilio García-Taengua , United Kingdom
DongDong Ge , USA
Khaled Ghaedi, Malaysia
Khaled Ghaedi , Malaysia
Gian Felice Giaccu, Italy
Agathoklis Giaralis , United Kingdom
Ravindran Gobinath, India
Rodrigo Gonçalves, Portugal
Peilin Gong , China
Belén González-Fonteboa , Spain
Salvatore Grasso , Italy
Fan Gu, USA
Erhan Güneyisi , Turkey
Esra Mete Güneyisi, Turkey
Pingye Guo , China
Ankit Gupta , India
Federico Gusella , Italy
Kemal Hacıefendioğlu, Turkey
Jianyong Han , China
Song Han , China
Asad Hanif , Macau
Hadi Hasanzadehshooiili , Canada
Mostafa Fahmi Hassanein, Egypt
Amir Ahmad Hedayat , Iran
Khandaker Hossain , Canada
Zahid Hossain , USA
Chao Hou, China
Biao Hu, China
Jiang Hu , China
Xiaodong Hu, China
Lei Huang , China
Cun Hui , China
Bon-Gang Hwang, Singapore
Jijo James , India
Abbas Fadhil Jasim , Iraq
Ahad Javanmardi , China
Krishnan Prabhakan Jaya, India
Dong-Sheng Jeng , Australia
Han-Yong Jeon, Republic of Korea
Pengjiao Jia, China
Shaohua Jiang , China

MOUSTAFA KASSEM , Malaysia
Mosbeh Kaloop , Egypt
Shankar Karuppannan , Ethiopia
John Kechagias , Greece
Mohammad Khajehzadeh , Iran
Afzal Husain Khan , Saudi Arabia
Mehran Khan , Hong Kong
Manoj Khandelwal, Australia
Jin Kook Kim , Republic of Korea
Woosuk Kim , Republic of Korea
Vaclav Koci , Czech Republic
Loke Kok Foong, Vietnam
Hailing Kong , China
Leonidas Alexandros Kouris , Greece
Kyriakos Kourousis , Ireland
Moacir Kripka , Brazil
Anupam Kumar, The Netherlands
Emma La Malfa Ribolla, Czech Republic
Ali Lakirouhani , Iran
Angus C. C. Lam, China
Thanh Quang Khai Lam , Vietnam
Luciano Lamberti, Italy
Andreas Lampropoulos , United Kingdom
Raffaele Landolfo, Italy
Massimo Latour , Italy
Bang Yeon Lee , Republic of Korea
Eul-Bum Lee , Republic of Korea
Zhen Lei , Canada
Leonardo Leonetti , Italy
Chun-Qing Li , Australia
Dongsheng Li , China
Gen Li, China
Jiale Li , China
Minghui Li, China
Qingchao Li , China
Shuang Yang Li , China
Sunwei Li , Hong Kong
Yajun Li , China
Shun Liang , China
Francesco Liguori , Italy
Jae-Han Lim , Republic of Korea
Jia-Rui Lin , China
Kun Lin , China
Shibin Lin, China

Tzu-Kang Lin , Taiwan
Yu-Cheng Lin , Taiwan
Hexu Liu, USA
Jian Lin Liu , China
Xiaoli Liu , China
Xuemei Liu , Australia
Zaobao Liu , China
Zhuang-Zhuang Liu, China
Diego Lopez-Garcia , Chile
Cristiano Loss , Canada
Lyan-Ywan Lu , Taiwan
Jin Luo , USA
Yanbin Luo , China
Jianjun Ma , China
Junwei Ma , China
Tian-Shou Ma, China
Zhongguo John Ma , USA
Maria Macchiaroli, Italy
Domenico Magisano, Italy
Reza Mahinroosta, Australia
Yann Malecot , France
Prabhat Kumar Mandal , India
John Mander, USA
Iman Mansouri, Iran
André Dias Martins, Portugal
Domagoj Matesan , Croatia
Jose Matos, Portugal
Vasant Matsagar , India
Claudio Mazzotti , Italy
Ahmed Mebarki , France
Gang Mei , China
Kasim Mermerdas, Turkey
Giovanni Minafò , Italy
Masoomah Mirrashid , Iran
Abbas Mohajerani , Australia
Fadzli Mohamed Nazri , Malaysia
Fabrizio Mollaioli , Italy
Rosario Montuori , Italy
H. Naderpour , Iran
Hassan Nasir , Pakistan
Hossein Nassiraei , Iran
Satheeskumar Navaratnam , Australia
Ignacio J. Navarro , Spain
Ashish Kumar Nayak , India
Behzad Nematollahi , Australia

Chayut Ngamkhanong , Thailand
Trung Ngo, Australia
Tengfei Nian, China
Mehdi Nikoo , Canada
Youjun Ning , China
Olugbenga Timo Oladinrin , United Kingdom
Oladimeji Benedict Olalusi, South Africa
Timothy O. Olawumi , Hong Kong
Alejandro Orfila , Spain
Maurizio Orlando , Italy
Siti Aminah Osman, Malaysia
Walid Oueslati , Tunisia
SUVASH PAUL , Bangladesh
John-Paris Pantouvakis , Greece
Fabrizio Paolacci , Italy
Giuseppina Pappalardo , Italy
Fulvio Parisi , Italy
Dimitrios G. Pavlou , Norway
Daniele Pellegrini , Italy
Gatheeshgar Perampalam , United Kingdom
Daniele Perrone , Italy
Giuseppe Piccardo , Italy
Vagelis Plevris , Qatar
Andrea Pranno , Italy
Adolfo Preciado , Mexico
Chongchong Qi , China
Yu Qian, USA
Ying Qin , China
Giuseppe Quaranta , Italy
Krishanu ROY , New Zealand
Vlastimir Radonjanin, Serbia
Carlo Rainieri , Italy
Rahul V. Ralegaonkar, India
Raizal Saifulnaz Muhammad Rashid, Malaysia
Alessandro Rasulo , Italy
Chonghong Ren , China
Qing-Xin Ren, China
Dimitris Rizos , USA
Geoffrey W. Rodgers , New Zealand
Pier Paolo Rossi, Italy
Nicola Ruggieri , Italy
JUNLONG SHANG, Singapore

Nikhil Saboo, India
Anna Saetta, Italy
Juan Sagaseta , United Kingdom
Timo Saksala, Finland
Mostafa Salari, Canada
Ginevra Salerno , Italy
Evangelos J. Sapountzakis , Greece
Vassilis Sarhosis , United Kingdom
Navaratnarajah Sathiparan , Sri Lanka
Fabrizio Scozzese , Italy
Halil Sezen , USA
Payam Shafigh , Malaysia
M. Shahria Alam, Canada
Yi Shan, China
Hussein Sharaf, Iraq
Mostafa Sharifzadeh, Australia
Sanjay Kumar Shukla, Australia
Amir Si Larbi , France
Okan Sirin , Qatar
Piotr Smarzewski , Poland
Francesca Sollecito , Italy
Rui Song , China
Tian-Yi Song, Australia
Flavio Stochino , Italy
Mayank Sukhija , USA
Piti Sukontasukkul , Thailand
Jianping Sun, Singapore
Xiao Sun , China
T. Tafsirojjaman , Australia
Fujiao Tang , China
Patrick W.C. Tang , Australia
Zhi Cheng Tang , China
Weerachart Tangchirapat , Thailand
Xiixin Tao, China
Piergiorgio Tataranni , Italy
Elisabete Teixeira , Portugal
Jorge Iván Tobón , Colombia
Jing-Zhong Tong, China
Francesco Trentadue , Italy
Antonello Troncone, Italy
Majbah Uddin , USA
Tariq Umar , United Kingdom
Muahmmad Usman, United Kingdom
Muhammad Usman , Pakistan
Mucteba Uysal , Turkey

Ilaria Venanzi , Italy
Castorina S. Vieira , Portugal
Valeria Vignali , Italy
Claudia Vitone , Italy
Liwei WEN , China
Chunfeng Wan , China
Hua-Ping Wan, China
Roman Wan-Wendner , Austria
Chaohui Wang , China
Hao Wang , USA
Shiming Wang , China
Wayne Yu Wang , United Kingdom
Wen-Da Wang, China
Xing Wang , China
Xiuling Wang , China
Zhenjun Wang , China
Xin-Jiang Wei , China
Tao Wen , China
Weiping Wen , China
Lei Weng , China
Chao Wu , United Kingdom
Jiangyu Wu, China
Wangjie Wu , China
Wenbing Wu , China
Zhixing Xiao, China
Gang Xu, China
Jian Xu , China
Panpan , China
Rongchao Xu , China
HE YONGLIANG, China
Michael Yam, Hong Kong
Hailu Yang , China
Xu-Xu Yang , China
Hui Yao , China
Xinyu Ye , China
Zhoujing Ye, China
Gürol Yildirim , Turkey
Dawei Yin , China
Doo-Yeol Yoo , Republic of Korea
Zhanping You , USA
Afshar A. Yousefi , Iran
Xinbao Yu , USA
Dongdong Yuan , China
Geun Y. Yun , Republic of Korea


Hyun-Do Yun , Republic of Korea
Cemal YİĞİT , Turkey
Paolo Zampieri, Italy
Giulio Zani , Italy
Mariano Angelo Zanini , Italy
Zhixiong Zeng , Hong Kong
Mustafa Zeybek, Turkey
Henglong Zhang , China
Jiupeng Zhang, China
Tingting Zhang , China
Zengping Zhang, China
Zetian Zhang , China
Zhigang Zhang , China
Zhipeng Zhao , Japan
Jun Zhao , China
Annan Zhou , Australia
Jia-wen Zhou , China
Hai-Tao Zhu , China
Peng Zhu , China
QuanJie Zhu , China
Wenjun Zhu , China
Marco Zucca, Italy
Haoran Zuo, Australia
Junqing Zuo , China
Robert Černý , Czech Republic
Süleyman İpek , Turkey

Contents

Laboratory Experiment and Numerical Analysis on the Precursory Hydraulic Process of Rainfall-Induced Slope Failure

Joon-Young Park  and Young-Suk Song 
Research Article (12 pages), Article ID 2717356, Volume 2020 (2020)




The Propagation of Landslide-Generated Impulse Waves and Their Impacts on the Moored Ships: An Experimental Investigation

Ping Mu, Pingyi Wang , Linfeng Han, Meili Wang, Caixia Meng, Zhiyou Cheng, and Haiyong Xu
Research Article (13 pages), Article ID 6396379, Volume 2020 (2020)



Effects of Rapid Water-Level Fluctuations on the Stability of an Unsaturated Reservoir Bank Slope

Jin-Zhu Mao, Jia Guo, Yong Fu , Wei-Peng Zhang, and Ya-Nan Ding
Research Article (10 pages), Article ID 2360947, Volume 2020 (2020)



Soil Fatigue from Induced Seismicity

Merissa L. Zuzulock , Oliver-Denzil S. Taylor , and Norbert H. Maerz 
Review Article (9 pages), Article ID 7030425, Volume 2020 (2020)

Research on the Disaster-Inducing Mechanism of Coal-Gas Outburst

Fengxiang Nie, Honglei Wang , and Liming Qiu 
Research Article (12 pages), Article ID 1052618, Volume 2020 (2020)

Mitigation Method of Rockfall Hazard on Rock Slope Using Large-Scale Field Tests and Numerical Simulations

Jinam Yoon, Hoki Ban , Youngcheol Hwang, and Duhee Park 
Research Article (6 pages), Article ID 3610651, Volume 2020 (2020)

Numerical Simulation Analysis of NPR Anchorage Monitoring of Bedding Rock Landslide in Open-Pit Mine

Kai Zhang, Xiaojie Yang, Xuebin Cui, Yong Wang, and Zhigang Tao 
Research Article (17 pages), Article ID 8241509, Volume 2020 (2020)

Development of Debris Flow Impact Force Models Based on Flume Experiments for Design Criteria of Soil Erosion Control Dam

Song Eu , Sangjun Im , and Dongyeob Kim 
Research Article (8 pages), Article ID 3567374, Volume 2019 (2019)

A Method for Cavity Scale Estimation Based on Ground-Penetrating Radar (GPR) Explorations: An Experimental Study

Jeong-Jun Park , Yoonseok Chung, and Gigwon Hong 
Research Article (13 pages), Article ID 1365759, Volume 2019 (2019)

Stability Analysis of Slope with Multiple Sliding Surfaces Based on Dynamic Strength-Reduction DDA Method


Shuhong Wang, Chengjin Zhu , Pengyu Wang, and Zishan Zhang
Research Article (12 pages), Article ID 2183732, Volume 2019 (2019)

Freeze-Thaw Cycle Effect on Sputtering Rate of Water-Saturated Yellow Sandstone under Impact Loading

Yunbing Hu , Tianzhu Duan , Penghui Xian , and Liang Chen 

Research Article (12 pages), Article ID 2549603, Volume 2019 (2019)

Laboratory Experiments on Breaching Characteristics of Natural Dams on Sloping Beds

Xiangang Jiang 

Research Article (14 pages), Article ID 5064093, Volume 2019 (2019)

Updating Soil Spatial Variability and Reducing Uncertainty in Soil Excavations by Kriging and Ensemble Kalman Filter

Yajun Li  and Kang Liu




Research Article (14 pages), Article ID 8518792, Volume 2019 (2019)

Rethinking the Water Leak Incident of Tunnel LUO09 to Prepare for a Challenging Future

Wen-Chieh Cheng , Ge Li , Annan Zhou , and Jian Xu 

Research Article (11 pages), Article ID 4695987, Volume 2019 (2019)

Correlation Analysis of Macroscopic and Microscopic Parameters of Coal Measure Soil Based on Discrete Element Method

Hong Zhang , Wei Liao , Junbo Lin, Bang Zhang, and Haoran Feng 

Research Article (14 pages), Article ID 1302682, Volume 2019 (2019)

Research Article

Laboratory Experiment and Numerical Analysis on the Precursory Hydraulic Process of Rainfall-Induced Slope Failure

Joon-Young Park  and Young-Suk Song 

Geo-Environmental Hazard Research Center, Geologic Environment Division, KIGAM, Daejeon 34132, Republic of Korea

Correspondence should be addressed to Young-Suk Song; yssong@kigam.re.kr

Received 27 September 2019; Revised 13 April 2020; Accepted 25 May 2020; Published 22 June 2020

Academic Editor: Kirk Hatfield

Copyright © 2020 Joon-Young Park and Young-Suk Song. This is an open access article distributed under the Creative Commons Attribution License, which permits unrestricted use, distribution, and reproduction in any medium, provided the original work is properly cited.

A combined analysis involving a laboratory test and numerical modeling was performed to investigate the hydraulic processes leading to slope failure during rainfall. Through a laboratory landslide test in which artificial rainfall was applied to a homogeneous sandy slope, the timing and configurations of multiple slides were identified. In addition, volumetric water content was measured in real time through the use of monitoring sensors. The measured volumetric water content data were then used to validate the relevance of the numerical modeling results. The validated numerical modeling of the laboratory-scale slope failures provided insight into the hydraulic conditions that trigger landslides. According to the numerical modeling results, the miniaturized slope in the laboratory test was saturated in a manner so that the wetting front initially progresses downward and then the accumulated rainwater at the toe of the slope creates a water table that advances toward the crest. Furthermore, each of the five sequential failures that occurred during this experiment created slip surfaces where the pore-water pressure had achieved full saturation and an excessive pore-water pressure state. The findings of this study are expected to help understand the hydraulic prerequisites of landslide phenomena.

1. Introduction

The continually increasing issue of damage resulting from landslides is a result of global climate change. Analysis of the changes in Korea's 10-year average temperature and precipitation from 1912 to 2010 showed that the average temperature rose by 1.8 degrees Celsius and precipitation increased by 19% [1]. Statistics indicate that the average rainfall in summer is increasing, whereas the number of rainy days is decreasing. That is, the rainfall characteristics of summer are stronger than in the past, and rainfall intensity is also increasing. Due to the increase in localized heavy rainfall, landslides occur more frequently throughout the country, with the most notable case being the Umyeonsan landslide that occurred in July 2011. In the case of the Umyeonsan landslide, rainfall data of the adjacent Seocho, Namhyeon, and Gwanak observatories show that the hourly rainfall was 62.5 mm–94.0 mm at 8:00 am when the landslide occurred [2]. Landslide damage totaled 2,382 ha over the

past 10 years (53,295 ha), with 53 casualties and 443 billion won in recovery costs.

Various research studies have focused on the occurrence of landslides and debris flows during rainfall, involving techniques such as theoretical analysis, numerical analysis, model experiments, and field monitoring. Recently, various types of laboratory model experiments have been conducted to analyze the mechanisms of landslides and slope failures. In Korea, certain studies were conducted to investigate the mechanism of landslides by causing failures under extreme artificial rainfall conditions [3, 4], whereas another study aimed to estimate the extent of spread after the occurrence of landslides [5]. In addition, Lee et al. [6] carried out experimental studies to investigate the characteristics of infiltration and drainage in model slopes during repeated rainfall. Kim et al. [7] conducted a series of landslide flume experiments to study responding sensitivities of various subsurface monitoring sensors. In the case of foreign countries, there are studies on landslide occurrence

mechanisms according to slope shape [8] as well as studies on surface runoff and soil erosion according to rainfall characteristics [9]. The occurrence of slope failure under various slope conditions during rainfall was experimentally investigated by Acharya et al. [10]; Gallage et al. [11]; and Lourenco et al. [12].

Variables such as volumetric water content and pore-water pressure are some of the most critical sources that govern transient causative factors of decreasing shear strength and the consequential loss of mechanical equilibrium. However, few studies have been conducted to comprehensively understand such precursory hydrologic and hydraulic behaviors that lead to the sliding of slopes. Although certain researchers [13–16] conducted purely experimental studies to investigate various changes in the subsurface during slope collapses, the findings could only provide insights at limited locations (i.e., locations of sensors).

With this context, this study conducted a laboratory-scale slope failure experiment in combination with numerical modeling to achieve comprehensive insights into the hydrologic and hydraulic processes of miniaturized and idealized landslides. For this purpose, a downsized sandy slope was formed and artificial rainfall was applied with a moderate intensity. During the experiment, the shape and type of the slope failures were analyzed, and the volumetric water content was monitored to be used as a prototype hydrologic variable in validating the relevance of the numerical modeling results. Thereafter, based on the numerical modeling results, the comprehensive saturation progress of the domain slope and the changes in the water flows that crossed boundaries (including runoff) were visually and quantitatively identified. Moreover, pore-water pressure conditions at the locations that formed slip surfaces were investigated by plotting numerically solved time-series data immediately prior to the failures.

2. Experimental Configurations

2.1. Apparatus of Laboratory Experiments. In order to simulate rainfall-induced slope failures and the corresponding subsurface hydrologic processes, experiments were performed using a set of laboratory test apparatus. Figure 1 shows a schematic diagram of the test apparatus, which is mainly comprised of a model chamber of a sandy slope, a rainfall simulation system, and a data management system: (1) The rainfall simulation system consists of a watering device with an oscillating nozzle, rainfall controller, and water tank. Rainfall intensity can be adjusted through the rainfall controller. (2) The data management system was installed to record the changes in hydrologic properties of the slope during rainfall. The instrument consists of TDR sensors, a data logger, and a computer. Decagon's 5TE soil moisture sensors were used as the TDR sensors to measure the change in the volumetric water content of the soil over time. Campbell Scientific CR1000M was used as the data logger to record data transmitted from the TDR sensors. (3) In the model chamber, a sandy slope was formed with a steep angle to be failure-prone under rainfall. As shown in

Figure 2(a), a sandy slope of a 35° gradient was formed at the bottom of the chamber, which is inclined by 30°. The depth of the soil layer was set as 35 cm considering the scale of the model chamber. A total of four TDR sensors were installed in two rows at specified depths. The rainfall intensity was adjusted to 50 mm/h. Figure 2(b) shows a side view of the model chamber with the sandy slope. One side of the model chamber was made of transparent tempered glass to observe collapses of the slope. The model chamber was open at the toe of the slope. As a result, rainwater that either runs off the surface or infiltrates into the slope could be drained out to a bucket under the chamber.

2.2. Experimental Procedure. The purpose of this study was to observe slope failure and to investigate the hydrologic processes in homogeneous sandy slopes through a slope model test. The experiment was performed by setting a fixed rainfall intensity of 50 mm/h and was carried out in the following order:

- ① A standard sample of Jumunjin sand from Korea was dried in an oven at 105°C for 24 hours and then additionally dried in air for 24 hours.
- ② Using compaction equipment with a rubber hammer and water sprayer, the dried sample was compacted in the model box and adjusted to 75% relative density with 4% volumetric water content. The compaction was conducted to ensure that the conditions of the model slope were homogeneous: (1) the soil mass and amount of distilled water required to produce the aforementioned density and wetness conditions were calculated using the given volume information of the model chamber; (2) three layers were compacted independently and piled up in sequence to ensure homogeneous and unified conditions.
- ③ Four TDR sensors were installed at 10 cm and 25 cm from the bottom of soil.
- ④ A rainfall intensity of 50 mm/h was applied using the rainfall simulation system.
- ⑤ The change in volumetric water content according to rainfall was measured and analyzed by the data management system in real time.
- ⑥ The slope behavior was filmed in real time and failure shapes of the slope were analyzed over the elapsed period.
- ⑦ The real-time monitored data on volumetric water content were analyzed and compared to the numerical modeling results of rainfall seepage.
- ⑧ Hydraulic conditions on slip surfaces within the slope were simulated and analyzed using the numerical modeling results.

3. Numerical Modeling Setup

In this study, numerical modeling was conducted for rainfall infiltration and seepage water flow of the miniaturized landslide phenomena. The numerical modeling aimed to

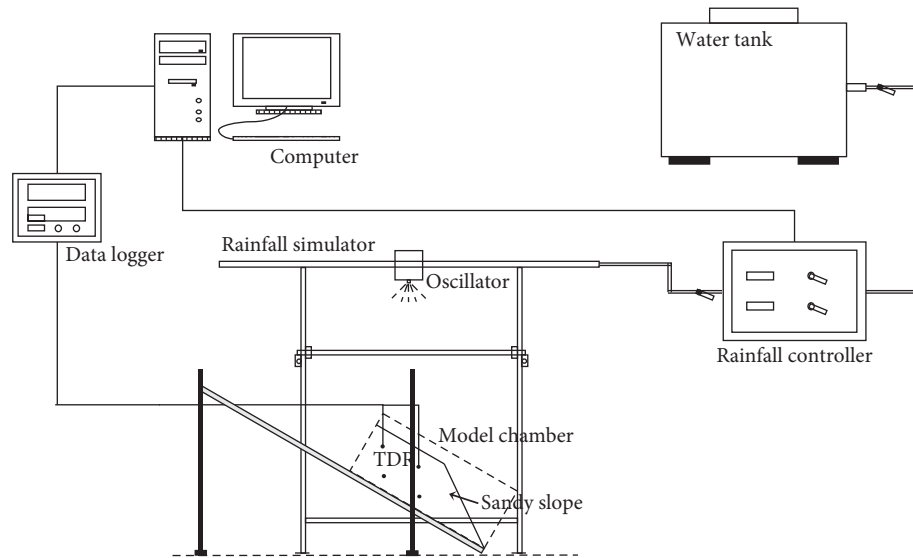


FIGURE 1: Schematic diagram of the model test apparatus.

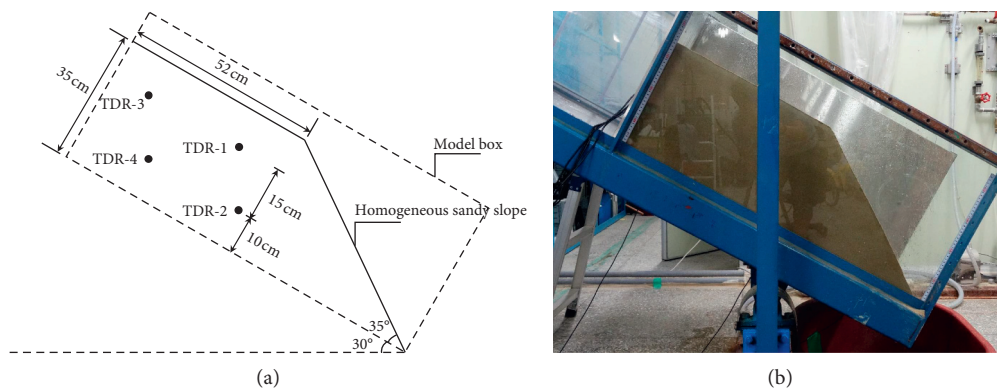


FIGURE 2: Model chamber of the sandy slope. (a) Geometry of the model slope and configuration of sensors. (b) Side view.

derive effective and valid data of hydraulic variables at any given point in the experiment domain, thereby assisting in understanding comprehensive hydraulic processes that lead to landslides. Field and laboratory experiments can only provide limited information with respect to these purposes. In the following sections, the components of the numerical modeling, such as material properties, domain geometry, and boundary and initial conditions, are specified in detail.

3.1. Material Properties. In order to construct the model slope composed of dense sandy ground for the laboratory experiment, Jumunjin standard sand was compacted to a relative density of 75%. Based on an ASTM test method (ASTM D 4254-83), the maximum and minimum dry unit weights were calculated. A series of laboratory tests were conducted to analyze the physical properties of Jumunjin standard sand. As shown in Table 1, the specific gravity is 2.62, the effective particle diameter is 0.42 mm, and the uniformity and curvature coefficients are 1.5 and 1.0, respectively. As a result, the sample falls within SP according to

the Unified Soil Classification System. Figure 3 shows the grain size distribution curve of Jumunjin standard sand. Considering that the slope of the curve is steep in the range between 0.4 and 0.9 mm, it is deduced that the particle size distribution is uniform.

In terms of unsaturated soil properties, Song et al. [18] used automatic test equipment to determine curve-fitting parameters for soil-water characteristic curves (SWCC) of Jumunjin standard sand with a relative density of 75%. The tests were conducted for both drying and wetting paths of SWCC. Based on the measurement dataset of matric suction and volumetric water content, SWCCs were fitted by applying the van Genuchten [19] model. Accordingly, the model parameters were determined for both the drying and wetting paths, as summarized in Table 2. Figure 4(a) depicts the drying and wetting paths of the fitted SWCC [17]. On the other hand, unsaturated hydraulic conductivity functions were estimated for both the drying and wetting paths based on the van Genuchten–Mualem approach [19, 20] and the aforementioned SWCC fitting parameters (Figure 4(b)). Drastic shifts in the slope of the SWCC above and below a

TABLE 1: Geotechnical engineering properties of Jumunjin standard sand.

Description	Symbol	Measured value
Specific gravity	G_s	2.621
Max. dry density	γ_{d-max}	1.613 g/cm ³
Min. dry density	γ_{d-min}	1.366 g/cm ³
Effective particle size	D_{10}	0.42 mm
Uniformity coefficient	C_u	1.5
Coefficient of curvature	C_c	1.0
Soil classification	USCS	SP
Internal frictional angle	Φ'	41.2°

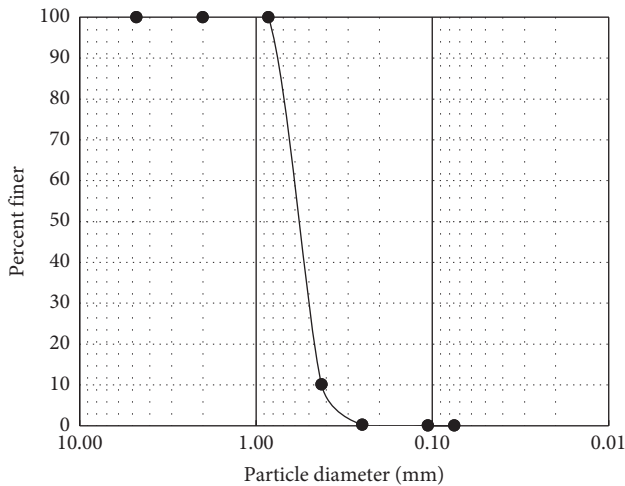


FIGURE 3: Grain size distribution curve of Jumunjin standard sand [17].

particular range of matric suction values (approximately 1~4 kPa) imply that unsaturated soil samples are expected to undergo drastic shifts in the matric suction decrement rate according to regular increments of degree of saturation. More specifically, samples with dry conditions will rapidly lose its high matric suction as it is wetted, until it reaches ~4 kPa matric suction (the first shifting section). Thereafter, matric suction will decrease at a drastically slower rate at the regular influx rate, whereas unsaturated hydraulic conductivity and consequential infiltration rate sharply increase. As the sample reaches near-full saturation at ~1 kPa matric suction (also referred to as the air-entry value), the second shifting section begins, where the remaining low matric suction will be rapidly lost by a small amount of influx until the fully saturated sample starts to exhibit excessive pore-water pressures. Due to the hysteresis behavior in unsaturated soils, the wetting path results in a lower effective saturation than the drying path, which in turn leads to a lower saturated hydraulic conductivity for the wetting path compared to the drying path (Table 2).

3.2. Numerical Domain and Boundary Conditions. The commercial finite element numerical code, SEEP/W (GeoSlope International Ltd., 2012), was used to describe the rainfall infiltration and subsurface water flow of the

experiment in this study. Figure 5 depicts the geometry of the domain (model slope) where a discretized mixed quad and triangle mesh is created. The element size was set to 1.5 cm, which led to the formation of the entire mesh comprised of 1409 nodes and 1325 elements. As the slope material (Jumunjin standard sand) was compacted and formed to an extent that it possesses a spatially uniform volumetric water content of 4%, the corresponding ground pore-water pressure was estimated as -3.5 kPa based on the SWCC (Figure 4(a)). This negative pore-water pressure value that is constant regardless of depth was set as an initial condition of the domain through steady-state analysis. As for the transient analysis that was conducted in sequence, several different types of boundary conditions were applied: (1) a constant zero flux condition was assigned to the left side edge and the bottom of the domain; (2) a constant rainfall flux of 50 mm/h (or $1.39E-03$ cm/s) was applied to the two upper edges that represent the ground surface. This rainfall flux rate was set as almost equal to the saturated hydraulic conductivity of Jumunjin standard sand (see Table 2) to prevent predominant overflowing as well as erosive losses of surficial soil. Through a series of laboratory experiments, Kim et al. [21] found that if the rainfall intensity is less than four times the saturated permeability of the ground, rainfall infiltrates the ground without much surface runoff while maintaining the saturation form as wetting-band progressions. It should be noted that, in the experiment, rainfall from the oscillating nozzle did not reach both ends of the soil, only reaching up to approximately 10 cm from each end of the slope surface. Therefore, the entire two upper edges (i.e., the slope surface) were set as a potential seepage face so that the boundary conditions of the nodes on the slope surface are reviewed at the end of each iteration to check if the conditions meet correct criteria and make adjustments as necessary. The settings would determine the desirable scale of the required seepage face for each time step. At the same time, the analysis was set to prevent rainwater from ponding on the slope surface boundary conditions. Instead, surface water was assumed to be immediately lost via runoff; this setting was possible in Seep/W with the precondition that a surface layer mesh with fine discretization exists on the slope surface boundaries (refer to the zoomed-in part of Figure 5). If numerical analysis is conducted for rainfall infiltration without constructing the surface layer mesh, excessive water that failed to infiltrate the ground would stack up and apply additional load, increasing positive pressure heads to any points located underground of the slope.

4. Results and Discussion

4.1. Retrogressive Failure and Analysis of Hydrologic Processes.

Figure 6 shows five failures that sequentially occurred in the sandy slope during the experiment of this study. As 95 min elapsed after the beginning of the rainfall, a marginal failure was first observed at the toe of the slope as an initiator of four successive slope failures that occurred within 25 min (from Figures 6(a)–6(d)). The failure scale gradually expanded, and thereafter, with a long interim dormant period of 111 min, the largest and final slope collapse was recorded at the

TABLE 2: Unsaturated soil parameters of Jumunjin standard sand with a relative density of 75%.

Condition	van Genuchten [19] SWCC fitting parameters					Saturated hydraulic conductivity k_s (cm/s)	
	α (kPa ⁻¹)	n	m	θ_s	θ_r		
$D_r = 75\%$	Drying	0.393	8.553	0.883	0.41	0.03	1.887×10^{-3}
	Wetting	0.593	5.561	0.820	0.39	0.03	1.482×10^{-3}

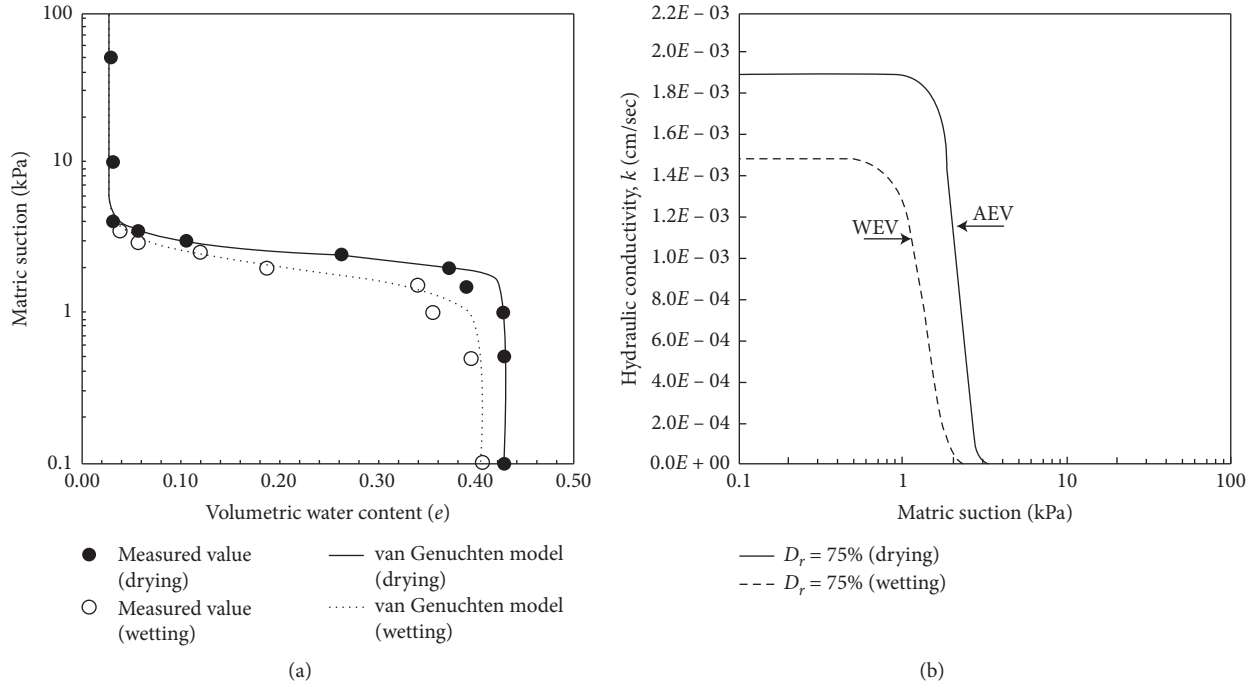


FIGURE 4: Unsaturated properties of Jumunjin standard sand with a relative density of 75% [17]. (a) SWCC. (b) Unsaturated hydraulic conductivity function.

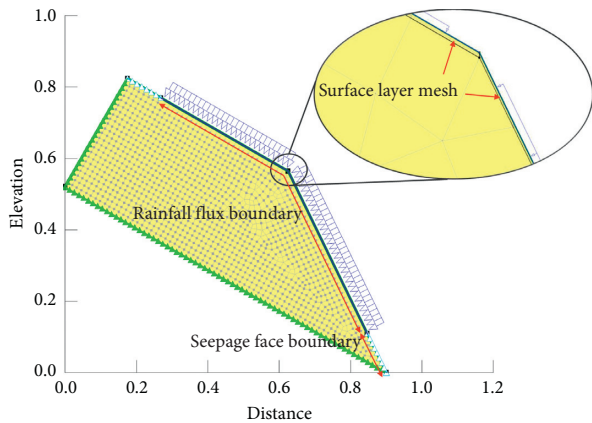


FIGURE 5: Domain and boundary conditions of seepage modeling and zoomed-in view of the surface layer mesh.

elapsed time of 239 min (Figure 6(e)). The characteristic failure mode that was observed in this study is deemed relevant as most precedent studies that conducted similar laboratory experiments on landslide initiation by applying moderate-intensity rainfalls on sandy slopes observed a

common slope failure phenomenon, the so-called retrogressive failure (e.g., Reid et al. [15]; Lourenço et al. [16]; and Wu et al. [22]). That is to say, multiple sequentially occurring slides progressed toward the crest (upslope), and these were accompanied by initial local failures or surface erosions at the toe of the slope.

Figure 7 shows the rainfall seepage process of the model slope that were computed from the numerical modeling. Initially, rainfall infiltrated the ground, advancing the wetting front downward (Figure 7(a)). The subsurface water flow tended to converge downslope and built up a water table from the toe of the slope where the drainage face is located (Figure 7(b)). Subsequently, the created water table progressively extended upslope (Figure 7(c)). However, after rising to a certain elevation, the water table maintained a constant elevation regardless of rainfall infiltration, as shown in Figure 7(d).

In order to verify the numerical modeling results, volumetric water content data as monitored by the four TDR sensors in the experiment were compared with the numerically solved volumetric water content data at the same locations (Figure 8). (1) Volumetric water content responded (by abruptly rising) when the wetting front or water

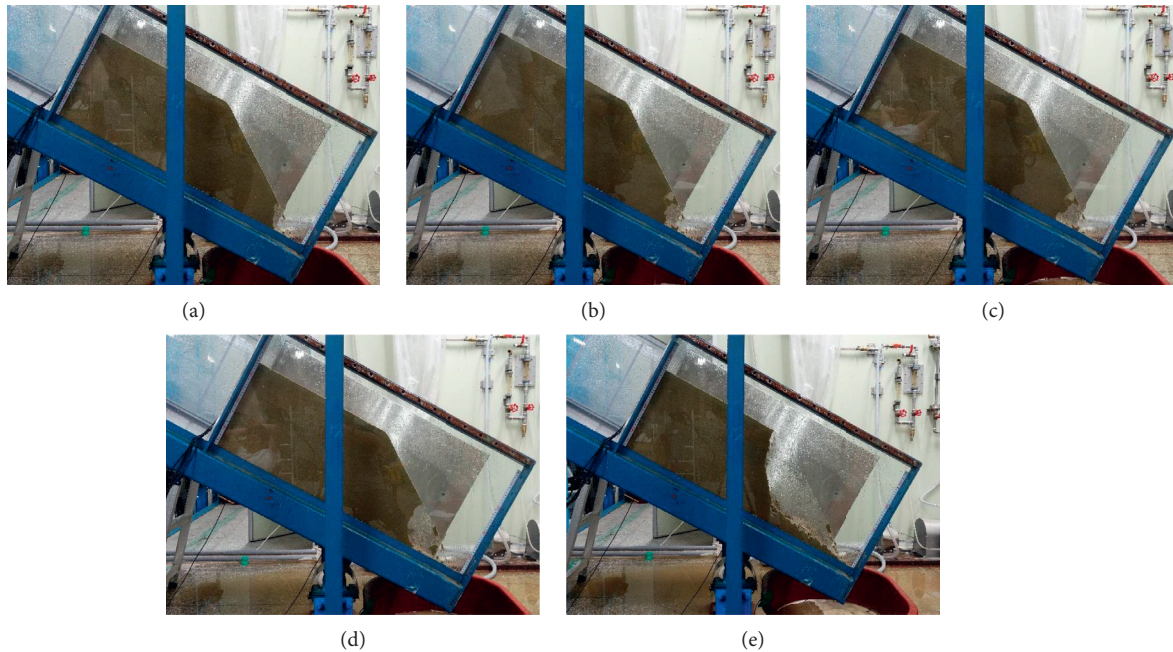


FIGURE 6: Side view of the slope at each moment of failure: (a) 1st failure (after 95 min); (b) 2nd failure (after 103 min); (c) 3rd failure (after 114 min); (d) 4th failure (after 128 min); (e) 5th failure and test completed (after 239 min).

table reached the measurement location. Therefore, the locations of TDR 1 and TDR 2, which are located relatively downslope, responded earlier than the other two locations. Moreover, TDR 1 was the first to respond as it was located closer to the ground surface than TDR 2. With the exception of the location of TDR 4, the response times of the other three locations in the experiment sufficiently coincided with the response times from the modeling results. As for the failure to predict the response of TDR 4, under the assumption that the sensors did not malfunction during the experiment, the water table may not have actually reached the bottom depth of the upslope where TDR 4 was located (refer to Figure 2(a) for the configuration of the TDR sensors). This may be due to the fact that the bottom layer of the soil was compacted to a relatively lower density, meaning that its drainage capacity was actually larger. (2) The measured volumetric water contents from the four sensors did not reach saturated conditions due to an experimental limitation: the soil was not compacted uniformly enough near the sensor locations to prevent the instruments from being damaged. This possibly led to larger voids in the soil and lower saturated water content values. (3) The volumetric water content of Modeling_TDR 3 exhibited a relatively gradual increase in the saturation progress and was overtaken by that of Modeling_TDR 4 from approximately the time of the 4th failure (refer to Figure 8). This is due to the water table progression shape: namely, in the upslope part near the crest, the downward-moving wetting front reached the shallow depth soil (i.e., the TDR 3 location) before the groundwater level reached the bottom depth soil, resulting in the shallow depth soil experiencing a matric suction loss earlier than the bottom depth soil (refer to Figure 7(a)–7(c)). However, after the 4th failure, the bottom depth soil (i.e., the

TDR 4 location) was occupied by the water table and entered into a positive pore pressure state earlier than the shallow depth soil (refer to Figure 7(d)). (4) Despite the aforementioned discordances at the TDR 4 location, it was concluded that the numerical modeling results are effective enough to represent hydraulic behaviors preceding slope failures. This is due to TDR 4 being located relatively far upslope of the failure locations among all sensors. In other words, the hydrologic conditions of the TDR 4 location were less likely to have significantly influenced the hydraulic behaviors at the failure interfaces.

The authors did not directly measure the amount of runoff during the experiment as runoff was not a significant factor governing the slope failure phenomena in this study. As aforementioned in Section 3.2, the artificial rainfall in the experiment was set to a sufficiently mild level to enable full penetration into the ground without producing runoff in the beginning stages. This facilitated the focus on subsurface hydrologic processes leading to failure. Additional experiments with smaller rainfall intensities were not conducted as the overall saturation progress prior to slope failure was expected to be similar with the only difference being in pace. The numerical analysis results that effectively represent the experiment also verify these assertions. Figure 9 shows the numerical analysis results of the changes in comprehensive rainwater flow rate across the boundaries (i.e., slope surface) over time. In Figure 9(a), positive values refer to flows into the system, whereas negative values refer to flows out of the system. Accordingly, it is interpreted that rainfall totally infiltrated the slope and no water was lost in the beginning through either runoff or the seepage face. However, from 52 to 53 min after rainfall initiation, a water table was created, which began to rise. The seepage face boundary nodes

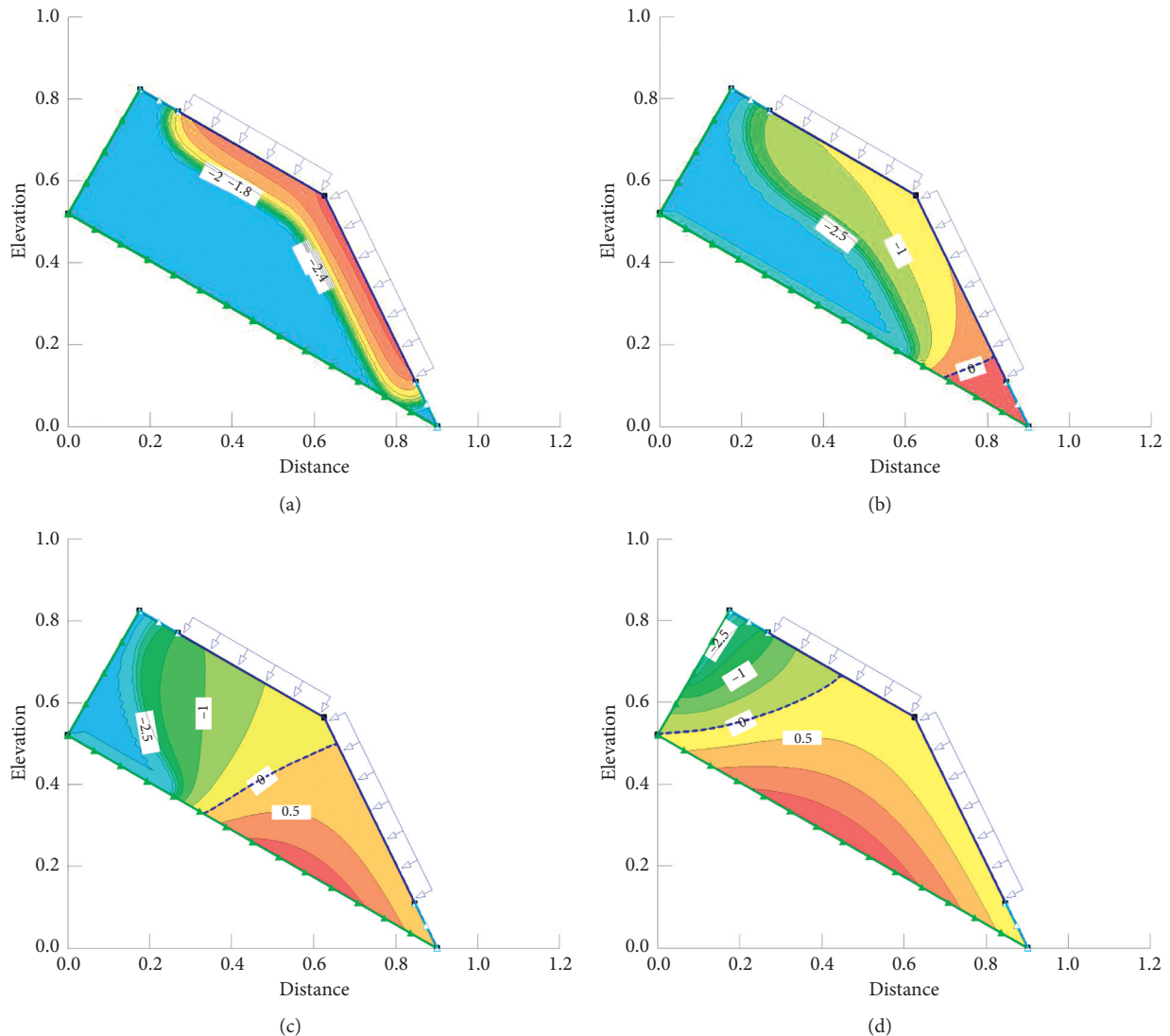


FIGURE 7: Seepage flow modeling results corresponding to elapsed times of (a) 30 min; (b) 60 min; (c) 128 min (at 4th failure); (d) 239 min (at 5th failure).

immediately discharged water as the nodes were overcome by the water table. Sequentially, the rainfall flux boundary nodes started to lose portions of the rainfall influx as runoff as the rising water table reached the nodes (refer to Figure 5 for the two boundary sections and refer to Figures 7 and 10 for the water table locations at various critical times). In the case of certain rainfall flux boundary nodes located at lower elevations, total rainfall influxes were lost as runoff and subsurface water flows were discharged as the water table continued to increase in elevation. Rainfall flux boundary nodes at higher elevations with gentler slopes lost significantly lower amounts of rainfall influx despite being surpassed by the water table. In Figure 9(b), the variation of the total runoff flow across the slope surface was plotted with respect to time. This was possible by subtracting the total amount of water flow that crossed the boundaries from the amount of total rainfall rate across the slope surface at each time step. The total amount of runoff flow gradually increased and approached the total rainfall rate. This indicates

that, as time elapsed to the end, only a small amount of rainfall could infiltrate at a few boundary nodes near the crest of the slope, whereas most of the rainfall overflowed the slope as runoff. Conclusively, it can be speculated that if the same experiment is conducted with smaller rainfall intensities, it will take longer for a water table to be formed and the elevation of the water table will increase at a slower rate. However, the overall pattern of water flux evolutions across the boundaries will be maintained.

4.2. Pore-Water Pressure Conditions Leading to Failure.

The relevance of the numerical modeling results in representing hydrologic processes of the laboratory experiment was validated through a comparative study of volumetric water content responses in Section 4.1. As a result, using the numerically solved data, observations of equivalent hydraulic processes prior to failure are possible at specific locations including slip surfaces. Figure 10(a) describes the

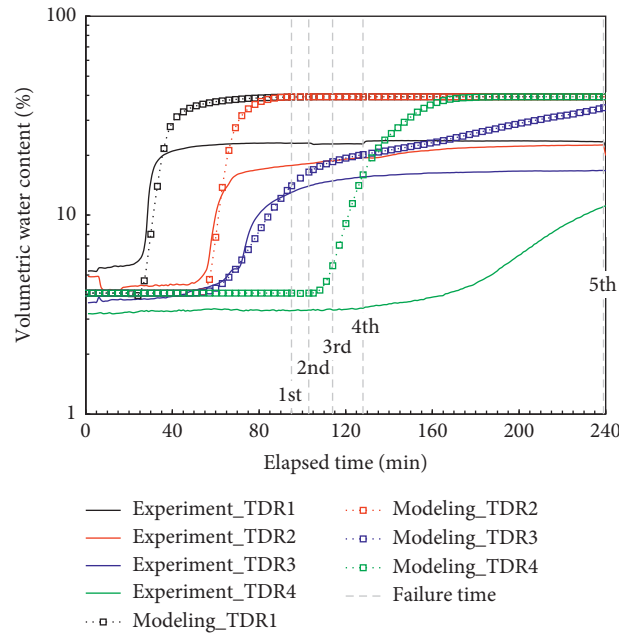


FIGURE 8: Comparison between the experiment and modeling results in terms of volumetric water content changes with respect to elapsed time at the four TDR sensor locations.

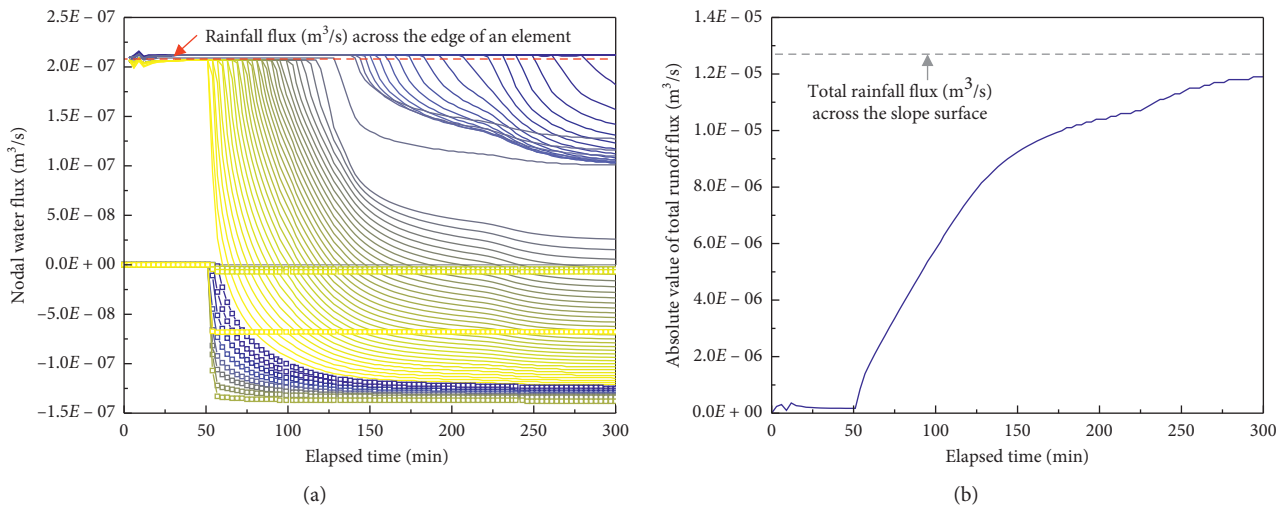


FIGURE 9: Change in comprehensive water flow across boundaries (i.e., slope surface) over time. (a) Individual nodal flow. (b) Total runoff flow. *The group of line plots are from the rainfall flux boundary nodes, whereas the group of “line and symbol” plots are from the seepage face boundary nodes (refer to Figure 5 for the two boundary section). **On a color spectrum from blue to yellow, the darkest blue line indicates a node at the highest elevation, whereas the brightest yellow line indicates a node at the lowest elevation. The color spectrum is applied to the two groups of plots independently.

slip surface shapes and configurations of the five failures that occurred in the experiment. The slip surface of the final 5th slope failure was larger than the slip surfaces of the first four failures. In the numerical modeling domain, the element node locations that correspond to the slip surface locations were selected and flagged as blue dots (from Figures 10(b)–10(f)). Finer discretization will be needed to select nodes of more exact locations that create smoother slip surfaces in future studies. In this study, pore-water pressure time-series data on the five slip surfaces, namely, the blue dots in

Figure 10, were collected and analyzed to determine the behavioral characteristics of pore-water pressure prior to the moment of failure. Figure 11 shows the plot of pore-water pressure evolutions leading to the five consecutive failures at the nodes corresponding to slip surface locations. Among these nodes, the nodes at shallow depths or the ground surface underwent abrupt losses of matric suction earlier than the nodes close to the bottom in the initial stages of the experiment. This was because the nodes at shallower depths were accessed more quickly by the downward-moving

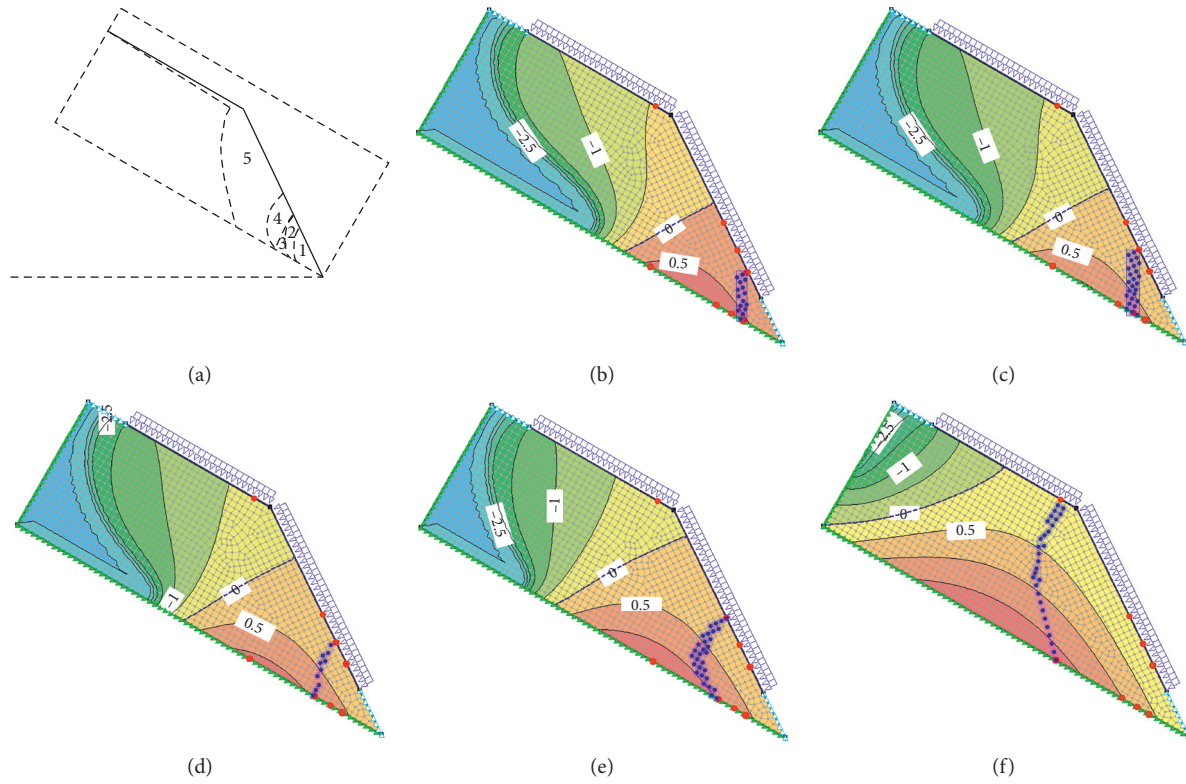


FIGURE 10: Slip surface shapes (a) and measuring points (blue dots) of pore-water pressure that constitute the slip surface of the (b) 1st failure; (c) 2nd failure; (d) 3rd failure; (e) 4th failure; (f) 5th failure.

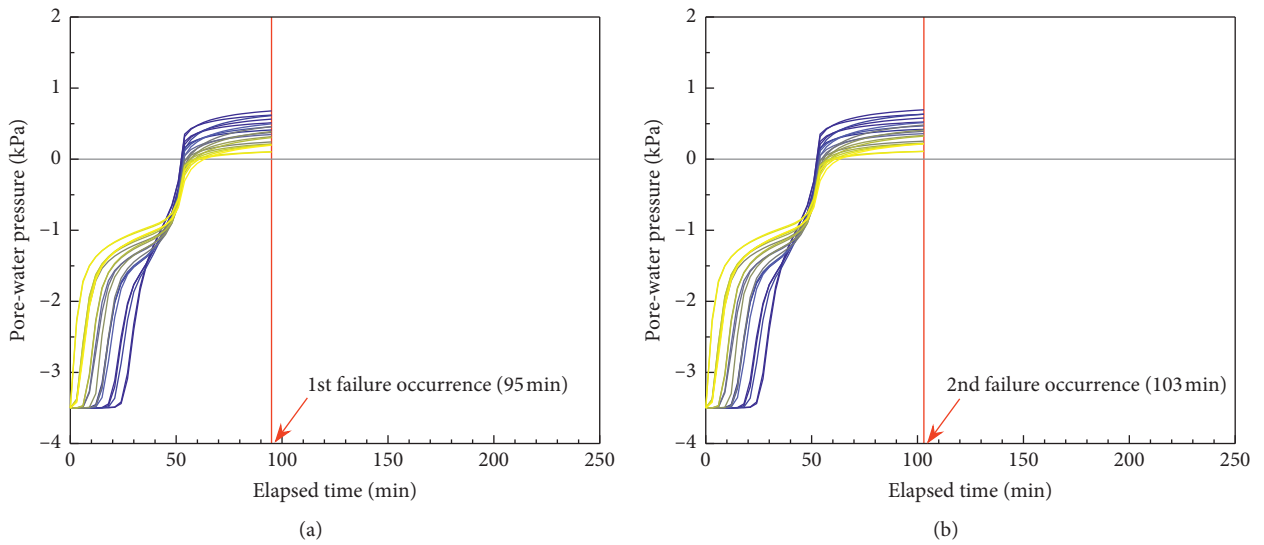


FIGURE 11: Continued.

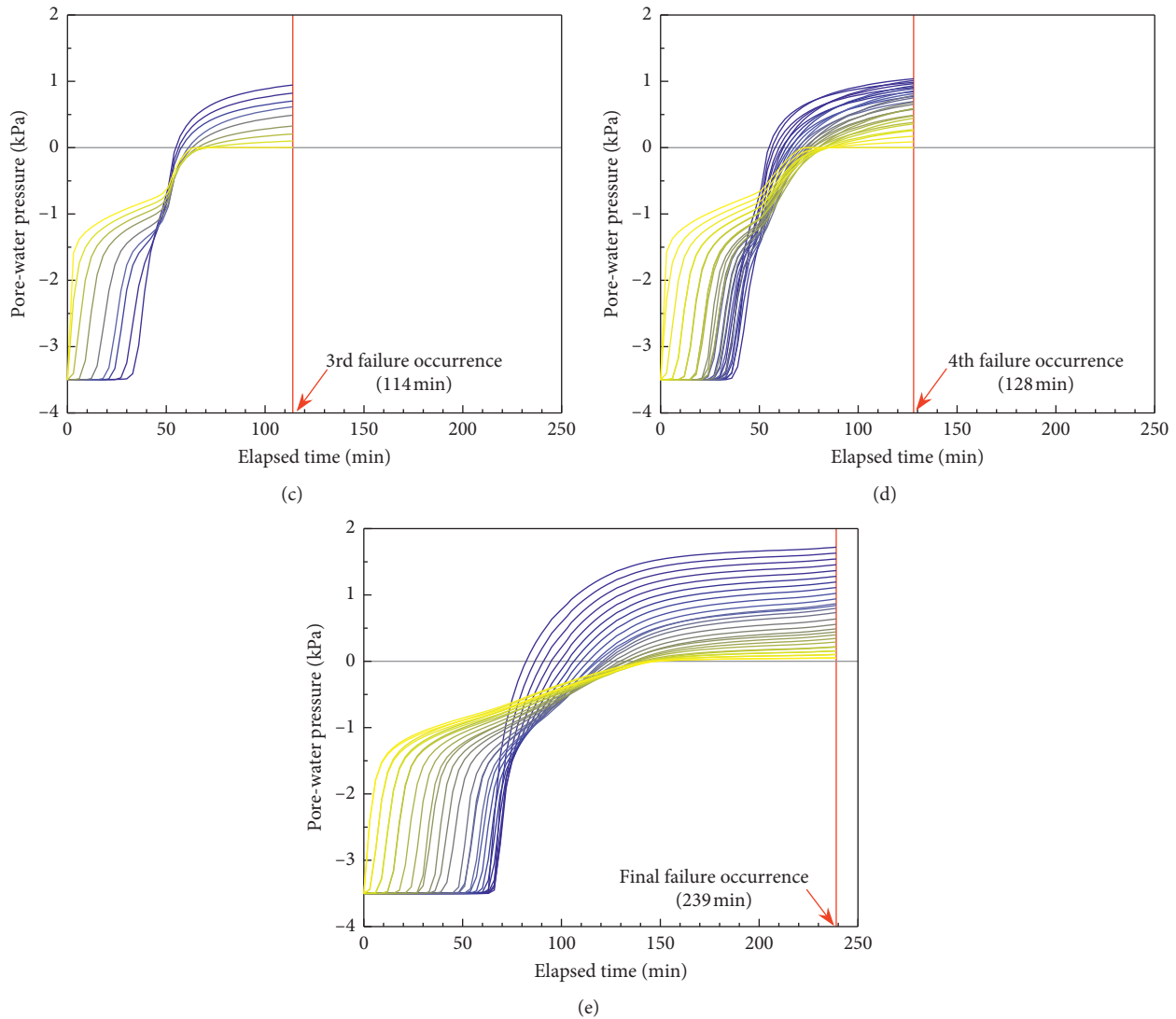


FIGURE 11: Evolutions of pore-water pressure leading to the five consecutive failures at the nodes corresponding to slip surface locations. *On a color spectrum from blue to yellow, the darkest blue line indicates a node at the lowest elevation, whereas the brightest yellow line indicates a node at the highest elevation. (a) At nodes corresponding to the 1st slip surface. (b) At nodes corresponding to the 2nd slip surface. (c) At nodes corresponding to the 3rd slip surface. (d) At nodes corresponding to the 4th slip surface. (e) At nodes corresponding to the 5th slip surface.

wetting front. On the other hand, the nodes at lower elevations generally exhibited greater excessive pore-water pressures as the elapsed time approached the moments of failure. This was because failures occurred below the water table (refer to Figure 10); thereby, the positive pore-water pressures of the nodes corresponding to slip surface locations were proportional to the corresponding vertical distance to the water table. From this analysis of the pore-water pressure conditions leading to the five failures, it was deduced that, in the case of sandy slopes, slope failure may occur when several prerequisites are satisfied: the soil at the expected slip surface is fully saturated and exhibits excessive pore-water pressure due to a water table that has been elevated to the ground surface or above the expected slip surface.

It should be noted that scale effects did not significantly lower the reliability of the results in this study despite being a well-known essential problem of small-scale experiments. This is because scale effects in landslide phenomena mainly involve stress conditions during sliding and consequent flow movement characteristics, not hydrologic or hydraulic processes prior to sliding. For example, dimensional analysis [23] is a powerful method that has been favored by researchers to “scale down” debris flow mixtures for laboratory experiments while maintaining geometric, dynamic, and kinematic similarity (e.g., [24–26]). Iverson et al. [13] also found that changes in pore-water pressure exerted by changes in volume of the soil mass (consolidation or swelling) during sliding depend on the initial porosity and the relative time scales for soil deformation and pore-

pressure diffusion. Therefore, this initial porosity condition has been a pivotal factor in laboratory experiments for simulating debris flow mobilizations. Despite such possible dissimilarities from full-scale natural phenomena in terms of the stress conditions during sliding and postfailure behaviors, the laboratory experiment in this study is deemed validated as the scope of this study focuses on providing insight into comprehensive hydraulic processes “prior to” slope failures.

5. Conclusions

In this study, hydrologic and hydraulic processes of the overall domain area that entailed multisliding landslides were identified through a combined analysis involving a laboratory experiment and numerical modeling. Furthermore, hydraulic prerequisites (or pore-water pressure conditions) for triggering landslides in sandy slopes were understood. Model experiments were carried out on homogeneous soils, and the saturation pattern of the slope due to rainfall infiltration was investigated using measuring devices and numerical modeling techniques. Furthermore, we described the slip surface shapes and configurations to identify the slip surface locations. Based on these locations, the evolutions of numerically solved pore-water pressure data leading to the failures were traced. Additional findings of this study are summarized as follows:

- (1) The model slope was observed to be saturated during rainfall from the surface to the bottom and thereafter from the toe to the crest due to the wetting front's downward progress and the subsequent water table increase, respectively.
- (2) The failure mode of the model slope was a retrogressive failure that started from the toe of the slope and subsequently extended upslope to the top of the slope. The slip surface was formed as a rotational failure type.
- (3) The response times of volumetric water content derived from the numerical modeling sufficiently coincided with the results from the experiment. The numerical modeling results were reasonable to represent the hydraulic processes of the model slope in the experiment.
- (4) The slope failures occurred as several subsurface hydraulic conditions were satisfied: full saturation, excessive pore-water pressure, and the hydrostatic pressure state.

Data Availability

The laboratory test and numerical modeling data used to support the findings of this study are available from the corresponding author upon request.

Conflicts of Interest

The authors declare that they have no conflicts of interest regarding this work.

Acknowledgments

This research was supported by the Basic Research Project (no. 20-3412-1) of the Korea Institute of Geoscience and Mineral Resources (KIGAM) funded by the Ministry of Science and ICT of Korea.

References

- [1] Korea Institute of Geoscience and Mineral Resources (KIGAM), *A Study on the Early Warning Technology of Landslides in Natural Terrain Under Extreme Rainfall through the Stereotactic Monitoring (2012M3A2A1050983)*, National Research Foundation of Korea, Ministry of Science, ICT and Future Planning, Daejeon, Republic of Korea, in Korean, 2017.
- [2] Korean Geotechnical Society (KGS), “Final report of project on investigating the causes and the establishing restoration of landslides in Mt. Woomyeon (KGS11-250),” Korean Geotechnical Society (KGS), Seoul Metropolitan City, Republic of Korea, in Korean, 2011.
- [3] B. G. Chae, Y. S. Song, Y. S. Seo, Y. C. Cho, and W. Y. Kim, “A test for characterization on landslides triggering and flow features of debris using a flume test equipment,” *The Journal of Engineering Geology*, vol. 16, no. 3, pp. 275–282, 2006, in Korean.
- [4] B. G. Chae, S. H. Lee, Y. S. Song, Y. C. Cho, and Y. S. Seo, “Characterization on the relationships among rainfall intensity, slope angle and pore water pressure by a flume test: in case of gneissic weathered soil,” *The Journal of Engineering Geology*, vol. 17, no. 1, pp. 57–64, 2007, in Korean.
- [5] Y. S. Song, B. G. Chae, and Y. S. Seo, “Proposal of method to estimate the runout distance of landslides induced by rainfall,” *Journal of the Korean Society of Civil Engineers*, vol. 27, no. 5C, pp. 343–352, 2007, in Korean.
- [6] K. Lee, H. Han, D. Chang, and D. Yoon, “Seepage behavior by artificial rainfall in weathered granite model slope,” *Journal of the Korean Geoenvironmental Society*, vol. 14, no. 12, pp. 5–12, 2013, in Korean.
- [7] D. Kim, J. Seo, C. Lee, and C. Woo, “Analysis on the behaviors of soil water characteristic sensors through rainfall-induced landslide flume experiments,” *Korean Society of Hazard Mitigation*, vol. 16, no. 6, pp. 209–218, 2016, in Korean.
- [8] W. N. Chien, R. H. Woo, and K. J. Kuo, “Failure mechanism of granular soil slopes under high intensity rainfalls,” *Journal of Geo Engineering*, vol. 7, no. 1, pp. 21–31, 2012.
- [9] Q. Ran, D. Su, P. Li, and Z. He, “Experimental study of the impact of rainfall characteristics on runoff generation and soil erosion,” *Journal of Hydrology*, vol. 424–425, pp. 99–111, 2012.
- [10] G. Acharya, T. A. Cochrane, T. Davies, and E. Bowman, “The influence of shallow landslides on sediment supply: a flume-based investigation using sandy soil,” *Engineering Geology*, vol. 109, no. 3–4, pp. 161–169, 2009.
- [11] C. Gallage, S. Jayakody, and T. Uchimura, “Effect of slope inclination on the rain-induced instability of embankment slopes,” in *Proceedings of the 2nd International Conference on Geotechnique, Construction Materials and Environment*, pp. 196–201, Kuala Lumpur, Malaysia, 2012.
- [12] S. D. N. Lourenço, G.-H. Wang, and T. Kamai, “Processes in model slopes made of mixtures of wettable and water repellent sand: implications for the initiation of debris flows in dry slopes,” *Engineering Geology*, vol. 196, pp. 47–58, 2015.

- [13] R. M. Iverson, M. E. Reid, N. R. Iverson et al., "Acute sensitivity of landslide rates to initial soil porosity," *Science*, vol. 290, no. 5491, pp. 513–516, 2000.
- [14] H. Moriwaki, T. Inokuchi, T. Hattanji, K. Sassa, H. Ochiai, and G. Wang, "Failure processes in a full-scale landslide experiment using a rainfall simulator," *Landslides*, vol. 1, no. 4, pp. 277–288, 2004.
- [15] M. E. Reid, R. G. LaHusen, and R. M. Iverson, "Debris-flow initiation experiments using diverse hydrologic triggers," in *Proceedings of the 1st International Conference on Debris-Flow Hazards Mitigation: Mechanics, Prediction and Assessment*, C. L. Chen, Ed, American Society of Civil Engineers, San Francisco, CA, USA, pp. 1–11, 1997.
- [16] S. D. Lourenço, K. Sassa, and H. Fukuoka, "Failure process and hydrologic response of a two layer physical model: implications for rainfall-induced landslides," *Geomorphology*, vol. 73, no. 1-2, pp. 115–130, 2006.
- [17] Y.-S. Song and W.-K. Hwang, "Numerical study of unsaturated infinite slope stability regarding suction stress under rainfall-induced infiltration conditions," *The Journal of Engineering Geology*, vol. 24, no. 1, pp. 1–8, 2014.
- [18] Y. S. Song, N. W. Lee, W. K. Hwang, and T. H. Kim, "Construction and application of an automated apparatus for calculating the soil-water characteristic curve," *Journal of Engineering Geology*, vol. 20, no. 3, pp. 281–295, 2010, in Korean.
- [19] M. T. van Genuchten, "A closed-form equation for predicting the hydraulic conductivity of unsaturated soils," *Soil Science Society of America Journal*, vol. 44, no. 5, pp. 892–898, 1980.
- [20] Y. Mualem, "A new model for predicting the hydraulic conductivity of unsaturated porous media," *Water Resources Research*, vol. 12, no. 3, pp. 513–522, 1976.
- [21] S. K. Kim, W. P. Hong, and Y. M. Kim, "Prediction of rainfall-triggered landslides in Korea," in *Proceedings of the International Symposium on Landslides*, pp. 989–994, Rotterdam, Netherlands, February 1992.
- [22] L. Z. Wu, Y. Zhou, P. Sun, J. S. Shi, G. G. Liu, and L. Y. Bai, "Laboratory characterization of rainfall-induced loess slope failure," *Catena*, vol. 150, pp. 1–8, 2017.
- [23] R. M. Iverson, "The physics of debris flows," *Reviews of Geophysics*, vol. 35, no. 3, pp. 245–296, 1997.
- [24] R. M. Iverson, "Scaling and design of landslide and debris-flow experiments," *Geomorphology*, vol. 244, pp. 9–20, 2015.
- [25] G. G. D. Zhou and C. W. W. Ng, "Dimensional analysis of natural debris flows," *Canadian Geotechnical Journal*, vol. 47, no. 7, pp. 719–729, 2010.
- [26] C. W. W. Ng, C. E. Choi, J. S. H. Kwan, R. C. H. Koo, H. Y. K. Shiu, and K. K. S. Ho, "Effects of baffle transverse blockage on landslide debris impedance," *Procedia Earth and Planetary Science*, vol. 9, pp. 3–13, 2014.

Research Article

The Propagation of Landslide-Generated Impulse Waves and Their Impacts on the Moored Ships: An Experimental Investigation

Ping Mu,^{1,2} Pingyi Wang ,^{1,2} Linfeng Han,³ Meili Wang,⁴ Caixia Meng,^{1,2} Zhiyou Cheng,^{2,5} and Haiyong Xu⁶

¹School of River and Ocean Engineering, Chongqing Jiaotong University, Chongqing 400074, China

²Key Laboratory of Hydraulic and Waterway Engineering of Ministry of Education, Chongqing Jiaotong University, Chongqing 400074, China

³School of Civil Engineering, Chongqing Jiaotong University, Chongqing 400074, China

⁴School of Architecture and Urban Planning, Chongqing Jiaotong University, Chongqing 400074, China

⁵School of Shipping and Naval Architecture, Chongqing Jiaotong University, Chongqing 400074, China

⁶Key Laboratory of Engineering Sediment, Tianjin Research Institute for Water Transport Engineering of Ministry of Transport, Tianjin 300456, China

Correspondence should be addressed to Pingyi Wang; py-wang@163.com

Received 14 July 2019; Revised 31 January 2020; Accepted 15 February 2020; Published 12 May 2020

Academic Editor: Zhongguo John Ma

Copyright © 2020 Ping Mu et al. This is an open access article distributed under the Creative Commons Attribution License, which permits unrestricted use, distribution, and reproduction in any medium, provided the original work is properly cited.

The effective prevention and reduction of the hazardous impact of landslide-generated impulse waves on the moored ships are crucial for the sustainable operation of the reservoirs. Although the investigations of landslide-generated impulse waves have been widely studied in the past decades, few efforts involved their impacts on the moored ships. The authors in this paper specifically examine the hazardous impact of the impulse waves on the moored ships by applying the physical experiments. Considering that the impulse wave was an external force acting on the mooring line, the impulse wave generation, propagation, and its impact on the moored ships are hence explored in detail. The results indicate that the impact of impulse waves on the moored ships was mainly due to the first wave amplitude and height, and an exponential function relationship between the relative wave height and wave crest amplitude was revealed. Furthermore, the attenuation of the maximum wave crest amplitude was approximated by a power exponential function. On this basis, the mooring tension could be calculated based on the linear relationship between the mooring tension and wave height. Ultimately, the safety of the moored ships in the port can be evaluated.

1. Introduction

As a worldwide secondary natural hazard, the impulse waves erupting in reservoirs have caused a range of catastrophic disasters and resulted in large economic losses. In general, impulse waves are generated by landslides and also referred to as landslide tsunamis [1, 2]. With great energy, the hazard of landslide-generated impulse waves can cause vast losses of life and properties, the destruction of critical infrastructure in wharf, and massive damage even overturns to the vessels. If such tremendous waves overtop the dam, the consequences are fatal for the downstream areas. In this regard, we take the

well-known Vajont landslide occurring in Italy in 1963 as a typical case, which killed almost 2000 persons and completely destroyed the downstream city of Longarone [3]. In this situation, to gain the desired sustainable operation of the reservoir, it is a common strategy for any country to pursue effective prevention and reduction of this natural hazard.

Hence, to solve the problem, the landslide-generated impulse waves occurring in reservoirs have attracted a wide range of international researchers in recent decades [4–7]. However, looking carefully at these existing studies, more attention has been paid to the characteristics of the hazard and the disaster losses, especially in the number of casualties

and economic losses based on the postdisaster investigation [4, 8, 9], while the moored ships in the port have received little attention. Thus, a research gap remains in the extant literature; namely, the moored ships against impulse waves have been ignored.

Against this unique background, as the largest hydroelectricity project in the world, the Three Gorges Reservoir (TGR) constructed on Yangtze River in China has been plagued with the serious natural hazard of landslide-generated impulse waves since its completion and delivery in 2003 [10]. Meanwhile, the water traffic is extremely heavy. For instance, the survey organized by the Yangtze River waterway administration indicated that about 138 million tons of cargo was transported through the reservoir in 2017 [11]. In other words, at any time, a large number of ships are moored in wharf. More importantly, in recent years some related catastrophic events have occurred [4]. Given these situations and the reported research gap, taking TGR as a typical case, undertaking the research of the hazardous impact of impulse waves on the moored ships is not only important but also necessary.

On the abovementioned basis, this study aims to examine the hazardous impact of impulse waves on the moored ships in TGR. We consider that the impact is largely constrained by the mooring tension of the line at the quay, whilst the damage of impulse waves is mainly due to wave height, especially the first waves [12, 13]. Additionally, the induced impulse waves will gradually attenuate over propagation distance [7, 12, 14]. Therefore, the detailed objectives of this paper are as follows: (1) to mimic impulse wave generation and explore its propagation and (2) to reveal the relationship between the mooring tension and impulse wave height; to the best of our knowledge, very few studies explored the hazardous impact of impulse waves in reservoirs on the moored ships in China and elsewhere. Hence, we innovate in the field of impulse waves and its disaster prevention by considering the moored ships in TGR.

The remainder of this paper is structured as follows. We describe the research methodology in the next section. Section 3 presents the results and discussion. Conclusions are drawn in the final section.

2. Methodology

2.1. Research Design. As emphasized by Huang et al. [15], due to the unique characteristics (e.g., short duration and sudden occurrence), the induced impulse waves are little on field measurements. To solve data constraints, in line with previous studies [7, 16–22], we select physical model to simulate and induce impulse waves and obtain the complicated data. On this basis, we analyze these data to fulfill the above research objectives. Thus, the following two-stage research design is planned, just exhibited in Figure 1.

2.2. Experimental Set-Up

2.2.1. The Three-Dimensional Basin. As mentioned in Section 2.1, the experimental study is selected to conduct this work. In this background, a physical model was built at 1 : 70

scale (for details also see Section 2.5), which was typically curved reach in the upper Yangtze River and generalized from the prototype of Jiangnan tuokou wharf reach. Figure 2 shows the schematic layout of the three-dimensional (3D) basin.

The total length of the basin was 48 m; the upstream and downstream straight were 28 m and 13 m, respectively. The radius of curvature for the intermediate portion was 7 m. The basin sides were covered with a concrete paste so as to enhance the roughness and make the model more realistic. The cross-section of the basin was trapezoidal, as shown in Figure 3, the top width was 8 m, and the bottom was 2.94 m. The slopes in the concave and convex banks were 33° and 20°, respectively.

2.2.2. The Wave-Making System. The waves were generated by a gravity type wave maker at the concave bank of the basin (see Figure 2). The wave-making system consisted of landslide, chute, wire mesh gate and chain hoist, and so on, as described in Figure 4. This chute allowed for predefining the slide geometry, including a slide width of 0.50 m, 1.00 m, and 1.50 m, and a landslide front edge allowing it to reach different still water depths, as well as a landslide impact angle with any value. A flexible wire mesh gate was placed in the front of the sliding chute to restrain the concrete blocks before the trials. When everything was ready, for instance, the water was still and the measuring equipment had been already debugged, the motion of landslide was triggered and accelerated due to gravity into the water body after suddenly manual release for the wire mesh gate. Clearly, the landslide is of great importance for the wave-making system; a special introduction hence will be presented in the following section.

2.2.3. The Landslide. Considering the similarity and deformability reported by Yavari-Ramshe, and Ataie-Ash-tiani. [23], the landslide was modeled by the granular concrete blocks containing five various geometric sizes (labelled as A1, A2, A3, A4, and A5) as illustrated in Table 1. Compared with other granular materials (e.g., PP-BaSO₄) in [24], the landslide materials of present experiments were more similar to the happening or potential landslides in TGR.

Tested landslide models with nine different sizes, including a constant landslide length of 1.00 m, a landslide width of 0.50 m, 1.00 m, and 1.50 m, and a landslide thickness of 0.20 m, 0.40 m, and 0.60 m, were carried out by adjusting the sliding cute geometrical shape (see Figure 4). As reported by Wiegel [19], the landslide length with a constant $l=1.00$ m was deemed to be appropriate based on the result that the landslide length has a slight influence on the primary wave. The landslide was composed of concrete blocks with an equal number of A1, A2, A3, A4, and A5. Based on the permutation and combination of concrete blocks, landslides were classified into nine classes encompassing S1, S2, S3, S4, S5, S6, S7, S8, and S9 to simulate and induce the impulse waves in our experiments; the detailed sizes and volumes of the landslides are shown in Table 2.

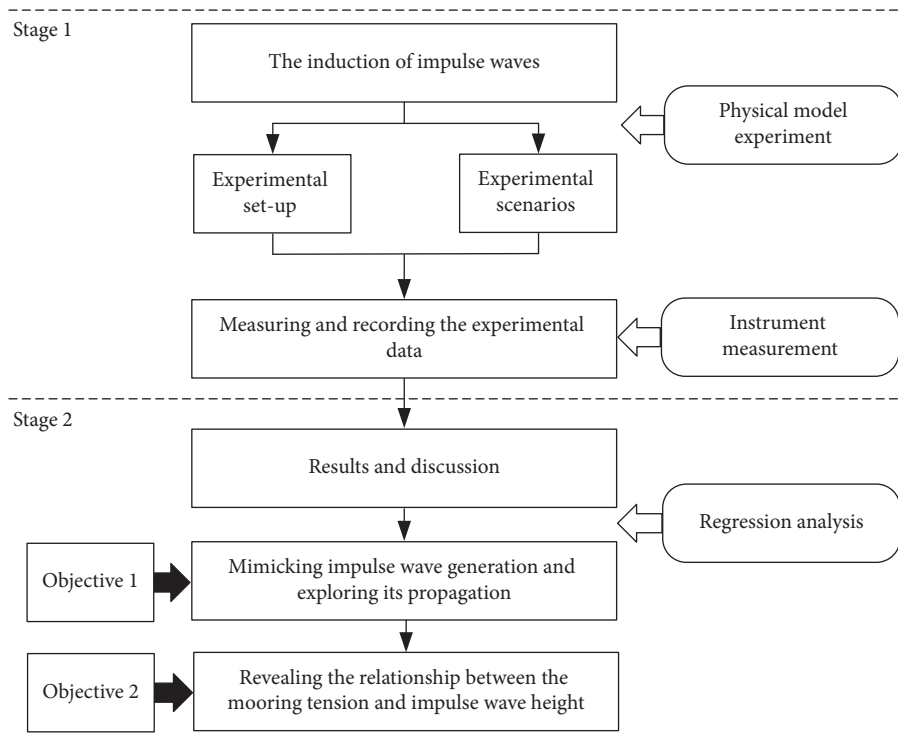


FIGURE 1: The research design of this paper.

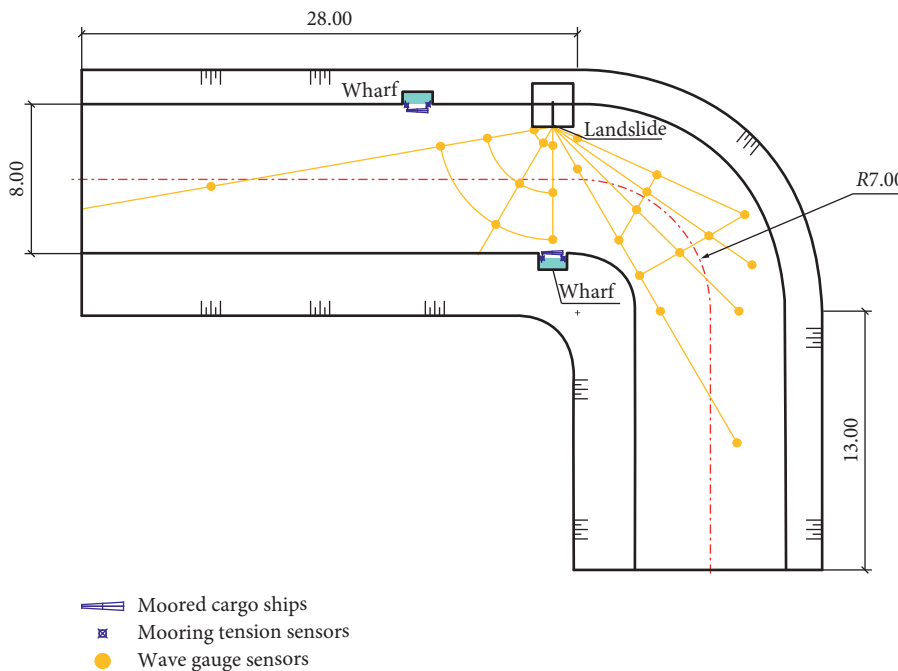


FIGURE 2: Schematic diagram of model experimental layout; geometrical measurements were in m.

2.2.4. *The Wharf and Cargo Ship.* The type of wharf used in the present study is “high-pile,” which is one of the most popular geometrical wharf designs in TGR as well [12]. Its structure is assumed as “rigid,” fixed in the basin. There was only one berth with two mooring bollards in the experimental model, and the length and width of the wharf were

1.50 m and 0.43 m, respectively. Cylinder piers with the diameter of 2.28 cm, line spacing 10.00 cm, were made by plastic pipes. In addition, the dock panel, beams, and stringers were all plastic, as illustrated in Figure 5. Given that the impulse waves propagated along with all directions, so two wharves were set: one was located the same shore of the

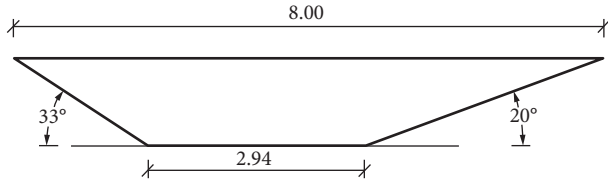


FIGURE 3: Cross-section of the basin; geometrical measurements were in m.

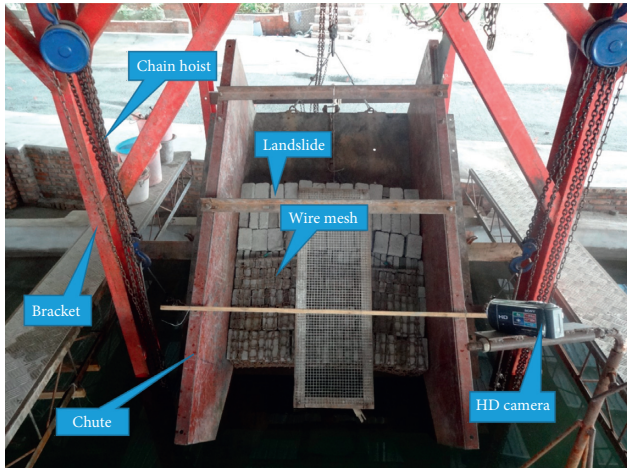


FIGURE 4: The wave-making system.

TABLE 1: Sizes of concrete blocks.

Block number	Length (cm)	Width (cm)	Thickness (cm)
A1	18	12	6
A2	12	8	4
A3	9	6	3
A4	6	4	2
A5	3	2	1

TABLE 2: Sizes and volume of landslides.

Landslide number	Length (m)	Width (m)	Thickness (m)	Volume (m ³)
S1	1.0	0.5	0.2	0.1
S2	1.0	1.0	0.2	0.2
S3	1.0	1.5	0.2	0.3
S4	1.0	0.5	0.4	0.2
S5	1.0	1.0	0.4	0.4
S6	1.0	1.5	0.4	0.6
S7	1.0	0.5	0.6	0.3
S8	1.0	1.0	0.6	0.6
S9	1.0	1.5	0.6	0.9

landslide (in concave bank) and the other one was placed on the opposite (in convex bank), both 6.37 m far from the location of the landslide occurrence.

As stated by Chen [25], approximately 88.98% of the ships operating in TGR are cargo ships, whilst about 90.79% of these ships are under 3000 DWT. Given this condition, the iron model ships (see Figure 5) were designed based on a

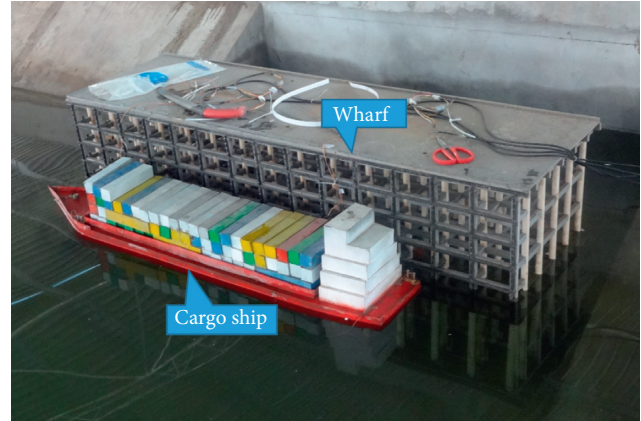


FIGURE 5: The experimental wharf and moored cargo ship in full-cargo condition.

prototype of 3000 DWT cargo ship. Primary parameters of the real and model ship are shown in Table 3. There were some conditions of the moored ships: light ship, half cargo, and full-cargo condition. Moreover, the most hazardous scene was that cargo ship is in full-cargo condition; hence, we only focused on the worst-case scenario.

The ships were moored on the port side by nylon ropes in the stern and head line, which were at an angle of 30° with the wharf front (see Figure 6). For the cargo ship in convex bank, the incident angle of the impulse waves was about 90°, because the impulse waves propagated towards the wharf. For the cargo ship in concave bank, the incident impulse waves angle was parallel to the quay because the waves flowed along it.

2.3. Experimental Scenarios. The experimental tests were carried out for 81 different scenarios of landslide-generated impulse waves by varying the parameters of the thickness (s), width (w), angle of landslide (α), and the still water depth in the basin (h). Landslide volume and angle may be changed by adding and removing concrete blocks and by varying the initial location of the chute, respectively. In line with the dispatching practice of reservoir flood in TGR, 145.00 m, 155.00 m, and 175.00 m were selected as the simulated water levels [15]. Based on our field surveys of the cross-section and the bottom elevation of the prototype, the water depths in the physical model corresponding with these three usual water levels can be calculated according to geometric similarity to be 0.74 m, 0.88 m, and 1.16 m (for details, see also Section 2.5). In addition, field investigation also reported that the distribution of landslide angle in TGR was from 20° to 60° and the average value was 36°. Hence, in the experiment, the angles were limited to 20°, 40°, and 60°.

2.4. Methods of Measuring and Recording Data. An HD camera (see Figure 4) was placed on a tripod to record the characteristic of the sliding process in a video format. Using MATLAB software, a series of images can be extracted from the video to calculate the landslide impact velocity.

TABLE 3: Primary parameters of the real and model ship.

Parameter	Real ship	Model ship
Length (m)	90	1.28
Depth (m)	4	0.057
Width (m)	16	0.228
Designed draft (m)	3.3	0.047
Block coefficient	0.8	0.8
Loaded displacement (t/g)	3000 t	8700 g

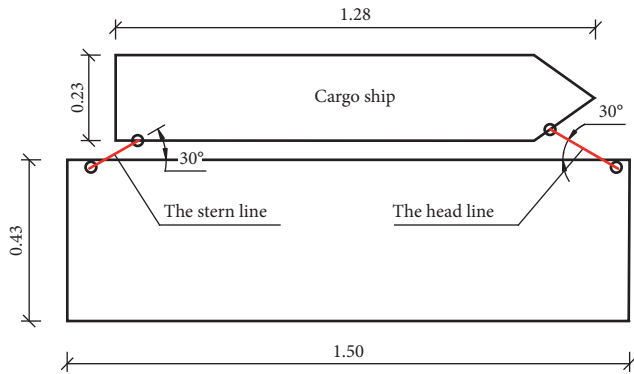


FIGURE 6: Mooring condition of cargo ship.

As exhibited in Figure 2, twenty-four wave gauges were placed in the basin for measuring the water surface displacement. Each sensor was partially submerged and corresponds to a channel with an identification number from 1 to 24 which returned voltage values. They could be converted to water level values at the designated spots by UBL-2 Ultrasonic Water Level/Wave Acquisition Analyzer (UWL/WLAA) developed by Southwest Water Transport Engineering Research Institute in China. The UWL/WLAA has been widely used in similar experimental measurements on account of high reliability and accuracy [14, 26].

Tension sensors (model number: BE120-2AA) were used for measuring the mooring tension of the lines restricting the moored cargo ship. There were two lines attached to the head and stern of the ship, with enough strength to contend against the impact force of waves at the wharf (see Figure 6). As a result, four elastic flaky sensors with an identification number from 1 to 4 which returned voltage values were used, as shown in Figure 2. These voltage values could be converted to the mooring tension through Dynamic Signal Test Analysis System (DSTAS). The signal acquisition frequency was 500 Hertz. Before the experiment, extensive efforts of calibration had been done. We acquired the mass-voltage curve by adding load from 0 g to 1200 g on the step of 100 g. The same calibration procedure had been repeated many times until satisfactory results could be obtained. For example, we had verified 3 times the elastic strain of Ch.1; the corresponding mass-voltage curves were depicted (see Figure 7), and the average value was finally adopted. Based on the mass-voltage curve of the materials and the relationship between mass and weight, the ultimate mooring tension-voltage value curve could be derived.

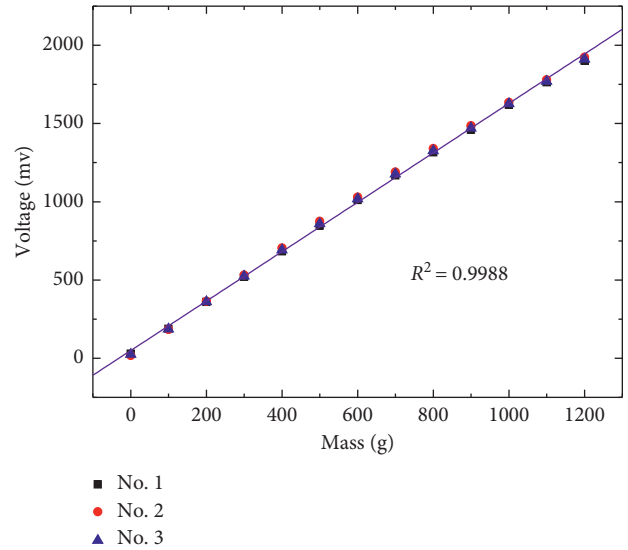


FIGURE 7: The force-voltage curve of elastic strain in Ch.1.

2.5. Scale Analysis. Additionally, a good physical model that can represent its real world prototype should satisfy geometric similarity, kinematic similarity, and dynamic similarity [27]. According to the Froude similitude, the similitude ratios of all parameters in present study are shown in Table 4.

There was a geometric similarity between the experimental and real world scenarios in the present tests, and geometric scale $\lambda_l = 70$. In the experiments, the landslide length, width, and thickness were 1.0 m, 0.5 m~1.5 m, and 0.2 m~0.6 m, respectively, representing the landslides with the length of 70 m, width of 35 m~105 m, and thickness of 14 m~42 m; the corresponding volume was 490~4410 m³ in the real world. For water levels 145 m, 155 m, and 175 m in the Jiangnan tuokou wharf reach, water depths were 51.8 m, 61.6 m, and 81.2 m, respectively. In the tests, the water depths were 0.74 m, 0.88 m, and 1.16 m with the scale factor $\lambda_l = 70$. For the slide impact velocity, the scale factor $\lambda_v = \lambda_l^{1/2} = \sqrt{70}$ based on the kinematic similarity criterion, and the landslide impact velocity ranged from 0.55 m/s to 2.68 m/s in the experiments, corresponding to the velocity 4.6 m/s~22.38 m/s in the real world. There was a high match between tests and real scenarios in TGR. Furthermore, the slide Froude number as a crucial dimensionless parameter that ranged from 0.178 to 0.993 based on $F_r = v_s/\sqrt{gh}$, where v_s was the landslide impact velocity and h was the still water depth.

The dynamic similarity of the physical model was based on the Froude similitude. To exclude the scale effect, the Weber number We and Reynolds number Re were used to estimate the influence of surface tension and the fluid viscosity effects, respectively [24]. In our experiments, Re and We were equal or greater than 300,000 and 5000, respectively; therefore the scale effects were negligible [28]. So the Froude similitude was suitable for the landslide-generated impulse wave phenomena, and the force scale $\lambda_F = \lambda_l^3 = 70^3$. Hence, the mooring tension in the real world $F_P = \lambda_F F_M$, where the F_M is the mooring tension in the experiment.

TABLE 4: Similitude ratios according to the Froude similitude.

Parameter	Fundamental dimension	Similitude ratio
Length	(L)	λ_l
Time	(T)	$\lambda_l^{1/2}$
Velocity	(LT ⁻¹)	$\lambda_l^{1/2}$
Force	(MLT ⁻²)	λ_l^3

3. Results and Discussion

3.1. Impulse Wave Generation and Propagation. By using the high speed camera, we clearly observed the entire process of the wave generation and propagation in the near field, as shown in Figure 8.

The figure shows that the first wave crest was generated and propagated away from the near field, whilst the first wave trough formed at the impact zone. Closely followed by the second wave crest and trough, after that, the water surface fell once and rose again, and the trailing wave train followed. In addition, observations also indicate that the first wave amplitude and height were the most significant and effective conditioning factors for the hazardous impact of impulse waves induced by landslides. In this regard, such finding is considered to be consistent with previous studies [14, 26]. Therefore, the first wave amplitude, height, and attenuation will be analyzed and discussed in the following sections.

3.1.1. Maximum Wave Amplitude. By analyzing the data recorded by 24 wave gauges of all the 81 experimental scenarios, it is not hard to find a common phenomenon that the impulse waves induced by landslide were nonlinear wave, and the wave crest amplitude was larger than the wave trough amplitude. Moreover, the first wave crest amplitude was the largest one, which is considered to be consistent with previous studies [29, 30]. Take Scenario 47 as an example, the water surface displacement recorded by six random wave gauges is plotted in Figure 9.

Apart from the aforementioned descriptive results, an expression for the maximum wave crest amplitude would be further explored. As emerged from previous empirical equation derived by Fritz et al. [29], the landslide velocity, landslide thickness, and still water depth were important factors governing the maximum crest amplitude. Nevertheless, their tests were conducted in a two-dimensional flume; the effect of landslide width was neglected. In this study, landslide width was an important factor governing the momentum transfer process. Hence, a modified empirical equation of the maximum crest amplitude was obtained based on our test data, as presented in

$$\frac{a_{cm}}{h} = 4.65F_r^{1.18}S^{0.77}B^{0.15}, \quad (1)$$

where a_{cm} is the maximum crest amplitude in the impulse wave generation zone; S and B are the relative landslide thickness and width, respectively; and h is the still water depth.

Unfortunately, the factor of landslide angle was not considered in the revealed expression, because the influence

of landslide angle on the first wave amplitude was controversial. For example, Huber and Hager [31] thought that the maximum wave crest amplitude increased with the impact angle increase, but Panizzo et al. [2] presented a contrary view that the wave crest amplitude decreased with the increase of landslide angle. In this study, the landslide with an angle 40° induced the highest wave crest amplitude when all other things were equal. It was coincident with the finding by Tang et al. [32], who reported that when the slide angle was in the lower band, the primary wave crest amplitude increased with the increase of the impact. However, as the landslide angle exceeded a threshold value, the wave crest amplitude decreased with the increase of the slide angle. In their work, the threshold value was about 37.5°. In general, the landslide angle had little effect on the maximum crest amplitude in our experiment, so it would be neglected.

3.1.2. Maximum Wave Height. In this section, wave height will be explored. For regular linear waves, the wave trough amplitude is strictly equal to the wave crest amplitude; namely, the wave height is twice the crest amplitude. However, for the impulse wave in present tests, the maximum trough amplitude always was less than or equal to the maximum crest amplitude. This is consistent with previous observations by Fritz et al. [29], who reported that the maximum crest amplitudes always matched or exceeded the maximum trough amplitudes. The same phenomenon has also been presented in the study of Xue et al. [33], who suggested that when $0.07 < a_{cm}/h < 1.05$, the expression for the relative maximum wave height could be addressed as

$$\frac{H_m}{h} = 1.07\left(\frac{a_{cm}}{h}\right)^{0.81}. \quad (2)$$

Herein, H_m is the maximum wave height in the impulse wave generation zone.

We further examined the applicability of existing empirical equation developed by Xue with our experimental data and found that the calculated value was less than the experimental value (see Figure 10). This phenomenon may be mainly attributed to the physical model; the tests conducted by Xue were in two-dimensional flume and the side wall restrained the impulse wave propagation. However, in this three-dimensional basin, the wall side had little effect on the propagation of the impulse waves. Given that situation, (2) was deemed to be basically applicable for this work. On this basis, referring to Xue the relative maximum wave height as a function of the relative maximum wave crest amplitude could be derived based our experimental data, as shown in

$$\frac{H_m}{h} = 1.39\left(\frac{a_{cm}}{h}\right)^{0.77}. \quad (3)$$

3.1.3. Maximum Wave Crest Amplitude Attenuation. Subsequently, the attenuation of maximum wave amplitude and wave height will be revealed. Considering that wave height and wave crest amplitude have been linked through

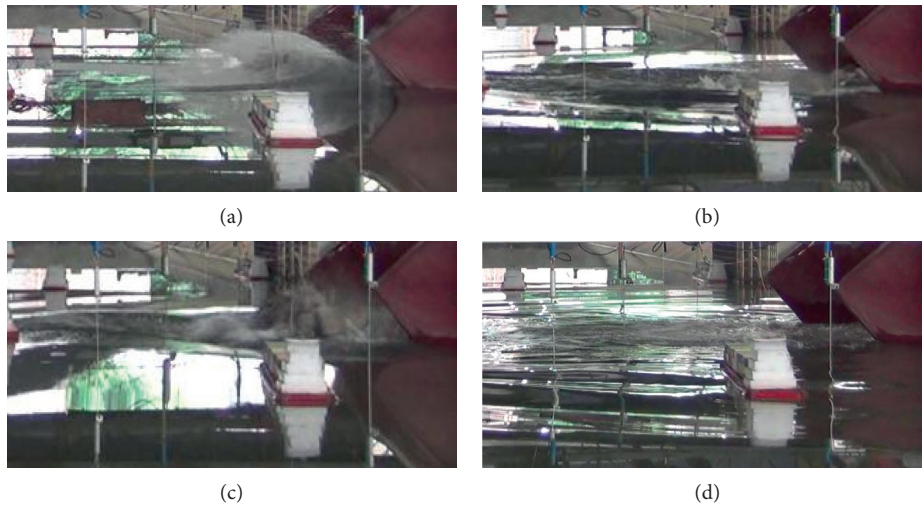


FIGURE 8: The process of impulse waves formation. (a) The first wave crest. (b) The first wave trough. (c) The following wave crest and trough. (d) Trailing wave train.

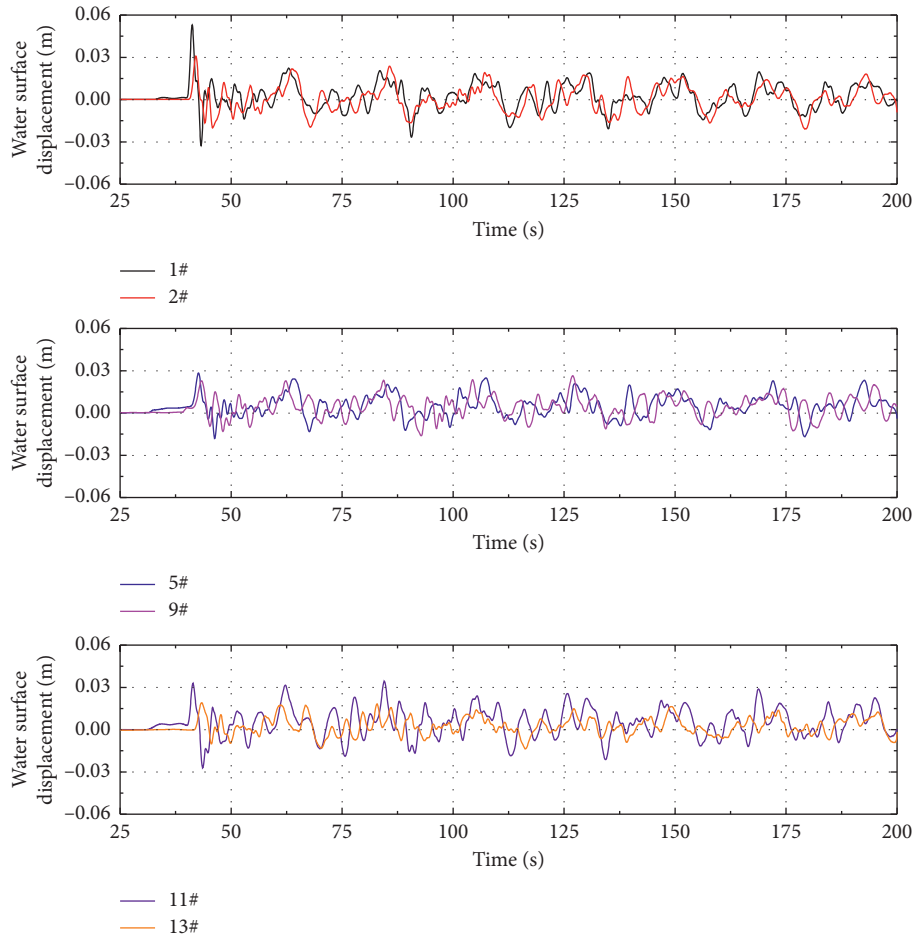


FIGURE 9: The water surface displacement from Scenario 47 with $l = 1.0$ m, $w = 0.5$ m, $s = 0.4$ m, $h = 0.88$ m, and $\alpha = 60^\circ$.

(3), only the maximum wave crest amplitude was analyzed in this section.

In line with the findings of Evers and Hager [34], our results report that the wave amplitude and energy of the

induced waves were maximal in near field and decayed gradually when they spread around. Moreover, it is found that the initial impulse waves attenuated sharply in the near-field region and then gradually propagated to the far-field

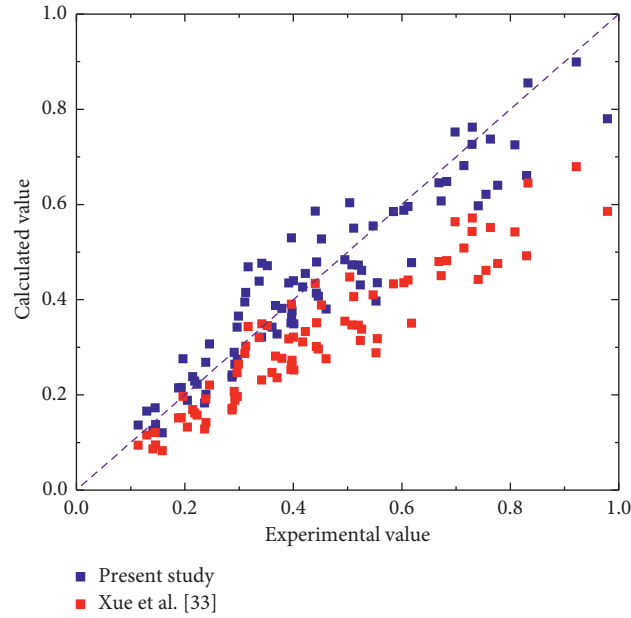


FIGURE 10: Experimental and calculated values of the impulse wave height.

region and attenuated slowly. However, experimental results indicate that there were no exactly the same patterns of the attenuation coefficient in the meandering and straight reaches. For the straight reaches, as shown in Figure 11, multiple regression analysis was adopted to obtain the wave crest amplitude attenuation based on all the experimental scenarios.

Figure 11 reveals that the attenuation of the wave crest amplitude only depended on the propagation distance r_x . Obviously, the wave crest amplitude was well featuring a power exponent attenuation, as seen in

$$\frac{a_{cx}}{a_{cm}} = \left(\frac{r_x}{r_{cm}} \right)^{-1.3}, \quad (4)$$

where a_{cx} was the wave crest amplitude in the propagation distance r_x and r_{cm} was the distance of the location between the place where landslide fell into water and the maximum wave crest amplitude reached.

Similarly, Figure 12 reveals the attenuation of the wave crest amplitude in meandering reaches. Obviously, the attenuation relied not only on the propagation distance r_x , but also on the radial angle with slide axis prolongation. Further, a regression function could be obtained, as shown in

$$\frac{a_{cx}}{a_{cm}} = \left(\frac{r_x}{r_{cm}} \right)^{-1.3/\sqrt{\cos\theta}}, \quad (5)$$

where θ was the radial angle with slide axis prolongation.

To sum up, the attenuation of the wave crest amplitude in both meandering and straight reaches was well characterized by a power exponent attenuation. This study was compared to previous studies such as Mohammed and Fritz [35] and Heller and Hager [36], who all thought that the attenuation law of wave crest amplitude could be described as a power function. Given that, these findings were

considered to be reliable. Based on these results, the impact of impulse waves on the moored ships will be explored in the next section.

3.2. The Impact of Impulse Waves on the Moored Ships

3.2.1. Maximum Mooring Line Tensions. As highlighted in Section 1, the hazardous impact of impulse waves on the moored ships will largely rely on the mooring tension [37]. In present study, the cargo ships were moored by the head and stern lines, which together reacted against the external force impacted by waves. Once any line was broken, the ships would be in danger. Hence, for all 81 tests, the maximum tension of the head and stern line in real world was calculated based on Froude similitude criterion, as shown in Figures 13 and 14. To better analyze the impact, the line's breaking load was also added into the figures, which was 190 kN according to the Load Code for Harbour Engineering (JTS 144-1-2010) [38] issued by the Ministry of Communications of the PRC.

In general, experimental results indicate that in both convex bank and concave bank the mooring tension was greater than the breaking load of the line in most cases. In other words, the moored ships were overall unsafe in the experiments. More specifically, in convex bank, Figure 13 presents the fact that the mooring tensions of the head line and the stern line were nearly equal because the lengths of the head and stern lines were exactly the same. These tensions were much larger than the breaking load of the mooring line in all cases, and the largest mooring tension was about 37 times more than the breaking load.

Similarly, in concave bank, Figure 14 reports that the mooring tension of the head line and the stern line was almost the same, and they were much larger than the breaking load of the mooring line in most cases. However,

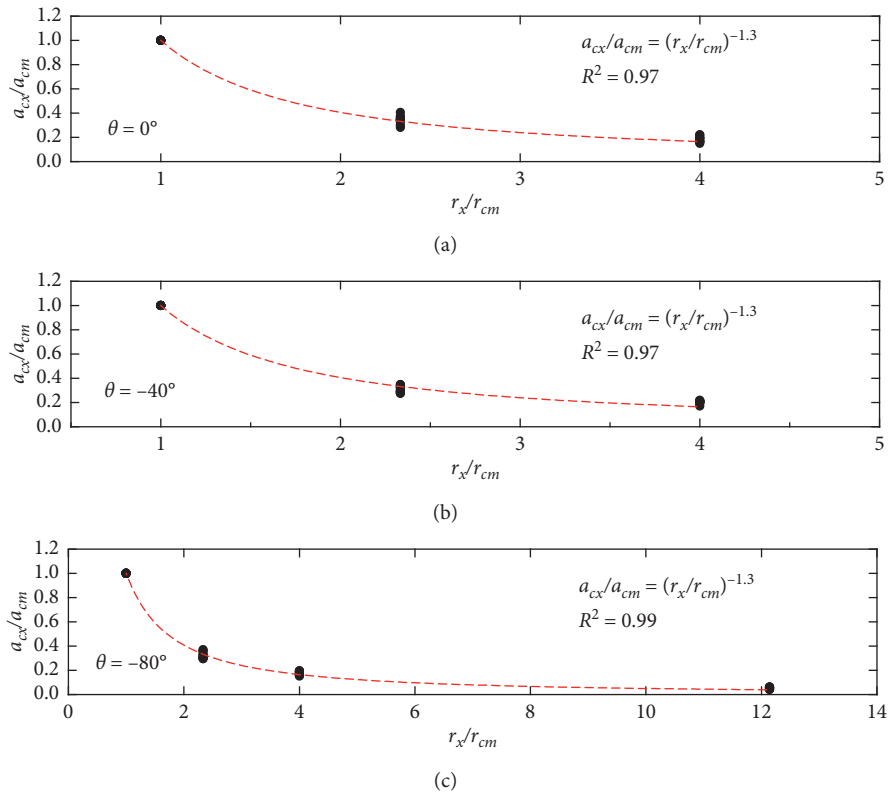


FIGURE 11: The attenuation law wave crest amplitude in straight reach.

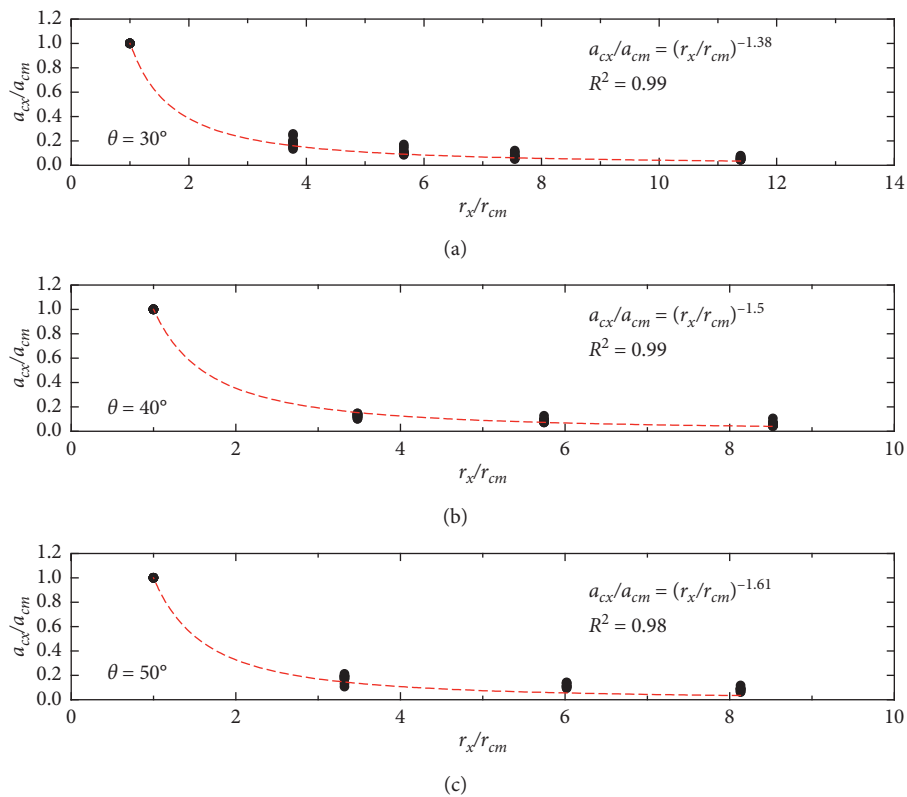


FIGURE 12: Continued.

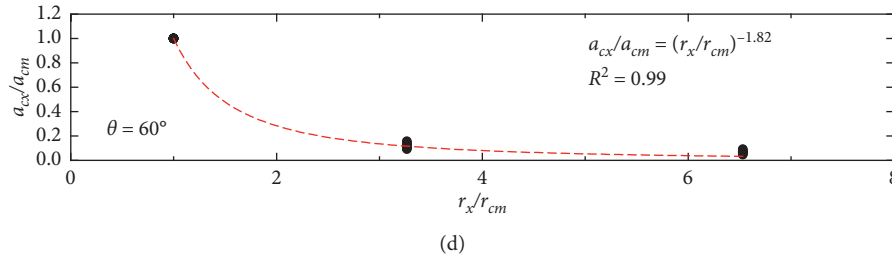


FIGURE 12: The attenuation law wave crest amplitude in meandering reach.

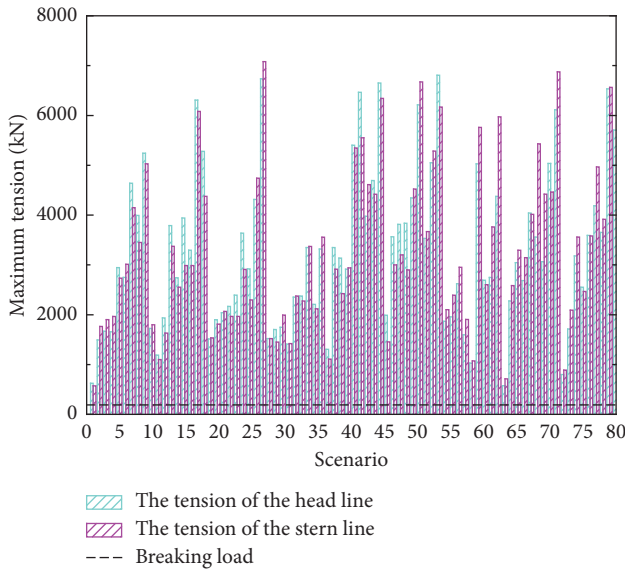


FIGURE 13: Maximum line tensions in convex bank.

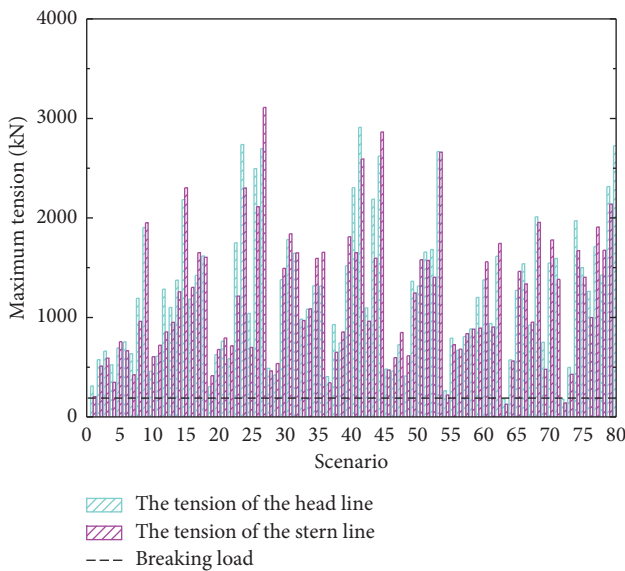


FIGURE 14: Maximum line tensions in concave bank.

compared to convex bank, the moored ship cable tension of both head line and stern line in concave bank was smaller. This was mainly due to two reasons: one was that the

reflection waves from the wharf increased the wave height in convex bank; the other was the incident angles of the impulse waves, which were parallel to the wharf in concave bank because the impulse wave flowed along it. As a result, the surging was the significant motion of the moored cargo ship against the landslide-generated impulse waves; that is to say, the moored ship moved on wave and primarily moved back and forth. This phenomenon also has been found by Ohgaki et al. [37], who reported the motion of the moored ship against the tsunami. For the moored cargo ship at the wharf of the convex bank, the incident angles of the impulse waves were perpendicular to the quay; hence the swaying was the primary motion of the moored cargo ship.

In a word, the moored ships in the ports were risk of cable breaking in our tests. However, the premise of the conclusion was that the distance between the port and the landslide was a specific value. To evaluate the safety of moored ship further in the distance, the relationship between the mooring tension and the aforementioned wave characteristics should be further revealed. However, considering that wave height and wave amplitude have been linked through (3), only the relationship in wave height was analyzed in next section.

3.2.2. *The Relationship between Mooring Tension and Wave Height.* At the test site, it was directly observed that the higher the wave height, the greater the mooring tension. On the basis of this experimental phenomenon, by applying the detailed test data, the relationship between mooring tension and wave height is obtained, as shown in Figure 15.

Figure 15 indicates that the relational expressions between the mooring tension and wave height could be expressed as the following, in convex bank and in concave bank, respectively:

$$F = 1520H_m, \tag{6}$$

$$F = 960H_m, \tag{7}$$

where F was the mooring tension and R^2 was 0.76 and 0.82, respectively.

It is understood that the mooring tension could be expressed as a linear function of wave height in both convex bank and concave bank. For this finding, Meng et al. [39] also reported similar result and argued that the relationship between the mooring tension and wave height was approximately linear. In that case, if H_m was estimated based

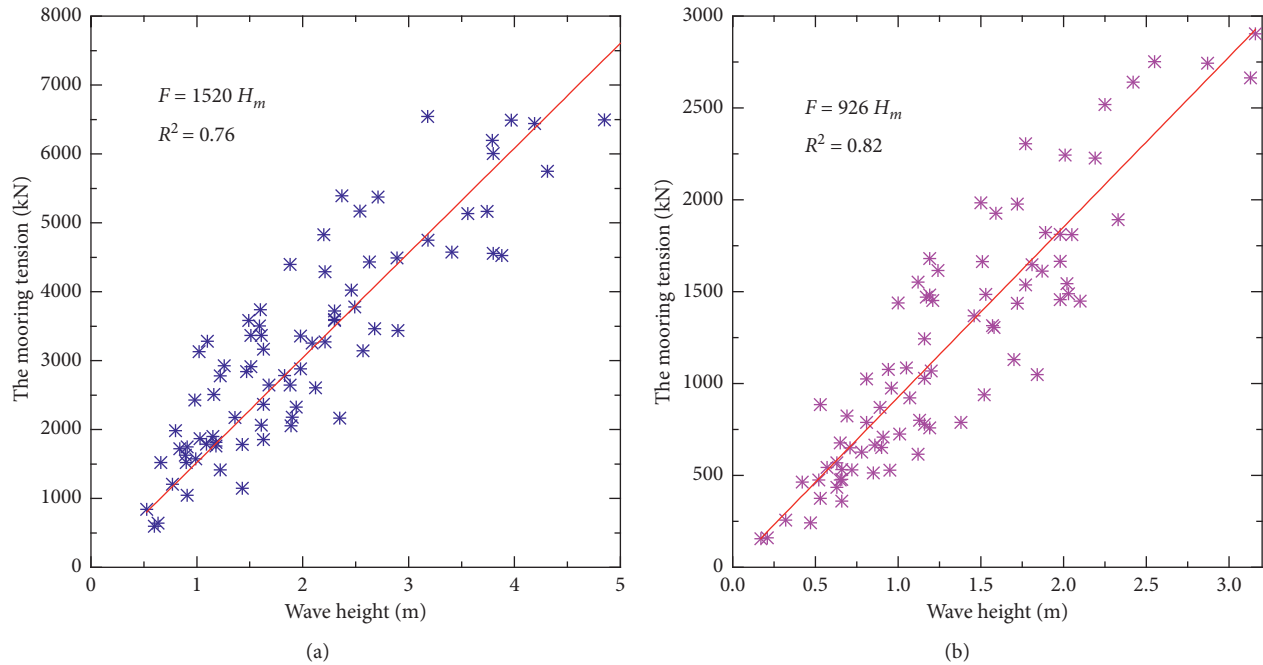


FIGURE 15: The relationship between mooring tension and wave height: (a) in convex bank and (b) in concave bank.

on (3), the mooring tensions could be calculated according to (6) and (7). Furthermore, when the calculated mooring tension is larger than the breaking load of the mooring line, the moored ship was dangerous. Conversely, the ship was safe.

4. Conclusions

To effectively prevent the natural hazard of landslide-generated impulse waves in reservoirs, we examined the hazardous impact on the moored ships in TGR. In detail, three-dimensional experiments of impulse waves were used to explore the impulse wave generation, propagation, and its impact on the moored ships. Based on laboratory results, the main conclusions were as follows:

- (1) The present experimental results indicate that the impact of impulse waves on the moored ships was mainly due to the first wave amplitude and height, which were attributable to four factors: the slide Froude number, the relative landslide thickness and width, and the still water depth. Unlike the linear regular wave, the relative wave height could be described as an exponential function of the relative wave crest amplitude.
- (2) The attenuation of the maximum wave crest amplitude was only attributable to the propagation distance in straight reach. However, the attenuation was influenced by the propagation distance and the radial angle in meandering reach. And both attenuation rules were approximated by a power exponential function.
- (3) For the moored cargo ships in the ports, the present experimental results demonstrate that they were unsafe because of the mooring line broken when

exposed against the impulse waves generated by landslides. Furthermore, the ship in convex bank was more dangerous than that in concave bank.

- (4) The mooring tensions of the head and stern lines were attributable to two factors, i.e., the wave height and the incident angle. Moreover, the mooring tension impacted by the incident angle of 90 deg was larger than that impacted by the incident angle of 0 deg. However, the effect on the mooring tension by any other incident angle should be further revealed in future work.

Data Availability

The data used to support the findings of this study are included herein.

Conflicts of Interest

The authors declare that they have no conflicts of interest.

Acknowledgments

This study was supported by the Chongqing Research Program of Basic Research and Frontier Technology (Grant No. cstc2017jcyjBX0070), the Science and Technology Research Program of Chongqing Municipal Education Commission (Grant Nos. KJQN201900718 and KJQN201800737), and China Postdoctoral Science Foundation (Grant No. 2016M592889XB).

References

- [1] S. N. Ward, "Landslide tsunami," *Journal of Geophysical Research: Solid Earth*, vol. 106, no. B6, pp. 11201–11215, 2001.

- [2] A. Panizzo, P. De Girolamo, and A. Petaccia, "Forecasting impulse waves generated by subaerial landslides," *Journal of Geophysical Research: Oceans*, vol. 110, no. 12, pp. 1–23, 2005.
- [3] S. N. Ward and S. Day, "The 1963 landslide and flood at vaiont reservoir Italy. A tsunami ball simulation," *Italian Journal of Geosciences*, vol. 130, no. 1, pp. 16–26, 2011.
- [4] B. Huang, Y. Yin, and C. Du, "Risk management study on impulse waves generated by Hongyanzi Landslide in Three Gorges reservoir of China on June 24, 2015," *Landslides*, vol. 13, no. 3, pp. 603–616, 2016.
- [5] L. Xiao, S. N. Ward, and J. Wang, "Tsunami squares approach to landslide-generated waves: application to Gongjiafang Landslide, Three Gorges Reservoir, China," *Pure and Applied Geophysics*, vol. 172, no. 12, pp. 3639–3654, 2015.
- [6] B. Huang, S. C. Wang, and Y. B. Zhao, "Impulse waves in reservoirs generated by landslides into shallow water," *Coastal Engineering*, vol. 123, pp. 52–61, 2017.
- [7] H. M. Fritz, W. H. Hager, and H.-E. Minor, "Landslide generated impulse waves," *Experiments in Fluids*, vol. 35, no. 6, pp. 505–519, 2003.
- [8] J. Wang, S. N. Ward, and L. Xiao, "Tsunami squares modelling of the 2015 June 24 hongyanzi landslide generated river tsunami in Three Gorges reservoir, China," *Geophysical Journal International*, vol. 216, no. 1, pp. 287–295, 2019.
- [9] B. Huang, Y. Yin, G. Liu, S. Wang, X. Chen, and Z. Huo, "Analysis of waves generated by Gongjiafang Landslide in Wu Gorge, Three Gorges Reservoir, on November 23, 2008," *Landslides*, vol. 9, no. 3, pp. 395–405, 2012.
- [10] B. Yang, K. Yin, T. Xiao, L. Chen, and J. Du, "Annual variation of landslide stability under the effect of water level fluctuation and rainfall in the three Gorges Reservoir, China," *Environmental Earth Sciences*, vol. 76, no. 16, p. 564, 2017.
- [11] P. D. LiuTao and L. Junwei, "Analysis of shipping development measures for Yichang to Wuhan section of Yangtze River mainstream," *Hydro-Science and Engineering*, vol. 1, pp. 76–84, 2019.
- [12] P. Wang, L. Han, T. Yu, and C. Meng, "Effects of landslide generated impulse waves on ship impact force for pile wharf," *Harbin Gongcheng Daxue Xuebao/Journal of Harbin Engineering University*, vol. 37, no. 6, pp. 878–884, 2016.
- [13] Z. Cheng, P. Wang, C. Yang, S. Wang, J. Zheng, and Y. Li, "Control mode of waterway traffic under dangerous mountain landslide conditions," *Xinan Jiaotong Daxue Xuebao/Journal of Southwest Jiaotong University*, vol. 53, no. 4, pp. 748–755, 2018.
- [14] P. Yuan, P. Wang, and Y. Zhao, "Model test research on the propagation of tsunamis and their interaction with navigating ships," *Applied Sciences*, vol. 9, no. 3, p. 475, 2019.
- [15] B. Huang, Y. Yin, S. Wang et al., "A physical similarity model of an impulsive wave generated by Gongjiafang Landslide in Three Gorges Reservoir, China," *Landslides*, vol. 11, no. 3, pp. 513–525, 2014.
- [16] E. Noda, "Water waves generated by landslides," *Journal of Waterway, Port, Coastal, and Ocean Engineering*, vol. 96, no. 4, pp. 835–853, 1970.
- [17] J. J. Monaghan and A. Kos, "Scott Russell's wave generator," *Physics of Fluids*, vol. 12, no. 3, pp. 622–630, 2000.
- [18] J. S. Russell, "Report on waves," in *Proceedings of the 14th Meeting of the British Association for the Advancement of Science*, York, UK, September 1844.
- [19] R. L. Wiegel, "Laboratory studies of gravity waves generated by the movement of a submerged body," *Transactions, American Geophysical Union*, vol. 36, no. 5, pp. 759–774, 1955.
- [20] P. Heinrich, "Nonlinear water waves generated by submarine and aerial landslides," *Journal of Waterway, Port, Coastal, and Ocean Engineering*, vol. 118, no. 3, pp. 249–266, 1992.
- [21] G. Sælevik, A. Jensen, and G. Pedersen, "Experimental investigation of impact generated tsunami; related to a potential rock slide, Western Norway," *Coastal Engineering*, vol. 56, no. 9, pp. 897–906, 2009.
- [22] F. Enet and S. T. Grilli, "Experimental study of tsunami generation by three-dimensional rigid underwater landslides," *Journal of Waterway, Port, Coastal, and Ocean Engineering*, vol. 133, no. 6, pp. 442–454, 2007.
- [23] S. Yavari-Ramshe and B. Ataie-Ashtiani, "On the effects of landslide deformability and initial submergence on landslide-generated waves," *Landslides*, vol. 16, no. 1, pp. 37–53, 2019.
- [24] V. Heller, W. H. Hager, and H.-E. Minor, "Scale effects in Subaerial Landslide generated impulse waves," *Experiments in Fluids*, vol. 44, no. 5, pp. 691–703, 2008.
- [25] H. Chen, *Research on the Safety of Vessel Traffic System within the Three Gorges Dam Waters*, Wuhan University of Technology, Wuhan, China, 2011.
- [26] L. Han and P. Wang, "Prediction of the maximum near-field wave amplitude of impulse waves generated by three-dimensional landslides based on momentum balance," *Yan-shilixue Yu Gongcheng Xuebao/Chinese Journal of Rock Mechanics and Engineering*, vol. 37, no. 11, pp. 2584–2592, 2018.
- [27] V. Heller, "Scale effects in physical hydraulic engineering models," *Journal of Hydraulic Research*, vol. 49, no. 3, pp. 293–306, 2011.
- [28] Z. Meng, "Experimental study on impulse waves generated by a viscoplastic material at laboratory scale," *Landslides*, vol. 15, no. 6, pp. 1173–1182, 2018.
- [29] H. M. Fritz, W. H. Hager, and H.-E. Minor, "Near field characteristics of landslide generated impulse waves," *Journal of Waterway, Port, Coastal, and Ocean Engineering*, vol. 130, no. 6, pp. 287–302, 2004.
- [30] F. M. Evers, W. H. Hager, and R. M. Boes, "Spatial impulse wave generation and propagation," *Journal of Waterway Port Coastal and Ocean Engineering*, vol. 145, no. 3, 2019.
- [31] A. Huber and W. H. Hager, "Forecasting impulse waves in reservoirs," in *Proceedings of the the 19th Congress On Large Dams C31*, Florence, Italy, 1997.
- [32] G. Tang, L. Lu, Y. Teng, Z. Zhang, and Z. Xie, "Impulse waves generated by subaerial landslides of combined block mass and granular material," *Coastal Engineering*, vol. 141, pp. 68–85, 2018.
- [33] H. Xue, Q. Ma, M. Diao, and L. Jiang, "Propagation characteristics of subaerial landslide-generated impulse waves," *Environmental Fluid Mechanics*, vol. 19, no. 1, pp. 203–230, 2018.
- [34] F. M. Evers and W. H. Hager, "Generation and spatial propagation of landslide generated impulse waves," in *Proceedings of the 35th International Conference on Coastal Engineering, ICCE 2016*, Antalya, Turkey, November 2016.
- [35] F. Mohammed and H. M. Fritz, "Physical modeling of tsunamis generated by three-dimensional deformable granular landslides," *Journal of Geophysical Research: Oceans*, vol. 117, no. C11, 2012.
- [36] V. Heller and W. H. Hager, "Impulse product parameter in landslide generated impulse waves," *Journal of Waterway, Port, Coastal, and Ocean Engineering*, vol. 136, no. 3, pp. 145–155, 2010.
- [37] K. Ohgaki, H. Yoneyama, and T. Suzuki, "Evaluation on safety of moored ships and mooring systems for a tsunami attack,"

in *Proceedings of the OCEANS 2008—MTS/IEEE Kobe Techno-Ocean*, Kobe, Japan, April 2008.

- [38] JTS 144-1-2010, *The Load Code for Harbour Engineering*, Ministry of Transport of the People's Republic of China, Beijing, China, 2010.
- [39] X. Meng, X. Gao, W. Zhang, and Y. Jiang, "A calculation method of mooring force induced by waves," *Journal of Tianjin University*, vol. 44, no. 7, pp. 593–596, 2011.

Research Article

Effects of Rapid Water-Level Fluctuations on the Stability of an Unsaturated Reservoir Bank Slope

Jin-Zhu Mao,¹ Jia Guo,² Yong Fu ,³ Wei-Peng Zhang,¹ and Ya-Nan Ding⁴

¹Changjiang Survey, Planning, Design and Research Co., Ltd. (CSPDR), Changjiang, Hubei 430015, China

²Department of Civil Engineering and Mechanics, Faculty of Engineering, China University of Geosciences, Wuhan, Hubei 430074, China

³Department of Ocean Science and Engineering, Southern University of Science and Technology, Shenzhen 518055, China

⁴State Key Laboratory of Water Resources and Hydropower Engineering Science, Institute of Engineering Risk and Disaster Prevention, Wuhan University, 299 Bayi Road, Wuhan 430072, China

Correspondence should be addressed to Yong Fu; fuyong@u.nus.edu

Received 27 July 2019; Revised 26 December 2019; Accepted 3 February 2020; Published 28 April 2020

Academic Editor: Khalid Abdel-Rahman

Copyright © 2020 Jin-Zhu Mao et al. This is an open access article distributed under the Creative Commons Attribution License, which permits unrestricted use, distribution, and reproduction in any medium, provided the original work is properly cited.

The instability of reservoir slope is likely to cause some severe natural hazards such as surge and barrier lake. In this study, the changes in seepage field and the distribution of the unsaturated zone of a reservoir bank slope subjected to rapid water-level fluctuations are investigated using the finite element method. The stability analysis of a reservoir slope under water-level fluctuation with a rate of 2 m/day is performed. The stability analysis is based on the theory of unsaturated soil mechanics and saturated-unsaturated seepage and accounts for the hydromechanical coupling effect. The changes in shear stress and strain as well as pore water pressure due to rapid water-level fluctuations are explicitly examined. Furthermore, the stability factor of safety, the underlying failure mechanism, and relevant influence factors are discussed. Based on the finite element analysis, it is found that the rapid loss of matrix suction would give rise to the surface landslide near the slope toe.

1. Introduction

The instability of reservoir slope is likely to cause some natural hazards such as surge and barrier lake when the reservoir water-level fluctuates rapidly (see, e.g., [1–3]). The danger derives from unsaturated residual soil due to rapid water-level fluctuations of a reservoir bank slope. A key influence factor is the matrix suction which varies according to the changes in water seepage and water infiltration line. As reported by Ng et al. [4], the rainfall infiltration would reduce the matrix suction, resulting in an increase in moisture content and soil permeability in unsaturated soil. The failure criterion of strength of unsaturated soil differs from that of saturated soil, which increases the difficulty of studying the stability of unsaturated soil slope [5]. Fredlund et al. [6] developed a Mohr-Coulomb shear strength theory for extensional unsaturated soil. Furthermore, Fredlund

et al. [7] proposed a slope stability evaluation method (GLE method) which accounts for the matric suction.

To investigate the stability of unsaturated soil slope, the theory of limit equilibrium with respect to unsaturated soil is commonly used. For example, Qi and Vanapalli [8] reported the formulation for calculating slope safety factor based on the strength theory of unsaturated soil and the limit equilibrium method and discussed the stability of unsaturated soil slope under rainfall infiltration. Liu et al. [9, 10] simulated the undrained shear strength as a random field to reflect the spatial variability of slope soil properties and combined the Monte Carlo method to determine the factor of safety. Hiroyuki et al. [11] reported that the influence factors for landslide stability in reservoir areas include the immersion of the reservoir water, the sharp decline of the reservoir water-level, and the rainstorm. Fredlund and Rahardjo [12] proposed a method for calculating the critical

height of vertical or nearly vertical slopes based on the theory of earth pressure in unsaturated soil. Fredlund et al. [13] put forth a nonlinear law for the variation of shear strength of unsaturated soil with matric suction based on the soil-water characteristic curve equation of unsaturated soil. Zhang et al. [14] and Luo and Ye [15] noticed that when the water-level fluctuates dramatically, the infiltration line and the matric suction field on the slope will change significantly and subsequently affect the stability of the bank slope. However, the slope reliability analysis as well as the changes in seepage field and the unsaturated zone of a reservoir bank slope subjected to rapid water-level fluctuations has not been discussed in these studies.

The effects of rapid water-level fluctuations on the stability of the reservoir slope in unsaturated soil still remain unclear. Unlike saturated soil, the interaction between pore air pressure and pore water pressure in unsaturated soil is more complicated. Firstly, the pore pressure in unsaturated soil may become negative, thereby reducing the effective soil stress [16]. Secondly, the water content and the permeability coefficient in unsaturated soil vary spatially which may cause soil-water content and permeability coefficient exhibiting spatial variability [17–19]. Thirdly, the failure criterion of strength of saturated soil differs from that of unsaturated soil. All these lead to the difficulty of studying the slope stability in unsaturated soil.

In this study, a genuine engineering case of reservoir landslide at Nuozhadu Reservoir area in Yunnan Province is examined using the finite element method. The hydraulic effect of water-level fluctuations on the interior of unsaturated soil slope is considered. The suction matrix is used to calculate the influence of a changing rate of water-level on the unsaturated soil of the typical landslide deposit H_{12} of an engineering example of bank slope investigation in Nuozhadu Reservoir area. In the stability analysis of the slope, the coupling effects of matrix suction in the unsaturated area, pore water seepage in the saturated area, and gravity stress field of rock and soil are taken into account. The results can serve as a reference for stability evaluation of reservoir bank and river side slopes and other related engineering areas (see, e.g., Chen et al. [20]).

2. Finite Element Model

2.1. Model Setup. By collecting of relevant data and field geological investigation in Nuozhadu Reservoir area, it is found that H_{12} is an ancient landslide accumulation body, which is located in the branch of Lancang River. Figure 1 shows the overall picture of the landslide accumulation body, with obvious landslide morphology. Figure 2 is a section sketch of H_{12} . The elevation of the front edge of the landslide is 660 m, the elevation of the back edge is 827 m, the height difference is about 207 m, and the volume of the landslide accumulation is 6 million cubic meters. The main sliding direction of the landslide is about 5° and the length of the main sliding direction is about 1000 m. The boundary of the landslide is basically clear. The boundary of both sides of the landslide is gully. The bedrock in the gully is exposed. The occurrence of the bedrock surface is 5° , which is less than 17° as shown in Figure 2. The landslide body slides along the

bedrock surface. The shape of the landslide accumulation body is as follows: the back edge of the accumulation body is steep, the slope in the middle part is gentle, and the slope at the shear outlet of the front edge is steep, which has typical landslide characteristics.

The reservoir bank slope is subjected to the water-level fluctuations at different rates. Figure 3 shows the schematic of a typical vertical cross section of a H_{12} landslide deposit which is obtained based on the basic geological survey and 1 : 10000 topographic map. The typical sections are intercepted reasonably. The orientation of the sections is consistent with the main sliding direction. The strata are divided into three layers. From top to bottom, the landslide deposits (gravel-bearing silty clay), the sliding zones are mainly strong weathered argillaceous sandstone and the magenta silty-argillaceous siltstone.

There is a horizontal displacement of the side walls and the vertical and horizontal ones. Regarding the boundary conditions, horizontal constraints are imposed on both sides of the model, and all nodes on the ground are added with horizontal and vertical constraints. There is water pressure on the slope, and the pressure value is determined by the reservoir water-level. According to the material composition of the landslide and the mechanical parameters of the adjacent rock and soil, the comprehensive calculation determines the calculation parameters as shown in Table 1.

The normal storage water-level is 812 m and the initial water-level is 625 m, which is lower than the toe of the landslide mass, i.e., the elevation of the landslide body. When the initial water-level is achieved, the river bed in the section is free of water. The reservoir is impounded in three stages: the first stage from the current water-level to 672.5 m, the second stage from 672.5 m to the dead water-level of 765 m, and the third stage from the dead water-level of 765 m to the normal water-level of 812 m. The cases modelled in the analysis of the landslide are shown in Table 2.

2.2. Computation Conditions. The finite element model is implemented using the SIGMA/W module of the commercial finite element software GeoStudio. This module is able to correctly model the stability behavior of an unsaturated slope which involves the coupling of seepage and stress-strain behavior of soil. The study that the slope stability analysis under unsaturated soil is calculated using the linear elasticity model implemented in GeoStudio 2007 is proposed by Oh et al. [21].

The soil and the bed rock of the landslide are modelled using an elastoplastic constitutive model and linear elastic constitutive model, respectively. Figure 4 shows the meshes of the landslide soil and bedrock domains. Based on the working conditions of Nuozhadu Reservoir in the periods of impoundment and operation, two scenarios are considered in this study. The parameters used in the analysis are displayed in Table 1.

2.3. Determination of Calculation Method. The fluid-soil interaction is explicitly considered as the finite element modelling. The soil is assumed to be a continuous medium.



FIGURE 1: Overall picture of the landslide accumulation body.

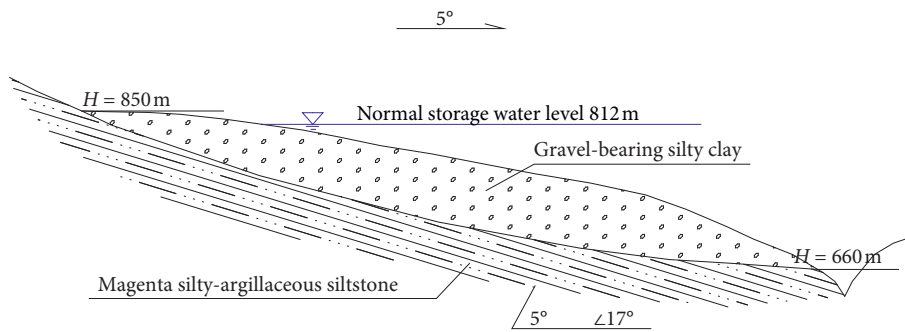


FIGURE 2: Schematic sketch of section H_{12} .

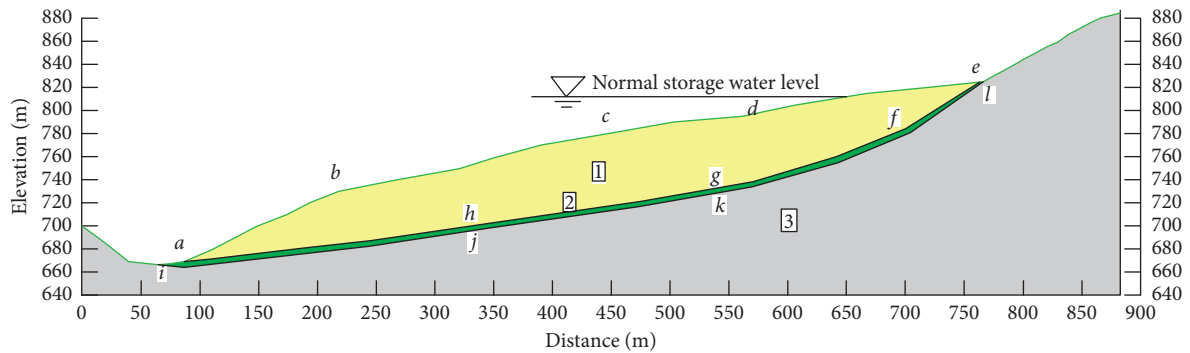


FIGURE 3: Schematic of a typical vertical cross section of landslide. Notes: Zone 1 (yellow part) is an accumulative body with an average thickness of 40 m; Zone 2 (narrow green part) is a slip zone with highly weathered argillaceous sandstone and an average thickness of about 3 m.

TABLE 1: Mechanical parameters of landslide accumulation and slide zone.

Parameter	Symbol	Value		Unit
		Landslide accumulation zone	Slip zone	
Cohesion of saturated soil	c	16.5	15	kPa
Internal friction angle of saturated soil	φ'	20	18	Degree
Internal friction angle caused by matrix suction	φ^b	16	16	Degree
Unit weight	γ	15.8	16	kN/m^3
Saturated unit weight	γ_{sat}	22	22	kN/m^3
Modulus of elasticity	E	17	15	MPa
Poisson's ratio	μ	0.25	0.3	—

The seepage is characterized by the static pore pressure and the hydrodynamic force, which is manifested by the osmotic pressure P applied to a certain action surface and the seepage

volume force f distributed in the seepage region. The former is the surface force, and the latter is physical strength; the expression is illustrated in

TABLE 2: Cases modelled in the analysis of landslide.

Case no.	Conditions	Research contents
Case 1	Water-level drops from 812 m to 765 m (2 m/day)	Stability
Case 2	Water-level increases from 672.5 m to 765 m (2 m/day)	Stability
Case 3	Water-level drops dramatically from 812 m to 765 m (2 m/day)	Hydromechanical behavior
Case 4	Water-level raises sharply from 672.5 m to 765 m (2 m/day)	Hydromechanical behavior

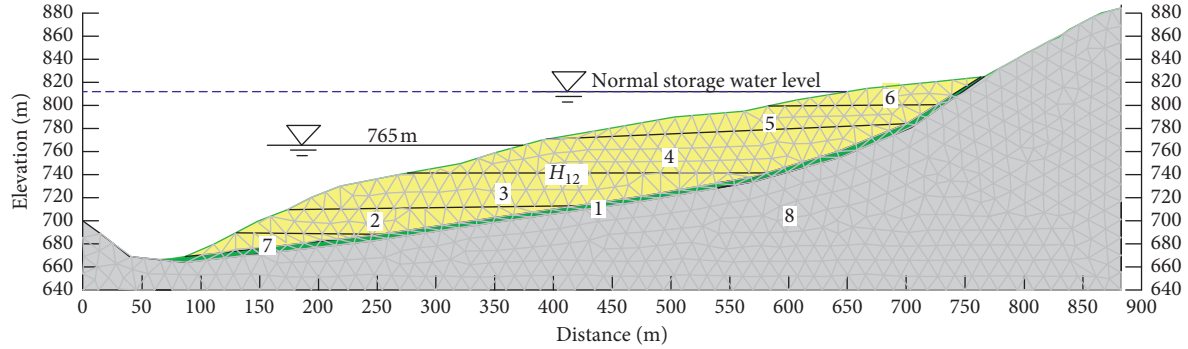


FIGURE 4: Meshing of finite element model.

$$\begin{cases} P = \gamma(H - z), \\ f = \gamma J_f. \end{cases} \quad (1)$$

On the other hand, the permeability coefficient k will change with the volumetric strain ε_v and porosity n , which in turn affects the seepage field. The expressions are given by

$$\begin{cases} k = k(n), \\ n = n(\varepsilon_v), \\ \varepsilon_v = \varepsilon_v(\sigma_{ij}). \end{cases} \quad (2)$$

The coupled fluid-soil interaction is implemented using nonlinear finite element method for slope stability analysis. The main steps include solving the seepage field through the initial permeability coefficient k_0 , and obtaining the head distribution so that the hydrostatic pressure and the permeation volume force can be calculated. The above results are then brought into the stress field, and the boundary conditions are combined to resolve the stress field. The volume strain is obtained, and the volume strain is substituted into (2) to solve the permeability coefficient k_1 . The above steps are repeated continuously until equilibrium is arrived to obtain the stress-strain distribution.

3. Results and Analysis

3.1. Cases 1 to 2. When analyzing the stability of the slope due to the sudden rise and fall of the water-level, consider the coupling effect of the seepage force and the stress field; that is, the seepage force is added to the landslide micro-unit, and the variation rate of 2 m/day is selected and analyzed. As shown in Figure 5, the reservoir water-level is reduced from 812 m to 765 m. Considering the finite element method stability calculation results of the unsaturated landslide deposits after the coupling of the seepage field and the stress

field, the results show the overall sliding. The stability factor is 1.123, which is generally stable.

When the reservoir water-level rises from 672.5 m to 765 m, the hydromechanical coupling effect is examined. During the analysis, the matric suction is reckoned. As shown in Figure 6, the factor of safety of the slope is 1.255.

In order to study the influence of the matric suction of unsaturated soil on the stability of unsaturated landslide deposits, the suction force is not considered; that is, the strength of the soil due to suction is removed in the software, and other parameters are unchanged, considering the effect of seepage force. The potential sliding conditions are shown in Figure 7. The factor of safety decreases from 1.255 to 1.138, which indicates that the matric suction has a positive effect on the slope stability when the water-level rises rapidly.

Compared with the rising condition of the reservoir water-level, the stability of the deposit body is superior to that of the sudden drop. The favorable factors for the antisliding of the reservoir water-level rising are schematically shown in Figure 8. Firstly, the reservoir water-level is suddenly raised, and the landslide body is subjected to the seepage force $F(K)$ addressed to the slope, which is beneficial to enhance the antisliding force. Secondly, during the abrupt rise of the water-level, the water will be pressed by a self-weight in a short period of time, which is perpendicular to the slope $F'(N)$. The slope foot increases the antislip force of the leading edge, which increases the stability of the entire slope. The unfavorable factors of water storage on slope stability also exist. After a period of water storage, the front edge of the slope is saturated, and the leading edge rock and soil itself will decrease due to water immersion strength, reducing the resistance. The sliding force causes a landslide. Because the leading edge of the slope is saturated by the upward pressure $F(N)$ of the water after the leading edge is saturated, the water seeps into the sliding surface to play a lubricating role, so that the anterior edge antisliding force

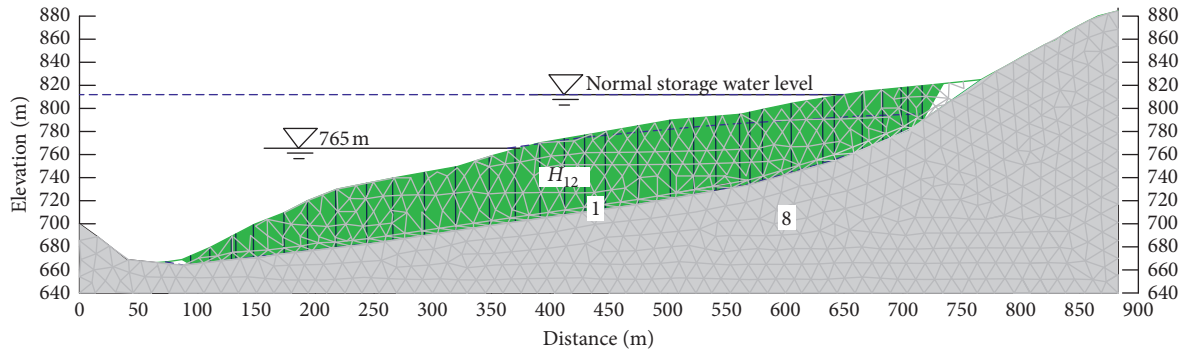


FIGURE 5: Potential sliding zone (green part) of Case 1 with water-level dropping from 812 m to 765 m at a rate of 2 m/day ($F_S = 1.123$).

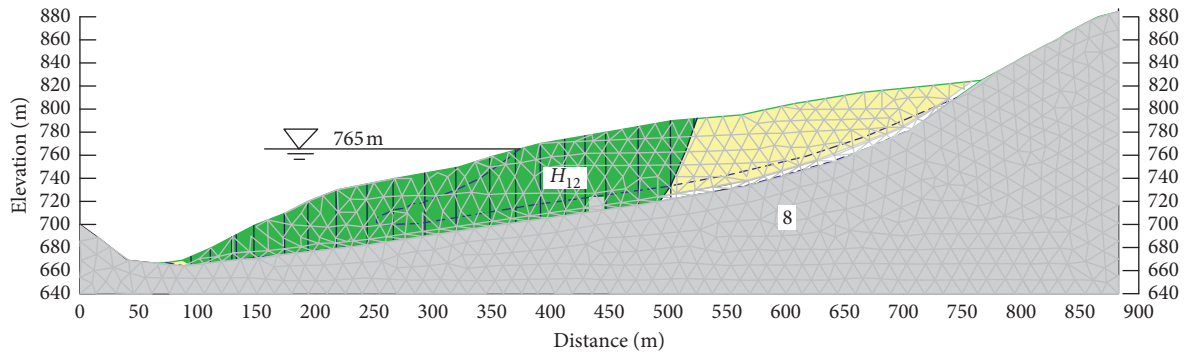


FIGURE 6: Potential sliding zone (green part) of Case 2 with water-level increases from 672.5 m to 765 m at a rate of 2 m/day, considering the hydromechanical coupling effect, and the suction force is considered ($F_S = 1.255$).

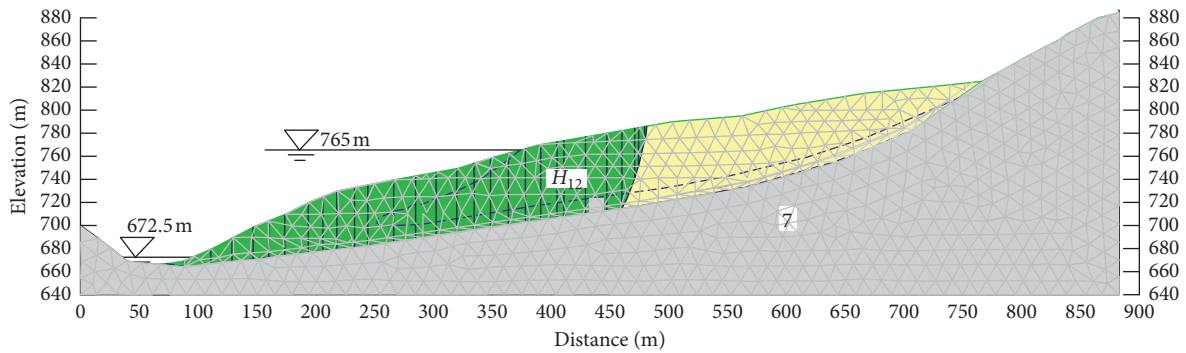


FIGURE 7: Potential sliding zone (green part) of Case 2 with water-level increases from 672.5 m to 765 m at a rate of 2 m/day, considering the hydromechanical coupling effect.

reduces. However, under the condition of water-level dropping at a rate of 2 m/day, the stability coefficient of the slope is broad and safe, indicating that the favorable factors are greater than the unfavorable factors.

The slope stability under the influence of the matrix suction in the unsaturated zone is also considered. It is found that when the matrix suction is calculated, the stability of the slope is likely to be improved, and the increase is mainly dominated by the range of the unsaturated zone. The larger the range, the greater the increase in stability. Under the condition of the reservoir water-level falling, the range of the unsaturated zone is not as large as that of the rising condition, so the unsaturated zone has less impact on the

stability of the slope under the precipitation condition. The above results suggest that the landslide accumulation body is stable under all the above-mentioned reservoir water-level fluctuation conditions. The calculation results are more accurate when the hydromechanical coupling effect is reckoned under unsaturated conditions.

3.2. Case 3. Figure 9 shows the seepage velocity field in landslide deposit H_{12} for Case 3 with water-level dropping from 812 m to 765 m at a rate of 2 m/day. As can be seen, the maximum seepage velocity occurs near the slope surface at water elevation of 765 m, i.e., a velocity of 2 m/day, which is

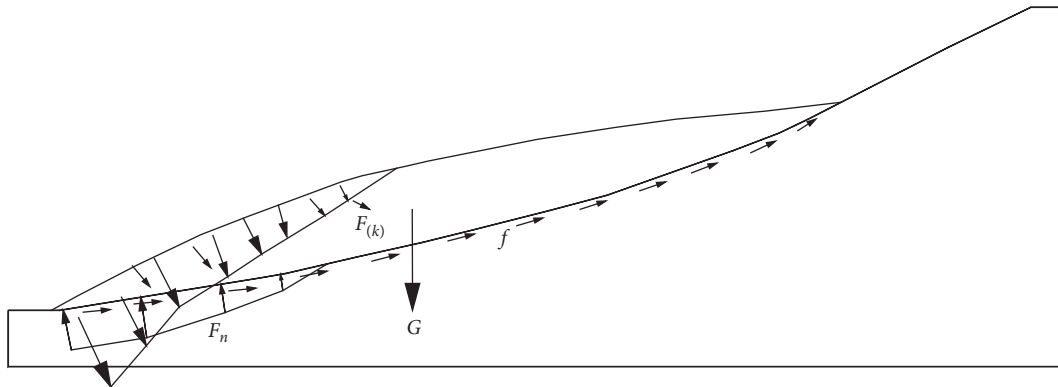


FIGURE 8: Schematic diagram of the force of the landslide body when the water-level rises suddenly.

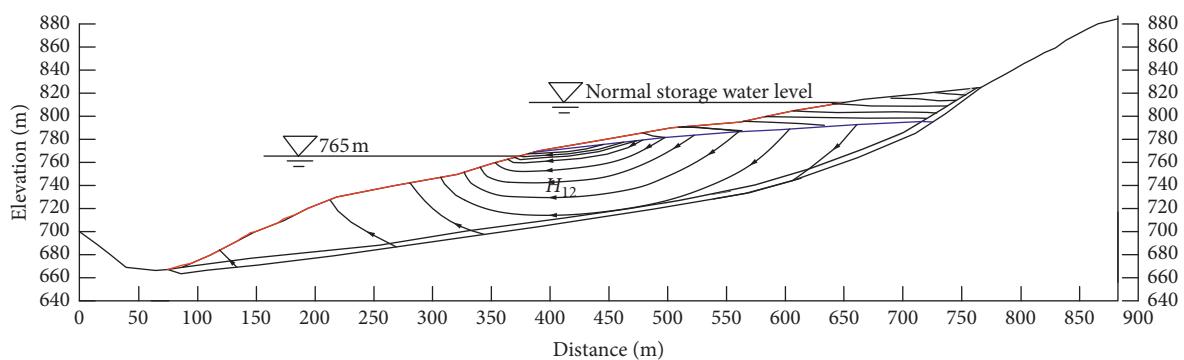


FIGURE 9: Seepage velocity field in landslide deposit H_{12} for Case 3 with water-level dropping from 812 m to 765 m at a rate of 2 m/day.

probably due to the relatively low soil permeability coefficient. The seepage velocity is a key influence factor on the stability of slopes [22]. This can be reflected from pore water pressure and saturation change. This effect would become more significant when the direction of flow velocity is the same as the sliding direction and the flow velocity is greater than the sliding velocity of the landslide.

Figure 10 shows the contours of the displacement, shear stress, and strain of the landslide for Case 3 with water-level dropping from 812 m to 765 m at a rate of 2 m/day. The displacement, shear stress, and strain distribution calculated by considering the coupling effect of the seepage field and the stress field are displayed in the displacement contour map along the horizontal and vertical directions. There is x -zero displacement at the 475 m of the landslide body. Due to the water pressure acting on the slope after water storage, the soil is consolidated and displaced along the positive direction of x -axis. The maximum displacement value is 0.31 m at x -axis of 200 m. At the trailing edge of the landslide body, due to the combined action of the sliding force and the seepage force, the trailing edge has a displacement along the negative x -axis direction, and the maximum value of 0.29 m is located at the trailing edge of the landslide. The displacement along y -axis is predominantly negative. The maximum settlement is 0.78 m, which is mainly due to soil consolidation caused by water pressure. The above results indicate that the potential failure mode is a typical thrust load-caused landslide.

The consequences of stress-strain calculation show that the shear stress is concentrated in the linear elastic model of the sliding bed; the maximum value reaches 2500 kPa. The landslide body is elastoplastic model, the shear stress is small, but the shear strain is large, and the shear strain at the landslide front and slip surface is great.

3.3. Case 4. Figure 11 shows the displacement, shear stress, and shear strain contours when the reservoir water-level rises from 672.5 m to 765 m at a rate of 2 m/day. From the dip displacement and stress-strain distribution contours, the following findings can be observed. Firstly, when the reservoir water-level rises, the displacement of the landslide body is lower than the reservoir water-level from 812 m to 765 m. The shear strain is much smaller. Because the reservoir water-level rises sharply, the projection of the seepage force direction and the sliding direction is negative, which offsets the effect of a part of the sliding force. Therefore, when the water-level rises, the displacement of the landslide body tends to be small. Secondly, at the elevation of 765 m, the seepage force exists along the opposite direction of the sliding direction, and the trailing edge receives the glide force caused by gravity; as a result, two zero displacement lines appear in the sliding body along x -axis displacement contour. In the shear strain contour map, two zero shear strain lines also appear in the sliding body. Thirdly, the shear stress distribution in the sliding body is the same as that

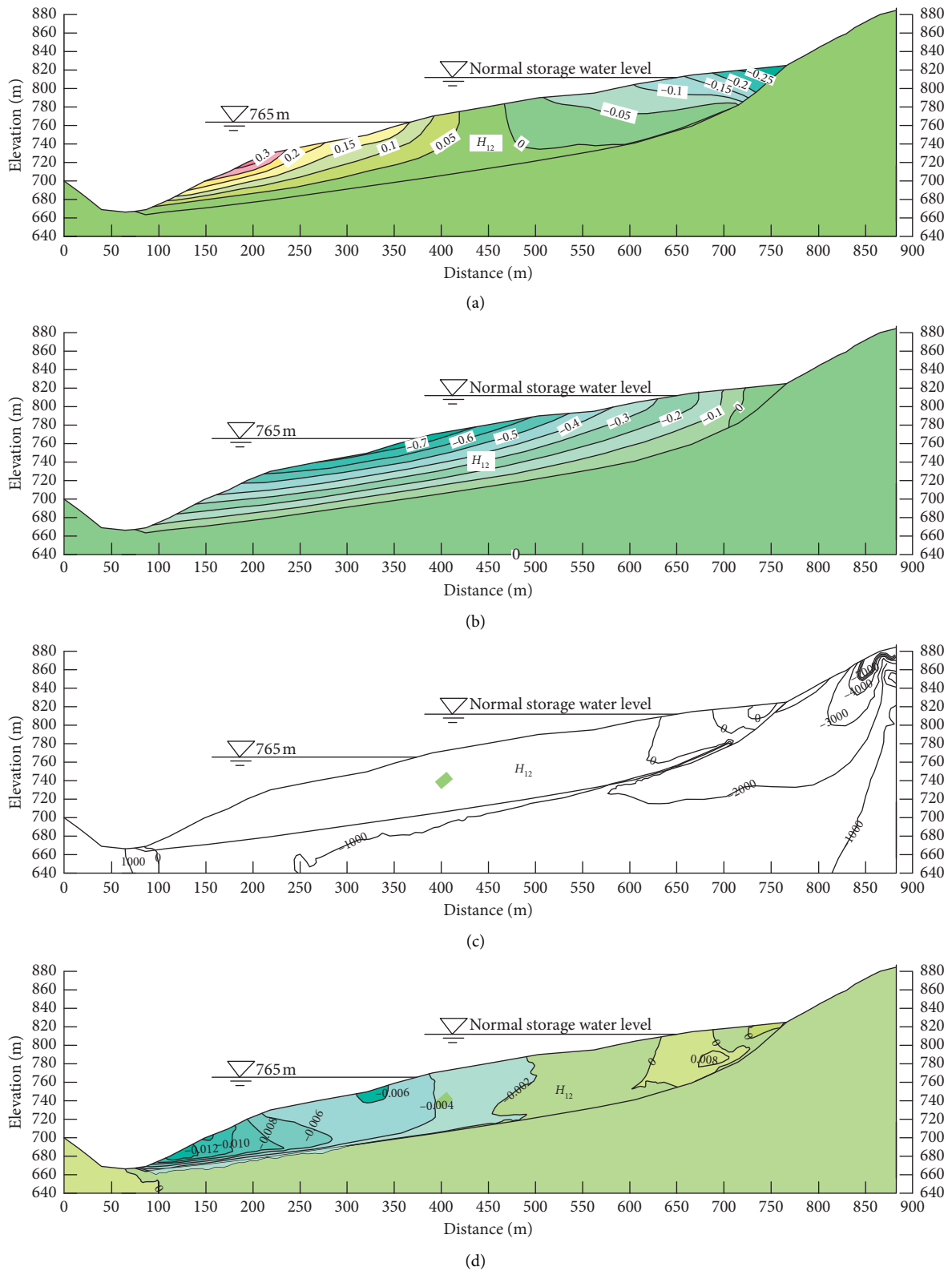
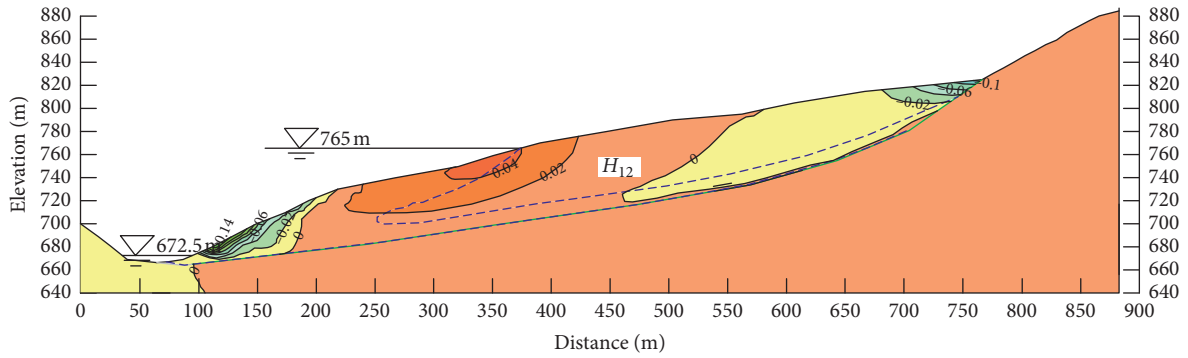
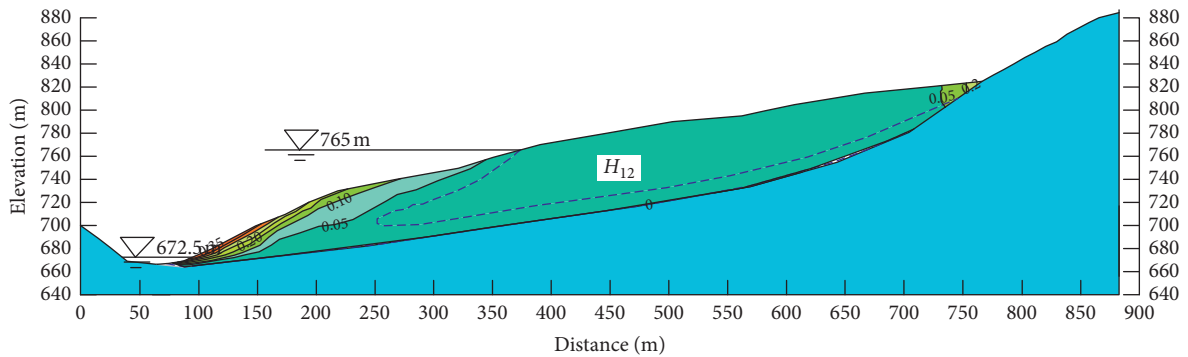


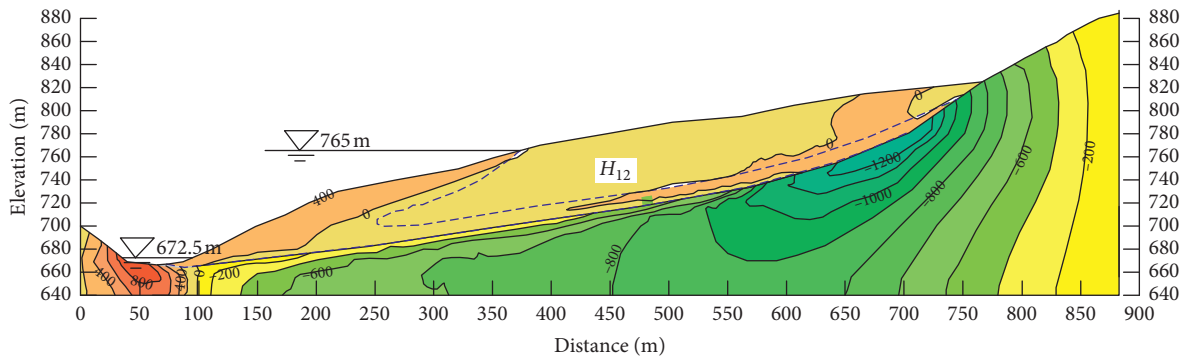
FIGURE 10: Soil behavior for Case 3 with water-level dropping from 812 m to 765 m at a rate of 2 m/day. (a) Horizontal displacement contour (unit: m). (b) Vertical displacement contour (unit: m). (c) Shear stress contour (unit: kPa). (d) Shear strain contour.



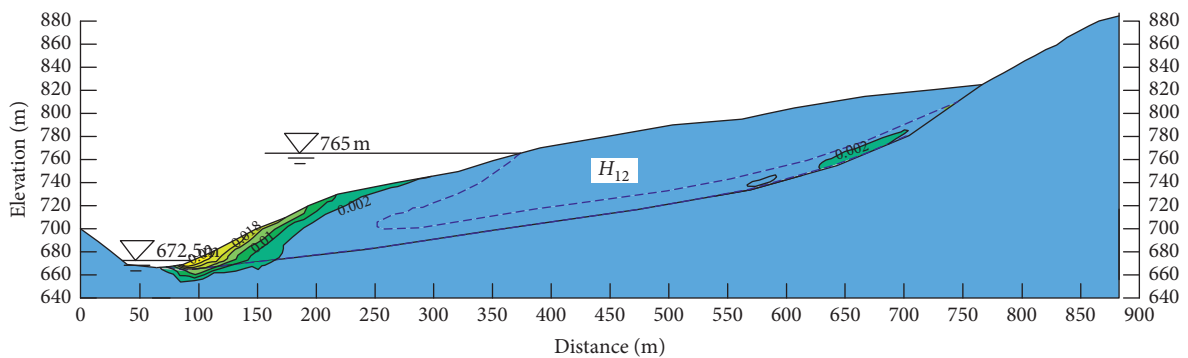
(a)



(b)



(c)



(d)

FIGURE 11: Soil behavior for Case 4 with water-level rising from 672.5 m to 765 m at a rate of 2 m/day. (a) Horizontal displacement contour (unit: m). (b) Vertical displacement contour (unit: m). (c) Shear stress contour (unit: kPa). (d) Shear strain contour.

under the precipitous drop condition, and the shear stress is large in the sliding bed. The shear strain distribution is great in the sliding body and small in the sliding bed.

4. Conclusions

Based on the study of rapid water-level fluctuations on the stability and hydromechanical behavior of an unsaturated reservoir bank slope, the following conclusions can be obtained.

- (1) The matrix suction should be considered when calculating the stability of unsaturated soil, which is beneficial for slope stability in unsaturated soil.
- (2) The stability of an unsaturated reservoir bank is weaker when the water-level drops dramatically and then rises sharply. The result is attributed to the orientation of seepage force being inclined to the outer edge of the slope when the water-level drops dramatically.
- (3) The coupled seepage-soil stress field should be considered in calculating the stability of an unsaturated reservoir bank slope when the water-level changes rapidly.
- (4) The unsaturated area of the slope body is becoming smaller after the water-level rises abruptly, which can make the reservoir bank slope be unstable.

In the process of water storage, due to the rapid disappearance of the matrix suction, it is not difficult to cause some shallow surface landslides. It is found that the most dangerous working condition for the bank slope is under deliberate storage and quick release of water. Compared with the rising condition of the reservoir water-level, the deposit body is more stable than that of the sudden water-level drop condition. When the matrix suction is reckoned, the stability of the slope is likely to be improved. A larger unsaturated zone often benefits the slope stability. This study is based on 2D model, and a more complete assessment should consider a 3D model of slope. As a multiphase material, the soil along the sliding surface should be spatially variable (see [23, 24]) which may also affect the failure mode and sliding velocity. These form strands of future work.

Data Availability

The data used to support the findings of this study are available from the corresponding author upon request.

Conflicts of Interest

The authors declare that they have no conflicts of interest.

Acknowledgments

This research was supported by the National Key Research and Development Program of China (Grant no. 2018YFC1505006) and the National Natural Science Foundation of China (Grant no. 51879203).

References

- [1] N. Liu, Z. Chen, J. Zhang, W. Lin, W. Chen, and W. Xu, "Draining the Tangjiashan barrier lake," *Journal of Hydraulic Engineering*, vol. 136, no. 11, pp. 914–923, 2010.
- [2] Y. Yin, B. Huang, W. Wang et al., "Reservoir-induced landslides and risk control in three gorges project on Yangtze river, China," *Journal of Rock Mechanics and Geotechnical Engineering*, vol. 8, no. 5, pp. 577–595, 2016.
- [3] K.-Q. Li, D.-Q. Li, P.-T. Li, and Y. Liu, "Meso-mechanical investigations on the overall elastic properties of multi-phase construction materials using finite element method," *Construction and Building Materials*, vol. 228, p. 116727, 2019.
- [4] C. W. W. Ng, L. T. Zhan, C. G. Bao, D. G. Fredlund, and B. W. Gong, "Performance of an unsaturated expansive soil slope subjected to artificial rainfall infiltration," *Géotechnique*, vol. 53, no. 2, pp. 143–157, 2003.
- [5] Y. Tang, W. Wu, K. Yin, S. Wang, and G. Lei, "A hydro-mechanical coupled analysis of rainfall induced landslide using a hypoplastic constitutive model," *Computers and Geotechnics*, vol. 112, pp. 284–292, 2019.
- [6] D. G. Fredlund, *Two-Dimensional Finite Element Program Using Constant Strain Triangles*, University of Saskatchewan Transportation and Geotech, Saskatoon, Canada, 1978.
- [7] D. G. Fredlund, J. Krahn, and D. E. Pufahl, "The relationship between limit equilibrium slope stability methods," *Proceedings of the International Conference on Soil Mechanics and Foundation Engineering*, vol. 3, pp. 409–416, 1981.
- [8] S. Qi and S. K. Vanapalli, "Influence of swelling behavior on the stability of an infinite unsaturated expansive soil slope," *Computers and Geotechnics*, vol. 76, pp. 154–169, 2016.
- [9] Y. Liu, H. Xiao, K. Yao, J. Hu, and H. Wei, "Rock-soil slope stability analysis by two-phase random media and finite elements," *Geoscience Frontiers*, vol. 9, no. 6, pp. 1649–1655, 2018.
- [10] Y. Liu, W. Zhang, L. Zhang, Z. Zhu, J. Hu, and H. Wei, "Probabilistic stability analyses of undrained slopes by 3D random fields and finite element methods," *Geoscience Frontiers*, vol. 9, no. 6, pp. 1657–1664, 2018.
- [11] N. Hiroyuki, "Discussions on reservoir landslide," *Bulletin of Soil and Water Conservation*, vol. 10, no. 1, pp. 53–64, 1990.
- [12] D. G. Fredlund and H. Rahardjo, *Soil Mechanics for Unsaturated Soils*, Wiley, Hoboken, NJ, USA, 1993.
- [13] D. G. Fredlund, A. Xing, M. D. Fredlund, and S. L. Barbour, "The relationship of the unsaturated soil shear strength to the soil-water characteristic curve," *Canadian Geotechnical Journal*, vol. 33, no. 3, pp. 440–448, 1996.
- [14] W. J. Zhang, L. T. Zhan, D. S. Ling, and Y. M. Chen, "Influence of reservoir water level fluctuations on stability of unsaturated soil banks," *Journal of Zhejiang University (Engineering Edition)*, vol. 40, no. 8, pp. 1365–1370, 2006.
- [15] X. H. Luo and H. Y. Ye, "Stability analysis of soil slope considering matric suction," *Rock and Soil Mechanics*, vol. 28, no. 9, pp. 1919–1922, 2007, in Chinese.
- [16] L. Zhang, F. Wu, Y. Zheng, L. Chen, J. Zhang, and X. Li, "Probabilistic calibration of a coupled hydro-mechanical slope stability model with integration of multiple observations," *Georisk: Assessment and Management of Risk for Engineered Systems and Geohazards*, vol. 12, no. 3, pp. 169–182, 2018.
- [17] D. H. Fredlund, D. P. Do, and D. Hoxha, "Effective elastic and hydraulic properties of fractured rock masses with high contrast of permeability: numerical calculation by an embedded fracture continuum approach," *Advances in Civil Engineering*, vol. 2019, Article ID 7560724, 21 pages, 2019.

- [18] T. M. H. Le, M. Sanchez, D. Gallipoli, and S. Wheeler, "Probabilistic study of rainfall-triggered instabilities in randomly heterogeneous unsaturated finite slopes," *Transport in Porous Media*, vol. 126, no. 1, pp. 199–222, 2019.
- [19] Y. Wheeler, L. Q. He, Y. J. Jiang, M. M. Sun, E. J. Chen, and F.-H. Lee, "Effect of in situ water content variation on the spatial variation of strength of deep cement-mixed clay," *Géotechnique*, vol. 69, no. 5, pp. 391–405, 2019.
- [20] G. Chen, Q.-Y. Li, D.-Q. Li, Z.-Y. Wu, and Y. Liu, "Main frequency band of blast vibration signal based on wavelet packet transform," *Applied Mathematical Modelling*, vol. 74, pp. 569–585, 2019.
- [21] S. Oh and N. Lu, "Slope stability analysis under unsaturated conditions: case studies of rainfall-induced failure of cut slopes," *Engineering Geology*, vol. 184, pp. 96–103, 2015.
- [22] R. L. Michalowski, "Slope stability analysis: a kinematical approach," *Géotechnique*, vol. 45, no. 2, pp. 283–293, 1995.
- [23] L. Li, C. Li, and C. He, "Analysis of mechanical response for a reinforced bedded rock slope under rainfall," *Advances in Civil Engineering*, vol. 2019, Article ID 9864230, 9 pages, 2019.
- [24] K.-Q. Li, D.-Q. Li, and Y. Liu, "Meso-scale investigations on the effective thermal conductivity of multi-phase materials using the finite element method," *International Journal of Heat and Mass Transfer*, vol. 151, p. 119383, 2020.

Review Article

Soil Fatigue from Induced Seismicity

Merissa L. Zuzulock ¹, Oliver-Denzil S. Taylor ², and Norbert H. Maerz ³

¹US Army Corps of Engineers, New York District, 5352 Delaware Ave., Joint Base MDL, NJ 08640, USA

²Geotechnical and Structures Laboratory, US Army Engineer Research and Development Center, 3909 Halls Ferry Road, Vicksburg, MS 39180, USA

³Missouri Science and Technology, Geological Engineering Department, 332 McNutt Hall, Missouri University of Science and Technology, Rolla, MO 65409-0410, USA

Correspondence should be addressed to Merissa L. Zuzulock; merissa.l.zuzulock@usace.army.mil

Received 1 August 2019; Accepted 21 January 2020; Published 15 April 2020

Guest Editor: Tae-Hyung Kim

Copyright © 2020 Merissa L. Zuzulock et al. This is an open access article distributed under the Creative Commons Attribution License, which permits unrestricted use, distribution, and reproduction in any medium, provided the original work is properly cited.

Induced seismicity and the effects on civil engineering systems are not completely understood and infrequently studied. One specific area that is not well known is soil fatigue which includes factors such as understanding the natural conditions of the subsurface as well as operational parameters under short duration impulse loads. With the increase of geinduced seismic activity, soil fatigue becomes of greater concern to structures in the vicinity of this seismic load. The foundations of these structures can be affected by impulse loads which can ultimately cause failure. The lack of quantitative data puts the reliability of these civil engineering systems at risk as they are not fully evaluated to determine if they are functioning as they are intended in the environments they are designed to support.

1. Introduction

Soil fatigue occurs prior to failure which makes it difficult to define as it is determined based on the acceptable level of risk the system can sustain. Determining factors for failure are usually based on social benefits and/or economic judgments that are difficult to quantify [1]. For purposes of this paper, soil fatigue can be defined as the magnitude of strain that a material can endure for a given number of cycles until a point of maximum strain where the soil begins to weaken. Similar to fatigue for other engineering structures bridges, roads, metals, etc., it is further defined as losing strength over time without catastrophic failure. However, such fatigue can ultimately lead to failure if left unchecked as it will continue to grow as the amount of applied impact load increases.

The increase in geoen지니어ed induced seismicity has created concerns for several civil engineering systems such as dams and levees. To date, the study of impacts from induced seismicity has been rare with indeterminate conclusions with significant volumes of research into the causality of geoen지니어ed induced seismicity. However, little

research has been completed into the accumulative effects of frequent collocated events as a single geoen지니어ed event is assumed to be minor to cause any damage or degradation of the overlying soil structure [2–4].

There is an abundance of literature regarding the study of single seismic event loading [5, 6], as well as the behavior of partially saturated soils under cyclic loading [7, 8]. However, these studies assume that the loading from geoen지니어ed induced seismicity can be treated as isolated single events where the soil structure can fully recover before the next loading. Induced seismicity records from throughout the Central United States illustrate regions of close spatiotemporal small magnitude events, i.e., swarms, wherein any isolated event would typically be considered insufficient to cause any surficial expression of damage [2, 3]. However, the cumulative effect of the close spatiotemporal swarms is not well understood and can potentially cause a fatigue condition within the soil.

To study soil fatigue, this paper presents a modified damage equation to account for degradation of soil structure as a result of low frequency impulsive loading, i.e., a proxy for spatiotemporal small magnitude events.

2. Geoengineered Activity and Induced Seismicity

Concerns regarding induced seismic activity have increased exponentially since 2009 due to the increase in the number of induced earthquakes magnitude (M) of 3.0 or larger [9]. Overall, the number of earthquakes in the central United States, M3.0 or larger, increased showing an average of around 300 earthquakes per year from 2009 to January 2016 [10]. In 2009 there were approximately 29 M3.0 or larger earthquakes with a large increase between 2009 and 2016 increasing to 330 M3.0 or larger earthquakes per year in 2016 [9].

A study was conducted in the western boundary of the stable Canadian craton using the three largest ground motion events: M4.0 and M4.2 near Fort St. John (FSJ), British Columbia, and an M3.9 in close proximity to the Rocky Mountain House (RMH) in Alberta that occurred between 30 July 2014 and 9 August 2014. The location selected for the study is a low-to-moderate seismic region which poses a large risk to infrastructure as it may not have been designed to resist strong ground motions because of the low probability of naturally occurring strong ground motions in the area [11]. In early investigations, the authors determined that moderate induced events (M4-5) could damage nearby infrastructure due to the shallow focal depth that can result in concentrated strong ground motions. The study was conducted using a sparse seismograph network to record the two events at FSJ, located anywhere from 15 km to several hundred km away. The recordings from these three events of $M \sim 4$ were then used to examine their ground motions along with their weakening with distance. When this study was conducted, the M4.2 event was the largest event related to hydraulic fracturing in the world. The two events at FSJ were determined through intensity assessments, ground motion characteristics, and focal depth estimations to be likely induced from hydraulic fracturing. They occurred at shallow (2–5 km) depths that could be felt at distances over 200 km at a maximum intensity of M4.2 for the largest event. The third event at RMH was M3.9 and was the strongest event in Alberta in more than a decade. The focal depths were determined to be between 4 km and 8 km and the area shows no records of oil and gas drilling in recent years. The RMH event was felt by nearby residents and had reported intensity of M4-5 and caused a shutdown of a nearby gas plant and a power outage that lasted for many hours. All of these events were widely felt and had the potential to cause damage to infrastructure.

A study in Oklahoma [9] shows a definite increase in earthquakes beginning in 2009 with a steep increase from 2014 to 2015. Oklahoma does have a history of seismicity but recent studies show that it is highly unlikely that these are caused through natural fluctuations in the rates of earthquakes. Central Oklahoma has created cause for concern especially since it has had more than 60 earthquakes at M4.0 to M4.8 starting in 2009 to the middle of 2016. There were larger events recorded in the same timeline that are currently under investigation due to the potential damaging effects of the seismic activity associated with the magnitude. One

major earthquake was in Prague, Oklahoma, registered at M5.6 and was recorded [12] in November 2011. It destroyed 14 homes, injured two people, and buckled some parts of the highway and 17 other states could feel the tremble [13]. The largest earthquake documented was in Pawnee, Oklahoma, which was recorded at M5.8 causing substantial damage to infrastructure [9]. The M5.8 earthquake in Pawnee, OK, in September 2016, was the biggest recorded in the state and could possibly be related to wastewater injection.

There is statistical data that supports this conceptual model that shows the seismic activity linked to the distance between the basement and the injection point. This data provides regulators with information on how pore pressure develops through the knowledge of existing faults and ambient stress levels [14]. The study included a gas extraction process as studied in Groningen, The Netherlands. The process established for gas production compacts the reservoir that causes the build-up of stress along faults. Because of preexisting offsets, compartment reservoirs that have varying compaction levels meet along the faults. The compaction differences can increase the built-up stress at the faults which can in turn increase the occurrence of earthquakes [14]. Through subsidence measurements used to calibrate reservoir compaction in models, it identified seismicity concentrated in locations of high subsidence and compaction. These induced events are recorded after a reduced reservoir pore pressure by ~ 10 MPa with the outcome of an increase in rock stress that is of similar magnitude [14]. This conflicts with observations in Oklahoma that shows pressure disturbances of ~ 0.1 MPa initiating earthquakes. This shows that the crust is critically stressed and has a subset of faults that are near failure that can cause activation through a small amount of disturbance of stress [14].

In both of these activities, location and timing of the induced seismic activity are controlled by the distribution of space and the make-up of preexisting faults with existing stress conditions prior to subsurface work [14]. The current assumption regarding the size of induced events is that failures from induced activity are confined within the volume of rock that is affected by changes in stress of fluid pressure. However, recent studies by Van der Elst et al. [15] and Galis et al. [16] contradict this assumption and show that earthquakes induced from human activity could potentially fail outside of the volume that is affected. So that size of the induced earthquake can be manipulated through preexisting natural fluctuations of stress along the fault similar to natural events [14]. In either case, evidence suggests the need to understand preexisting faults as well as their stress level. Mitigation measures need to include both operational parameters, i.e., volume produced and volume injected, but must also include knowledge of the status of faults within the subsurface. This can be identified through hydromechanical modeling, operation parameters calibrated by independent measures through the use of InSAR to identify surface deformations [14].

A study was conducted by Zalachoris and Rathje [17] to develop ground motion models (GMMs) for small to moderate sized, potentially induced earthquake events in Texas, Oklahoma, and Kansas. The team created a database

with events with epicenters in those specific locations through the use of the Incorporated Research Institutions for Seismology (IRIS), 2018. Events that had at least 3 ground motions and at magnitudes that were greater than 3.0 were used for this effort which included 4,528 ground motions that were recorded during 376 events with hypocentral distances at less than 500 km. In an effort to quantify site amplifications, the team used the P-wave seismogram method that uses theoretical wave propagation considerations as well as recordings from seismic stations to estimate the VS30 at 251 seismic station locations within the defined area. In addition, the team investigated the relationship between geologic conditions and VS30 estimates at each location. This new model predicts smaller ground motions than other models and predicts an increase in ground motions at hypocentral distances less than or equal to 20 km. The newly scaled VS30 was determined to be weaker than other models and less amplified at VS30 <600 m/s [17]. It should be noted that there is an abundance of research into the source initiation and spectral characteristics of induced seismicity (see, e.g., [18–20]).

There have been several notable studies investigating the seismic vulnerability of structures to induced seismicity (see, e.g., [21–25]). These studies illustrate that there exists the potential for structural susceptibility for moderate to slight damage from induced seismicity. While the severity of the potential damage to structures from induced seismic events may not be as significant as HAZUS models based on the New Madrid Seismic Zone, these results clearly indicate that the potential damage is not insignificant. To further illustrate damage potential on structures from the increase in seismicity in parts of the central United States, a recent study by Liu et al. [25] identified that nonstructural components of structures have the potential to sustain damage from induced events as well as increased risk towards potential building collapse. In particular, Chase et al. [22] indicated that in the case of light-frame wood structures the structural damage and fragility did not seem to be accumulating with sequential seismic loadings. Liu et al. [25] calculated life-safety risk from the USGS 2016 one-year seismic hazard model as well as the fragility curves that are defined in the 2015 NEHRP (National Earthquake Reduction Program) Provisions. These results indicate that life-safety risks for modern buildings, in areas that are close to active induced seismic zones, have the potential to exceed the risks calculated from the 2015 NEHRP provisions' report that considers natural seismicity alone [25]. Therefore, if non-structural components can sustain damage and increase the potential risk of structural collapse from induced seismicity, then the logical question is as follows: "Can the fatigue of the subsurface yield similar increased risk?" Moreover, do sequential induced seismic events have an accumulative effect on the fragility or fatigue of the subsurface?

3. Laboratory Observations of Soil Fatigue for Impulsive versus Cyclic Loading

To determine the reliability of a system, an object is assessed to determine failure which is the lack of ability of a system to function normally under the same specified conditions for

the same amount of time [1]. In the case of soil mechanics, the point of failure is determined via an ultimate, or peak, failure condition, typically occurring when the strains exceed between 2% and 5%. However, failure of the soil structure can occur at a significantly lower strain [26, 27]. This loss of soil structure stiffness can result in small-scale collapses, i.e., small-strain compression, yielding, or settlement, as the soil element transitions to the next quasi-stable soil structure. If the excitation sources, e.g., impulses from pile driving, occur at a rate where the soil structure is continually forced to transition to the next quasi-stable state, the summation of the small-strain compression can cause superstructures, e.g., buildings and infrastructure, to exceed allowable design tolerances without causing an ultimate failure, e.g., structural collapse. This behavior defines the soil fatigue process. As subjective as failure is, soil fatigue is as well and far more difficult to identify as the experience which is usually known as the factor of safety is unknown [1]. This makes it difficult to quantify soil fatigue from close proximity spatiotemporal small magnitude events.

In a study conducted by the Engineering Research and Development Center, Geotechnical and Structures Laboratory (ERDC-GSL), laboratory tests were conducted to show the difference in dynamic behavior of near-surface partially saturated sand in reference to the potential for liquefaction from both cyclic and impulse loadings [28]. The outcome of these tests identifying the effects of near-surface soils with equivalent sinusoidal loads does not show the same strains as impulse loads to represent seismic waveforms that are irregular [28]. The 0.3% axial strain yield threshold is used based on a study conducted by [29] to identify significant limiting strain at the beginning of movement from pile strikes that began around 0.3% ϵ_{da} . The study consisted of a series of cyclic tests shown in Table 1 with the number of cycles needed to attain a certain double amplitude axial strain, ϵ_{da} , as shown in Figure 1. The results suggest that an exponential increase in the rate of strain starts to occur at around 0.3% ϵ_{da} , which is prior to the ultimate failure threshold of 5% ϵ_{da} . Additionally, it was observed that 47% of the completed tests reached 0.1% ϵ_{da} within the first cycle which suggests that the use of 0.1% as a yield initiation threshold would be overly conservative. Further tests identified that the capacity at 0.3% ϵ_{da} is about half of the difference of 0.1% and 5% ϵ_{da} and is about the mean of the distribution of the capacity-strain threshold, as shown in Figure 1 [29]. Therefore, a yield initiation, or fatigue, threshold of 0.3% ϵ_{da} as the maximum allowable fatigue stain for saturated dynamic loading is justified.

Taylor et al. [28] identify changes in dynamic behavior of near-surface partially saturated sand illustrating the strain potential from comparable cyclic and impulse loading wherein ten partially drained triaxial impulse and cyclic tests were conducted on poorly graded medium-fine beach sand with 24% saturation with a confinement of 10 kPa. An ultimate failure criterion of 2.5% axial strain was imposed based on samples tested through triaxial testing for a qualitative comparison of the loading requirements needed to cause an ultimate failure condition; see Figure 2 and Table 2 [28]. The test results showed no signs of liquefaction

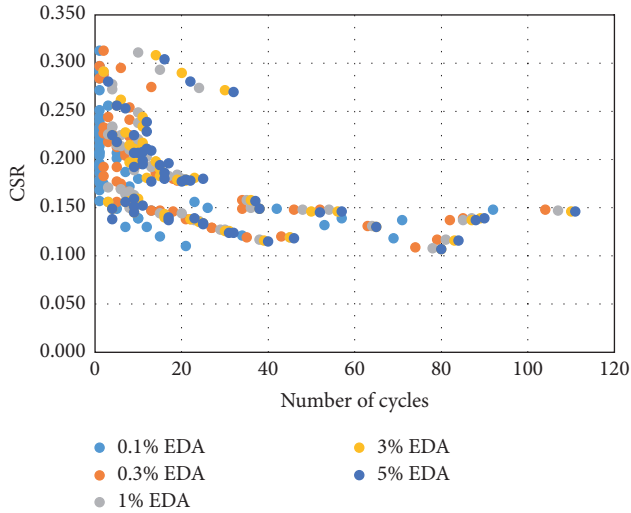


FIGURE 1: Data from Taylor [29] comparing number of cycles to initiate varying strains.

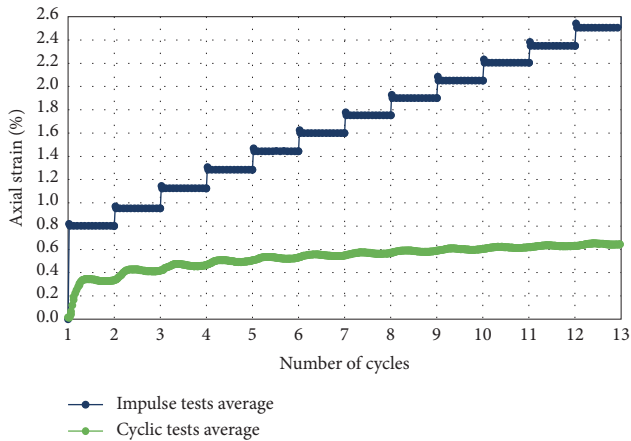


FIGURE 2: Comparison of impulse loading and uniform 1 Hz cyclic loading.

study cyclic and impulse loads with respect to near-surface seismic resistance. As shown by the data, cyclic loads, the increase in axial strain is nonlinear and has a logarithmic trend with a low number of cycles followed by a large increase at 50 cycles which identifies the potential for softening of the soil; however, this is not enough to reach liquefaction. On the other hand, impulse loads showed the increase in strain to be linear after an initial loading spike which identifies a constant strain [28].

4. Determining Damage Potential from Soil Fatigue

It is feasible through innovative processes to determine damage from soil fatigue that will allow engineers to identify when the system is not functioning as it should. Most studies are focused on the effects of cyclic soil degradation on soil strengths but neglect including potential damage from impulse loads. In addition, the damage accumulation effects from earthquake swarm

events are largely unknown. Newmark's [30] sliding block analysis touches on this concept but focuses on a single earthquake with a distinct number of times the acceleration exceeds the threshold. The focus of this paper is to consider multiple events in close proximity where each event has a single time the acceleration exceeds a threshold value. Based on Taylor et al. [28], it is important that cyclic and impulse loading tests are treated differently so equation (1) is introduced to identify a more accurate picture of liquefaction from induced seismic events. To consider the seismic design of a structure in this paper, a conceptual model is provided to analyze the equations presented in this paper.

The pseudostatic slope stability method is a commonly used procedure to determine slope stability under seismic loading that was introduced by Seed [31]. It was further improved by Bray and Travararou [32, 33] to better rationalize the identification of the seismic coefficient used in the analysis. This method uses a probabilistic seismic slope displacement model to determine slope stability under seismic loading. It uses the yield coefficient (k_y), the initial fundamental time period of the sliding mass (T_s), along with a degraded time period of spectral acceleration (S_a) $1.5T_s$, (M being the moment magnitude of the earthquake, and ε being the normal distributed random variable. Equation (1) represents the number of nonzero seismic displacement (D) events:

$$\begin{aligned} \ln(D) = & -1.10 - 2.83 \ln(k_y) - 0.333(\ln(k_y))^2 \\ & + 0.566 \ln(k_y) \ln(S_a(0.39)) + 3.04 \ln(S_a(1.5T_s)) \\ & - 0.244(\ln(S_a(1.5T_s)))^2 + 1.50T_s + 0.278 \\ & \cdot (M - 7) \pm \varepsilon. \end{aligned} \quad (1)$$

The example presented in this paper is created as an example for potential settlement from earthquake swarm events on a standard office building. The below slope stability analysis was completed through the use of the Seismic Landslide Movement Modeled using Earthquake Records (SLAMMER) program created for the USGS [34]. The program is used to analyze permanent deformations of slopes to identify how they behave during an earthquake. The Bray and Travararou [32] method was used for this analysis with the use of existing data incorporated into the SLAMMER system as well as assumptions that were used to calculate displacement. Using the data included in the SLAMMER system, shown in Figures 3 and 4, the below record was used as a sample product for the calculations used in the Bray and Travararou flexible (coupled) method with a modification of the earthquake magnitude from M7 to M4 to represent the potential for damage at small magnitudes [34].

The Bray and Travararou flexible coupled method was selected to estimate permanent displacement from a single deterministic event or the probability of exceeding specific permanent displacements [34]. The flexible analysis estimates the nonzero displacement as well as the probability of

TABLE 2: Test results from equivalent cyclic and impulse loading [4].

Specimen	Test program	Initial water content (%)	Posttest water content				Number of cycles to 2.5% ϵ_a
			Top (%)	Middle (%)	Bottom (%)	Average (%)	
SP200-I-1	Impulse	5.53	4.20	6.24	7.63	6.02	13
SP200-I-2	Impulse	5.51	4.87	5.89	6.83	5.86	11
SP200-I-3	Impulse	5.55	4.77	5.77	7.77	6.10	16
SP200-I-4	Impulse	5.54	4.69	5.85	9.07	6.54	14
SP200-I-5	Impulse	5.56	4.75	5.85	6.92	5.84	11
SP200-I-6	Impulse	5.55	4.37	5.25	7.87	5.83	15
SP200-I-7	Impulse	5.37	4.95	5.89	7.49	6.11	16
SP200-I-8	Impulse	5.59	4.36	5.33	7.25	5.65	9
SP200-I-9	Impulse	5.55	4.86	5.63	7.99	6.16	10
SP200-I-10	Impulse	5.58	4.41	6.56	8.15	6.37	11
<i>Average</i>	<i>Impulse</i>	5.53	4.62	5.83	7.70	6.05	12
SP200-C-1	Cyclic	5.53	4.91	6.17	6.87	5.98	96
SP200-C-2	Cyclic	5.71	4.14	5.62	7.05	5.60	n/a
SP200-C-3	Cyclic	5.68	4.59	6.19	7.50	6.09	n/a
SP200-C-4	Cyclic	5.48	4.47	5.77	6.87	5.70	n/a
SP200-C-5	Cyclic	5.59	5.54	8.04	9.40	7.66	n/a
SP200-C-6	Cyclic	5.59	4.65	5.17	6.25	5.36	n/a
SP200-C-7	Cyclic	5.58	4.52	5.51	7.35	5.79	n/a
SP200-C-8	Cyclic	5.54	4.38	5.89	7.03	5.77	n/a
SP200-C-9	Cyclic	5.57	4.60	5.07	7.04	5.57	74
SP200-C-10	Cyclic	5.53	4.63	4.89	7.29	5.60	63
<i>Average</i>	<i>Cyclic</i>	5.58	4.64	5.83	7.27	5.91	n/a

The screenshot shows the SLAMMER software interface. At the top, there are menu options: Getting Started, Rigorous Analyses, Simplified Empirical Models, Manage/Add Records, Utilities, and User Guide. Below the menu, there are three steps: Step 1: Select records, Step 2: Select analyses, and Step 3: Perform analyses and view results. A search area is present with 'Search records by properties' and 'Select individual records' buttons. The 'Earthquake' dropdown is set to 'Cape Mendocino 1992' and the 'Record name' dropdown is set to 'CPM-000'. Below this, there is a 'Records selected (units as indicated above):' section with a table. The table has columns: Earthquake, Record, Magnitude, Arias intensity, Duration (s-95%), PGA, PGV, Mean period, Epicentral distance, Focal distance, Rupture distance, Focal mechanism, and Analyze. The selected record is 'Cape Mendocino ... CPM-000' with a magnitude of 7.1, Arias intensity of 5.958, and duration of 6.2. At the bottom, there are buttons for 'Group Manager', 'Clear table', 'Clear highlighted record(s)', and 'Go to Step 2: Select analyses'. A status bar at the very bottom indicates '1 of 1 records selected for analysis'.

FIGURE 3: Soil properties from SLAMMER.

zero displacement. Figure 5 shows the correlation of the yield coefficient to the median displacement from data shown in Table 3. The data shows little to no displacement based on the above parameters.

In an effort to identify soil fatigue from earthquake swarms and show that induced seismic events have shorter dominating peak accelerations as well as shorter durations (2) was modified from Allotey and Nagger [35] damage equation to replace

cyclic loading with impulse loading as well as adding an additional nonlinear stress dependent variable:

$$D = D(N, N_f(S)) = (N_f(S))^{\Theta(S)}, \quad (2)$$

where D is the constant stress-controlled loading, fatigue damage function that is assumed to be a single valued deterministic figure that is nondimensional, and nondecreasing part of the stress ratio under a given number of

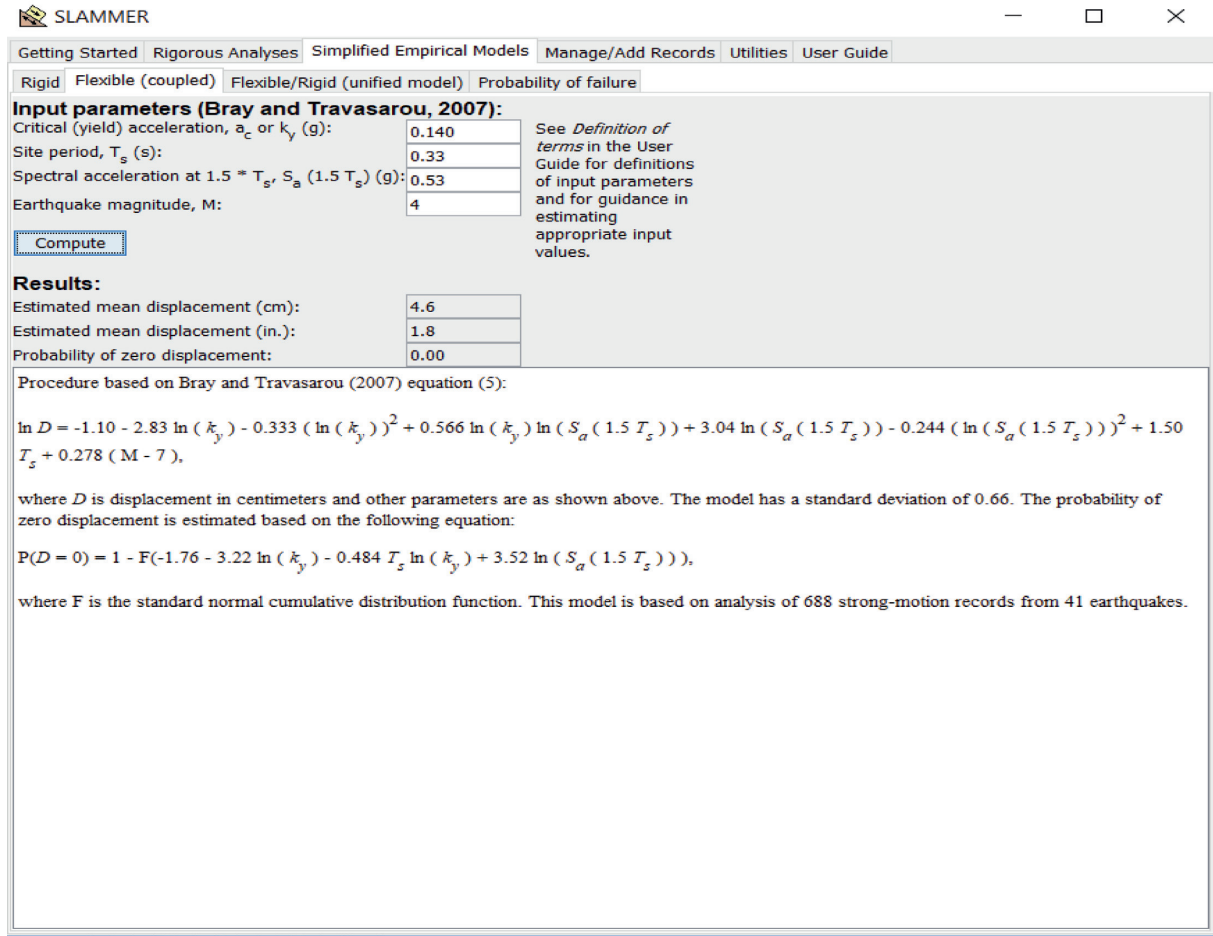


FIGURE 4: Bray and Travarasrou [32] displacement analysis from SLAMMER.

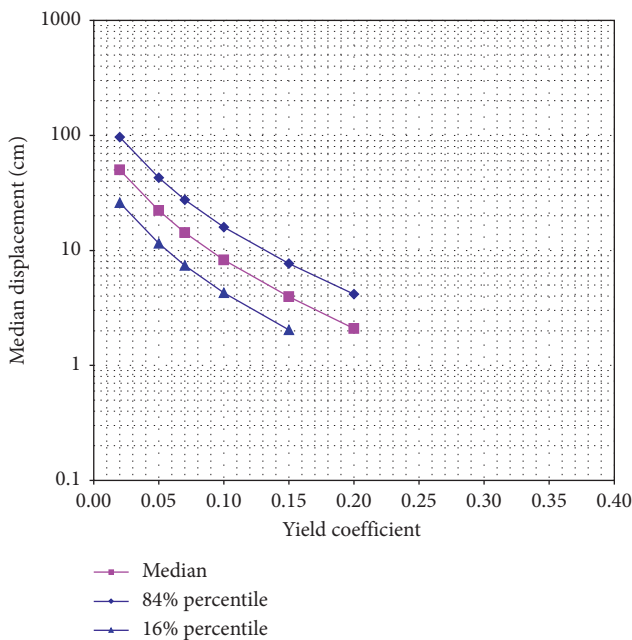


FIGURE 5: Bray and Travarasrou [32] comparison of displacement to yield coefficient.

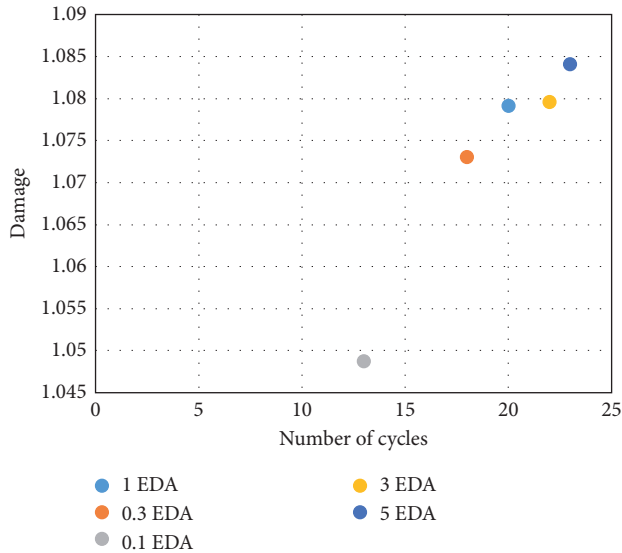
TABLE 3: Bray and Travarasrou dependence on k_y [32].

Dependence on k_y	P ($D = "0"$)	D (cm)	D_{median} (cm)	D_1 (cm)	D_3 (cm)
0.020	0.00	50.1	50.1	96.5	26.0
0.05	0.00	22.2	22.2	42.7	11.5
0.07	0.00	14.3	14.3	27.5	7.4
0.1	0.00	8.3	8.3	15.9	4.3
0.15	0.01	4.0	4.0	7.7	2.0
0.2	0.07	2.2	2.1	4.2	0.9
0.3	0.47	0.9	0.3	1.3	<1
0.4	0.82	0.4	<1	0.2	<1

cycles. N is the current number of cycles elapsed at the stress ratio S and $N_f(S)$ is the number of cycles of the stress ratio, S , to reach failure. Failure is defined as soil fatigue which is determined to be the magnitude of strain that a material can endure for a given number of cycles until a point of maximum strain where the soil no longer functions as intended. The stress ratio, S , is the initial mean effective confining stress and Θ is a nonlinear function with loading cycles that is a stress dependent variable in the applied stress (CSR) and confining pressure. As the stress levels vary, the damage rate

TABLE 4: Changes in D .

Number of cycles to failure (N)	ε_{da}	S	$\Theta(S)$	D
13	0.1	0.147	0.0735	1.048752
18	0.3	0.146	0.073	1.073081
20	1	0.144	0.072	1.079136
22	3	0.138	0.069	1.079640
23	5	0.139	0.0695	1.084126

FIGURE 6: Comparison of change in D to strain.

changes; depending on the sequence of loading, the life of fatigue can be less than or greater than one [36]. A threshold of 0.3% strain allows a comparison of cyclic loading vs impulse loading [29].

In contrast to the previous analysis from Bray and Travarasrou [32] that did not register damage, Table 4 and Figure 6 show that when being modified from cyclic loading to impulse loading, the damage rate changes at varying stress levels. These results identify degradation to the soil structure that might not be seen immediately but overtime can cause failure if left unchecked. This level of damage can be catastrophic in infrastructure that is constructed to a certain level based on the existing seismic design criteria. Using this method, the data identifies the potential failure from settlement due to earthquake swarms and should be considered in seismic evaluations.

5. Conclusion

Induced seismicity or induced earthquakes have become of great concern in recent years as rates of these events continue to grow. The inducement of seismicity from underground and surface mining, extraction of oil and gas, reservoir impoundments, and injection of fluids into geologic formations at the subsurface has been understood for some time now; however, these studies neglect incorporating the potential effects that these impulse loads may have on civil engineering systems. One of these potential effects is soil fatigue which can be considered a slow weakening of

material because of sources external to the structure that act upon the reliability of it. This should be considered in current evaluation standards and studied to determine if the structure can sustain impulse loading that occurs at shallow depths to identify issues with the foundation prior to failure.

The introduction of a new damage equation is an extension of the Allotey and Nagggers [35] model that modifies the loading criteria to impulse in lieu of cyclic to get a better depiction of soil degradation from induced seismic events. It was further modified to include a nonlinear function with loading cycles that is a stress dependent variable for both applied stress and confining pressure. The limitation of the Allotey and Nagger [35] model to determine soil degradation from induced seismic events was based on cyclic loads which do not depict strains that develop from impulse loads. Based on the reformulation of the equation, a better picture of potential damage effects to soils near the surface under impulse loading can be attained. This redundancy is needed as the existing process to access damage to infrastructure from induced seismicity is not adequate as it requires a better understanding of the failure modes and threshold limits within the Seismic Hazard and vulnerabilities structures that are not well equipped to survive seismic loading. Moreover, the difficulty in quantifying the seismic hazard for induced event continues as the hazard is not completely understood and changes in geoenvironmental locations, activities, and technologies are ever present. However, thorough innovative processes and further studies on this particular topic will allow for a better assessment and determination of detrimental degradation to be observed at the subsurface.

Data Availability

All data used to support the findings of this study can be obtained via the published references.

Conflicts of Interest

The authors declare that they have no conflicts of interest.

Acknowledgments

The authors would like to acknowledge M.D. Antwine, W.W. Berry, A.L. Cunningham, W.R. Rowland, and K.E. Winters of the US Army Engineer Research and Development Center for their assistance in experimental execution. The laboratory research was funded through the US Army, Acquisition, Logistics and Technology (ASAALT) and US Army Corps of Engineers.

References

- [1] M. E. Harr, *Reliability Based Design in Civil Engineering*, Dover Publications, Inc., New York, NY, USA, 1996.
- [2] O.-D. S. Taylor, A. P. Lester, and T. A. Lee, "Hazard and risk potential of unconventional hydrocarbon development-induced seismicity within the central United States," *Natural Hazards Review*, vol. 16, no. 4, 2015.
- [3] O.-D. S. Taylor, A. P. Lester, and T. A. Lee, "Unconventional hydrocarbon development hazards within the central United

- States: report 1, overview and potential risk to infrastructure,” Technical report ERDC/GSL TR-15-26, US Army Engineer Research and Development Center, Vicksburg, MS, USA, 2015.
- [4] O.-D. S. Taylor, A. Lester III, T. A. Lee, and M. H. McKenna, “Can small magnitude induced seismic events actually cause damage?” *Natural Hazards Challenges in Civil Engineering*, vol. 2018, Article ID 2056123, 5 pages, 2018.
 - [5] I. M. Idriss and R. W. Boulanger, *Soil Liquefaction during Earthquakes*, p. 237, Earthquake Engineering Research Institute, University of California, Davis, CA, USA, 2008.
 - [6] H. Seed and I. I. M. Bolton, “A simplified procedure for evaluating soil liquefaction potential,” in *Earthquake Engineering Research Center, Report No. EERC-70-9*, University of California, Berkeley, CA, USA, 1970.
 - [7] E. Eseller-Bayat, M. K. Yegian, A. Alshawabkeh, and S. Gokyer, “Liquefaction response of partially saturated sands I: experimental results,” *Journal of Geotechnical and Geoenvironmental Engineering*, vol. 139, no. 6, pp. 863–871, 2013.
 - [8] M. Okamura and Y. Soga, “Effects of pore fluid compressibility on liquefaction resistance of partially saturated sand,” *Soils and Foundations*, vol. 46, no. 5, pp. 695–700, 2006.
 - [9] P. Folger and M. Tiemann, *Human-Induced Earthquakes from Deep-Well Injection: A Brief Overview*, Congressional Research Service, Washington, DC, USA, 2016.
 - [10] J. L. Mahani, “Myths and facts wastewater injection, hydraulic fracturing, enhanced oil recovery, and induced seismicity,” *Seismological Research Letters*, vol. 86, no. 4, pp. 1060–1067, 2015.
 - [11] G. Atkinson, K. Assatourians, B. Cheadle, and W. Greig, “Ground motions from three recent earthquakes in Western Alberta and Northeastern British Columbia and their implications for induced-seismicity hazard in eastern regions,” *Seismological Research Letters*, vol. 86, no. 3, pp. 1022–1031, 2015.
 - [12] K. M. Keranen, H. M. Savage, G. A. Abers, and E. S. Cochran, *Potentially Induced Earthquakes in Oklahoma, USA: Links between Wastewater Injection and the 2011 M 5.7 Earthquake Sequence*, Geological Society of America, Boulder, CO, USA, 2013.
 - [13] A. Kuchment, “Drilling for earthquakes,” *Scientific American*, vol. 315, no. 1, pp. 46–53, 2016.
 - [14] T. Candela, B. Wassing, J. T. Heege, and L. Buijze, “How earthquakes are induced,” *Science*, vol. 360, no. 6389, pp. 598–600, 2018.
 - [15] N. J. Van der Elst, M. T. Page, D. A. Weiser, T. H. W. Goebel, and S. M. Hosseini, “Induced earthquake magnitudes are as large as (statistically) expected,” *Journal of Geophysical Research: Solid Earth*, vol. 121, no. 6, pp. 4575–4590, 2016.
 - [16] M. Galis, J. P. Ampuero, P. M. Mai, and F. Cappa, “Induced seismicity provides insight into why earthquake ruptures stop,” *Science Advances*, vol. 3, no. 12, Article ID eaap7528, 2017.
 - [17] G. Zalachoris and E. M. Rathje, “Ground motion model for small-to-moderate earthquakes in Texas, Oklahoma, and Kansas,” *Earthquake Spectra*, vol. 35, no. 1, pp. 1–20, 2019.
 - [18] F. Khosravikia, P. Clayton, and Z. Nagy, “Artificial neural network-based framework for developing ground-motion models for natural and induced earthquakes in Oklahoma, Kansas, and Texas,” *Seismological Research Letters*, vol. 90, no. 2, pp. 604–613, 2019.
 - [19] L. Quinones, H. R. DeShon, S. Jeong et al., “Tracking induced seismicity in the Fort Worth basin: a summary of the 2008–2018 north Texas earthquake study catalog,” *Bulletin of the Seismological Society of America*, vol. 109, no. 4, pp. 1203–1216, 2019.
 - [20] J. I. Walter, C. Frohlich, and T. Borgfeldt, “Natural and induced seismicity in the Texas and Oklahoma panhandles,” *Seismological Research Letters*, vol. 89, no. 6, pp. 2437–2446, 2018.
 - [21] M. Barba-Sevilla, B. Baird, A. Liel, and K. Tiampo, “Hazard implications of the 2016 Mw 5.0 cushioning, OK earthquake from a joint analysis of damage and InSAR data,” *Remote Sensing*, vol. 10, no. 11, p. 1715, 2018.
 - [22] R. E. Chase, A. B. Liel, N. Luco, and B. W. Baird, “Seismic loss and damage in light-frame wood buildings from sequences of induced seismicity,” *Earthquake Engineering and Structural Dynamics*, vol. 48, no. 12, pp. 1365–1383, 2019.
 - [23] F. Khosravikia, A. Potter, and V. Prakhov, *Seismic Vulnerability and Post-event Actions for Texas Bridge Infrastructure*, FHWA/TX-18/0-6916-1, Center for Transportation Research, Austin, TX, USA, 2018.
 - [24] F. Khosravikia, J. Kurkowski, and P. Clayton, “Fragility of masonry veneers to human-induced Central US earthquakes using neural network models,” *Journal of Building Engineering*, vol. 28, Article ID 101100, 2020.
 - [25] T. Liu, N. Luco, and A. B. Liel, “Increases in life-safety risks to building occupants from induced earthquakes in the Central United States,” *Earthquake Spectra*, vol. 35, no. 2, pp. 471–488, 2019.
 - [26] O.-D. S. Taylor, A. L. Cunningham, K. E. Martin, R. E. Walker, M. H. McKenna, and P. G. Kinnebrew, “Near-surface soils: ultrasonic near-surface inundation testing,” *Near Surface Geophysics*, vol. 17, no. 4, pp. 331–344, 2019.
 - [27] O.-D. S. Taylor, K. E. Winters, W. W. Berry, L. A. Walshire, and P. G. Kinnebrew, “Near-surface soils: self-supported unconfined drained sand specimens,” *Canadian Geotechnical Journal*, vol. 56, no. 3, pp. 307–319, 2019.
 - [28] O.-D. S. Taylor, K. E. Winters, W. W. Berry, and M. L. Zuzulock, “Dynamic failure potential of partially saturated sand under ultra-low confining pressures,” in *Proceedings of Geotechnical Earthquake Engineering and Soil Dynamics*, Austin, TX, USA, June 2017.
 - [29] O.-D. S. Taylor, *Use of an Energy-Based Liquefaction Approach to Predict Deformation in Silts Due to Pile Driving*, University of Rhode Island, South Kingstown, RI, USA, 2011.
 - [30] N. M. Newmark, “Effects of earthquakes on dams and embankments,” *Géotechnique*, vol. 15, no. 2, pp. 139–160, 1965.
 - [31] H. B. Seed, “Considerations in the earthquake-resistant design of earth and rockfill dams,” *Geotechnique*, vol. 29, no. 3, 1979.
 - [32] J. D. Bray and T. Travararou, “Simplified procedure for estimating earthquake-induced deviatoric slope displacements,” *Journal of Geotechnical and Geoenvironmental Engineering*, vol. 133, no. 4, pp. 381–392, 2007.
 - [33] J. D. Bray and T. Travararou, “Pseudostatic slope stability procedure,” in *Proceedings of the 5th International Conference on Earthquake Geotechnical Engineering*, pp. 10–13, Santiago, Chile, 2011.
 - [34] R. W. Jibson, E. M. Rathje, M. W. Jibson, and Y. W. Lee, *SLAMMER—Seismic Landslide Movement Modeled Using Earthquake Records*, US Geological Survey Techniques and Methods, Reston, VA, USA, 2014.
 - [35] N. Allotey and M. H. El Naggar, “A consistent soil fatigue framework based on the number of equivalent cycles,” *Geotechnical and Geological Engineering*, vol. 26, no. 1, pp. 65–77, 2008.
 - [36] W. V. Paepegem and J. Degrieck, “Effects of load sequence and block loading on the fatigue response of fiber-reinforced composites,” *Mechanics of Advanced Materials and Structures*, vol. 9, no. 1, pp. 19–35, 2002.

Research Article

Research on the Disaster-Inducing Mechanism of Coal-Gas Outburst

Fengxiang Nie,¹ Honglei Wang ,² and Liming Qiu ^{2,3}

¹School of Resources and Safety Engineering, China University of Mining and Technology (Beijing), Beijing 100083, China

²School of Civil and Environmental Engineering, University of Science & Technology Beijing, Beijing 100083, China

³Guangxi Key Laboratory of Disaster Prevention and Engineering Safety, Guangxi University, Nanning 530004, China

Correspondence should be addressed to Honglei Wang; wang_hl007@163.com and Liming Qiu; qiulm@ustb.edu.cn

Received 25 July 2019; Revised 29 October 2019; Accepted 4 November 2019; Published 29 March 2020

Academic Editor: Antonio Formisano

Copyright © 2020 Fengxiang Nie et al. This is an open access article distributed under the Creative Commons Attribution License, which permits unrestricted use, distribution, and reproduction in any medium, provided the original work is properly cited.

In China, coal-gas outburst is seriously affecting safety of the coal mine. To improve the safety status of underground coal mining, this work investigated the evolution process and occurrence mechanism of coal-gas outburst under the coupling action of stress and gas. Results show that increasing either gas pressure or in-situ stress can make coal destroy and destabilize, and the contribution of gas pressure to coal failure is twice that of in-situ stress. In ultradeep coal mining, coal-gas outburst may occur even under the condition of low gas pressure due to large in-situ stress. Moreover, the larger the mining depth is, the lower the gas index is required for disaster occurrence. The results have certain guiding significance for coal energy mining and the control of coal-gas outburst in deep coal mining.

1. Introduction

With the development of society, people's demand for mineral resources has gradually increased, and coal mining has gradually shifted to the deep part of the earth, leading to more and more dynamic disasters during the production, which poses a threat to the safety of energy and miners' lives [1, 2]. In recent years, with the increase of mining depth, coal and gas outburst disasters have begun to occur in some low gas mines, which contradicts previous research experience. This indicates that with the increase of mining depth, the mechanical properties of deep coal and rock have changed, and the mechanism of coal and gas outburst is different from that of shallow coal. The mechanism of coal and gas outburst in deep mining and low-gas condition is an urgent problem to be studied [3, 4].

The occurrence of coal dynamic disasters is mainly because of coal destabilization and failure caused by the gestation, development, propagation, and coalescence of microcracks. When coal and rock mass are damaged under load, different kinds of primary cracks gradually expand and penetrate. Rock failure caused by crack growth is an

important subject in rock mechanics research. Many scholars have performed a lot of research on the law of crack propagation in coal and rock. In the early 20th century, scholars have started to explore the production and propagation of cracks [5], and comprehensive experimental studies on the interaction of the gestation and development of cracks in rocks began in the middle of the last century and have achieved rich progresses [6–8]. Research results show that, under compressive load, the development of cracks, existing and newly gestated due to ground pressure inside rocks, first from the tips of these cracks and gradually propagate in the direction parallel to compressive direction [9]. When the cracks are short, their propagation is mainly under the control of the local stress field. With their expansion, they interact with adjacent microcracks, resulting in crack coalescence and eventual rock failure [10].

Studies on the mechanical properties and cracking behaviors of a single crack in the conditions of both dynamic and quasi-static strain rates have shown that shear cracks are dominant in the action of dynamic load while tensile cracks are dominant in the action of quasi-static load [11–16] In our

work, we observed three different types of cracks and believed that the fracturing processes of opened and closed cracks are similar and the friction along the crack direction strengthens the cohesion of coal, which are conducive to the coalescence of shear cracks. cracks' gestation and coalescent stresses, which are conducive to the coalescence of shear cracks.

In recent years, with the mining depth ever increasing, dynamic disaster manifested that themselves in the deep coal seams with low gas frequently. Under the complex environment of deep coal seam, coal is subjected to larger tectonic stress. Under the influence of mining or other disturbance, internal microcracks of coal undergo gestation, development, and coalescence, lead to the dynamic disasters, such as extensive roof and floor fractures, rock burst, coal and gas outburst, and others. Therefore, the occurrence of deep coal and rock dynamic disasters is the result of instability failure of gas-bearing coal under the combined action of high stress and gas. Many researchers, from the aspects of coal cracks gestation and propagation as well as the fracture mechanics, massively studied coal and gas outbursts and similar dynamic disasters are caused by coal destabilization. Qiu et al. [17] found that coal crack had fractal characteristics by comparing the photos of crack development in the process of coal failure under load. Li et al. [18] determined the physical laws that govern crack propagation in coal, a fracture mechanics model. Pre-existing cracks tend to branch towards the damage in the coal matrix while induced fractures tend to connect with other cracks nearby. According to crack propagation, the abutment pressure area in an underground mine was divided into six zones and the field data are consistent with the theoretical and experimental results. Kong et al. [19] studied the dynamic mechanical characteristics and the fracture mechanism of gas-bearing coal based on SHPB experiments and found that gas-bearing coal can produce more cracks under impact load. Zhao et al. [20], based on the theories of coal spherical shell failure, coal spallation, and coal powder pneumatic conveying, studied the flow state and transport mechanism of coal and gas outbursts. Chai et al. [21] comprehensively considered crack gestation and propagation evolution under both compressive and tensile shear stresses and introduced the initial damage tensor of cracks and the additive damage tensor after crack gestation and propagation into their user-defined constitutive model. Zuo et al. [22] separately established the axial crack closure model and the axial crack propagation model to study the variation characteristics of axial cracks with stress and strain. Zhao et al. [23] used a 3D mesoscopic monitoring software for dynamic evolution of the coal surface microstructure as the main research equipment to examine the propagation law of cracks on the coal surface under impact load. He and Wang [24] further analyzed the general law of the deformation and failure process of a composite from the aspects of both damaged crack evolution process and the mechanics of interactions of different media. Xie et al. [25] theoretically analyzed the role of mining the released coal seam in preventing coal and gas outburst based on the basic theory of fracture mechanics and further proposed a new method for preventing coal and gas outburst from both aspects of reducing the coal's stress intensity factor and improving the fracture toughness. Wang et al. [26] found the mechanical genesis of stress concentration at crack tips

from the angle of fracture mechanics and believed that rock (coal) and gas outburst is a dynamic phenomenon in which cracks fall in instability and failure when the stress intensity factor at crack tips reaches the fracture toughness of the rock.

Fedorchenko and Fedorov [27] consider the nonstationary, equilibrium velocity approach of the nonuniform environment mechanics and solved the coal and gas outburst problem. Zhao et al. [20] used the gas-solid plug flow formation analysis to propose a new view of the gas-distributed process as a reciprocating air knife of high pressure that cuts the ejected coal powders. Gao [28] studied the mechanism of coal and gas outburst in Shimen uncovering coal under the influence of the structure. Through laboratory simulation and numerical calculation, it was found that stress concentration in the process of protrusion induced by coal in the fault area under compressive stress increased the elastic potential of the coal body, and the gas caused the coal body to be unstable and thrown. Xu et al. [29] believed that coal and gas outburst are caused by the microelement destruction of coal and gas and thus constructed a coal-rock microelement model to analyze the damage of the coal-rock microbody region and the generation of protruding regions. Zhang [30] analyzed the dynamic mechanical characteristics of coal, the energy dissipation characteristics under dynamic load, and the effect of dynamic load on coal and gas outburst through various research methods and concluded that the combined effect of the sudden load input energy and the gas expansion energy leads to coal and gas outburst. Wang et al. [31] analyzed the effects of different stresses on coal and gas outbursts. It is believed that the in-situ stress can affect the outburst by affecting the gas emission intensity. However, under the conditions of deep high stress and low gas, the research on the influence of geostress and gas pressure on coal and rock dynamic disasters is rarely reported.

The process of damage and disaster evolution of coal and rock is extremely complex. Especially, the study of crack initiation, development, and structural instability fracture of gas-bearing coal and rock under stress-gas action in deep mine is insufficient. There is no consensus on the mechanism of coal and rock dynamic disasters in deep mining, especially on the mechanism of low-index outburst disasters. This is of great practical significance for the prevention and control of gas disasters under deep mining. According to the theory of rock fracture mechanics, we first analyze the types of crack growth and stress intensity factors of coal and rock. Then, based on the theory of strain energy density factor, the influence of in-situ stress, gas pressure, and physical and mechanical properties of coal on the internal crack growth of the coal body is studied. Finally, the mechanism of coal body failure and outburst occurrence at the working face is discussed and analyzed. Our conclusions can provide a theoretical basis for more accurate prediction of coal and gas outburst and more reasonable determination of predictive indicators.

2. Analysis on Crack Propagation in Gas-Bearing Coal under Load

2.1. Analysis of Crack Initiation Conditions of Coal and Rock Containing Gas. Irwin [32] divided simple cracks into three

types, as shown in Figure 1. Type I crack is open cracks, which means that under tensile stress perpendicular to the crack surface, the crack surface moves in the direction perpendicular to itself. Both Type II and Type III cracks are shear cracks, of which Type II cracks slip along the direction parallel to the crack strike, while Type III cracks slip along the direction perpendicular to the crack strike.

Feng [33] studied the stress distribution characteristics of the surrounding rock in the coal roadway and pointed out that in a certain range of roadway lateral displacement, the vertical stress of coal increases and the horizontal stress continues to decrease. The difference between the two will continue to increase. The surrounding rock gradually changed from three-way compression to only two-way compression, the stress balance state will be broken, and the deformation failure would occur. The research results of Wang et al. [34] show that the characteristics of coal macro-meso mechanical coupling failure and instability under uniaxial compression are consistent with the results of FLAC3D numerical simulation and the damage of coal observed in the field which will further explain how to simplify the failure process of coal on the coal wall in front of the working face to the problem of uniaxial compression. The vertical in-situ stress σ_m of deep seam is far greater than the minimum principal stress σ_3 . The stress state of the coal at the coal wall in front of the working face can be simplified into a uniaxial compression problem of the ground stress σ_m . Figure 2(a) shows the state of stress on the characteristic unit of the cracked coal, REV. From the figure, REV subjects to the uniaxial compression by σ_m and contains a crack with a length of $2a$ and an angle of $0 < \alpha < \pi/2$ to the direction of the maximum principal stress. The crack contains free gas with a pressure of P_0 . Because a large amount of adsorbed gas in the coal matrix will be desorbed in the form of free gas in the process of crack growth; the free gas pressure of P_0 will remain unchanged in the process of crack growth.

For the ground stress σ of the coal body at the coal wall in front of the face, we decompose it into a pair of normal stress σ_x and σ_y , and a pair of shear stress τ_{xy} and τ_{yx} . The long-axis direction of the crack is Y -axis and the short axis direction is X -axis. The equilibrium of normal stress σ_y , and shear stress τ_{xy} on the crack tip in the y -axis direction shows that the normal stress σ_{x-p} and the shear stress τ_{yx} in the x -axis direction are the main factors that cause the crack growth. When the crack surface is closed by pressure, i.e., $\sigma_x > P$, there is friction distribution on the crack surface, and the crack growth belongs to type II crack growth. The paper analyzes the influence of friction on K_{II} in formula (4). Generally, the fracture width of the coal body is millimeter or even nanometer, which is very small compared with the coal seam size. Therefore, in the analysis of the influence of the friction force generated by the decomposed normal stress on the crack growth, the friction force is equivalent to the uniform shear force in the infinite far field. Figure 2(b) shows the stress state of an elliptical crack in the Cartesian coordinate system set with its short and long axis directions corresponding to the x - and y -axis. The singular term of the stress component at the crack front in the polar coordinates is expressed as follows:

$$\begin{cases} \sigma_{\pi} = \frac{1}{2\sqrt{2\pi r}} \left[K_I \left(\cos \frac{\theta}{2} (3 - \cos \theta) \right) + K_{II} (3 \cos \theta - 1) \sin \frac{\theta}{2} \right], \\ \sigma_{\theta\theta} = \frac{1}{2\sqrt{2\pi r}} \cos \frac{\theta}{2} [K_I (1 + \cos \theta) + 3K_{II} \sin \theta], \\ \tau_{r\theta} = \frac{1}{2\sqrt{2\pi r}} \cos \frac{\theta}{2} [K_I \sin \theta + K_{II} (3 \cos \theta - 1)], \end{cases} \quad (1)$$

where K_I and K_{II} are the stress intensity factors of Type I and II cracks, respectively.

Set $h = P_0/\sigma_m$, and the equivalent normal stress, σ_N , on the surface of the crack inside the loaded gas-bearing coal is

$$\sigma_N = P_0 - \sigma_m \sin^2 \alpha = \sigma_m (h - \sin^2 \alpha). \quad (2)$$

Analysis of equations (1) and (2), one can find that

- (1) When $h \leq \sin^2 \alpha$, the gas pressure is less than the normal stress of the ground stress in the long-axis direction of the crack. Under the stress, the crack surface has to close, leading to crack closure and friction distribution on the crack surface. The crack propagation is a type II propagation with the equivalent shear stress on the crack surface, and τ_e can be computed by the following formula:

$$\tau_e = \sigma_m [\sin \alpha \cos \alpha + f_d (h - \sin^2 \alpha)], \quad (3)$$

where f_d is the friction coefficient of the crack tips and $\tau_e > 0$. The stress intensity factor of the crack is

$$\begin{aligned} K_I &= 0, \\ K_{II} &= \sigma_m [\sin \alpha \cos \alpha + f_d (h - \sin^2 \alpha)] \sqrt{\pi a}. \end{aligned} \quad (4)$$

Set $M = \sqrt{a/2r}$ and inserting equation (4) into equation (1) finds the circular stress as follows:

$$\sigma_{\theta\theta} = \frac{3}{2} M \sigma_m \cos \frac{\theta}{2} \sin \theta [\sin \alpha \cos \alpha + f_d (h - \sin^2 \alpha)]. \quad (5)$$

- (2) When $h > \sin^2 \alpha$, that is, the gas pressure is greater than the normal stress of the ground stress in the direction of the crack's long axis. The friction on the crack surface caused by the normal stress equals zero, and the equivalent shear stress, τ_e , on the crack surface is

$$\tau_e = \sigma_m \sin \alpha \cos \alpha. \quad (6)$$

The stress intensity factor of the crack is

$$\begin{aligned} K_I &= \sigma_m (h - \sin^2 \alpha) \sqrt{\pi a}, \\ K_{II} &= \sigma_m \sin \alpha \cos \alpha \sqrt{\pi a}. \end{aligned} \quad (7)$$

Putting equation (7) into equation (1), find the circular stress as follows:

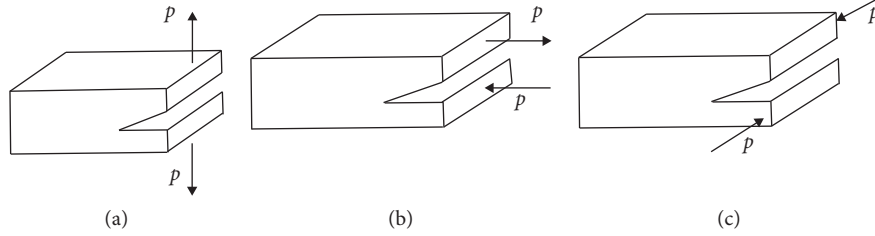


FIGURE 1: Three basic types of cracks Anderson [3]. (a) Type I. (b) Type II. (c) Type III.

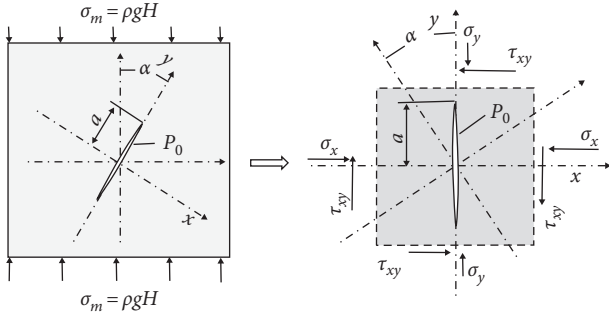


FIGURE 2: Stress state of cracks in front of the working face.

$$\sigma_{\theta\theta} = \frac{1}{2} M \sigma_m \cos \frac{\theta}{2} \left[(1 + \cos \theta)(h - \sin^2 \alpha) + 3 \sin \alpha \cos \alpha \sin \theta \right]. \quad (8)$$

Erdogan and Sih [35], based on their experimental observations, proposed the maximum circular tensile stress criterion and applied the maximum circular stress theory to explain the cracking initiation of two-dimensional Type I, Type II, and Type I-II composite cracks. The criterion holds that if a crack propagates in the direction θ corresponding to $\sigma_{\theta\theta\max}$, the direction satisfies the following conditions:

$$\frac{\partial \sigma_{\theta\theta}}{\partial \theta} = 0, \quad \frac{\partial^2 \sigma_{\theta\theta}}{\partial \theta^2} < 0. \quad (9)$$

The maximum circular stress theory holds that the crack propagation initiates when $\sigma_{\theta\theta\max}$ meets the following condition:

$$\sigma_{\theta\theta} = \big|_{\theta=\theta_0} = \sigma_{\theta\theta\max} > \sigma_c. \quad (10)$$

Equation (10) is the so-called initiation condition of crack propagation inside the loaded gas-bearing coal.

For closed cracks, the stress intensity factor is obtained from formula (4), while for the nonclosed crack, the stress intensity factor is obtained from formula (7). It can be seen from formulas (4) and (7) that the first part of the stress intensity factor K_{II} of the type II closed crack is the same as that of the type II nonclosed crack and is related to the shear stress τ_{yx} decomposed by the ground stress in the axial direction of the crack. The combined force of the normal stress decomposed from the ground stress in the direction of short axis and gas is related to the stress intensity factors K_{II} of closed crack and K_I nonclosed crack.

2.2. Analysis of Crack Propagation Type. Utilizing the values of stresses applied on the crack surface, τ_{xy} and σ_N , one can divide the crack propagation in the loaded gas-bearing coal into three types: Type I, Type II, and Type I-II composite cracks. Figure 3 shows the stress state and crack propagation type on the crack surface.

- (1) When $h \leq \sin 2\alpha$, $\tau_e = 0$ and the crack direction $\alpha = \pi/2$ and $h \leq 1$, $\tau_{xy} = 0$, $\sigma_N \leq 0$, that is, the gas pressure is less than the ground stress, the horizontal crack has $K_I = 0$ and $K_{II} = 0$. Thus, the crack surface is closed under the stress and there is a crack disturbing stress in the matrix.
- (2) When the crack direction $\alpha = 0$ and $\alpha = \pi/2$ and $h > 1$, $\tau_{xy} = 0$, $\sigma_N > 0$, that is, the vertical crack, or the horizontal crack at the time when gas pressure is greater than the ground stress, the crack has $K_I \neq 0$ and $K_{II} = 0$. Thus, the crack propagation belongs to Type I, and the crack starts to expand if it meets the maximum circular stress cracking condition, i.e., $\partial \sigma_{\theta\theta} / \partial \theta = 0$ and $\partial^2 \sigma_{\theta\theta} / \partial \theta^2 < 0$, from which, it follows

$$\theta_0 = 0. \quad (11)$$

Thus, the second-order partial derivative of $\sigma_{\theta\theta}$ with respect to θ is bigger than zero, which is the solution to this problem. Putting equation (11) into equation (5), we find the maximum circular stress as follows:

$$\sigma_{\theta\theta\max} = M \sigma_m (h - \sin^2 \alpha). \quad (12)$$

- (3) When $h \leq \sin^2 \alpha$, $\sigma_{xy} \neq 0$, $\sigma_N \leq 0$, and the oblique crack has $K_I = 0$ and $K_{II} \neq 0$, the gas pressure is less than the normal stress of the ground stress in the long axis direction of the crack. Thus, the crack surface is subjected to stress and the crack in its expanding process will produce a friction against crack propagation. The crack propagation belongs to Type II, and the crack that begins to expand needs to meet the maximum circular stress cracking condition, i.e., $\partial \sigma_{\theta\theta} / \partial \theta = 0$ and $\partial^2 \sigma_{\theta\theta} / \partial \theta^2 < 0$, from which it follows

$$\theta_0 = \arccos \frac{1}{3} = -70.53^\circ, \quad (13)$$

where $\theta = -\arccos(1/3)$ can make the second-order partial derivative of $\sigma_{\theta\theta}$ with respect to θ bigger than zero. Thus, $\theta = -\arccos(1/3)$ is the solution to this problem. Inserting

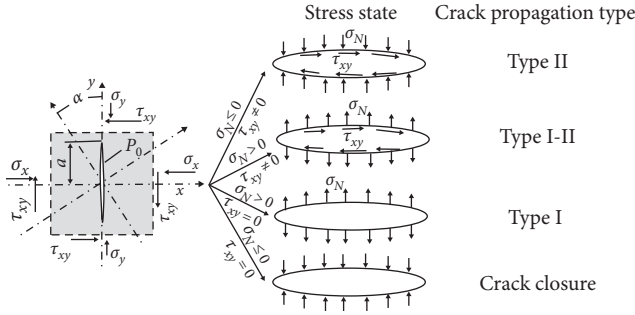


FIGURE 3: Crack stress state and crack propagation type.

equation (13) into equation (5), we find the maximum circular stress:

$$\sigma_{\theta\theta} = \frac{2}{\sqrt{3}} M \sigma_m [\sin \alpha \cos \alpha + f_d (h - \sin^2 \alpha)]. \quad (14)$$

- (4) When $h > \sin 2\alpha$, $\tau_{xy} \neq 0$, and $\sigma_N > 0$, that is, the gas pressure greater than the normal stress of the ground stress in the long axis direction of the crack and the oblique crack has $K_I \neq 0$ and $K_{II} \neq 0$. Thus, the crack that begins to propagate needs to satisfy the maximum circular stress rupture condition, that is, $\partial \sigma_{\theta\theta} / \partial \theta = 0$ and $\partial \sigma_{\theta\theta} / \partial \theta < 0$, from which one finds

$$\cos \frac{\theta}{2} [K_I \sin \theta + K_{II} (3 \cos \theta - 1)] = 0. \quad (15)$$

The solution that makes the abovementioned equation be of physical significance is

$$\theta_0 = -2 \arctan \frac{\sqrt{1 + 8(K_{II}/K_I)^2 - 1}}{4(K_{II}/K_I)}. \quad (16)$$

Inserting equations (7) and (16) into equation (5), we find the maximum circular stress to be

$$\sigma_{\theta\theta \max} = \frac{1}{2} M \sigma_m \cos \frac{\theta_0}{2} [(1 + \cos \theta_0)(h - \sin^2 \alpha) + 3 \sin \alpha \cos \alpha \sin \theta_0]. \quad (17)$$

From equations (12), (14), and (17), clearly, the circular stress at the crack tips of the loaded gas-bearing coal is the function of the crack angle, α , and the relationship between the maximum circular stress at the crack tips and the crack angle is shown in Figure 4.

It can be seen from Figure 4 that the maximum circular stress at the crack tips shows a trend of increase before decrease with the increase of the angle between the crack direction and its maximum principal stress. According to the maximum circular stress criterion, when the maximum circular stress at the crack tip, $\sigma_{\theta\theta}$, is greater than the tensile strength of the coal body, σ_c , the crack of the coal body begins to expand, that is, for a certain stress state, if the presence of α_{\max} and α_{\min} makes the crack angle α satisfy $\alpha_{\max} < \alpha < \alpha_{\min}$, and the crack propagation starts.

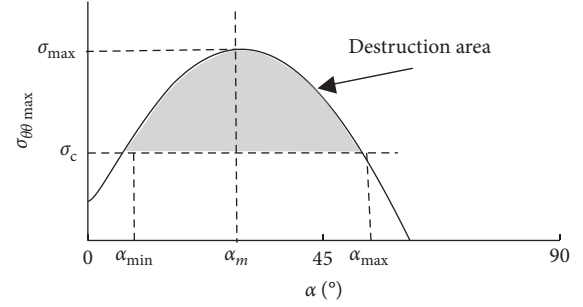


FIGURE 4: Relationship between circular stress at the crack tip and crack angle.

3. Process Analysis of Dynamical Disasters due to Gas-Bearing Coal Fracture

3.1. Analysis of Factors Influencing Maximum Circular Stress on Loaded Gas-Bearing Coal

3.1.1. Effect of Ground Stress on Maximum Circular Stress. At gas pressure $P = 1$ MPa and the friction coefficient $f_d = 0.6$, the relationship of the circular stress at the crack tips in the loaded gas-bearing coal to the ground stress is shown in Figure 5(a). From the figure, it is clear that the circular stress keeps constant at different ground stresses when the crack angle is 0° . As the angle increases, the circular stress begins to increase. When the angle reaches 29.4° , the circular stress simultaneously reaches its peaks. At this time, the circular stress corresponding to σ_m of 5 MPa, 10 MPa, 15 MPa, and 20 MPa is 2.33 MPa, 3.96 MPa, 5.60 MPa, and 7.23 MPa, respectively. When the angle further enlarges, the circular stress shows a tendency to decrease. When the angle is 58.8° , the stress remains the same. When the angle is greater than 58.8° , the lower the ground stress, the higher the circular stress. Data fitting finds that the maximum circular stress is positively correlated to the ground stress, which can be expressed as $\sigma_{\theta\theta \max} = 0.3269 \sigma_m + 0.6928$, as shown in Figure 5(b).

3.1.2. Effect of Gas Pressure on the Maximum Circular Stress. When the ground stress $\sigma_m = 10$ MPa and the friction coefficient $f_d = 0.6$, the relationship of the circular stress at the tips of cracks in the loaded gas-bearing coal to gas pressure is shown in Figure 6(a). From the figure, it is clear that when the crack angle is 0° , the maximum circular stress equals to the gas pressure, and as the angle increases, the circular stress begins to increase. When the gas pressure is at 0 MPa, 0.5 MPa, 1.5 MPa, and 3.0 MPa, the angle α_m corresponding to the maximum circular stress of 3.27 MPa, 3.62 MPa, 4.31 MPa, and 5.28 MPa is 28.7° , 28.9° , 30.2° , and 32.1° , respectively. When the angle further grows, the circular stress shows a downward trend. Data fitting finds that the maximum circular stress is positively correlated with the ground stress, which can be expressed as $\sigma_{\theta\theta} = 0.6761P + 3.2772$, as shown in Figure 6(b). The maximum circular stress has linear relationship with both ground stress and gas pressure, and the corresponding proportion coefficient are 0.3269 and

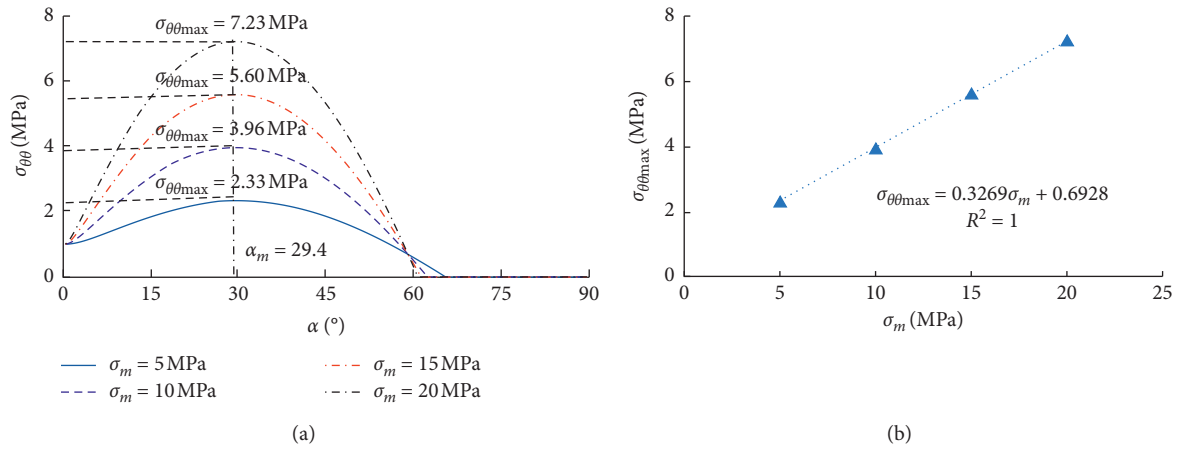


FIGURE 5: Effect of ground stress on maximum circular stress.

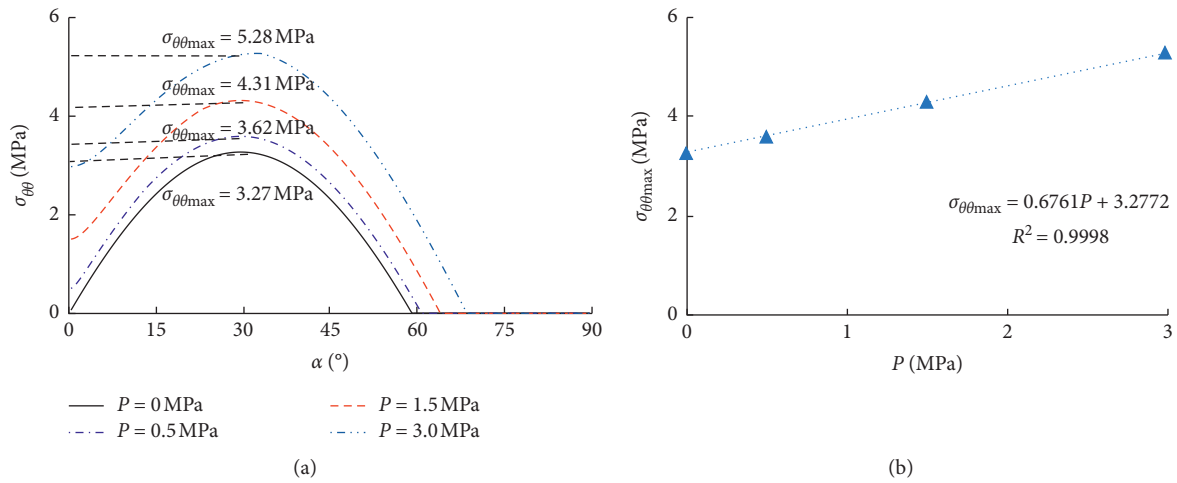


FIGURE 6: Effect of gas pressure on maximum circular stress.

0.6761, respectively. In other words, the destructive power of increasing the same gas pressure to the coal is about twice of that of increasing the ground stress. The maximum circular stress has a negative power function correlation with the friction coefficient. Therefore, the main factor affecting the maximum circular stress is the gas pressure of cracks inside the coal seam. At high ground stress, smaller gas pressure can lead to coal failure.

3.1.3. Effect of Friction Coefficient on the Maximum Circular Stress. Figure 7(a) shows the relationship of the circular stress at the tips of cracks in the loaded gas-bearing coal to the friction coefficient at ground stress $\sigma_m = 10$ MPa and gas pressure $P = 1$ MPa. From Figure 7(a), it is evident that when the crack angle is less than 20.4° , the crack propagation belongs to Type I-II composite. At this time, the maximum circular stress is independent of the friction coefficient. When the crack angle is greater than 20.4° , the maximum circular stress reduces with the friction coefficient increasing. When the friction coefficient is 0, 0.4, 0.6, and 0.8, the angle α_m corresponding to the maximum circular stress of

5.77 MPa, 4.37 MPa, 3.96 MPa, and 3.70 MPa is 45° , 34.5° , 29.4° , and 25.8° , respectively, and when the angle further increases, the circular stress shows a decreasing trend. Data fitting finds that the maximum circular stress is positively correlated to the ground stress, which can be expressed as $\sigma_{\theta\theta\max} = 5.4679 \exp(-0.422^* f_d)$, as shown in Figure 7(b).

3.2. Mechanism of Dynamic Disaster Evolution in Gas-Bearing Coal Seam

3.2.1. Analysis of Coal Fracture Process in Front of Working Face. A change in the state of stress inside a coal in front of the working face will in turn cause a change in both fracture and gas fields [36], as shown in Figure 8. Under the mining disturbance, the coal in front of the working face undergoes three stages, namely, elastic stress stage or stage I, ground stress and gas pressure failure stage or stage II, and gas-tearing coal stage or stage III [37]. In the stage I, as the working face advances, the two mutually perpendicular tangential stresses increase continuously and the radial stress decreases ceaselessly. During this time, the coal under their

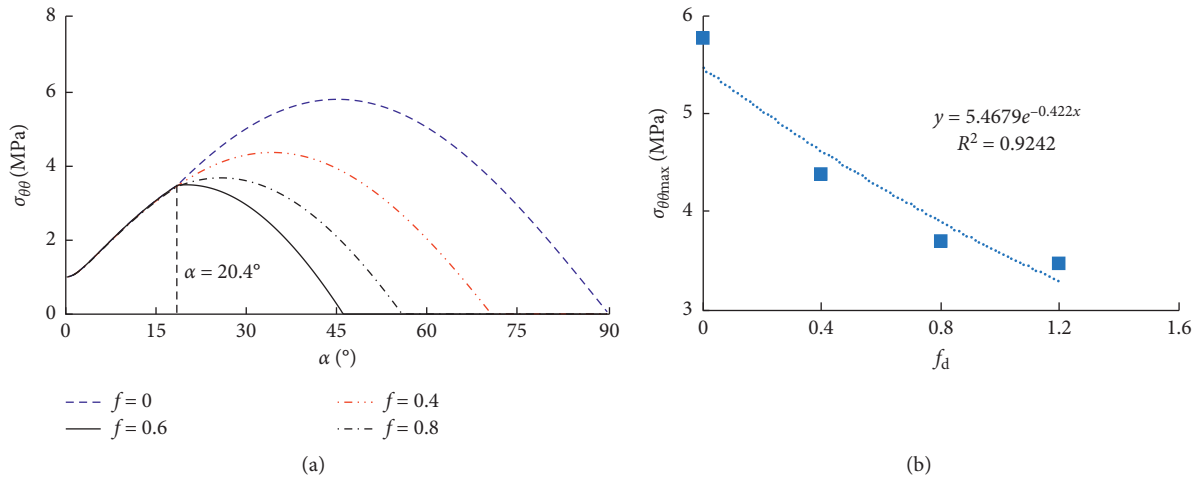


FIGURE 7: Effect of the friction coefficient on maximum circular stress.

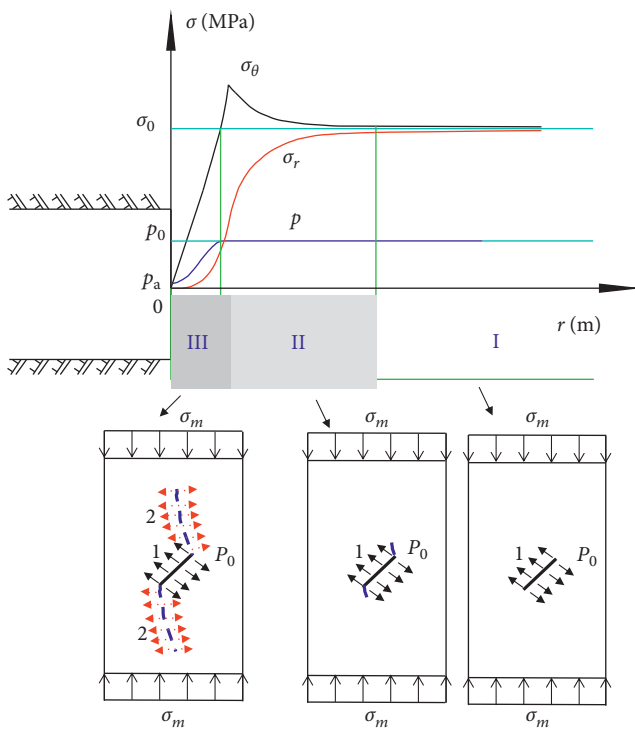


FIGURE 8: The stress state of coal in front of the working face.

actions is still in the elastic stress stage. When the tangential stress constantly increases and the radial stress continually reduces, the critical condition of crack growth is reached under the action of ground stress and gas pressure. Some of the cracks begin to expand, thus, part of the coal undergoes fracture, and the front of the working face enters the ground stress and gas pressure damage stage or stage II. Under the joint action of ground stress and gas pressure, the cracks inside the gas-bearing coal propagate and the presence of gas in the coal accelerates both tensile and shear damages of coal. Thus, coal is very prone to rapid crack expansion and the front of the working face enters gas-tearing coal (III) stage. After crack propagation, from equations (12), (14), and (17),

clearly, the ability of gas pressure to break the coal body is positively proportional to the square root of the crack length a , and the asymptote of crack expansion orients toward the direction of the maximum principal stress, as shown in Figure 8. The ground stress-induced tensile force $\sigma_{\theta\theta}$ gradually decreases, and the gas effect gradually strengthens in the later stage of coal crack propagation.

A shallow mine has smaller ground stress, thus it is necessary to combine with higher gas pressure so as to initiate crack propagation in coal [38]. Coal fracturing requires greater gas pressure to do work, that is, it needs higher gas pressure. When coal mining extends to the deep part of coal mines, the larger ground stress can initiate crack propagation, and the crack length can be extended to be longer. The capacity of the gas pressure to break the coal increases rapidly with crack expansion. Although it is also possible to crack coal under the action of lower gas pressure, the gas threshold to initiate dynamic phenomenon reduces.

3.2.2. Deep Stress-Gas Disaster Evolution Process. The geological conditions of mines with dynamic disasters are generally complex. Gao et al. [39], Song and Zhang [40], Jia et al. [41], Li et al. [42], and Qiu et al. [43] have studied the influence of faults, folds, and other geological structures on coal and gas outburst. The former research results show that in the abnormal geological structure, under the disturbance of mining, it can produce greater unbalanced force. In the deep mine, this kind of unbalanced stress phenomenon is more intense. Under the action of large unbalanced stress and gas pressure, the coal body breaks, and the unstable failure causes the coal-rock dynamic disaster. The evolution process of the disaster is shown in Figure 9.

- (1) Gestation stage: this stage experienced a series of events as the natural sedimentary formation, geological structure, and mining process of coal mass. The existence of geological structures such as faults affects the distribution of stress in the coal and changes its physical and mechanical properties, and

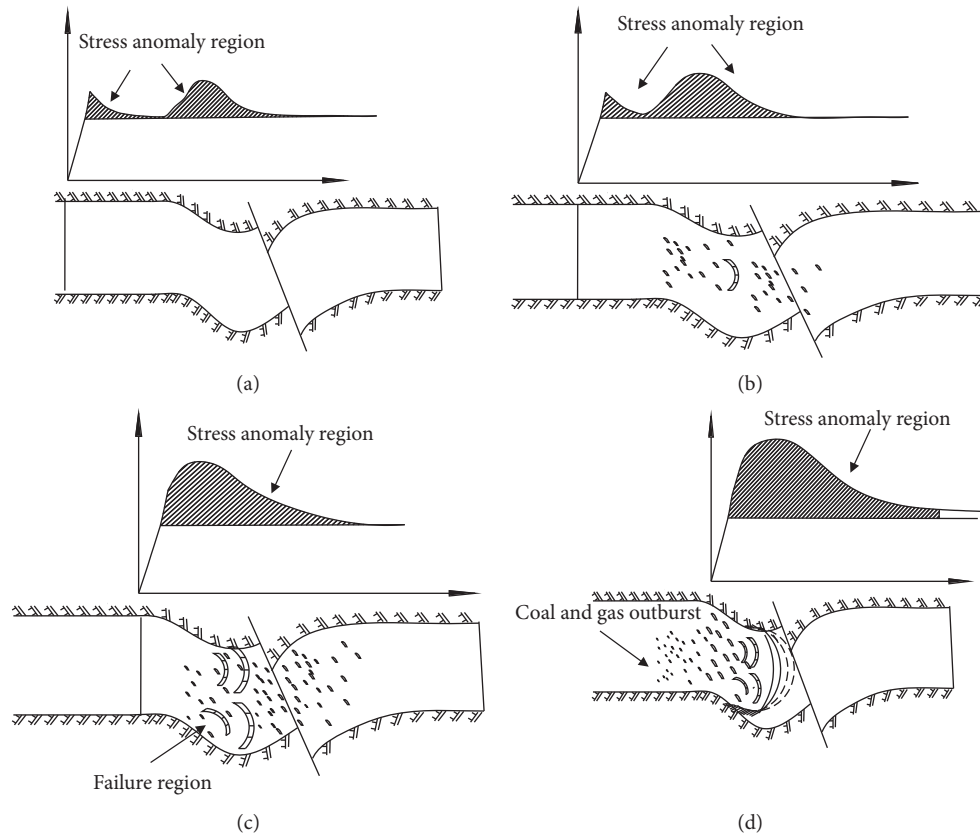


FIGURE 9: Evolution model of deep low gas dynamic disaster.

the mining operation destructs the mechanical balance in coal around the roadway. The strength, stress distribution, and gas pressure of coal in the coal seam are constantly changing, while the formed low-strength coal, abnormal stress distribution, and gas accumulated areas all provide a good breeding environment for the evolution of dynamic disasters in deep coal seams with low gas pressure.

- (2) Formation stage: under deep mining conditions, coal is subjected to a higher stress and accumulates more elastic energy. At this time, the coal seam has stable stress distribution and is in its equilibrium. The presence of faults and similar geological structures breaks the original stress distribution, forming the stress concentration in the fault and construction area, which reaches the maximum near the fault. In the coal seam-mining process, the mining-formed plastic zone continues to near the structure-formed plastic zone. The mining stress and tectonic stress are superimposed on each other, causing the stress state of the coal seam to be changed and the original stress balance system in the coal-rock mass to be broken. When the stress exceeds the ultimate strength of the coal, the coal will crack.
- (3) Expansion stage: the effect of gas on coal is generally divided into two aspects: the corrosive action

of adsorbed gas on the skeleton of coal and the mechanical action of free gas on the skeleton of coal. Both adsorbed and free gases make the strength of coal decrease and its brittleness increase. Meanwhile, as a fluid, free gas flows in micropores and microcracks of coal, making coal more susceptible to tensile damage. The effect of gas on coal is also affected by stress. When coal has a lower fracture degree, the effect of the low gas content on coal is not obvious; when coal has a higher fracture degree, fine coal under gas pressure will migrate outward. Deep coal mines have higher ground stress and accumulate a large amount of energy, which can provide a sufficient power source for the occurrence of coal dynamic disasters. Under the joint action of both stress and gas, the deformation and fracture of coal ever increases. Only when the pressure of gas in coal meets the condition for blowing crushed coal, gas-induced dynamic disaster will outburst.

- (4) End stage: after the occurrence of gas outburst and other dynamic disasters, coal accumulates massive elastic energy due to gas expansion, which cannot provide a sufficient power source for coal dynamic disasters, thus resulting in the termination of gas dynamic disasters.

4. Discussion

4.1. The Joint Effect of Different In-Situ Stress and Different Gas Pressure. Figures 5 and 6, respectively, show the influence of ground stress on the maximum hoop stress under the same gas pressure and the influence of gas pressure on the maximum hoop stress under the same in-situ stress. In coal mine, the ground stress and gas pressure are usually different, so it is necessary to discuss the effect of different ground stress and gas pressure. For this reason, four sets of simulation values of gas pressure and ground stress are designed, which are shown in Table 1. When the tensile strength of the coal sample is 1.15 MPa in the experiment, the variation curves of maximum circular stress at the tip of the internal crack of the four coal samples with the crack angle are analyzed by equations (12), (14), and (17), as shown in Figure 10. It can be seen from Figure 10 that when the ground stress is 5 MPa and the gas pressure is 0.1 MPa (the black line), the crack angle range that can make the stress exceed the bearing capacity of the coal body is about $10^{\circ}\sim 40^{\circ}$. Therefore, only a small number of coal body cracks can expand, the damage area is small, and it is difficult to have no significant damage. When the ground stress is 15 MPa and the gas pressure is 1.5 MPa (the orange line), the crack angle range that can make the stress exceed the bearing capacity of the coal body is about $0^{\circ}\sim 52^{\circ}$. When the ground stress is 30 MPa and the gas pressure is 3 MPa (the red line), although the ground stress exceeds the orange line, the crack angle range that can make the stress exceed the bearing capacity of the coal body is about $2^{\circ}\sim 49^{\circ}$ and the damage capacity is lower than the orange line. In conclusion, it is easy to explain the critical value of coal and gas disasters.

The larger in-situ stress in deep mine can fully break the coal body, and only a small gas pressure is needed to eject the broken coal body to generate dynamic phenomenon. However, the ground stress of the shallow mine is small, so it needs high gas pressure to break the coal body. Therefore, the effective gas critical value of coal and rock dynamic disaster early warning verified in the shallow part is not applicable to the deep mining mine, and the gas critical value of coal and rock dynamic disaster early warning in the deep mine should be smaller than that in the shallow mine [44–48].

4.2. Analysis of the Causes of Excessive Gas Generation in Coal and Gas Outburst Process. Coal and gas outburst is an extremely complicated mechanical process. It is generally believed that its development process is affected by comprehensive action of ground stress and gas [49]. Coal crack expansion is an inevitable step of coal and gas outburst [50]. In the process of coal and gas outburst, the amount of outburst gas is often much higher than the actual gas content of the prominent coal body, up to several tens or hundreds of times [51]. For example, the coal and gas outburst in the Daping Coal Mine in 2004 outbursts 1894 tons of rocks and about $25 \times 10^4 \text{ m}^3$ gas with average gas volume per ton of coal being $132 \text{ m}^3/\text{t}$. In China, the measured gas content in the coal seam of medium and high-grade coal and anthracite

TABLE 1: Modeling scheme.

Number	Gas pressure (MPa)	Load stress (MPa)
1	0.1	5
2	0.1	15
3	1.5	15
4	0.1	30

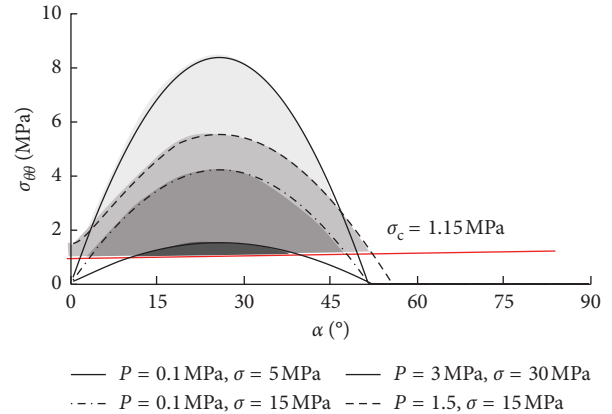


FIGURE 10: Variation of the maximum circular stress at the crack tip of four coal samples with the crack angle.

coal is $10\text{--}30 \text{ m}^3/\text{t}$, with the highest of $36 \text{ m}^3/\text{t}$, which is obviously lower than the amount of gas outburst [52]. Even considering the gas stored in the surrounding rocks in the process of gas production and gas outburst, the amount of gas present in the coal seam is far from being able to compensate for the difference between the gas content and the amount of Lan's adsorption.

Coal is a porous medium with pores and cracks, which contains a large number of macroscopic cracks and microscopic cracks and endogenous cracks and exogenous cracks [53]. In the process of coal formation, the gas generated per ton of coal is as high as $200\text{--}300 \text{ m}^3$, most of which can dissipate through coal's porous and fracture systems, and only part of it remains in the coal seam. The porous system of the coal seam is divided into closed pores-fractures and connected fractures. Because of the extremely poor permeability of the coal matrix, there are high gas pressure gradient between the closed pore fracture and the connected fractures, which forms favorable conditions for storage of high-pressure gas inside the closed pores and fractures. The directly measured gas pressure is the gas pressure in the opened pores, which is much lower than that in the closed pores and fractures.

The deformation and failure of coal is the result of cracks and fractures development. The new-formed cracks will connect some pores and fractures. The volume of the pores and fractures will increase after coal damaged under load, which indicates that under the action of ground stress and gas pressure, part of closed fissures communicate with open fractures. The closed fissures inside the coal seam can be transformed into open fissures, and the internal gas may be involved in coal and gas outburst processes such as coal body

crushing and throwing, which also explains that closed-fracture cracking is connected with the coal's pore and fracture system to release the internal gas in coal and gas outburst process under the action of high ground stress and high gas pressure. Therefore, in the process of outburst, the amount of outburst gas is often much higher than the measured coal-gas content. In the process of outburst prediction, the amount of gas generated by the fractured coal should also be comprehensively investigated together with analyzing the total amount of gas.

5. Conclusions

Gas dynamic disasters are still one of the important research directions of safety science, and the frequency of occurrence is increasing, which poses a threat to the safety of miners' lives and property. It is beneficial for controlling the occurrence of disasters to reveal stress-gas coupling function and the occurrence law of gas dynamic disaster under the condition of deep mining. The main conclusions of this paper are as follows:

- (1) The maximum circular stress at the crack tip showed a trend of decrease with the increase of the angle between the crack and the maximum principal stress and increases linearly with the increase of gas pressure and ground stress. The destructive capacity of increasing the same gas pressure on the coal body is about twice of that of the ground stress and had a negative power function relationship with the friction coefficient of coal.
- (2) In the process of dynamic disaster, crack propagation and penetration of coal under the joint action of ground stress and gas pressure is an important gestation stage. The superposition of large tectonic stress and mining stress in the geological structural zone can cause crack expansion and penetration, leading to fully broken of the coal body, which is prone to dynamic phenomena.
- (3) In the shallow mining process, small ground stress needs work together with a large gas pressure to make coal body cracks to expand and penetrate, resulting in dynamic disaster. When the mining extends to the deep ground, the large ground stress can initiate crack expansion. Thus, even under the action of lower gas pressure, it is also possible to break the coal body with reduced gas threshold of the dynamic phenomenon, which is prone to the occurrence of the dynamic phenomenon of the low index.
- (4) There are a large number of closed fissures inside the coal body. The high-pressure gas existing inside the closed fissure is an important source of excess gas in the process of coal and gas outburst. Therefore, in the process of predicting coal and gas outburst, the amount of gas generated by coal body fragmentation should be also comprehensively investigated except analysis of the total amount of gas.

Data Availability

The data used to support the findings of this study are available from the corresponding author upon request.

Conflicts of Interest

The authors declare that they have no conflicts of interest.

Acknowledgments

This work was supported by the Systematic Project of Guangxi Key Laboratory of Disaster Prevention and Structural Safety (2019ZDK013), the Fundamental Research Funds for the Central Universities (FRF-TP-18-081A1), and the China Postdoctoral Science Foundation (2018M641201).

References

- [1] B. Li, N. Li, E. Wang, X. Li, Y. Niu, and X. Zhang, "Characteristics of coal mining microseismic and blasting signals at Qianqiu coal mine," *Environmental Earth Sciences*, vol. 76, p. 722, 2017.
- [2] L. Qiu, E. Wang, D. Song et al., "Measurement of the stress field of a tunnel through its rock EMR field of a tunnel through its rock EMR," *Journal of Geophysics and Engineering*, vol. 14, no. 4, pp. 949–959, 2017.
- [3] T. L. Anderson, *Fracture Mechanics: Fundamentals and Applications*, CRC Press, Boca Raton, FL, USA, 2005.
- [4] X. He, X. Liu, B. Nie, and D. Song, "FTIR and Raman spectroscopy characterization of functional groups in various rank coals," *Fuel*, vol. 206, pp. 555–563, 2017.
- [5] A. Griffith, "VI the phenomena of rupture and flow in solids," *Philosophical Transactions of the Royal Society of London. Series A, Containing Papers of a Mathematical or Physical Character*, vol. 221, no. 582–593, pp. 163–198, 1921.
- [6] C. H. Park and A. Bobet, "Crack initiation, propagation and coalescence from frictional flaws in uniaxial compression," *Engineering Fracture Mechanics*, vol. 77, no. 14, pp. 2727–2748, 2010.
- [7] H. Lee and S. Jeon, "An experimental and numerical study of fracture coalescence in pre-cracked specimens under uniaxial compression," *International Journal of Solids and Structures*, vol. 48, no. 6, pp. 979–999, 2011.
- [8] J. Reinoso, P. Durand, P. Budarapu, and M. Paggi, "Crack patterns in heterogenous rocks using a combined phase field-cohesive interface modeling approach: a numerical study," *Energies*, vol. 12, no. 6, p. 965, 2019.
- [9] D. Song, E. Wang, L. Qiu, H. Jia, P. Chen, and M. Wei, "Response of coal rock apparent resistivity to hydraulic fracturing process," *Geomechanics and Engineering*, vol. 14, no. 6, pp. 581–588, 2018.
- [10] M. F. Ashby and S. D. Hallam, "The failure of brittle solids containing small cracks under compressive stress states," *Acta Metallurgica*, vol. 34, no. 3, pp. 497–510, 1986.
- [11] H. Li, S. Shi, B. Lin, J. Lu, Q. Ye, Y. Lu et al., "Effects of microwave-assisted pyrolysis on the microstructure of bituminous coals," *Energy*, vol. 187, Article ID 115986, 2019.
- [12] X. P. Zhou, H. Cheng, and Y. F. Feng, "An experimental study of crack coalescence behaviour in rock-like materials containing multiple flaws under uniaxial compression," *Rock Mechanics and Rock Engineering*, vol. 47, no. 6, pp. 1961–1986, 2014.

- [13] Y. Niu, Z. Li, E. Wang, R. Shen, Z. Cheng, X. Gao et al., "Study on characteristics of EP responding to coal mining," *Engineering Fracture Mechanics*, vol. 224, Article ID 106780, 2020.
- [14] B. Li, N. Li, E. Wang, X. Li, Z. Zhang, X. Zhang et al., "Discriminant Model of Coal Mining Microseismic and Blasting Signals Based on Waveform Characteristics," *Shock and Vibration*, vol. 2017, Article ID 6059239, 2017.
- [15] C. Zou, L. N. Y. Wong, J. J. Loo, and B. S. Gan, "Different mechanical and cracking behaviors of single-flawed brittle gypsum specimens under dynamic and quasi-static loadings," *Engineering Geology*, vol. 201, pp. 71–84, 2016.
- [16] C. H. Park and A. Bobet, "Crack coalescence in specimens with open and closed flaws: a comparison," *International Journal of Rock Mechanics and Mining Sciences*, vol. 46, no. 5, pp. 819–829, 2009.
- [17] L. Qiu, D. Song, X. He, E. Wang et al., "Multifractal of electromagnetic waveform and spectrum about coal rock samples subjected to uniaxial compression," *Fractals*, 2020.
- [18] L. Li, S. Yan, Q. Liu, and L. Yu, "Micro-and macroscopic study of crack propagation in coal: theoretical and experimental results and engineering practice," *Journal of Geophysics and Engineering*, vol. 15, no. 4, pp. 1706–1718, 2018.
- [19] X. Kong, E. Wang, S. Li, H. Lin, Z. Zhang, and Y. Ju, "Dynamic mechanical characteristics and fracture mechanism of gas-bearing coal based on SHPB experiments," *Theoretical and Applied Fracture Mechanics*, vol. 105, Article ID 102395, 2020.
- [20] W. Zhao, Y. Cheng, P. Guo, K. Jin, Q. Tu, and H. Wang, "An analysis of the gas-solid plug flow formation: new insights into the coal failure process during coal and gas outbursts," *Powder Technology*, vol. 305, pp. 39–47, 2017.
- [21] H. Chai, P. Cao, and Y. Zhao, "Implementation and application of constitutive model for damage evolution of fractured rock mass," *Chinese Journal of Geotechnical Engineering*, vol. 32, no. 7, pp. 1047–1053, 2010.
- [22] J. Zuo, Y. Chen, and H. Song, "Evolution of pre-peak axial crack strain and nonlinear model for coal-rock combined body," *Chinese Journal of Geotechnical Engineering*, vol. 39, no. 9, pp. 1609–1615, 2017.
- [23] H. Zhao, H. Zhang, and Z. Wang, "Study on effects of impact load on coal sample surface crack propagation characteristics," *Journal of China University of Mining & Technology*, vol. 47, no. 2, pp. 280–288, 2018.
- [24] T. He and L. Wang, "Research on damage evolution laws of rock-coal-rock combination based on particle discrete element model," *Safety in Coal Mines*, vol. 49, no. 7, pp. 205–208, 2018.
- [25] S. Xie, F. Zhao, and C. Chen, "Breaking mechanics analysis on mining protective seam to prevent coal and gas outburst," *Coal Science and Technology*, vol. 4, pp. 22–25, 2007.
- [26] Z. Wang, Y. Li, and R. Li, "Fault gas outburst in roadway and determination of critical thickness of prevention rock pillar," *Chinese Journal of Underground Space and Engineering*, vol. 11, no. 4, pp. 1060–1065, 2015.
- [27] I. A. Fedorchenko and A. V. Fedorov, "Gas-dynamic stage of the coal and gas outburst with allowance for desorption," *Journal of Mining Science*, vol. 48, no. 1, pp. 15–26, 2012.
- [28] K. Gao, *Similar Simulation Test of Induce Coal and Gas Outburst during the Uncovering Tectonic Soft Coal by Crosscut*, Anhui University of Science and Technology, Huainan, China, 2013.
- [29] M. G. Xu, K. Q. Dong, and Y. C. Dong, "Mechanism of coal and gas outburst with microelement destruction," *Journal of Xi'an University of Science and Technology*, vol. 34, no. 3, pp. 249–254, 2014.
- [30] W. Q. Zhang, *Study on Mechanical Property of Soft Coal under Impact Load and its Effect to Coal and Gas Outburst*, Anhui University of Science and Technology, Huainan, China, 2015.
- [31] H. Wang, B. Zhang, L. Yuan, G. Yu, and W. Wang, "Gas release characteristics in coal under different stresses and their impact on outbursts," *Energies*, vol. 11, no. 10, p. 2661, 2018.
- [32] G. R. Irwin, "Analysis of stress and strains near the end of a crack extension force," *Journal of Applied Mechanics*, vol. 24, pp. 361–364, 1957.
- [33] Y. L. Feng, "Study on surrounding rock stress distribution characteristics and sidewall failure mechanism of seam gateway," *Coal Science and Technology*, vol. 48, no. 1, pp. 183–191, 2018.
- [34] J. Wang, Z. Wang, and S. Yang, "A coupled macro-and meso-mechanical model for heterogeneous coal," *International Journal of Rock Mechanics and Mining Sciences*, vol. 94, pp. 64–81, 2017.
- [35] F. Erdogan and G. C. Sih, "On the crack extension in plates under plane loading and transverse shear," *Journal of Basic Engineering*, vol. 85, no. 4, pp. 519–525, 1963.
- [36] L. Qiu, Z. Li, E. Wang et al., "Characteristics and precursor information of electromagnetic signals of mining-induced coal and gas outburst," *Journal of Loss Prevention in the Process Industries*, vol. 54, pp. 206–215, 2018.
- [37] Y. Niu, X. Song, Z. Li, E. Wang, Q. Liu, Z. Zhang et al., "Experimental study and field verification of stability monitoring of gas drainage borehole in mining coal seam," *Journal of Petroleum Science and Engineering*, Article ID 106985, 2020.
- [38] J. Liu, *Experimental Study on the Evolution Process and Mechanism of Coal and Gas Pressure*, China University of Mining and Technology, Beijing, China, 2014.
- [39] M. Gao, S. Zhang, J. Li, and H. Wang, "The dynamic failure mechanism of coal and gas outbursts and response mechanism of support structure," *Thermal Science*, vol. 23, no. Suppl.3, pp. 867–875, 2019.
- [40] W. H. Song and H. W. Zhang, "Research on the mechanism of tectonic stress field evolution for coal and gas outburst," *Applied Mechanics and Materials*, vol. 325–326, pp. 1352–1356, 2013.
- [41] T. Jia, Z. Feng, G. Wei, and Y. Ju, "Shear deformation of fold structures in coal measure strata and coal-gas outbursts: constraint and mechanism," *Energy Exploration & Exploitation*, vol. 36, no. 2, pp. 185–203, 2018.
- [42] W. Li, T. Ren, A. Busch et al., "Architecture, stress state and permeability of a fault zone in Julishan coal mine, China: implication for coal and gas outbursts," *International Journal of Coal Geology*, vol. 198, pp. 1–13, 2018.
- [43] L. Qiu, D. Song, Z. Li, B. Liu, and J. Liu, "Research on AE and EMR response law of the driving face passing through the fault," *Safety Science*, vol. 117, pp. 184–193, 2019.
- [44] Q. Tu, Y. Cheng, P. Guo, J. Jiang, L. Wang, and R. Zhang, "Experimental study of coal and gas outbursts related to gas-enriched areas," *Rock Mechanics and Rock Engineering*, vol. 49, no. 9, pp. 3769–3781, 2016.
- [45] J. Sobczyk, "A comparison of the influence of adsorbed gases on gas stresses leading to coal and gas outburst," *Fuel*, vol. 115, pp. 288–294, 2014.
- [46] J. Cao, H. Sun, B. Wang et al., "A novel large-scale three-dimensional apparatus to study mechanisms of coal and gas outburst," *International Journal of Rock Mechanics and Mining Sciences*, vol. 118, pp. 52–62, 2019.
- [47] H. Li, Z. Feng, D. Zhao, and D. Duan, "Simulation experiment and acoustic emission study on coal and gas outburst," *Rock*

- Mechanics and Rock Engineering*, vol. 50, no. 8, pp. 2193–2205, 2017.
- [48] C. Zhang, J. Xu, G. Yin, S. Peng, Q. Li, and Y. Chen, “A novel large-scale multifunctional apparatus 21 to study the disaster dynamics and gas flow mechanism in coal mines,” *Rock Mechanics and Rock Engineering*, vol. 52, no. 8, pp. 2889–2898, 2019.
- [49] Q. Hu and G. Wen, *Mechanical Mechanism of Coal and Gas Outburst*, Science Press, Beijing, China, 2013.
- [50] Z. Zhao and Y. Tan, “Study on the mechanism of crack propagation of coal under gas pressure,” *Mining Research and Development*, vol. 6, pp. 37–39, 2008.
- [51] B. B. Beamish and P. J. Crosdale, “Instantaneous outbursts in underground coal mines: an overview and association with coal type,” *International Journal of Coal Geology*, vol. 35, no. 1–4, pp. 27–55, 1998.
- [52] P. D. Gamson, B. B. Beamish, and D. P. Johnson, “Coal microstructure and micropermeability and their effects on natural gas recovery,” *Fuel*, vol. 72, no. 1, pp. 87–99, 1993.
- [53] Z. Feng and Y. Zhao, “Control of rock fissure scale on its deformation and failure,” *Chinese Journal of Rock Mechanics and Engineering*, vol. 27, no. 1, pp. 78–83, 2007.

Research Article

Mitigation Method of Rockfall Hazard on Rock Slope Using Large-Scale Field Tests and Numerical Simulations

Jinam Yoon,¹ Hoki Ban ,² Youngcheol Hwang,³ and Duhee Park ¹

¹Department of Civil and Environmental Engineering, Hanyang University, Seoul 04753, Republic of Korea

²Department of Civil Engineering, Kangwon National University, Samcheok 25913, Republic of Korea

³Department of Civil Engineering, Sangji University, Wonju 26339, Republic of Korea

Correspondence should be addressed to Hoki Ban; hban@kangwon.ac.kr and Duhee Park; dpark@hanyang.ac.kr

Received 26 September 2019; Accepted 21 November 2019; Published 23 March 2020

Guest Editor: Young-Suk Song

Copyright © 2020 Jinam Yoon et al. This is an open access article distributed under the Creative Commons Attribution License, which permits unrestricted use, distribution, and reproduction in any medium, provided the original work is properly cited.

This paper presents the mitigation of rockfall hazard on the large-scale rock slope using the field tests with numerical simulation. To this end, field tests including the pendulum test and real rock falling tests were performed to investigate the rock movements such as rotation, repulsion, and speed. In the simulation, the validation of the developed model followed by calibration processes was made on the field tests. In this study, a simple and new method was proposed to mitigate the rockfall hazard using the so-called sand pool made by ditching and then filling sand where the rock should be stopped or arrested. The results showed that the sand pool method was very effective and economical.

1. Introduction

The rock falling occasionally causes a disastrous situation when it falls down to the road and facilities. The conventional methods to protect or mitigate rockfall hazard are concrete barrier (rigid) or rockfall fence (flexible). These methods have somewhat drawbacks in terms of maintenance. For concrete barrier, it can be severely damaged when the rock hits continuously the barrier. In addition, the construction/reconstruction cost of concrete barrier is high [1]. For the rockfall fence, even though construction cost is comparatively low, the capability of protection is low and perforation of net may occur, the so-called bullet effect [2, 3, 4]. In this study, a simple and new method was introduced to mitigate the rockfall hazard using the so-called sand pool. The sand pool was made by ditching and then filling sand where the rock should be stopped or arrested. The capability of the sand pool to stop or arrest the rockfall was examined. Based on its capability, the size of the sand pool was determined. In order to examine the capability of the sand pool, the integrated field tests with numerical simulation were performed. In the field tests, a total of four pendulum tests using two large cranes and a concrete ball (1 ton) were performed to obtain the restitution

coefficient of rock. The rock falling tests were also conducted on the real rock slopes to investigate the movements of rock such as rotation, repulsion, and speed. The rock was pushed at top of the slope which has 214 m of height and 230 m of length in the vertical direction and horizontal direction, respectively. When the rock falls, two major parameters governing the rock movement are the friction coefficient and restitution coefficient. As stated earlier, the restitution coefficient was obtained from the pendulum tests, whereas the friction coefficient was determined from the calibration process of numerical simulation on the representative slope. After calibration processes, the validation of the developed model was made on different sections of slopes where the field tests were performed. The results showed that the proposed sand pool method was very effective and economic. In addition, maintenance can be simply done by removing the arrested rocks and replacing sand without compaction.

2. Field Tests

Two field tests such as the pendulum test and rock-dropping test were conducted in the field. The details of each test are described in the following subsections.

2.1. Pendulum Test. A total of four pendulum tests using two large cranes and a concrete ball (1 ton) were performed to obtain the restitution coefficient of rock as shown in Figure 1.

Two out of four tests were performed on the upper part of the rock wall, and the others were done on the lower part of the rock wall. The details of the concrete ball used in the test are presented in Table 1.

The restitution coefficients were obtained by measuring the distance from the wall to the position where the concrete ball was bounced as presented in Figure 2 and were calculated as expressed in the following equation:

$$C_R = \sqrt{\frac{h_v}{H_v}}, \quad (1)$$

where C_R is the restitution coefficient, H_v is the initial distance from concrete ball to wall, and h_v is the maximum distance from the concrete ball to the wall after being bounced.

Figure 2 presents the initial and final positions of the concrete ball. Figure 2(a) shows the initial position of the concrete ball and measured distance from the wall before hitting the wall, representing H_v in equation (1). Figure 2(b) presents the final position of the concrete ball and measured maximum rebounded distance from the wall, representing h_v in equation (1). As a result, the restitution coefficient (C_R) was computed as 0.48 by substituting 8.39 for H_v and 1.91 for h_v in equation (1).

The test results are presented in Table 2. Potential energy, velocity, and restitution coefficient for all four tests are listed in the table. The velocity in the table was calculated when the concrete ball hit the wall.

As presented in Table 2, the average restitution coefficients of upper and lower parts of the rock wall were 0.52 and 0.4, respectively. From the literature [5], the range of the restitution coefficient is 0.8-0.9 for solid rock and 0.3 for soft rock. Hence, it can be said that the restitution coefficient from the pendulum test is in between reasonable range.

2.2. Rock-Dropping Test. The rock-dropping tests were conducted on the real rock slopes to investigate the movements of rock such as rotation, repulsion, and speed. The rock was pushed from the top of the slope which was 214 m high and 230 m long in the vertical direction and horizontal direction, respectively, as presented in Figure 3. This rock slope has berms with 15 m height and 4 m width. Total of 13 rocks were dropped, and the repulsion height, speed, and location where the rock hit were measured using a high-speed camera and drone. As seen in the figure, the trees in the berms reduced the energy of rock dropping and finally stopped the rock, resulting in that the most of rocks were stopped in the trees and a few rocks dropped down to the bottom.

From the test, the height of bounced rock from the berm was measured using the high-speed camera. In addition, the velocity of the dropping rock was measured by means of both high-speed camera and drone. The results are presented in Table 3.

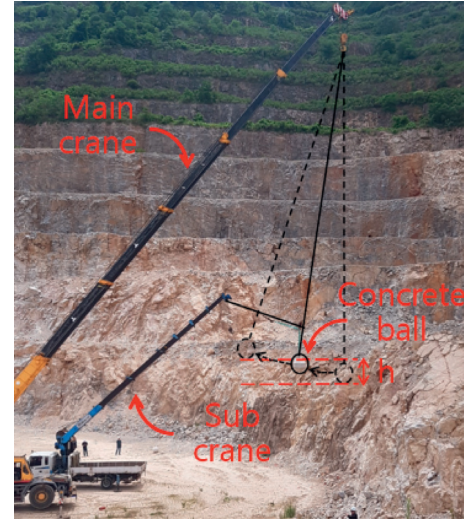


FIGURE 1: Overview of the pendulum test.

TABLE 1: Details of the concrete ball used in the pendulum test.

Weight (kg)	Shape	Size (cm)
1000		(1) 23 × 23
		(2) 23 × 33
		(3) 33 × 33

3. Numerical Simulation

The numerical simulations were conducted using commercial finite element software, ABAQUS [6]. When the rock falls, two major parameters governing the movement of rock are friction coefficient and restitution coefficient. The restitution coefficient was obtained from the pendulum test, and friction coefficient was determined as 0.2 from the calibration process by comparing with the results of the field test (as shown in Figure 3(d)). The pendulum test was simulated to obtain damping coefficient which is an input parameter for the simulation.

As shown in Figure 4, the dynamic analysis was performed by considering the entering speed and repulsion speed of concrete ball of 5.54 m/sec and 2.21 m/sec, respectively.

From the simulation and calibration process, the damping coefficient of 800 was obtained as an input parameter for the real rock-dropping simulation.

In the simulation of rock dropping, the slope and rock were modeled as rigid and solid, respectively; the rock moved only by the gravity force, and its behavior was governed by restitution and friction coefficient as seen in Figure 5(a).

As presented in Figure 5(b), the dots in red represents the location of the touched ground and the solid line in red represents the rock movement from the simulation. Due to the environmental conditions in the field, Figure 5(b) showed a little discrepancy between the field test and simulation result.

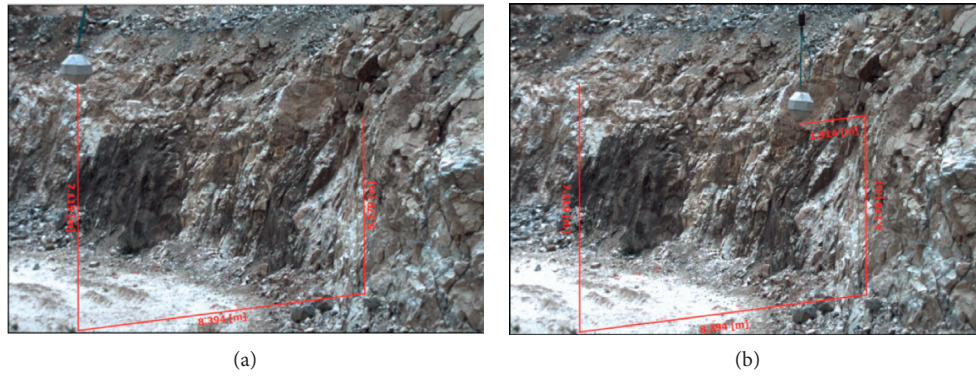
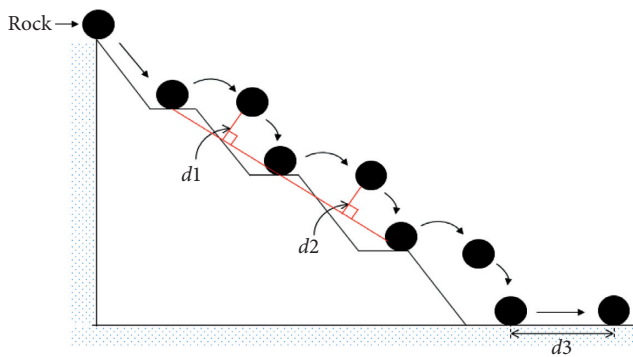


FIGURE 2: Pendulum test for the restitution coefficient: (a) initial position; (b) final position.

TABLE 2: Pendulum test results.

Test		Energy (kJ)	Velocity (m/s)	C_R
Upper part	#1	19.11	6.18	0.48
	#2	18.52	6.09	0.56
	Average	18.82	6.14	0.52
Lower part	#1	18.03	6.01	0.51
	#2	15.97	5.65	0.33
	Average	17.00	5.83	0.42



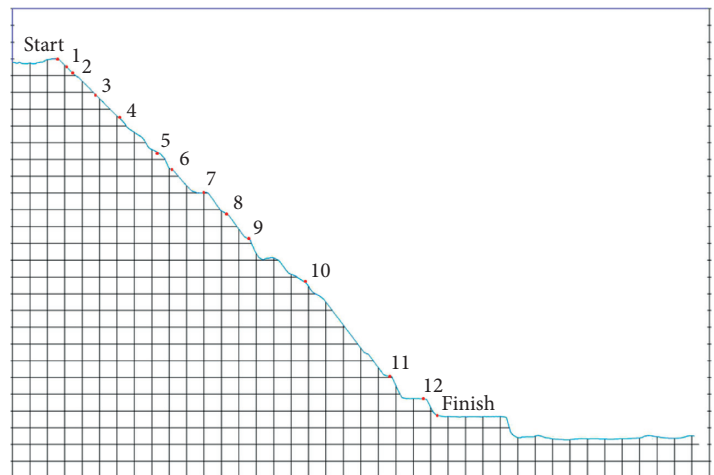
(a)



(b)



(c)



(d)

FIGURE 3: Rock-dropping test: (a) measurement scheme; (b) dropping direction; (c) height measurement; (d) touching location.

TABLE 3: Rock-dropping test results.

Height from berm (m)	Velocity of dropping rock (m/s)		
Maximum	5.24	Drone	9.9
Average	2.99	High-speed camera	10.1

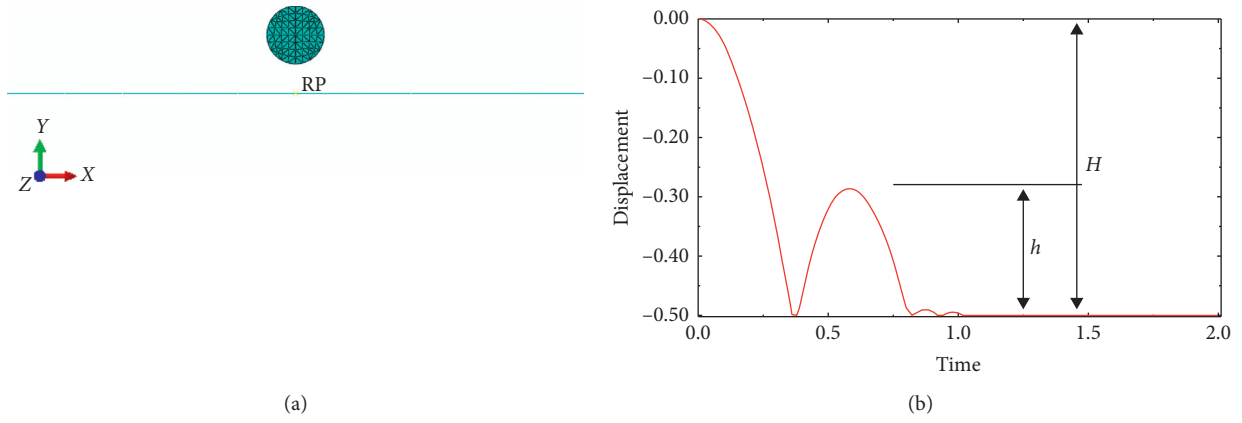


FIGURE 4: Simulation of the pendulum test: (a) mesh for simulation; (b) result of simulation.

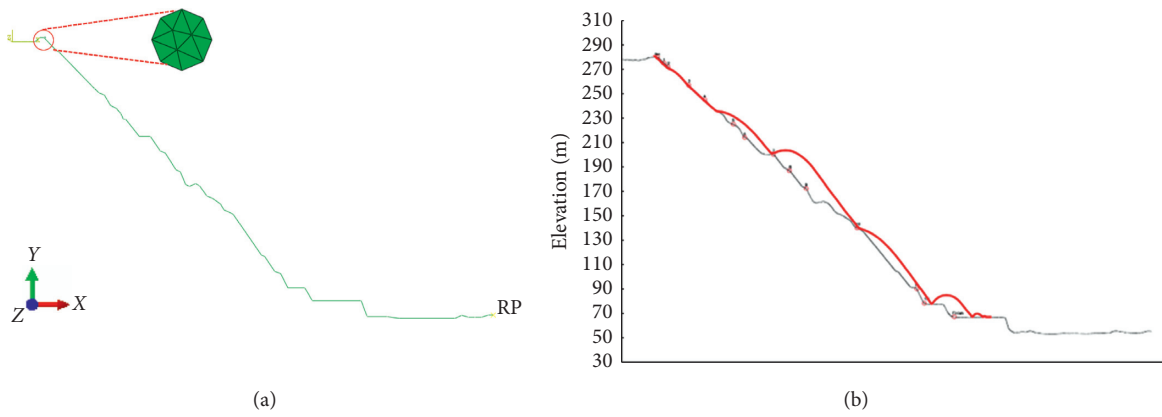


FIGURE 5: Numerical simulation: (a) mesh for simulation; (b) simulation result.

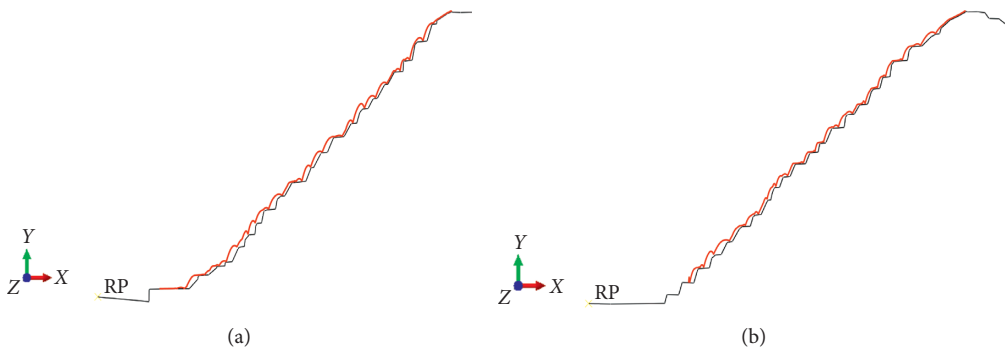


FIGURE 6: Continued.

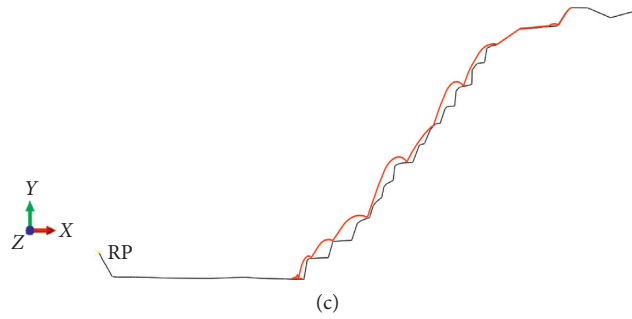


FIGURE 6: Rock-dropping simulation to which the developed model applied: (a) section 1; (b) section 2; (c) section 3.

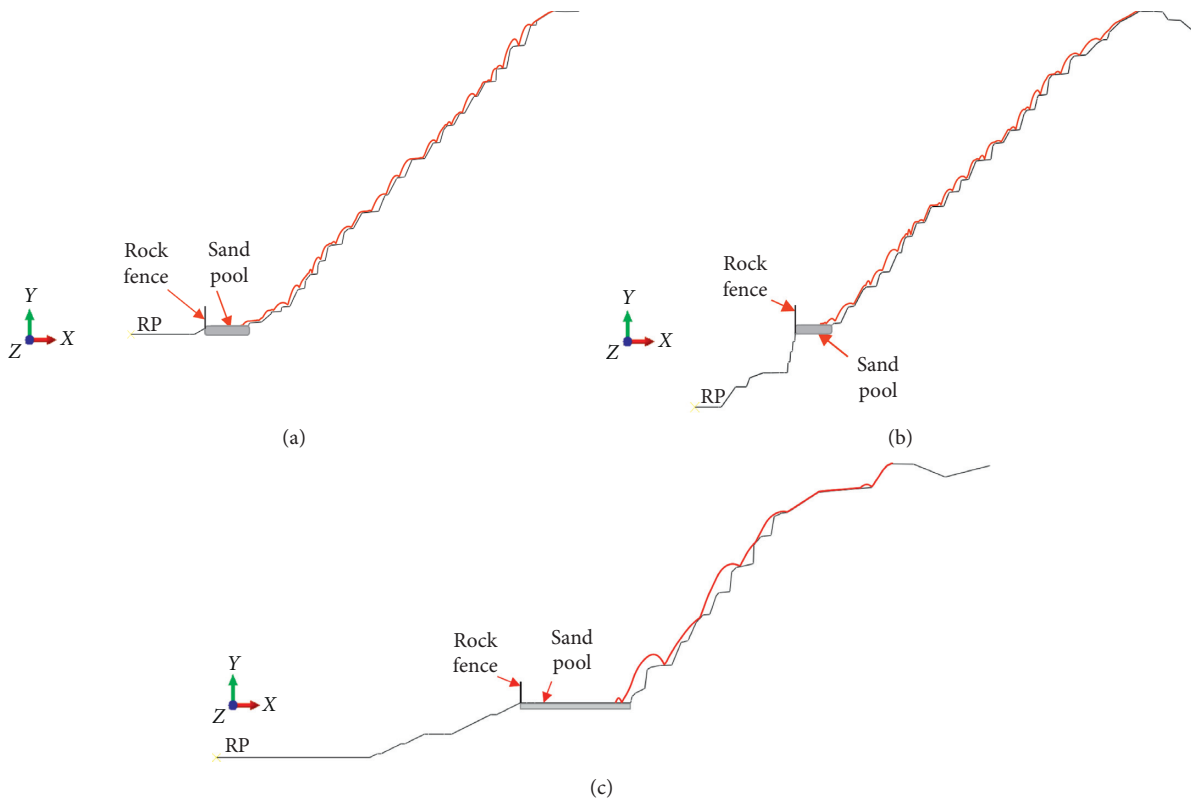


FIGURE 7: Results of rock-dropping simulations with sand pool: (a) section 1; (b) section 2; (c) section 3.

This discrepancy may be the fact that the real slope had many trees that enabled to reduce the rock movement (bounce, rotation, and speed), whereas the slope in the simulation was ideally/simplely assumed; that is, the rock movement was controlled only by the restitution coefficient and friction of the slope. Despite of this discrepancy, it can be said that the result of simulation showed a good agreement with field test.

4. Mitigation Method

The developed model was applied to the three different sections of the slope as presented in Figure 6. These sections were selected from the real slope (as shown in Figure 3(b)).

As shown in Figure 6, the rock dropped down to the bottom and lower parts of the slope that might give a rise to a dangerous situation if there was a building or structure. For

section 1, the long distance was needed to stop the rock compared to the other sections. This is because the rock jumps longer and spins more at a gentle slope as seen in Figure 6(c).

In order to mitigate/reduce the hazardous situation, the sand pool and rock fence were placed in the lower part of the slope as shown in Figure 7. The high coefficient of friction was applied to the sand pool that is generally used in the simulation of arresting/stopping the golf ball in the sand trap. As seen in Figure 7, the rock was arrested/stopped in the sand pool with small movement compared to the results of Figure 6 that the rock rolled down to the bottom of the slope.

5. Conclusions

This study presents integrated field test-computational efforts to investigate the effects of newly developed mitigation

method of rockfall hazard. Based on the test results and simulations, the following conclusions are made.

- (i) The restitution coefficient of the rock slope obtained from the pendulum tests was 0.47 which is in between the reference value solid rock of 0.8 to soft soil of 0.3
- (ii) The friction coefficient was obtained from the calibration process by comparing the rock-dropping test with the simulation.
- (iii) The developed model was applied to the three different slope sections with/without sand pool. The rock rolled down to the bottom of the slope without sand pool. On the contrary, the rock was stopped/arrested after a small movement with sand pool.
- (iv) The newly developed mitigation method provides a good advantage in terms of maintenance by simply removing the arrested/acclulturated rocks.

Data Availability

The field test and numerical simulation data used to support the findings of this study are included within the article.

Conflicts of Interest

The authors declare that there are no conflicts of interest regarding the publication of this paper.

Acknowledgments

This research was supported by the Korea Agency for Infrastructure Technology Advancement under the Ministry of Land, Infrastructure and Transport of the Korean government (Grant number 20CTAP-C152052-02).

References

- [1] A. Patnaik, A. Musa, S. Marchetty, and R. Liang, "Full-scale testing and performance evaluation of rockfall concrete barrier," *Transportation Research Record*, vol. 2252, no. 1, pp. 27–36, 2015.
- [2] A. Mentani, A. Giacomini, O. Buzzi, L. Govoni, G. Gottardi, and S. Fityus, "Numerical modelling of a low energy rockfall barrier: new insight into the bullet effect," *Rock Mechanics and Rock Engineering*, vol. 49, no. 4, pp. 1247–1262, 2016.
- [3] N. Sashiharan, B. Muhunthan, T. C. Badger, S. Shu, and D. M. Carradine, "Numerical analysis of the performance of wire mesh and cable net rockfall protection system," *Engineering Geology*, vol. 88, no. 1-2, pp. 121–132, 2006.
- [4] M. Spadari, A. Giacomini, O. Buzzi, and J. P. Hambleton, "Prediction of the bullet effect for rockfall barrier: a scaling approach," *Rock Mechanics and Rock Engineering*, vol. 45, no. 2, pp. 131–144, 2012.
- [5] B. Peng, "Rockfall trajectory analysis: parameter determination and application," Thesis, University of Canterbury, Christchurch, New Zealand, 2000.
- [6] Dassault System, ABAQUS/Standard User's Manual v. 6.14, Simulia, Johnston, RI, USA, 2014.

Research Article

Numerical Simulation Analysis of NPR Anchorage Monitoring of Bedding Rock Landslide in Open-Pit Mine

Kai Zhang,^{1,2} Xiaojie Yang,^{1,2} Xuebin Cui,^{1,2} Yong Wang,^{1,2} and Zhigang Tao ^{1,2}

¹State Key Laboratory for Geomechanics & Deep Underground Engineering, China University of Mining & Technology, Beijing 100083, China

²School of Mechanics and Civil Engineering, China University of Mining & Technology, Beijing 100083, China

Correspondence should be addressed to Zhigang Tao; taozhigang@263.net

Received 15 July 2019; Revised 16 November 2019; Accepted 25 November 2019; Published 6 January 2020

Academic Editor: Jiang Jin

Copyright © 2020 Kai Zhang et al. This is an open access article distributed under the Creative Commons Attribution License, which permits unrestricted use, distribution, and reproduction in any medium, provided the original work is properly cited.

Nanfen open-pit iron mine is the largest single open-pit mine in Asia. Because of the lag of the extension project, the section has slowly spread in the shape of “V,” and disasters such as landslides occur frequently. In this study, first, the NPR anchor cable monitoring, which shows supernormal mechanical characteristics and can realize the monitoring and early warning target for the whole landslide process and early warning curve of bedding rock “2016-1101 landslide” in the lower wall of Nanfen open-pit mine, was analyzed, revealing the failure process of the bedding rock landslide and the force evolution characteristics of the NPR anchor cable. Then, based on the Fish language in FLAC3D and 3DEC software, the mechanical model of the NPR anchor cable was constructed, and numerical simulation was performed on the whole process of “16-1101 landslide” induced by accumulation of old landslide body. The results of this study indicate that the stress monitoring curves and failure characteristics of the NPR anchor cables in the whole process of landslide by the two numerical simulation methods are basically consistent with the field measurement results, providing a theoretical and practical basis for the mechanistic analysis and numerical simulation of other similar slopes.

1. Introduction

Under the blasting, rainfall, and human activity, the rock mass of slope weakens, causing a large number of engineering disasters [1–6]. The disaster because of large deformation during a landslide in an open-pit mine not only causes huge economic losses but also seriously threatens the safety of life and property of the staff in the mine. Reducing the casualties and property losses caused by landslides and forecasting them have been a research hotspot. The key to affecting the reliability and authenticity of forecasting results is to timely and accurately monitor and simulate the data. Based on this, the study and development of landslide monitoring methods have become the most basic measure to improve the effectiveness of the prediction results. At present, the monitoring methods widely used include deformation monitoring, physical field monitoring, water monitoring, and external trigger monitoring [7–10]. Allasia et al. proposed a new method called Advanced Displacement

Monitoring System for Early Warning for near real-time monitoring of surface displacement caused by landslides [11]; Choon et al. monitored and analyzed the slope displacement of Basel coal mine in Indonesia using a GPS system, and a GIS model combining the fuzzy theory and analytical hierarchy process was established to evaluate the slope instability of open-pit mines [12]. In recent years, satellite remote sensing technology monitoring methods (SAR, INSAR, and D-INSAR) have been widely used in landslide monitoring leading to significant results [13–16]. Based on previous investigation and our experience with Saito’s method, an improved Saito curve was drawn with four stages corresponding to the displacement process of the position on the back of the landslide [17]. However, these landslide monitoring methods are basically based on observing the surface displacement, cracks, and settlements. These factors are necessary conditions for the occurrence of landslides rather than sufficient conditions. Therefore, carrying out the advance warning of landslide disasters is

impossible. He et al. proposed that “sliding force is greater than the shear strength, and it is the necessary and sufficient condition for landslide generation.” Based on this, they constructed the mechanical model of “sliding force monitoring” and developed an NPR anchor cable with constant resistance characteristics, which can adapt to landslide monitoring in deep deformation conditions [18–21]. On this basis, a wireless sensor network was built based on the GPRS dual-channel platform using Zigbee technology, and a multisource system cloud service platform was established for landslide monitoring to adapt to the complex environment sloping disaster monitoring and early warning system [22–26]. Although they successfully monitored and warned of many dangerous landslides, they neither established the NPR anchor cable numerical calculation model and nor carried out the numerical simulation of the whole process of landslide monitoring and early warning.

Similarly, the numerical simulation analysis of landslide geological disasters is also a key method for investigation in the field of slope engineering. At present, a series of numerical methods such as finite difference method and finite volume method for different types of sliding bodies have been developed. Model establishment and control theory include discrete element method (DEM), discontinuous deformation, DAN, smooth particle hydrodynamics, particle flow code (PFC), and tsunami ball. Some numerical simulation software such as FLAC, UDEC, PFC, 3DEC, and Geoslope have emerged. Many researchers carried out a series of simulations on the slope instability and damage by these methods and software achieving significant results. Maihemuti et al. used the three-dimensional rapid Lagrangian analysis program (FLAC3D, 4.0) of geotechnical engineering to numerically simulate the deformation and failure process of the bank slope rock and obtained the deformation mechanism of the E20 bank slope [27]. Li et al. combined C++ programming technology and finite difference method and realized the three-dimensional numerical simulation of slope through the intelligent inversion analysis of the structural parameters of the soil slope [28]. The traditional continuous numerical calculation method has been widely used by the predecessors, and the practicability and effectiveness of the finite element method and boundary element method have been fully confirmed [29–32]. At the same time, Munjiza et al. combined the finite element method suitable for the analysis of continuous problems with the discrete element method suitable for transient, contact detection, contact interaction, and other discrete problems [33]. Some scholars explored the integrated continuity and discontinuity methods, known as the finite element-discrete element method for the numerical simulation of material cracking and fracture after slope instability [34–37]. However, the NPR anchor cable monitoring, numerical modeling, and simulation analysis in the whole process of landslides are rarely investigated. Based on the monitoring data and the engineering geological conditions of “2016-1101 landslide,” in this study, we established the NPR anchor cable numerical calculation model and carried out numerical simulation on the monitoring of “2016-1101 landslide” through the Fish language in FLAC3D and 3DEC

software. The whole process of monitoring and early warning of Newtonian force of typical landslide in Nanfen open-pit mine was established, laying a good theoretical foundation for the layout of the monitoring points of the Newtonian force and slope stability analysis in Nanfen open-pit mine in the future.

2. Structural Composition and Static Tensile Mechanical Properties of the NPR Anchor Cable

2.1. Structural Composition of the NPR Anchor Cable. The NPR anchor cable is different from the traditional PR anchor cable and has improved constant resistance and large deformation mechanical characteristics. Figure 1 shows the structural composition of the NPR anchor cable, mainly including mechanical sensors, anchor cables (steel strands), constant resistance bodies, constant resistance bushings, top covers, backing plates, filling new materials, and other equipment.

Normally, the force applied on the anchor cable is offset by the static friction between the constant resistance body and the constant resistance casing. When the load applied to the anchor cable is larger than the constant resistance design load value, the body begins to move along the inner wall of the casing and absorbs the load energy through the structural deformation, leading to constant resistance and large deformation.

2.2. The Mechanical Model for NPR Anchor Cable. The constant resistance body is the core part of the constant resistance and large deformation anchor cable, and its structure is shown in Figure 2 [18].

Among them, α is the angle of constant resistance body, h is the effective length of constant resistance body, a is the inner radius of constant resistance casing, b is the outer radius of constant resistance casing, u is the radial deformation, V is the elongation of anchor cable bundle, P_0 is the external load, M is the mass of constant resistance body, $\delta(z)$ is the inner wall deformation of constant resistance casing of $A - B$ section at z from the top of constant resistance body, p' is the acting stress of constant resistance body to constant resistance casing, and $p'(z)$ is the action stress of $A - B$ profile constant resistance casing to constant resistance body. The mechanical model of the rheostat is as follows [18]:

$$\begin{aligned}
 P_0 &= 2\pi f I_s I_c, \\
 I_s &= \frac{E(b^2 - a^2)\tan\alpha}{a[a^2 + b^2 - \mu(b^2 - a^2)]}, \\
 I_c &= \frac{ah^2}{2} \cos\alpha + \frac{h^3}{3} \sin\alpha,
 \end{aligned} \tag{1}$$

where P_0 is the constant resistance (kN), f is the static friction coefficient, I_s is the elastic constant of the constant resistance sleeve, I_c is the geometric constant of the constant

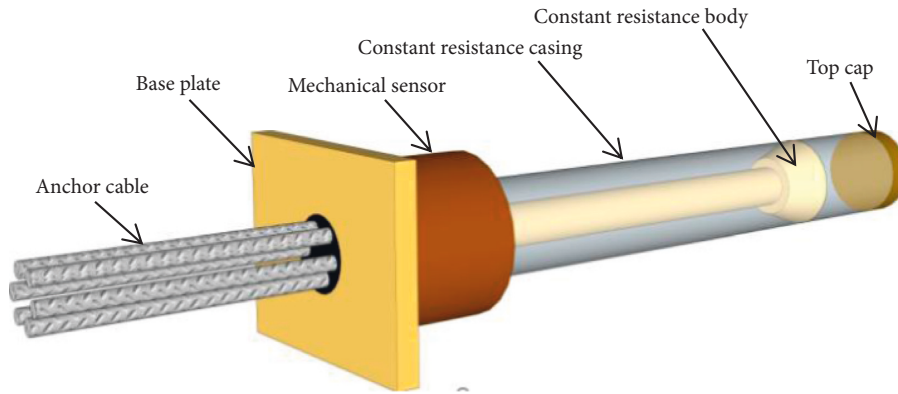


FIGURE 1: Structure diagram of constant resistance large deformation anchor cable.

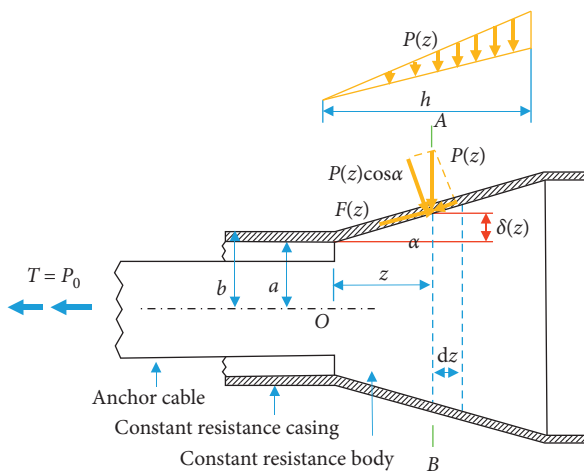


FIGURE 2: Analysis of the axial stress of the constant resistance device.

resistance body, E is the elastic modulus of the material, and μ is Poisson's ratio of the material.

The constant resistance value of the NPR anchor cable is related to the material size of the constant resistance body and the external load.

2.3. Extraordinary Statics and Its Test

2.3.1. Testing System. In order to verify and investigate the supermechanical properties such as tensile properties, negative Poisson's ratio (NPR) characteristics, and constant resistance specialty of the anchor cables in this study, we used "the static tensile test system of HWL-2000 NPR anchor cables," developed by the State Key Laboratory of Deep Geotechnical Mechanics and Underground Engineering, China University of Mining and Technology (Beijing). The anchor cables are numbered as "MS-01-01," "MS-01-02," and "MS-01-03," and their physical parameters are listed in Table 1.

The test system mainly includes a data acquisition and processing system, a liquid crystal display system, a hydraulic power system, and an anchorage and tension system. The maximum tensile force is 2,000 kN; the resolution of the

tensile force is 3.3×10^{-6} ; and the strain rate and tension are in the ranges 0–200 mm/min and 30–5000 mm, respectively. Figure 3 shows the schematic diagram of the static stretching system.

2.3.2. Result Analysis

- (1) Tensile properties and constant resistance characteristics of the constant resistance and large deformation anchor cables

Figure 4 shows the static tensile test curve of the test piece anchor cable, indicating the following:

- (a) From the beginning of the tension to the failure of the anchor cable, it has an average elongation of 1960 mm, showing an extraordinarily large deformation capacity.
 - (b) During the static tension, the axial force of the anchor cable rises to the maximum constant resistance (850 kN) in a short time and then becomes constant at 850 kN, exhibiting a remarkable constant resistance characteristic.
- (2) Negative Poisson's ratio effect of the constant resistance large deformation anchor cable structure

The cable structure with a constant resistance and large deformation under axial elongation also undergoes radial structural expansion. Figure 5 shows the NPR anchor cable resistor used in the experiment.

The outer diameters of the cross sections 1-1 and 2-2 in two vertical directions were measured using a Vernier caliper. The interval is 100 mm, and the length of the casing is read. Figures 6(a) and 6(b) show the diameters of the three groups of the constant resistance casing in 1-1 and 2-2 directions, respectively.

- (1) The initial average diameters before and after the test in the 1-1 direction are 121.42 mm and ~125.42 mm, respectively. The expansion in the 1-1 direction before and after the test is ~4 mm.
- (2) The initial average diameters before and after the test in the 2-2 direction are 121.50 and ~125.66 mm,

TABLE 1: Anchor cable parameters.

Anchor cable number	Anchor cable length L_1 (mm)	Constant resistance sleeve length L_2 (mm)	Constant resistance body length L_3 (mm)
MS-01-01	2854	2005	150
MS-01-02	2856	2007	150
MS-01-03	2860	2010	150

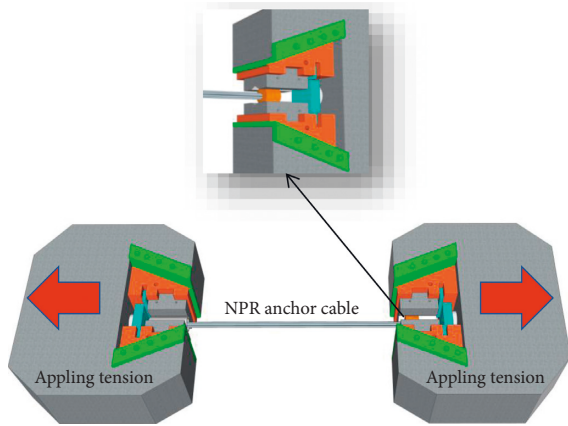


FIGURE 3: Schematic diagram of the static stretching system.

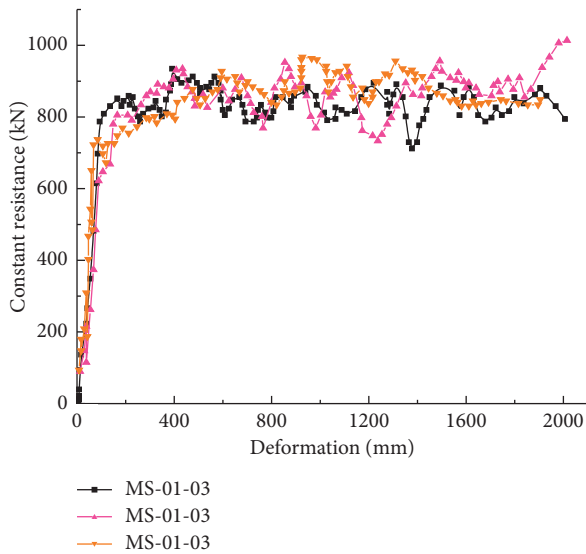


FIGURE 4: Static tensile test curve of the anchor cable.

respectively. The expansion in the 2-2 direction before and after the test is ~ 4.16 mm.

In summary, the large deformation anchor cable with a constant resistance has supernormal tensile properties, NPR characteristics, and constant resistance characteristics.

- (3) Geological conditions, landslide monitoring system, and distribution characteristics of monitoring point.

3.1. Topography, Geomorphology, and Stratigraphic Lithology. Nanfen open-pit iron mine (Figure 7) of the Benxi Steel Group is located 25 km south of Benxi City, Liaoning

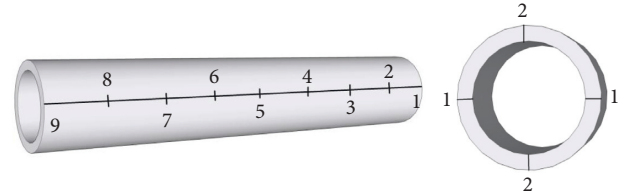


FIGURE 5: NPR anchor cable resistor.

Province. Its terrain undulates greatly. The relative elevation difference is generally 300–400 m, and the maximum elevation is 500 m. The overall topography is high in the east and low in the west, and the mountain trend is close to the east and west. It is a middle-high mountain area with a denudation structure. The orebody is a monoclinic structure. The east and west sides of the stope are the lower and upper walls of the monoclinic structure, respectively.

The strata in the stope are relatively complex. First, the Anshan group (mainly composed of mica quartz schist, epidote amphibolite schist, magnetite quartz, quartz chlorite schist, mica quartz schist, and gneissic migmatite) was widely developed, followed by the Liaohe group of the Proterozoic (mainly composed of quartzite, phyllite, and marble), sinian strata (mainly composed of quartzite and shale), and the quaternary strata of the Cenozoic (lithologically including sand, gravel, clay soil, and gravel).

3.2. Geological Structure and Hydrometeorological Characteristics. The geological structure in the mining is the fold structure and fault structure dominated by the inverted anticline (the inverted dome structure of the Heibeishan mountain, the inverted anticline of the open-pit mine, and the F1 fault structure). The core drilling data show obvious inverted anticline morphology and fault structure (Figure 8).

The mining area belongs to the north temperate monsoon climate. The annual average rainfall and the maximum daily rainfall are close to 900 and 300 mm, respectively. Rainfall mainly concentrates in the summer. Besides, the annual temperature difference is relatively large; the extreme minimum temperature in the winter is close to -33°C , while the extreme maximum temperature in the summer is close to 38°C ; and the annual average temperature is 8.2°C . Groundwater also plays an important role in the region. The ice and snow melt in the rainy and winter-spring alternating seasons. The water seriously affects the stability of the landslide body, thus increasing the difficulty in mining operations.

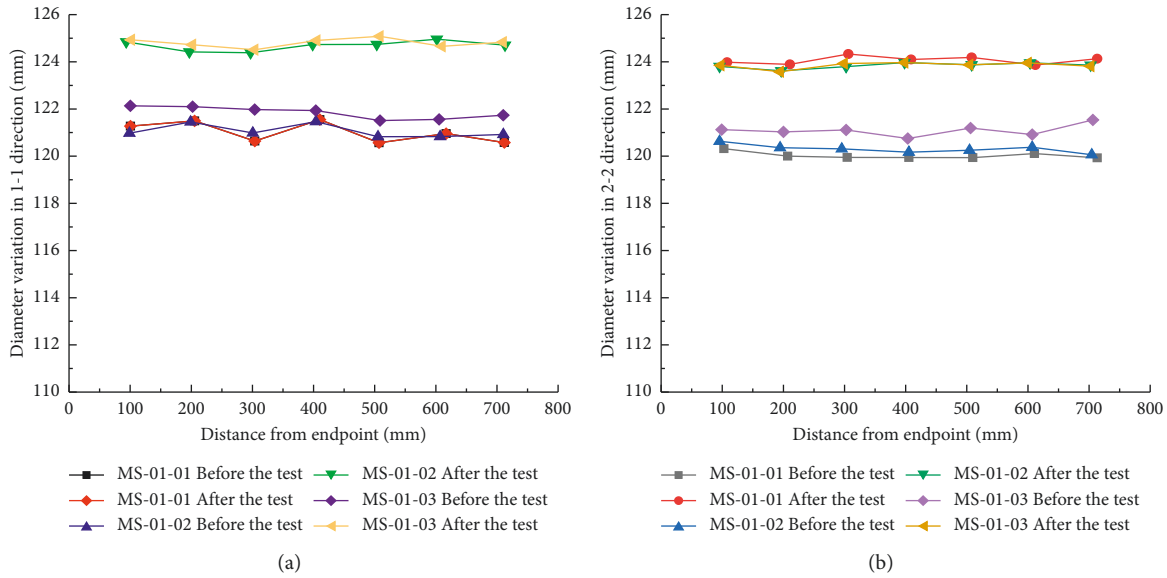


FIGURE 6: Diameter variation of constant resistance casing before and after the test: (a) diameter variation of 1-1 section; (b) diameter variation of 2-2 section.

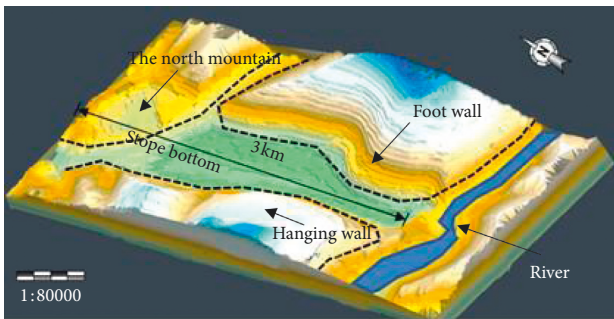


FIGURE 7: Mine mining site shape and landform.

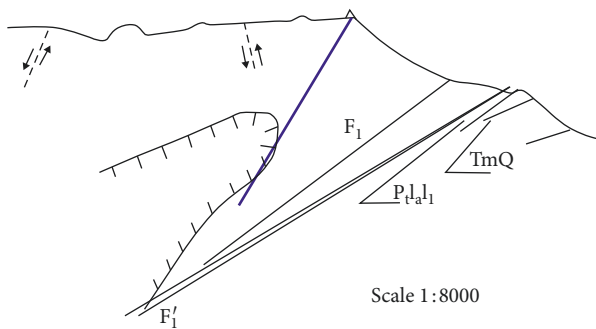


FIGURE 8: Reverse anticline shape and fault structure in the mining area.

3.3. Distribution Characteristics of Monitoring Point

3.3.1. Monitoring System. The landslide observation system is divided into indoor and outdoor monitoring systems.

The indoor landslide monitoring system (Figure 9) mainly consists of a GPRS data receiver, a BeiDou satellite signal receiver, an automatic data analysis and processing

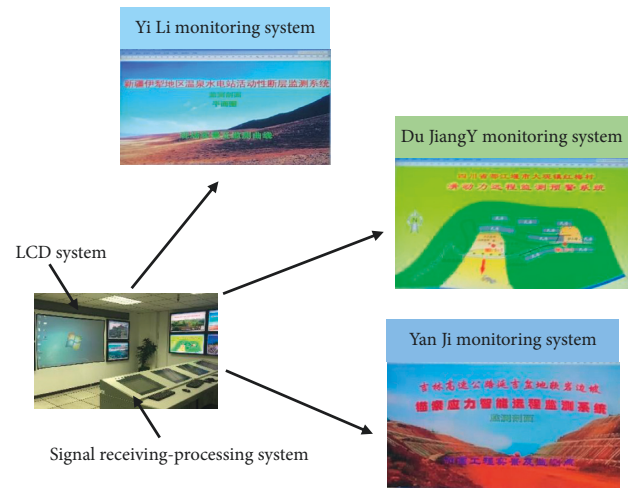


FIGURE 9: Indoor monitoring system.

system, a 3D automatic search system, and a liquid crystal display system.

The outdoor landslide monitoring system (Figure 10) mainly consists of a signal transmission system, a power supply system, a mechanical transmission device, and a mechanical signal acquisition and conversion device. Among them, the power supply system contains 100a colloidal battery overcharge, a 85 W monocrystalline silicon solar panel, and a dedicated controller, guaranteeing 24 h of working status. The mechanical transmission devices include mechanical sensors. The signal transmission system includes a BeiDou machine and an antenna. There are also anchored piers, poles, and other equipment.

Data transmission and aggregation in the monitoring area are mainly based on the data transmission topology (Figure 11).

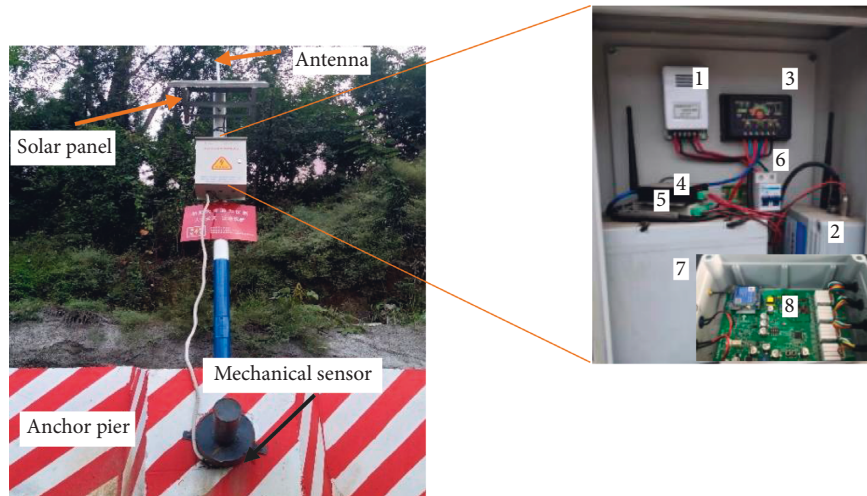


FIGURE 10: Outdoor system equipment: 1, power supply (12 V); 2, power supply (9 V); 3, solar controller; 4, communication node; 5, GPRS-DTU; 6, switch; 7, solar battery; 8, data acquisition device.

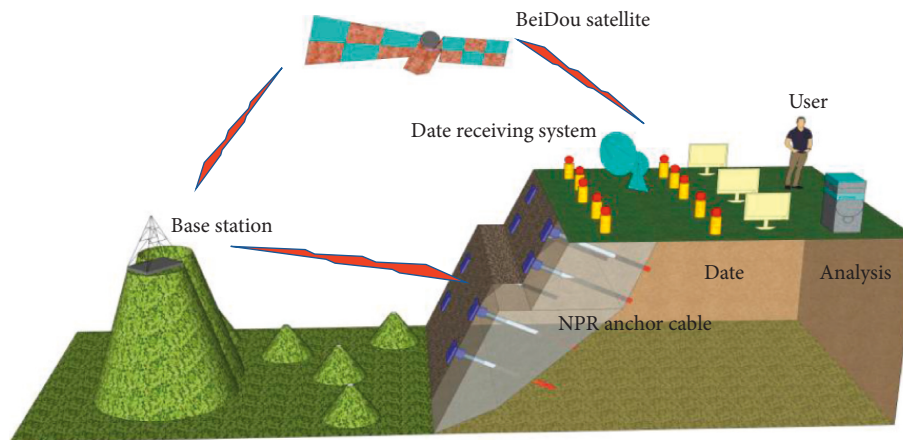


FIGURE 11: Data transmission topology.

3.3.2. *Mechanism of Large Deformation Control.* NPR anchor cable plays an important role in controlling the large deformation of the slope:

- (1) Before the slope slides (Figure 12(a)): assembly of a new anchor cable equipment and application of prestress

Before excavation, the slope is in equilibrium. According to the survey and construction design, holes are drilled in the design depth, the anchor cable is extended into the tunnel, and the anchorage section is grouted and reinforced; besides, the free end is molded, and the installation of equipment is completed, followed by applying the prestressing force.

- (2) Slope sliding (Figure 12(b)): energy absorption process of the “NPR structure”

When the slope is about to slip or begin to slip, the original mechanical equilibrium state between the slope and NPR anchor cable will be destroyed, causing slip. As the slip exceeds a certain limit, the constant resistance body will absorb energy with

increasing deformation in the casing, effectively increasing or avoiding the breaking of the anchor cable, thus avoiding the sudden collapse of the slope and the failure of the monitoring equipment.

- (3) After the slope slides (Figure 12(c)): controlling the sliding body

In the case of large deformation, the elastic energy is released, the deformation energy inside the slope is less than the design constant resistance P of the resistor, the axial force F of the anchor cable is less than the friction force, and the soil body reaches a new equilibrium and stable state.

Therefore, the anchor cable can not only realize the monitoring and early warning of the slope landslide but also reinforces the slope.

3.3.3. *Distribution Characteristics of the Monitoring Point.* With the continuous exploitation of deep mineral resources, landslides, rolling stones, and other geological disasters

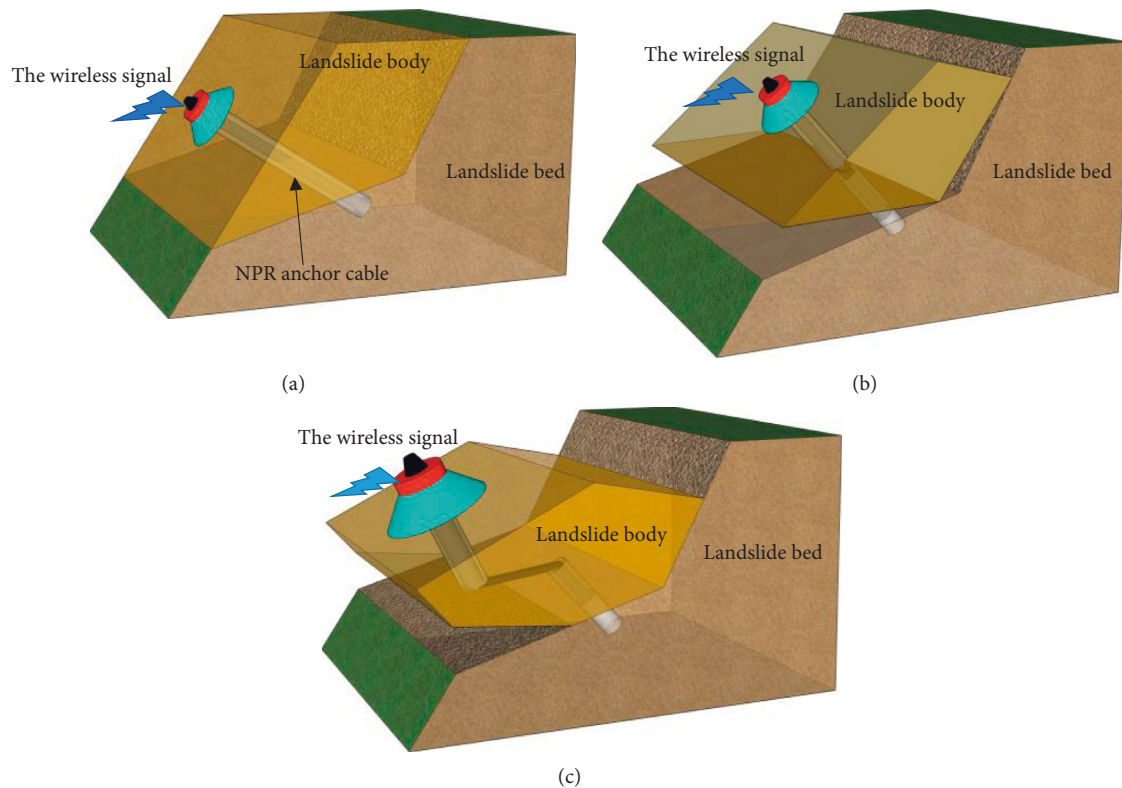


FIGURE 12: Process of interaction between NPR anchor and slope: (a) before the slope slides; (b) slope sliding; (c) after the slope slides.

occur frequently. In June 2015, nine new NPR anchor monitoring points were introduced in the 478–502 m platform range of the stope working face. The buried depth is in the range 55–84 m, the angle of incidence is 45° , and the azimuth angle is 84° . As shown in Figure 13(a), the red marking dots are the new monitoring points, and the A-A' section of the monitoring area is shown in Figure 13(b).

4. Numerical Simulation and Analysis of “16-1101 Landslide” NPR Monitoring

4.1. Characteristic Analysis of “16-1101 Landslide”. At 8:30 on September 14th, 2016, the No. 478-3 curve rose to point D, and the system issued a “long-term warning”; at 10:20 on October 1st, 2016, because of a working shovel under 430 m steps, the sliding force curve of No. 478-3 suddenly rose to point F, and the system issued a “medium-term warning.” The mine leaders asked all large machinery and extension workers to evacuate; at 23:52 on October 31st, 2016, the curve suddenly appeared. On November 1st, 2016, at 3:40, the monitoring system reported the occurrence of the landslide, producing a loud noise. The broken rock and soil mass rolled down along the slope and piled up on the 430 m step. The failure characteristics of the slope top behind the landslide are shown in Figure 14.

4.2. Numerical Simulation Analysis of the “16-1101” Landslide. In this section, the field monitoring data of “16-1101 landslide” in Nanfen open-pit iron mine was calculated by

FLAC3D and 3DEC numerical simulation software to realize the recurrence of the landslide process. The numerical analysis model of the NPR anchor cable was constructed by Fish language in numerical simulation software. The model was analyzed, and the calculation was performed for the 16-1101 landslide to investigate the similarities and differences between the simulation and the actual monitoring results.

4.2.1. Principle of Large Deformation Design of NPR Anchor Cable in Numerical Simulation Software. The NPR anchor reinforcement unit is generally defined by geometric parameters, material parameters, and anchorage agent characteristics. The axial stiffness of the bolt K is expressed by

$$K = \frac{AE}{L}, \quad (2)$$

where A is the cross-sectional area of the reinforcement, E is the elastic modulus of the bolt, and L is the length of the bolt.

Conventional anchor cables do not have large deformation characteristics. For the NPR anchor cables, with constant resistance and large deformation characteristics, it is necessary to set the end of the anchor section with conventional anchorage strength and the end of the free section as the rigid contact with the rock mass through Fish language in the modeling process. The principle of large deformation is as follows: applying axial force at the end of the NPR anchor cable, when the axial force reaches the design constant resistance P , the anchor cable will produce axial deformation, until the maximum deformation is

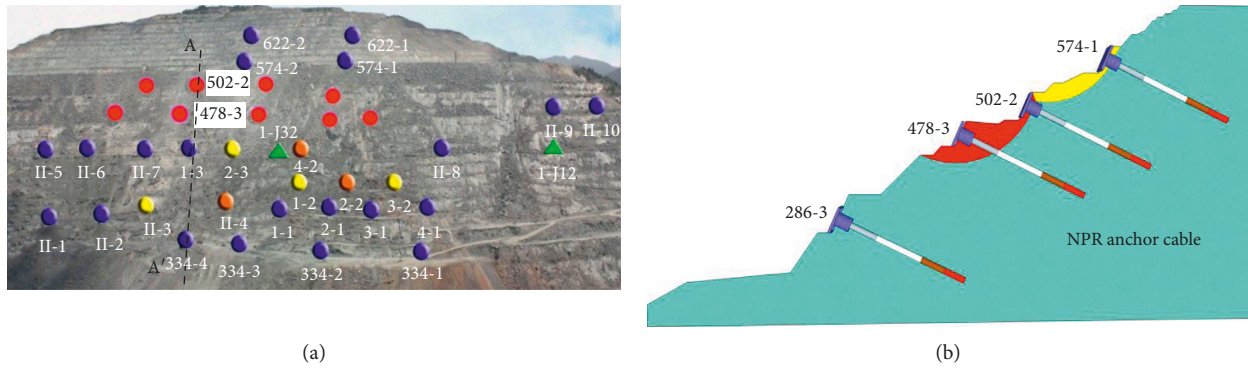


FIGURE 13: Monitoring point distribution: (a) added monitoring point distribution characteristics; (b) section A-A' of the monitoring area.

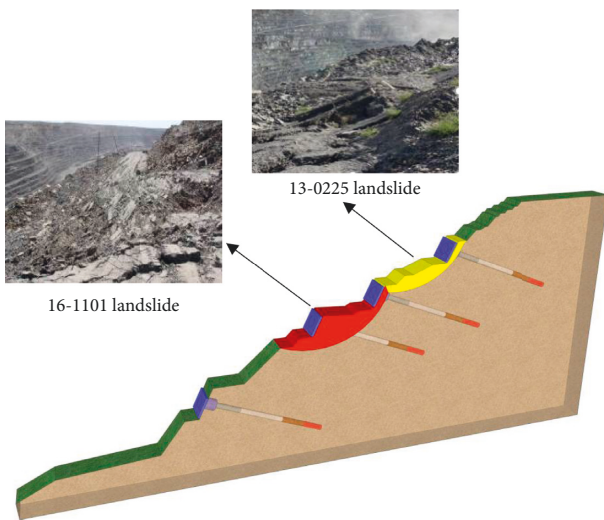


FIGURE 14: Characteristics of the “16-1101 landslide.”

reached, the failure of anchorage agent will be judged, and the anchor cable unit will be released to achieve the effect of large deformation.

4.2.2. Numerical Model Establishment of the 16-1101 Landslide. Calibration of model boundary and elevation: the maximum width of the old landslide body and “16-1101 landslide body” is 50 m, and the elevation limits are in the ranges 502–550 m and 430–502 m. Because the width of the model boundary is 2.5 times larger than the width of the target body, the height range of the model is 277–634 m, and the strike direction length is 200 m. In order to simulate the spatial relationship between the upper and lower sliding bodies and the interface characteristics of the sliding body during the start-up process, setting the interface elements between the sliding body and the rock foundation is necessary. The back, bottom, and both sides of the landslide body have a fixed boundary, and the upper and front parts have a free boundary.

4.2.3. Landslide Numerical Simulation Based on FLAC3D. The NPR anchor cable model was constructed by FLAC3D software, as shown in Figure 15. The static tensile mechanical properties are shown in Figure 16.

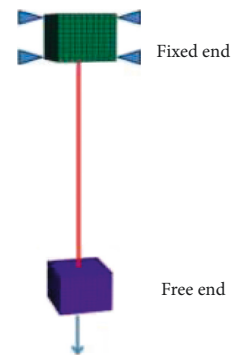


FIGURE 15: The NPR anchor cable model.

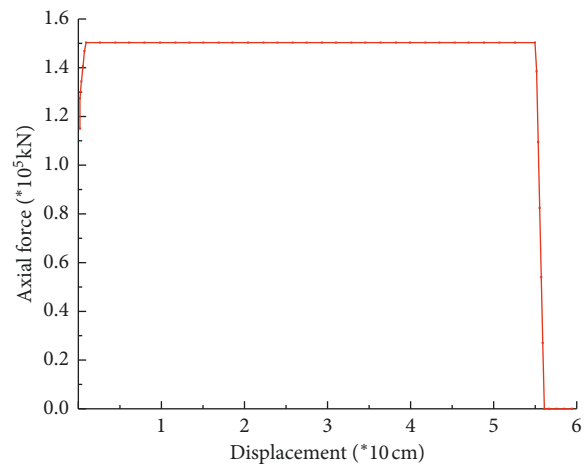


FIGURE 16: The static tensile mechanical properties.

(1) Insertion of the NPR Anchor Cable Model. The parameters of the NPR anchor cable model were determined by the coordinates of the monitoring points of the deep sliding force and buried depth of the NPR anchor cable: inclination angle, 30°; length, 75 m; preload force, 40 kN; and constant resistance value, 85 kN. The excavation length of the 430 platform shovel is set to 70 m. The rock mechanical parameters are as follows (Table 2).

Figure 17 shows the double-sliding body model.

TABLE 2: Parameters of rock mechanics.

Rock mass name	Bulk weight (kg/m ³)	Bulk modulus (GPa)	Shear modulus (GPa)	Cohesion (kPa)	Friction angle (°)	Tensile strength (MPa)
Basement	2873	20	10.9	420	36	1.5
Sliding mass	2580	5.2	2.10	70	27	0.2

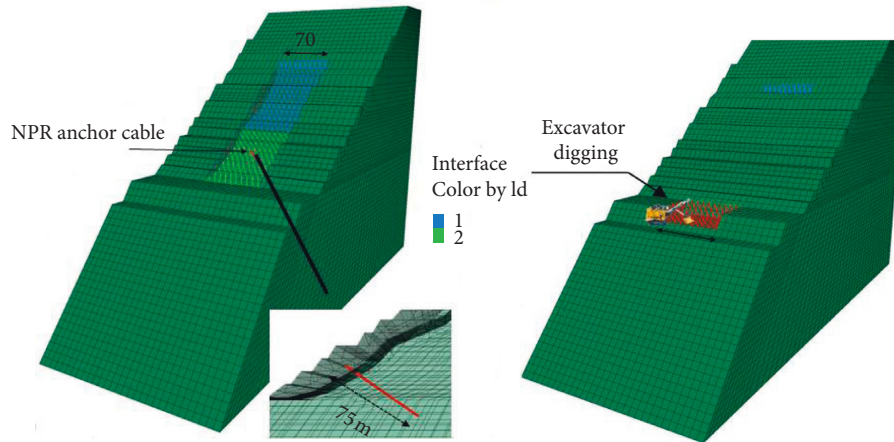


FIGURE 17: Construction of double-sliding body model.

(2) Analysis of Simulation Results

(i) Numerical simulation analysis of the old landslide (Figure 18)

Principles of simulation:

- (a) When the maximum unbalance force F is $<1e-5$, the software determines the landslide as stable.
- (b) When the calculation exceeds 10,000 steps and the model is still unstable, the calculation is stopped, and the model is considered to be in a plastic flow state.
- (c) Observe the strain increment contour of the sliding surface. When the sliding surface passes through, the software determines the sliding surface instability and stops calculation.

According to these three principles, the maximum displacement of the old landslide after stabilization is ~1.3 m. The landslide body is basically located at the set position of the contact surface of the model. When the slope slides, the strength of the contact surface is set as the actual strength of the sliding surface and then slides until reaching the stable state.

(ii) Numerical simulation analysis of “16-1101 landslide” (Figure 19)

The numerical simulation of “16-1101 landslide” was carried out by setting both the velocity and deformation of the old landslide in the calculation as zero.

After the appearance of “16-1101 landslide,” the old landslide body “resurrected” and then slipped, and the 502 m step appeared staggered. The direct cause of the ultimate

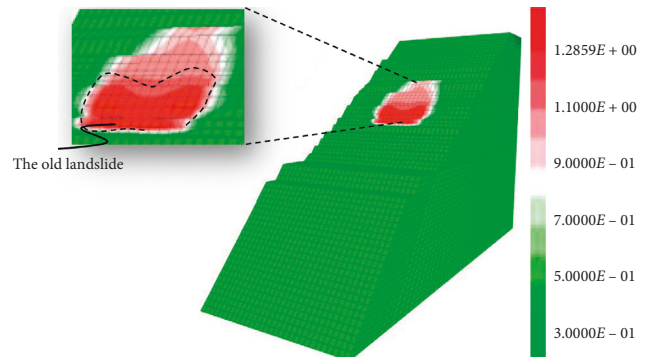


FIGURE 18: Displacement contour of the old landslide after stabilization.

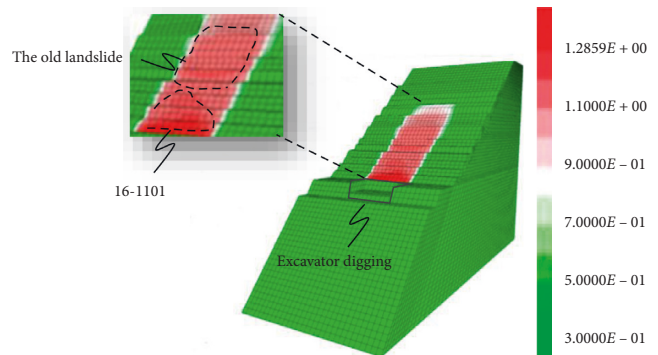


FIGURE 19: “16-1101 landslide” instability displacement contour.

instability of the whole slope is the transfixion of the sliding surface, and the antisliding force is less than the sliding force. Therefore, in practical calculation, the strength of the contact

TABLE 3: Strength degradation stages criteria.

Stage classification	Normal stiffness (GPa)	Tangential stiffness (GPa)	Cohesive strength (kPa)	Friction angle (°)
First stage	10	10	148	21
Second stage	10	10	36	20
Third stage	10	10	25	19
Fourth stage	10	10	18	18

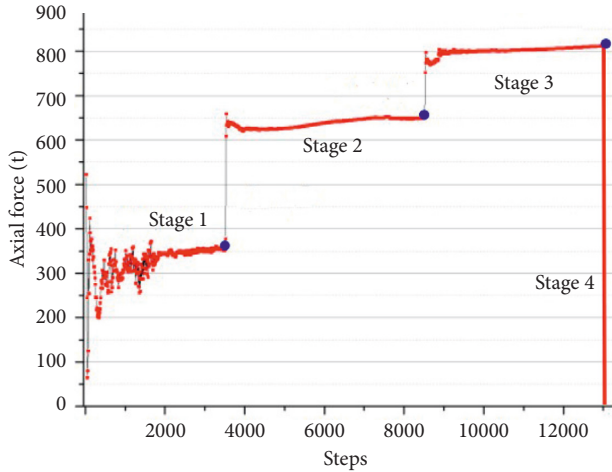


FIGURE 20: Stairs of axis force change of NPR anchor cables.

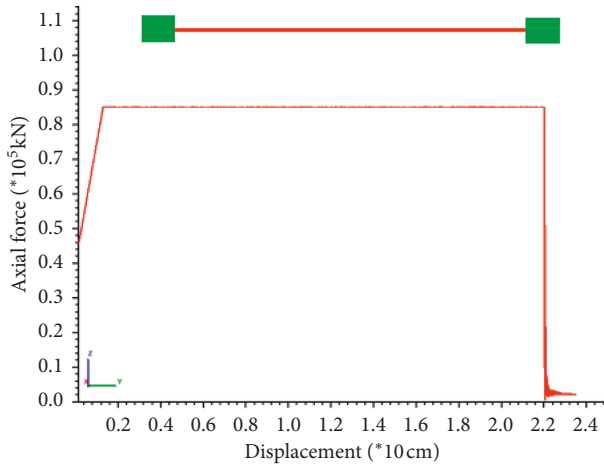


FIGURE 21: NPR anchor cable model and its static tensile properties.

surface (sliding surface) should also be decreased in stages to investigate the rock mass instability. The strength of the contact surface should be divided into stages from the stable state to the final sliding state, as listed in Table 3.

The axial force variation in the NPR anchor cables located at 478 m steps in the landslide body is also divided into four stages, as shown in Figure 20.

The four stages shown in Figure 20 are as follows:

Stage 1 (shovel excavation at the foot of the slope): the axial force of the NPR anchor cable increases gradually because of the disturbance of shovel excavation on the 430 m steps.

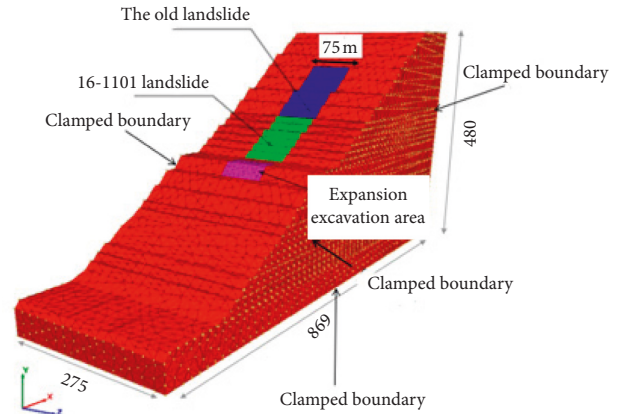


FIGURE 22: Model building and meshing.

Stage 2 (old sliding body revival): with the excavation of the electric shovel, the sliding force of the slope increases, the old sliding body revives, the strength of the weak interlayer of the sliding surface decreases gradually, and the axial force of the NPR anchor cable increases sharply; however, the sliding surface does not produce relative displacement.

Stage 3 (relative displacement of 16-1101 slip surface): the slope has reached the safety threshold because of the shovel excavation, microcracks appear in the rock mass, relative displacement of the slip surface begins to appear, and the axial force of the NPR anchor cable increases suddenly.

Stage 4 (16-1101 landslide facing slip warning): the sliding surface completely loses its stability and sends out early warning information.

In summary, the actual monitoring results and simulation results are in close agreement, providing a theoretical and practical basis for the mechanistic analysis and numerical simulation calculation of other similar slopes.

4.2.4. *Landslide Numerical Simulation Based on 3DEC.* The NPR anchor cable model was constructed by 3DEC software, and the static tension and mechanical characteristics were simulated, as shown in Figure 21.

The boundary of the old landslide body and “16-1101 landslide body” and the boundary of the excavation area of the shovel are shown in Figure 22.

The NPR anchor parameters are listed in Table 4.

The rock mechanical parameters are listed in Table 5.

(1) The double-sliding model is shown below (Figure 23).

TABLE 4: Parameters of anchor cable.

Anchor cable	Length (m)	Inclination (°)	Preload (kN)	Value of consistence (kN)
	75	30	400	850

TABLE 5: Parameters of rock mechanics.

Rock mass name	Bulk weight (kg/m ³)	Bulk modulus (GPa)	Shear modulus (GPa)	Cohesion (kPa)	Friction angle (°)	Tensile strength (MPa)
Basement	2900	40	18	420	36	1.5
Sliding mass	2500	20	8	70	27	0.2

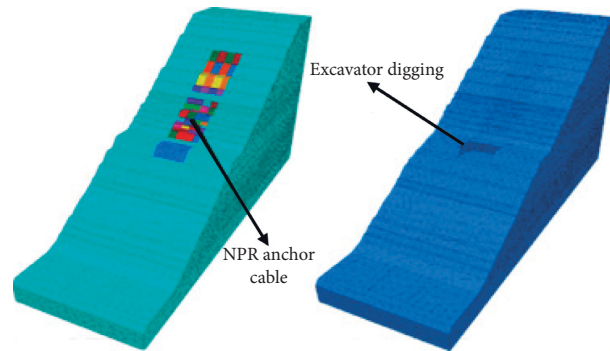


FIGURE 23: Double-sliding model created by 3DEC.

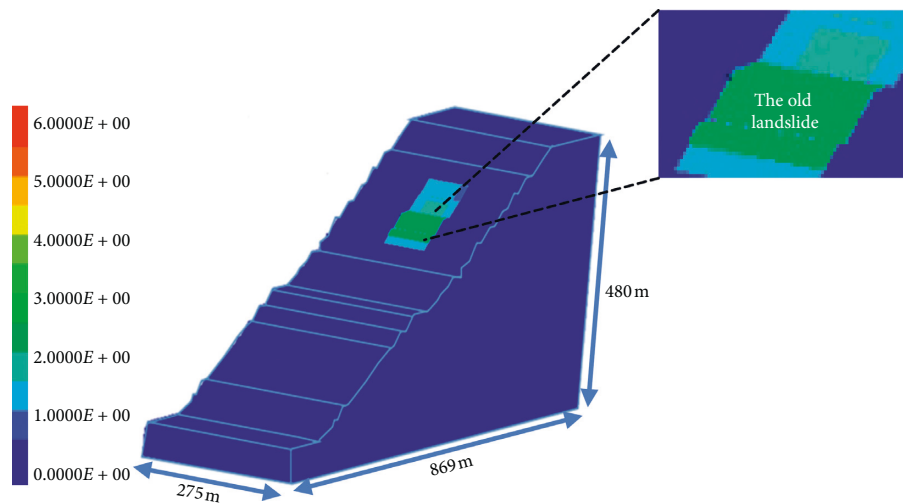


FIGURE 24: Displacement contour after landslide stabilization.

(1) Analysis of the Simulation Results

- (i) The Mohr–Coulomb elastic-plastic model was used to observe the displacement contours of the slip surface, settlement curve, and NPR cable axial force curve.
- (ii) The sign of the stability of the slope is that the subsidence curve does not change, but the calculation is continued.

As shown in Figure 24, the maximum displacement of the old landslide is 1.2 m after stabilization. The landslide body is basically located at the set position of the contact surface of the model. When the landslide starts, the strength of the contact surface is set to the actual strength of the sliding

surface and then slides to the stable state. Because of the reinforcement of multiple anchor cables with constant resistance and large deformation, the 16-1101 sliding body does not slip and disintegrate as a whole, but only emerges from the tongue. In the present extrusion failure mode, tension fracture occurs in the middle and rear edges.

- (iii) Numerical simulation analysis of “16-1101 landslide”

The speed and deformation of the old landslide body set to zero to fully consider the effect of the accumulated load caused by the old landslide body. The numerical simulation of the “16-1101 landslide” started, and the typical three-

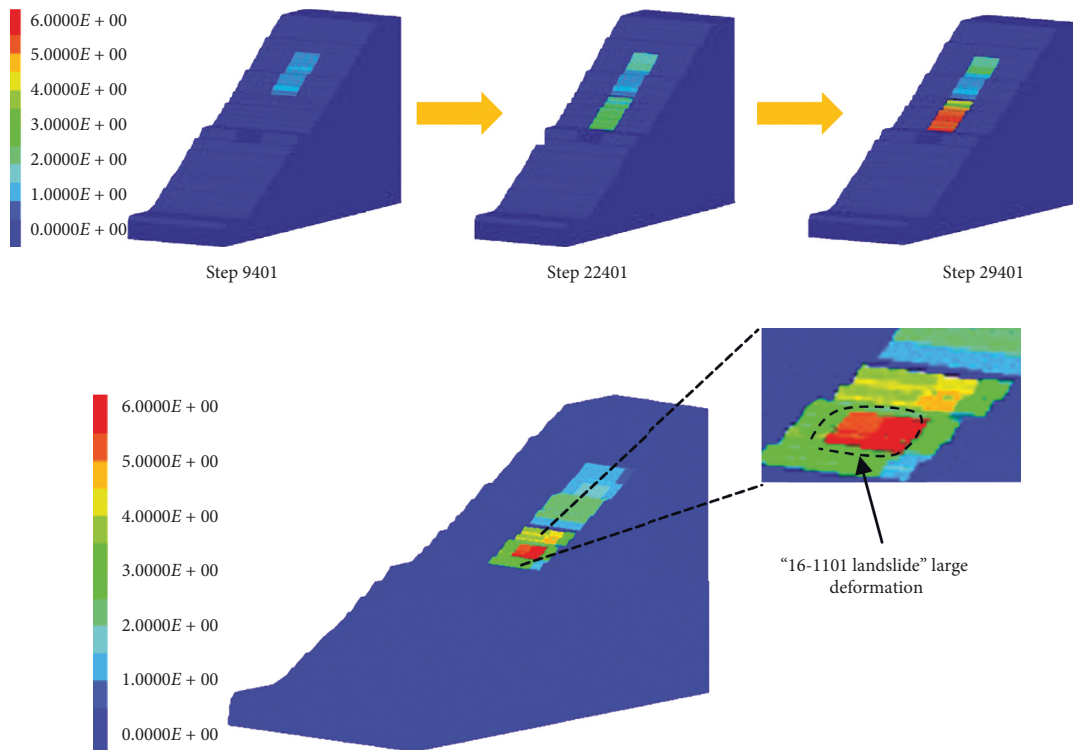


FIGURE 25: 16-1101 landslide instability displacement contour.

TABLE 6: Criteria of strength degradation stages.

Stage classification	Normal stiffness (GPa)	Tangential stiffness (GPa)	Cohesive strength (kPa)	Friction angle (°)
First stage	9	14	148	21
Second stage	9	12	36	20
Third stage	9	10	25	19
Fourth stage	9	8	18	18

step process was used to reproduce the entire landslide instability process.

The “16-1101 landslide” started as a second landslide after the instability of the old landslide body in the upper part. Figure 25 shows the displacement change contour (intercepting steps 9401, 22401, and 29401), and the final displacement contour of the landslide more intuitively shows the whole process of the “16-1101 landslide” instability. The direct cause of the ultimate instability of the whole slope is the penetration of the sliding surface, and the antisliding force is less than the sliding force, gradually deteriorating the strength of the old landslide body. Therefore, in practical calculation, the strength of the contact surface (sliding surface) should be weakened to decrease the rock mass instability. The strength of the contact surface should be divided into stages from the stable state to the final sliding state, as listed in Table 6.

After the start of “16-1101 landslide,” the axial force variation characteristics of the NPR anchor cable, the elongation variation curve of the anchor cable, the vertical relative displacement curve of monitoring point 1 on the upper edge of the old landslide body, and the vertical

relative displacement curve of monitoring point 2 on the upper edge of “16-1101 landslide” are shown in Figure 26.

Figure 27 shows the monitoring point 1 of the subsidence at the upper edge of the old landslide body and monitoring point 2 of the subsidence at the upper edge of the “16-1101 landslide.”

The four stages shown in Figure 26 are summarized as follows:

Stage 1 (shovel excavation at the foot of the slope): the slope body is affected by the disturbance of shovel excavation on 430 m steps. The axial force of the NPR anchor cable increases from 400 kN to 530 kN, and its elongation reaches 0.3 m. The sliding distance is 0.6 m. Stage 2 (revival of the old sliding body): with the excavation of the electric shovel, the sliding force of the slope rock mass increases and then the old sliding body revives, the strength of weak sliding surface decreases gradually, and the axial force of the NPR anchor cable increases sharply; the curve of the axial force monitoring increases rapidly to 680 kN, the elongation of the anchor cable reaches 0.64 m, and the relative displacement of sliding surface is 1.54 m.

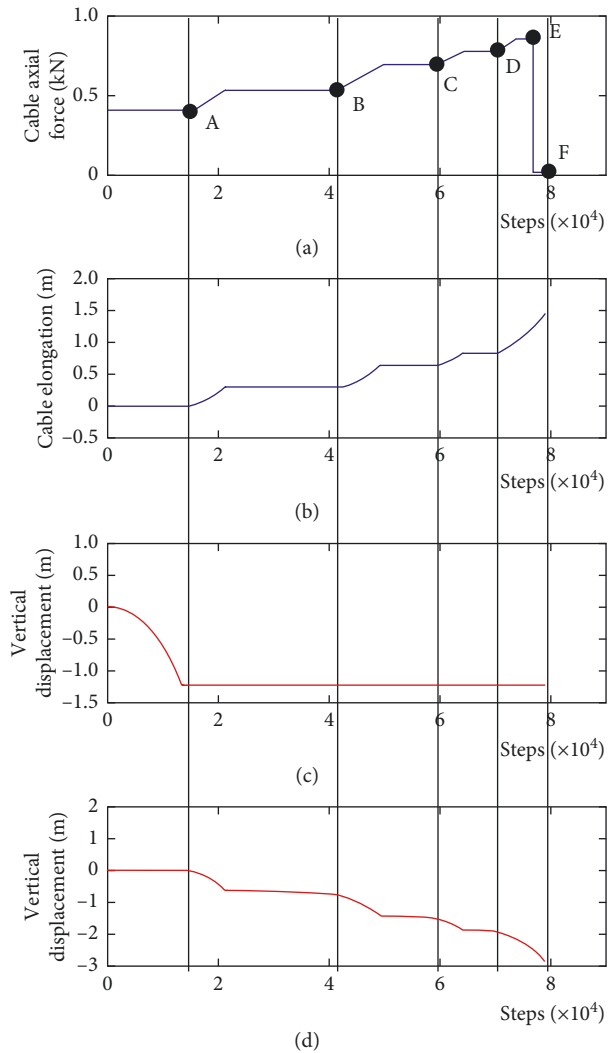


FIGURE 26: Monitoring curve of 16-1101 landslide by 3DEC software: (a) anchor cable force; (b) anchor cable elongation; (c) vertical relative displacement of monitoring point 1; (d) vertical relative displacement of monitoring point 2.

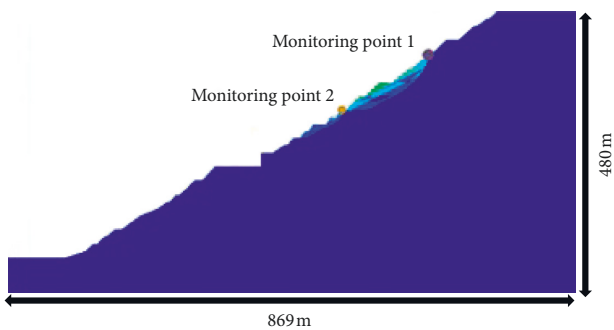


FIGURE 27: Layout of the landslide settlement.

Stage 3 (relative displacement of the 16-1101 slip surface): the slope reached the safety threshold because of shovel excavation. There are microcracks in the rock mass. The slip surface begins to displace relatively. The axial force of the NPR anchor cable rises rapidly to 770 kN, the elongation of the anchor cable reaches

0.84 m, and the slip body generates a relative displacement of 1.87 m along the potential slip surface.

Stage 4 (16-1101 slope near landslide warning): the axial force of the NPR anchor cable continues to rise to a constant resistance of 850 kN. When the relative displacement of the sliding surface reaches 2.54 m, the sliding surface completely loses stability, the anchor cable fails, the axial force suddenly drops to 18 kN, and the anchor cable extends to 1.45 m, eventually sending out warning information.

According to the landslide process, three typical steps are selected in the displacement slice contour to reproduce the landslide process, as shown in Figure 28.

The slope failure simulated by 3DEC is in close agreement to the field investigation parameters: “16-1101 landslide” has an actual settlement of 3.5 m at the top; the slope of the middle part is broken, and the crack zone appears; the sinking amount is 12 m; a compression deformation zone is formed at the bottom, and a settlement is in the range 2-3 m. It is accumulated at a

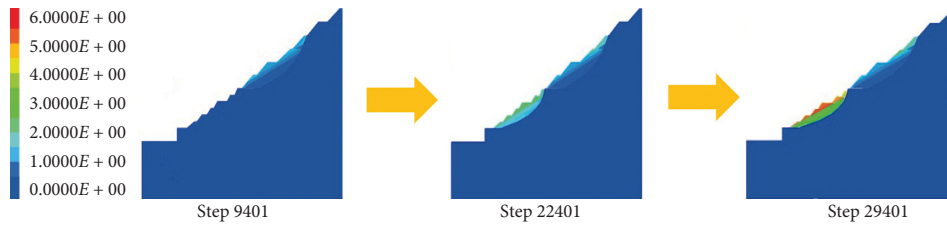


FIGURE 28: Key point displacement slice contour.

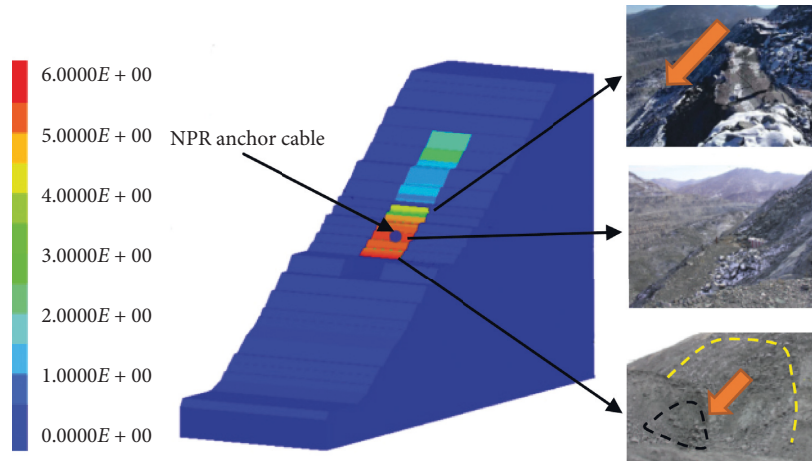


FIGURE 29: Comparison of simulation results with field conditions.

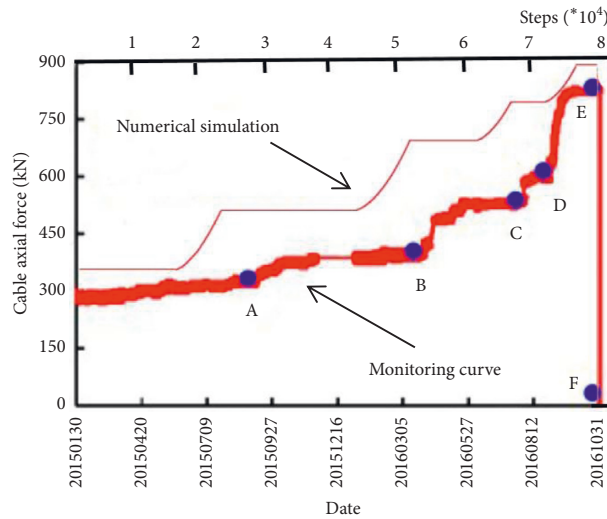


FIGURE 30: Comparison of numerical simulation curve and monitoring curve.

height of 430 m platform at the bottom. Figure 29 shows that the simulation results are consistent with the actual field situation.

The NPR anchor cables built at 478 m steps in the landslide body were further selected, and numerical simulation was performed on the whole process of landslide. The change in the axial force curve was observed (Figure 30), indicating that the curves were significantly consistent with the field monitoring curves, providing a theoretical and practical basis for the analysis of landslide mechanism and numerical simulation calculation of other similar slopes.

4.3. Comparison of the Simulation Results Obtained by *FLAC3D* and *3DEC* Software. The whole landslide process was simulated and analyzed by *FLAC3D* and *3DEC* software. The monitoring curve characteristics and the landslide displacement distribution contour obtained by the two software were compared as follows.

4.3.1. Comparison of the Monitoring Curves. The axial force changes in the NPR anchor cables were monitored by

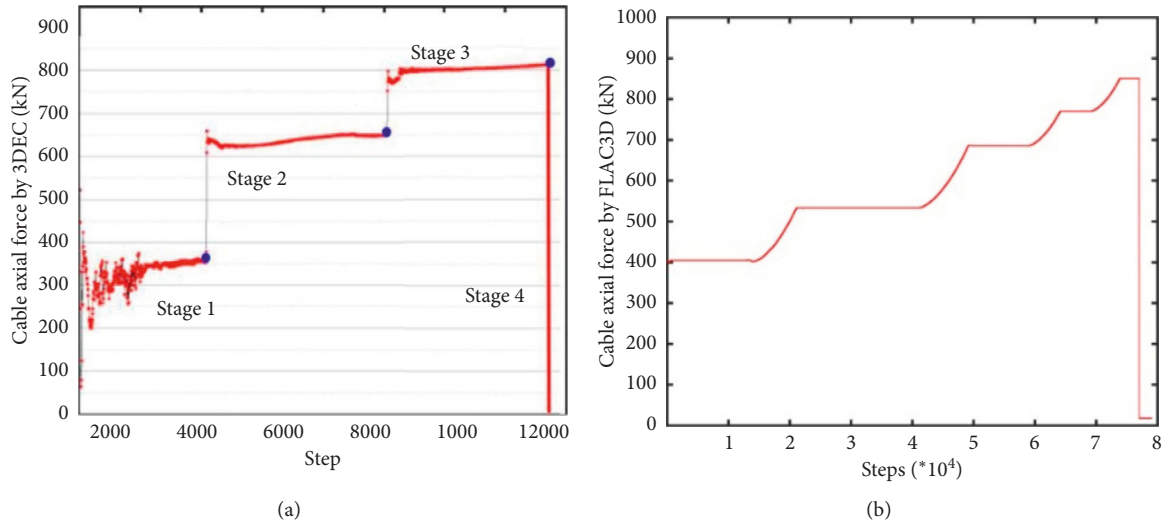


FIGURE 31: Comparison of the axial force variation curve of the NPR anchor cable.

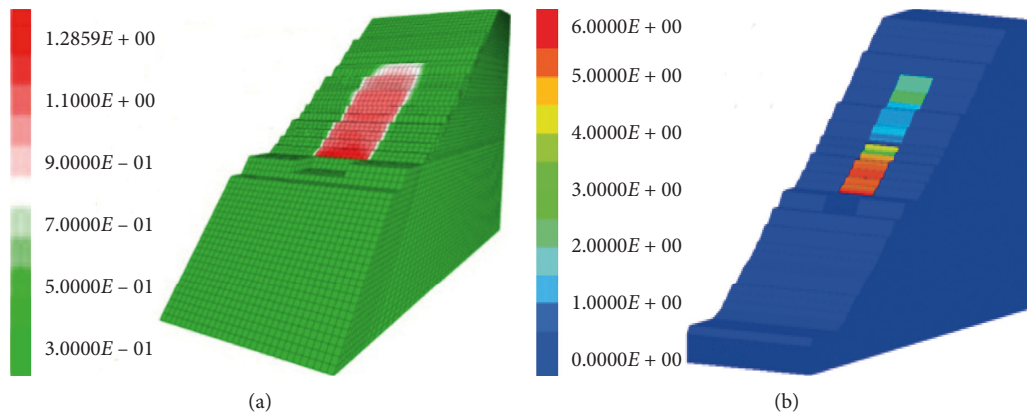


FIGURE 32: Comparison of displacement distribution contour after the landslide instability process.

FLAC3D and 3DEC software. The comparison shows that both have four different degrees of cracks, with identical curve trend and characteristics. As shown in Figure 31, the curves of the axial force variation of the anchor cables were simulated by FLAC3D and 3DEC software in Figures 31(a) and 31(b), respectively.

4.3.2. Comparison of Landslide Displacement Contour. The landslide instability process was also simulated by FLAC3D software and 3DEC software, as shown in Figure 32. Figure 32(a) is simulated by FLAC3D, and the maximum deformation is ~ 5 m; Figure 32(b) is simulated by 3DEC, and the maximum displacement is ~ 6 m, showing a very small difference.

5. Conclusions

In this study, numerical simulation was carried out on the whole process of large deformation and failure of 16-1101 landslide, and the following conclusions were obtained:

- (1) Based on the theory of Cataclysm mechanics, a large deformation numerical calculation model of the NPR anchor cable was constructed, and the simulated curve has a significant constant resistance effect, confirming that the large deformation can be achieved without damage.
- (2) The numerical analysis model of the NPR anchor cable with constant resistance large deformation was constructed by Fish language in the finite element numerical simulation software FLAC3D, and it is embedded in the “2016-1101 landslide,” achieving the numerical simulation of monitoring and warning of Newtonian force. The comparison between the numerical simulation results and the field measurement results shows good agreement between the simulation monitoring curve and the field monitoring curve and proves that this model can be used to monitor the landslide model of Nanfen open-pit mine.
- (3) The numerical calculation model of the NPR anchor cable was constructed by the discrete element

software 3DEC. The numerical simulation monitoring curve of the anchor cable force shows four times of rise and one time of decline, coinciding with the field monitoring curve. The numerical simulation calculation of the whole process monitoring and early warning target of 16-1101 landslide in Nanfen open-pit iron mine was realized, indicating that the model can be used in Nanfen open-pit mine.

- (4) The numerical simulation results of the landslide by FLAC3D and 3DEC software were compared and analyzed, indicating a significant consistency between them. The characteristic cracks are relatively consistent, and the trend of landslide also coincides. The maximum deformation is in the range 5-6 m, with a small difference, thus providing a theoretical and practical basis for the mechanistic analysis and numerical simulation of other similar slopes.

Data Availability

The data used to support the findings of this study are included within the article.

Conflicts of Interest

The authors declare that they have no conflicts of interest.

Acknowledgments

This study was supported by the Zhejiang Province Key R&D Projects (No. 2019C03104) and the Fundamental Research Funds for the Central Universities, SCUT (No. 2015QB02).

References

- [1] Y. Li, S. Zhang, and X. Zhang, "Classification and fractal characteristics of coal rock fragments under uniaxial cyclic loading conditions," *Arabian Journal of Geosciences*, vol. 11, no. 9, p. 201, 2018.
- [2] Z. Qin, H. Fu, and X. Chen, "A study on altered granite meso-damage mechanisms due to water invasion-water loss cycles," *Environmental Earth Sciences*, vol. 78, no. 14, p. 428, 2019.
- [3] J. Wang, S.-c. Li, L.-p. Li, P. Lin, Z.-h. Xu, and C.-l. Gao, "Attribute recognition model for risk assessment of water inrush," *Bulletin of Engineering Geology and the Environment*, vol. 78, no. 2, pp. 1057–1071, 2019.
- [4] S. Zhang, Y. Li, B. Shen, X. Sun, and L. Gao, "Effective evaluation of pressure relief drilling for reducing rock bursts and its application in underground coal mines," *International Journal of Rock Mechanics and Mining Sciences*, vol. 114, pp. 7–16, 2019.
- [5] W. Sun, H. Du, F. Zhou, and J. Shao, "Experimental study of crack propagation of rock-like specimens containing conjugate fractures," *Geomechanics and Engineering*, vol. 17, pp. 323–331, 2019.
- [6] X. J. Yang, C. W. Hu, M. C. He et al., "Study on presplitting blasting the roof strata of adjacent roadway to control roadway deformation," *Shock and Vibration*, vol. 2019, Article ID 3174898, 16 pages, 2019.
- [7] T. Kamai, "Monitoring the process of ground failure in repeated landslides and associated stability assessments," *Engineering Geology*, vol. 50, no. 1-2, pp. 71–84, 1998.
- [8] R. Ohbayashi, Y. Nakajima, H. Nishikado, and S. Takayama, "Monitoring system for landslide disaster by wireless Sensing node network," in *Proceedings of the 2008 SICE Annual Conference*, pp. 1704–1710, Tokyo, Japan, August 2008.
- [9] G. Puglisi, A. Bonaccorso, M. Mattia et al., "New integrated geodetic monitoring system at Stromboli volcano (Italy)," *Engineering Geology*, vol. 79, no. 1-2, pp. 13–31, 2005.
- [10] B. A. Reevea, G. F. Stickley, D. A. Noon, and I. D. Longstaff, "Developments in monitoring mine slope stability using radar interferometry," in *Proceedings of the 2000 IEEE International Geoscience and Remote Sensing Symposium*, pp. 2325–2327, Honolulu, HI, USA, July 2000.
- [11] P. Allasia, A. Manconi, D. Giordan, M. Baldo, and G. Lollino, "ADVICE: a new approach for near-real-time monitoring of surface displacements in landslide hazard scenarios," *Sensors*, vol. 13, no. 7, pp. 8285–8302, 2013.
- [12] S. Choon, Y. Jung, P. Hyeong-Dong, and Y. Choi, "Failure prediction for weak rock slopes in a large open-pit mine by GPS measurements and assessment of landslide susceptibility," *The Journal of Engineering Geology*, vol. 20, pp. 243–255, 2010.
- [13] M. E. Hartwig, "Detection of mine slope motions in Brazil as revealed by satellite radar interferograms," *Bulletin of Engineering Geology and the Environment*, vol. 75, no. 2, pp. 605–621, 2016.
- [14] T. Carlà, V. Tofani, L. Lombardi et al., "Combination of GNSS, satellite InSAR, and GBInSAR remote sensing monitoring to improve the understanding of a large landslide in high alpine environment," *Geomorphology*, vol. 335, pp. 62–75, 2019.
- [15] L. He, L. Wu, S. Liu, Z. Wang, C. Su, and S.-N. Liu, "Mapping two-dimensional deformation field time-series of large slope by coupling DInSAR-SBAS with MAI-SBAS," *Remote Sensing*, vol. 7, no. 9, pp. 12440–12458, 2015.
- [16] A. Michellini, N. Coli, F. Coppi et al., "Advanced data processing of ground-based synthetic aperture radar for slope monitoring in open pit mines," in *Proceedings of the 2015 24th International Mining Congress of Turkey*, pp. 420–427, Antalya, Turkey, April 2015.
- [17] S. J. Miao, X. Hao, X. L. Guo, Z. M. Wang, and M. C. Liang, "Displacement and landslide forecast based on an improved version of Saito's method together with the Verhulst-Grey model," *Arabian Journal of Geosciences*, vol. 10, no. 3, p. 53, 2017.
- [18] M. He, W. Gong, J. Wang et al., "Development of a novel energy-absorbing bolt with extraordinarily large elongation and constant resistance," *International Journal of Rock Mechanics and Mining Sciences*, vol. 67, pp. 29–42, 2014.
- [19] M. He, C. Li, W. Gong, L. R. Sousa, and S. Li, "Dynamic tests for a Constant-Resistance-Large-Deformation bolt using a modified SHTB system," *Tunnelling and Underground Space Technology*, vol. 64, pp. 103–116, 2017.
- [20] M. He, Y. Wang, and Z. Tao, "A new early-warning prediction system for monitoring shear force of fault plane in the active fault," *Journal of Rock Mechanics and Geotechnical Engineering*, vol. 2, no. 3, pp. 223–231, 2010.
- [21] M. C. He, Y. J. Wan, J. Yang, P. Zhou, Q. Gao, and Y. B. Gao, "Comparative analysis on stress field distributions in roof cutting non-pillar mining method and conventional mining method," *Journal of China Coal Society*, vol. 43, pp. 626–637, 2018.
- [22] Z. G. Tao, C. Zhu, X. H. Zheng, and M. C. He, "Slope stability evaluation and monitoring of Tonglushan ancient copper mine relics," *Advances in Mechanical Engineering*, vol. 10, no. 8, pp. 1–16, 2018.

- [23] Z. G. Tao, Z. Zhu, W. S. Han et al., "Static tension test and the finite element analysis of constant resistance and large deformation anchor cable," *Advances in Mechanical Engineering*, vol. 10, no. 12, pp. 1–13, 2018.
- [24] Z. G. Tao, C. Zhu, Y. Wang, J. M. Wang, M. C. He, and B. Zhang, "Research on stability of an open-pit mine dump with fiber optic monitoring," *Geofluids*, vol. 2018, Article ID 9631706, 20 pages, 2018.
- [25] Z. Tao, Y. Wang, C. Zhu, H. Xu, G. Li, and M. He, "Mechanical evolution of constant resistance and large deformation anchor cables and their application in landslide monitoring," *Bulletin of Engineering Geology and the Environment*, vol. 78, no. 7, pp. 4787–4803, 2019.
- [26] Z. Li, Y. Jiang, Z. Tao, and M. He, "Monitoring prediction of a rockslide in an open-pit mine and numerical analysis using a material instability criterion," *Bulletin of Engineering Geology and the Environment*, vol. 78, no. 3, pp. 2041–2053, 2019b.
- [27] B. Maihemuti, E. Z. Wang, T. Hudan, and Q. J. Xu, "Numerical simulation analysis of reservoir bank fractured rock-slope deformation and failure processes," *International Journal of Geomechanics*, vol. 16, no. 2, 2016.
- [28] J. Li, Y. Gao, Y. Li, B. Cui, and Z. Deng, "Intelligent back analysis of constitutive parameters for soil slope based on unified strength theory," in *Proceedings of the 2011 2nd ISRM International Young Scholars' Symposium on Rock Mechanics, Rock Mechanics: Achievements and Ambitions*, pp. 941–945, Beijing, China, October 2011.
- [29] T.-H. Yang, W.-H. Shi, P.-T. Wang, H.-L. Liu, Q.-L. Yu, and Y. Li, "Numerical simulation on slope stability analysis considering anisotropic properties of layered fractured rocks: a case study," *Arabian Journal of Geosciences*, vol. 8, no. 8, pp. 5413–5421, 2015.
- [30] L. Jing, "A review of techniques, advances and outstanding issues in numerical modelling for rock mechanics and rock engineering," *International Journal of Rock Mechanics and Mining Sciences*, vol. 40, no. 3, pp. 283–353, 2003.
- [31] D. Stead, J. S. Coggan, and E. Eberhardt, "Realistic simulation of rock slope failure mechanisms: the need to incorporate principles of fracture mechanics," *International Journal of Rock Mechanics and Mining Sciences*, vol. 41, no. 3, p. 466, 2004.
- [32] D. Stead, E. Eberhardt, and J. S. Coggan, "Developments in the characterization of complex rock slope deformation and failure using numerical modelling techniques," *Engineering Geology*, vol. 83, no. 1–3, pp. 217–235, 2006.
- [33] A. Munjiza, T. Bangash, and N. W. M. John, "The combined finite-discrete element method for structural failure and collapse," *Engineering Fracture Mechanics*, vol. 71, no. 4–6, pp. 469–483, 2001.
- [34] M. Barla, G. Piovano, and G. Grasselli, "Rock Slide Simulation with the combined finite-discrete element method," *International Journal of Geomechanics*, vol. 12, pp. 711–721, 2011.
- [35] D. Elmo, D. Stead, E. Eberhardt, and A. Vyazmensky, "Applications of finite/discrete element modeling to rock engineering problems," *International Journal of Geomechanics*, vol. 13, no. 5, pp. 565–580, 2013.
- [36] O. K. Mahabadi, A. Lisjak, A. Munjiza, and G. Grasselli, "Y-Geo: new combined finite-discrete element numerical code for geomechanical applications finite-discrete element numerical code for geomechanical applications," *International Journal of Geomechanics*, vol. 12, no. 6, pp. 676–688, 2012.
- [37] A. Munjiza, D. R. J. Owen, and N. Bicanic, "A combined finite-discrete element method in transient dynamics of fracturing solids," *Engineering Computations*, vol. 12, no. 2, pp. 145–174, 1995.

Research Article

Development of Debris Flow Impact Force Models Based on Flume Experiments for Design Criteria of Soil Erosion Control Dam

Song Eu ¹, Sangjun Im ¹ and Dongyeob Kim ²

¹Department of Forest Sciences, Seoul National University, Seoul 08826, Republic of Korea

²Division of Research Planning and Coordination, National Institute of Forest Science, Seoul 02455, Republic of Korea

Correspondence should be addressed to Dongyeob Kim; dongyeob.kim1@gmail.com

Received 26 September 2019; Accepted 22 November 2019; Published 31 December 2019

Guest Editor: Young-Suk Song

Copyright © 2019 Song Eu et al. This is an open access article distributed under the Creative Commons Attribution License, which permits unrestricted use, distribution, and reproduction in any medium, provided the original work is properly cited.

Soil erosion control dams are widely used as part of measures to reduce damage caused by debris flow all over the world. Engineering considerations are needed for proper design of erosion control dams, but in the Republic of Korea, the impact force of debris flow is not fully reflected in the current design criteria of the dam. Against this backdrop, this study was conducted to estimate the impact force of debris flow for the practical purpose of designing erosion control dam. Simulated flume experiments were performed to develop the relationship to estimate the flow velocity as well as the impact force of debris flow. Experimental results showed that increases both in sediment mixture volume and flume slope gradient led to an increase in flow velocity. Especially, it was found that as clay content increased gradually, the flume slope gradient had greater impact on the increase of flow velocity. Also, it was proved that the impact force of debris flow was well fitted to the hydrodynamic model as it showed linear correlation with the flow velocity. Then, the debris-flow velocity model was established based on the factor related to the debris-flow velocity. Finally, the dynamic model to estimate the impact force of debris flow was introduced utilizing correlations between the established debris-flow velocity model and Froude number. Both models which were developed with using statistically significant watershed characteristics succeeded in explaining the experiment results in a more accurate way compared to existing models. Therefore, it is highly expected that these models can be fully utilized to estimate impact force of debris flow which will be required to design erosion control dams in practical use through overcoming their identified limitations.

1. Introduction

Debris flow refers to a geological phenomenon in which mixture of sediment and water consisting of various soil particles ranging from fine clay to large boulder rushes down a mountainside at high velocity [1]. While debris flow occurs from various causes generally, particularly, in South Korea, localized heavy rain in summer is the main reason for debris flow [2]. In most cases, landslide-induced sediment at hillside becomes debris flow as it flows into a mountain stream. Such debris flow was rarely found in South Korea until the 1980s when the government almost completed reforestation. However, since 2000, its occurrence has been on the gradual increase to become the type of sediment-related disaster inflicting the biggest damage. The average landslide-damaged area was 715 ha per year in 2000s while it

was 313 ha per year during 1981–1999 [3]. Recently, debris flow that killed tens of people and caused hundreds of property damage occurred at Mt. Umyeon in Seoul, the capital city of South Korea, in July 2011. It is the first sediment-related disaster in South Korea which occurred and brought massive damage to the center of the urbanized area. Since the devastating landslide occurred in the city, the paradigm shift was introduced in the formulation of land disaster policy focused on from “mountain area” to “sphere of daily life.”

The most common countermeasures against debris flow include structure measure, nonstructure measure, and watershed management. The method of employing soil erosion control dam (ECD) is to block debris flow directly with structure. It is the most applicable as well as effective in urban areas with high population density and intensive land

use. To perform the function of ECDs as debris-flow barriers or breaker structures in urban area, dynamic features of debris flow shall be considered in the design of structures. In nations such as Japan and Austria, a number of debris barriers have been constructed to block debris flow directly under the design criteria considering the impact force of debris flow.

Generally, it is difficult to quantitatively measure the impact force of debris flow at the field. Therefore, modeling approach has been employed to calculate the force which utilizes the dynamics of flow characteristics of debris flow and impact force [4–7]. The hydrodynamic model is applied and used well in practical use because it can provide the clear and explicit understanding on the physical phenomenon of “impact” with physical factors such as density and flow velocity of debris flow [8–10]. In order to utilize the hydrodynamic model to estimate the impact force of debris flow, it is most important to estimate the debris-flow velocity. Various methods have been applied so far from simple empirical model to precise numerical analysis. Despite high accuracy of numerical analysis models, it is not used widely for both challenges in practice: (i) it is difficult to attain the parameter at the field and (ii) observed data to verify the results are insufficient. For these reasons, a simple empirical model has been commonly used to estimate the flow velocity of debris flow.

In the past, the focus had been placed on the “soil conservation” to restore degraded mountainous areas rather than “disaster prevention” to protect against debris flow directly when ECDs were constructed. Thus, except for static characteristics of sediment pressure and water pressure, dynamic characteristics such as impact force of debris flow were not fully considered in the design of ECDs. Therefore, it is urgent and necessary to establish the estimation of impact force of debris flow applicable to the situation of South Korea and design standard for construction of ECD. The size of debris flow in South Korea is relatively small when compared to that of Australia and Japan with a high frequency of debris flow. Moreover, the construction budget including design per each unit—250 million Korean Won (≈ 200 thousand USD) per unit—is cheaper. For these reasons, the impact force of debris flow shall be calculated with the cost-effective way.

From this point of view, the current study was conducted to suggest that impact force of debris flow be incorporated in designing ECDs. As part of this effort, it was intended not only to estimate the flow velocity of debris flow by using design factors of debris barrier or watershed characteristics but also to develop a model to calculate the impact force based on the flow velocity. We tried to clearly identify the relations between two factors, flow velocity and impact force, by conducting debris-flow flume experiments, and to derive the models to estimate flow velocity and impact force of debris flow, respectively.

2. Materials and Methods

2.1. Experimental Flume. Small-sized flume (Figure 1) employed for the debris-flow experiment was made of

transparent polycarbonate (PC), and it has $0.2\text{ m} \times 0.3\text{ m}$ rectangular section whose total length is 2.0 m. The upper part of the flow path is linked with sediment mixture storage tank whose capacity is 0.48 m^3 equipped with manually operated movable gate. Force plate with load cell is attached to the bottom of the flow path to measure the impact force of a sediment mixture. The gradient of the flume is adjustable manually by 5° interval within ranges from 20° to 40° .

2.2. Sediment Mixture of Experiment. To simulate the key feature of debris flow in flume experiment, various mixed sets of clay, sand, and gravel combined with water were employed. The result of field investigation around watersheds of Mt. Umyeon where debris flow event occurred in 2011 was reflected to decide the composition of sediment mixture. SMG [11] indicates that the largest diameter size of boulders found in the debris flow was 1.5–2.0 m. The diameter of gravel, representative of large particle, was set as 5 mm in average based on the length ratio of experiment flume and the real debris flow, 1 : 300. It was reported that both silt and clay accounted for about 50% of the total particle composition of colluvium layers in the site [11]. However, the ratio of sand and clay was set as 1 to 1, the same ratio of the field, while it was hard to satisfy dynamic similarity if considering the length ratio of 1 : 300.

After considering particle composition of sediment mixture, we chose two factors of “total volume” and “viscosity” among various characteristics of sediment mixtures that could affect to flow velocity and flow depth. A total of nine types of sediment mixture were provided by classifying each factor (total volume and viscosity) into three levels, respectively (Table 1). Specifically, the volume of sediment mixture was classified into three sizes—small (indexing “S,” $5.03 \times 10^{-3}\text{ m}^3$), medium (indexing “M,” $6.65 \times 10^{-3}\text{ m}^3$), and large (indexing “L,” $8.35 \times 10^{-3}\text{ m}^3$). As for viscosity, clay content was divided into 21% (A), 25% (B), and 29% (C) of the total weight of sediment mixture. Except for both factors, the density of $1,676\text{ kg}\cdot\text{m}^{-3}$ and gravitational water contents of 0.36 of sediment mixture were fixed to the same value in each set of sediment mixture.

2.3. Experimental Condition and Result Analysis. For measurement of flow velocity and impact force of sediment mixtures, flume experiments were repeated three times for every nine types of sediment mixtures with different volumes and clay contents under three conditions of flume gradients, 25° , 30° , and 35° . Whenever we implemented experiments, water and soil of the sediment mixture were fully mixed before it was put into the storage of the flume. Afterwards, they were continuously stirred even just before the storage gate opened to minimize separation. And then, the storage gate was opened to discharge the sediment mixture. The video camera was installed to capture how sediment mixtures were flowing, and the impact force was measured when the sediment mixture reached the plate attached with the load cell at the bottom of the flow path.

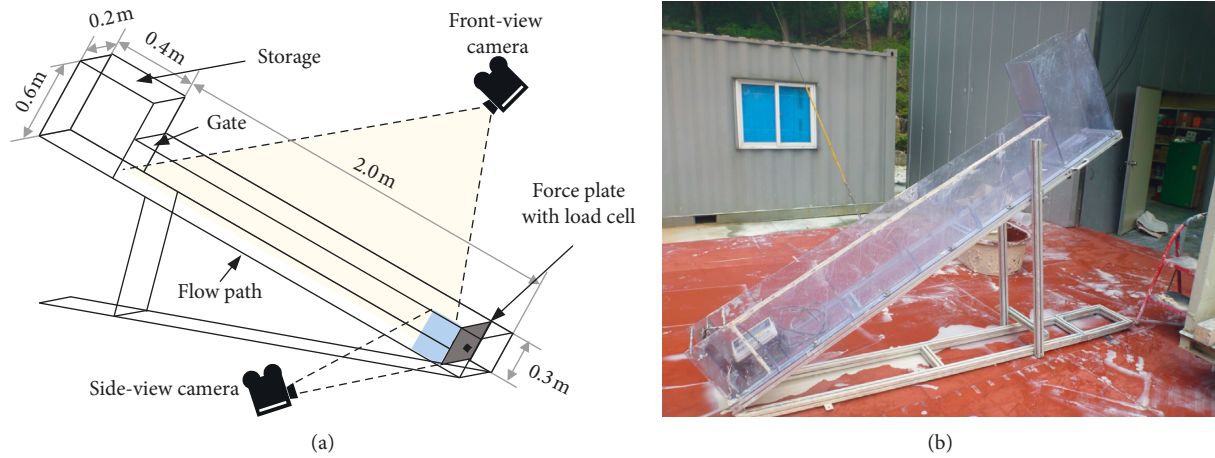


FIGURE 1: Schematic design (a) and photograph (b) of experimental flume and measuring instrument.

TABLE 1: Overview of mean (\pm the standard error of the mean) sediment mixture properties.

Volume index	Viscosity index	Total volume (10^{-3} m^3)	Weight (kg)	Density (kg m^{-3})	Clay (kg)	Sand (kg)	Gravel (kg)	Water (10^{-3} m^3)
S	A	5.02 ± 0.03	8.40 ± 0.03	1672.38 ± 0.03	1.80 ± 0.03	1.80 ± 0.03	1.80 ± 0.03	3.00
	B	5.04 ± 0.02	8.40 ± 0.02	1667.67 ± 0.02	2.10 ± 0.02	2.10 ± 0.02	1.20 ± 0.02	3.00
	C	5.04 ± 0.03	8.40 ± 0.03	1668.35 ± 0.03	2.40 ± 0.03	2.40 ± 0.03	0.60 ± 0.03	3.00
M	A	6.74 ± 0.03	11.20 ± 0.03	1661.37 ± 0.03	2.40 ± 0.03	2.40 ± 0.03	2.40 ± 0.03	4.00
	B	6.59 ± 0.07	11.20 ± 0.07	1701.43 ± 0.07	2.80 ± 0.07	2.80 ± 0.07	1.60 ± 0.07	4.00
	C	6.61 ± 0.04	11.20 ± 0.04	1694.24 ± 0.04	3.20 ± 0.04	3.20 ± 0.04	0.80 ± 0.04	4.00
L	A	8.34 ± 0.02	14.00 ± 0.02	1679.52 ± 0.02	3.00 ± 0.02	3.00 ± 0.02	3.00 ± 0.02	5.00
	B	8.37 ± 0.02	14.00 ± 0.02	1672.15 ± 0.02	3.50 ± 0.02	3.50 ± 0.02	2.00 ± 0.02	5.00
	C	8.36 ± 0.04	14.00 ± 0.04	1675.18 ± 0.04	4.00 ± 0.04	4.00 ± 0.04	1.00 ± 0.04	5.00

“S, M, and L” mean different volume conditions (about $5.03 \times 10^{-3} \text{ m}^3$, $6.64 \times 10^{-3} \text{ m}^3$, and $8.35 \times 10^{-3} \text{ m}^3$, respectively) and “A, B, and C” mean different clay contents (about 21%, 25%, and 29% of total weight, respectively).

Flow characteristics of the sediment mixtures were obtained by using an image analysis method with two cameras (30 fps). The flow velocity was analyzed from the front-view camera image while the flow depth was estimated from the side-view camera image. As the flow velocity, we used velocity of the snout of the sediment mixture just before its impact to the force plate of the flume. Also, maximum depth of the snout of the sediment mixture at 0.1 m away from the force plate was used as flow depth. Load cell (Model MN-100L by CAS) and data logger of 80 Hz sampling frequency (Model CI-201A by CAS) were used to measure the impact force of the flow.

The experiment results, such as relationships among flow velocity, flow depth, and impact force of sediment mixture, were statistically analyzed to propose relevant models. Statistical analysis on the correlation of flow velocity, impact force, and experimental parameters such as volume and clay contents of sediment mixture and flume slope gradient was conducted by utilizing three-way ANOVA. Furthermore, model parameters for debris-flow impact force model were induced based on the experiment results, and regression analysis was employed to identify the relationship between the coefficient of the model and Froude number (Fr) that represented the flow characteristics. R software ver. 3.3.2 was utilized for such statistical analysis and introducing the model.

3. Results and Discussion

3.1. Results of Flume Experiments

3.1.1. Consideration of Similarity. We compared Froude numbers between flume experiment and real debris flow events in the previous studies to review reproducibility of the debris flow. The results of flume experiments in the current study showed the Fr of 2.3–9.1. It is hard to compare Fr of the Mt. Umyeon debris flow event in 2011 as we have no measured flow velocity. Fr of debris flow generally ranges from 0 to 3 in the gentle gradient of less than 25° [6, 12]. Exceptionally, it was also reported that it ranged from 5 to 7 in some case [5, 12]. In small-scaled flume experiments [12, 13] which were assessed to reproduce the phenomenon of debris flow, Fr ranged from 1.2 to 12. In conclusion, it displays a tendency that the Fr range in the flume experiment is in accordance with previous studies. Therefore, it can be concluded that the current study reproduced the debris flow.

3.1.2. Variations of Flow Characteristics and Impact Force under Experimental Conditions. As shown in Figure 2, the results indicated that the flow velocity of sediment mixture tended to increase when the flume gradient and volume of

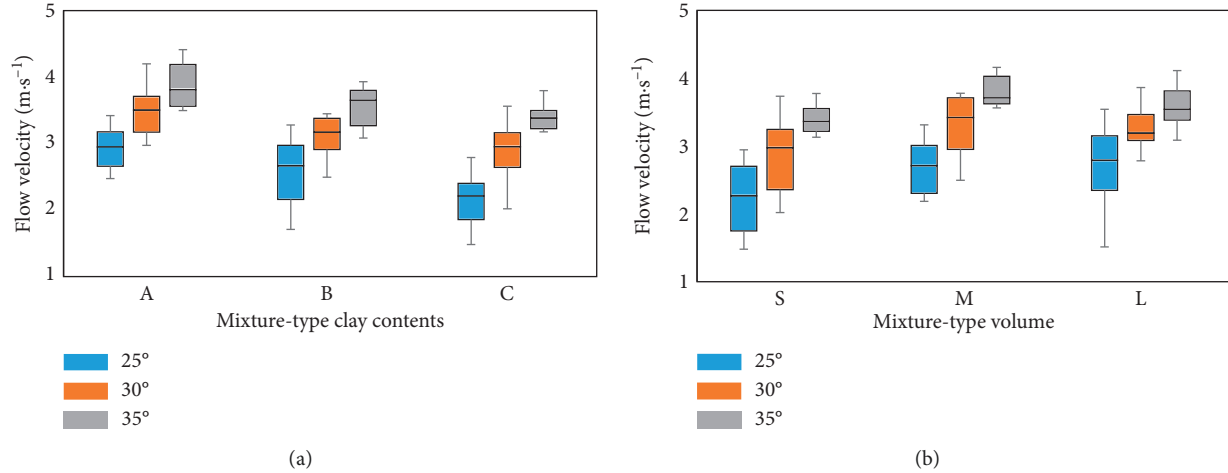


FIGURE 2: The change of flow velocity according to clay contents (a) and mixture volume (b) as slope condition changes.

the mixture increased while clay content decreased (Table 2). Especially, it showed that the higher the clay content was, the greater impact the flume gradient had on the increase of velocity of sediment mixture. While an increase of flume gradient or volume enhanced gravity force to make flow velocity faster, it was proved that energy loss caused by internal shear friction originated from increased clay content led to flow velocity reduction [14, 15].

It was found that the flow depth of sediment mixture was statistically related to the volume ($r = 0.53$, p value < 0.01) despite a statistically weak correlation between the flume slope and the clay content (Figure 3). Generally, a correlation between total volume and flow depth of debris flow is well known [16], but it is assumed that such a weak correlation among flow depth of sediment mixture, clay content, and flume slope might be affected by several factors such as measurement errors due to video camera performance and status of mixture which was not fully mixed.

The experiment results showed that flume gradient, volume, and clay content of sediment mixture were statistically significant with the impact force of sediment mixture with the significance level of 99% (ANOVA). Meanwhile, it appeared to be an interaction between the flume gradient and clay content (p value < 0.01). Considering the relation between flow velocity and impact force expressed as a hydrodynamic model, it seems to reflect that the increase rate of flow velocity with increasing slope tended to vary depending on the clay content.

3.1.3. Relationship between Flow Characteristics and Impact Force of Sediment Mixture. Figure 4 shows flow velocity and flow depth of sediment mixture with impact force, respectively. According to Figure 4, while flow velocity was in the linear correlations with impact force, linear correlations between the flow depth and impact force was weak.

In previous studies [6, 12], a hydrodynamic model indicates that there is a linear correlation between the square of flow velocity and impact force of debris flow, but the results showed that impact force had a close linear correlation with flow velocity as the exponent of flow velocity in the

TABLE 2: The result of ANOVA of the flow velocity and experimental variables.

	Degree of freedom	F value	p value ($>F$)
MR	2	25.49	< 0.01
V	2	17.63	< 0.01
S	2	80.42	< 0.01
MR * V	4	1.04	0.39
MR * S	4	1.06	0.38
V * S	4	1.71	0.16
MR * V * S	8	0.62	0.75
Residual	75		

“MR” is mixing ratio, “V” is volume, and “S” is channel slope.

experiment is close to one. It is because the coefficient of a hydrodynamic model exhibits the linear correlations with Fr^{-1} [12]. Because Fr^{-1} is dimensionless coefficient that is proportional to flow velocity, impact force shows the linear correlations with flow velocity by multiplying Fr^{-1} and square of flow velocity in the case where it is expressed only as flow velocity as shown in Figure 4(a).

3.2. Estimation of the Debris-Flow Velocity Model. Most existing debris-flow velocity models were expressed as the function of channel slope and flow quantity that is represented as flow depth [5, 14] or instant discharge [16]. Meanwhile, flow depth or instant discharge are closely correlated with total sediment discharge [10, 16], and the results of flume experiments also showed the similar relationship between flow depth and total volume of mixture. Considering this correlation, the current study built the function of flume gradient and volume of water-sediment mixture to estimate the velocity of debris flow based on the results of the flume experiments. The experiment results indicated that changes in the debris-flow velocity at certain flume gradient were affected by clay content, “viscosity.” Based on the results, a power function of the viscosity of sediment mixture was set as an exponent of flume gradient. The following equation to estimate the velocity of debris flow was established:

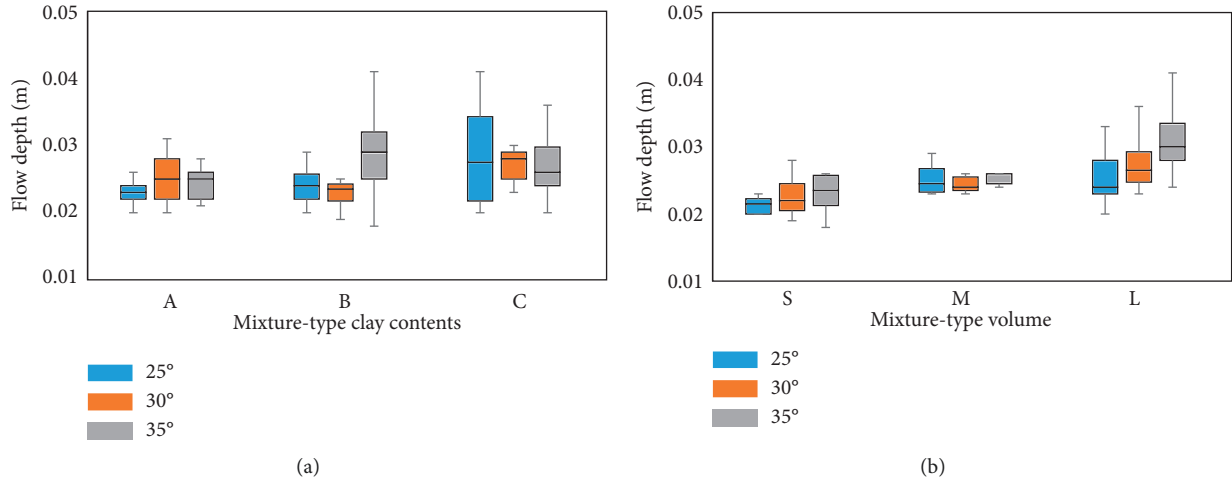


FIGURE 3: The change of flow depth according to clay contents (a) and mixture volume (b) as slope condition changes.

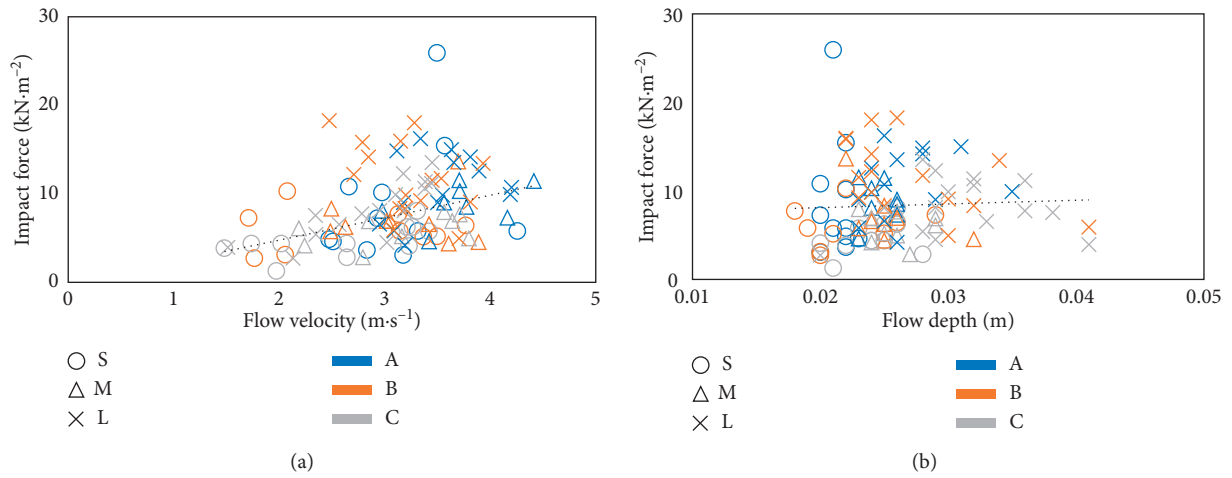


FIGURE 4: The relationship between impact force and flow behavior. The horizontal axis is flow velocity (a) and flow depth (b). Circle, triangle, and cross symbols mean “S, M, and L” of volume condition. Blue, orange, and gray colors mean “A, B, and C” of viscosity condition.

$$v = C_e S^\alpha Cr^\beta V^\gamma, \quad (1)$$

where v represented the velocity of debris flow (m·s⁻¹), S is the gradient of the flume (m·m⁻¹), Cr is the viscosity factor, V is the volume of sediment mixture (m³), and C_e , α , β , and γ are all constants. It follows how the values of constants α , β , γ , and C_e were calculated step by step.

- (i) Volume constant γ : volume constant γ at clay content of A, B, and C by each flume gradient was calculated to 0.1966 (p value < 0.01), 0.3936 (p value < 0.01), and 0.3484 (p value < 0.05), respectively. If the dimensions of both sides of equation (1) are different due to flow depth or exponent constant of the volume, the constant C_e is to have dimension L to offset this. As indicated in Rickmann [16] and Eu and Im [14], if we use the constant whose dimension is L, it is hard to explain

debris flow in reality because of the scale problem. Therefore, in the current study, we assumed γ as a dimensionless value, that is, 0.33 ($\approx 1/3$), for better applicability at the site.

- (ii) Empirical constant C_e : Because γ was determined, both side of equation (1) were divided by $V^{1/3}$, and it is expressed as equation (2). Then, to determine C_e , we conducted the regression analysis of power model. Meanwhile, it was hard to calculate C_e using simple power model regression since the exponent of S also expressed as a power function form which has α and β as unknown. Thus, to minimize unknown, the power model regression was derived in clay content A, B, and C, separately; it was expressed as equation (3)–(5), respectively. As the result C_e in equation (3)–(5) showed very small variation, we estimated the value of C_e as the average value of 25.91 from equation (3)–(5).

$$\text{Base: } \frac{v}{V^{1/3}} = C_e S^b, \quad (2)$$

$$\text{Case (A): } \frac{v}{V^{1/3}} = 25.60 S^{0.63}, \quad R^2 = 0.5759, \quad p \text{ value} < 0.01, \quad (3)$$

$$\text{Case (B): } \frac{v}{V^{1/3}} = 25.52 S^{0.86}, \quad R^2 = 0.5394, \quad p \text{ value} < 0.01, \quad (4)$$

$$\text{Case (C): } \frac{v}{V^{1/3}} = 26.62 S^{1.12}, \quad R^2 = 0.5555, \quad p \text{ value} < 0.01. \quad (5)$$

(iii) α and β : equation (6) was produced when applying the logarithm (ln) to both sides of the equation and leaving b in the right hand. Here, b was according to equation (1):

$$\frac{\ln(v/V^{1/3}) - \ln C_e}{\ln S} = b = \alpha Cr^\beta. \quad (6)$$

To obtain values of α and β , we substituted values of flume experiment results to equation (6). As for viscosity index, we applied the universal value of water-to-clay ratio that had been utilized in Jeong [17] instead of clay content in soil which exhibited greater variability. In the study of Jeong [17], the liquidity index (LI) was utilized to assess the viscosity of debris flow. Atterberg limits were evaluated as the amount of fine particles less than 425 microns, which corresponded to clay in the sediment mixture employed in the current study. Therefore, it was reasonable to apply water-to-clay ratio as in equation (6) when considering the correlation with Atterberg limits. We assumed equation (6) as regression equation of power function, and the results on the value of constant α and β were produced as $\alpha = 1.54$ (p value < 0.01) and $\beta = -1.76$ (p value < 0.01). Finally, equation (7) was produced after substituting the constant value of γ , C_e , α , and β , which had been derived from (i) to (iii):

$$v = 25.91 S^{1.54 Cr^{-1.76}} V^{0.33}. \quad (7)$$

Equation (7) was the debris-flow velocity model derived by using the experimental result in the current study. Comparing the derived model and existing models [14, 16] with using the experimental result, Table 3 showed that coefficient of variance (CV) and root mean square error (RMSE) of the derived model were the smallest. The reason was assumed that CV of C_e value in equation (7) was small enough to be less affected by scale than other models. C_e has T^{-1} dimension, the same dimension with shear rate closely related to shearing stress of fluid. The shear stress is affected by the viscosity of fluid and surface roughness of stream bed. Especially, C_e cannot fully reflect roughness conditions of stream bed of debris flow in reality because smooth flume bed without certain treatment to adjust roughness was utilized in the experiments. Therefore, more precise C_e value

can be introduced if the shear stress model considering the roughness of stream bed is utilized to estimate it.

3.3. *Estimation of Debris-Flow Impact Force Model.* The model to calculate the flow velocity of debris flow was assumed as equation (7), and we also tried to introduce the hydrodynamic model, equation (8), to calculate the impact force of debris flow based on equation (7):

$$p_{\text{peak}} = a \rho v^2, \quad (8)$$

where p_{peak} represents the impact force of debris flow, a is a coefficient, ρ is the density (unit weight) of debris flow, and v is the velocity of debris flow. Various studies [12, 20, 21] indicated that a in equation (8) and Fr have power function relationships. By utilizing results of the debris-flow flume experiment and the observed debris flow event [12], correlations between coefficient a and Fr can be estimated as Figure 5 and equation (9). Especially, equation (9) is similar to relation of a and Fr ($a = 4.5 \text{Fr}^{-1.2}$), which were estimated by the wide range of Fr of 1.2 to 12 suggested by the previous study [13] with small-sized flume experiment. After considering related precedent studies, we can reach the conclusion that the relation between a and Fr in the current study produced a general result which can be applied to wide range of Fr.

$$a = 4.77 \text{Fr}^{-1.27}, \quad R^2 = 0.6648, \quad p \text{ value} < 0.01. \quad (9)$$

Finally, estimation of the debris-flow impact force model after combining equations (7)–(9) is concluded as

$$p_{\text{peak}} = 3.20 \text{Fr}^{-1.27} \rho S^{3.09 Cr^{-1.76}} V^{0.67} \text{ (unit: kPa)}. \quad (10)$$

Components of equation (10), sediment discharge, content of fine particles in soil, and flume gradient, are closely related with necessary components for designing an ECD. Conducting field survey for designing ECD in South Korea includes topography investigation, soil investigation, and estimation of sediment discharge. Therefore, it was assumed that no additional expense would be required except the field survey cost if equation (10) was employed. Moreover, equation (10) also considers fine soil particle into the calculation of the impact force of debris flow. Recently, several studies indicated the possibility that fine soil particles can be fluidized caused by phase shift, which can lead to an increase in density and flow regime changes of debris flow accordingly [22, 23]. These recent findings were well reflected into equation (10).

However, there are limitations which shall be resolved to estimate impact force of debris flow by utilizing equation (10) to reflect it in designing ECDs in practice. First, the estimation method for moisture content in sediment or debris flow shall be considered. Although the moisture content is an important factor to decide density and volume of debris flow and flow characteristics, it is hard to accurately estimate the moisture content when real debris flow occurs in the field. Furthermore, there is also uncertainty as “sediment discharge volume,” representative of “volume V ” in the current study, is utilized as an input variable. Because debris flow undergoes

TABLE 3: Summary of the result of the comparison of velocity estimation models.

	Formula	Notation (unit)	Coefficient	RMSE	CV	Reference
			Value (mean \pm standard error)			
Newtonian laminar flow	$\nu = (1/3)(\rho g/\mu)H^2S$	μ ($\text{kg}\cdot\text{m}^{-1}\cdot\text{s}^{-2}$)	0.73 ± 0.03	1.32	0.50	[5]
Dilatant flow	$\nu = (2/3)\xi H^{3/2} S^{1/2}$	ξ ($\text{m}^{-1/2}\cdot\text{s}^{-1}$)	2044.80 ± 58.08	1.14	0.29	[5, 18]
Newtonian turbulent flow	$\nu = (1/n)H^{2/3} S^{1/2}$	n ($\text{m}^{-1/3}\cdot\text{s}$)	0.0221 ± 0.0006	0.62	0.26	[5, 19]
Voellmy flow	$\nu = C_1 H^{1/2} S^{1/2}$	C_1 ($\text{m}^{-1/2}\cdot\text{s}^{-1}$)	25.57 ± 0.46	0.56	0.18	[16]
This study	$\nu = C_e S^{1.54} Cr^{-1.76} V^{1/3}$	C_e (s^{-1})	25.60 ± 0.31	0.37	0.12	

The value of each coefficient is expressed as “mean \pm standard error.” RMSE is the root mean square error and CV means the coefficient of variance.

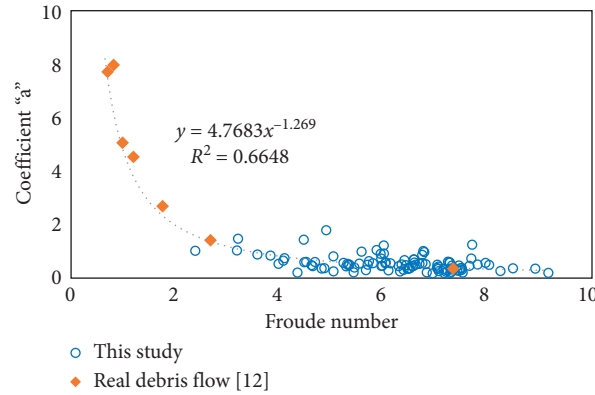


FIGURE 5: The relationship between the coefficient of hydrodynamic model for impact force and Froude number. Blue circles show the results of this experiment, and orange diamonds represent data of real debris flow [12].

phases of soil erosion and deposition repeatedly in the process of its flowing, it is difficult to identify the precise amount of sediment discharge at a certain point. To overcome these challenges, several studies tried to calculate velocity as well as the impact force of debris flow by utilizing instant flux. However, it was not reflected into the current study due to limitations on experimental equipment. Lastly, the applicability of the developed models to “real” debris flow event was not fully examined in the current study. The debris flow cases of the previous studies [5, 12] did not fully support information of variables required in equation (10), and their flow velocity as well as impact force was also estimated by employing empirical models. The applicability of equation (10) was not fully examined due to these difficulties of field data use. Therefore, field application shall be reviewed after utilizing observed values in large-scale flume experiment or real debris flow cases in the future.

Comprehensively, the model, equation (10), shall be improved and verified by conducting further experiments to be utilized in practice. However, even after such model is improved and verified through additional experiment, it has its own limitations because it is inevitable to assume under which conditions in the field (such as soil moisture content) debris flow will occur. As the suggested models in the current study are expressed in simple empirical formula, they cannot estimate dynamic characteristics of debris flow and its temporal changes of the impact force in detail like numerical models [23, 24]. Despite such challenges, equation (10) is meaningful for following reasons: (i) under few practical assumptions, impact force of debris flow can be easily estimated cost effectively in South Korea in a situation

in which related design criteria are insufficient and (ii) the model was developed through flume experiments considering soil and topographic characteristics in South Korea while we had inadequate observation equipment for debris flow in field. In this sense, the current study results can lay the foundation for further related experiments in the future.

4. Conclusions

This study was preliminary work to suggest that impact force of debris flow shall be considered in designing ECDs in South Korea. As part of this effort, the flume experiments were conducted to develop the model to estimate the impact force of debris flow. Correlations among sediment mixture conditions, flow characteristics, and impact force of the experiments were statistically analyzed, and both models to calculate debris-flow velocity and impact force were introduced successively. Especially, we applied characteristics of soil and topography in South Korea into the models as part of efforts to consider regional conditions of the site where debris flow can occur. Besides, we utilized the design factor of ECDs as input variables of the model to estimate the impact force of debris flow for cost efficiency.

In conclusion, in given conditions of South Korea, the developed model can be applicable enough at a practical level even though there are some clear limitations that shall be resolved by conducting further experiments. It is highly expected that this model can be utilized better at the site with some improvements through additional experiments. If we

can obtain sufficient field observation data on debris flow in the future, the model can be much advanced in practice.

Data Availability

The data used to support the findings of this study are available from the corresponding author upon request.

Conflicts of Interest

The authors declare that there are no conflicts of interest regarding the publication of this paper.

Acknowledgments

This study was carried out with the support of “R&D Program for Forest Science Technology (Project no. 2017061B10-1919-AB01)” provided by Korea Forest Service (Korea Forestry Promotion Institute).

References

- [1] O. Hungr, S. G. Evans, M. J. Bovis, and J. N. Hutchinson, “A review of the classification of landslides of the flow type,” *Environmental and Engineering Geoscience*, vol. 7, no. 3, pp. 221–238, 2001.
- [2] D. Kim, E. J. Lee, B. Ahn, and S. Im, “Landslide susceptibility mapping using a grid-based infiltration transient model in mountainous regions,” in *Landslide Science for a Safer Geoenvironment*, vol. 2, pp. 425–429, Springer, Cham, Switzerland, 2014.
- [3] Korea Forest Service, “Landslide statics,” 2018, http://www.forest.go.kr/newkfsweb/html/HtmlPage.do?pg=/lsls/UI_LSIS_1000_050101.html&orgId=lsls&mn=KFS_02_06_05_07_01.
- [4] A. Armanini, “On the dynamic impact of debris flows,” in *Recent Developments on Debris Flows*, vol. 64, pp. 208–226, Springer, Berlin, Germany, 1997.
- [5] O. Hungr, G. C. Morgan, and R. Kellerhals, “Quantitative analysis of debris torrent hazards for design of remedial measures,” *Canadian Geotechnical Journal*, vol. 21, no. 4, pp. 663–677, 1984.
- [6] C. Scheidl, M. Chiari, R. Kaitna et al., “Analysing debris-flow impact models, based on a small scale modelling approach,” *Surveys in Geophysics*, vol. 34, no. 1, pp. 121–140, 2013.
- [7] J. Suda, A. Strauss, F. Rudolf-Miklau, and J. Hübl, “Safety assessment of barrier structures,” *Structure and Infrastructure Engineering*, vol. 5, no. 4, pp. 311–324, 2009.
- [8] J. Hübl, G. Nagl, J. Suda, and F. Rudolf-Miklau, “Standardized stress model for design of torrential barriers under impact by debris flow (according to Austrian standard regulation 24801),” *International Journal of Erosion Control Engineering*, vol. 10, no. 1, pp. 47–55, 2017.
- [9] J. Kwan, “Supplementary technical guidance on design of rigid debris-resisting barriers,” GEO report 270, Geotechnical Engineering Office, Hong Kong, 2012.
- [10] Natural Institute for Land and Infrastructure Management, *Manual of Technical Standard for Designing Sabo Facilities against Debris Flow and Driftwood*, Technical Note of NILIM 365, Ministry of Land, Infrastructure and Transport, Tokyo, Japan, 2007.
- [11] Seoul Metropolitan Government, *Supplemental Investigation Report of Causes of Umyeonsan Landslides*, Seoul Metropolitan Government, Seoul, Republic of Korea, 2014.
- [12] D. Proske, J. Suda, and J. Hübl, “Debris flow impact estimation for breakers,” *Georisk: Assessment and Management of Risk for Engineered Systems and Geohazards*, vol. 5, no. 2, pp. 143–155, 2011.
- [13] J. Hübl and G. Holzinger, “Kleinmasstaebliche modellversuche zur wirkung von murbrechern,” WLS report 50.3, Universität für Bodenkultur, Vienna, Austria, 2003.
- [14] S. Eu and S. Im, “Examining velocity estimation equations of debris flow using small-scaled flume experiments,” *Journal of Korean Forest Society*, vol. 106, no. 4, pp. 424–430, 2017, in Korean.
- [15] J. D. Parsons, K. X. Whipple, and A. Simoni, “Experimental study of the grain-flow, fluid-mud transition in debris flows,” *The Journal of Geology*, vol. 109, no. 4, pp. 427–447, 2001.
- [16] D. Rickenmann, “Empirical relationships for debris flows,” *Natural Hazards*, vol. 19, no. 1, pp. 47–77, 1999.
- [17] S. W. Jeong, “Grain size dependent rheology on the mobility of debris flows,” *Geosciences Journal*, vol. 14, no. 4, pp. 359–369, 2010.
- [18] T. Takahashi, “Debris flow,” *Annual Review of Fluid Mechanics*, vol. 13, no. 1, pp. 57–77, 1981.
- [19] D. O. K. Lo, “Review of natural terrain landslide debris-resisting barrier design,” GEO report 104, Geotechnical Engineering Office, Hong Kong, 2000.
- [20] A. Armanini, M. Larcher, and M. Odorizzi, “Dynamic impact of a debris flow against a vertical wall,” in *Proceedings of the 5th International Conference on Debris-Flow Hazards Mitigation: Mechanics, Prediction, and Assessment*, pp. 1041–1049, Padua, Italy, June 2011.
- [21] C. Scheidl, B. McArdeall, G. Nagl, and D. Rickenmann, “Debris flow behavior in super- and subcritical conditions,” in *Proceedings of the 7th International Conference on Debris-Flow Hazards Mitigation*, pp. 437–442, Golden, CO, USA, June 2019.
- [22] K. Nakatani, T. Furuya, Y. Hasegawa, K. Kosugi, and Y. Satofuka, “Study on fine sediment phase change factors and influence on debris flow behavior,” *Journal of the Japan Society of Erosion Control Engineering*, vol. 70, no. 6, pp. 3–11, 2018, in Japanese.
- [23] T. Uchida, Y. Nishiguchi, K. Nakatani et al., “New numerical simulation procedure for large-scale debris flows (Kanakols),” *International Journal of Erosion Control Engineering*, vol. 6, no. 2, pp. 58–67, 2013.
- [24] M. Cesca and V. D’Agostino, “Comparison between FLO-2D and RAMMS in debris-flow modelling: a case study in the Dolomites,” *WIT Transactions on Engineering Sciences*, vol. 60, pp. 197–206, 2008.

Research Article

A Method for Cavity Scale Estimation Based on Ground-Penetrating Radar (GPR) Explorations: An Experimental Study

Jeong-Jun Park ¹, Yoonseok Chung,² and Gigwon Hong ³

¹Incheon Disaster Prevention Research Center, Incheon National University, 119 Academy-ro, Yeonsu-gu, Incheon 22012, Republic of Korea

²Korea Conformity Laboratories, 199 Gasan digital1-ro, Geumcheon-gu, Seoul 08503, Republic of Korea

³Institute of Technology Research and Development, Korea Engineering & Construction, 3-16, Jungdae-ro 25-gil, Songpa-gu, Seoul 05661, Republic of Korea

Correspondence should be addressed to Gigwon Hong; gigwon_hong@kecgroup.kr

Received 27 September 2019; Accepted 22 November 2019; Published 27 December 2019

Guest Editor: Young-Suk Song

Copyright © 2019 Jeong-Jun Park et al. This is an open access article distributed under the Creative Commons Attribution License, which permits unrestricted use, distribution, and reproduction in any medium, provided the original work is properly cited.

This study described the results of experiments comparing the cavity scales obtained from the GPR exploration with the direct excavation of the identified cavity scales. The first experiment was carried out on the actual roadway, and the additional experiment was carried out on the mock-up site to prevent the cavity collapse under the ground. It was confirmed that the soil depth of the predicted cavity and the identified cavity was similar, but the predicted cavity scales by GPR exploration overestimated the longitudinal and cross-sectional widths compared with the identified cavity scales. Based on the correlation between the cavity scales predicted by GPR exploration and the cavity scales identified in the mock-up test, an empirical formula for estimating the cavity scales was proposed.

1. Introduction

In Seoul, Korea, there have been large and small ground subsidence since 2014, which have become a social issue. Most ground subsidence occurred in the pavement of urban areas, and the main causes are supposed to be the improper construction of water supply pipes, sewers, gas pipes, and subways under the pavement. The analysis of the location of the roadway cavity that occurred in the past five years in Seoul revealed that 81% of cavities occurred at a depth less than 0.8 m, 17% of cavities occurred at a depth between 0.8 m and 1.5 m, and 2% of cavities occurred at a depth more than 1.5 m from the pavement surface. Therefore, 98% of the cavities were distributed within 1.5 m depth, the average depth of underground utilities, and the cavity scale was small and mainly occurred in the shallow layer. Such cavities are likely to expand over time and lead to ground subsidence [1].

Ground subsidence due to cavity can bring about various problems, such as casualties, decrease of the safety of the structures, and indirect social costs. Therefore, ground subsidence should be prevented through the exploration and recovery of the cavity under the pavements [2, 3].

Recently, to avoid affecting the flow of traffic, cavity exploration under the pavement has used the mobile multi-GPR (ground-penetrating radar). The location, depth, and cavity scale can be calculated by obtaining waveform GPR data for the cavity under the pavements. The cavity scale can be calculated by confirming the availability of the cavity from the parabolic cross section based on the theory of cavity waveform analysis. Generally, the horizontal axis of the cavity waveform shows the measurement distance, and the vertical axis shows the depth. Furthermore, the cavity scale is calculated by estimating the scale in each direction through the longitudinal and cross-sectional measurements of the image of the cavity waveforms. However, the cavity scale can

be confirmed accurately only through excavation during the restoration process.

On the other hand, cavity exploration and the calculation of the scale are normally divided into two processes: (1) GPR exploration and (2) endoscopic investigation. The GPR exploration calculates the cavity scale on the longitudinal and cross-sectional directions; then, the endoscopic investigation films the inside of the cavity to confirm its depth and width. Considering the cavity scale (height and width), the thickness of the pavement, and the amount of cracks in the pavement, the results of the primary exploration and secondary investigation allow us to determine the level of danger of the cavity. According to the cavity management guidelines established by the city of Seoul, the dangerousness of the cavity is determined on four levels: emergency, priority, general, and observation. Emergency and priority levels indicate the level of danger that the cavity must be restored immediately, while the general and monitoring levels mean that the cavity may expand to a higher level. Therefore, there should be an exact calculation of the cavity scale to monitor the expansion process of the cavity from the general and observation levels to a more dangerous level. Furthermore, the exact calculation of the cavity scale is also important to determine the costs (e.g., materials and equipment) for the restoration of the cavity, if the cavity is at the emergency or priority levels.

Current methods for the measurement of cavity scales are excavating the cavity directly, which leads to social indirect costs due to traffic control as well as the direct costs associated with the excavation and restoration process. Since a difference occurs between the estimation of the cavity scale obtained through the direct excavation and the cavity scale obtained from the GPR exploration, the reliability of the GPR exploration results is degraded. Therefore, in order to ensure the reliability of the GPR exploration results, it is necessary to enhance the accuracy of the cavity scale calculation based on the GPR exploration.

This study compares the cavity scales obtained from the GPR exploration and the direct excavation of the identified cavity. The first exploration was carried out on the actual roadway, and the second exploration was carried out on the mock-up site to prevent the cavity collapse by placing Styrofoam under the ground. Therefore, the study suggests a GPR exploration method for predicting the actual cavity scales by comparing the GPR exploration results with the identified cavity scales.

2. GPR Exploration and Methods for Cavity Scale Calculation

2.1. Principles of GPR Exploration. The ground-penetrating radar emits electromagnetic waves into the underground and receives the electromagnetic waves reflected from a boundary with different electrical properties (e.g., conductivity and permittivity). This system is widely used to investigate the reserves of the resources in mines, buried structures, and terrane information in geophysics [4–6]. GPR exploration is a method to explore the shallow subjects or structures with high resolution by using the transmission

of the electromagnetic waves with frequencies higher than tens of MHz and is commonly used as a nondestructive test for the survey of underground pipes under the pavements, cavities as well as cavity exploration of tunnels [7, 8].

The principles of the GPR exploration are shown in Figure 1. The electromagnetic waves emitted from the transmitter antenna are reflected, bent, diffracted, and recorded as waveforms by the reception antenna. The GPR exploration identifies the size and location of the anomalous object by analyzing the changing patterns of the waveforms according to the characteristics of the anomalous object (e.g., boundary, utilities, cavities, and so on) [9].

The high-frequency bandwidth between 10 MHz and 1 GHz used in the GPR exploration falls under the transmission area in which displacement currents are superior compared to conduction currents, and the behavior of the electromagnetic wave remains under the control of the wave equation. The most interesting behavioral characteristics of the GPR waves in the area of the electromagnetic waves are the attenuation and speed. Under the assumption of flat electromagnetic waves, the attenuation (α , [dB/m]) and the phase constant (β , [rad/m]) of the wave area are shown in equations (1) and (2):

$$\alpha = \frac{\sigma}{2} \frac{\mu}{\varepsilon}, \quad (1)$$

$$\beta = \omega \mu \varepsilon. \quad (2)$$

The symbol σ refers to the electrical conductivity (S/m), ε is the permittivity (F/m), μ is the permeability (H/m), and ω is the frequency. Therefore, as the conductivity of the medium increases and the permittivity decreases, the GPR waves show significant attenuations and become irrelevant to the frequency. However, in areas with a frequency higher than 100 MHz, the attenuation rapidly increases due to relaxation effects, and the depth of investigation of the GPR system that uses a wavelength higher than 100 MHz decreases rapidly.

Under the assumption that the penetration ratio of the rocks that constitute the underground is identical to that within a vacuum ($\mu = \mu_0$), the GPR transmission speed (v , [m/ns]) can be defined as in equation (3). The transmission speed of the GPR wave is not related to the frequency and depends only on the permittivity:

$$v = \frac{c}{\sqrt{\varepsilon\gamma}} = \frac{0.3}{\sqrt{\varepsilon\gamma}}. \quad (3)$$

The minimum size of the object that can be explored is called resolution; it varies according to the soil, and it is half of the length of a single wavelength (λ_l). The base wavelength must increase to increase the resolution. However, when the base wavelength increases and the resolution increases accordingly, the depth of the investigation decreases due to an increase of attenuation. When selecting an antenna, the depth of the investigation should be prioritized over the resolution if there is no information on the depth or permittivity of the object. It should be noted that the speed of the GPR wave is a function of the permittivity,

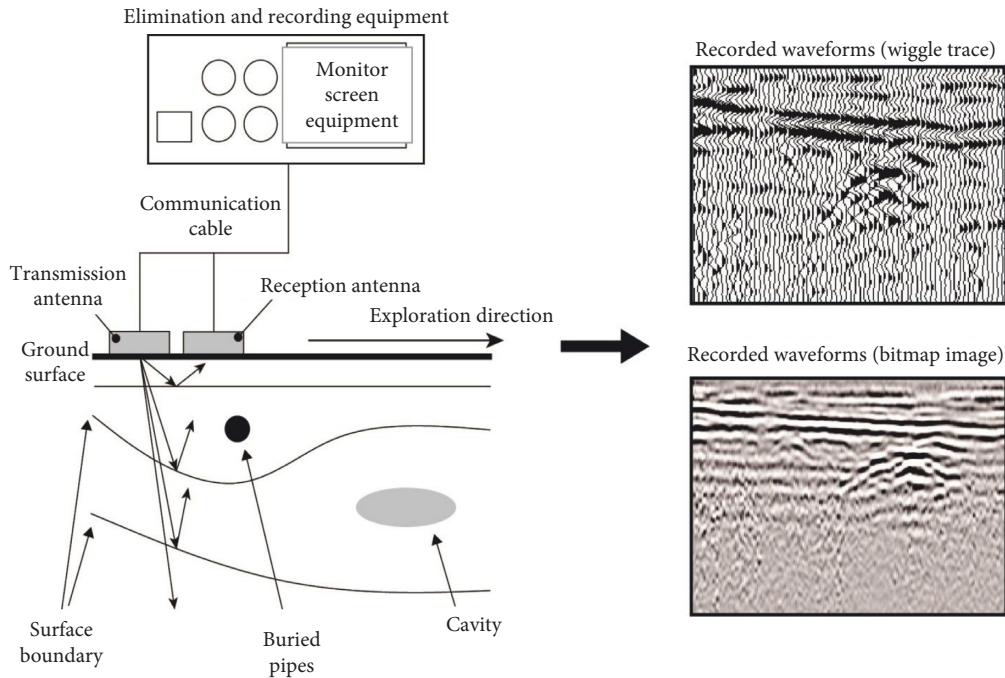


FIGURE 1: Schematic of the GPR system and waveforms.

and the resolution varies according to the medium. The minimum frequency is decided by the resolution, and the maximum frequency is influenced by the depth of the investigation and the scale of the seismic noise as shown in Table 1.

According to the characteristics of the underground medium, the frequency used for GPR explorations should be appropriately changed according to the stratum of the exploration subject, the status of the surface of the earth, the status of the underground water, and the surrounding environment. When using an antenna with a high base frequency of 500 MHz, the depth of the exploration varies according to the permittivity and the electrical conductivity of the underground, which is generally between 2 m and 3 m. If the surface is an asphalt pavement, the penetration depth is reduced to 1 to 2 m, as the energy of the electromagnetic waves to penetrate to the bottom weakens, reflecting much energy at the boundary of the packaging [10].

GPR reflections transmitted through a pavement structure can determine sublayer electromagnetic properties [11–13]. The electromagnetic property measured more frequently by pavement engineers is the dielectric constant (ϵ) because it is primarily influenced by soil water content [14]. From the perspective of material engineering, soils are composite material systems comprised of inorganic minerals, organic particles, water, and air. As a result, the dielectric characteristics of the soil are a function of the dielectric constants of the individual soil components, the volume fraction of each component, their geometrics, and the electrochemical interactions between the components [15]. Table 2 summarizes the published dielectric constants of typical pavement soil constituents [14].

When a low-frequency antenna of 100 MHz is used to increase the penetration depth, it is difficult to distinguish the reflective signals from shallow areas due to the interference of the direct waves emitted from the transmission antenna to the reception antenna. Therefore, the electrical characteristics of the underground medium and the frequency used for the exploration should be investigated in advance to ensure the appropriate exploration depths and resolution.

2.2. Analysis of the Cavity Exploration and the Calculation of the Cavity Scale. As shown in Figure 2, the GPR exploration equipment used in this study is mounted on a vehicle. Its base frequency is 400 MHz, and the exploration depth on paved pavements is within 2 m. This is effective in detecting the cavities and underground utilities of 0.15 m or larger within the depth of one meter (0.3 m within 2 m of depth). In addition with the multichannel GPR exploration equipment, there are three-dimensional interpretations, which allow us to detect abnormal signals according to the difference in materials as well as in the permittivity of identical materials.

The GPR exploration equipment consists of GPR antennae, surface image camera, GPS measurement equipment, and positioning cameras, which allow us to identify the exact location of abnormal signals from the surface. In addition, the integrated analysis program of the multichannel GPR and the positioning system increase the reliability of the exploration results.

First, the exploration uses a piece of software that records and controls the exploration data and sets the antenna arrangement, sampling intervals, and initial values of the data locations. The data are obtained by constructing a reception

TABLE 1: Relationship between the variables of underground electrical characteristics, GPR exploration, and frequency.

Measurement variable	Permittivity			Conductivity			Frequency		
	Low	→	High	Low	→	High	Low	→	High
Velocity of electromagnetic wave	Fast	→	Slow	—	—	—	—	—	—
Attenuation	High	→	Low	Low	→	High	Low	→	High
Depth of investigation	Shallow	→	Deep	Deep	→	Shallow	Deep	→	Shallow
Wavelength	Long	→	Short	—	—	—	Long	→	Short
Resolution	Low	→	High	—	—	—	Low	→	High

TABLE 2: Dielectric values of the typical pavement soil and layer constituents.

Constituent	Dielectric value
Air	1
Freshwater	8
Ice	4
Bedrock (granite)	5–7
Clay	25–40
Silt	16–30
Silty sand	7–10
Sand subbase	4–6
Gravel base	4–7
Glacial till	8–18
Asphalt concrete	4–8
Slag asphalt concrete	8–15
Portland cement concrete	8–10
Bitumen bound base	6–7
Cement bound base	8–10

and transmission channel, DMI, and exploration system. Afterwards, the results are analyzed through data processing, such as preprocessing, interpolation, and migration of data, using the analysis programs for exploration data. The sectional data analyses are conducted according to the channels through the integrated management of the positioning system and then comparing and analyzing the abnormal locations with the surface clips, filtering the signals from objects such as underground utilities and manholes.

On the other hand, if the GPR exploration consists of a one-dimensional arrangement and detects cavities or underground pipes, the target is represented as a parabola on the GPR data. Therefore, the system is able to obtain data from detecting the strength of the reception signal and the delay in transmitting and receiving the electromagnetic waves.

As shown in Figure 3, when the GPR sensors shown with red dots are aligned, there is a particular object (cavity or underground pipe) below them, and the GPR sensors transmit and receive individual electromagnetic waves, the delay becomes longer as the sensor is further away from the target object; as the distance increases, the strength of the signal reflected back is weakened. If this is represented in a two-dimensional space with time axis and sensor arrangement direction, it assumes a parabolic shape. The parabola has a gradual slope for materials with low permittivity and has a steeper slope for materials with high permittivity [16]. The slope waveform has a parabolic shape, and the major type of waveform is shown in Figure 4.

Figure 5 shows a method to differentiate the cavity according to the white and black parts of the waveform, based on the fact that air and medium have different permittivities. It shows a reflected form in the case of homogeneous medium and cavity. In the case of a homogeneous medium without cavity under the pavement, depending on the direction of the depths, the relative permittivity increases and the phase switches from black to white. When there are cavities under the pavements, the permittivity decreases in the direction of the depth, reversing the phase of the reflecting waves by 180 degrees and switching the phase from white to black [17–19].

In the results of the cavity explorations, the horizontal axis and the vertical axis represent the distance and depth, respectively, and the exploration results are interpreted as the reflection patterns shown in the cross-section planes. In the clip of the results of the planes, the color shows the strength of the electromagnetic waves that are transmitted and allows us to distinguish between cavities and underground pipes according to the characteristics of the trace waveforms. However, although the depth of the explored abnormal object is determined by the continuous observation of the electromagnetic waves and the permittivity constant of the medium, there may be errors as it is difficult to determine accurately the permittivity constant according to the medium.

The abnormal signals from the clips of the planes should be selected first to analyze the signal of the cavity. There are patterns of straight lines in the case of underground pipe; however, a pattern formed in a particular area along the boundary that shows an extreme change in amplitude is considered a cavity, and the cavity is determined by the combination of the plane, longitudinal, and cross sections. As mentioned previously, the signals for the cavity through the clips of the longitudinal sections are shown in a parabolic shape; the depths are identified through the distance between the apical area, where large changes begin; finally, the surface and the longitudinal lengths are identified through the width of each end of the parabola. Generally, the longitudinal and cross-sectional widths of the cavity waveforms are calculated in the range between 60 and 100% of each end, but when it is needed, migration is first conducted, which is followed by the analysis of the reflection states. Using these methods, the examples of calculation based on the width of each end of the parabola from the cavity waveforms obtained from GPR exploration are shown in Figure 6.

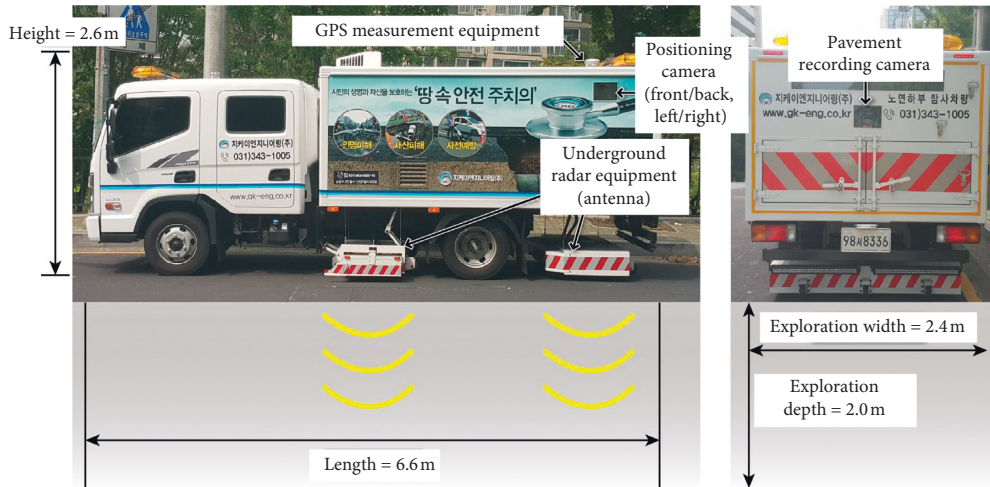


FIGURE 2: Extended multichannel GPR exploration equipment mounted on a vehicle.

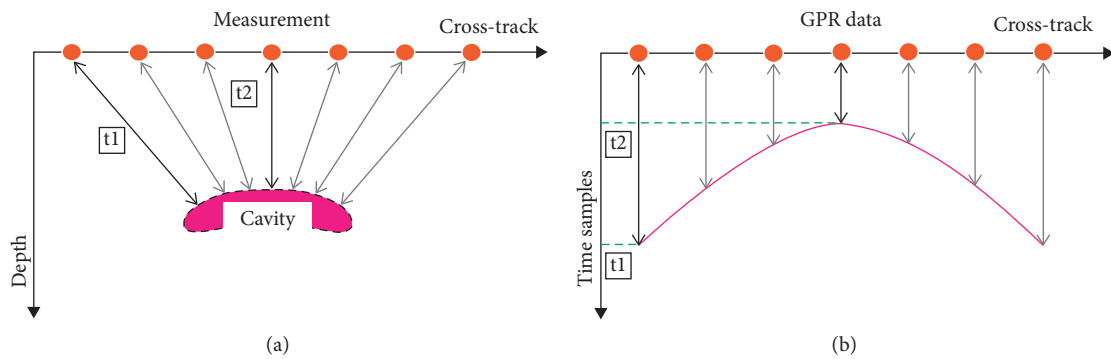


FIGURE 3: Parabolic signature in the GPR Data. (a) GPR detection. (b) Parabola projection of GPR data.

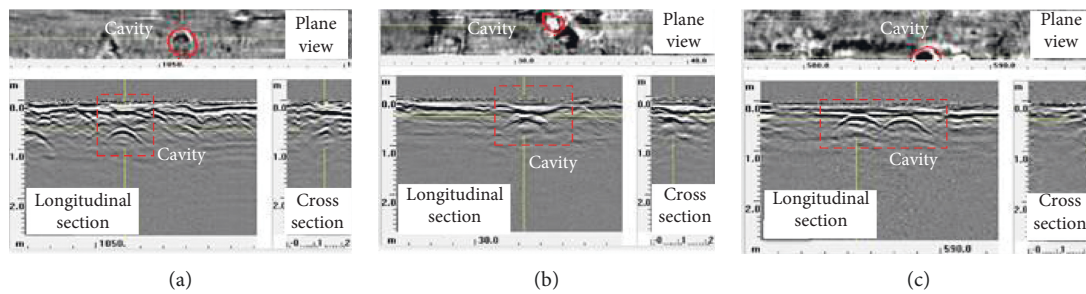


FIGURE 4: Common types of cavity waveforms. (a) Wedge type. (b) Box type. (c) Continuous type.

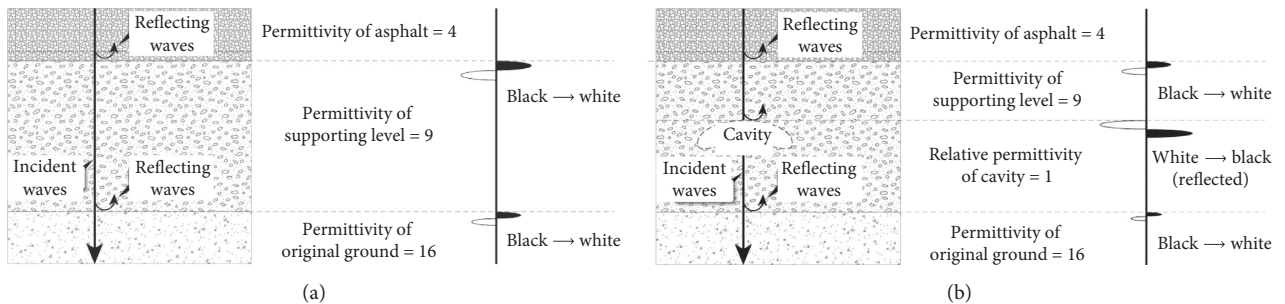


FIGURE 5: Reflected status of the polarity of the reflected wave. (a) In medium of homogeneous typical strata. (b) In cavity.

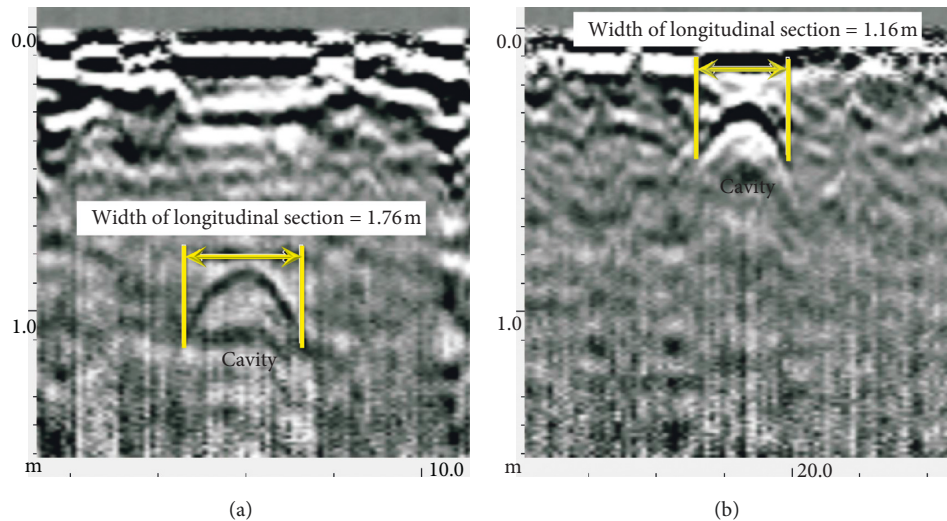


FIGURE 6: Measurement example of scale (soil depth and width) by the cavity waveforms. (a) Depth: 0.9 m and width: 1.0 m. (b) Depth: 0.3 m and width: 0.5 m.

3. A Comparison of Evaluation Results on the Cavity Scale

3.1. Evaluation Methods. The calculation of the cavity scales according to the GPR waveforms is extremely important to evaluate the danger levels for managing the cavity. The cavity scales are calculated at a set ratio by considering the permittivity of the medium under the pavements, based on the total width of the lower parabola of the cavity waveform obtained from the longitudinal section and the cross section.

Therefore, in this study, we compared the cavity scales calculated on the basis of the exploration of the cavity with those identified through direct excavation. To evaluate the calculation results of the cavity scales through GPR exploration, the soil depth on the top of the cavity and the cavity scale were compared for 10 cavities in three regions. Based on the results, the relationships between the predicted cavity and the identified cavity were analyzed.

3.2. Evaluation Results. Figure 7 illustrates the relationship between the depths of the predicted cavity and the identified cavity. The ratio of the identified soil depth and the predicted soil depth was analyzed in order to evaluate the error bound of the soil depth on the cavity. The result showed that the difference between the identified soil depth and the predicted soil depth was about 12% to 19%, when the identified soil depth was more than 0.4 m. This result means that the GPR exploration depth is limited. Although some data have differences, the relationship between the identified soil depth and the predicted soil depth is close to 1:1 gradient. Therefore, it was confirmed that the predicted soil depth from the pavement layer was approximately the same as the identified soil depth.

Table 3 and Figure 8 show the results of the analysis of the relationship between the soil depths of the identified cavity, the soil depth of the predicted cavity according to the GPR waveforms, and the total width (longitudinal and cross-

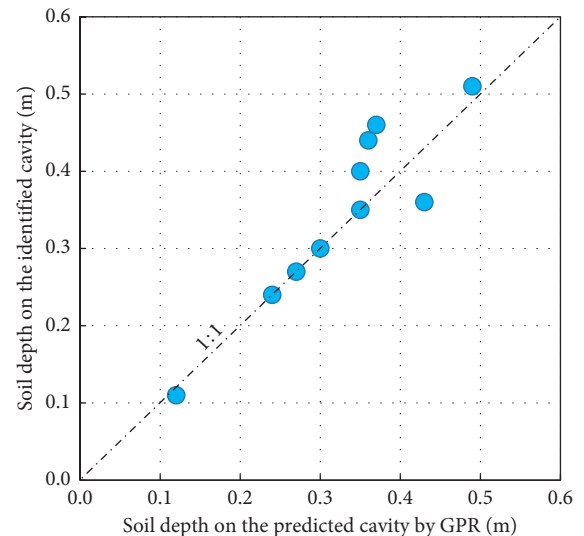


FIGURE 7: Relationship of the soil depth on the predicted cavity and the identified cavity.

sectional widths). As shown in Table 3, the soil depth of the identified cavity was from 0.11 m to 0.51 m, and the soil depth was divided into three ranges based on the depth relationship (see Figure 8) between the locations of the predicted cavity and the identified cavity. As a result of calculating the arithmetic mean of the soil depth by the range of the identified cavity, the mean soil depths of each range were 0.23 m, 0.37 m, and 0.47 m, respectively. Based on these results, the minimum, maximum, and the mean of the predicted cavity according to soil depths were compared. The results showed that, as the soil depth decreased, the soil depths of the predicted cavity and the identified cavity were almost identical, and this is identical to the qualitative results shown in Figure 7. Furthermore, as the soil depth increased, the differences in the longitudinal width of the predicted cavity increased; however, the differences in the cross-section width were similar.

TABLE 3: Calculation results of mean difference in the scale of the predicted cavity according to the soil depth of the identified cavity.

Average soil depth of the identified cavity [soil depth range] (m)	Difference in soil depth (m)			Difference in longitudinal section (m)			Difference in cross section (m)		
	Minimum	Maximum	Mean	Minimum	Maximum	Mean	Minimum	Maximum	Mean
0.23 [0.11~0.30]	-0.07	0.01	-0.02	0.00	0.35	0.17	0.00	0.40	0.25
0.37 [0.35~0.40]	-0.05	0.00	-0.02	0.10	0.30	0.20	0.10	0.60	0.28
0.47 [0.44~0.51]	-0.09	-0.02	-0.06	0.20	0.60	0.40	0.20	0.40	0.28

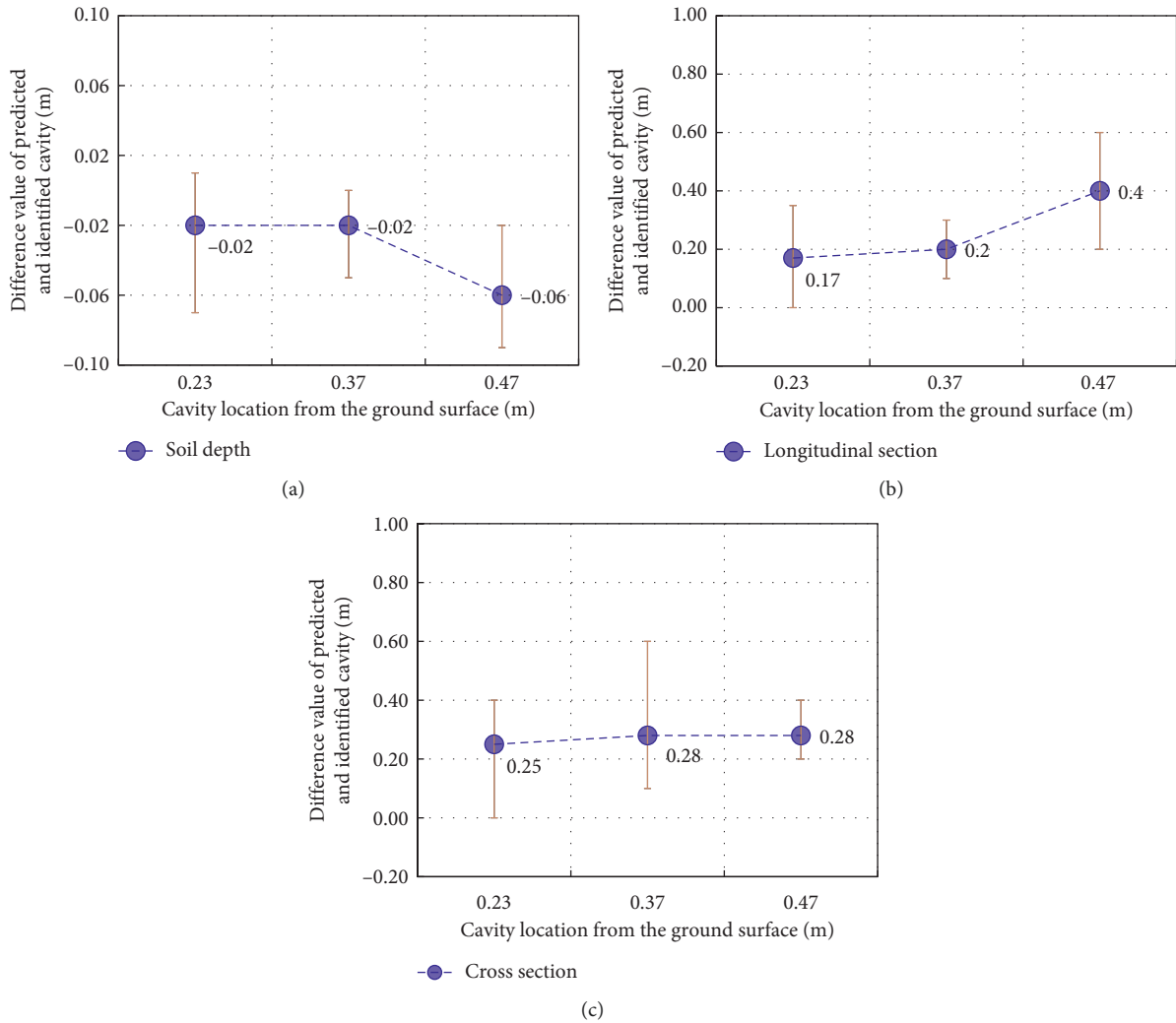


FIGURE 8: Difference between the predicted cavity scale and the identified cavity scale according to the location of the cavity. (a) Soil depth. (b) Longitudinal section. (c) Cross section.

The difference in the widths of the predicted cavity and the identified cavity as well as the scale ratios were calculated for the longitudinal and cross sections to compare the cavity scales of the predicted cavity and the identified cavity, as shown in Table 4. First, according to the soil depth of the location of the cavity, the differences in the widths of the predicted cavity and the longitudinal and cross sections of the identified cavity were compared. As a result, it was generally difficult to confirm a specific tendency for the difference in scales of the identified and the predicted cavity in longitudinal and cross sections according to the soil depth

at the top of the cavity, as shown in Figure 9. This may be due to irregular differences in scales because of some collapses of the soil around the cavity due to external drilling along with the errors of the analysis. Therefore, we concluded that there was no significant relationship between the scales of the identified cavity and the predicted cavity, according to the soil depth of the cavity. In addition, we also analyzed the ratio of the total width of the GPR waveforms in a parabolic form and the scales of the identified cavity (scales of identified cavity ($C_{\text{identified}}$)/scales of predicted cavity ($C_{\text{predicted}}$)). As shown in Figure 10, the ratio of the scales of

TABLE 4: Calculation results of the difference in scales between the predicted cavity and the identified cavity according to the soil depth.

Analyzed cavities	Soil depth (m)	Identified cavity (m)		Difference of predicted and identified values (m)		$C_{\text{identified}}/C_{\text{predicted}}$ (%)	
		Longitudinal section	Cross section	Longitudinal section	Cross section	Longitudinal section	Cross section
Cavity 1	0.11	1.00	0.90	0.30	0.30	76.9	75.0
Cavity 2	0.24	0.50	0.40	0.35	0.40	58.8	50.0
Cavity 3	0.27	1.50	1.20	0.00	0.00	100.0	100.0
Cavity 4	0.30	1.60	0.50	0.00	0.30	100.0	62.5
Cavity 5	0.35	1.00	0.50	0.30	0.10	76.9	83.3
Cavity 6	0.36	1.60	2.10	0.10	0.60	94.1	77.8
Cavity 7	0.40	1.20	0.65	0.20	0.15	85.7	81.3
Cavity 8	0.44	0.70	1.40	0.60	0.20	53.8	87.5
Cavity 9	0.46	1.80	0.40	0.20	0.40	90.0	50.0
Cavity 10	0.51	1.00	0.95	0.40	0.25	71.4	79.2

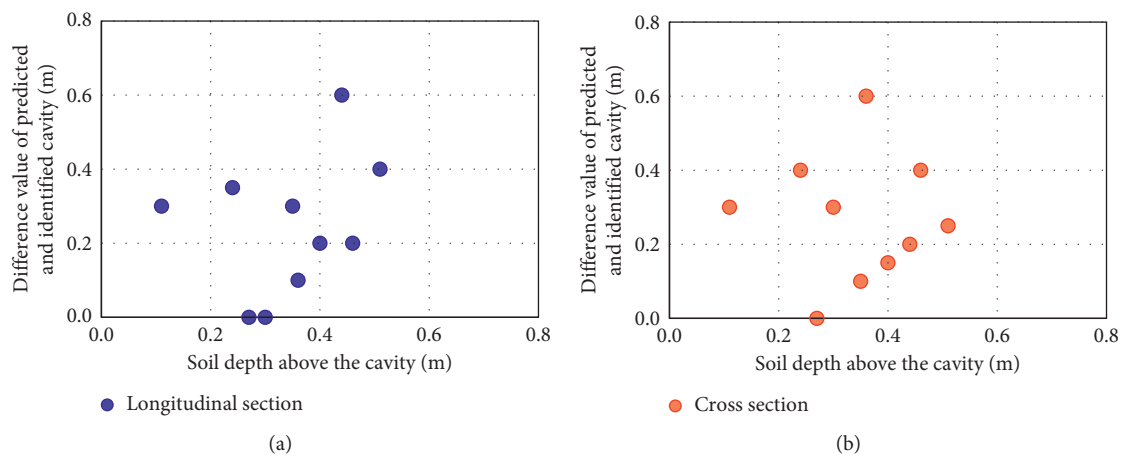


FIGURE 9: Relationship between the differences in cavity scales according to the soil depth. (a) Longitudinal section. (b) Cross section.

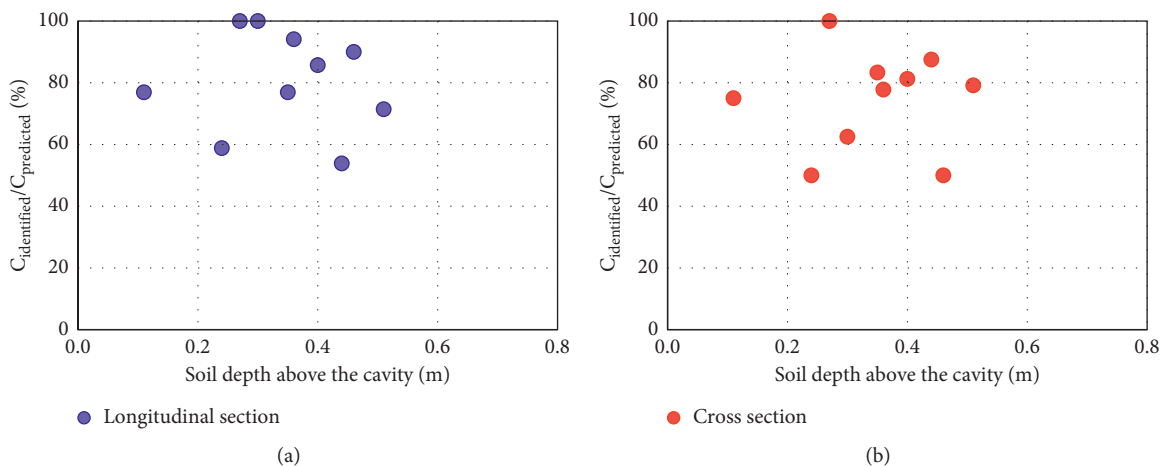


FIGURE 10: Relationship of the cavity scale ratio according to the soil depth. (a) Longitudinal section. (b) Cross section.

the identified cavity to the total width of the predicted cavity was between 53.8% and 100% for the longitudinal sections and between 50% and 100% for the cross sections. In other words, it is estimated that the cavity explored through GPR was larger compared to the actual cavity.

Although the soil depths on the top of the predicted cavity and the identified cavity were similar, there were no strict tendencies for the differences and the ratios of the cavity scales. The reason may be the collapses and sinks of some cavities during the examination process, and so, the

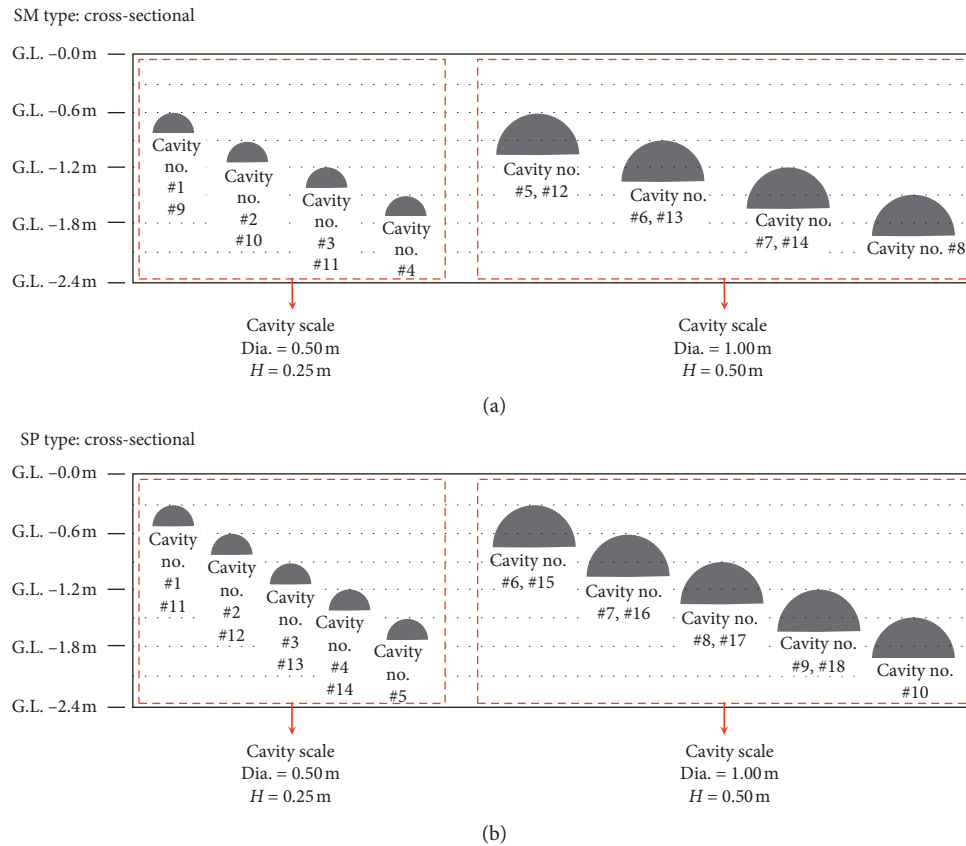


FIGURE 11: Experiment types. (a) Detailed map of SM type. (b) Detailed map of SP type.

study suggested a calculation method of the cavity scale through a test-bed experiment that artificially structuralizes mock-up cavities.

4. Evaluation of the Cavity Scale Based on a Test-Bed Experiment

Although the relationship between the predicted and identified cavity scales was evaluated based on the field data, it was difficult to derive a clear correlation. Therefore, this study attempted to compare the cavity scales through the ratio and difference of the predicted and the identified cavities based on a mock-up test and attempted to suggest a calculation method for cavity scales.

4.1. Construction of the Mock-Up Cavities and the Experimental Methods. In the test-bed experiment, the mock-up cavities were constructed in 32 locations considering the on-site condition according to the depth and the scale of the cavity. The mock-up cavity used Styrofoam in a hemispherical structure with 0.5 m and one meter in diameter and 0.25 m and 0.5 m in height and was planted in the ground. The reason for using Styrofoam was that a previous study showed that the permittivity constant of Styrofoam is similar to that of air [20]. The vertical locations of the mock-up cavities were 0.3 m, 0.6 m, 0.9 m, 1.2 m, and 1.5 m from the ground surface, and the space between each cavity was 0.3 m.

After excavating the ground, Styrofoam was placed in the planned locations, which were then covered in backfill soil. For the backfill soil of the top of the mock-up cavities, we used SM (silty sand) and SP (sand mixed with silt), which are commonly used in Korea as backfill soils. The GPR explorations used the same equipment as described for the previous experiment.

The purpose of this experiment was to suggest a method to quantitatively estimate the cavity scale through a comparison between the predicted cavity and the identified cavity. Therefore, there must be an excavation of cavity that can be clearly compared to the mock-up cavities. However, after simulating the mock-up cavities, it was found to be difficult to obtain clear GPR exploration results due to the collapses of some cavities and the irregular pavement surface of the unpaved pavements. Hence, we used the test results of 10 cases only that were relatively clear and, thus, comparable with the mock-up cavities. The summary of the experiment types is shown in Figure 11.

4.2. Results and Discussion. Table 5 shows the soil depth and the longitudinal and cross sections of the predicted cavity (GPR exploration results) and the identified cavity (mock-up cavities) according to the soil types. The soil depths of the predicted cavity and the identified cavity were approximately -0.06 m to 0.04 m, which were similar. This is similar to the results of experiments on cavities on the roadway. However, the difference in the longitudinal width of the

TABLE 5: Calculation results of the difference in soil depths and scales between the predicted cavity and the identified cavity.

Type	Cavity no.	Soil depth (m)			Longitudinal section (m)			Cross section (m)		
		Predicted cavity	Identified cavity	Difference	Predicted cavity	Identified cavity	Difference	Predicted cavity	Identified cavity	Difference
SM	#5	0.63	0.60	0.03	1.45	1.00	0.45	1.50	1.00	0.50
	#12	0.54	0.60	-0.06	1.53	1.00	0.53	1.50	1.00	0.50
	#13	0.84	0.90	-0.06	1.76	1.00	0.76	1.80	1.00	0.80
SP	#1	0.26	0.30	-0.04	0.83	0.50	0.33	0.80	0.50	0.30
	#11	0.32	0.30	0.02	0.86	0.50	0.36	0.90	0.50	0.40
	#6	0.32	0.30	0.02	1.30	1.00	0.30	1.30	1.00	0.30
	#15	0.28	0.30	-0.02	1.22	1.00	0.22	1.30	1.00	0.30
	#2	0.54	0.60	-0.06	1.03	0.50	0.53	1.10	0.50	0.60
	#7	0.64	0.60	0.04	1.59	1.00	0.59	1.60	1.00	0.60
	#16	0.59	0.60	-0.01	1.52	1.00	0.52	1.50	1.00	0.50

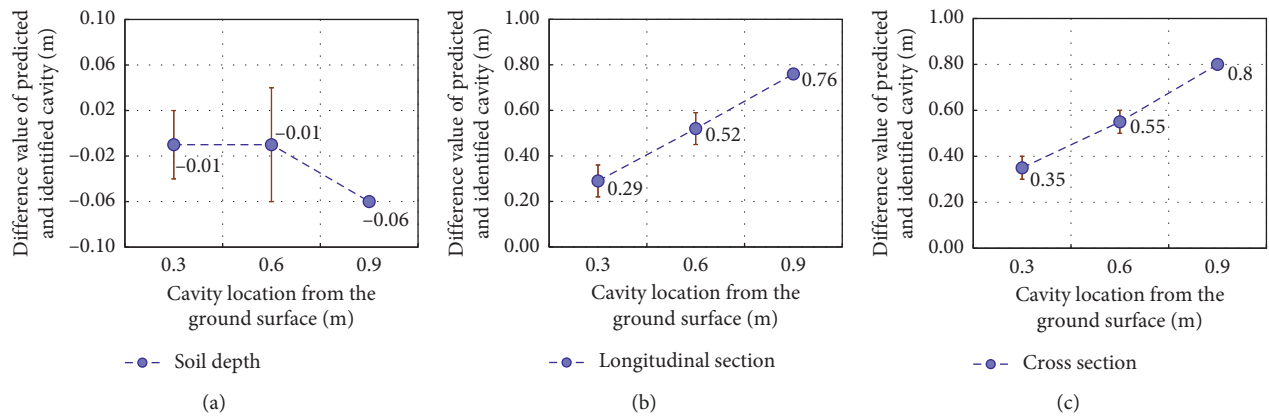


FIGURE 12: Difference between the predicted cavity scale and the identified cavity scale according to the location of the cavity. (a) Soil depth. (b) Longitudinal section. (c) Cross section.

predicted cavity and the identified cavity was found to be 0.22 m to 0.76 m depending on the depth of the cavity, and the difference in cross-sectional width was found to be 0.30 m to 0.80 m.

Figure 12 shows the results of the correlation analysis using the mean differences between the predicted cavity and the identified cavity concerning the soil depth, longitudinal sections, and cross sections when the buried depths were at 0.3 m, 0.6 m, and 0.9 m, respectively. The results show that when the soil depths were at 0.3 m and 0.6 m, there were not many differences in the vertical location of the predicted cavity and the identified cavity, but as the soil depth increased, the difference increased as well. This is also similar to the tendency shown in the experiment on cavities on the roadway. However, as the soil depth increases, the differences in the longitudinal and cross sections of the predicted cavity and the identified cavity continuously increased. Based on these results, we were able to show that, as the depth of the cavity (soil depth) increases, the scales of longitudinal and cross sections of the predicted cavity were larger than those of the identified cavity.

Table 6 shows the scale ratio of the predicted cavity and the identified cavity according to the conditions of the experiment. The scale ratio was determined as the ratio of the identified cavity to the predicted cavity on the soil depth,

longitudinal width, and cross-sectional width. The results showed that the scale ratio of soil depth was 94% to 111%, and the scale ratios of the longitudinal and cross sections were 49% to 82% and 45% to 77%, respectively. There was a small difference in the scale ratio of soil depth between the predicted cavity and the identified cavity, but the scale ratio of the longitudinal and cross-sectional width was large. This shows that the cavity scales predicted by GPR explorations are larger than the actual cavities for the scale ratios of the longitudinal and cross sections. Although the scale of soil depth predicted by the GPR exploration is relatively reliable, there is a possibility that the exploration results for the longitudinal and cross-sectional width reveal large errors.

On the other hand, soil types did not show particular relationships with buried depth, cavity scale, and scale ratio. This is because there are no large differences in permittivity according to the types of SM and SP, as suggested by Saarenketo [21].

4.3. Suggestions of Evaluation Method for Prediction of the Cavity Scale. It is extremely difficult to estimate the scale of a cavity in the ground accurately. Based on the results of the mock-up test, we found no relationship between the cavity scale and the soil type. However, it was found that the GPR

TABLE 6: Calculation results of the scale ratio.

Soil type	Cavity no.	Soil depth (m)	Cavity scale (longitudinal section = cross section) (m)	Cavity height (m)	Scale ratio (identified cavity/predicted Cavity)		
					Soil depth (%)	Longitudinal section (%)	Cross section (%)
SM	#5	0.6			95	69	67
	#12	0.6	1.0	0.5	111	65	67
	#13	0.9			107	57	56
SP	#1	0.3	0.5	0.25	115	60	63
	#11	0.3			94	58	56
	#6	0.3	1.0	0.5	94	77	77
	#15	0.3			107	82	77
	#2	0.6	0.5	0.25	111	49	45
	#7	0.6	1.0	0.5	94	63	63
	#16	0.6			102	66	67

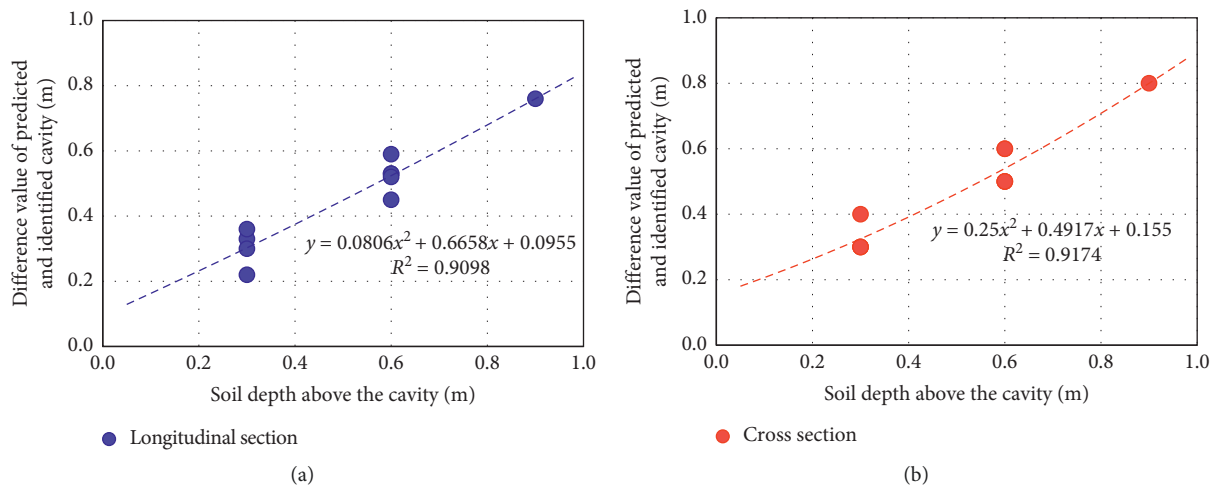


FIGURE 13: Correlation of the cavity scale according to the soil depth. (a) Longitudinal section. (b) Cross section.

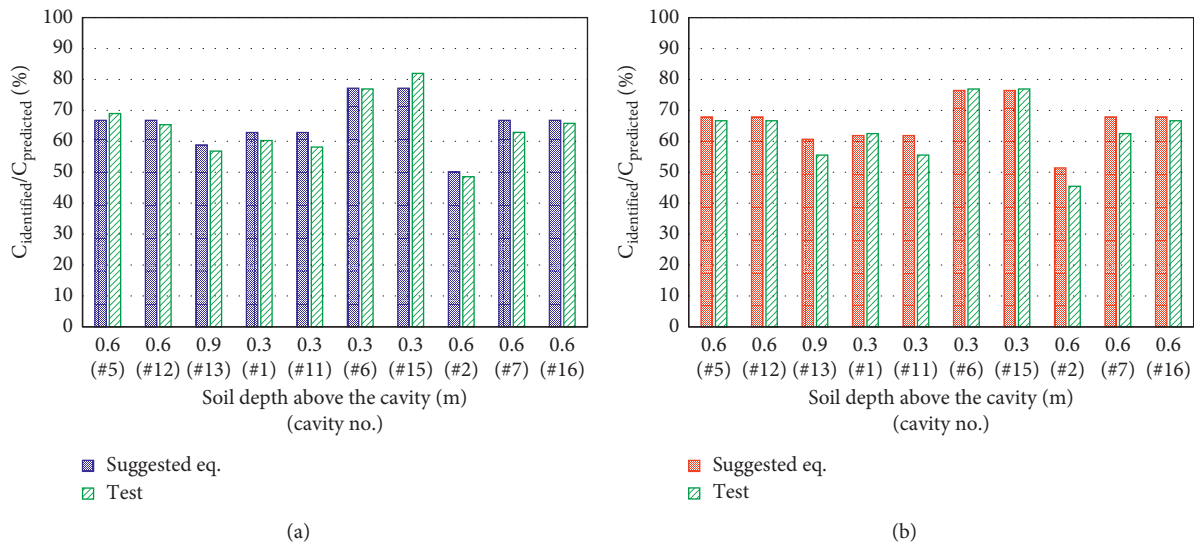


FIGURE 14: Evaluation results by the applied evaluation method. (a) Longitudinal section. (b) Cross section.

exploration results were relatively accurate in estimating the depth of the cavity (soil depth). In addition, as the soil depth increases on top of the cavity, the plane scales of the cavity

(longitudinal and cross sections) are predicted to be larger than the actual scales. Therefore, based on the relationship between the structuralized mock-up cavity (identified

cavity) scale and the predicted cavity scale by the results of GPR exploration (see Table 5), we suggest a formula to estimate the cavity scale using the differences (predicted cavity minus identified cavity) in the longitudinal and cross sections, according to the soil depth as shown in Figure 13. Considering the nonlinear increasing trend of the difference of the plane scale of the cavity in the experimental cases according to the increase of the soil depth, the formula was determined as a second-order polynomial.

We compared the scale ratio of the cavity predicted from the mock-up test and the scale ratio calculated with the proposed formula as shown in Figure 14. The scale ratio obtained by applying the formula was generally larger than the scale ratio obtained from the results of the experiment. In particular, the increase rate was larger for the cross sections, where the differences in scale were relatively large in comparison to the longitudinal scale. Therefore, it is possible to quantitatively estimate the cavity scale based on the calculation method suggested in this study. However, the formula should be applied to more cavity data to enhance its reliability.

5. Conclusions

In this study, the GPR exploration method was carried out on both actual roadway and mock-up site to compensate for the problems caused by excavation and restoration process. An empirical GPR exploration method for predicting the actual cavity scales by comparing the GPR exploration results with the identified cavity scales was suggested. The results are summarized as follows:

- (1) This study compared the cavity scales obtained from GPR exploration results and the direct excavation of the identified cavity. It was confirmed that the predicted soil depth by GPR exploration was similar to the identified soil depth, but the predicted cavity scale by GPR exploration overestimated the longitudinal and cross-sectional widths compared to the identified cavity scale.
- (2) In the experiment on the actual roadway, there was no clear trend for the differences and the ratios of the cavity scales between GPR exploration results and identified cavity. The reason is assumed to be the collapse of cavity during the examination process. Thus, an additional mock-up test was performed to prevent the cavity collapse by placing Styrofoam under the ground. Although the soil depth of the predicted cavity and the identified cavity was similar, the difference in the longitudinal and cross-sectional widths increased as the soil depth increased. Therefore, cavity scales predicted by GPR explorations were larger than the actual cavities for the scale ratios of the longitudinal and cross sections.
- (3) Based on the correlation between the predicted cavity scales by GPR exploration and the cavity scales identified in the mock-up test, it is possible to qualitatively estimate the cavity scales using the empirical formula proposed in this study.

Data Availability

The data used to support the findings of this study are available from the corresponding author upon request.

Conflicts of Interest

The authors declare that they have no conflicts of interest.

Acknowledgments

This work was supported by Korea Environment Industry & Technology Institute (KEITI) through Public Technology Program based on Environmental Policy Project, funded by the Korea Ministry of Environment (MOE) (no. 2016000700001).

References

- [1] *A Study on the Mechanisms of Pavement Subsurface Cavity and its Management Plans*, in Korean, Seoul City, South Korea, 2016, in Korean.
- [2] J. J. Park, H. S. Shin, Y. Chung, S. K. You, and G. Hong, "A study on the open cut restoration of underground cavity using concrete mat," *Journal of Korean Geosynthetics Society*, vol. 18, no. 1, pp. 55–65, 2019.
- [3] H. Y. Chae, "Study on subsurface collapse of pavement surface and cavity search in urban area," *Tunnel & Underground Space*, vol. 27, no. 6, pp. 387–392, 2017.
- [4] D. J. Daniels, "Ground penetrating radar," in *Encyclopedia of RF and Microwave Engineering*, John Wiley & Sons, Inc., Hoboken, NJ, USA, 2005.
- [5] N. J. Cassidy, R. Eddies, and S. Dods, "Void detection beneath reinforced concrete sections: the practical application of ground penetrating radar and ultrasonic techniques," *Journal of Applied Geophysics*, vol. 74, no. 4, pp. 263–276, 2011.
- [6] Y. V. Kang and H. Hsu, "Application of ground penetrating radar to identify shallow cavities in a coastal dyke," *Journal of Applied Science and Engineering*, vol. 16, no. 1, pp. 23–28, 2013.
- [7] Korean Society of Earth and Exploration Geophysicists, *Practical Guidelines for Geophysical Exploration*, Korean Society of Earth and Exploration Geophysicists, Daejeon, South Korea, 2011, in Korean.
- [8] Y. S. Han, "Numerical analysis and exploring of ground condition during groundwater drawdown environment in open-cut type excavation," *Journal of the Korean Geotechnical Society*, vol. 34, no. 11, pp. 93–105, 2018.
- [9] A. Arisona, M. Nawawi, K. S. Ishola, and L. O. Safiuddin, "Forward modeling of ground penetration radar for the reconstruction of models response profiles using synthetic data," *Journal of Geology & Geophysics*, vol. 6, no. 3, p. 3, 2017.
- [10] C. Berthelot, D. Podborochynski, T. Saarenketo, B. Marjerison, and C. Prang, "Ground-penetrating radar evaluation of moisture and frost across typical saskatchewan pavement soils," *Advances in Civil Engineering*, vol. 2010, Article ID 416190, 9 pages, 2010.
- [11] K. Grote, S. Hubbard, and Y. Rubin, "GPR monitoring of volumetric water content in soils applied to highway construction and maintenance," *The Leading Edge*, vol. 21, no. 5, pp. 482–504, 2002.
- [12] K. Grote, S. Hubbard, J. Harvey, and Y. Rubin, "Evaluation of infiltration in layered pavements using surface GPR reflection

- techniques,” *Journal of Applied Geophysics*, vol. 57, no. 2, pp. 129–153, 2005.
- [13] A. Benedetto and S. Pensa, “Indirect diagnosis of pavement structural damages using surface GPR reflection techniques,” *Journal of Applied Geophysics*, vol. 62, no. 2, pp. 107–123, 2007.
- [14] T. Saarenketo and T. Scullion, “Ground penetrating radar applications on roads and highways,” Tech. Rep. 1923-2F, Texas Transportation Institute, College Station, TX, USA, 1994.
- [15] M. D. Knoll and R. Knight, “Relationships between dielectric and hydrogeologic properties of sand-clay mixtures,” in *Proceedings of the 5th International Conference on Ground Penetration Radar*, pp. 45–61, Englewood, CO, USA, 1994.
- [16] H. Kong, S. Kim, M. Kim, and S. Han, “A preprocessing method for ground penetrating radar based land-mine detection system,” *Journal of the Institute of Electronics and Information Engineers*, vol. 50, no. 4, pp. 931–941, 2012.
- [17] I. L. Al-Qadi, S. Lahouar, and A. Loulizi, “GPR: From the state-of-the-art to the state-of-the-practice,” in *Proceedings of the International Symposium of Non-destructive Testing in Civil Engineering*, Berlin, Germany, September 2003.
- [18] L. B. Conyers, “Analysis and interpretation of GPR datasets for integrated archaeological mapping,” *Near Surface Geophysics*, vol. 13, no. 6, pp. 645–651, 2015.
- [19] A. P. Annan, “11. Ground-penetrating radar,” *Near-Surface Geophysics*, vol. 13, pp. 357–438, 2005.
- [20] I. L. Al-Qadi, Z. Leng, S. Lahouar, and J. Baek, “In-place hot-mix asphalt density estimation using ground-penetrating radar,” *Transportation Research Record: Journal of the Transportation Research Board*, vol. 2152, no. 1, pp. 19–27, 2010.
- [21] T. Saarenketo, *Electrical properties of road materials and subgrade soils and the use of ground penetrating radar in traffic infrastructure surveys*, Ph.D. thesis, University of Oulu, Oulu, Finland, 2006.

Research Article

Stability Analysis of Slope with Multiple Sliding Surfaces Based on Dynamic Strength-Reduction DDA Method

Shuhong Wang, Chengjin Zhu , Pengyu Wang, and Zishan Zhang

School of Resources and Civil Engineering, Northeastern University, Shenyang 110819, China

Correspondence should be addressed to Chengjin Zhu; zhuchengjin@cumt.edu.cn

Received 15 July 2019; Revised 23 September 2019; Accepted 1 October 2019; Published 11 November 2019

Academic Editor: Yinshan Tang

Copyright © 2019 Shuhong Wang et al. This is an open access article distributed under the Creative Commons Attribution License, which permits unrestricted use, distribution, and reproduction in any medium, provided the original work is properly cited.

The present study aims to elucidate the problem of a rock mass structural plane with a range of damage degrees and the numerical model selection for analysis of a slope with multiple sliding surfaces. Based on the relative displacement between blocks, the dynamic strength reduction-discontinuous deformation analysis (hereinafter referred to as DSR-DDA) method is proposed for studying slopes with multiple sliding surfaces. The slope-slider classic case was used to test the displacement threshold. The model was applied to the stability analysis of multiple sliding surfaces of a high rock slope in the Fushun West Open-Pit Mine. The results show that when the displacement threshold is set to 1 mm, the error between the DSR-DDA results and the theoretical solution is within 0.5%, which satisfies the calculation requirements. The most dangerous slip surface in the Fushun West Open-Pit Mine slope was identified. Based on the numerical slope model after the first landslide, the position of the secondary slip surface was then identified. The failure mode is traction sliding failure, and the middle and lower oil shales play a key role in the slope stability. This study recommends that mining of the remaining oil shale should stop to avoid causing large-scale landslides in the upper part of the slope and landslides at the pit-city boundary.

1. Introduction

Large-scale geographical areas have complicated geological and instability conditions. A high slope with an open pit forms large areas prone to secondary instability after initial instability, resulting in a secondary sliding surface. The high rock slope is affected by the bedding structure, which complicates the stability problem of the slope. Therefore, it is necessary to elucidate the stability of rock high slopes with multiple potential sliding surfaces through research [1–8].

There are two commonly used calculation methods in slope stability analysis: the limit equilibrium method (LEM) [9–11] and finite element method (FEM) [12–14]. Compared with the FEM, the LEM has a high computational efficiency. The safety factor is solved by geometric assumptions based on known or assumed slip surfaces, but the constitutive relationship of rock and soil during slope slip is ignored [15]. In recent years, with the rapid

development of FEMs and the combination of strength reduction methods, models no longer need to presuppose the position of the sliding surface. The safety factor and corresponding potential sliding surface are easy to obtain. The limitation lies in the safety factor and singularity of the sliding surface solution. Cala et al. [16] pioneered a new strength-reduction method, which identified the most dangerous instability surface based on the conventional method. The authors determined the number of steps N for the first slip and continued to increase the reduction factor; then, the results of the $1.1N$ step were calculated. The corresponding secondary potential instability surface and safety factor were successively obtained. However, there is a need to further study these methods for the stability analysis of slopes with multiple sliding surfaces.

Discontinuity is an intrinsic property of a rock mass. The discontinuous deformation analysis (DDA) proposed by Shi [17] has unique advantages in simulating

large block displacement and large deformation. DDA has also been rapidly developed in the field of slope engineering. Maclaughlin et al. [18] simulated the plane and arc failure modes of inclined slopes and found that the results had better accuracy than those of the conventional analysis methods. Hatzor and Feintuch [19] showed the validity of DDA results for the full dynamic analysis of dynamically charged monolithic slopes. Beyabanaki [20] presented existing blocks in discontinuity failure analysis as deformable disks. Jiang and Zheng [21] proposed an effective method to correct the error in the increase in volume caused by a large rotation. Morgan and Aral [22] proposed a hydrogeological model to model hydraulic breaks using deformed breakdown analysis. This model complies with the Griffith model. The elasticity problem of a large rotation has been previously studied [23]. Perturbations occur in the initial DDA because the first-order shift function is used to describe the block's movement. Yu and Yin [24] have improved some algorithms and processes used to analyze the deformation of discontinuities. Biran and Hatzor [25] compared the DDA with a powerful discrete structure and component numerical modeling method. Zheng et al. [26] used the dual form of this method to solve the problem of opening and closing iterations and strong applied forces. Fu et al. [27] combined the border element method with the DDA to achieve synchronous deformation modeling and displacement modeling. Fan et al. [28, 29] used virtual work theory to improve the accuracy of deformation and large rotation error estimation and proposed a new method to identify and analyze the contact blocks. Fu et al. [30] applied the vector sum method (VSM) to the DDA to calculate the slope stability safety factor based on the actual stress state and vector and algorithm. There is a lack of studies regarding the stability analysis of a slope with multiple sliding surfaces using these methods.

Shahami et al. [31] studied the effects of external loading changes on the rock block displacements in the DDA method. The results show that the effects of external forces on the stability of the blocky rock mass depend on the magnitude of the applied forces and the dimensions of the blocks that constitute the rock mass. Gong et al. [32] proposed the improved DDA (IDDA) method, which could more effectively provide a unified formulation to simulate the nonlinear deformation and failure behaviors of jointed rock masses. Chen et al. [33] clarified the postfailure behavior of a landslide using a two-dimensional (2D) DDA and provided comprehensive information on the initiation and evolution of the landslide. Fan et al. [34] introduced a partitioned finite element and interface element (PFE/IE) interactive method and analyzed the dynamic behaviors of structures with discontinuous deformations. Moreover, PFE/IE improves the computational efficiency because the nonlinear iteration is limited to the possible contact region. Liu et al. [35] extended the flat-top partition of the unity method

that could obtain a stiffness matrix with a small condition number and avoid the linear dependence problem to rock dynamic analyses to simulate the effect of the discontinuity and dynamic loading.

The key problem in the development of slope stability evaluation is the safety factor and solution of the corresponding slip surface. Previously, the strength reduction method mostly assumes a uniform reduction in a rock mass. In an actual situation, the mechanical properties of the structural plane mainly determine the mechanical properties of the rock mass. However, the structural damage of a rock mass does not exhibit the same degree of damage through time. After the first instability of the slope, the block position and stress redistribute. Therefore, the secondary slip surface should be analyzed using the slope model after the first instability. In the past, the secondary sliding surface of the slope was studied. Few studies have considered the actual situation. To solve this problem, we draw on the advantage of DDA to calculate the displacement and consider the relative displacement between blocks. We proposed a multiple-sliding-surface search based on the DSR-DDA method and evaluated the slope stability. This method is mainly applied to solve rock mass stability problems, especially for large-scale rock masses with numerous structural planes. Moreover, this method can consider the variation in damage along a rock mass structural plane and help with numerical model selection in the analysis of a slope with multiple sliding surfaces. By analyzing a rock mass using this method, we can easily determine the safety factor and corresponding slip surface. Thus, measures can be taken to prevent the instability of a rock mass over time. We used an inclined plane slider to test the displacement threshold and verify the feasibility and accuracy of the proposed method and attempted to apply this approach to the stability analysis of a rock high slope in the Fushun West Open-Pit Mine.

2. Methodology

2.1. Main Features of the DDA. The DDA uses a first-order displacement function to express the motion parameters of each block and assumes that the stress and strain are constant [36]. The displacement vector of each block contains 6 variables as follows:

$$D = (u_0, v_0, r_0, \varepsilon_x, \varepsilon_y, \gamma_{xy})^T, \quad (1)$$

where (u_0, v_0) is the rigid displacement of a specific point (x_0, y_0) in the block; r_0 is the rotation angle of the block around a specific point (x_0, y_0) ; and $\varepsilon_x, \varepsilon_y, \gamma_{xy}$ is the positive strain and the shear strain of the block, respectively. The displacement (u, v) of any point (x, y) in the block is as follows:

$$\begin{aligned}
\begin{Bmatrix} u \\ v \end{Bmatrix} &= [T]\{D\} \\
&= \begin{bmatrix} 1 & 0 & -(y-y_0) & (x-x_0) & 0 & (y-y_0)/2 \\ 0 & 1 & (x-x_0) & 0 & (y-y_0) & (x-x_0)/2 \end{bmatrix} \\
&\quad \cdot \begin{Bmatrix} u_0 \\ v_0 \\ r_0 \\ \varepsilon_x \\ \varepsilon_y \\ \gamma_{xy} \end{Bmatrix}.
\end{aligned} \tag{2}$$

The overall equilibrium equation of the system based on the principle of minimum potential energy is as follows:

$$\begin{bmatrix} K_{11} & K_{12} & \cdots & K_{1n} \\ K_{21} & K_{22} & \cdots & K_{2n} \\ \cdots & \cdots & \ddots & \cdots \\ K_{n1} & K_{n2} & \cdots & K_{nn} \end{bmatrix} \begin{Bmatrix} D_1 \\ D_2 \\ \vdots \\ D_n \end{Bmatrix} = \begin{Bmatrix} F_1 \\ F_2 \\ \vdots \\ F_n \end{Bmatrix}, \tag{3}$$

where K_{ij} is a 6×6 submatrix in the coefficient matrix; K_{ii} is determined by the material properties and geometric parameters of the block unit; K_{ij} ($i \neq j$) is determined by the contact conditions between block i and block j ; $[D_i]$ and $[F_i]$ are 6×1 submatrices; D_i is the deformation variable ($d_{1i}, d_{2i}, d_{3i}, d_{4i}, d_{5i}, d_{6i}$) block i ; and F_i is the load assigned to the six deformation variables on block i .

2.2. DSR-DDA Method Displacement Threshold. To consider the dissimilarity of the damage along the block structure surface in the real situation, it is proposed that the shear strength of the block structure surface is reduced so that the displacement change does not exceed the threshold value. We used the classic slope slider case to test the displacement threshold of the shear strength reduction. The model is shown in Figure 1. The rock mass parameters are shown in Table 1. In the program calculation, the shear strength parameters of the structural plane of the block are set at regular intervals (10,000 steps, each time step is 0.001 s). According to the relationship between the relative displacement change in the block and the threshold value, only the structural plane with the displacement change that satisfies the requirements was selected. Then, the reduction increases by 0.001 from 1.000 until a sharp deformation occurs, at which time the value of the safety factor of the slope slip surface is determined. The program calculates the simulated reduction process that is consistent with the damage degradation of the rock mass material under actual conditions.

The theoretical safety factor of the simple slope model is as follows:

$$F_s = \frac{\tan \varphi}{\tan \alpha}. \tag{4}$$

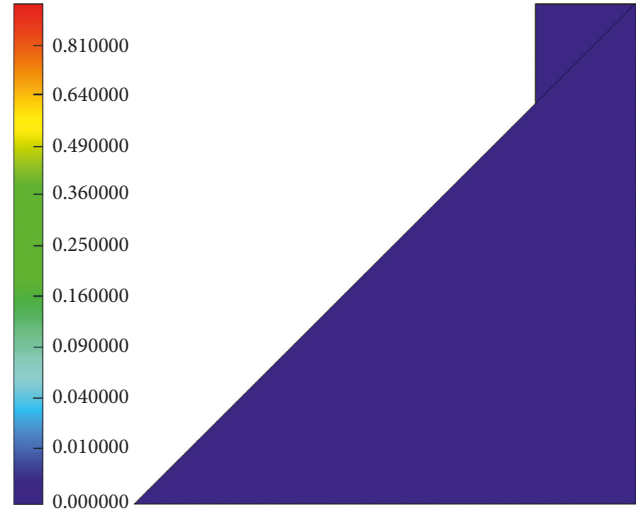


FIGURE 1: Model of the sliding block along the slope.

Figure 2 shows the variation in the model safety factor and error percentage of the analytical solution with the displacement threshold under different values of the in-plane friction angle φ . This graph shows that, regardless of the value of the internal friction angle φ , when the displacement threshold approaches 1 mm, the safety factor is near its maximum value. There is a significant dip in the error percentage of the analytical solution, which indicates that the error is relatively small, within 0.5%. The displacement threshold is temporarily taken as 1 mm. The results of the analytical solution are consistent. Hence, the DSR-DDA method satisfies the calculation requirements and can guarantee a certain calculation accuracy.

Finding the exact solution of the contact force between the blocks is the core step in solving the total equilibrium equation. In each time step, it is necessary to redetermine the application of the spring and position of the spring. It is necessary to repeatedly generate a solution to solve the total stiffness matrix. The process of application and removal of the rigid spring is called an open-close iteration. There are three states of contact: opening, sliding, and locking. The criteria to determine the mode change are shown in Table 2.

Based on the above analysis, the DSR-DDA method is implemented in the program as shown in Figure 3.

3. Rock Slope Model and Parameters of Fushun Western Open-Pit Mine

3.1. Overview of the Rock Slope in Fushun Western Open-Pit Mine. The Fushun West Open-Pit Mine is located in the southeastern part of Fushun City and has a mining history of more than 100 years. It has formed “Asia’s largest pit” with a length of 6.6 km, a width of 2.2 km from north to south, and a depth of 400–500 m, representing a total volume of 1.7 billion cubic kilometers. The northern part of the coal-mining pit is adjacent to the urban area of Fushun City. If a landslide occurs in the northern slope, it will cause a large number of casualties and major property loss, seriously affecting the safety of all nearby construction facilities and endangering the safety of

TABLE 1: Mechanical properties of the slope model.

Number	Density ($\text{kg}\cdot\text{m}^{-3}$)	E (MPa)	Cohesion (MPa)	Friction ($^{\circ}$)	Poisson's ratio	Theoretical safety factor
01	2700	1000	40	50	0.35	1.192
02	2700	1000	40	55	0.35	1.428
03	2700	1000	40	60	0.35	1.732
04	2700	1000	40	65	0.35	2.145
05	2700	1000	40	70	0.35	2.747
06	2700	1000	40	75	0.35	3.732
07	2700	1000	40	80	0.35	5.671

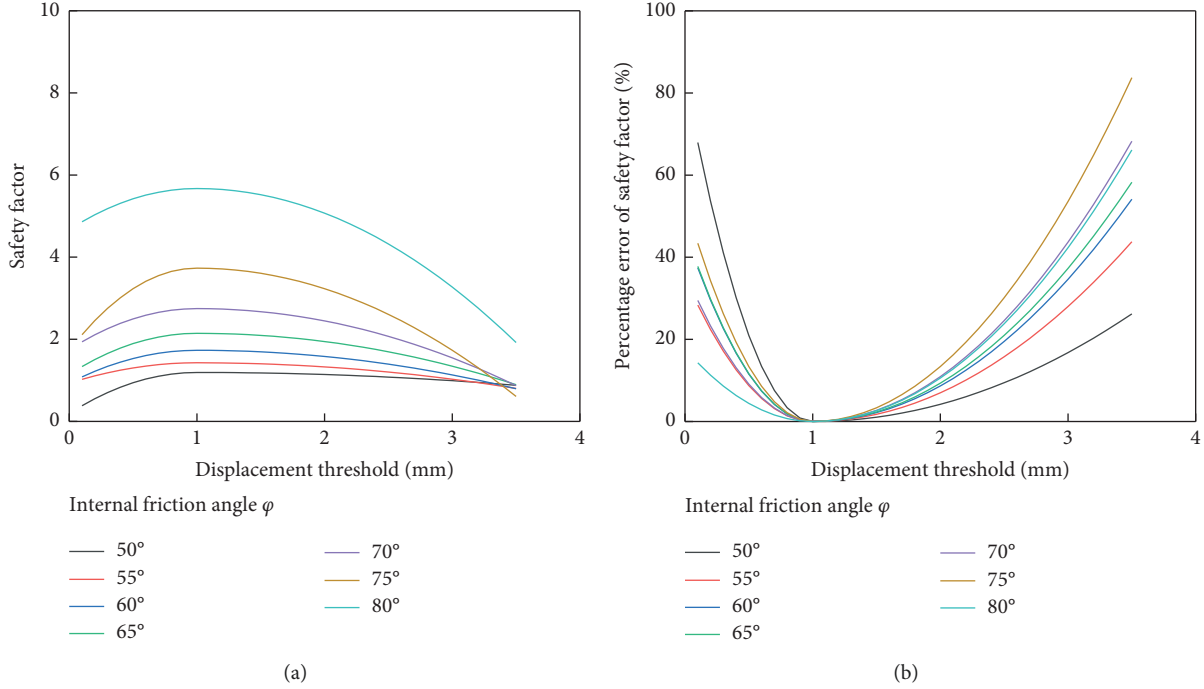


FIGURE 2: Curve of safety factor and its error with the displacement threshold: (a) safety factor; (b) percentage error of safety factor.

TABLE 2: Contact status table.

Contact switch	Contact condition	Contact force
Open-open	$N > 0$	No
Open-sliding	$N < 0, S > f $	Yes
Open-locked	$N < 0, S < f $	Yes
Sliding-open	$N > 0$	No
Sliding-sliding	$N < 0, S > f $ or $N < 0, \psi = -\text{sgn } f$	Yes
Sliding-locked	$N < 0, S < f $ or $N < 0, \psi = \text{sgn } f$	Yes
Locked-open	$N > 0$	No
Locked-sliding	$N < 0, S > f $	Yes
Locked-locked	$N < 0, S < f $	Yes

¹ N is the normal contact force, S is the shear contact force, ψ is the direction of shear displacement, and f is the frictional force.

the entire city. The layout of the Fushun West Open-Pit Mine and the northern part of the western slope are shown with a geological section map in Figure 4.

3.2. Calculation Analysis Model and Parameters.

Discontinuous structures such as joints and fissures play a controlling role in the deformation of a rock mass. The accuracy of the information acquisition of the structural plane is critical to the accuracy of the numerical simulation analysis. Using high-precision and high-efficiency unmanned aerial vehicle technology, deterministic structural plane information is accurately acquired to generate a point cloud model [37]. The DJI Phantom 4 Pro and control system are shown in Figure 5.

The definition of inclination requires that the surface structure of the rock mass is known, including the normal vector of the plane where the production is located, assuming that the equation representing the structural plane is as follows:

$$Z = AX + BY + C, \quad (5)$$

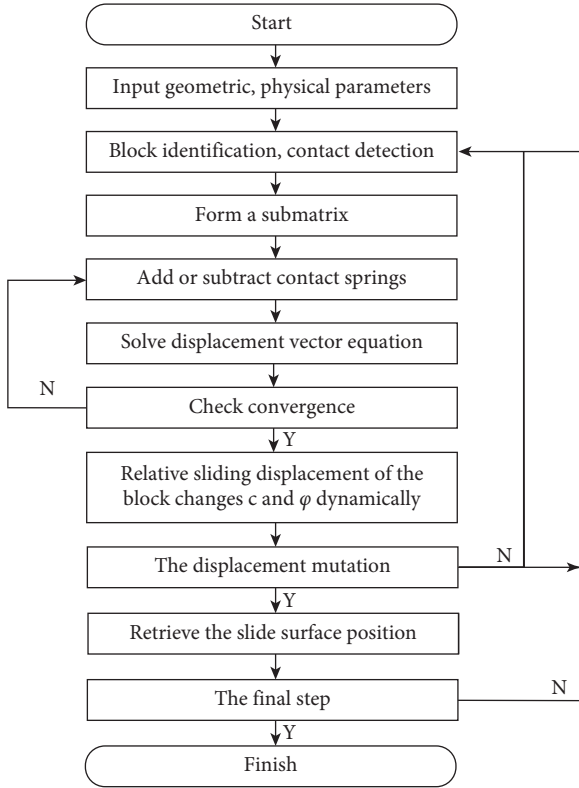


FIGURE 3: Flow chart of the DDA procedures.

where A , B , and C are plane parameters, and the plane normal vector n is $(-A, -B, 1)$. Along the structural plane, for any n points that are not collinear ($n > 3$), we can obtain the following equation:

$$\begin{bmatrix} X_1 & Y_1 & 1 \\ X_2 & Y_2 & 1 \\ X_3 & Y_3 & 1 \\ \dots & \dots & \dots \\ X_n & Y_n & 1 \end{bmatrix} \cdot \begin{bmatrix} A \\ B \\ C \end{bmatrix} = \begin{bmatrix} Z_1 \\ Z_2 \\ Z_3 \\ \dots \\ Z_n \end{bmatrix}. \quad (6)$$

The least squares method is used to solve (A, B, C) as follows:

$$\begin{bmatrix} A \\ B \\ C \end{bmatrix} = \left(\begin{bmatrix} X_1 & Y_1 & 1 \\ X_2 & Y_2 & 1 \\ X_3 & Y_3 & 1 \\ \dots & \dots & \dots \\ X_n & Y_n & 1 \end{bmatrix}^T \begin{bmatrix} X_1 & Y_1 & 1 \\ X_2 & Y_2 & 1 \\ X_3 & Y_3 & 1 \\ \dots & \dots & \dots \\ X_n & Y_n & 1 \end{bmatrix} \right)^{-1} \begin{bmatrix} X_1 & Y_1 & 1 \\ X_2 & Y_2 & 1 \\ X_3 & Y_3 & 1 \\ \dots & \dots & \dots \\ X_n & Y_n & 1 \end{bmatrix}^T \begin{bmatrix} Z_1 \\ Z_2 \\ Z_3 \\ \dots \\ Z_n \end{bmatrix}. \quad (7)$$

From the conversion formula, the dip direction is as follows:

$$\alpha = \arctan \left| \frac{B}{A} \right|. \quad (8)$$

The dip angle is as follows:

$$\beta = \left| \arctan \left(\sqrt{A^2 + B^2} \right) \right|. \quad (9)$$

The point cloud parameters of the structural plane are selected. The plane equation is fitted according to the point cloud information, and the structural surface morphology is determined. The calculation results of some occurrences are shown in Table 3, and the structural plane production statistics are obtained. The statistical cloud chart of the structural plane is shown in Figure 6.

The acquired structural plane information is imported into the DSR-DDA program, and the structural plane mesh cuts the rock mass to form a block unit in the DSR-DDA. Figure 7 shows a model of the example for numerical analysis.

The natural stress field takes only gravity into account and does not include the regional tectonic stress. According to the geological exploration and test results, the parameters in Table 4 are obtained. The cohesion and friction in Table 4 are the implied cohesion and friction values of the rock mass structural plane. In the numerical calculation, the shear strength parameters of the structural plane of the block are reduced at a certain time step (10,000 steps, each time step is approximately 0.001 seconds) along the structural plane where the relative displacement change in the block is reached or exceeded, and the reduction factor changes from 1.000. Initially, this time step is consistent with the damage degradation of the rock mass material.

4. Stability Analysis of the Rock Slope in Fushun Western Open-Pit Mine

4.1. Field Displacement Monitoring. The cumulative displacement values measured at different depths in each inclined hole during two months are shown in Figure 8.

The analysis of Figure 8 shows that the total displacement value of the measured point in the first 100 m of hole 69002 greatly varies with time. The magnitude of displacement sharply increases near a depth of 100 m, which indicates that the rock mass near the inclined hole slips. There is a tendency to continue sliding, and the sliding surface is approximately 100 m from the slope. The total displacement of the measuring point in the first 20 m of hole 55026 occurs relatively fast, and there is a trend of continued growth. The change in displacement at the subsequent measuring point is not obvious and tends to be stable. It is speculated that instability exists in the rock mass above the measuring hole. The displacement of the measuring point in hole 74003 slowly increases with time, with no obvious regularity, and tends to be stable; thus, the stability of the rock mass in this area is better than those at other holes.

4.2. DSR-DDA Numerical Calculation Analysis. To further determine the potential slip surface position of the slope, according to the DSR-DDA method, the shear strength parameters are dynamically reduced, and the progressive instability of the slope was characterized. The slip surface and corresponding safety factor were measured. The feasibility of the method was verified by identifying the most dangerous slip surface and secondary slip surface in the slope. Figures 9 and 10 show the first instability and secondary instability of the slope. The legend in these figures indicates the displacement of the block at the current time step. For example, 0.706876 indicates that the block moves 0.706876 mm in the current time step.

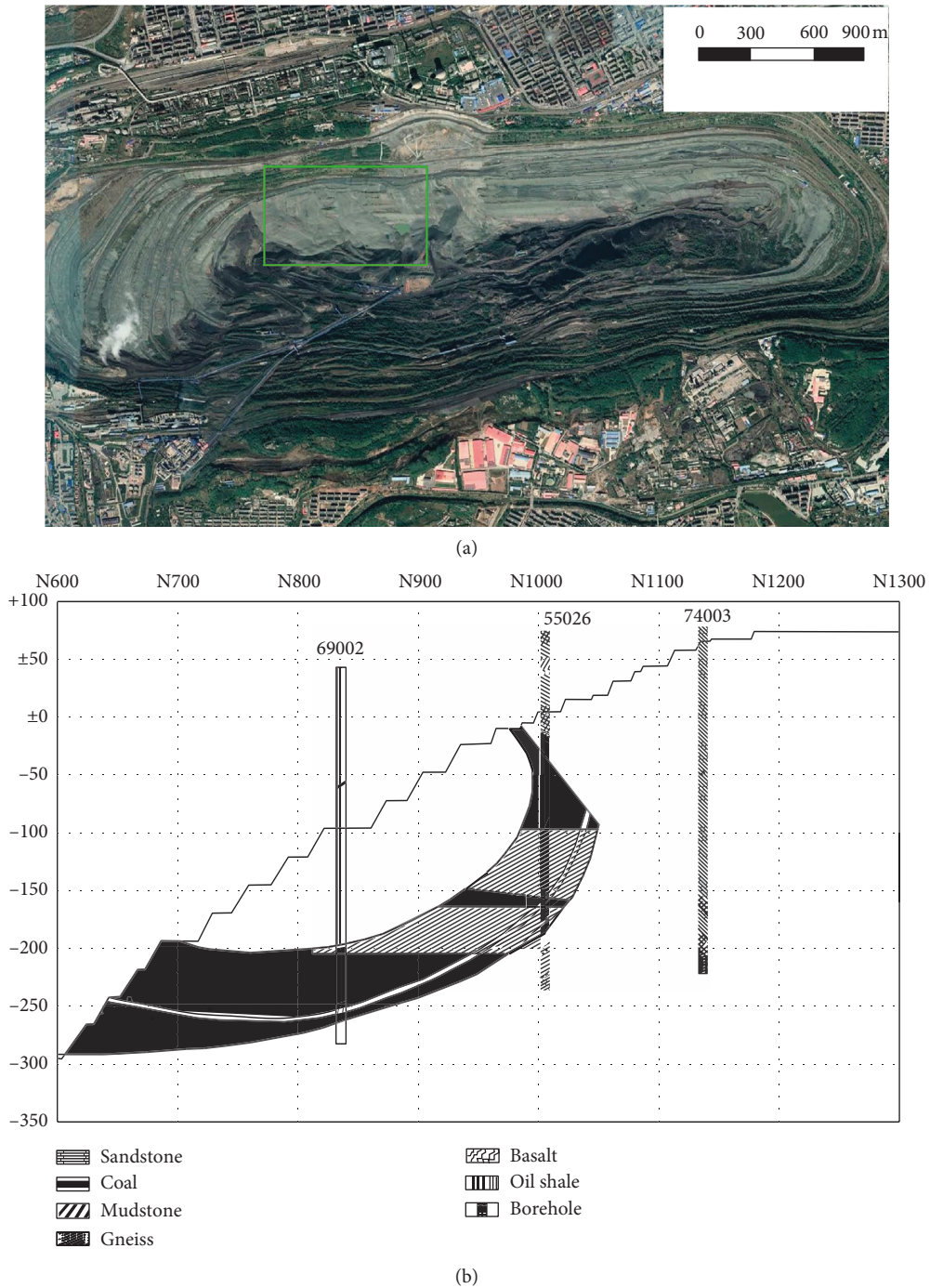


FIGURE 4: Layout of the Fushun West Open-Pit Mine and the northern part of the western slope in the geological section map: (a) Fushun West Open-Pit Mine; (b) geological section map.

Before the 1.360×10^6 time step, the displacement of the monitoring points of each block and the overall slope of the block remain basically stable. When the calculation is at step 1.360×10^6 , the slope quickly deforms, the reduction factor reaches 1.136, and the displacement of the corresponding block sharply increases. The subsequent deformation also shows a gradual increasing trend. The overall deformation of the slope shows that the lower landslide body slips along the corresponding sliding surface, which indicates that the slope

is unstable for the first time. The safety factor corresponding to the most dangerous slip surface was 1.136.

According to the block large deformation data and DSR-DDA program image, the slope slip surface appears at a depth of approximately 100 m in hole 69002. The large deformation of the rock mass occurs above the sliding surface. The position of the deep part of hole 55026 does not significantly change, and only the block in the near-surface position is displaced. There is no obvious deformation of the

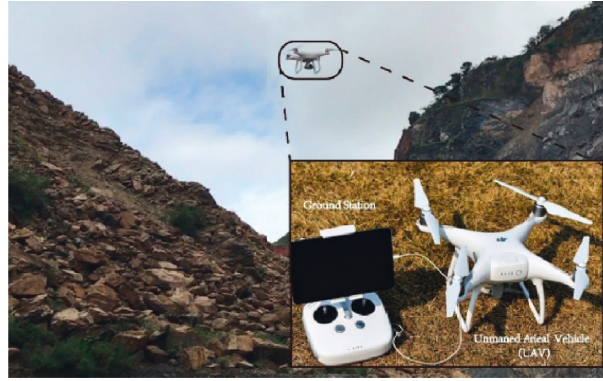


FIGURE 5: DJI Phantom 4 Pro and control system.

TABLE 3: Yield calculation results.

Number	Structural plane equation parameter			Structural plane information		
	A	B	C	Dip direction (°)	Dip angle (°)	The length of the trace (m)
01	0.368	0.245	0.621	33.7	35.5	6.55
02	0.440	-1.270	0.265	109.0	78.9	6.70
03	0.337	2.824	0.324	263.2	83.5	8.53
04	-1.380	3.452	0.443	291.8	83.2	4.26
05	0.455	2.088	0.266	282.3	82.9	2.88
06	-0.100	1.480	0.185	265.9	82.9	1.20
07	-0.640	5.600	0.247	96.6	73.2	5.88
08	0.316	0.882	0.201	250.3	77.9	1.47
09	0.447	1.703	0.247	284.7	89.0	2.06
10	57.150	-28.400	0.433	26.5	89.6	1.95

rock mass in hole 74003. These characteristics are consistent with the on-site monitoring data, which further proves the feasibility of the method.

After the first instability of the slope, the block position and internal stress are redistributed. The slope modeling continued after the first instability process to identify the secondary slip surface.

Before step 1.890×10^6 , the slope tends to be stable. When the calculation is completed at step 1.890×10^6 , the reduction factor reaches 1.189. The slope again quickly deforms and forms a secondary slip surface. Its corresponding safety factor is 1.189. The slope of the first slope is larger than the first slope instability. The slope strength is slightly reduced after the first instability occurs, which is notably different from the results obtained by the conventional analysis.

The failure mode of the slope of the Fushun West Open-Pit Mine is traction-type sliding failure. The middle and lower oil shales play a key role in the stability of the slope. Therefore, the remaining oil shale cannot be continuously mined to avoid large-scale landslides from initiating in the upper part of the slope and to avoid landslides at the pit-city boundary.

5. Discussion

In this paper, we theoretically confirmed the necessity and significance of dynamically reducing the strengths of rock mass structural planes. We further revealed the effects of the

problem of different degrees of damage of rock mass structural planes and the problem of numerical model selection for analyzing slopes with multiple sliding surfaces. We determined the displacement threshold to reduce the error between DSR-DDA and the theoretical solution. Then, we used these methods in the stability analysis of the northern slope of the Fushun West Open-Pit Mine.

In addition, the slope strength is slightly reduced after the first instability occurs, which is quite different from the results obtained by conventional analysis [38, 39]. We infer that the first instability landslide body cannot be ignored in the conventional analysis because it protects the secondary landslide body with a high safety factor, mainly because the position and stress of the block are redistributed after the first instability of the slope. Therefore, the secondary slip surface should be analyzed using the slope model after the first instability, which was not fully considered in previous studies.

Although there are advantages in the DSR-DDA method for slope-stability analysis and large-deformation slope-instability analysis, there are still weaknesses in the precision of the method. It is difficult to complete slope failure experiments in the laboratory. The displacement threshold is set by the DSR-DDA numerical simulation test, which makes the accuracy of the results overly dependent on the accuracy of the DSR-DDA program. Therefore, the results suggest that, in the future, different projects will require simulation training to improve their accuracy and that similar laboratory experiments should be attempted. For further study,

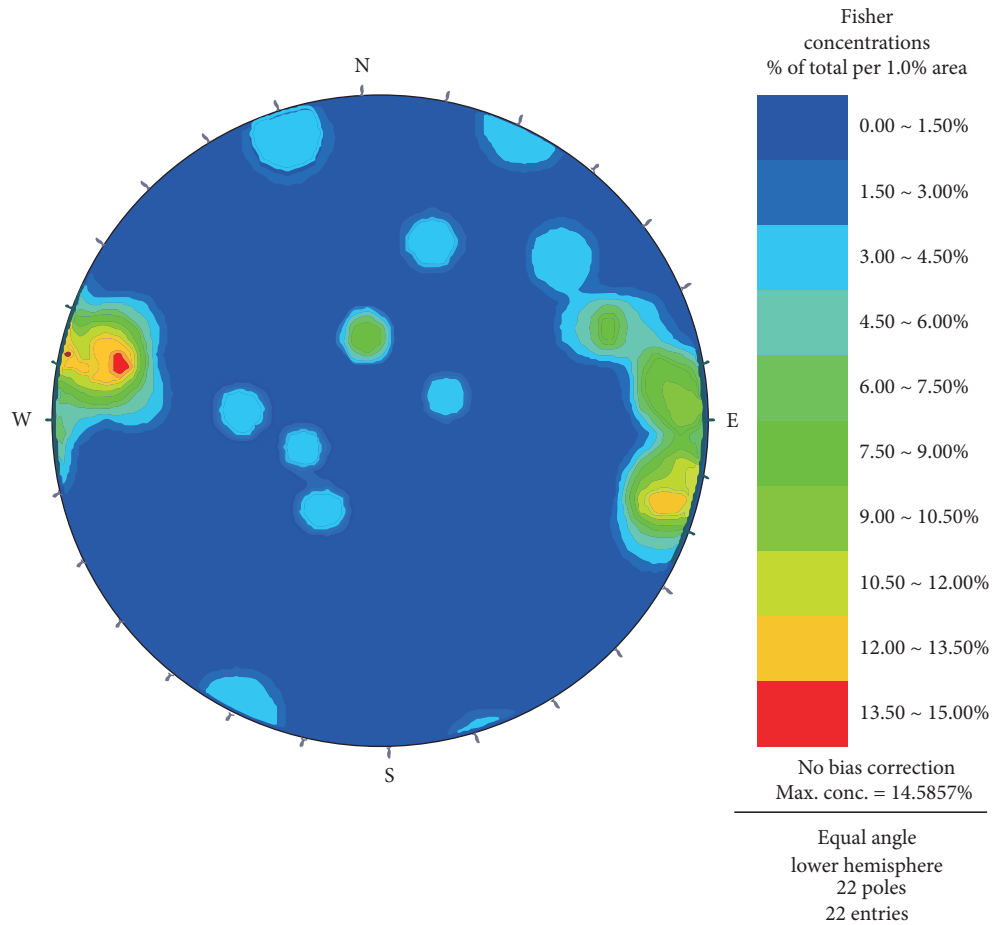


FIGURE 6: Statistical cloud chart of the structure surface.

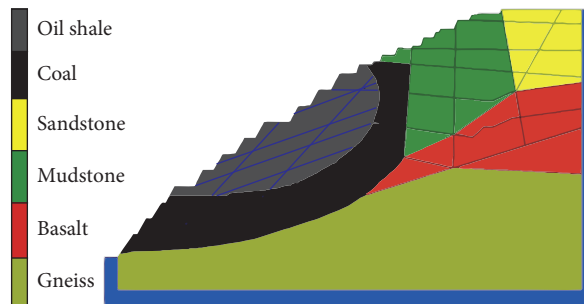


FIGURE 7: DDA model of the slope in the Fushun West Open-Pit Mine for numerical calculation and analysis.

TABLE 4: Mechanical parameters of the slope model.

Lithology	Density ($\text{kg}\cdot\text{m}^{-3}$)	E (GPa)	Cohesion (MPa)	Friction ($^{\circ}$)
Oil shale	2100	16.5	3.5	26
Coal	1500	12.0	4.7	25
Sandstone	2300	15.2	20.0	19
Mudstone	2500	12.5	33.0	20
Basalt	2800	57.5	27.0	25
Gneiss	2800	38.2	32.0	29

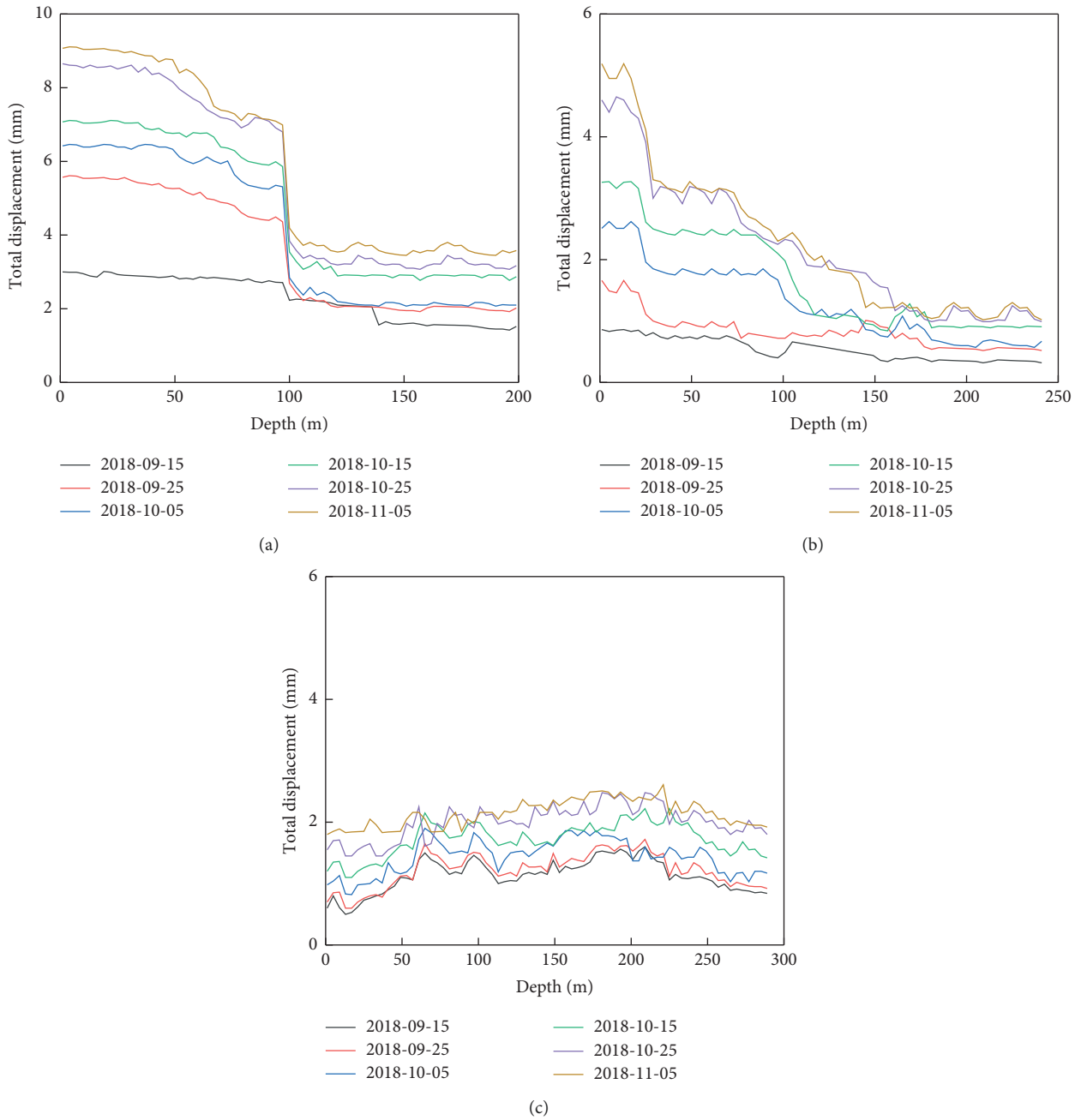


FIGURE 8: Cumulative displacements of the monitoring point in surveying the inclined hole: (a) surveying inclined hole 69002; (b) surveying inclined hole 55026; (c) surveying inclined hole 74003.

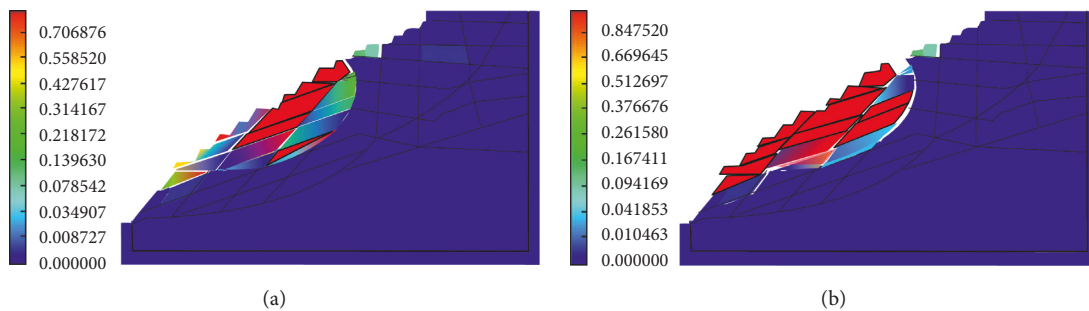


FIGURE 9: Continued.

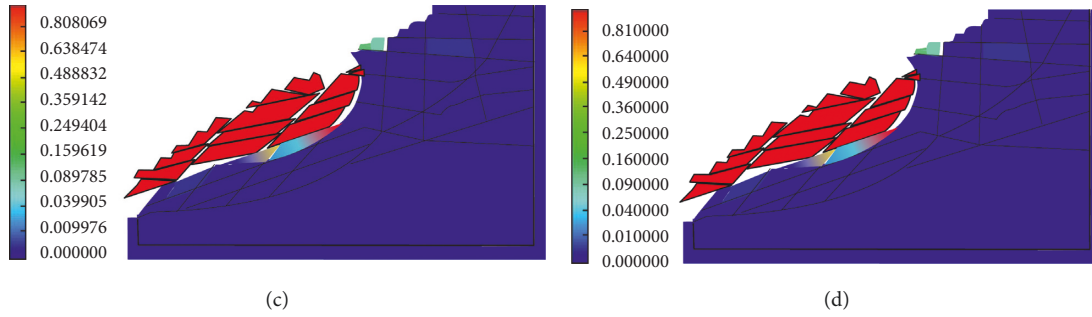


FIGURE 9: First failure process of the northern slope in the Fushun West Open-Pit Mine: (a) step 1.361×10^6 ; (b) step 1.363×10^6 ; (c) step 1.365×10^6 ; (d) step 1.367×10^6 .

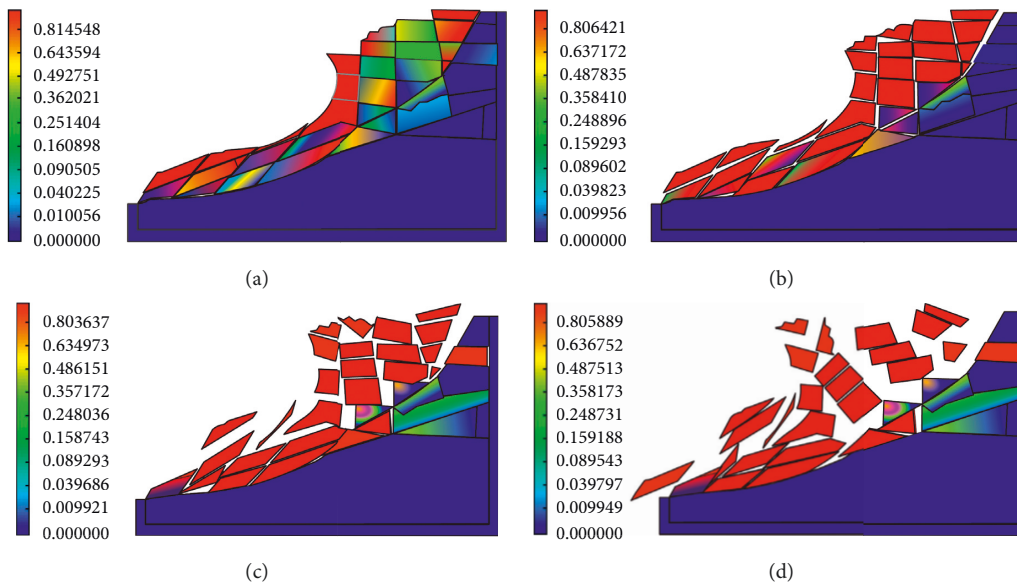


FIGURE 10: Second failure process of the northern slope in the Fushun West Open-Pit Mine: (a) step 1.892×10^6 ; (b) step 1.894×10^6 ; (c) step 1.896×10^6 ; (d) step 1.898×10^6 .

this method will be improved to solve the problems of tunnel assessment and the failure mechanisms of different rocks [40–42].

6. Conclusions

This study aims to elucidate the problem of different degrees of damage along a rock mass structural plane and numerical model selection for analyzing slopes with multiple sliding surfaces. Furthermore, a series of numerical simulations and on-site monitoring data were used to study the mechanism controlling different degrees of damage along a rock mass structural plane. The following conclusions have been drawn from this study:

- (1) A DSR-DDA method controlled by the displacement threshold is proposed. The basic process of calculating the safety factor of a slope with multiple sliding surfaces by the DSR-DDA method is provided, contributing a new method for slope-stability analysis.

- (2) The feasibility and calculation accuracy of the DSR-DDA method are verified by the case of the classic slope slider. The displacement threshold is 1 mm, and the dynamic strength of the rock mass is reduced under different degrees of damage. Furthermore, the heterogeneity of the rock mass structural surface damage was analyzed.
- (3) Based on the DSR-DDA method, the stability of multiple sliding surfaces of the northern slope of the Fushun West Open-Pit Mine was analyzed. The most dangerous slip surface and secondary slip surface position were determined, proving that the slope is prone to slipping. The results suggest that there is a requirement of dynamic change in the model for accurate slope surface stability analysis. The results indicate that the failure mode of the slope was traction sliding failure. The middle and lower oil shales play a key role in the stability of the slope. Therefore, the remaining oil shale cannot be continuously mined to avoid large-scale landslides and

landslides along the pit-city boundary in the upper part of the slope.

Data Availability

The data used to support the findings of this study are available from the corresponding author upon request.

Conflicts of Interest

The authors declare no conflicts of interest.

Authors' Contributions

Shuhong Wang and Chengjin Zhu contributed equally.

Acknowledgments

The authors gratefully acknowledge the financial support from the National Natural Science Foundation of China (Nos. 51474050 and U1602232), Fundamental Research Funds for the Central Universities (No. N17010829), Doctoral Scientific Research Foundation of Liaoning Province (Nos. 20170540304 and 20170520341), and Research and Development Project of Guizhou University of Engineering Science (Grant No: G2018016).

References

- [1] C. Zhu, Z. Tao, Y. Shen, and S. Zhao, "V shaped gully method for controlling rockfall on high-steep slopes in China," *Bulletin of Engineering Geology and the Environment*, vol. 78, no. 4, pp. 2731–2747, 2019.
- [2] Y. Li, S. Zhang, and X. Zhang, "Classification and fractal characteristics of coal rock fragments under uniaxial cyclic loading conditions," *Arabian Journal of Geosciences*, vol. 11, no. 9, p. 201, 2018.
- [3] S. Zhang, Y. Li, B. Shen, X. Sun, and L. Gao, "Effective evaluation of pressure relief drilling for reducing rock bursts and its application in underground coal mines," *International Journal of Rock Mechanics and Mining Sciences*, vol. 114, pp. 7–16, 2019.
- [4] Z. Qin, H. Fu, and X. Chen, "A study on altered granite meso-damage mechanisms due to water invasion-water loss cycles," *Environmental Earth Sciences*, vol. 78, p. 428, 2019.
- [5] F.Q. Ren, C. Zhu, and M. C. He, "Moment tensor analysis of acoustic emissions for cracking mechanisms during schist strain burst," *Rock Mechanics and Rock Engineering*, vol. 3, pp. 1–18, 2019.
- [6] Z. Tao, Y. Wang, C. Zhu et al., "Mechanical evolution of constant resistance and large deformation anchor cables and their application in landslide monitoring," *Bulletin of Engineering Geology and the Environment*, vol. 78, no. 7, pp. 4787–4803, 2019.
- [7] G. Shi, X. Yang, H. Yu, and C. Zhu, "Acoustic emission characteristics of creep fracture evolution in double-fracture fine sandstone under uniaxial compression," *Engineering Fracture Mechanics*, vol. 210, pp. 13–28, 2019.
- [8] S. Wang and P. Ni, "Application of block theory modeling on spatial block topological identification to rock slope stability analysis," *International Journal of Computational Methods*, vol. 11, no. 1, pp. 903–914, 2014.
- [9] N. R. Morgenstern and V. E. Price, "The analysis of the stability of general slip surfaces," *Géotechnique*, vol. 15, no. 1, pp. 79–93, 1965.
- [10] Y. Zheng, C. Chen, T. Liu, H. Zhang, K. Xia, and F. Liu, "Study on the mechanisms of flexural toppling failure in anti-inclined rock slopes using numerical and limit equilibrium models," *Engineering Geology*, vol. 237, pp. 116–128, 2018.
- [11] S.-H. Jiang, J. Huang, C. Yao, and J. Yang, "Quantitative risk assessment of slope failure in 2-d spatially variable soils by limit equilibrium method," *Applied Mathematical Modelling*, vol. 47, pp. 710–725, 2017.
- [12] O. Simon, T. Franz, and F. S. Helmut, "Finite element analysis of slope stability problems using non-associated plasticity," *Journal of Rock Mechanics and Geotechnical Engineering*, vol. 10, no. 6, pp. 1091–1101, 2018.
- [13] Y. Liu, W. Zhang, L. Zhang, Z. Zhu, J. Hu, and H. Wei, "Probabilistic stability analyses of undrained slopes by 3D random fields and finite element methods," *Geoscience Frontiers*, vol. 9, no. 6, pp. 1657–1664, 2018.
- [14] L. Li, S. X. Liu, J. X. Li, and W. Jia, "Numerical simulation of oblique and multidirectional wave propagation and breaking on steep slope based on FEM model of Boussinesq equations," *Applied Mathematical Modelling*, vol. 71, pp. 632–655, 2019.
- [15] J. M. Duncan, "State of the art: limit equilibrium and finite-element analysis of slopes. discussion and closure," *Journal of Geotechnical Engineering*, vol. 122, no. 7, pp. 577–596, 1996.
- [16] M. Cala, J. Flisiak, and A. Tajdus, "Slope stability analysis with modified shear strength reduction technique," in *Proceedings of the Ninth International Symposium on Landslides: Evaluation and Stabilization*, Rio de Janeiro, Brazil, 2004.
- [17] G.-H. Shi and R. E. Goodman, "Two dimensional discontinuous deformation analysis," *International Journal for Numerical and Analytical Methods in Geomechanics*, vol. 9, no. 6, pp. 541–556, 1985.
- [18] M. Maclaughlin, N. Sitar, D. Doolin, and T. Abbot, "Investigation of slope-stability kinematics using discontinuous deformation analysis," *International Journal of Rock Mechanics and Mining Sciences*, vol. 38, no. 5, pp. 753–762, 2001.
- [19] Y. H. Hatzor and A. Feintuch, "The validity of dynamic block displacement prediction using DDA," *International Journal of Rock Mechanics and Mining Sciences*, vol. 38, no. 4, pp. 599–606, 2001.
- [20] S. A. R. Beyabanaki, B. Ferdosi, and S. Mohammadi, "Validation of dynamic block displacement analysis and modification of edge-to-edge contact constraints in 3-D DDA," *International Journal of Rock Mechanics and Mining Sciences*, vol. 46, no. 7, pp. 1223–1234, 2009.
- [21] W. Jiang and H. Zheng, "An efficient remedy for the false volume expansion of DDA when simulating large rotation," *Computers and Geotechnics*, vol. 70, pp. 18–23, 2015.
- [22] W. E. Morgan and M. M. Aral, "An implicitly coupled hydrogeomechanical model for hydraulic fracture simulation with the discontinuous deformation analysis," *International Journal of Rock Mechanics and Mining Sciences*, vol. 73, pp. 82–94, 2015.
- [23] J.-H. Wu, "The elastic distortion problem with large rotation in discontinuous deformation analysis," *Computers and Geotechnics*, vol. 69, pp. 352–364, 2015.
- [24] Y. Yu and J. Yin, "Some modifications to the process of discontinuous deformation analysis," *Journal of Rock Mechanics and Geotechnical Engineering*, vol. 7, no. 1, pp. 95–100, 2015.
- [25] G. Yagoda-Biran and Y. H. Hatzor, "Benchmarking the numerical discontinuous deformation analysis method," *Computers and Geotechnics*, vol. 71, pp. 30–46, 2016.

- [26] H. Zheng, P. Zhang, and X. Du, "Dual form of discontinuous deformation analysis," *Computer Methods in Applied Mechanics and Engineering*, vol. 305, pp. 196–216, 2016.
- [27] G. Y. Fu, G. W. Ma, and X. L. Qu, "Boundary element based discontinuous deformation analysis," *International Journal for Numerical and Analytical Methods in Geomechanics*, vol. 41, no. 7, pp. 994–1015, 2017.
- [28] H. Fan, H. Zheng, and J. Zhao, "Discontinuous deformation analysis based on strain-rotation decomposition," *International Journal of Rock Mechanics and Mining Sciences*, vol. 92, pp. 19–29, 2017.
- [29] H. Fan, H. Zheng, and J. Wang, "A generalized contact potential and its application in discontinuous deformation analysis," *Computers and Geotechnics*, vol. 99, pp. 104–114, 2018.
- [30] X. Fu, Q. Sheng, Y. Zhang, J. Chen, S. Zhang, and Z. Zhang, "Computation of the safety factor for slope stability using discontinuous deformation analysis and the vector sum method," *Computers and Geotechnics*, vol. 92, pp. 68–76, 2017.
- [31] M. H. Shahami, A. Y. Bafghi, and M. F. Marji, "Investigating the effect of external forces on the displacement accuracy of discontinuous deformation analysis (DDA) method," *Computers and Geotechnics*, vol. 111, pp. 313–323, 2019.
- [32] B. Gong, C. A. Tang, and S. Y. Wang, "Simulation of the nonlinear mechanical behaviors of jointed rock masses based on the improved discontinuous deformation and displacement method," *International Journal of Rock Mechanics and Mining Sciences*, vol. 122, 2019.
- [33] K.-T. Chen and J.-H. Wu, "Simulating the failure process of the Xinmo Landslide using discontinuous deformation analysis," *Engineering Geology*, vol. 239, pp. 269–281, 2018.
- [34] S. Fan, T. Li, X. Liu, L. Zhao, Z. Niu, and H. Qi, "A hybrid algorithm of partitioned finite element and interface element for dynamic contact problems with discontinuous deformation," *Computers and Geotechnics*, vol. 101, pp. 130–140, 2018.
- [35] X. Liu and Z. Zhao, "Dynamic analysis with flat-top partition of unity-based discontinuous deformation analysis," *Computers and Geotechnics*, vol. 98, pp. 35–47, 2018.
- [36] G. H. Shi, "Discontinuous deformation analysis: a new numerical model for the statics and dynamics of deformable block structures," *Engineering Computations*, vol. 9, no. 2, pp. 157–168, 1992.
- [37] S. Wang, Z. Zhang, C. Wang, C. Zhu, and Y. Ren, "Multistep rocky slope stability analysis based on unmanned aerial vehicle photogrammetry," *Environmental Earth Sciences*, vol. 78, no. 8, pp. 260–275, 2019.
- [38] Y. Tu, X. Liu, Z. Zhong, and Y. Li, "New criteria for defining slope failure using the strength reduction method," *Engineering Geology*, vol. 212, pp. 63–71, 2016.
- [39] J. Song, Q. Fan, T. Feng, Z. Chen, J. Chen, and Y. Gao, "A multi-block sliding approach to calculate the permanent seismic displacement of slopes," *Engineering Geology*, vol. 255, pp. 48–58, 2019.
- [40] J. Wang, S.-C. Li, L.-P. Li, P. Lin, Z.-H. Xu, and C.-L. Gao, "Attribute recognition model for risk assessment of water inrush," *Bulletin of Engineering Geology and the Environment*, vol. 78, no. 2, pp. 1057–1071, 2019.
- [41] G. Feng, Y. Kang, Z.-D. Sun, X.-C. Wang, and Y.-Q. Hu, "Effects of supercritical CO₂ adsorption on the mechanical characteristics and failure mechanisms of shale," *Energy*, vol. 173, pp. 870–882, 2019.
- [42] W. Sun, H. Du, F. Zhou, and J. Shao, "Experimental study of crack propagation of rock-like specimens containing conjugate fractures," *Geomechanics and Engineering*, vol. 17, no. 4, pp. 323–331, 2019.

Research Article

Freeze-Thaw Cycle Effect on Sputtering Rate of Water-Saturated Yellow Sandstone under Impact Loading

Yunbing Hu ¹, Tianzhu Duan ¹, Penghui Xian ¹ and Liang Chen ²

¹China Coal Technology and Engineering Group Chongqing Research Institute, Chongqing 400039, China

²State Key Laboratory for Geomechanics and Deep Underground Engineering of China University of Mining and Technology, Xuzhou, Jiangsu Province 221008, China

Correspondence should be addressed to Tianzhu Duan; duantianzhu@163.com

Received 22 June 2019; Revised 15 September 2019; Accepted 23 September 2019; Published 6 November 2019

Guest Editor: Tae-Hyung Kim

Copyright © 2019 Yunbing Hu et al. This is an open access article distributed under the Creative Commons Attribution License, which permits unrestricted use, distribution, and reproduction in any medium, provided the original work is properly cited.

In order to explore the impact of freeze-thaw temperature on the sputtering rate of water-saturated yellow sandstone under impact loading, in this paper, the Hopkinson pressure bar is used to conduct impact loading test on the water-saturated yellow sandstone at the same strain rate (74.22 s^{-1}) under five different freeze-thaw temperatures. After impact loading, the yellow sandstone fragments are graded and screened by using the sizing screen, and the mass of fragments with different particle sizes after screening is counted. By transforming the fragments into spheres with the corresponding particle sizes, and combining the dissipated energy, the surface specific energy of yellow sandstone with different freeze-thaw temperatures is calculated. Finally, the sputtering rate of the fragments is obtained by using the relationship of total work, dissipated energy, and kinetic energy. The main conclusions are as follows: The freeze-thaw temperature has a significant effect on the fracture degree of yellow sandstone. The lower the freeze-thaw temperature is, the higher the fracture degree of yellow sandstone is, and the smaller the particle size distribution of fragments is. The fractal dimension of yellow sandstone increases with the decrease of freeze-thaw temperature, indicating that the damage of yellow sandstone is more serious. The dissipative energy of yellow sandstone increases with the decrease of freezing temperature, while the kinetic energy increases gradually when the freeze-thaw temperature is -30°C to -15°C and decreases gradually when the freeze-thaw temperature is -15°C to -5°C . The surface area and surface specific energy of yellow sandstone fragments both increase with the increase of freeze-thaw temperature. And the sputtering rate of yellow sandstone fragments increases gradually at freezing temperature from -30°C to -15°C and decreases gradually at -15°C to -5°C . Therefore, from the perspective of dynamic destruction process, the sputtering of yellow sandstone fragments at freezing temperatures of -15°C , -20°C , and -30°C is more intense than that at -5°C and -10°C . The results can provide some guidance for production in winter and winter regions.

1. Introduction

In the frost area, the seasons change obviously, and the rainfall or groundwater is abundant, so the temperature difference between day and night in this area is too large, which will easily lead to the phenomenon of freezing and thawing of water-saturated rocks [1, 2]. The process of freezing and thawing affects the stability of water-saturated rocks [3]. However, in the process of coal open-pit mining and tunnel tunneling, in addition to freezing-thawing phenomenon, it is often accompanied by the impact load on rocks. Under the impact load, the energy inside the rocks

accumulates and releases rapidly for a short time [4, 5], resulting in rock fragments sputtering around. Therefore, it is of great significance to take freeze-thaw temperature as a prominent factor to study the impact load and freeze-thaw cycle on the sputtering rate of water-saturated yellow sandstone.

As a brittle material with disordered internal pores, rock has a significant impact on rock crack evolution under freeze-thaw conditions [6–10]. When the water-saturated rock is under freeze-thaw conditions, the water connects microcracks and generates expansion [11] in the rock, which aggravates the development of these cracks. The

development of these cracks is mainly manifested in the following aspects: on the one hand, the size of these cracks is further increased [12]; on the other hand, the crack tip continues to extend; meanwhile, in the local cracks, adjacent cracks close due to expansion of ice, while the size of cracks without water filling shrinks [13]. In addition, freezing and thawing will also have an impact on the water polymer. When the temperature drops, some water polymer particles inside the rock shrink, leading to local collapse, which affects the overall internal structure of the rock to a certain extent [14]. Due to the change of pore structure inside the rock, the physical and mechanical parameters of the rock change, such as compressive strength [15–17], tensile strength [18], damage [19], acoustic emission [20–22], pore structure [23], and resistivity [24, 25]. Ince et al. [26] collected 10 volcanic clastic rock samples from Cappadocia for test. Water-saturated rock was frozen in 12 hours at $-18 \pm 2.5^\circ\text{C}$ and then thawed for 12 hours at $32 \pm 2.5^\circ\text{C}$, so after 30 times, the compressive strength, P wave velocity, dry density, point load strength index, and coefficient of durability test of samples after the freeze-thaw cycle were measured. So the multiple linear regression equations of the above parameters are obtained, and the equations can well predict the impact of the freeze-thaw cycle on rock compressive strength in other areas. Zhou et al. [27] conducted large-scale triaxial tests on roadbed gravel soil samples after the freeze-thaw cycle. And it is found that the elastic modulus and shear strength of soil-rock mixture decreased after the freeze-thaw cycle.

Moreover, with the introduction of some advanced equipment, such as Hopkinson pressure bar test system, the high-speed camera, and other advanced equipment, a large number of scholars used Hopkinson pressure bar test system to carry out the impact load test on rocks treated by freeze-thaw cycle. It is found that freeze-thaw cycle has an important influence on physical and mechanical parameters and energy dissipation of water-saturated rocks under high strain rate [28–33]. This influence is mainly reflected in the different internal structures of water-saturated rocks treated with different freeze-thaw cycle temperatures under high strain rate, leading to differences in energy transformation within the rocks. Wang et al. [34–36] studied the effects of impact loading and freeze-thaw cycle (freeze-thaw temperature ranges from -20°C to 20°C , with cycles of 0, 5, 10, 15, and 25 times, respectively) on the damage of red sandstone. It is found that the peak strength and elastic modulus of red sandstone after freeze-thaw decrease with the increase of cycle times when the strain rates are different. But the damage, which is defined by total power and dissipated energy, increases with the increase of cycle times. Ke et al. [37, 38] conducted NMR tests on rocks after freeze-thaw cycle (freeze-thaw temperature ranges from -20°C to 20°C , with cycles of 0, 20, 60, 100, and 140 times, respectively) and did dynamic experiments on rocks under strain rate (75 s^{-1}) using the SHPB system. It is found that, with the increase of freeze-thaw cycle, the porosity of sandstone increases, the evolution of pore size tends to be uniform, the dynamic peak stress decreases, and the energy absorption increases. Therefore, this series of research results

shows that freeze-thaw has an important influence on the evolution law of physical and mechanical parameters of water-saturated rocks, and the change of physical and mechanical parameters will eventually affect the absorption and transformation of internal energy of rocks under external loads.

At present, some scholars mainly focus on the impact of freeze-thaw on physical and mechanical properties and energy dissipation of rocks by changing the internal structure of rocks and rarely study the change law of rock fragments sputtering rate under the impact load [39], especially taking the freeze-thaw cycle into a prominent factor. Therefore, in this paper, the freeze-thaw cycles of the water-saturated yellow sandstone were performed for 8 times at -5°C , -10°C , -15°C , -20°C , and -30°C , respectively. Then, impact tests were carried out on the yellow sandstone samples after freeze-thaw cycles. The impact of freeze-thaw cycles on the sputtering rate of fragments was studied by using the relationship between fragments and energy. And the results can be used to guide the sputtering rate of rock burst in seasonal frost zone.

2. Test Equipment and Methods

2.1. Preparation of Freeze-Thaw Samples

2.1.1. The Production Process of Original Sample. In this paper, the sample was selected from a mine in Inner Mongolia. After drilling, cutting, and polishing, the original sample was finally made into a cylinder of $25 \times 50\text{ mm}$ (height \times diameter). According to the test requirements, the nonparallelism at both ends of the cylinder is less than 0.5%, and the flatness of the end face is ensured. The final samples are shown in Figure 1.

2.1.2. Water Saturation of Yellow Sandstone Samples. The prepared original sample was placed in the electric thermostatic drying box DHG9076 and dried at 105°C for 24 hours. The quality of yellow sandstone samples before and after drying was recorded for several times until the quality difference was less than 0.01 g, which means that the yellow sandstone has been dried off at this time.

Then, the dried samples were placed in a sealed tank and pumped with water and air for 24 hours at a vacuum pressure of -0.09 MPa , until there was no bubble overflow on the surface of the samples, and then, the pressure of the sealed tank was adjusted to the standard atmosphere. When the mass change of the sample is less than 0.01 g, it is considered that the sample has been saturated at this time. The saturation rate of the sample obtained by forced saturation treatment with vacuum extraction method is 5.71%. All the saturated patterns were divided into five groups, three in each group.

2.1.3. Freeze-Thaw Process of Yellow Sandstone Samples. The samples after water saturation were placed in the freezer and thermostat for freeze-thaw cycle treatment [40, 41]. In the freezer, the water-saturated samples experienced two



FIGURE 1: Yellow sandstone samples.

hours of temperature changing, falling from 25°C to -5°C, -10°C, -15°C, -20°C, and -30°C, respectively. When the sample reaches the set temperature, it is kept in a freezer for six hours and then placed in a thermostat of 25°C for two hours. This process is repeated for 7 times, and the total number of freeze-thaw cycles is 8 times. The temperature change process is shown in Figure 2.

The standard model of saturated yellow sandstone after freeze-thaw cycle was subjected to uniaxial compression test. The physical parameters of saturated yellow sandstone after freeze-thaw cycle were obtained as shown in Table 1.

2.2. Test Equipment and Methods. This impact load test equipment is carried out by Hopkinson pressure bar system, as shown in Figure 3. The experimental system includes dynamic loading system, pressure bar system, energy absorption system, and signal acquisition and processing system. During the test, the bullet strikes the incident bar, and the velocity of the impact bar is measured by the speedometer. The incident and reflected wave signals are collected by the strain gauge on the incident bar, and the transmitted wave signals are collected by the strain gauge on the transmission bar.

Figure 4 shows the SHPB impact test system. In order to observe the dynamic damage process of yellow sandstone, high-speed camera was used.

Test process: firstly, a certain amount of Vaseline is daubed on both ends of the sample, and it is fixed in the middle of the incidence bar and transmission bar. Next, the control valve and high-speed camera are opened, and when the set pressure is reached in the launching chamber, the bullet is driven by gas to hit the incident bar to complete the impact test. During the test, the velocity of the impact bar was obtained by the speedometer, the data of incident wave, reflected wave, and transmitted wave were collected by the strain gauge on the incident bar and transmission bar, and the whole process of sample destruction was captured by the high-speed camera. The typical incident, reflected, and transmitted waves obtained in this experiment are shown in Figure 5.

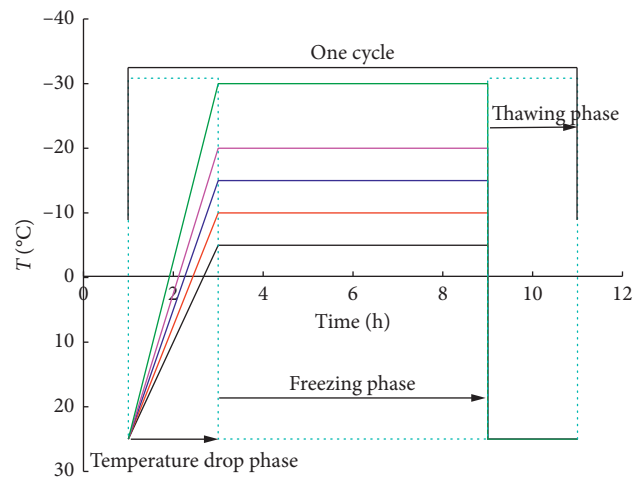


FIGURE 2: Temperature-time curve of freeze-thaw cycle.

3. Effect of Freeze-Thaw Temperature on Macroscopic Properties of Yellow Sandstone

3.1. Effect of Freeze-Thaw Temperature on Stress-Strain Curve of Yellow Sandstone. Figure 6 shows the stress-strain curve of yellow sandstone at different temperatures. It can be seen that the stress-strain curve of yellow sandstone at different temperatures has a certain temperature effect, which is mainly reflected in the following:

- (1) The mechanical properties of yellow sandstone have obvious temperature effect with the change of temperature. For the stress-strain curve, the slope of linear elastic rising stage and the postpeak descending stage decreases gradually.
- (2) Different freezing-thawing temperatures have significant effects on peak strength, peak strain, and dynamic elastic modulus of water-saturated yellow sandstone.

From the above stress-strain curve, it can be seen that the mechanical properties are significantly affected by

TABLE 1: Physicomechanical parameters of sandstone under different freeze-thaw temperatures.

Freezing and thawing temperature T (°C)	Number	σ_s (MPa)		ε_s (10^{-3})		E_s (GPa)	
		Single sample	Average value	Single sample	Average value	Single sample	Average value
25	T0-1	34.56		13.25		4.61	
	T0-2	34.18	34.82	13.52	13.62	4.41	4.43
	T0-3	35.72		14.09		4.27	
-5	T1-1	30.78		13.68		4.15	
	T1-2	29.39	30.57	14.47	14.29	4.23	4.28
	T1-3	31.54		14.73		4.47	
-10	T2-1	29.38		15.34		3.81	
	T2-2	30.82	30.29	15.12	15.26	4.04	3.99
	T2-3	30.67		15.31		4.12	
-15	T3-1	27.54		15.52		3.44	
	T3-2	29.19	28.57	15.87	15.51	3.15	3.35
	T3-3	28.98		15.13		3.45	
-20	T4-1	25.41		17.54		3.35	
	T4-2	26.09	26.43	17.07	17.34	2.95	3.06
	T4-3	27.79		17.41		2.87	
-30	T5-1	25.41		18.86		2.72	
	T5-2	23.66	24.39	19.00	18.71	2.58	2.80
	T5-3	24.09		18.26		3.10	

Note: σ_s is the uniaxial compressive strength, ε_s is the peak strain, and E_s is the elastic modulus.

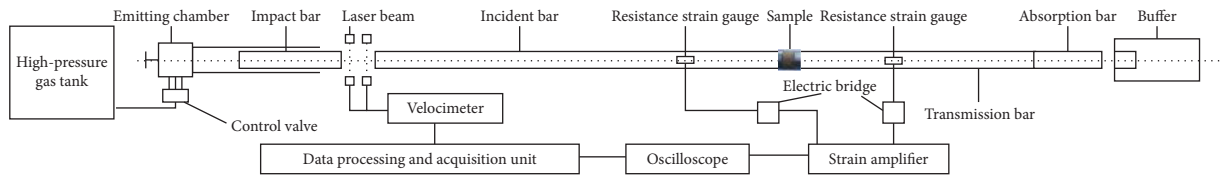


FIGURE 3: Hopkinson pressure bar system.



FIGURE 4: Hopkinson impact apparatus.

temperature. This is because the lower the freeze-thaw temperature is, the more obvious the development and expansion of internal cracks in the sample will be, which will lead to the reduction of the internal integrity of the sample. Finally, the physical properties of the sample will change under the impact load.

3.2. Particle Size Distribution of Yellow Sandstone Fragments at Freeze-Thaw Temperature. Particle size distribution is the macroscopic manifestation of rock damage [40]. The analysis of particle size distribution can directly reflect the impact of freeze-thaw temperature on the damage degree of sandstone. In order to describe the particle size distribution

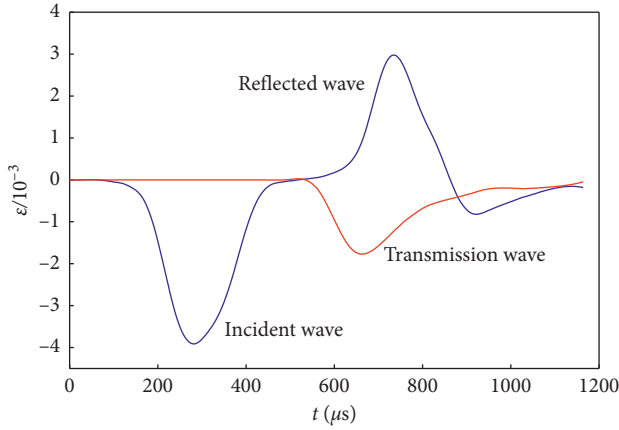


FIGURE 5: The shock signal of SHPB test.

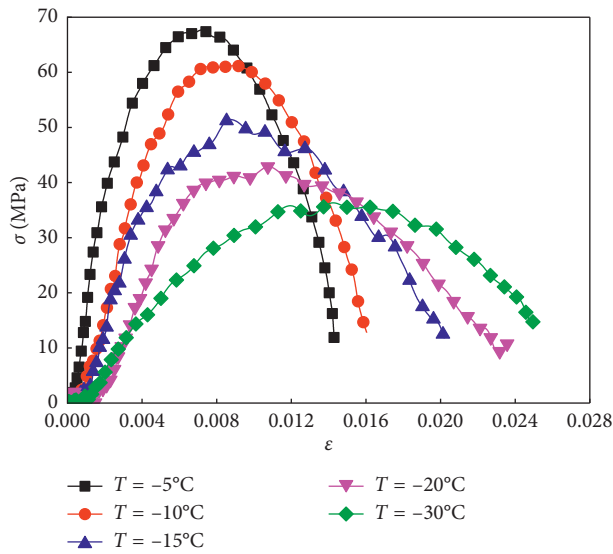


FIGURE 6: Stress-strain curves of yellow sandstone at different temperatures.

rule of sandstone scientifically, the fragmentation degree of sandstone fragments at different temperatures is screened by using a grading sieve. Since the smallest size of the pieces is 0 mm, the largest size of the original pattern is 50 mm, so this place is classified as 0–1 mm, 1–2.5 mm, 2.5–4 mm, 4–6 mm, 6–8.5 mm, 8.5–11 mm, 11–13 mm, 13–15 mm, and 15–50.0 mm. After screening, electronic scales with high sensitivity are used to weigh each level of fragments and record the test data. Therefore, the fraction of the mass of fragments in the whole mass in the range of particle size η_{li} is calculated by the following equation [42]:

$$\eta_{li} = \frac{m_{li}}{M}, \quad (1)$$

where η_{li} is the mass occupied by fragments with this particle size, m_{li} is the mass of fragments with this particle size, and M is the total mass of samples.

Secondly, the percentage between the mass of fragments at all levels m_{li} and the initial total mass of samples m_d after screening is defined as the percentage of fragments η_{li} ; then, the average particle size of fragments in each grading group

d_{li} is multiplied by the mass percentage of fragments under this particle size η_{li} to obtain the size percentage of the group in all particle sizes δ . At last, the percentage of particle size of fragments at all levels of the sample was accumulated to obtain the average particle size of the fragments. The relevant calculation expressions were as follows:

$$\delta = \sum_{i=1}^9 \delta_{li} = \sum_{i=1}^9 \eta_{li} d_{li}, \quad (2)$$

where i is the number of grading sieve level, $i = 1, 2, 3, \dots, 9$, and d_{li} is the average particle size of the fragments in each level, which is calculated by taking the average mesh size of the two levels before and after the grading sieve.

Figure 7 shows the particle size distribution of yellow sandstone under different freeze-thaw temperatures. It can be seen that, with the decrease of freeze-thaw temperature, the proportion of fragments with large particle size (15–50 mm) of yellow sandstone decreases, while that with small particle size increases. However, the overall average particle size shows a nearly linear downward trend.

4. Influence of Freeze-Thaw Temperature on Energy Distribution of Yellow Sandstone

4.1. Calculation Method of Dissipated Energy and Total Absorption Energy of Yellow Sandstone. Yellow sandstone is a typical physical change in the process of impact load, which is a process of transforming mechanical energy into internal energy [42–45]. However, the ultimate damage of yellow sandstone is a state instability phenomenon after internal energy accumulation reaches its limit driven by external energy [42]. Therefore, the energy carried by the stress wave can be calculated by the following equation [42, 44, 45]:

$$W = \frac{AC}{E} \int_0^t \sigma^2(t) dt = ACE \int_0^t \varepsilon^2(t) dt, \quad (3)$$

where A is the cross-sectional area of the incident bar and the transmission bar, which is 1963.49 mm²; E is the elastic modulus of the input bar and the transmission bar, which is 210 GPa; and C is the one-dimensional stress wave velocity. Since both the incident bar and the transmission bar are rigid bodies, C is related to the density and elastic modulus E of the incident bar. The relationship between them can be expressed in the following equation [42, 44, 45]:

$$C = \sqrt{\frac{E}{\rho}}. \quad (4)$$

According to equations (3) and (4), the incident energy W_I , reflected energy W_R , and transmitted energy W_T in the dynamic impact process of SHPB can be expressed as [42, 44, 45]

$$\begin{cases} W_I = ACE \int_0^t \varepsilon_i^2(t) dt, \\ W_R = ACE \int_0^t \varepsilon_r^2(t) dt, \\ W_T = ACE \int_0^t \varepsilon_t^2(t) dt, \end{cases} \quad (5)$$

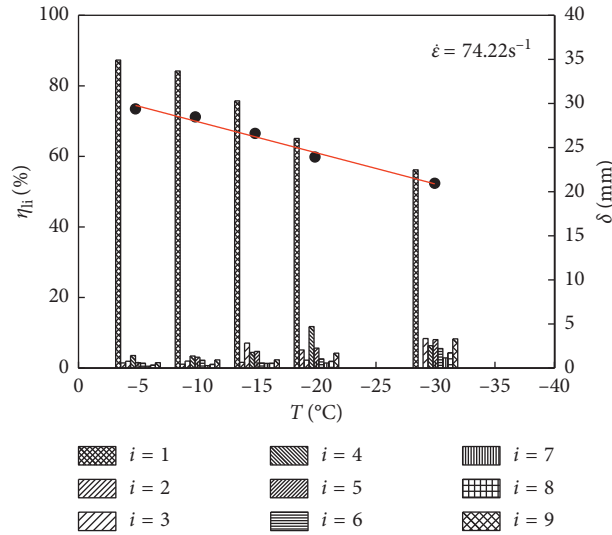


FIGURE 7: Distribution of yellow sandstone fragments at different freeze-thaw temperatures.

where W_I , W_R and W_T are incident energy, reflected energy, and transmitted energy, respectively, $\varepsilon_i(t)$ represents the strain under the action of the incident stress wave, $\varepsilon_r(t)$ represents the strain under the action of the reflected stress wave, and $\varepsilon_t(t)$ represents the strain under the action of the transmitted stress wave.

Based on the relationship between incident energy, reflected energy, and transmitted energy, the dissipated energy of sandstone under impact failure W_L can be finally obtained, as shown in the following equation [42, 44, 45]:

$$W_L = W_I - W_R - W_T. \quad (6)$$

In the process of studying the total absorption energy of yellow sandstone, the work done by external forces causes the deformation of yellow sandstone, so the area enclosed by the stress-strain curve and the X-axis is the total absorption energy U [44, 46], as shown in the following equation:

$$U = \int \sigma d\varepsilon. \quad (7)$$

4.2. Influence of Freeze-Thaw Temperature on Each Energy Variation of Sandstone. For brittle rocks, the effect of external impact is an input process of external energy to rocks [39]. When the rock is subjected to external mechanical energy, the absorption energy is converted to the internal energy of the rock, and when the energy accumulates more than the energy storage limits, the rock fractures, and the absorbed energy will transform into damage energy, plasticity energy, kinetic energy, heat and friction heat energy, radiant energy, and other forms of energy [43]. The research results show that the damage energy and kinetic energy account for 95% of all energies [45], so it is approximately believed that the total absorption energy of yellow sandstone under impact is converted into damage energy and kinetic energy [45, 46], and their relationship is shown in the following equation:

$$U = W_L + U_e. \quad (8)$$

Figure 8 shows the relationship between energy and freeze-thaw temperature in yellow sandstone. It can be seen that, under the same strain rate and different freeze-thaw temperatures, the total absorption energy of yellow sandstone changes little, about 34 J. With the increase of freeze-thaw temperature, the dissipation energy was 20.19 J at -30°C and was 27.81 J at -5°C . And the former increases by 37.74%. However, the kinetic energy first increases and then decreases with the increase of freeze-thaw temperature. It was the maximum of 12.49 J at -15°C and was the minimum of 6.39 J at -5°C .

It can be seen from the changing relationship between the energy of the water-saturated yellow sandstone and the freeze-thaw temperature, water fills the cracks in the internal communication of the yellow sandstone. When the temperature drops rapidly, the water changes from liquid state to solid state, making the volume larger. Due to the time required for temperature transfer, the water on the outer surface of the yellow sandstone first condenses into solid ice when the temperature drops rapidly. And at this time, the internal cracks of the yellow sandstone are in a closed state. As the temperature continues to drop, the water from the outside to the inside changes from liquid to solid, which causes the volume of water to increase gradually. As the yellow sandstone is in a state of saturation, the water has filled all the connected pores and cracks in the interior of rocks, and the increase in the volume of water exerts an expansive force on the internal pores and cracks, causing the crack tips to be tensed apart from each other, or the bonding force of adjacent interfaces to be weakened [47]. When the temperature rises and the water is dissolved, the water flows from the original crack to the newly sprouted crack and redistributes in the yellow sandstone. And then the ice continues to exert an expansive force on the crack tip when refrozen. Therefore, when the temperature is lower, the temperature drops more rapidly within the same time, and

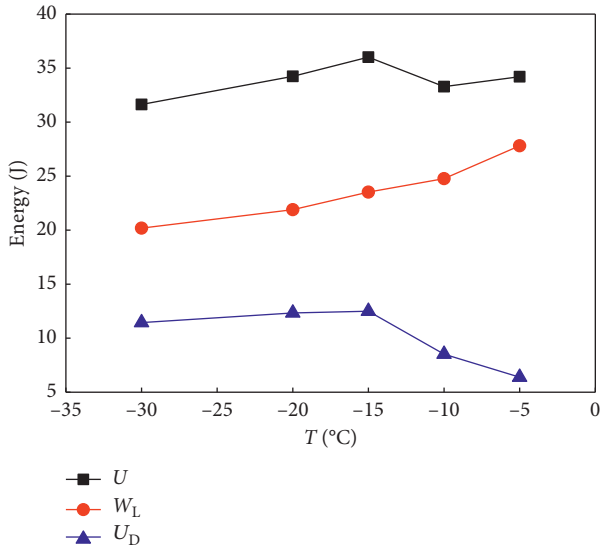


FIGURE 8: The relationship between each energy and freeze-thaw temperature in yellow sandstone.

the expansion force effect on crack growth and adhesion reduction is more obvious [48].

Due to the influence of freeze-thaw temperature, the ratio of total energy transforming into dissipated energy and kinetic energy depends on the physical and mechanical properties and the loading mode of yellow sandstone when it is subjected to impact load. At the same strain rate, as the temperature decreases, the cohesive force inside the yellow sandstone decreases, and the energy required to form the same crack area is less, thus the dissipated energy is smaller.

Meanwhile, in the process of dynamic impact compression, the transformation of internal energy of yellow sandstone leads to a dynamic process from deformation to damage sputtering of yellow sandstone [39, 43], which is characterized by the transformation and balance of total energy, dissipated energy, and kinetic energy. For a specific freeze-thaw temperature, there is a specific energy state corresponding to it.

5. Influence of Freeze-Thaw Temperature on Sputtering Rate of Sandstone

5.1. Influence of Freeze-Thaw Temperature on Sandstone Surface Energy. For sandstone, a brittle material, the dissipated energy is mainly in the form of surface energy that separates fragments from each other [43]. In order to further explore the influence of freeze-thaw temperature on yellow sandstone, fragments with different particle sizes are simplified into spheres of corresponding sizes, as shown in Figure 9 [42, 43].

The number of spheres within the diameter range of screening is calculated according to the following equation [42, 43]:

$$n_i = \frac{m_{li}}{4\rho r_i^3 \pi/3}, \quad (9)$$

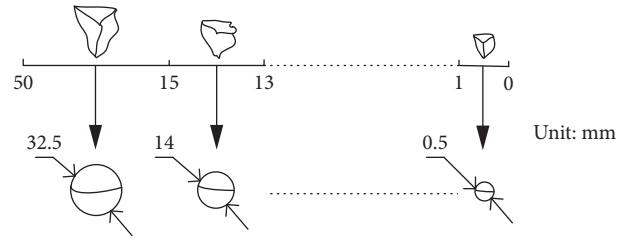


FIGURE 9: The schematic diagram of the fragments transformed into a sphere [40].

where n_i is the quantity of sphere with dimension i ; m_i is the mass of sphere with dimension i ; ρ is the density of yellow sandstone, as 2395 Kg/m^{-3} ; and r_i is the sphere radius transformed with dimension i .

Formula (9) can be used to obtain the number of spheres with different particle sizes, so that the surface area of fragments can be further calculated (10). By subtracting the upper and lower surface area and side area of the cylinder when it is not damaged from the surface area of all fragments, the internal damage area can be obtained, as shown in the following equation [42, 43]:

$$S = \sum_{i=1}^9 4n_i \pi r_i^2 - 2\pi r h - 2\pi r^2, \quad (10)$$

where r is the radius of sandstone sample in the impact test and h is the height of sandstone sample in the impact test.

When the yellow sandstone is done work by external force, the energy accumulated inside will work on the yellow sandstone, leading to the fragmentation of each other, and the sum of energy required by the separation of all fragments is damage energy. As a brittle material, the dissipated energy of the yellow sandstone can be regarded as the surface energy when the yellow sandstone is broken, so the relationship between surface energy and dissipated energy is as follows [42–44]:

$$W_L = S\gamma. \quad (11)$$

Since most dissipated energy acts on the separation of all fragments, the relationship between dissipated energy and the surface area of fragments can be used to obtain the surface specific energy of sandstone fragments at per unit area [42–44]:

$$\gamma = \frac{W_L}{S}. \quad (12)$$

Figure 10 shows the effect of freeze-thaw temperature on surface specific energy of sandstone. It can be seen from the figure that the broken surface area of yellow sandstone decreases gradually with the increase of freeze-thaw temperature. When the freeze-thaw temperature is -30°C , the broken surface area of yellow sandstone is 362.35 cm^2 . When the freeze-thaw temperature is -5°C , the broken surface area of yellow sandstone is 105.30 cm^2 , which decreases by 70.94% compared with that at -30°C . By fitting the surface area of yellow sandstone fragments with the freeze-thaw temperature, it is found that the surface area of yellow

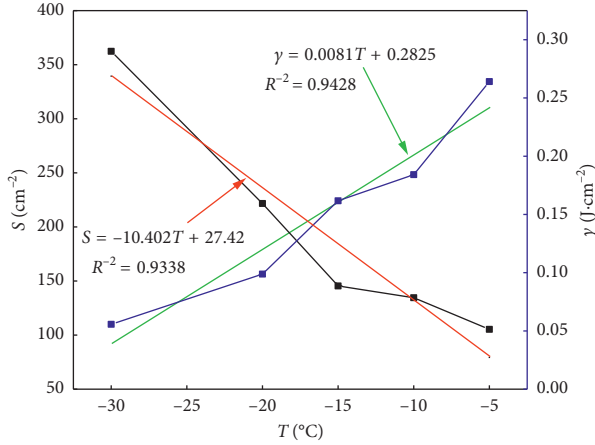


FIGURE 10: Effect of freeze-thaw cycle on surface energy of sandstone.

sandstone fragments decreases linearly with the increase of freeze-thaw temperature. However, the surface specific energy of yellow sandstone increases gradually with the increase of freeze-thaw temperature. When the freeze-thaw temperature is -30°C , the surface specific energy of yellow sandstone can be $0.056\text{ J}\cdot\text{cm}^{-2}$. When the freeze-thaw temperature is increased to -5°C , the surface specific energy of yellow sandstone can be increased to $0.264\text{ J}\cdot\text{cm}^{-2}$, which increases by 373.99% compared with that at -30°C . By fitting the surface specific energy of yellow sandstone with the freeze-thaw temperature, it is found that the surface specific energy of yellow sandstone decreases linearly with the increase of freeze-thaw temperature.

The lower the freezing-thawing temperature is, the faster the water condenses, which leads to the reduction of the cohesive force within the yellow sandstone. At the same strain rate, yellow sandstone with low freeze-thaw temperature requires a little energy to separate fragments from each other, which is consistent with the relationship between the freeze-thaw temperature and the average particle size of fragments.

5.2. Influence of Freeze-Thaw Cycle on Sputtering Rate of Yellow Sandstone. When the water-saturated yellow sandstone after freeze-thaw cycle is subjected to impact load, a part of the whole absorbed energy converts into dissipated energy to separate fragments from each other and the other part converts into kinetic energy of fragments. In order to study the influence of freeze-thaw temperature on the sputtering rate of fragments of yellow sandstone, assume that the kinetic energy ratio is K , so the total absorbed energy of yellow sandstone in the impact process is distributed as follows [43]:

$$\begin{cases} \sum_{i=1}^9 \frac{2}{3} \rho \pi r_i^3 v^2 = kU, \\ \left(\sum_{i=1}^9 4\pi n_i r_i^2 - 2\pi RH - 2\pi R^3 \right) \gamma = (1-K)U, \end{cases} \quad (13)$$

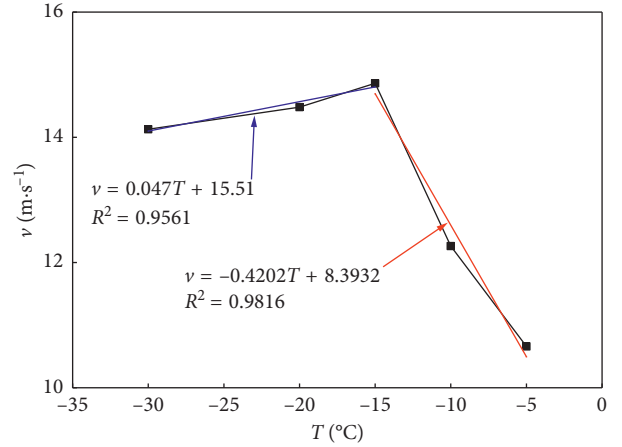


FIGURE 11: Relationship between the sputtering rate and temperature.

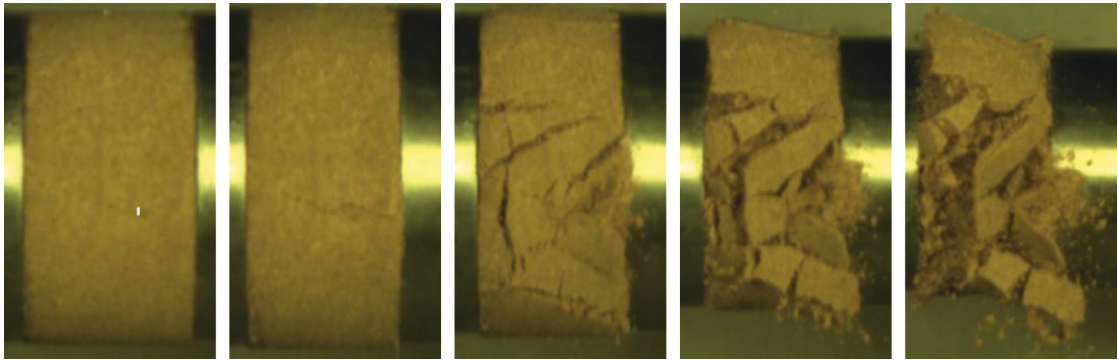
where v is the sputtering rate of the fragments and K is the proportion of kinetic energy in the total energy of yellow sandstone.

According to equation (13), the sputtering rate of yellow sandstone fragments after crushing under the impact load is v , and the final expression is shown in the following equation [43]:

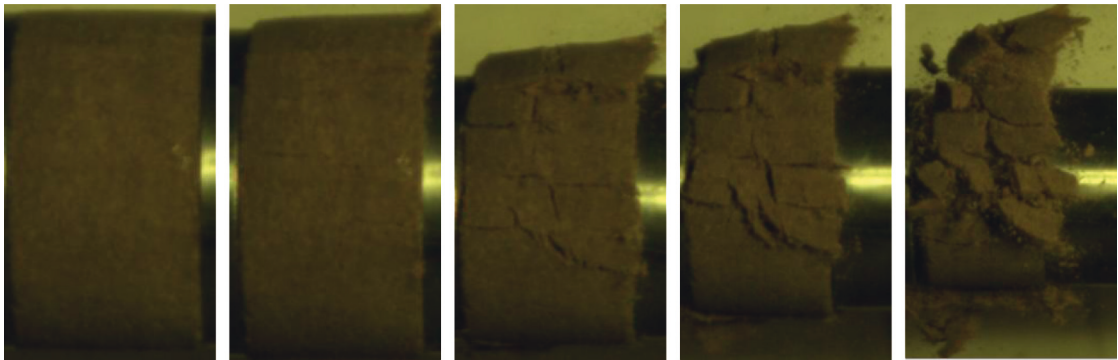
$$\left(v = \sqrt{\frac{k}{1-k} \frac{4\pi(3R^2H/4)^{2/3} \left(\sum_{i=1}^9 n_i \right)^{1/3} - 2\pi RH - 2\pi R^2}{1/2\rho\pi R^2 H}} \gamma \right) \quad (14)$$

According to equations [13] and [14] and the energy value of yellow sandstone calculated previously, the sputtering rate of yellow sandstone fragments under the impact load can be obtained. By combining the sputtering rate and freeze-thaw temperature, the variation rule between them can be obtained.

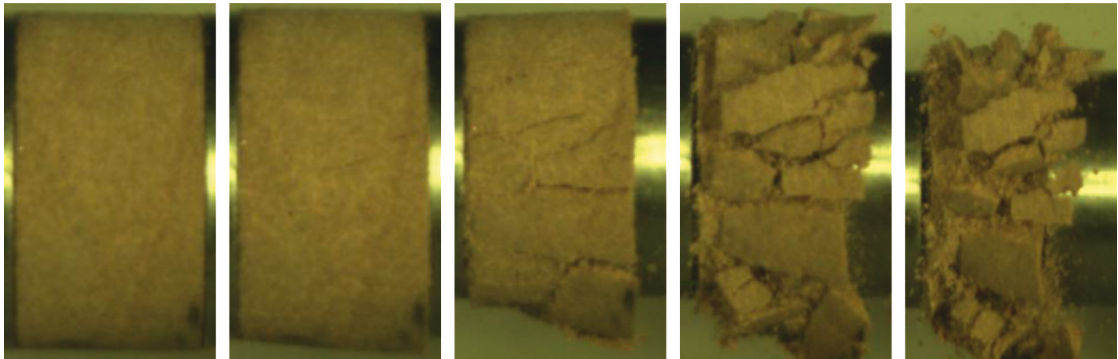
Figure 11 shows the relationship between the sputtering rate of yellow sandstone fragments and temperature. It can be seen from the figure that there are significant differences between the deceleration rate of yellow sandstone fragments and the freeze-thaw temperature. The main performance is that, when the freeze-thaw temperature ranges from -30°C to -15°C , the sputtering rate of yellow sandstone fragments gradually increases with the increase of freeze-thaw temperature. When the temperature is -30°C , the sputtering speed of yellow sandstone fragments is $14.13\text{ m}\cdot\text{s}^{-1}$. When the temperature is -15°C , the sputtering speed of yellow sandstone fragments is $14.86\text{ m}\cdot\text{s}^{-1}$, which increases by 5.20% compared with that at -30°C . However, when the freeze-thaw temperature ranges from -15°C to -5°C , the sputtering rate of yellow sandstone fragments gradually increases with the increase of freeze-thaw temperature. When the temperature is -5°C , the sputtering rate of yellow sandstone fragments is $14.13\text{ m}\cdot\text{s}^{-1}$, which increased by 28.27% compared with that at -15°C .



(a)



(b)



(c)



(d)

FIGURE 12: Continued.

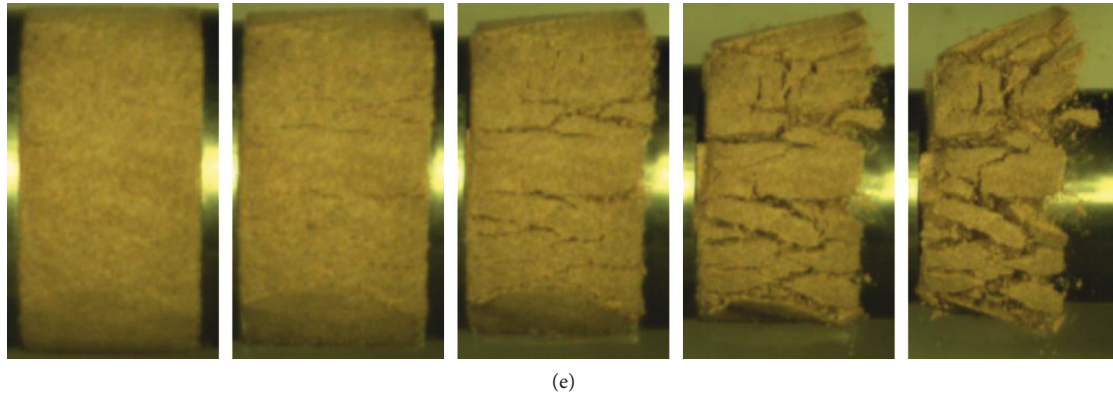


FIGURE 12: The macroscopic damage process of yellow sandstone under different freeze-thaw temperatures: (a) $T = -5^{\circ}\text{C}$, (b) $T = -10^{\circ}\text{C}$, (c) $T = -15^{\circ}\text{C}$, (d) $T = -20^{\circ}\text{C}$, and (e) $T = -30^{\circ}\text{C}$.

5.3. High-Speed Photography of Dynamic Failure Process of Yellow Sandstone under Different Freeze-Thaw Temperatures.

In order to observe the impact of freeze-thaw temperature on the whole fracture process of yellow sandstone more intuitively, high-speed camera is adopted to film the whole process of impact load on yellow sandstone with different freeze-thaw temperatures. The dynamic fracture process of yellow sandstone can be recorded by high-speed camera. So the initiation of cracks, cracking development, fragment separation, and fragmentation sputtering process of yellow sandstone can be observed from the deformation and failure of yellow sandstone in the whole process. And five typical state pictures are selected, which are, respectively, the first contact of the incident bar with the sample, the first visible crack of the sample surface, the complete distribution of the sample cracks, the separation of the sample fragments, and the sputtering of the separated fragments to the surrounding areas.

Figure 12 shows the macroscopic damage process of yellow sandstone under different freeze-thaw temperatures. From the dynamic failure process of yellow sandstone, we can get the following information: It can be seen that the deformation and failure process of yellow sandstone under impact at different freeze-thaw temperatures are roughly the same, which all go through stages of compaction, crack generation, crack growth, fragment separation, and fragmentation sputtering. But the stages are different. When the freeze-thaw temperature is lower, the crack density of yellow sandstone is higher and the final fracture is more severe, which is consistent with the previous particle size distribution. The effect of freezing and thawing temperature on the sputtering rate of the saturated yellow sandstone is mainly reflected in the fact that the fragments are separated from each other and sputtered in the direction of rod motion. The higher the sputtering rate, the greater the distance from the center of mass of the fragments and the smaller the distance from the system axis. According to the final sputtering results, the freezing and thawing temperatures of -15°C , -10°C , and -5°C are more severe than those of -20°C and -30°C , and the freezing and thawing temperature is -15°C . The fragmentation at $^{\circ}\text{C}$ is the most severe,

which is consistent with the sputtering rate of the yellow sandstone fragments at different temperatures.

6. Conclusions

In this paper, firstly, Hopkinson pressure bar is used to conduct dynamic impact on the water-saturated yellow sandstone treated with five different freeze-thaw temperatures under the same strain rate. Secondly, the yellow sandstone fragments after impact are screened by a grading sieve, and the mass of fragments with different particle sizes after screening is counted. Then, fragments with different particle sizes are transformed into spheres with corresponding particle sizes. So the surface specific energy of yellow sandstone at different freeze-thaw temperatures can be obtained by combining dissipative energy. Finally, the sputtering rate of the fragments is obtained by using the relationship of total energy, dissipated energy, and kinetic energy. The main conclusions are as follows:

- (1) The elastic modulus and peak stress decrease with the decrease of freeze-thaw temperature, while the peak strain and unloading elastic modulus decrease with the freeze-thaw temperature, indicating the mechanical properties of freeze-thaw temperature on saturated yellow sandstone. The impact is significant, and the freeze-thaw temperature changes to some extent change the internal structure of the yellow sandstone, reducing its crucible bearing capacity and resistance to deformation. The freeze-thaw temperature has a significant effect on the damage of the yellow sandstone. The lower the freezing temperature, the more obvious the damage of the yellow sandstone. The smaller the particle size distribution of the fragments, the lower the freeze-thaw temperature, the weaker the interface adhesion of the yellow sandstone, the same strain. At the rate, the lower the freeze-thaw temperature is, the more severe the yellow sandstone is destroyed, and the internal damage is more serious.
- (2) The dissipated energy of yellow sandstone increases with the decrease of freezing temperature. The relationship

between dissipative energy and freeze-thaw temperature indicates that more cracks are formed inside the yellow sandstone. The generation of these cracks consumes more energy. The kinetic energy gradually increases at a freeze-thaw temperature of -30°C to -15°C and gradually decreases at -15°C to -5°C . The variation of kinetic energy with freeze-thaw temperature shows that the distribution of internal energy of the yellow sandstone is different for the same loading rate.

- (3) The surface area of the yellow sandstone fragments increases with the increase of the freezing and thawing temperature, the surface specific energy decreases with the decrease of the freezing temperature, and the surface specific energy decreases with the temperature, indicating that the saturated yellow sandstone is different. At freezing and thawing temperature, the bond strength per unit area is gradually weakened. Under the impact load with the same strain rate, the yellow sandstone with weaker interface force is more likely to break up to form more fragments, thus showing freezing and thawing. The lower the temperature, the larger the surface area of the fragments.
- (4) The freezing and thawing temperature is -5°C , -10°C , -15°C , -20°C , -30°C . The sputtering conditions of -15°C , -10°C , and -5°C compared with -20°C and -30°C are more severe, and the freezing and melting temperature of -15°C is the most severe, indicating that the freezing and thawing temperature is lowered. The sputtering conditions of -15°C , -10°C and -5°C compared with -20°C and -30°C are more severe, and the freezing and melting temperature of -15°C is the most severe, indicating that the freezing and thawing temperature is lowered. The surface specific energy of the saturated yellow sandstone changes its energy distribution ratio. Therefore, under the impact load with the same strain rate, the freezing rate of the freeze-thaw temperature is -15°C .

Data Availability

The data used to support the findings of this study are available from the corresponding author upon request.

Conflicts of Interest

The authors declare that they have no conflicts of interest.

Acknowledgments

The authors gratefully acknowledge the financial support of this study provided by the "National Science and Technology Major Project (2016ZX05045002-003)."

References

- [1] M. A. Coombes, H. A. Viles, and H. Zhang, "Thermal blanketing by ivy (*Hedera helix* L.) can protect building stone from damaging frosts," *Scientific Reports*, vol. 8, no. 1, p. 9834, 2018.
- [2] T. C. Hales and J. J. Roering, "Climatic controls on frost cracking and implications for the evolution of bedrock landscapes," *Journal of Geophysical Research: Earth Surface*, vol. 112, no. F2, 2007.
- [3] N. A. Beier and D. C. Segó, "Cyclic freeze-thaw to enhance the stability of coal tailings," *Cold Regions Science and Technology*, vol. 55, no. 3, pp. 278–285, 2009.
- [4] H. P. Xie, Y. Ju, and L. Y. Li, "Criteria for strength and structural failure of rocks based on energy dissipation and energy release principles," *Chinese Journal of Rock Mechanics and Engineering*, vol. 24, no. 17, pp. 3003–3010, 2005.
- [5] H. P. Xie, Y. Ju, L. Y. Li et al., "Energy mechanism of deformation and failure of rock masses," *Chinese Journal of Rock Mechanics and Engineering*, vol. 27, no. 9, pp. 1729–1739, 2008.
- [6] N. West, E. Kirby, A. A. Nyblade, and S. L. Brantley, "Climate preconditions the Critical Zone: elucidating the role of subsurface fractures in the evolution of asymmetric topography," *Earth and Planetary Science Letters*, vol. 513, pp. 197–205, 2019.
- [7] M.-C. Eppes and R. Keanini, "Mechanical weathering and rock erosion by climate-dependent subcritical cracking," *Reviews of Geophysics*, vol. 55, no. 2, pp. 470–508, 2017.
- [8] P. Viklander, "Laboratory study of stone heave in till exposed to freezing and thawing," *Cold Regions Science and Technology*, vol. 27, no. 2, pp. 141–152, 1998.
- [9] R. S. Anderson, S. P. Anderson, and G. E. Tucker, "Rock damage and regolith transport by frost: an example of climate modulation of the geomorphology of the critical zone," *Earth Surface Processes and Landforms*, vol. 38, no. 3, pp. 299–316, 2013.
- [10] J. Kruschwitz and J. Bluhm, "Modeling of ice formation in porous solids with regard to the description of frost damage," *Computational Materials Science*, vol. 32, no. 3-4, pp. 407–417, 2005.
- [11] J. R. Blachere and J. E. Young, "Failure of capillary theory of frost damage as applied to ceramics," *Journal of the American Ceramic Society*, vol. 57, no. 5, pp. 212–216, 1974.
- [12] M. Fener and İ. Ince, "Effects of the freeze-thaw (F-T) cycle on the andesitic rocks (Sille-Konya/Turkey) used in construction building," *Journal of African Earth Sciences*, vol. 109, pp. 96–106, 2015.
- [13] D. H. Everett, "The thermodynamics of frost damage to porous solids," *Transactions of the Faraday Society*, vol. 57, pp. 1541–1551, 1961.
- [14] J. Park, C.-U. Hyun, and H.-D. Park, "Changes in microstructure and physical properties of rocks caused by artificial freeze-thaw action," *Bulletin of Engineering Geology and the Environment*, vol. 74, no. 2, pp. 555–565, 2015.
- [15] Y. Inada and K. Yokota, "Some studies of low temperature rock strength," *International Journal of Rock Mechanics and Mining Sciences & Geomechanics Abstracts*, vol. 21, no. 3, pp. 145–153, 1984.
- [16] F. Bayram, "Predicting mechanical strength loss of natural stones after freeze-thaw in cold regions," *Cold Regions Science and Technology*, vol. 83-84, pp. 98–102, 2012.
- [17] H. Deng, S. Yu, J. Deng et al., "Experimental investigation on energy mechanism of freezing-thawing treated sandstone under uniaxial static compression," *KSCE Journal of Civil Engineering*, vol. 23, no. 3, pp. 1–9, 2019.
- [18] V. Penttala and F. Al-Neshawy, "Stress and strain state of concrete during freezing and thawing cycles," *Cement and Concrete Research*, vol. 32, no. 9, pp. 1407–1420, 2002.

- [19] M. Koniorczyk, D. Gawin, and B. A. Schrefler, "Modeling evolution of frost damage in fully saturated porous materials exposed to variable hygro-thermal conditions," *Computer Methods in Applied Mechanics and Engineering*, vol. 297, pp. 38–61, 2015.
- [20] D. Codeglia, N. Dixon, G. J. Fowmes, and G. Marcato, "Analysis of acoustic emission patterns for monitoring of rock slope deformation mechanisms," *Engineering Geology*, vol. 219, pp. 21–31, 2017.
- [21] J. B. Murton, O. Kuras, M. Krautblatter et al., "Monitoring rock freezing and thawing by novel geoelectrical and acoustic techniques," *Journal of Geophysical Research: Earth Surface*, vol. 121, no. 12, pp. 2309–2332, 2016.
- [22] L. Girard, S. Gruber, S. Weber, and J. Beutel, "Environmental controls of frost cracking revealed through in situ acoustic emission measurements in steep bedrock," *Geophysical Research Letters*, vol. 40, no. 9, pp. 1748–1753, 2013.
- [23] V. G. R. De Argandoña, A. R. Rey, C. Celorio, L. M. S. del Río, L. Calleja, and J. Llavona, "Characterization by computed X-ray tomography of the evolution of the pore structure of a dolomite rock during freeze-thaw cyclic tests," *Physics and Chemistry of the Earth, Part A: Solid Earth and Geodesy*, vol. 24, no. 7, pp. 633–637, 1999.
- [24] C. H. Sondergeld and C. S. Rai, "Velocity and resistivity changes during freeze-thaw cycles in Berea sandstone," *Geophysics*, vol. 72, no. 2, pp. E99–E105, 2007.
- [25] P. A. Duvillard, A. Revil, Y. Qi, A. Soueid Ahmed, A. Coperey, and L. Ravel, "Three-dimensional electrical conductivity and induced polarization tomography of a rock glacier," *Journal of Geophysical Research: Solid Earth*, vol. 123, no. 11, pp. 9528–9554, 2018.
- [26] I. Ince and M. Fener, "A prediction model for uniaxial compressive strength of deteriorated pyroclastic rocks due to freeze-thaw cycle," *Journal of African Earth Sciences*, vol. 120, pp. 134–140, 2016.
- [27] Z. Zhou, K. Xing, H. Yang, and H. Wang, "Damage mechanism of soil-rock mixture after freeze-thaw cycles," *Journal of Central South University*, vol. 26, no. 1, pp. 13–24, 2019.
- [28] C. M. Steelman, C. S. Kennedy, D. C. Capes, and B. L. Parker, "Electrical resistivity dynamics beneath a fractured sedimentary bedrock riverbed in response to temperature and groundwater-surface water exchange," *Hydrology and Earth System Sciences*, vol. 21, no. 6, pp. 3105–3123, 2017.
- [29] T. Yamabe and K. M. Neaupane, "Determination of some thermo-mechanical properties of Sirahama sandstone under subzero temperature condition," *International Journal of Rock Mechanics and Mining Sciences*, vol. 38, no. 7, pp. 1029–1034, 2001.
- [30] Q. Li, L. Chen, Z. Sui et al., "Dynamic analysis and criterion evaluation on rockburst considering the fractured dissipative energy," *Advances in Mechanical Engineering*, vol. 11, no. 3, article 1687814019825906, 2019.
- [31] J. Kodama, T. Goto, Y. Fujii, and P. Hagan, "The effects of water content, temperature and loading rate on strength and failure process of frozen rocks," *International Journal of Rock Mechanics and Mining Sciences*, vol. 62, pp. 1–13, 2013.
- [32] S. Demirdag, "Effects of freezing-thawing and thermal shock cycles on physical and mechanical properties of filled and unfilled travertines," *Construction and Building Materials*, vol. 47, pp. 1395–1401, 2013.
- [33] K.-P. Zhou, B. Li, J.-L. Li, H.-W. Deng, and F. Bin, "Microscopic damage and dynamic mechanical properties of rock under freeze-thaw environment," *Transactions of Nonferrous Metals Society of China*, vol. 25, no. 4, pp. 1254–1261, 2015.
- [34] P. Wang, J. Xu, S. Liu, S. Liu, and H. Wang, "A prediction model for the dynamic mechanical degradation of sedimentary rock after a long-term freeze-thaw weathering: considering the strain-rate effect," *Cold Regions Science and Technology*, vol. 131, pp. 16–23, 2016.
- [35] P. Wang, J. Xu, S. Liu, H. Wang, and S. Liu, "Static and dynamic mechanical properties of sedimentary rock after freeze-thaw or thermal shock weathering," *Engineering Geology*, vol. 210, pp. 148–157, 2016.
- [36] P. Wang, J. Xu, X. Fang, and P. Wang, "Energy dissipation and damage evolution analyses for the dynamic compression failure process of red-sandstone after freeze-thaw cycles," *Engineering Geology*, vol. 221, pp. 104–113, 2017.
- [37] B. Ke, K. Zhou, H. Deng et al., "NMR pore structure and dynamic characteristics of sandstone caused by ambient freeze-thaw action," *Shock and Vibration*, vol. 2017, Article ID 9728630, 10 pages, 2017.
- [38] B. Ke, K. Zhou, C. Xu, H. Deng, J. Li, and F. Bin, "Dynamic mechanical property deterioration model of sandstone caused by freeze-thaw weathering," *Rock Mechanics and Rock Engineering*, vol. 51, no. 9, pp. 2791–2804, 2018.
- [39] L. Y. Li, Y. Ju, Z. W. Zhao et al., "Energy analysis of rock structure under static and dynamic loading conditions," *Journal of China Coal Society*, vol. 34, no. 6, pp. 737–741, 2009.
- [40] C. Liu, H. Deng, H. Zhao, and J. Zhang, "Effects of freeze-thaw treatment on the dynamic tensile strength of granite using the Brazilian test," *Cold Regions Science and Technology*, vol. 155, pp. 327–332, 2018.
- [41] D. Ma, Q. Ma, and P. Yuan, "SHPB tests and dynamic constitutive model of artificial frozen sandy clay under confining pressure and temperature state," *Cold Regions Science and Technology*, vol. 136, pp. 37–43, 2017.
- [42] A. Lu, S. Hu, M. Li et al., "Impact of moisture content on the dynamic failure energy dissipation characteristics of sandstone," *Shock and Vibration*, vol. 2019, Article ID 6078342, 10 pages, 2019.
- [43] Z. Zhang and F. Gao, *Energy Evolution Mechanism during Rock Deformation and Failure*, China University of Mining and Technology, Beijing, China, 2013.
- [44] L. Y. Li, Z. J. Xu, H. P. Xie et al., "Failure experimental study on energy laws of rock under differential dynamic impact velocities," *Journal of China Coal Society*, vol. 36, no. 12, pp. 2007–2011, 2011.
- [45] L. Ming, *Research on Rupture Mechanisms of Coal Measures Sandstone under High Temperature and Impact Load*, China University of Mining and Technology, Xuzhou, China, 2014.
- [46] S. Hu, *Study on Mechanical Properties and Energy Response Characteristics of High-Porosity Concrete under Cyclic Loading and Unloading*, China University of Mining and Technology, Xuzhou, China, 2018.
- [47] O. Coussy and P. Monteiro, "Unsaturated poroelasticity for crystallization in pores," *Computers and Geotechnics*, vol. 34, no. 4, pp. 279–290, 2007.
- [48] M. J. Setzer, "Micro-ice-lens formation in porous solid," *Journal of Colloid and Interface Science*, vol. 243, no. 1, pp. 193–201, 2001.

Research Article

Laboratory Experiments on Breaching Characteristics of Natural Dams on Sloping Beds

Xiangang Jiang ^{1,2}

¹School of Civil Engineering, Sichuan Agricultural University, Dujiangyan 611830, China

²Sichuan Higher Education Engineering Research Center for Disaster Prevention and Mitigation of Village Construction, Sichuan Agricultural University, Dujiangyan 611830, China

Correspondence should be addressed to Xiangang Jiang; jxgjim@163.com

Received 23 July 2019; Revised 12 August 2019; Accepted 20 August 2019; Published 20 October 2019

Academic Editor: Chiara Bedon

Copyright © 2019 Xiangang Jiang. This is an open access article distributed under the Creative Commons Attribution License, which permits unrestricted use, distribution, and reproduction in any medium, provided the original work is properly cited.

Natural dams formed by landslides may produce disastrous floods after dam outburst. However, studies on the breaching characteristics of natural dams on sloping beds systematically are still at an early stage, and especially the relationship between breach width and depth is still unclear. In this paper, results of a series of laboratory tests that assessed seven different flume bed slope angles are presented. The results show that 3 stages of breaching process of natural dams on different bed slopes were observed. According to the results, headward erosion was the main force for enlargement of breach when bed slope was relatively small. With the increasing of bed slope, the effect of tractive erosion on longitudinal development of breach was enhanced. The discharge hydrographs were unimodal for all the bed slopes. The peak discharge increased first and then decreased with the increasing of bed slope. The elapsed time from the start of breach formation to the moment of peak discharge decreased with the increasing of bed slope. The difference between different bed slopes was larger when the bed slope was small or large, and the relationship between duration and bed slope had the same characteristics. With the increasing of bed slope, the ratio of breach width to breach depth rose to 1 and then decreased with the increasing of bed slope angle. A result of the present work is a function of the relationship between the breach width and depth for which it is possible to calculate them. This function is based on a shape parameter that linearly decreases with bed slope. The relationship between shape parameter and bed slope was developed to calculate the shape parameter with an additional relationship between shape parameter and mean diameter of particles. Combined with the experimental data and filed data of Tangjiashan natural dam, the shape parameter was calculated, and the function was validated.

1. Introduction

Excessive rainfall and earthquakes often cause landslide, which can fall into river channels and block the river. This is called a natural dam [1]. More than 50% of natural dams failed by overtopping, and 85% failed within 1 yr of formation [2]. Hazardous flooding may occur after failure of the dams. For example, in 1786, the natural dam in Dadu River failed and caused a severe flood, killing 100,000 people [3].

Many researchers investigated the field and selected data about the natural dam, such as dam height, dam width, dam volume, and so on. And then, dataset about natural dams were primarily established. For example, Eisbacher and

Clague, Pirocchi, and Casagli and Ermini investigated natural dams in Alpine mountains [4–6]; Costa and Schuster collected 460 natural dams' data worldwide [2]; Clague and Evans included landslide dams from the Canadian cordillera [7]; Chai et al. included 147 landslide dams from China [8]; Peng and Zhang collected 1239 landslide dam cases and developed a database [9]; and some famous landslide dams occurred recent years [10–14]. Data are derived from the cases inventoried by the authors and from cases collected from review work. These data mainly include the height, width, length, area, and volume of natural dams. With these data, some qualitative analysis could be carried out, such as the safety of natural dams could be evaluated with geomorphologic factors based on an analysis of 84 episodes of

selected natural dams worldwide [15]; and breaching parameters could be predicated with some field data [10, 16]. However, few breaching photographs, videos, and field data were recorded when natural dams failed by limited observation technology. In such way, the characteristics of breaching for natural dams, especially the overtopping mode, are not able to make clear with above-mentioned field data.

The size of the breach and the magnitude of the resulting flood are controlled by many factors, which include geomorphological factors, e.g., bed slope and dam's geometry, sediment characteristics, and so on. Many researchers have studied the influence of dam's geometry on failure process and discharge hydrograph and found a steeper downstream slope of dam could result in a larger peak discharge and shorter duration [17–20]. The breaching process may differ notably due to different compositions of fine and coarse particles. And, the fines contents or median diameter of the dam materials have an important effect on the discharge [17, 18, 21–26]. The rate of inflow could also change the erosion process during the failure process and then affect the breach development and outflow [19, 27]. However, there are few studies about influence of bed slope on breaching characteristics of natural dams until now.

The breaching characteristics of natural dams include both the evolution of breaching discharge and spatial evolution of breach. The evolution characteristics of breach discharge mainly include characteristics of discharge hydrographs, peak discharge, and breaching time. The evolutionary characteristics of breach mainly entail variation of breaching depth and width. However, at present, the process of breaching discharge has been studied separately from the characteristics of breach [18, 24, 28], so thorough analysis about the breaching characteristics by considering these two aspects comprehensively have failed.

The breach development is actually the relationship between breach width and depth. Because of the limitations of observation technology, the existing research can hardly confirm the quantitative relationship between breach depth and width, leaving a research gap. Although Coleman et al. proved that the breach shape can be described by a parabolic equation through experimental observation [17], the case is different from natural dams. Pickert et al. and Do et al. obtained breach longitudinal and transverse profiles at different stages, but the definite relationships between the two directions are unclear [23, 29]. Zhu et al. studied in detail the variation of breach longitudinal profiles, but the regularities of breach widening have not been studied [30].

In field, the natural dam could block river and gully. The bed of river is usually gentle, and the bed of gully is steep. In this paper, the bed slope was designed from 1° to 13° to simulate natural dams located in both river and gully. This paper aims to improve the understanding of influence of bed slope on breaching characteristics of natural dams triggered by overtopping. In this paper, a series of flume tests to study the breaching characteristics of natural dams on sloping beds are presented. Firstly, the influences of bed slope angles on breach discharge

hydrograph, peak discharge, time to peak discharge, duration, breach depth, and breach width are analyzed. Then, the relationship between breach width and depth is discussed. In the end, the relationships between parameters in the breach width-depth function and bed slope are investigated.

2. Experimental Setup and Procedure

2.1. Experimental Prototype and Materials. The experimental models are based on the Zongqu natural dam prototype. The Zongqu natural dam was formed after Wenchuan earthquake and overtopped in 2009 [31]. The Zongqu gully is located about 7 km in the south of Maoxian County, Sichuan province, which is a primary tributary on the left bank of Minjiang River. The entire basin is located in the southeast of Sichuan Plateau (Figure 1). The longitudinal section of Zongqu natural dam is similar to the shape of a trapezoid. The top crest width and the height of the dam were both approximately 30 m. The length across the river was approximately 60 m. The bed slope was approximately 4° at the location of the natural dam. The upstream and downstream slopes of the dam were approximately 34° and 17° , respectively. The materials in the dam were block rocks, gravels, sand, silt, and clay. The content of block rocks with diameters of 100–300 cm was approximately 5%. The content of particles 30–100 cm in diameter was approximately 60%, and 35% of particles had a diameter less than 30 cm. We set the length ratio $\lambda_L = 1 : 100$ in the present models. The experimental material with a diameter of 1–3 cm was 5%, 0.3–1 cm was approximately 60%, and less than 0.3 cm was about 35%. In addition, to avoid the influence of viscosity of flow on the breaching process, the content of clay particles should not be large. The content of clay particles was 1.872% in the present models. The median diameter D_{50} was 0.48 cm. The initial dry density was 1.72 g/cm^3 . The grain-size distribution curve of the experimental materials is shown in Figure 2. Before each test run, we weighed approximately 300 kg of material that fits the gradation curve and watered the composition.

2.2. Experimental Setup. Based on the length ratio λ_L , the dam crest width and height were both 30 cm for the experimental models. Natural dam breaching is a free water surface process dominated by gravity, followed the Froude principle. If λ_L is scale ratio, based on the Froude number $F = v/(gL)^{0.5}$, with v being the velocity, g being the gravity acceleration, and L being the length, the scale ratio for inflow discharge is $\lambda_L^{0.5}$. Based on small watershed convergence model, reasoning formula method was used to calculate the designed inflow rate of Zongqu watershed. The characteristic value of catchment area of the basin was taken from the area above Zongqu natural dam by a topographic map of 1 : 50000; the catchment area was 15 km^2 , and the main channel length was 7.5 km. The confluence parameters, designed storm value, etc., were obtained according to the Handbook for Calculation of Storm Floods in the Medium and Small Watersheds of Sichuan Province [32]. When design frequency was 2%, the calculated

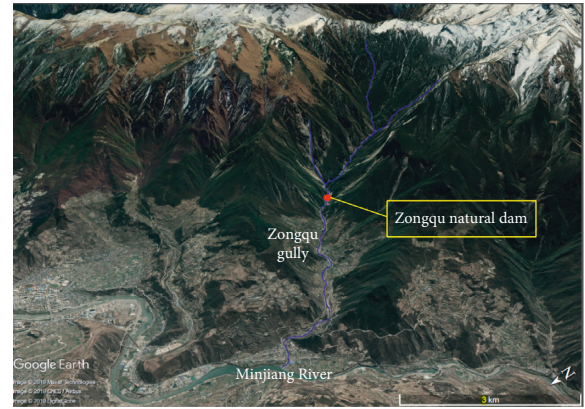
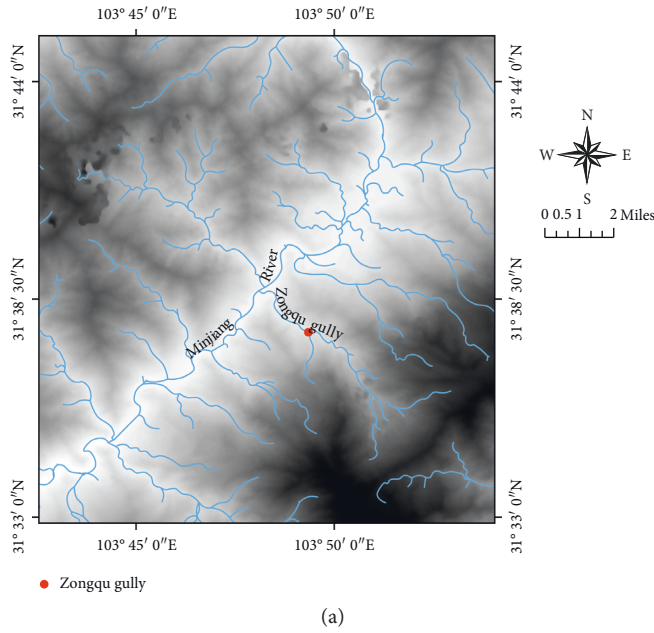


FIGURE 1: Location of the Zongqu gully and Zongqu natural dam. (a) Location of the Zongqu gully (b) Location of the Zongqu natural dam in the gully.

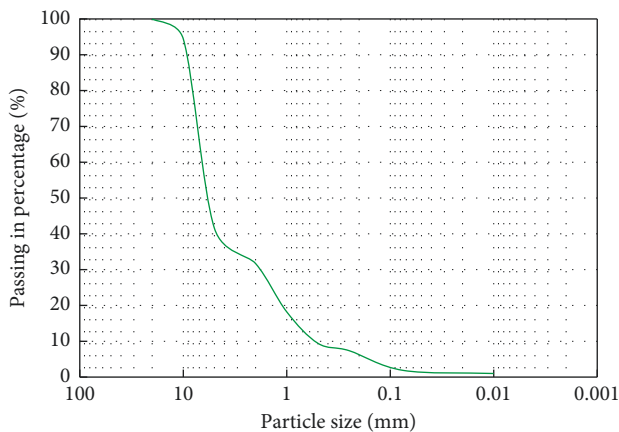


FIGURE 2: Particle size distribution of the material.

peak discharge at the section of the dam was set as actual inflow rate of Zongqu natural dam. Therefore, the discharge ratio $\lambda_Q = \lambda_L^{2.5} = 1 : 100000$, and the inflow rate in the tests was about 1.0 L/s.

A half-width of dam was chosen and scaled down with λ_L . The initial breach was beside the flume wall, assuming a little effect of the flume sidewall on the breach flow and a symmetric breach advance (Figure 3). It is noted that very small flow depths with low Reynolds number might generate some delay in the breach discharge due to viscous and capillarity effects at the interfaces of glass/water and grain/water up to the point at which a turbulent flow is fully developed at the beginning of overtopping. However, these effects have minor importance due to the fast increasing breach discharge [23]. This assumption is supported by the findings of Schmocker and Hager [28] for small-scale models [23].

The experiments were carried out in a 15 m long, 0.3 m wide, and 0.6 m deep flume, and the adjustable slope angle was 0–30°. The flume was made of tempered glass to clearly see the breach bottom during the breaching process. The width of the dam crest W and initial dam height H_b were both 30 cm. We preset an initial triangular breach at one side of the dam. Both of its depth and width were 4 cm (Figure 3). The inflow discharge was accurately controlled by an electromagnetic flowmeter. The tests involved the use of a movable riverbed with thickness of 5 cm, which was made of the same materials with the dam. As the boundary condition, a plate with a height of 5 cm was set at the end of the flume. In the experiments, the upstream slope toe of the dam was set up at a distance of 10 m from the intank. The experimental setup is shown in Figure 3.

For the first test, we set the flume bed slope as 1°, and the upstream and downstream slopes of the dam were set as 30° and 20°, respectively. θ is the flume slope, and β is the downstream slope of the dam. Then, other six tests with flume bed slope of 2°, 3°, 7°, 9°, 11°, and 13° were set, whose other conditions except lake volume before the dam were the same with the first test.

A piezometer was buried in front of the dam. The piezometer recorded the depth of water upstream of the dam, and the data were collected by a computer automatically.

2.3. Measurements. The upstream water pressure could be recorded by the piezometer set at the upstream of the dam. According to the principle of hydrostatic pressure, the water level in front of the dam could be converted by the water pressure, and the breaching discharge in the failure process was calculated based on the water balance equation:

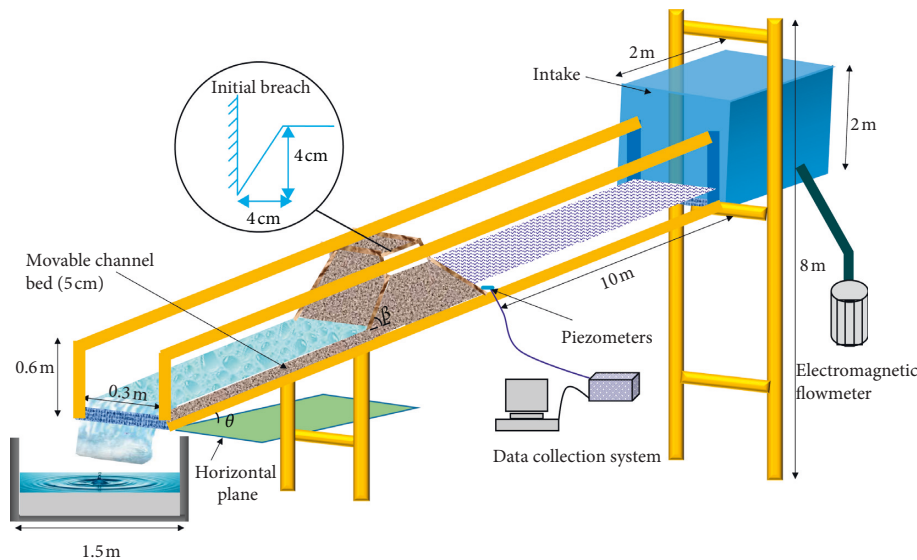


FIGURE 3: A sketch of the flume and its hydrological equipment. It shows the full size and shape of the dam and the size of the initial breach.

$$Q = q_{in} - \frac{dW}{dt}, \quad (1)$$

where Q is the outflow discharge, L/s; q_{in} is the inflow discharge, L/s; t is time, s; and W is the volume of reservoir as a function of water surface elevation.

Cameras were set in different places around the dam. A grid paper was set on the side glass of the flume to measure the height of the breach bottom. The accuracy of the measurement reached 5 mm. Combining the measured height of the breach bottom and the initial dam height, the breach depth could be determined.

3. Experimental Results

3.1. General Features. The results show that the breaching characters of dams in the tests, which included outflow characters, erosion characters, and breach enlargement characters, were similar. And, the overtopping process of all experiments had three same phases. At the first stage (0- t_1), the sediment at the breach of dam crest was dominated by the suspended load movement. And, the sediments accumulated at the downstream slope and formed an obvious slope turning point. The breach slope collapsed intermittently on a small scale, and the breach shape in this stage approached to a rectangle. The slope turning point reached the intersection point of downstream slope and breach bottom when $t = t_1$ (Figure 4(a)). At the second stage (t_1 - t_2), backward erosion became serious with more water outflow. The backward erosion reached upstream slope when $t = t_2$ (Figure 4(b)). In this stage, there were break points at downstream slope, which was the characteristic of backward erosion. The strength of erosion under the slope of the break point became slower, while the upper slope became stronger. When the slope break point moved to the upstream slope, the elevation of water upstream showed a sudden decline (Figure 4(d)). The shape of the breach was similar to a

trapezoid. The deepening and widening of breach in this stage was the most rapid one. At stage three (t_2 - t_3), the outflow discharge was gradually decreased, and the water depth became shallow and sand carrying capacity was gradually weakened. And, a coarse layer which protected the lower particles from being washed away was formed (Figure 4(c)). At that moment, the motion of water and sand could reach a new balance, indicating the end of the failure process. The shape of breach was also like a trapezoid during this stage.

3.2. Characteristics of Breach Discharge. Figure 5 shows the discharge hydrographs of the natural dam with seven slope angles (1° , 2° , 3° , 7° , 9° , 11° , and 13°). As is shown, in different slope conditions, the breach discharge increases as time increases and then reaches the peak discharge; subsequently, the breach discharge decreases gradually. This feature indicates that breach discharge at different slopes has strong unsteady characteristics. The figure reflects the smaller the bed slope is, the longer breaching time is, and the fatter the curve is. The peak discharge is only one for all conditions. It means that the bed slope does not change the number of peak discharge point for hydrograph.

The relationship between peak discharge and bed slope is shown in Figure 6. According to the form of the curve, peak discharge increases with the increase in slope when the slope is less than 3° . However, it gradually decreases when the slope is larger than 3° . The main reason for causing this phenomenon is that when the slope is below 3° , the water upstream dam is abundant for outflowing, and, the bed slope is the controlling factor for breach development. As the slope increases, the shear force of outflow is strengthened, and the breach expansion is accelerated, which causes larger outflow. Therefore, the peak discharge increases gradually along with the increase in slope. When slope becomes more than 3° , the pre-dam storage capacity decreases with the increase in

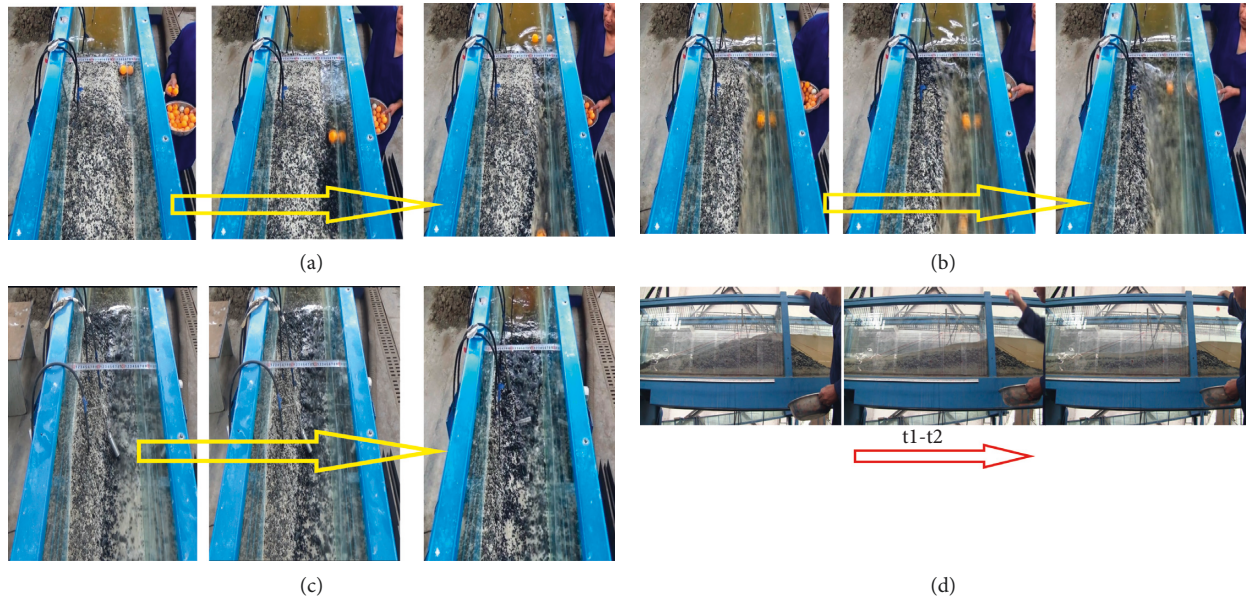


FIGURE 4: Images of dam and flow at different times, showing overtopping erosion is the dominant factor for dam failure. (a) Stage I for dam failure process, 0-t1 period. (b) Stage II for dam failure process, t1-t2 period. (c) Stage III for dam failure process, t2-t3 period. (d) The longitudinal profiles of the dam in Stage II. It shows a whole backward erosion process.

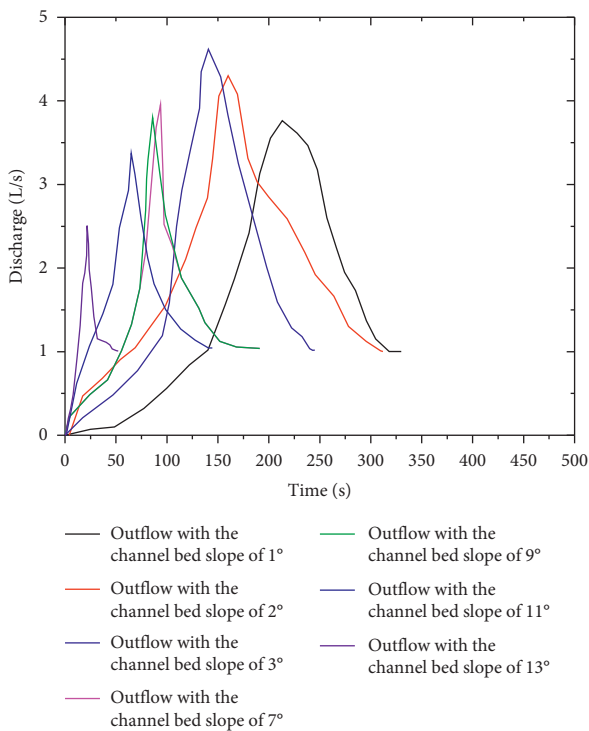


FIGURE 5: Breach discharge hydrographs for different channel bed slopes.

slope. Although the erosion ability is strengthened with the increase in slope, the decrease of predam storage capacity contributes to insufficient outflow discharge. This causes the decrease in peak discharge with the increase in bed slope. Thus, in this condition, predam storage capacity is the main factor that affects peak discharge. At the same time, in the

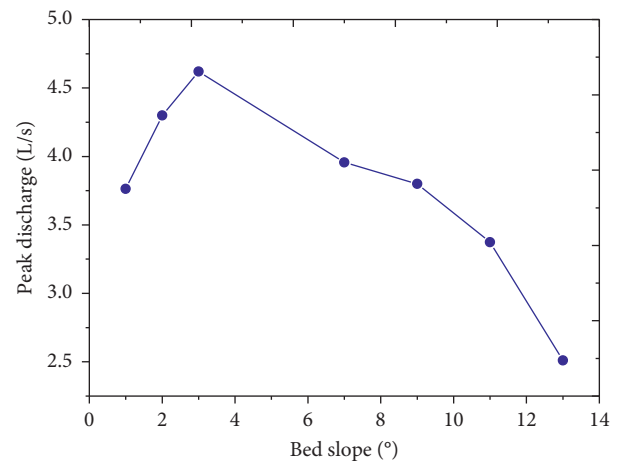


FIGURE 6: The relationship between peak discharges and bed slopes.

growth stage of peak discharge, it grows faster when slope is 2°-3° than that of 1°-2°. And, in the decreasing stage of peak discharge, it decreases faster when slope is 9°-13° than that of 3°-9°. It indicates that the steeper the slope is, the greater the increment of peak discharge in growth stage is and the decline rate of peak discharge in decrease stage is.

Figure 7 shows the bed slope could shorten the duration of hydrographs and time from test start to the moment of peak discharge. It means the larger bed slope could decrease the dam's life span and advance the peak discharge. The figure indicates that the duration and time from test start to the moment of peak discharge with the bed slope are nonlinear relationships. When bed slopes are smaller than 3° and larger than 9°, the duration and time from test start to the moment of peak discharge decrease more quickly than the others. The average reduction rate of

duration and time to peak curve are 23 s and 16 s, respectively per bed slope, indicating duration decreases more quickly than time from test start to the moment of peak discharge.

3.3. Characteristics of Breach Development. Figure 8 shows longitudinal profiles of natural dam with different slopes. As is shown, under different slope conditions, dam crest has different degrees of bending characteristics. Especially, after a period of breaching time, break point is formed on the dam crest, that is the symbol of headward erosion. Under different slope conditions, the failure process is basically the same, including slow overcurrent, headward erosion, and rebalance of sediment and water. Thus, it means that the variation of slope does not change characteristics of failure process. Breach longitudinal profiles in that seven slopes all show that strong headward erosion existed in stage II. The number of break point decreases as the bed slope becomes larger. Compared with the residual dam height in different slopes, as the slope increases, residual dam height decreases gradually.

Figure 9 shows the relationships between breach width and depth during failure process. It is seen that the breach width increases when the breach deepens. At the early and late stage of breach growth, the breach widens slowly. Otherwise, the breach widens rapidly, in which the curve is similar to the shape “S”. Overall, the curves of breach depth and width at any time are partly located above the straight line with a slope of $K=1$, when the slope is $1^\circ\text{--}3^\circ$. While the slope is more than 7° , all curves are located basically below that straight line. It indicates that during the development of breach, the breach width increases faster than depth when the slope is relatively small. Nevertheless, it is the opposite as for the steeper slopes. When the failure process is over, as slope increases, the breach width-depth graphs firstly approach the straight line with a slope of $K=1$ and then get away from it. It indicates that the breach width-to-depth ratio increases to 1, and then decreases as the slope increases.

4. Relationships between Width and Depth of Breach

Based on the experimental data, we converted breach width and depth to dimensionless values. The dimensionless breach depth D^* and width W^* are set as follows:

$$\begin{aligned} D^* &= \frac{D}{H_d}, \\ W^* &= \frac{W}{H_d}, \end{aligned} \quad (2)$$

where D (cm) and W (cm) are breach depth and width, respectively, and H_d (cm) is the dam height.

To obtain the functional relation between W^* and D^* , all the test data were fitted as shown in Figure 10. This figure shows that all the fitting curves fit the experimental data well, and the fitting curves could be expressed by the following equation:

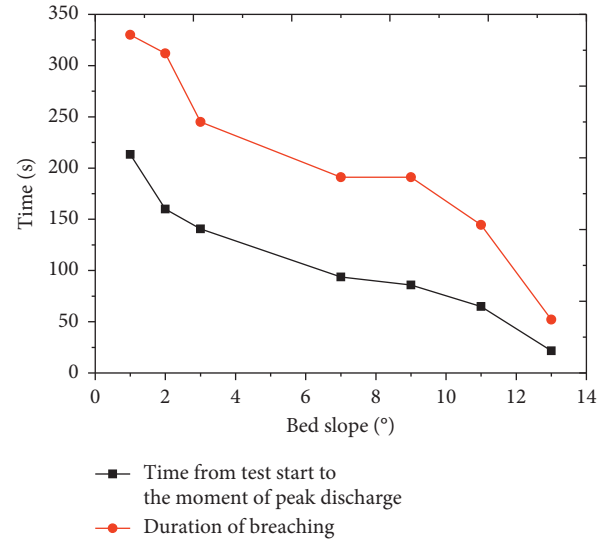


FIGURE 7: The relationship between time from test start to the moment of peak discharge and duration of hydrograph and bed slopes.

$$W^* = \frac{\eta}{1 + e^{(-k(D^* - \gamma))}}, \quad (3)$$

where η , k , and γ are parameters. The parameter η reflects the possible maximum breach width; k is the shape parameter, which represents steep or gentle of the curve, reflecting growth rate of breach. If the absolute value of k is larger, the breach width increases faster. On the contrary, the width expands slower with a smaller k . The parameter γ reflects the corresponding depth of the breach when it reaches half of the maximum breach width.

Figure 11 shows the influence of slope on breaching parameters η , k , and γ . It indicates that η increases with θ and then decreases, but the relation between γ and θ is opposite. The larger θ is, the smaller k becomes. Furthermore, the parameters k and θ agree with linear relationship.

5. Discussion

Lang, Zhang, and Huang calculated the peak discharge and velocity at the peak discharge based on the hydrological data in the field of the Zongqu natural dam, and considered the peak discharge of $300\text{--}600\text{ m}^3/\text{s}$ and the velocity of approximately 34 m/s at the peak discharge time [33, 34]. For the experimental model with the flume bed slope of 1° , the peak discharge is 3.8 L/s , which agrees with the field data transformed value of $3\text{--}6\text{ L/s}$ based on the scale ratio. Meanwhile, the velocity of the outflow surface was measured to be approximately 3.2 m/s at the peak discharge moment, which was approximately equal to the field data transformed value of 3.4 m/s based on the scale ratio. These findings mean that the hydraulic parameters in model test are consistent with the field data. Also, it indicates that the boundary effect on the motion of outflow may not be serious in the tests. In such way, laboratory tests may model the hydraulic characteristics of the natural dam.

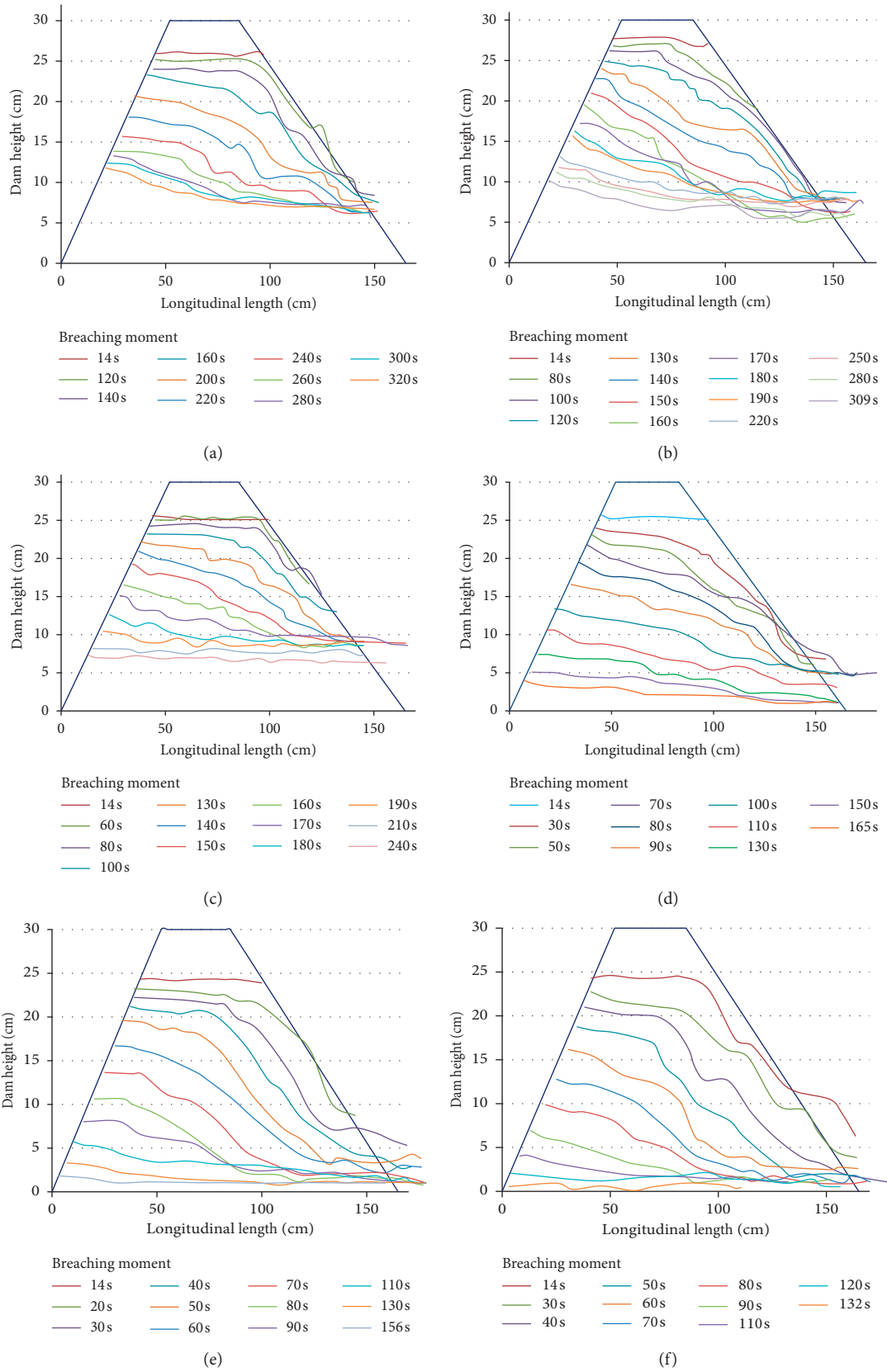


FIGURE 8: Continued.

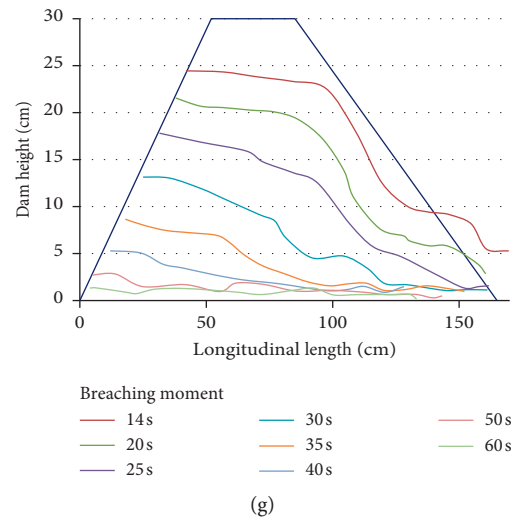


FIGURE 8: Longitudinal profiles of the dam during failure process for different channel bed slopes at different times. (a) Bed slope of 1° . (b) Bed slope of 2° . (c) Bed slope of 3° . (d) Bed slope of 7° . (e) Bed slope of 9° . (f) Bed slope of 11° . (g) Bed slope of 13° .

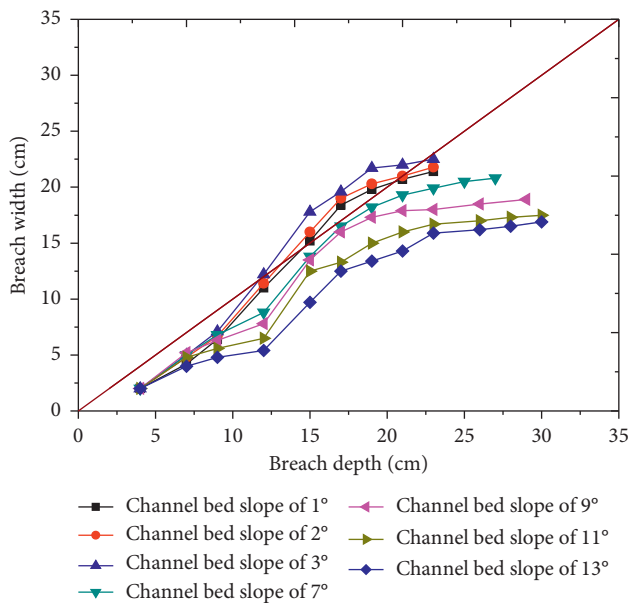


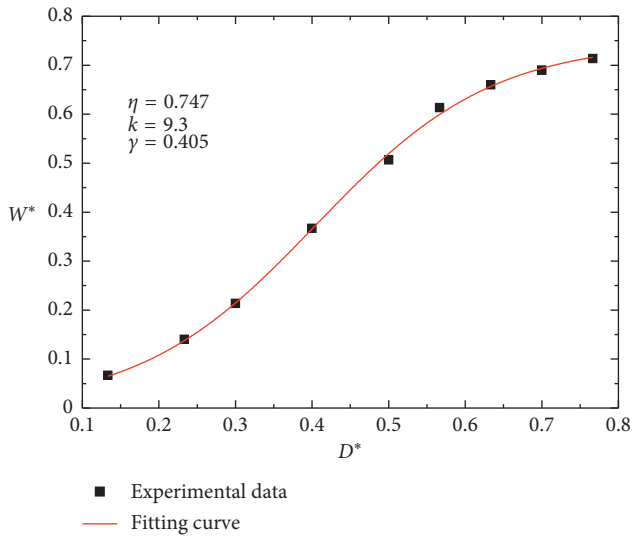
FIGURE 9: The relationship between breach width and depth for different bed slopes.

Natural dams are not only common in rivers with small bed slopes, but also in the gully with large bed slopes. Previous studies and conclusions are mostly focused on the dam failure on small bed slope. This paper shows the breaching process of natural dams on different bed slopes, especially the large bed slope. It also clearly reflects the relationship between breaching parameters and the bed slope. It should be noted that this paper just intends to study the influence of bed slope on breaching process of natural dams. However, the lake volume changes indeed when changing the bed slope and keeping the other parameters the same. It means that the bed slope of the channel could change both the topographical condition and hydraulic condition. However, the bed slope and lake

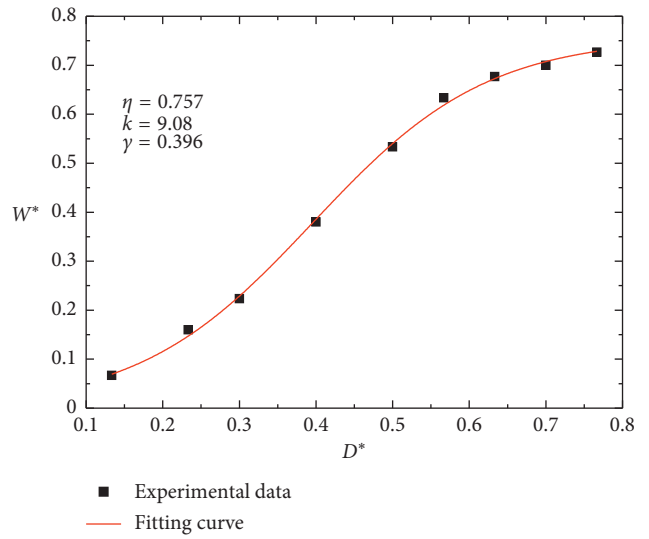
volume are dependent, and the lake volume is a function of bed slope. In this respect, the independent variable is only bed slope.

After the natural dam formation, the researchers concern the outflow peak discharge during the failure process. When analyzing the peak discharge, it is often estimated based on lake volume, which is called parameter model [35]. In general, it has a negative correlation between lake volume and bed slope. In such methods, the relationship between peak discharge and bed slope is a negative correlation. Figure 12 shows the relationship between peak discharge and bed slope for the experiments in this paper based on Evans's and Hagen's methods [36, 37]. It shows that the peak discharge decreases with the bed slope which is inconsistent with the experimental data. In addition, the calculated values are less than the experimental values. It is observed that the trend of the calculated values is similar to the experimental data when the bed slope is large, but opposite with the small bed slope. It is worth mentioning that the parameter model almost ignored the influence of bed slope on peak discharge. It does not agree well with the field situation, such as the natural dam in the gully with a large bed slope. For such a dam in gully, it should not only consider the variation of lake volume induced by bed slope but also the variation of erosion rate induced by bed slope. In such way, the results and conclusions in this paper may provide some references to peak discharge calculation for natural dam with different bed slopes.

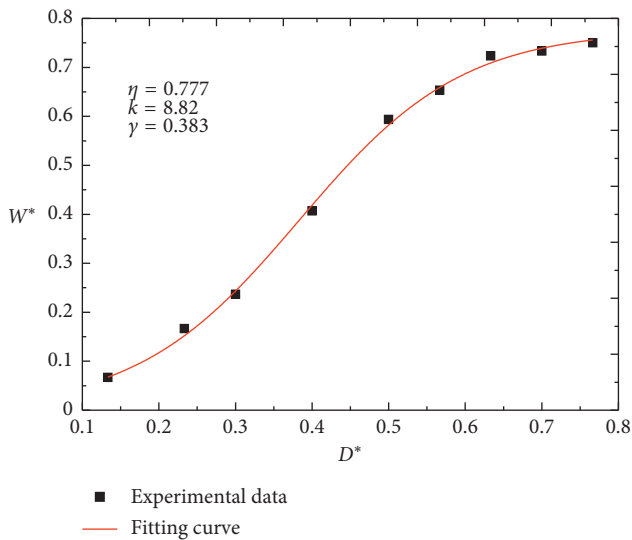
A lot of calculation methods about discharge are related to water head and breach width [38–41]. It is obvious that the water head could be calculated if the breach bottom is known together with the water balance equation. The breach bottom is influenced by erosion only. If we know the erosion rate, the evolution characteristics of breach bottom/breach depth could be obtained. And, it is



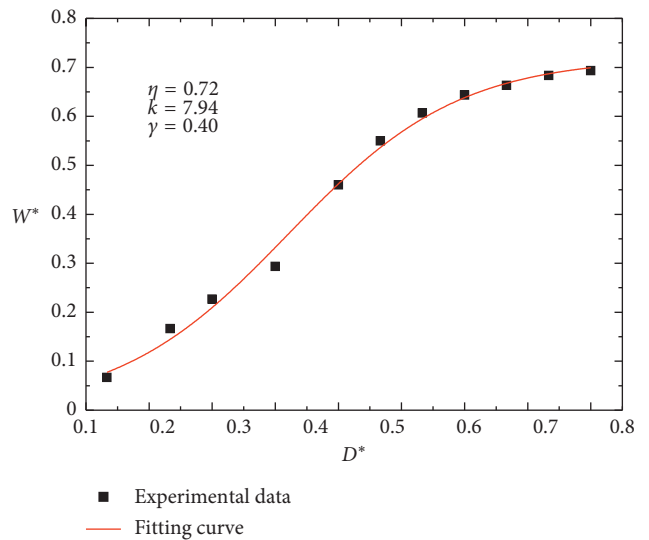
(a)



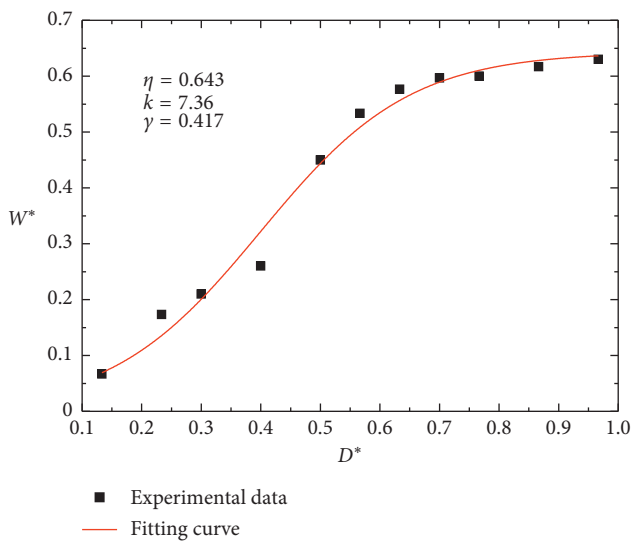
(b)



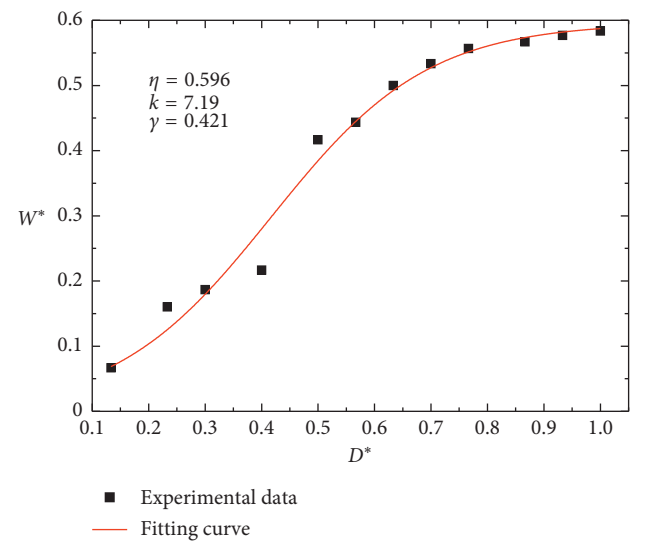
(c)



(d)

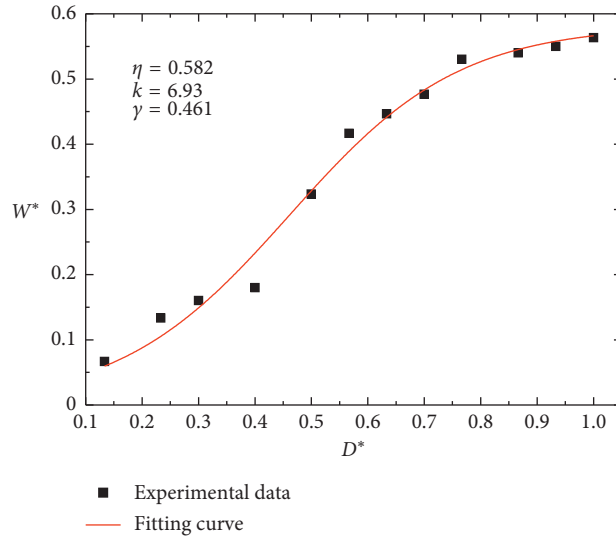


(e)



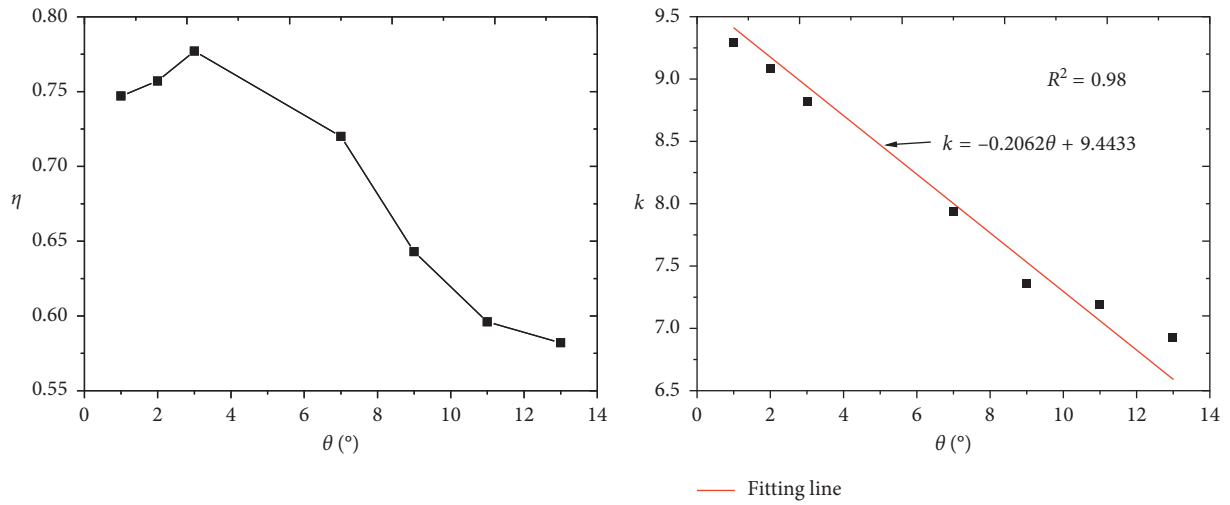
(f)

FIGURE 10: Continued.



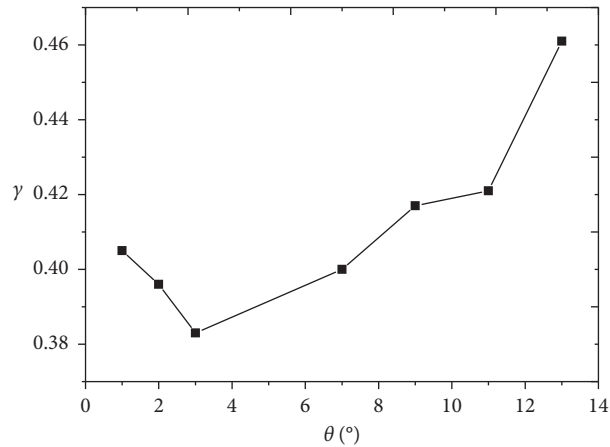
(g)

FIGURE 10: The relationship between the experimental data and fitting curves for W^* and D^* . The parameters η , k , and γ in fitting equation (3) are shown in each figure. (a) Bed slope of 1° . (b) Bed slope of 2° . (c) Bed slope of 3° . (d) Bed slope of 7° . (e) Bed slope of 9° . (f) Bed slope of 11° . (g) Bed slope of 13° .



(a)

(b)



(c)

FIGURE 11: The relationships between parameters in equation (3) and bed slopes. (a) The relationship between η and bed slopes. (b) The relationship between k and bed slopes. (c) The relationship between γ and bed slopes.

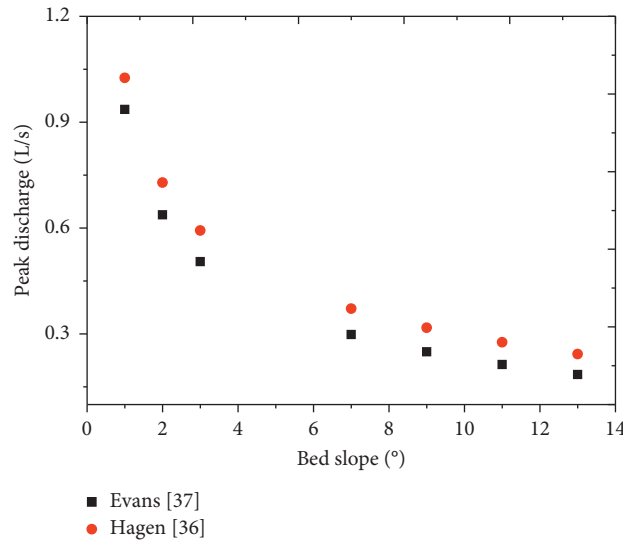


FIGURE 12: The relationship between calculated peak discharge values with Evans’s and Hagen’s methods [36, 37] and bed slopes.

not difficult to calculate the erosion rate at present. The methods for erosion rate calculation could refer to Van Rijn, Chang and Zhang, and Wu [42–44]. The breach width is an important parameter to calculate outflow discharge. The breach width is mainly caused by lateral erosion and breach side slope collapse. At present, the lateral erosion rate is assumed to be equal to the incised erosion rate. In fact, the shear stress of outflow is different along the breach. Therefore, Osman and Thorne indicated that the above assumption may be uncorrected [45]. It is noted that there is still not a calculation method of lateral erosion rate for noncohesive materials. Although many models analyzed breach slope collapse based on force equilibrium, sometimes the failure plane is not linear or circle as the assumption of models [46]. In addition, the collapse of breach side slope is random indeed in field of natural dams. In such way, the breach width calculation value may be far from the observed value based on the complex method (i.e., the addition of lateral erosion and collapse of breach side slope). Therefore, another practical and effective method may be developed avoiding calculating lateral erosion and collapse of breach side slope. Based on such thought, the relationship between breach width and depth intend to be determined. After all, the incised erosion rate is easier to obtain than the later erosion rate. Moreover, it may be a new way for getting breach width based on the breach depth which is more easy to obtain.

From the data of Jiang et al. [26], the relationship between parameter k in equation (3) and medium diameter of dam material could be obtained (Figure 13). So, the parameter k could be calculated with the relationship between k and medium diameter first and then improve the parameter with the relationship between k and bed slope. The parameter η reflects the maximum breach width after the dam failure. This parameter could be calculated with the method provided by Peng and Zhang [9]. The last parameter in equation (3) is γ . If the initial breach width and depth are

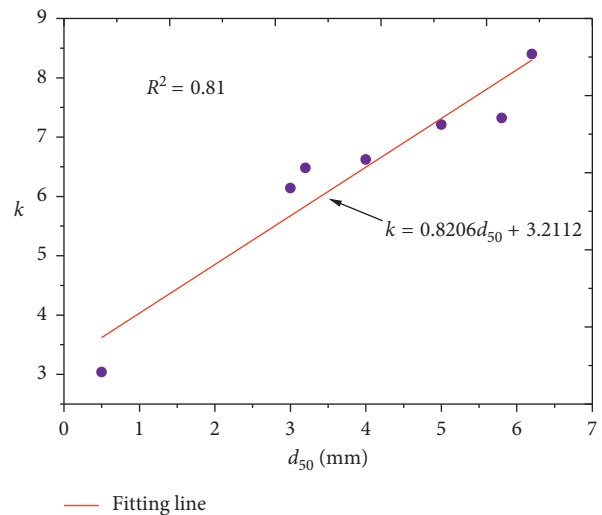


FIGURE 13: The relationship between parameter k and medium diameters. The data are from Jiang et al. [26].

given, the parameter could be calculated, and then the equation (3) is confirmed.

The formula developed in this paper, e.g., equation (3), is also validated with data provided by Coleman et al. and Pickert et al. [17, 23] (Figure 14). It is clear that the breach width and depth described in Coleman et al. and Pickert et al. also obey the formation of equation (3) [17, 23].

The Tangjiashan natural dam is the largest natural dam caused by Wenchuan earthquake. The dimensionless breach depth and width data during Tangjiashan dam failure are shown in Figure 15.

The initial breach width and depth are about 11.5 m and 10 m [47]. Firstly, based on the relationship between parameter k and medium diameter in Figure 13, $k = 19.62$. Then, modifying the parameter k according the relationship between k and bed slope in Figure 11(b), the final value of $k = 18.27$ is obtained. The value of parameter η equals to 2.06

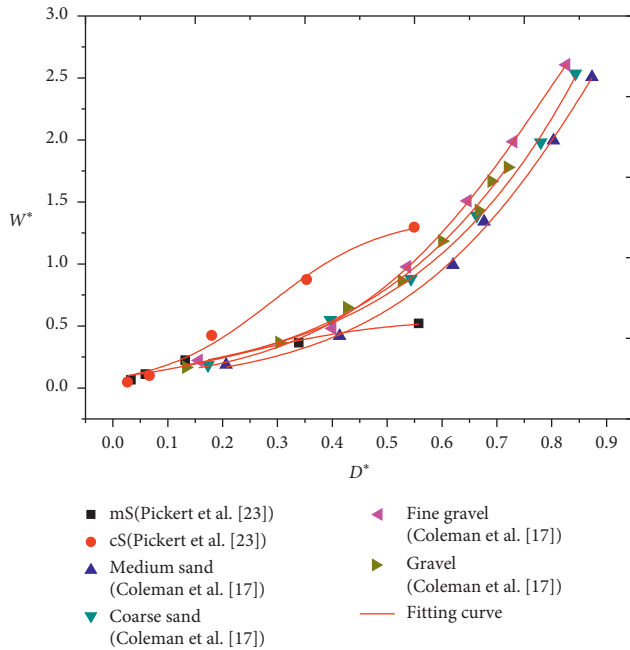


FIGURE 14: The relationships between breach width and depth in dimensionless formation. The scatter points were measured data by Coleman et al. [17] and Pickert et al. [23]. The fitting curve in the figure is analyzed based on equation (3).

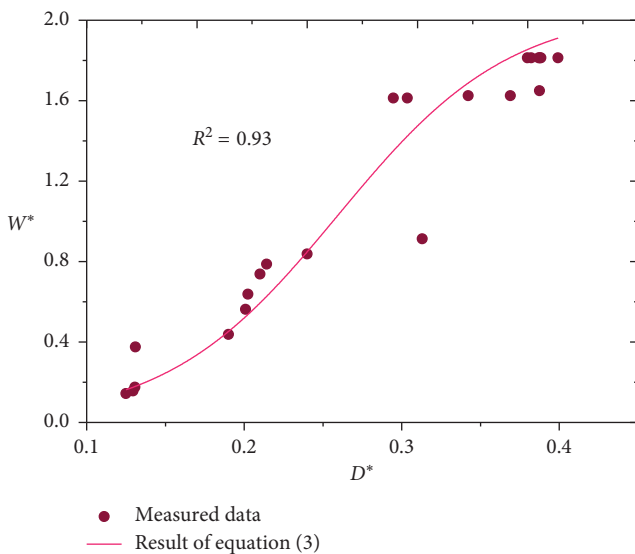


FIGURE 15: The dimensionless breach width and depth of the Tangjiashan natural dam. The points in the figure are the field data recorded during Tangjiashan natural dam failure process. The fitting curve is the simulated results of equation (3).

based on the method provided by Peng and Zhang [9]. On the basis of the initial breach width and depth of the Tangjiashan natural dam, the parameter γ could be calculated as 0.26 with equation (3). Figure 15 shows the results of simulated breach width and depth with equation (3). It indicates that the calculated values are close to the measured values. It proves the equation (3) is feasible to evaluate the breach size.

6. Conclusions

A series of tests were conducted to investigate the failure process of natural dam on sloping beds. In the present experiments, overtopping erosion was the primary mechanism of natural dam failure. The breaching process of natural dams on different sloping beds was divided into three breach phases. Headward erosion plays a dominant role during the erosion process.

The discharge hydrographs are unimodal no matter bed slope is large or not. With the increase in slope, peak discharge increases at first and then decreases while breaching time decreases gradually. The time from test start to the moment of peak discharge becomes earlier as bed slopes become bigger. The rate of decreasing for the time from test start to the moment of peak discharge and duration decreases first and then increases with the increase in bed slope.

As slope increases, breach width-to-depth ratio tends to be 1 and then to be less than 1. The breach width and depth follow a logistic equation formula. There are two parameters that could reflect the maximum breach size in the equation. Also, a shape parameter in the equation has a linear relationship with bed slope. With breaching data of experiments and Tangjiashan natural dam, it proves that the breach width and depth could be simulated well with the formula developed in this paper.

Data Availability

The data used to support the findings of this study are available from the corresponding author upon request.

Conflicts of Interest

The authors declare that there have no conflicts of interest.

Acknowledgments

The authors acknowledge financial support provided by the National Natural Science Foundation of China (no. 41807289) and Sichuan Province Fundamental Scientific Research (no. 18ZA0374).

References

- [1] T. Takahashi, *Debris Flow: Mechanics, Prediction and Countermeasures*, Taylor & Francis, London, UK, 2007.
- [2] J. E. Costa and R. L. Schuster, "The formation and failure of natural dams," *Geological Society of America Bulletin*, vol. 100, no. 7, pp. 1054–1068, 1988.
- [3] H. J. Chai, H. C. Liu, Z. Y. Zhang, and Z. W. Xu, "The distribution, causes and effects of damming landslides in China," *Journal of the Chengdu Institute of Technology*, vol. 27, no. 3, pp. 302–307, 2000, in Chinese.
- [4] G. H. Eisbacher and J. J. Clague, *Destructive Mass Movements in High Mountains: Hazard and Management*, Geological Survey of Canada, Ottawa, Canada, 1984.
- [5] A. Pirocchi, "Laghi di sbarramento per frana nelle Alpi: tipologia ed evoluzione," *Atti I convegno Nazionale Giovani Ricercatori in Geologia Applicata*, vol. 93, pp. 128–136, 1992.

- [6] N. Casagli and L. Ermini, "Geomorphic analysis of landslide dams in the Northern Apennine," *Transactions of the Japanese Geomorphological Union*, vol. 20, no. 3, pp. 219–249, 1999.
- [7] J. J. Clague and S. G. Evans, "Formation and failure of natural dams in the Canadian Cordillera," Bulletin 464, Geological Survey of Canada, Ottawa, Canada, 1994.
- [8] H. J. Chai, H. C. Liu, and Z. Y. Zhang, "The catalog of Chinese landslide dam events," *Journal of Geological Hazards and Environment Preservation*, vol. 6, no. 4, pp. 1–9, 1995, in Chinese.
- [9] M. Peng and L. M. Zhang, "Breaching parameters of landslide dams," *Landslides*, vol. 9, no. 1, pp. 13–31, 2012.
- [10] Z. M. Shi, X. Xiong, M. Peng et al., "Risk assessment and mitigation for the Hongshiyuan landslide dam triggered by the 2014 Ludian earthquake in Yunnan, China," *Landslides*, vol. 14, no. 1, pp. 269–285, 2017.
- [11] L. Zhang, T. Xiao, J. He, and C. Chen, "Erosion-based analysis of breaching of Baige landslide dams on the Jinsha River, China," *Landslides*, vol. 16, no. 10, pp. 1965–1979, 2019.
- [12] X. M. Fan, W. Zhan, X. Dong et al., "Analyzing successive landslide dam formation by different triggering mechanisms: the case of the Tangjiawan landslide, Sichuan, China," *Engineering Geology*, vol. 243, pp. 128–144, 2018.
- [13] C. T. Stefanelli, V. Vilimek, A. Emmer, and F. Catani, "Morphological analysis and features of the landslide dams in the Cordillera Blanca, Peru," *Landslides*, vol. 15, no. 3, pp. 507–521, 2018.
- [14] L. Nibigira, H. B. Havenith, P. Archambeau, and B. Dewals, "Formation, breaching and flood consequences of a landslide dam near Bujumbura, Burundi," *Natural Hazards and Earth System Sciences*, vol. 18, no. 7, pp. 1867–1890, 2018.
- [15] L. Ermini and N. Casagli, "Prediction of the behaviour of landslide dams using a geomorphological dimensionless index," *Earth Surface Processes and Landforms*, vol. 28, no. 1, pp. 31–47, 2003.
- [16] G. G. D. Zhou, M. Zhou, M. S. Shrestha et al., "Experimental investigation on the longitudinal evolution of landslide dam breaching and outburst floods," *Geomorphology*, vol. 334, pp. 29–43, 2019.
- [17] S. E. Coleman, D. P. Andrews, and M. G. Webby, "Overtopping breaching of noncohesive homogeneous embankments," *Journal of Hydraulic Engineering*, vol. 128, no. 9, pp. 829–838, 2002.
- [18] Z. Cao, Z. Yue, and G. Pender, "Landslide dam failure and flood hydraulics. Part I: experimental investigation," *Natural Hazards*, vol. 59, no. 2, pp. 1003–1019, 2011.
- [19] L. Schmocker and W. H. Hager, "Plane dike-breach due to overtopping: effects of sediment, dike height and discharge," *Journal of Hydraulic Research*, vol. 50, no. 6, pp. 576–586, 2012.
- [20] J. S. Walder, R. M. Iverson, J. W. Godt, M. Logan, and S. A. Solovitz, "Controls on the breach geometry and flood hydrograph during overtopping of noncohesive earthen dams," *Water Resources Research*, vol. 51, no. 8, pp. 6701–6724, 2015.
- [21] M. W. Morris, M. A. A. M. Hassan, and K. A. Vaskinn, "Breach formation: field test and laboratory experiments," *Journal of Hydraulic Research*, vol. 45, no. 1, pp. 9–17, 2007.
- [22] C. Gregoretto, A. Malturo, and S. Lanzoni, "Laboratory experiments on the failure of coarse homogeneous sediment natural dams on a sloping bed," *Journal of Hydraulic Engineering*, vol. 136, no. 11, pp. 868–879, 2010.
- [23] G. Pickert, V. Weitbrecht, and A. Bieberstein, "Breaching of overtopped river embankments controlled by apparent cohesion," *Journal of Hydraulic Research*, vol. 49, no. 2, pp. 143–156, 2011.
- [24] L. Schmocker, P.-J. Frank, and W. H. Hager, "Overtopping dike-breach: effect of grain size distribution," *Journal of Hydraulic Research*, vol. 52, no. 4, pp. 559–564, 2014.
- [25] S.-C. Chen, T.-W. Lin, and C.-Y. Chen, "Modeling of natural dam failure modes and downstream riverbed morphological changes with different dam materials in a flume test," *Engineering Geology*, vol. 188, pp. 148–158, 2015.
- [26] X. G. Jiang, J. H. Huang, Y. W. Wei et al., "The influence of materials on the breaching process of natural dams," *Landslides*, vol. 15, no. 2, pp. 243–255, 2018.
- [27] L. Liu, D. Zhong, H. Zhang, and X. Li, "Experimental and numerical study of a landslide dam failure due to overtopping," *Journal of Tsinghua University (Science and Technology)*, vol. 53, no. 4, pp. 583–588, 2013.
- [28] L. Schmocker and W. H. Hager, "Modelling dike breaching due to overtopping," *Journal of Hydraulic Research*, vol. 47, no. 5, pp. 585–597, 2009.
- [29] X. K. Do, M. Kim, H. P. T. Nguyen, and K. Jung, "Analysis of landslide dam failure caused by overtopping," *Procedia Engineering*, vol. 154, pp. 990–994, 2016.
- [30] Y. Zhu, P. J. Visser, J. K. Vrijling, and G. Wang, "Experimental investigation on breaching of embankments," *Science China Technological Sciences*, vol. 54, no. 1, pp. 148–155, 2011.
- [31] N. Liu, Z. L. Cheng, and P. Cui, *Dammed Lake and Risk Management*, Science Press, Beijing, China, 2013, in Chinese.
- [32] Water Resources Department of Sichuan Province China, *Handbook for Calculation of Storm Floods in the Medium and Small Watersheds of Sichuan Province*, Water Resources Department, Chengdu, China, 1984.
- [33] J. Zhang and E. Huang, "Safety analysis of dammed lakes in Wenchuan earthquake," *Advanced Engineering Sciences*, vol. 42, no. 1, pp. 107–112, 2010, in Chinese.
- [34] S. L. Lang, "Forecast on dam-break discharge and hydrologic condition led to overflow burst of landslide dam in Zongqu Gully," *Science Technology and Engineering*, vol. 15, no. 22, pp. 113–117, 2015, in Chinese.
- [35] M. W. Pierce, C. I. Thornton, and S. R. Abt, "Predicting peak outflow from breached embankment dams," *Journal of Hydrologic Engineering*, vol. 15, no. 5, pp. 338–349, 2009.
- [36] V. K. Hagen, "Reevaluation of Design Floods and Dam Safety," in *Proceedings of 14th Congress of International Commission on Large Dams*, Rio de Janeiro, Brazil, 1982.
- [37] S. G. Evans, "The maximum discharge of outburst floods caused by the breaching of man-made and natural dams," *Canadian Geotechnical Journal*, vol. 23, no. 3, pp. 385–387, 1986.
- [38] V. P. Singh and C. A. Quiroga, "A dam-breach erosion model: I. Formulation," *Water Resources Management*, vol. 1, no. 3, pp. 177–197, 1987.
- [39] D. L. Fread, *BREACH: An Erosion Model for Earthen Dam Failures*, National Weather Service, Silver Spring, MD, USA, 1988.
- [40] J. S. Walder and J. E. O'Connor, "Methods for predicting peak discharge of floods caused by failure of natural and constructed earthen dams," *Water Resources Research*, vol. 33, no. 10, pp. 2337–2348, 1997.
- [41] A. L. Rozov, "Modeling of washout of dams," *Journal of Hydraulic Research*, vol. 41, no. 6, pp. 565–577, 2003.
- [42] L. C. V. Rijn, "Sediment pick-up functions," *Journal of Hydraulic Engineering*, vol. 110, no. 10, pp. 1494–1502, 1984.
- [43] D. S. Chang and L. M. Zhang, "Simulation of the erosion process of landslide dams due to overtopping considering

- variations in soil erodibility along depth,” *Natural Hazards and Earth System Science*, vol. 10, no. 4, pp. 933–946, 2010.
- [44] W. Wu, “Simplified physically based model of earthen embankment breaching,” *Journal of Hydraulic Engineering*, vol. 139, no. 8, pp. 837–851, 2013.
- [45] A. M. Osman and C. R. Thorne, “Riverbank stability analysis. I: Theory,” *Journal of Hydraulic Engineering*, vol. 114, no. 2, pp. 134–150, 1988.
- [46] M. Morris, G. Hanson, and M. Hassan, “Improving the accuracy of breach modelling: why are we not progressing faster?,” *Journal of Flood Risk Management*, vol. 1, no. 3, pp. 150–161, 2008.
- [47] Z. Chen, L. Ma, S. Yu et al., “Back analysis of the draining process of the Tangjiashan barrier lake,” *Journal of Hydraulic Engineering*, vol. 141, no. 4, p. 05014011, 2014.

Research Article

Updating Soil Spatial Variability and Reducing Uncertainty in Soil Excavations by Kriging and Ensemble Kalman Filter

Yajun Li ¹ and Kang Liu²

¹School of Engineering and Technology, China University of Geosciences (Beijing), Beijing, China

²School of Civil and Hydraulic Engineering, Hefei University of Technology, Hefei, China

Correspondence should be addressed to Yajun Li; y.j.li@cugb.edu.cn

Received 16 June 2019; Revised 14 September 2019; Accepted 19 September 2019; Published 20 October 2019

Guest Editor: Young-Suk Song

Copyright © 2019 Yajun Li and Kang Liu. This is an open access article distributed under the Creative Commons Attribution License, which permits unrestricted use, distribution, and reproduction in any medium, provided the original work is properly cited.

Field measurements can be used to improve the estimation of the performance of geotechnical projects (e.g., embankment slopes and soil excavation pits). Previous research has utilised inverse analysis (e.g., the ensemble Kalman filter (EnKF)) to reduce the uncertainty of soil parameters, when measurements are related to performance, such as inflow, hydraulic head, and deformation. In addition, there are also direct measurements, such as CPT measurements, where parameters (i.e., tip resistance and sleeve friction) can be directly correlated with, e.g., soil deformation and/or strength parameters, where conditional simulation via constrained random fields can be used to improve the estimation of the spatial distribution of parameters. This paper combines these two (i.e., direct and indirect) methods together in a soil excavation analysis. The results demonstrate that the parameter uncertainty (and thereby the uncertainty in the response) can be significantly reduced when the two methods are combined.

1. Introduction

Soil properties are spatially varying due to mineralogical compositions, stress histories, and geological disposal processes [1–3]. Therefore, in a routine site investigation program where soil samples are tested at some places, soil property values at unsampled locations cannot be interpolated or extrapolated with perfect certainty (i.e., due to the spatial variability). However, it is often desirable to predict those property values (with as little uncertainty as possible) at those locations, in order to reduce the uncertainties in the soil structural responses.

Conditional random field approaches that aim to reduce the uncertainty are available to generate realisations of random fields, constrained by the direct measurement data at sampling locations. The Monte Carlo process is often involved in those approaches. Bayesian updating based on Markov Chain Monte Carlo (MCMC) can be used to generate multiple realisations of soil properties. For example, Li et al. [4] used MCMC for generating conditioned random fields of depth to bedrock in the geologic profiles.

An alternative way is to use kriging combined with an unconditional random field generator [5]. Kriging provides a best linear unbiased estimation of spatially random properties at unsampled locations, by weighing the sampled measurements according to the covariance (variogram) [6]. Multiple realisations of soil properties can also be generated to investigate the uncertainty in structure responses. For instance, Li et al. [5] used kriging to generate the random fields of undrained shear strength by using the direct cone penetration test (CPT) data.

Apart from the “direct” measurement data, monitoring data of the soil structure performance is quite often available. Conditional simulation of random fields of soil properties and of the soil structures on or around these soils can be also achieved by using these indirect soil response data and inverse modelling techniques. For example, making use of all deflection measurements along an inclinometer, Lo and Leung [7] showed that Bayesian methods can be used to update subsurface soil spatial variability in order to improve the prediction of the response of a braced excavation. Vardon et al. [8] used the ensemble Kalman filter (EnKF) to

reduce the uncertainty in slope stability based on hydraulic measurements via inverse analysis.

However, conditional simulation based on both direct and indirect measurements is surprisingly scarce in geotechnical engineering, except the study by Li et al. [4], who claimed that their approach can take account of both sources of measurement data, although they provided an explicit relationship between the response and the property of interest in their case. The relationship between the soil response and soil property, however, does not have an explicit form in most cases. Therefore, this paper presents a framework for uncertainty reduction in soil deposits with spatial variability by conditioning a random field using both direct soil property measurements and indirect soil response measurements. A numerical soil excavation example was used to demonstrate the improvement of soil property field and the soil deformation estimations during various stages of excavation. The idea is to show the efficiency of the two sources of information when used to condition the random fields of soil properties and their relative contribution to the overall uncertainty reduction in the performance.

2. RF Model: Unconditional Random Field Generation

Random fields (RF) are used for representing spatially variable soil properties, and they have found extensive use in practical geotechnical applications [9]. They are usually used in combination with the finite element method to investigate the uncertainties in the soil structure response. There are various methods of representing random fields in finite element analysis [10, 11], including: (i) midpoint or nodal point method [12], in which the field within the domain of an element is described by a single random variable representing the value of the field at a central point of the element; (ii) spatial averaging method [13], which describes the field within each element in terms of the spatial average of the field over the element; (iii) shape function method [14], which describes the random field within an element in terms of a set of nodal values and corresponding shape functions; and (iv) series expansion method, such as Karhunen–Loeve expansion, which expresses the field in terms of its spectral decomposition [15].

Classical statistical characteristics of soil properties, in the case of describing the soil properties as single variables, include the parameters defining the probability distribution of the variable, such as the mean value (μ), standard deviation (σ) or variance (σ^2), and coefficient of variation (COV) ($V = \sigma/\mu$). In the case of spatial variability, an additional parameter, the scale of fluctuation (SOF) (θ) [16], which measures the distance over which soil property values show relatively strong correlation from point to point in space, should be introduced.

The local average subdivision (LAS) method, which falls in the category of “spatial averaging”, is used in this paper to generate random field realisations of spatially varying soil properties, using the aforementioned soil statistical parameters and a certain form of spatial correlation function parametrized by SOF. In the case that the scale of fluctuation

is direction-dependent, the anisotropy of correlation distance of the soil spatial heterogeneity ($\xi = \theta_h/\theta_v$) is modelled by defining different values of SOF in the vertical and horizontal directions (i.e., θ_v and θ_h , respectively) for horizontally deposited soil mass. This has previously been reported and implemented, for example, by Hicks and Samy [17] and Hicks and Spencer [18] and Li et al. [19] in 2D and 3D, respectively.

A frequently used autocorrelation function for generating random fields is of the exponential form and is used in this study; that is,

$$\rho(\tau_1, \tau_2) = \exp\left(-\sqrt{\left(\frac{2\tau_1}{\theta_1}\right)^2 + \left(\frac{2\tau_2}{\theta_2}\right)^2}\right), \quad (1)$$

where τ is the lag distance between two points in space and subscripts 1 and 2 denote the vertical and lateral coordinate direction, respectively.

Note that the local average subdivision (LAS) algorithm itself is incapable of preserving correlation anisotropy [20]. In case an anisotropic field is desired, an isotropic random field (i.e., $\theta_1 = \theta_2$) can initially be generated, and this isotropic field can then be postprocessed to give the target anisotropic random field. That is, an anisotropic field can be obtained by squashing and/or stretching the isotropic field in the vertical and/or horizontal directions, respectively. However, due to the scarcity of data intensity in the horizontal direction, the horizontal characterization of spatial correlation is often less frequently seen in geotechnical engineering. Although evidence has shown that correlation of soil properties tends to be stronger in the horizontal direction than that in the vertical direction, this paper focuses on isotropic correlation to show the effect of conditioning. It is believed that the effect only differs in the magnitude of uncertainty reduction for an anisotropically correlated field.

3. RF Model: Conditional Random Field Generation via Kriging and EnKF

Conditional random fields using kriging and EnKF are used in this paper to investigate their effects on reducing the uncertainties of spatially varying soil parameter realisations and thereby on the uncertainty reduction of soil excavation displacements. Random fields of soil properties conditioned on direct property measurements and/or indirect response measurements via kriging and EnKF are briefly introduced here, respectively.

3.1. Generation of Conditional Random Fields via Kriging. The generation of a conditional random field involves two steps [5]: (i) generation of an unconditional random field, $\mathbf{E}_{ru}^i(\mathbf{x}) = (E_1, E_2, \dots, E_n)^T$, of the spatial variability of soil properties (where \mathbf{x} denotes a location in space, n is the number of locations representing the random field, and i denotes the realisation number); (ii) conditioning the random field, e.g., kriging estimates, \mathbf{E}_{km} , based on measured

values at $\mathbf{x}_j (j = 1, 2, \dots, N_k)$ and kriging estimates, \mathbf{E}_{ks}^i , based on unconditionally (or randomly) simulated values at the same positions $\mathbf{x}_j (j = 1, 2, \dots, N_k)$, where N_k is the number of direct measurement locations, are combined with \mathbf{E}_{ru}^i from step (i) to give the conditional random field, \mathbf{E}_{rc}^i , that is,

$$\mathbf{E}_{rc}^i(\mathbf{x}) = \mathbf{E}_{km}(\mathbf{x}) + (\mathbf{E}_{ru}^i(\mathbf{x}) - \mathbf{E}_{ks}^i(\mathbf{x})). \quad (2)$$

It is noted that the superscript i is absent in the aforementioned equation for $\mathbf{E}_{km}(\mathbf{x})$. This is because the kriging estimation based on measurements does not need to be performed for each realisation of the random field; it only needs to be performed once and it is the same for all realisations.

3.2. Generation of Conditional Random Fields via EnKF. This paper uses the method developed by the second author in an earlier study [8] and the method description partly reproduces their wording. The method is now presented in the context of a soil excavation problem for easy understanding. The EnKF method follows an iterative process, in which each iteration contains two steps: forecast and update. For applying the EnKF to stochastic soil excavation problems, a state vector has to be constructed to incorporate both unknown local deformation parameters (e.g., elastic modulus) and measurements of soil displacements. This is expressed as

$$\mathbf{Z}_i = \begin{pmatrix} \mathbf{E}^i \\ \mathbf{d}^i \end{pmatrix}, \quad (3)$$

where subscript i represents an realisation of the ensemble;

$$\mathbf{E}^i = (E_1, E_2, \dots, E_n)^T, \quad (4)$$

is the vector of normally distributed elastic modulus ($\mathbf{E}^i = \mathbf{E}_{rc}^i$ for conditional random fields based on kriging and $\mathbf{E}^i = \mathbf{E}_{ru}^i$ for unconditional random fields);

$$\mathbf{d}^i = (d_1, d_2, \dots, d_m)^T, \quad (5)$$

is the vector of displacements computed at the measurement locations; n and m are the number of unknown elastic modulus values and soil displacement measurements, respectively.

In this investigation, the number of unknown elastic modulus values is equal to the number of elements in the finite element mesh. In the EnKF, an ensemble of N state vectors is used to simulate the initial estimation of the elastic modulus field, that is,

$$\mathbf{Z} = [\mathbf{Z}_1, \mathbf{Z}_2, \dots, \mathbf{Z}_N]. \quad (6)$$

In the forecasting step of each iteration, the ensemble of state vectors is forecasted to the second (i.e., update) step by the model describing the problem (i.e., the finite element model), that is,

$$\mathbf{Z}_t = F(\mathbf{Z}_{t-1}), \quad (7)$$

where t is the iteration number in the EnKF. In this case, the soil excavation model is utilised to compute the displacements

for all realisations of the ensemble, based on the updated elastic modulus fields from the end of the previous iteration. After the forecasting step, the computed displacements at the measurement locations in the forecasted ensemble of state vectors are compared with the collected "real" displacement measurements. The ensemble of state vectors is then updated (with respect to elastic modulus) by

$$\begin{aligned} \mathbf{Z}_t^{\text{udt}} &= \mathbf{Z}_t^f + \mathbf{K}_G(\mathbf{D} - \mathbf{H}\mathbf{Z}_t^f), \\ \mathbf{D} &= [\mathbf{d}^1, \mathbf{d}^2, \dots, \mathbf{d}^N], \\ \mathbf{d}^i &= \mathbf{d}^* + \boldsymbol{\varepsilon}_i, \end{aligned} \quad (8)$$

where $\mathbf{Z}_t^{\text{udt}}$ is the matrix containing the ensemble of updated state vectors, of dimensions $(m+n) \times N$, and \mathbf{Z}_t^f is the corresponding matrix of state vectors resulting from the forecasting step; \mathbf{D} is the matrix of measurement data perturbed by noise, of dimensions $m \times N$; \mathbf{d}^i is a vector of perturbed measurements; \mathbf{d}^* is the vector of real measurements; and $\boldsymbol{\varepsilon}_i$ is a vector of measurement errors added to the real measurements in order to create perturbed measurements. Each element in the error vector $\boldsymbol{\varepsilon}_i$ is randomly selected from a normal distribution with a zero mean and a variance defined by the input measurement error. Here, \mathbf{R} is a matrix based on $\boldsymbol{\varepsilon}_i$, that is,

$$\begin{aligned} \mathbf{R} &= \frac{\mathbf{e}\mathbf{e}^T}{N-1}, \\ \mathbf{e} &= (\boldsymbol{\varepsilon}_1, \boldsymbol{\varepsilon}_2, \dots, \boldsymbol{\varepsilon}_N). \end{aligned} \quad (9)$$

Also, with reference to equation (3), \mathbf{H} is the measurement operator which relates the state vector to the measurement points; it is in the form of $\mathbf{H} = [\mathbf{0} \mid \mathbf{I}]$, where $\mathbf{0}$ is an $m \times n$ null matrix and \mathbf{I} is an $m \times m$ identity matrix. \mathbf{K}_G is the Kalman gain derived from the minimization of the posterior error covariance of the ensemble of state vectors, that is,

$$\mathbf{K}_G = \mathbf{P}_t^f \mathbf{H}^T (\mathbf{H} \mathbf{P}_t^f \mathbf{H}^T + \mathbf{R})^{-1}, \quad (10)$$

$$\mathbf{P}_t^f = \frac{1}{N} (\mathbf{Z}_t^f - \bar{\mathbf{Z}}_t^f) (\mathbf{Z}_t^f - \bar{\mathbf{Z}}_t^f)^T,$$

where \mathbf{P}_t^f is the error covariance matrix of the ensemble of forecasted state vectors and $\bar{\mathbf{Z}}_t^f$ is the ensemble mean of \mathbf{Z}_t^f , that is,

$$\bar{\mathbf{Z}}_t^f = \mathbf{Z}_t^f \mathbf{1}_N, \quad (11)$$

where $\mathbf{1}_N$ is a matrix in which each element is equal to $1/N$.

At the end of the iteration process, the ensemble mean is considered to be the best estimate of the elastic modulus field, and the soil displacement field can then be updated based on the best estimation.

It is worth noting that kriging can also be used to interpolate the soil responses such as displacements to produce a kriged displacement field. However, the displacement monitoring points are often not intensive enough to allow an accurate estimation of the covariance between displacements

at different points. This form of conditioning is not pursued in this study.

4. Methodology: The Random Finite Element Method

The random finite element method (RFEM) is used to compute the geotechnical structure (e.g., soil excavation) response (e.g., displacement) within a Monte Carlo framework [9]. The procedure is as follows:

- (1) Generate random property fields (either conditional or unconditional), for example, using the local average subdivision (LAS) method [21] (combined with kriging for conditional fields), based on the soil property statistics, e.g., mean, standard deviation, and spatial correlation structure (type of correlation function and horizontal and vertical scales of fluctuation, θ_h and θ_v , respectively);
- (2) Map (conditional or unconditional) random field cell values onto the finite elements within the finite element mesh modelling the given problem (in this case, a soil excavation problem);
- (3) Carry out a traditional finite element (FE) analysis (e.g., staged excavation) [22];
- (4) Repeat the aforementioned steps for multiple realisations in a Monte Carlo analysis (e.g., the number of realisations $N_{mc} = 1000$ in this case) until the output statistics (e.g., mean and standard deviation of the soil displacement) converge.

For a given set of statistics, a probability distribution of the displacement response can be obtained.

An existing finite element program [22] capable of simulating sequential soil excavation is used in this investigation. The excavation is simulated by the removal of elements and the application of forces thus generated to the new boundary. The boundary forces at the i th stage of an excavation are given by

$$F_i = \int_V \mathbf{B}^T \boldsymbol{\sigma}_{i-1} dV - \int_V \mathbf{N}^T \gamma dV, \quad (12)$$

where \mathbf{B} is the strain-displacement matrix, V is the excavated volume, \mathbf{N} is the element shape function, and γ the soil unit weight. The first term is the nodal internal resisting force vector due to the stresses $\boldsymbol{\sigma}$ in the removed elements, and the second term is the reversal of the nodal body-load forces of the removed elements assuming γ (the body-load due to gravity) is acting downwards (negative in this case).

A hypothetical soil excavation problem is considered in this study. Figure 1 shows the finite element mesh of the vertical excavation problem (4 m \times 4 m domain with an element size of 0.5 m \times 0.5 m). The boundary conditions are fixed base and rollers on left and right sides. The meshes used were made up of 8-node quadrilateral elements. Nonlinear elasto-plastic behaviour was assumed with the shear strength defined by a Mohr-Coulomb failure envelope with parameters c and ϕ . A viscoplastic algorithm was used to redistribute the violating stresses in an iterative manner.

Reduced integration was used throughout the mesh. A soil deposit characterised by undrained shear strength $c_u = 9$ kPa was to be excavated in sequence. The unit weight of the soil is $\gamma = 20$ kN/m³, and Poisson's ratio is $\nu = 0.49$. The elastic modulus is assumed to be spatially variable, with a mean of $\mu_E = 1.0 \times 10^5$ kPa, coefficient of variation of $V_E = 0.2$, and an isotropic scale of fluctuation of $\theta = 1$ m. For the present case, the vertical excavation is to occur in 4 steps, leading to a cut of depth 2 m. As can be seen from Figure 1, the first excavation removes elements 5–8, and the second excavation removes elements 13–16 and so on until the fourth excavation. For a vertical cut consisting of undrained clay with a strength of 9 kPa, Taylor [23] predicts a critical height of approximately 1.73 m which is well within the range of the 4th excavation. Twelve inclinometers have been “instrumented on-site” to monitor the displacement field during excavation and these are shown in Figure 1 as well. In order to investigate how the conditional simulation affects the response uncertainties in displacements, a node in the mesh has been selected as the target node to investigate the uncertainty reduction and this is also shown in Figure 1.

Note that LAS has been used to generate 1000 random fields as initial ensemble members. It has also been used to generate a single reference realisation, based on the same statistics as used for the ensemble. This is to represent “real” values of elastic modulus (as might be obtained from the field) and has been used in the FE excavation analysis to produce “real” data of monitored displacements (i.e., at 12 locations) to be assimilated.

Note also that usually soil excavations are supported by structural elements during excavation [24, 25]. This paper, however, investigates the excavation problem without referring to specific supports for simplicity, partly due to the excavation being only 2 m deep. Soil excavation is a typical soil-structure interaction problem where either the soil performance or the structural element performance may be unsatisfactory during excavation. A more realistic analysis considering the performance of both the soil and the structural element is an ongoing research subject for authors (i.e., for deep excavations).

5. Results and Discussion of Conditional Simulation of Soil Excavation

This section presents the results of the conditional simulation of a soil excavation problem stated in the previous section. The results are presented here in three categories, i.e., when direct information or indirect response information is used or when these two sources of information are combined.

5.1. Conditional Simulation via Kriging (Direct Information).

Soil elastic modulus can be measured from laboratory or in situ tests. It can also be estimated based on correlation with other soil properties [26]. In the laboratory, it can be determined from the triaxial test or from the oedometer test (indirectly). On-site, it can be estimated from the standard penetration test (SPT), cone penetration test (CPT),

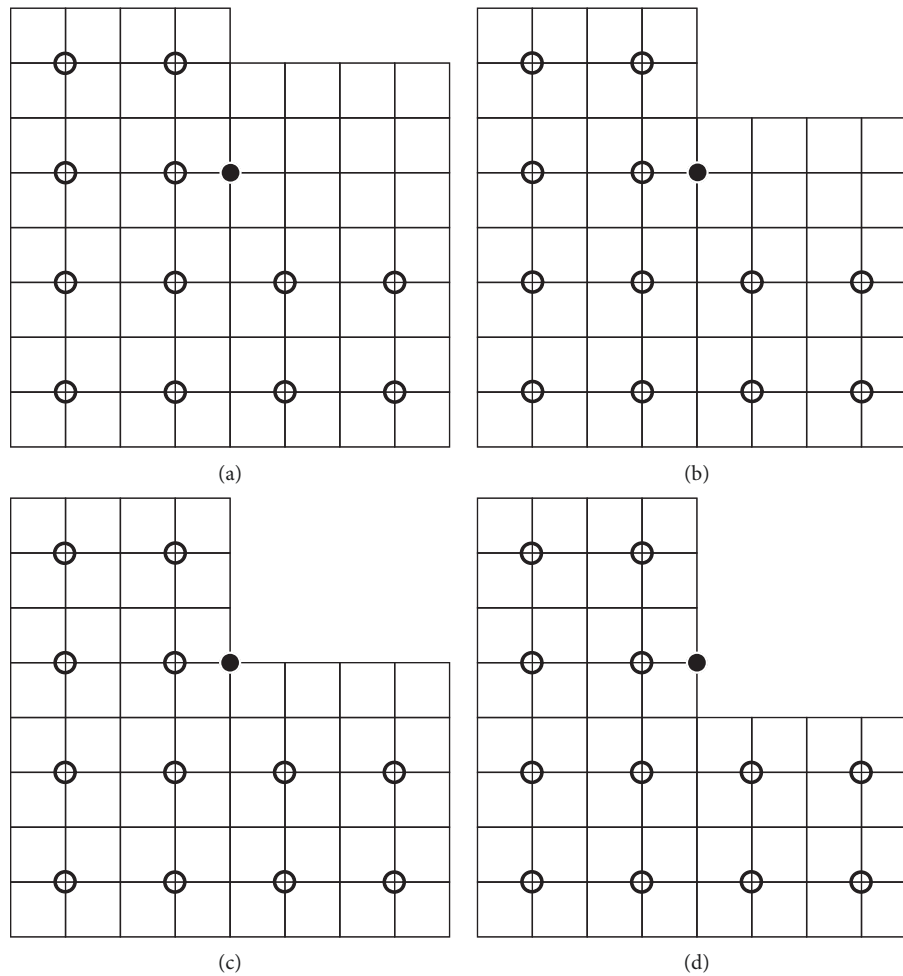


FIGURE 1: Finite element mesh and excavation sequence: 1st layer excavation (a), 2nd layer excavation (b), 3rd layer excavation (c), and 4th layer excavation (d) (circles indicate 12 displacement measurement locations, and the dot indicates the target node where uncertainties in displacements are to be investigated).

pressuremeter test or dilatometer test (indirectly). This paper assumes that the elastic modulus is estimated based on correlation with soil undrained shear strength, which is in turn correlated with CPT measurements. Therefore, known measurements are assumed to be arranged in the form of columns of elements in the following sections, i.e., in the same way as CPTs are taken.

Figures 2 and 3 show two example realisations of the elastic modulus fields, respectively, for the case where one CPT is taken at the second column. In both figures, various fields are presented in the following sequence: an unconditional field, an conditional field, a kriged field based on randomly generated values at measurement locations, and the kriged field based on measurement values. The field values are shown in grey scale, with black cells denoting small values and white cells high values. Also, the two figures use the same global color scale in order to better compare between realisations. It is seen that the variation between realisations reduces upon conditioning, i.e., variations between figures 2(b) and 3(b) are less apparent than variations between figures 2(a) and 3(a). Moreover, the kriged fields are smoother (either based on random values or measurement

values), compared to both conditional and unconditional fields. This highlights the difference between random field simulation and kriging estimation, i.e., random field simulation reproduces the spatial variation of the measured field whereas kriging estimation typically has a smoothing effect on real data.

Similar to Figures 2 and 3, Figures 4 and 5 show two example realisations of the elastic modulus fields, when two CPTs are taken at the 2nd and 7th column, respectively. It is seen that by preserving the measurement values at the 7th column, the updated random fields (Figures 4(b) and 5(b)) become closer to the reference (actual) field (see Figure 6(a)); i.e., those realisations that include unrealistic values in the vicinity of the additional measurements have been updated.

Figures 7(a)–7(f) shows the normalised histograms and fitted probability density functions (PDF) of the horizontal (X) and vertical (Y) displacements of the target point, in the first three consecutive excavation steps, for unconditional simulation and conditional simulation honoring one CPT and two CPTs. It is worth noting that the displacements are relatively small due to the use of a large mean elastic modulus. The dashed vertical line in the figure represents the

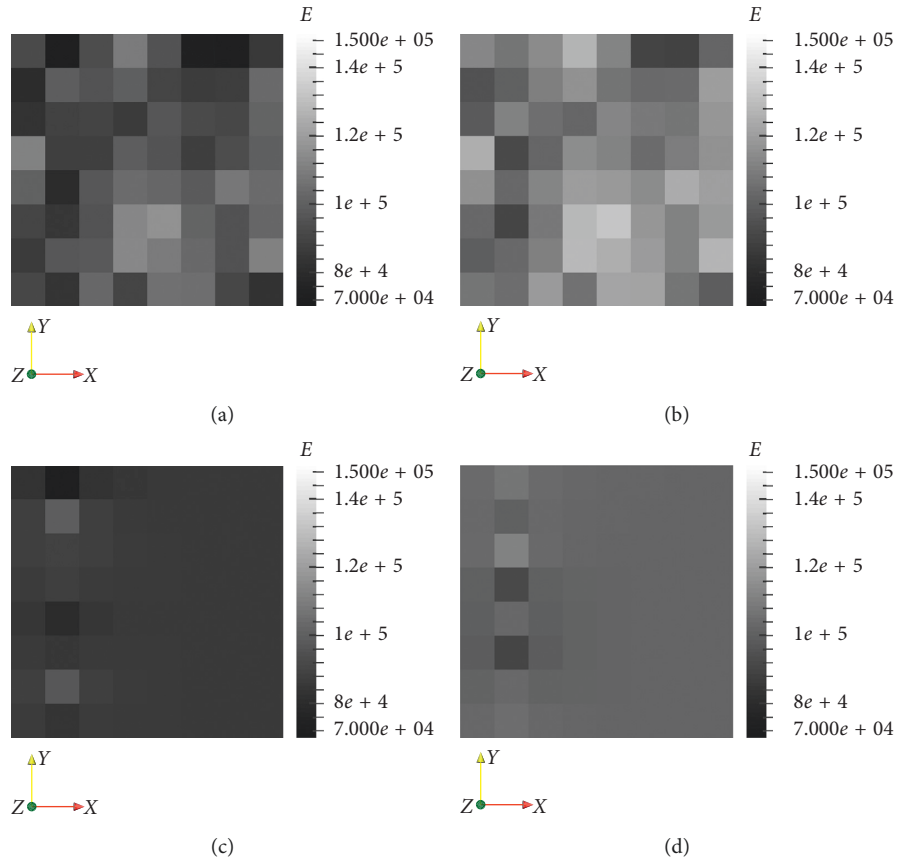


FIGURE 2: Example realisation i for unconditional field (a), conditional field (b), kriged field based on random field values at measurement locations (c), and kriged field based on measurement values (d), 1 CPT.

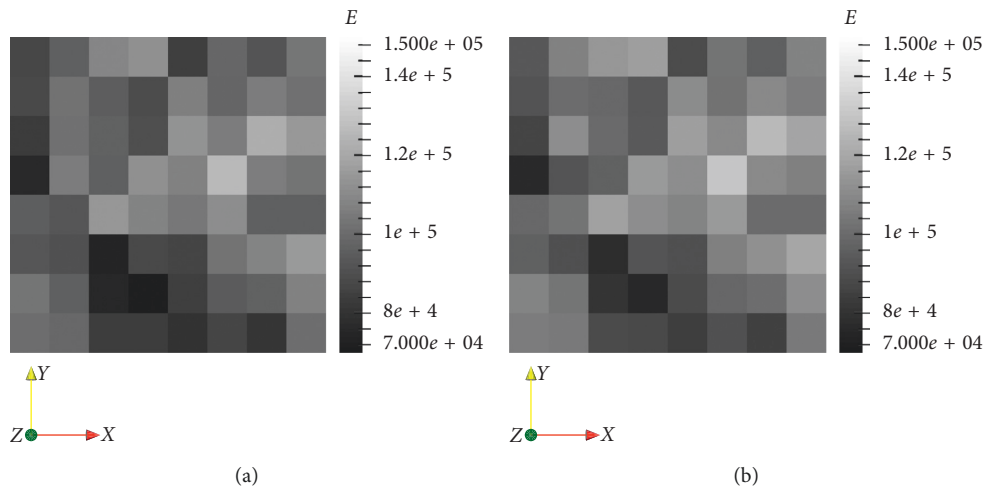


FIGURE 3: Continued.

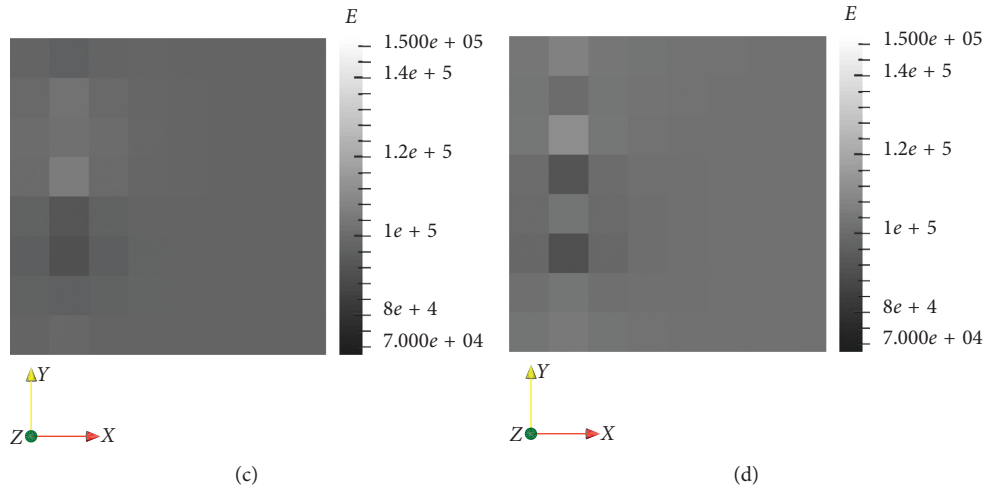


FIGURE 3: Example realization j for unconditional field (a), conditional field (b), kriged field based on random field values at measurement locations (c), and kriged field based on measurement values (d), 1 CPT.

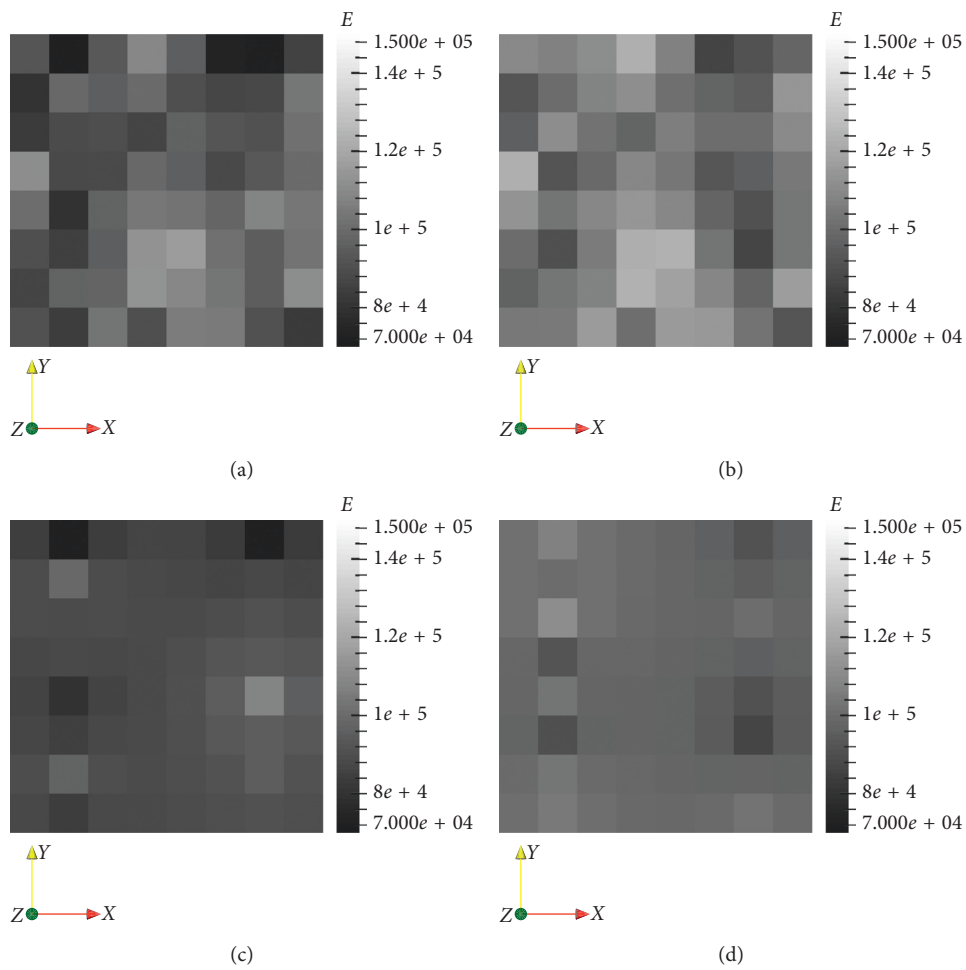


FIGURE 4: Example realization i for unconditional field (a), conditional field (b), kriged field based on random field values at measurement locations (c), and kriged field based on measurement values (d), 2 CPTs.

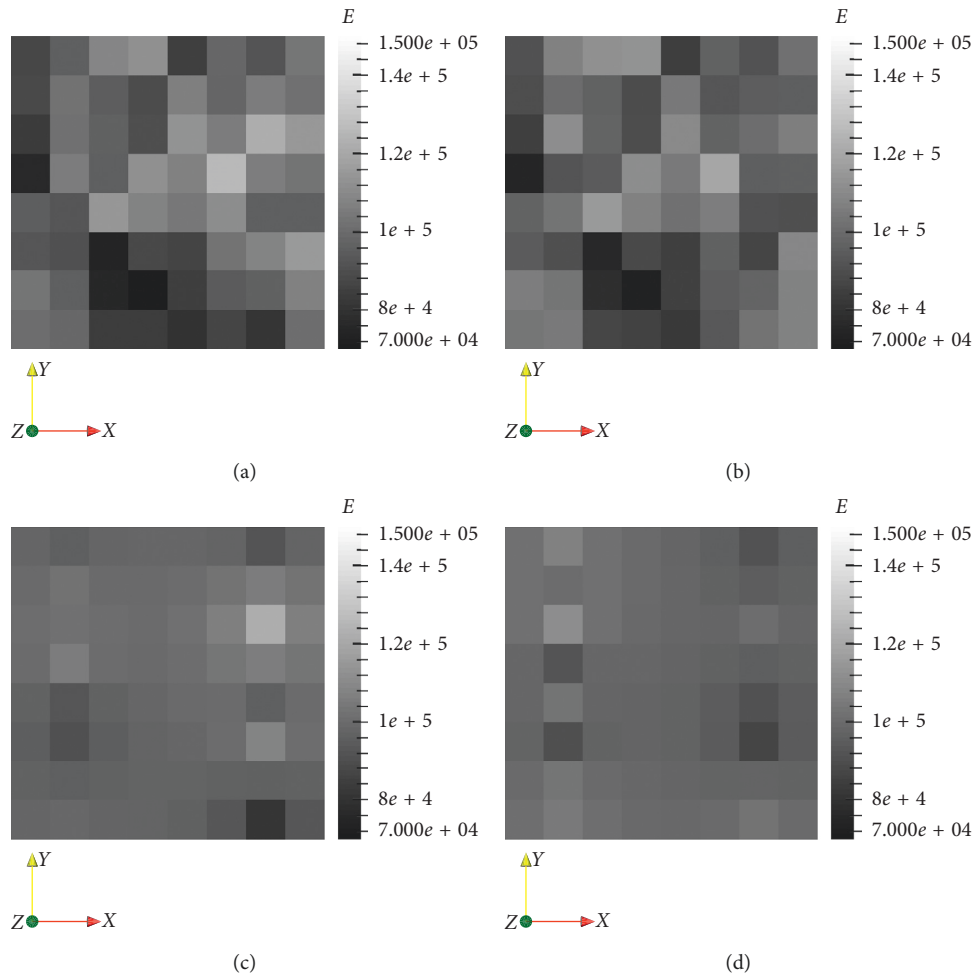


FIGURE 5: Example realisation j for unconditional field (a), conditional field (b), kriged field based on random field values at measurement locations (c), and kriged field based on measurement values (d), 2 CPTs.

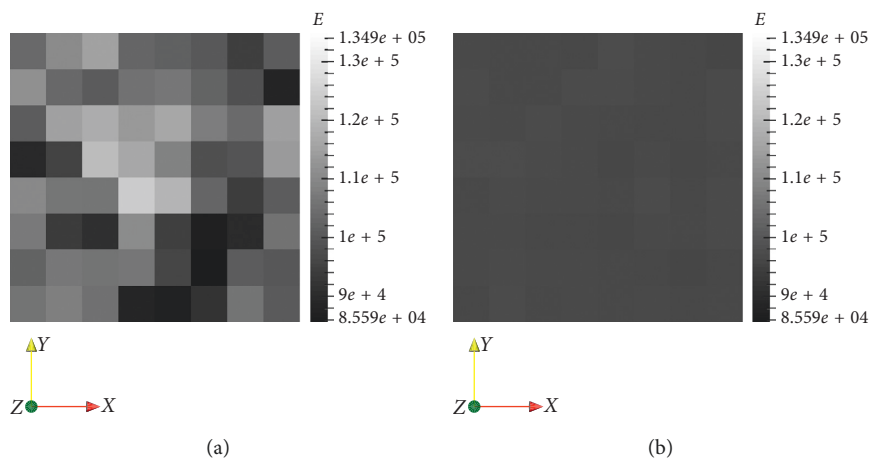


FIGURE 6: Continued.

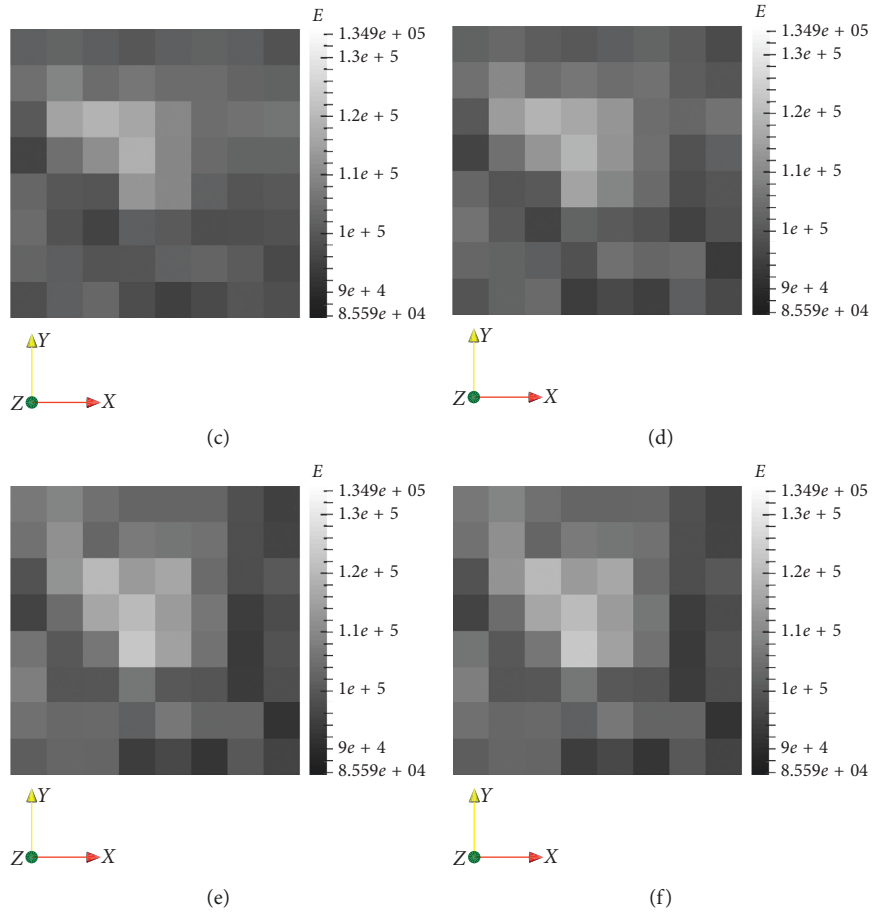


FIGURE 6: Reference field (a), initial estimation (i.e., ensemble mean) (b), updated estimation after excavating the 1st layer (c), updated estimation after excavating the 2nd layer (d), updated estimation after excavating the 3rd layer (e), and updated estimation after excavating the 4th layer (f).

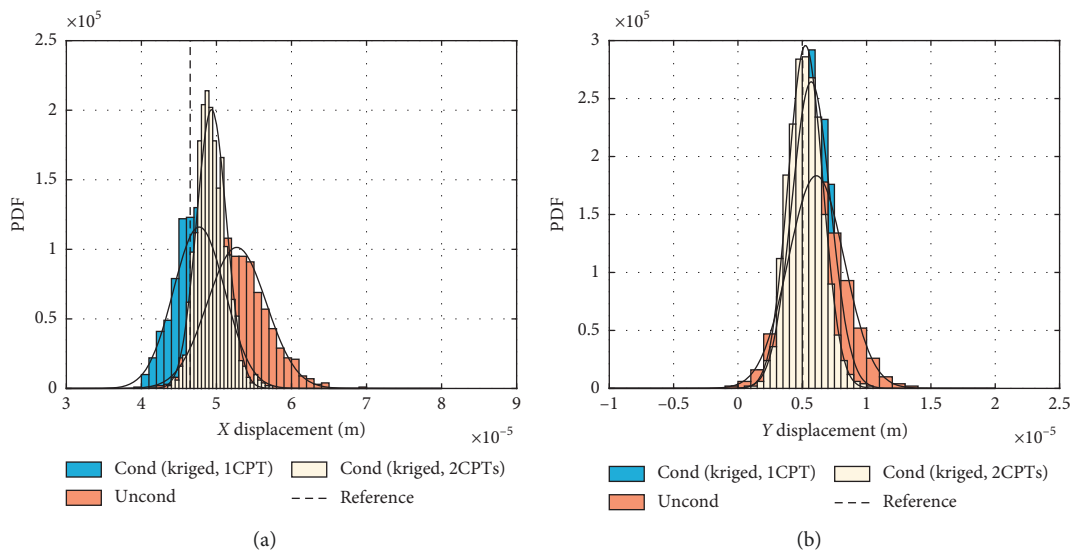


FIGURE 7: Continued.

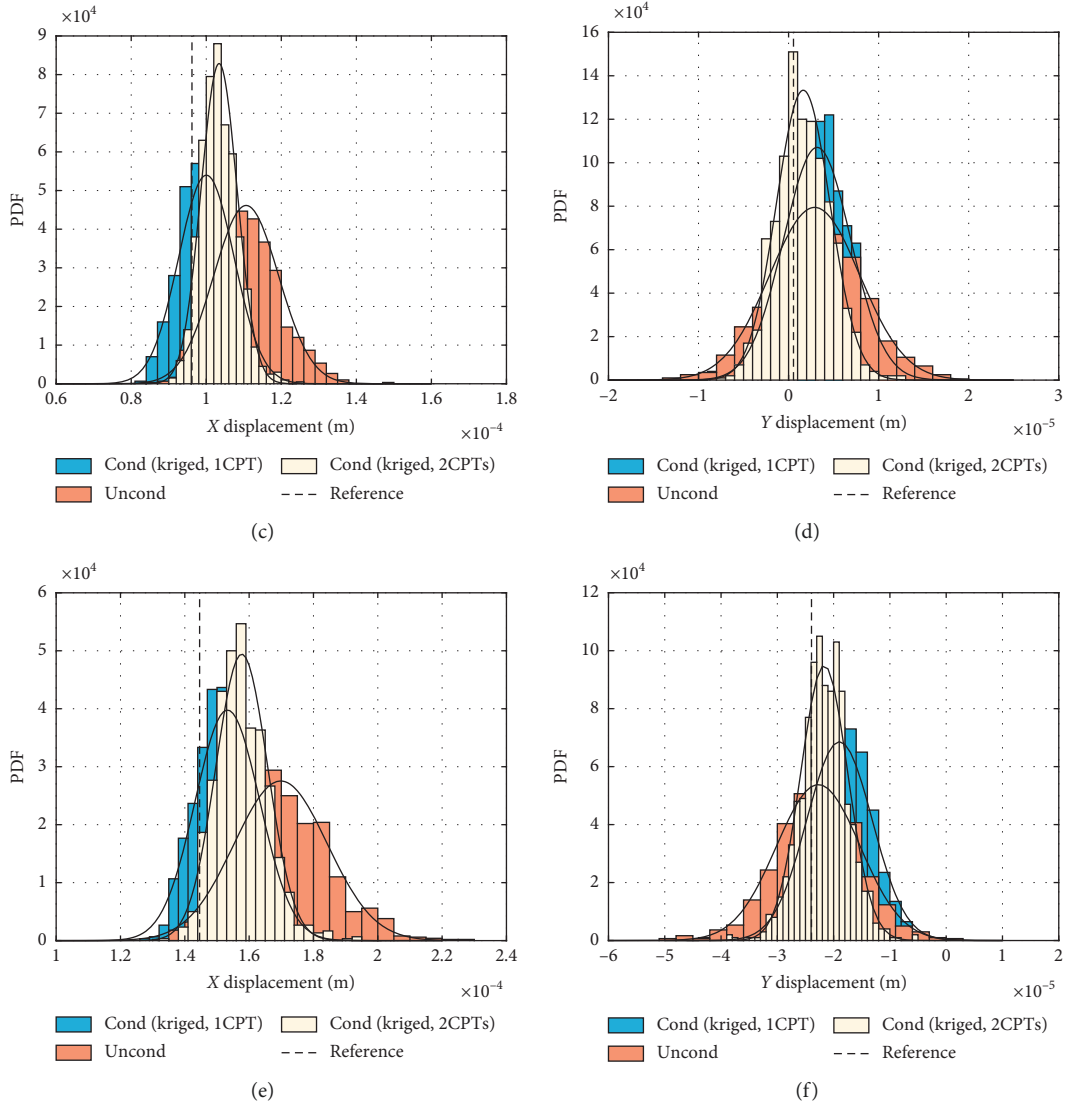


FIGURE 7: PDF of target point displacements in excavation steps 1–3: comparison between unconditional simulation and conditional simulation based on 1 CPT measurement and 2 CPT measurements. (a) First layer excavation (X), (b) first layer excavation (Y), (c) second layer excavation (X), (d) second layer excavation (Y), (e) third layer excavation (X), and (f) third layer excavation (Y).

reference value, that is, the FE analysis calculated value based on the reference field. It is seen that the uncertainties in the displacements reduce as a result of including the measurement values in the elastic modulus field. Moreover, the uncertainty reduction (i.e., as indicated by the decreasing standard deviation of the probability distribution) when considering two CPTs is larger compared to that when considering only one CPT. In order to quantify the uncertainty reduction, a performance-based uncertainty reduction ratio is defined as

$$u_d^i = \sigma_{\text{cond}}^i / \sigma_{\text{uncond}}^i, \quad (13)$$

where σ_{cond}^i and σ_{uncond}^i denote the standard deviation of the probability distribution of the i th step X or Y displacements of the target points in the conditional and unconditional simulation, respectively. In this case, $u_d^1 = 0.8739$ for 1 CPT

conditioning and $u_d^1 = 0.5060$ for 2 CPTs when assessing the uncertainties in the 1st step X displacement of the target point. The uncertainty reduction ratios of the X and Y displacements in the three excavation steps are shown in Tables 1 and 2, respectively.

5.2. Conditional Simulation via EnKF (Indirect Information).

The measured responses, i.e., displacements, are used in this section to investigate the effect of the inclusion of such indirect information on the probability distributions of the excavation displacements. To facilitate understanding, a flowchart in the case of a soil excavation problem is shown in Figure 8. Similar to the previous section, probability updating is presented specifically for the target point, although the analysis has more or less the same effect on other node points.

TABLE 1: Uncertainty reduction ratio u_d^i in X displacements.

Excavation step	Conditional 1 CPT	Conditional 2 CPTs	Conditional EnKF	Conditional 1 CPT + EnKF	Conditional 2 CPTs + EnKF
1	0.8739	0.5060	—	—	—
2	0.8548	0.5568	0.4861	0.4085	0.2640
3	0.6921	0.5571	0.3368	0.2520	0.1827

TABLE 2: Uncertainty reduction ratio u_d^i in Y displacements.

Excavation step	Conditional 1 CPT	Conditional 2 CPTs	Conditional EnKF	Conditional 1 CPT + EnKF	Conditional 2 CPTs + EnKF
1	0.6936	0.6202	—	—	—
2	0.7244	0.5958	0.6106	0.4592	0.3914
3	0.7846	0.5669	0.4907	0.3757	0.3492

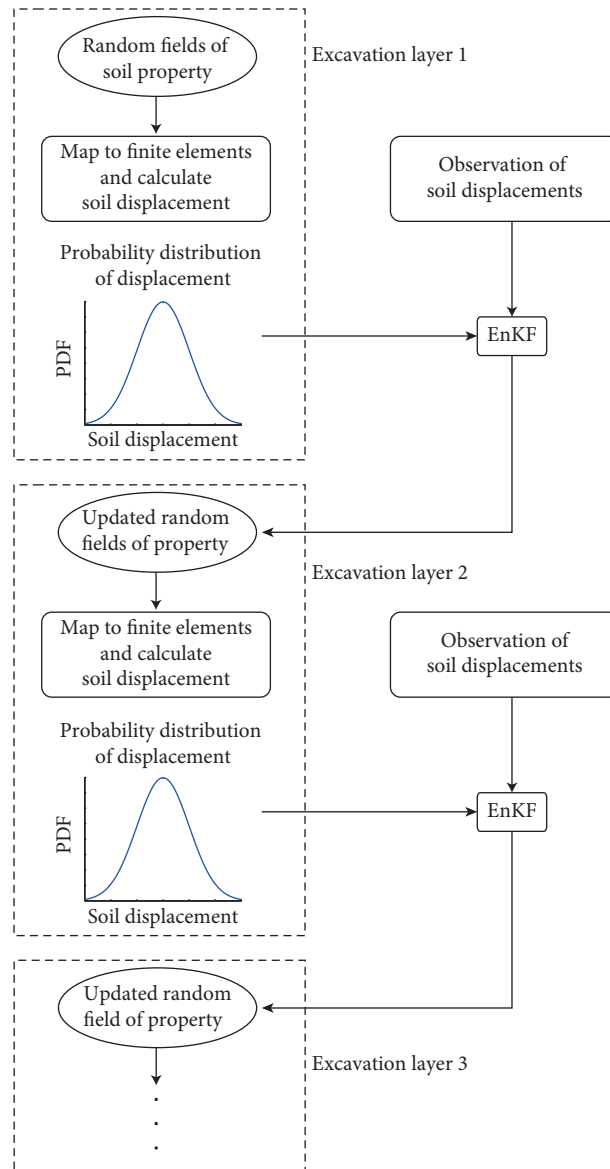


FIGURE 8: Flowchart of the conditional simulation via EnKF.

In order to reduce the uncertainties in the displacement responses, the inverse modelling technique EnKF is used. Figure 6 shows the initial estimation of the field

when there are no displacement measurements and the updated field estimation after 4 excavation layers, respectively. The reference field is also shown in the figure. It

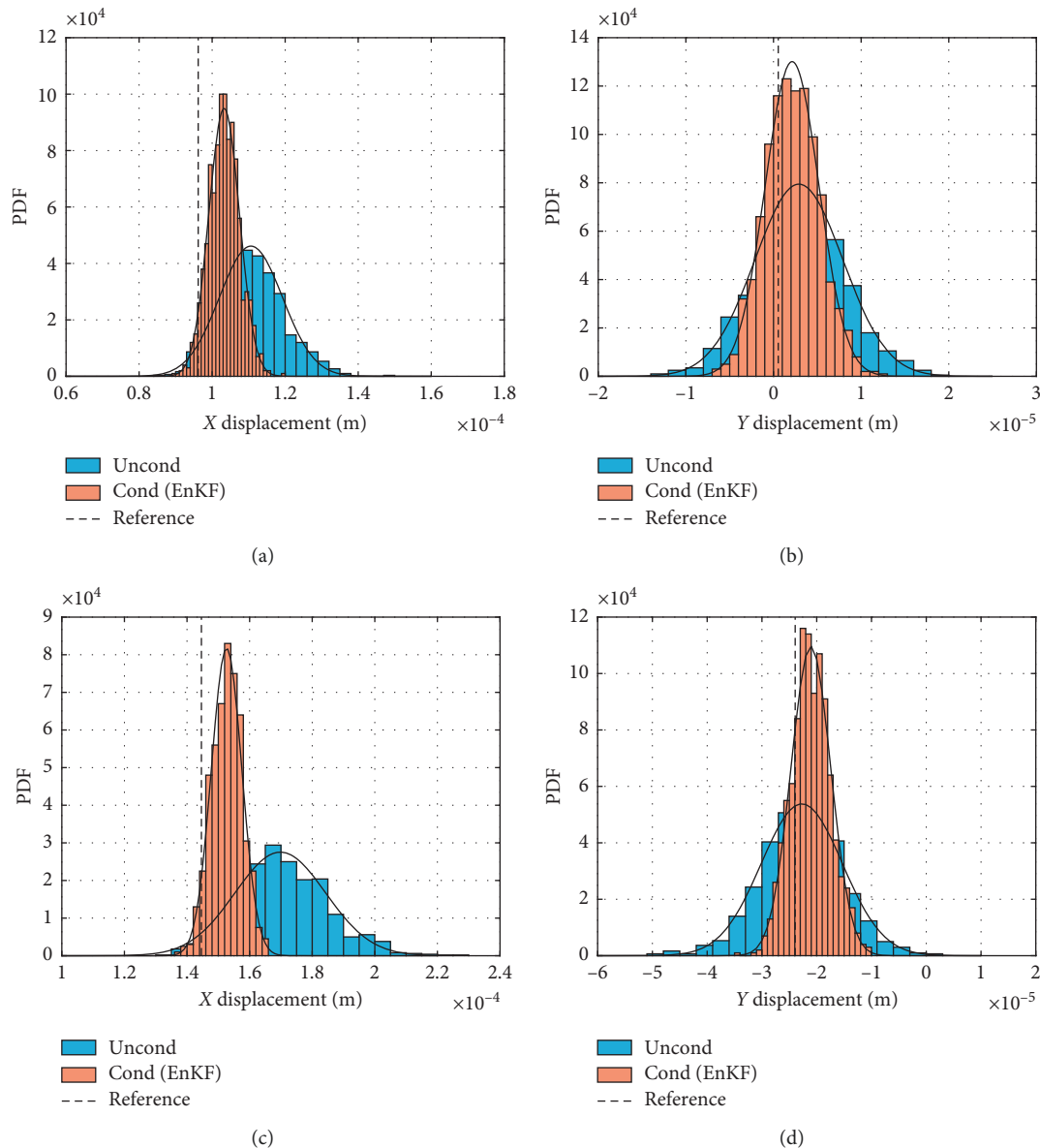


FIGURE 9: PDF of target point displacements in excavation steps 2-3: comparison between unconditional simulation and conditional simulation based on displacement measurements. (a) Second layer excavation (X), (b) second layer excavation (Y), (c) third layer excavation (X), and (d) third layer excavation (Y).

is seen that after the first excavation step, the field estimation starts to improve. After the second excavation layer, the field estimation is closer to the reference field. The field resembles the reference field after the 3rd and 4th excavation layer.

Figure 9 shows the effect of updating the elastic modulus field on the probability distributions of the target point displacements in the 2nd and 3rd excavation steps, respectively. It is seen that the conditional simulation via EnKF reduces the displacement variation, i.e., it reduces the variance of the distribution. The distribution moves closer to the reference values that are obtained from the reference field. Also, a comparison with previous conditional simulation results (i.e., Figures 7(c)–7(f) and Tables 1 and 2) indicates that conditional simulation via EnKF has a larger

effect on the uncertainty reduction than conditional simulation via kriging 1 CPT measurement (at the 2nd column in this case), although the differences are smaller for conditional simulation via kriging 2 CPTs. Note that the relative effect of EnKF and kriging may change for a different case. It is a function of a number of factors including the number and relative arrangement of displacement monitoring points and the number and relative positioning of direct measurements (e.g., CPT).

5.3. Conditional Simulation via Both Kriging and EnKF. The two techniques have been combined in this section to investigate the effect on the excavation problem, as more often both direct measurements and indirect monitoring

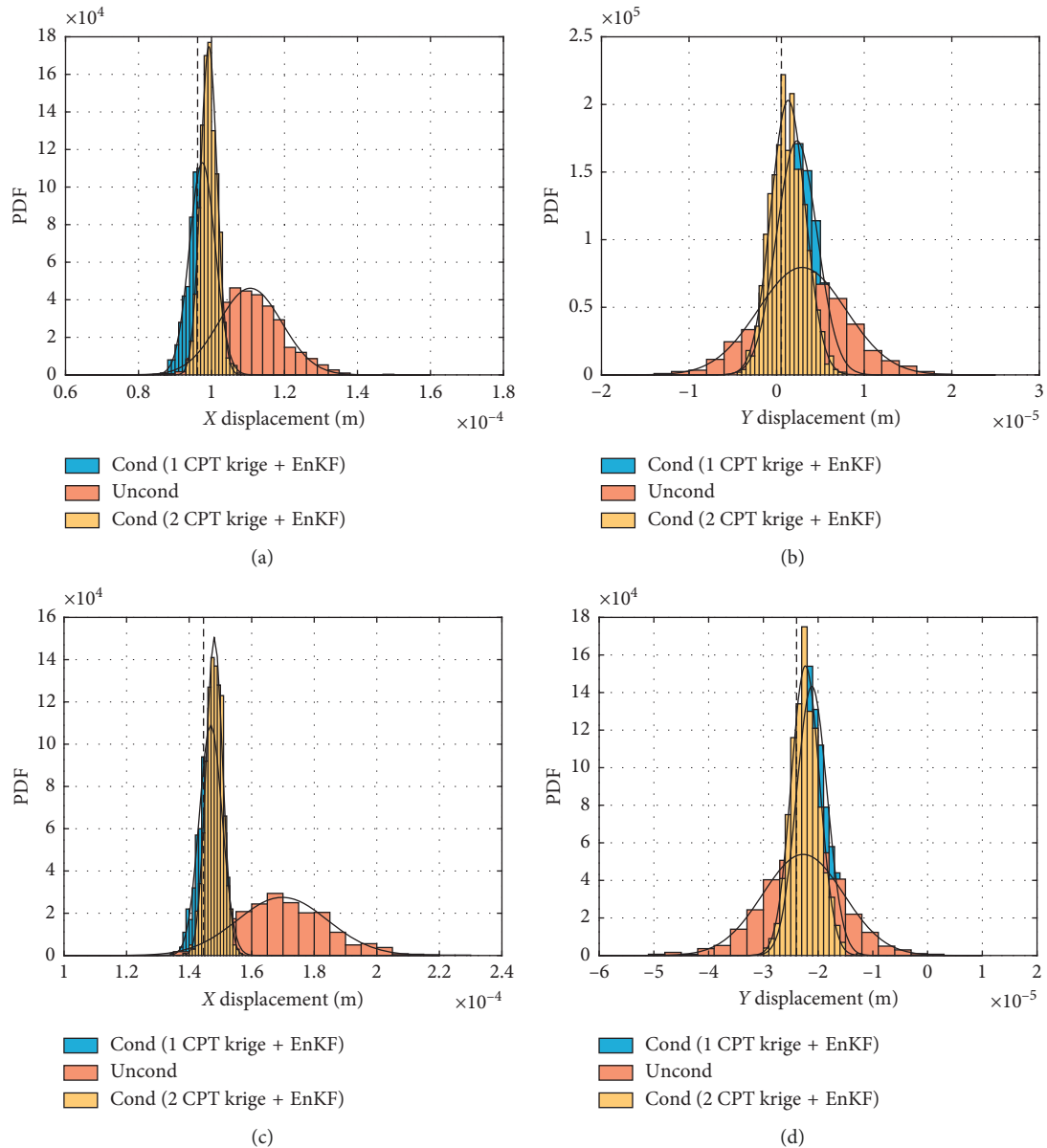


FIGURE 10: PDF of target point displacements in excavation steps 2-3: comparison between unconditional simulation and conditional simulation based on CPT and displacement measurements. (a) Second layer excavation (X), (b) second layer excavation (Y), (c) third layer excavation (X), and (d) third layer excavation (Y).

data are available. Figure 10 shows PDFs of displacement responses of the target point for the unconditional simulation, the conditional simulation via EnKF and kriging 1 CPT, and the conditional simulation via EnKF and kriging 2 CPTs. In contrast to EnKF (Figure 9) or kriging (Figure 7) alone, combining EnKF and kriging produces a probability distribution that is narrower and closer to the reference value. The uncertainty reduction ratios shown in Tables 1 and 2 clearly demonstrate this effect.

6. Conclusions

The paper presents a framework to reduce uncertainty in soil spatial variability and thus in soil structure performance through conditional simulation of the soil property field, by making use

of either the direct measurement data or the indirect response monitoring data. A hypothetical soil excavation example is used to demonstrate the updating of the probability distributions of soil displacement in the series of excavation steps.

It is first shown that conditional simulation based on direct measurements can reduce the range of possible field realisations and therefore the uncertainty (indicated by the variance of the probability distribution) in the displacement responses. Then it is illustrated that the EnKF can be used efficiently to improve the knowledge on the soil property field (i.e., soil elastic modulus in this case) and on the displacement probability of the excavation pit. It is found that in the present study, the EnKF is more efficient in reducing the displacement uncertainty than kriging only one CPT test. Although increasing the number of direct CPT

measurements reduces the difference between the two, the conditional simulation based on EnKF is still more efficient in most cases. However, the performance of the two conditional simulations is believed to be dependent on the arrangement and number of direct measurement points and indirect monitoring points and the degree of spatial variability (i.e., the spatial fluctuation scale of the soil property in the ground).

Nevertheless, the results show that conditional simulation that makes use of all the available data (i.e., direct and indirect) can more effectively improve the prediction of soil displacements than conditional simulation that takes advantage of either one source of data. Moreover, EnKF can be effectively used to sequentially update the property field, following the excavation sequence. The implication is that this updating process can be continued step by step to direct and refine the construction process.

Data Availability

The data used to support the findings of this study are available from the corresponding author upon request.

Conflicts of Interest

The authors declare that they have no conflicts of interest.

Acknowledgments

The first author appreciates the financial support of the National Natural Science Foundation of China (grant no. 41807228) and the Fundamental Research Funds for the Central Universities (grant no. 2652017071), and the second author appreciates the financial support of the National Natural Science Foundation of China (grant no. 51908175).

References

- [1] K. K. Phoon and F. H. Kulhawy, "Characterization of geotechnical variability," *Canadian Geotechnical Journal*, vol. 36, no. 4, pp. 612–624, 1999.
- [2] Y. J. Li, *Reliability of long heterogeneous slopes in 3D- model performance and conditional simulation*, Ph.D. thesis, Delft University of Technology, Delft, Netherlands, 2017.
- [3] M. A. Hicks and Y. Li, "Influence of length effect on embankment slope reliability in 3D," *International Journal for Numerical and Analytical Methods in Geomechanics*, vol. 42, no. 7, pp. 891–915, 2018.
- [4] X. Y. Li, L. M. Zhang, and J. H. Li, "Using conditioned random field to characterize the variability of geologic profiles," *Journal of Geotechnical and Geoenvironmental Engineering*, vol. 142, no. 4, Article ID 04015096, 2015.
- [5] Y. J. Li, M. A. Hicks, and P. J. Vardon, "Uncertainty reduction and sampling efficiency in slope designs using 3D conditional random fields," *Computers and Geotechnics*, vol. 79, pp. 159–172, 2016.
- [6] D. G. Krige, "A statistical approach to some mine valuation and allied problems on the witwatersrand," M.S. thesis, University of the Witwatersrand, Johannesburg, Gauteng, South Africa, 1951.
- [7] M. K. Lo and A. Y. Leung, "Bayesian updating of subsurface spatial variability for improved prediction of braced excavation response," *Canadian Geotechnical Journal*, vol. 56, no. 8, pp. 1169–1183, 2018.
- [8] P. J. Vardon, K. Liu, and M. A. Hicks, "Reduction of slope stability uncertainty based on hydraulic measurement via inverse analysis," *Georisk: Assessment and Management of Risk for Engineered Systems and Geohazards*, vol. 10, no. 3, pp. 223–240, 2016.
- [9] G. A. Fenton and D. V. Griffiths, *Risk Assessment in Geotechnical Engineering*, John Wiley & Sons, New York, NY, USA, 2008.
- [10] C. C. Li and A. Der Kiureghian, "Optimal discretization of random fields," *Journal of Engineering Mechanics*, vol. 119, no. 6, pp. 1136–1154, 1993.
- [11] H. G. Matthies, C. E. Brenner, C. G. Bucher, and C. Guedes Soares, "Uncertainties in probabilistic numerical analysis of structures and solids-stochastic finite elements," *Structural Safety*, vol. 19, no. 3, pp. 283–336, 1997.
- [12] A. Der Kiureghian and J. B. Ke, "The stochastic finite element method in structural reliability," in *Stochastic Structural Mechanics*, pp. 84–109, Springer, New York, NY, USA, 1987.
- [13] E. Vanmarcke and M. Grigoriu, "Stochastic finite element analysis of simple beams," *Journal of Engineering Mechanics*, vol. 109, no. 5, pp. 1203–1214, 1983.
- [14] W. K. Liu, T. Belytschko, and A. Mani, "Random field finite elements," *International Journal for Numerical Methods in Engineering*, vol. 23, no. 10, pp. 1831–1845, 1986.
- [15] K. K. Phoon, S. P. Huang, and S. T. Quek, "Simulation of second-order processes using Karhunen-Loeve expansion," *Computers & Structures*, vol. 80, no. 12, pp. 1049–1060, 2002.
- [16] E. H. Vanmarcke, "Probabilistic characterization of soil profiles," in *Site Characterization & Exploration*, pp. 199–219, ASCE, Evanston, Illinois, USA, 1978.
- [17] M. A. Hicks and K. Samy, "Influence of heterogeneity on undrained clay slope stability," *Quarterly Journal of Engineering Geology and Hydrogeology*, vol. 35, no. 1, pp. 41–49, 2002.
- [18] M. A. Hicks and W. A. Spencer, "Influence of heterogeneity on the reliability and failure of a long 3D slope," *Computers and Geotechnics*, vol. 37, no. 7–8, pp. 948–955, 2010.
- [19] Y. J. Li, M. A. Hicks, and J. D. Nuttall, "Comparative analyses of slope reliability in 3D," *Engineering Geology*, vol. 196, pp. 12–23, 2015.
- [20] G. A. Fenton, "Error evaluation of three random-field generators," *Journal of Engineering Mechanics*, vol. 120, no. 12, pp. 2478–2497, 1994.
- [21] G. A. Fenton and E. H. Vanmarcke, "Simulation of random fields via local average subdivision," *Journal of Engineering Mechanics*, vol. 116, no. 8, pp. 1733–1749, 1990.
- [22] I. M. Smith and D. V. Griffiths, *Programming the Finite Element Method*, John Wiley & Sons, New York, NY, USA, 2005.
- [23] D. W. Taylor, "Stability of earth slopes," *Journal of the Boston Society of Civil Engineers*, vol. 24, pp. 197–246, 1937.
- [24] Z. Luo, S. Atamturktur, C. H. Juang, H. Huang, and P. S. Lin, "Probability of serviceability failure in a braced excavation in a spatially random field: fuzzy finite element approach," *Computers and Geotechnics*, vol. 38, no. 8, pp. 1031–1040, 2011.
- [25] W. Gong, C. Juang, and J. Martin, "A new framework for probabilistic analysis of the performance of a supported excavation in clay considering spatial variability," *Géotechnique*, vol. 67, pp. 546–552, 2016.
- [26] K.-K. Phoon and F. H. Kulhawy, "Evaluation of geotechnical property variability," *Canadian Geotechnical Journal*, vol. 36, no. 4, pp. 625–639, 1999.

Research Article

Rethinking the Water Leak Incident of Tunnel LUO09 to Prepare for a Challenging Future

Wen-Chieh Cheng ^{1,2,3}, Ge Li ^{2,3}, Annan Zhou ⁴, and Jian Xu ^{2,3}

¹Key Laboratory of Western China's Mineral Resource and Geological Engineering, Ministry of Education, Xi'an 710054, China

²School of Civil Engineering, Xi'an University of Architecture and Technology, Xi'an 710055, China

³Shaanxi Key Laboratory of Geotechnical and Underground Space Engineering (XAUAT), Xi'an 710055, China

⁴School of Engineering, Royal Melbourne Institute of Technology (RMIT), Melbourne, Victoria 3001, Australia

Correspondence should be addressed to Wen-Chieh Cheng; s2428030@gmail.com

Received 26 June 2019; Revised 3 September 2019; Accepted 10 September 2019; Published 7 October 2019

Academic Editor: Fan Gu

Copyright © 2019 Wen-Chieh Cheng et al. This is an open access article distributed under the Creative Commons Attribution License, which permits unrestricted use, distribution, and reproduction in any medium, provided the original work is properly cited.

Incident often occurs while deepening excavation pit and/or tunnelling underground pipelines although serious attention from practitioners, engineers, and scientists has received. Prevention and mitigation of incident have thus been deemed to be the key in developing sustainable infrastructure in urban areas. This study analyses and discusses an extensive water leak incident taken place throughout the parallel tunnels LUO09 construction in the soft alluvial deposits in Kaohsiung, Taiwan. Dumping sand bags and quick-set cement intervened the incident but in vain. The water leak incident is initiated by the piping. The existing vehicle underpass causes the jet-grout columns installed not exactly in the plumb. Their overlapping is estimated to be less than the design value of 60 cm, and some seepage-prone weak zones are thus developed. The measured hydraulic gradient being equal to 12.1 and existence of seepage-prone weak zones are deemed as the main cause initiating the water leak incident. The pinhole test results highlight not only the nonplastic nature of the Kaohsiung silt but also its vulnerability to piping under large hydraulic gradients. Some bullet points that indicate what engineers should do or avoid are learned and summarised.

1. Introduction

Braced excavation and/or shield tunnelling in soft ground with high piezometric levels leads to a high potential to trigger water leak incident. Such water leak into excavation pit or sewage pipeline can result in-ground collapse and damages to adjoining facilities. Prevention of such a leaking incident has thus been deemed to be the key in developing sustainable infrastructure in urban areas. Jo et al. [1] indicated that the migration of the fine particles mainly contributed to the ground sinking incident occurred in Seoul, Korea. Hou et al. [2] declared that the combined effects of the sewage pipeline corrosion, soil strength deterioration, and construction disturbance triggered a 20 m long, 14 m wide, and 12 m deep cave-in throughout soft soil tunnelling of Beijing metro line 10. Chen et al. [3] indicated

that the ground collapse occurred in a 15.7 m deep excavation in very sensitive clay in Hangzhou, China caused damages to the retaining structure and the water main and led to ground sinking of a road next to the excavation. Feng and Lu [4] reported that the bislurry grouting failed to stop the seepage causing a failure of retaining structure installed in very thick sand layers with a high phreatic surface during a metro station excavation in Nanchang, China. Tan and Lu [5] indicated that a flawed slab connector embedded in the silt and sand layers has been deemed as being the main cause to lead to a sudden outburst of groundwater while deepening a subway excavation in Shanghai, China. The above studies indicate that incident often occurs, accompanied with significant casualties and economic losses, while developing infrastructure in urban areas [6–15] and relates mostly the phenomenon of water leak despite several protective

measures available [15–23]. In spite that serious attention has been drawn, consensus on prevention and mitigation measures has not reached yet.

The objectives of this study are (1) to analyse and discuss the water leak incident occurred while deepening the middle sump pit of the parallel tunnels LUO09, (2) to reveal the triggering mechanism, with reference to the testimony from the men at work and the field measurements, and (3) to suggest preventive measures against similar leaking incident.

2. Description of Case History

2.1. Background. Two 837 m long, 6.1 m wide parallel tunnels LUO09 were excavated using the shield tunnelling method. A 6.24 m diameter earth pressure balance (EPB) shield was responsible for tunnel boring operations. Their ends are linked to the stations O7 and O8 of the Kaohsiung metro system, and a cross passage with a middle sump pit at 32.6 m depth was built for safety purpose. Several boreholes that penetrate through a 42 m thick alternating layer of soft clay and silty sand and into a more than 30 m thick silty gravel were installed providing a detailed description of the field geological conditions (Figure 1). The groundwater level was at 5–6 m depths below the ground surface.

A series of 3.2–3.5 m diameter jet-grout columns at the depth of 35 m, with a mutual overlapping of 60 cm, were installed in the vicinity of the cross passage using the super jet-midi (SJM) method because of the surrounding silty sand of high permeability [26]. The grouting tubes, while boring operations, were installed with horizontal included angles because of the existing overlying vehicle underpass. Upon completion of the cross passage, the 3.3 m diameter sump pit was excavated.

2.2. Incident, Associated Damage, and Remedial Measure. It was noticed that an outburst of mud water occurred while excavating to near the bottom of the sump pit (Figure 2(a)). Authorities immediately responded to the water ingress event by dumping sand bags and quick-set cement but in vain. Men at work soon heard sounds of breaks at liner joints of the tunnel on the south side, with water leaked into the tunnel from the ripped liner joints. The water also carried away fine particles, and the tunnel due to this reason lost contact with the ground leading to stepwise surface settlement in the longitudinal direction. More soil, while the settled cone expanded upwards, fell by slipping along the vertical wall of the vehicle underpass and passing through the ripped liner joints into the tunnel. Not only serious ground loss but also two undermined water mains transferred the soil into more flowable debris, causing a large surface cave-in on the south side (Figures 2(c) and 3(a)).

The ground loss also caused the tunnel on the north side to sink, accompanied by the offsets of the liners (Figure 3(b)). The soil fell into the tunnel mainly from the liner offset at the junction between the tunnel and the cross passage, leading to another surface cave-in (Figures 2(d) and 3(a)). To summarise, the amount of earth and quick-set cement dumped to fill the surface cave-ins was estimated to

be as much as 12,000 m³, whereas the water inflow, resulting from the two undermined water mains, was approximately 2,000 m³. Then, a 2-year rehabilitation was carried out to resume the traffic and its activities are detailed as follows (Figure 4):

- (i) Two watertight plugs within the tunnels at some distance from the point of water ingress were to secure the watertight effectiveness with additional jet-grout blocks
- (ii) Porewater within the surrounding soil was frozen using the ground freezing method
- (iii) Diaphragm walls of 1.5 m in thickness to retain the excavation-induced lateral loads were constructed at the depth of 60 m
- (iv) Dewatering wells screened at the bottom of the tunnels were constructed to secure the excavation face dry
- (v) The removal of the undermined vehicle underpass was conducted upon completion of Region “II” excavation
- (vi) New tunnel liners were erected following completion of Region “I” excavation
- (vii) Controlled low-strength materials (CLSM) was backfilled to the bottom of new vehicle underpass allowing for new vehicle underpass installation
- (viii) CLSM was backfilled to the surface

2.3. Field Instrumentation Data. Such serious ground loss caused two surface cave-ins to be developed on the south and north sides, respectively. The tunnel on the south side and the vehicle underpass due to loss of the contact with surrounding ground significantly settled 2.7 m and 1 m, respectively. The tunnel on the north side showed a relatively small settlement of 0.16 m. Additionally, the adjacent railway also measured some settlements and track relative displacements. As discussed, the diaphragm walls with the frozen ground and soilcrete blocks aimed to secure the watertight effectiveness while progressing the rehabilitation. The rehabilitation including the removal of undermined vehicle underpass and the erection of new tunnel liners as well as the installation of new vehicle underpass was performed when the water inside the walls was drained using the pumping wells and when the earth inside was removed. Therefore, the proposed layout of monitoring instruments (Figure 5) intended not only to observe the groundwater level and surface settlement variations while progressing the rehabilitation but to assess the associated environmental impacts.

Prior to progressing the rehabilitation, a group-well pumping test was performed using eight pumping wells installed inside the diaphragm walls. Figure 6 presents the variations of the groundwater levels and the number of pumping wells opened during the group-well pumping test. The group-well pumping test consisted of the pumping phase and recovery phase, and each phase continued for about 7 consecutive days. Table 1 lists the monitoring

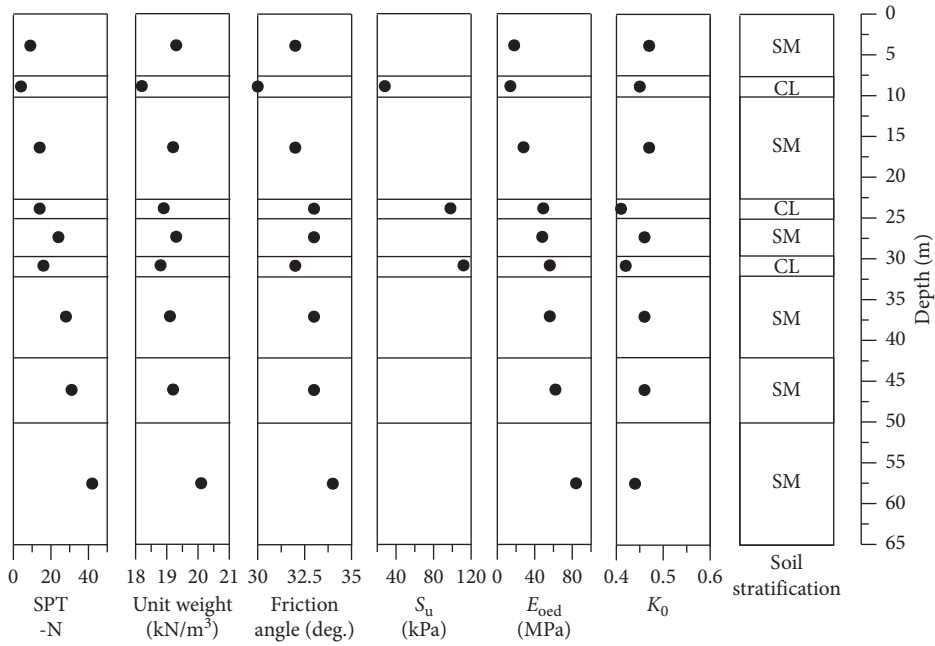
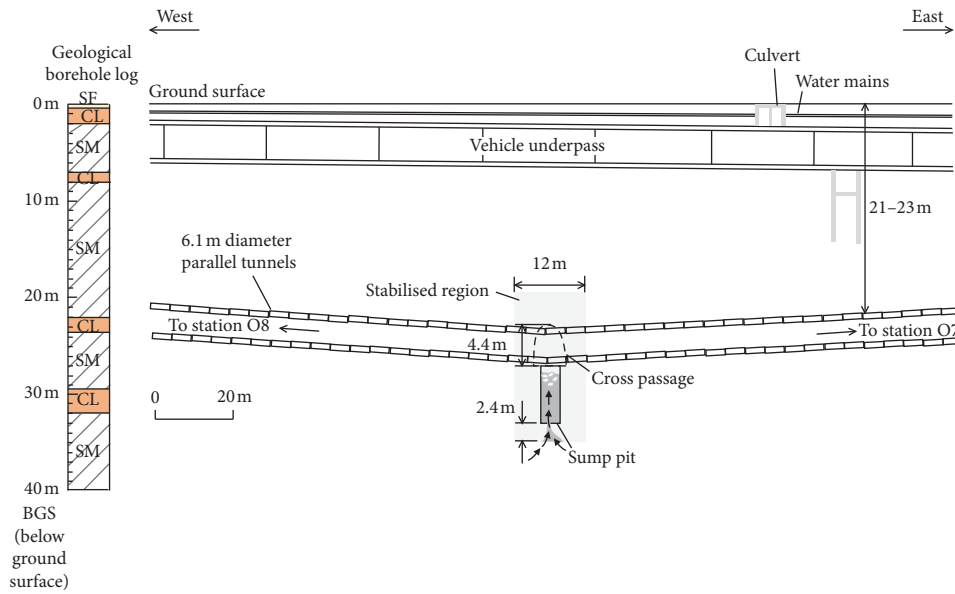


FIGURE 1: Soil properties profile. CL = silty clay; SM = silty sand; S_u = undrained shear strength; K₀ = earth pressure coefficient at rest; E_{oed} = elastic modulus from oedometer test.



(a)
FIGURE 2: Continued.

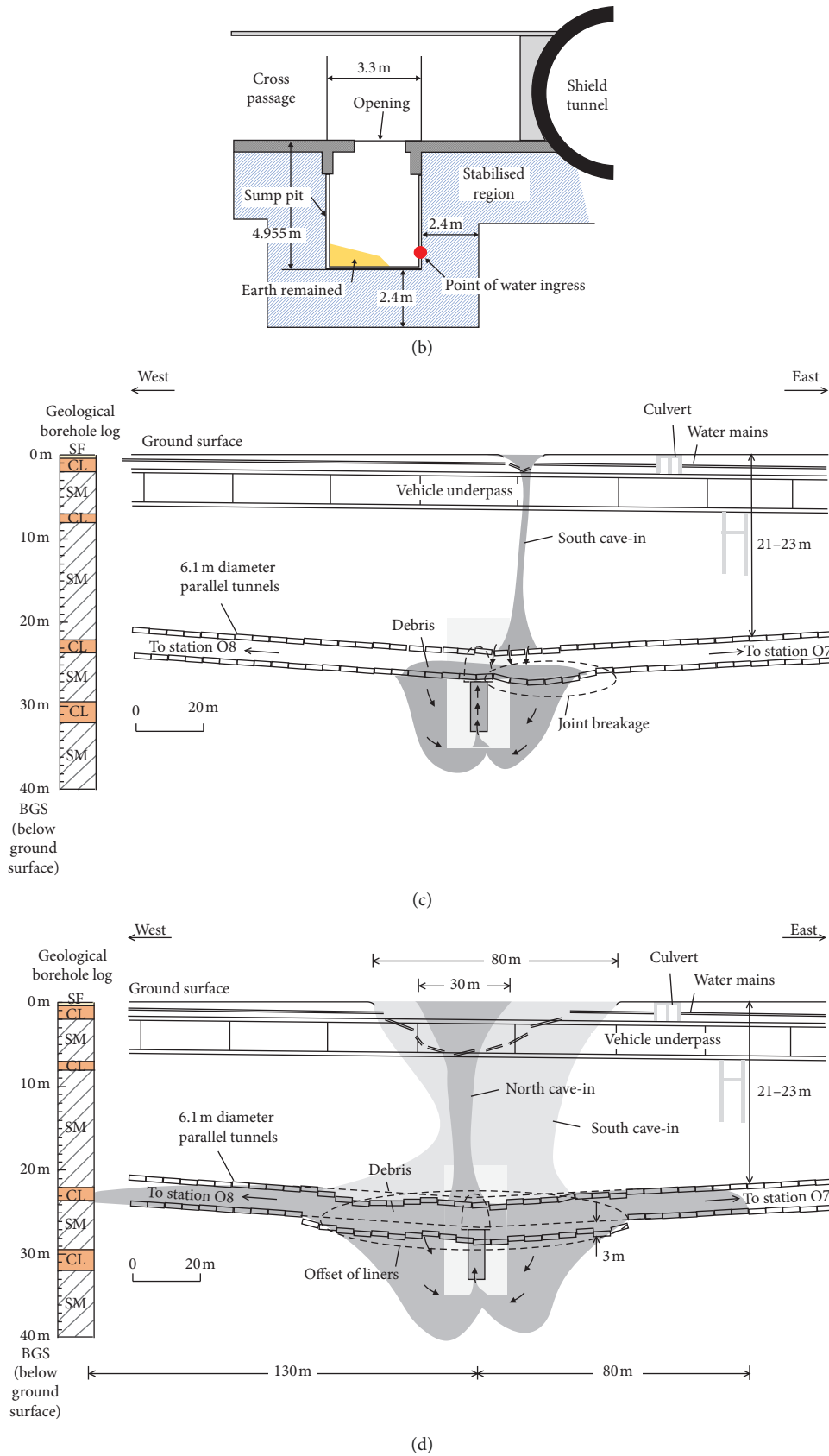


FIGURE 2: Scenario for progressing the water leak incident: (a) water leak (SF: backfill; SM = silty sand; CL: low plasticity clay), (b) illustration of the shortest path for groundwater seepage, (c) formation of the surface cave-in on the south side, and (d) formation of the surface cave-in on the north side (SF: backfill; SM = silty sand; CL: low plasticity clay).

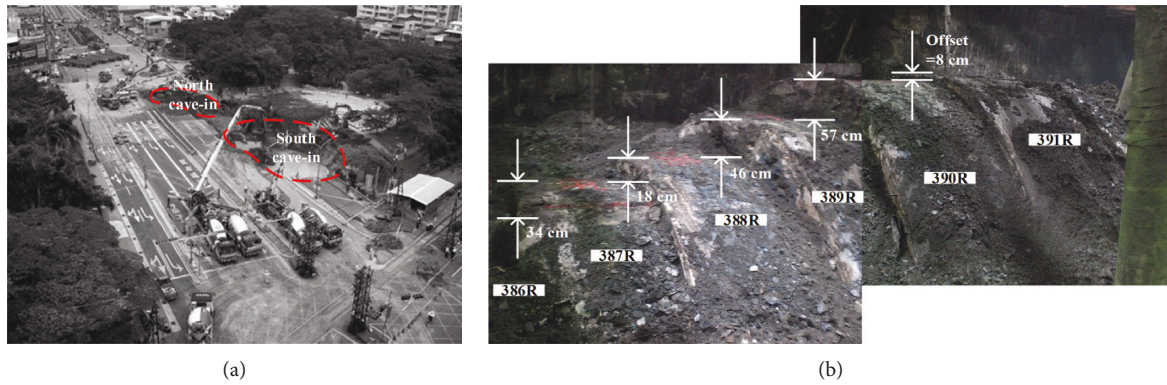


FIGURE 3: Photos taken from the water leak incident: (a) two surface cave-ins and (b) offsets of tunnel liners.

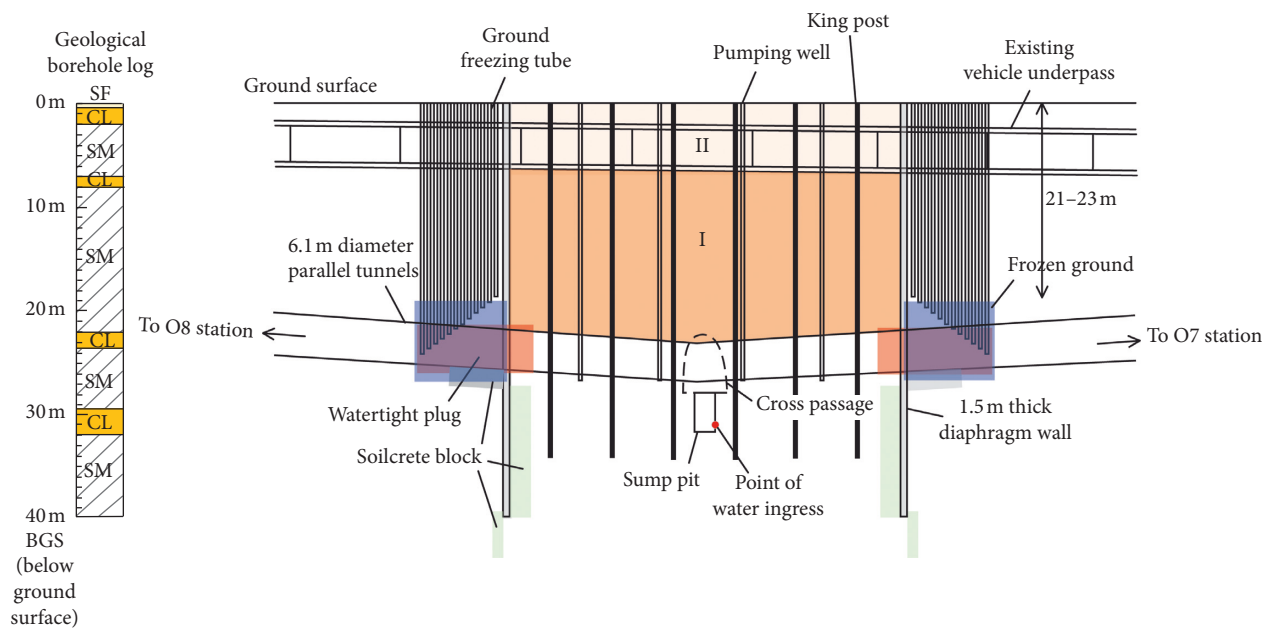


FIGURE 4: Schematic illustration for progressing the rehabilitation. Note: Soil in Regions I and II to be removed in the rehabilitation and then backfilled to the surface upon completion of the tunnel liners erection and new vehicle underpass installation. Note: soil in Regions I and II to be removed in the rehabilitation and then backfilled to the surface upon completion of the tunnel liners erection and new vehicle underpass installation. SF: backfill; SM = silty sand; CL: low plasticity clay.

instruments used in the test. It can be seen from Figure 6 that the groundwater levels in the observation wells OW-S1, OW-S2, OW-04, and OW-10 declined sharply to the 33–35 m depths in the very beginning of the pumping phase and maintained almost constant until the end of the pumping phase. A similar tendency, but with smaller variation, was observed from the observation wells OW-02 and OW-08. There was a sudden increase in the groundwater levels right before the completion of the pumping phase, most likely because of the recharge effect resulting from a rainfall. The recovery rates of the observation wells OW-S1, OW-S2, OW-04, and OW-10 gradually declined from 1.2 m/day in the beginning of the recovery phase to 0.1–0.2 m/day in the end of the recovery phase. Except the duration of rainfall, the groundwater level in the observation well OW-14 remained almost constant, indicating that the group-well pumping

appeared to have negligible influence on the groundwater level outside the diaphragm walls, which also indicated good watertight effectiveness.

Figure 7 shows the variations of the ground surface settlements while progressing the rehabilitation. The surface settlement point SM-T1 measured the smallest settlement, compared with the surface settlement points SM-T2, SM-T3, SM-T4, SM-A, SM-B, and SM-C. Similarly, the surface settlement points SM-01, SM-02, SM-04, SM-06, and SM-07 measured the relatively small settlements, compared with the surface settlement points SM-03 and SM-05. This phenomenon is due to the fact that the indicated surface settlement points were all close to the short side of excavation pit and the diaphragm walls of the short side due to its larger bending stiffness than those of the long side exhibited smaller lateral deflection and surface settlements. Despite

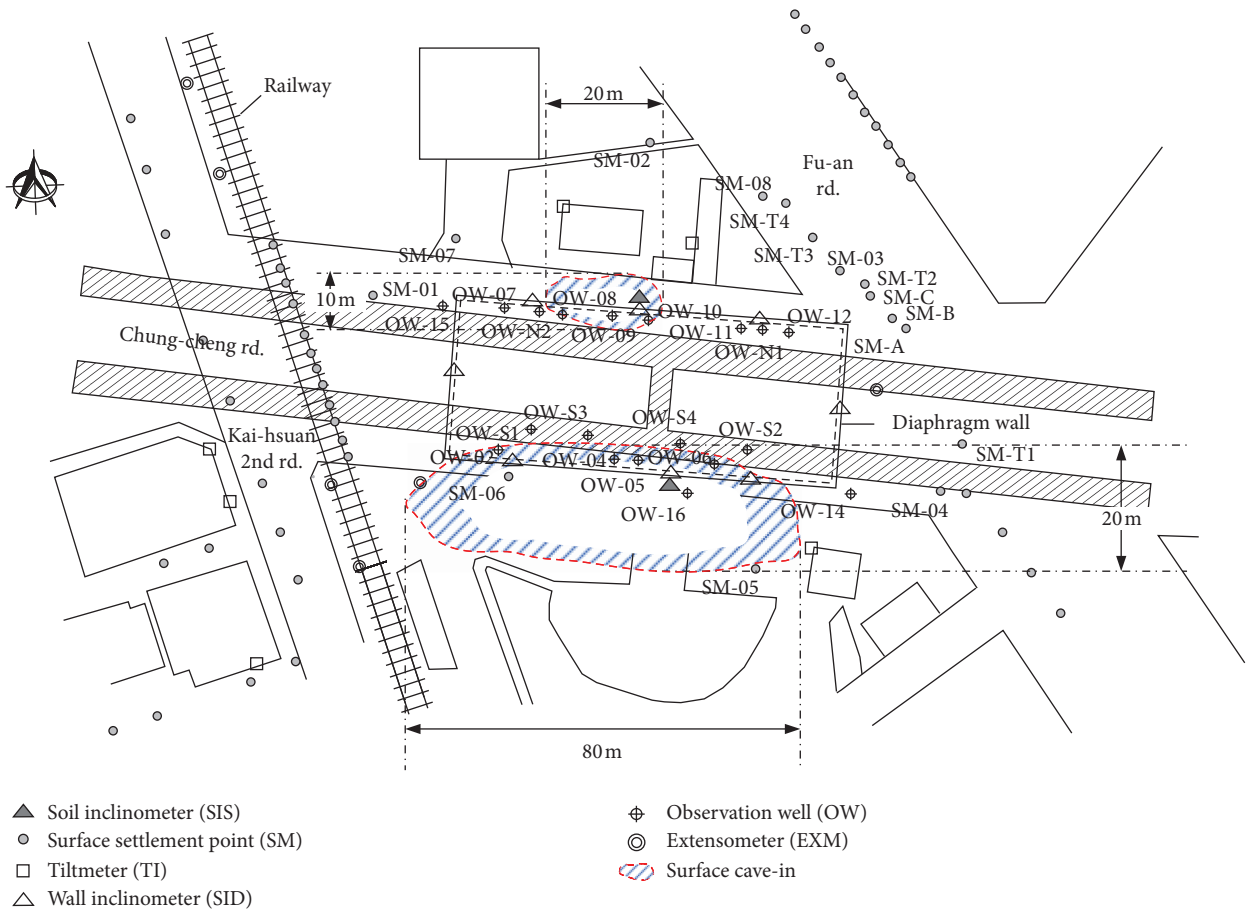


FIGURE 5: Layout of monitoring instruments and locations of surface cave-ins.

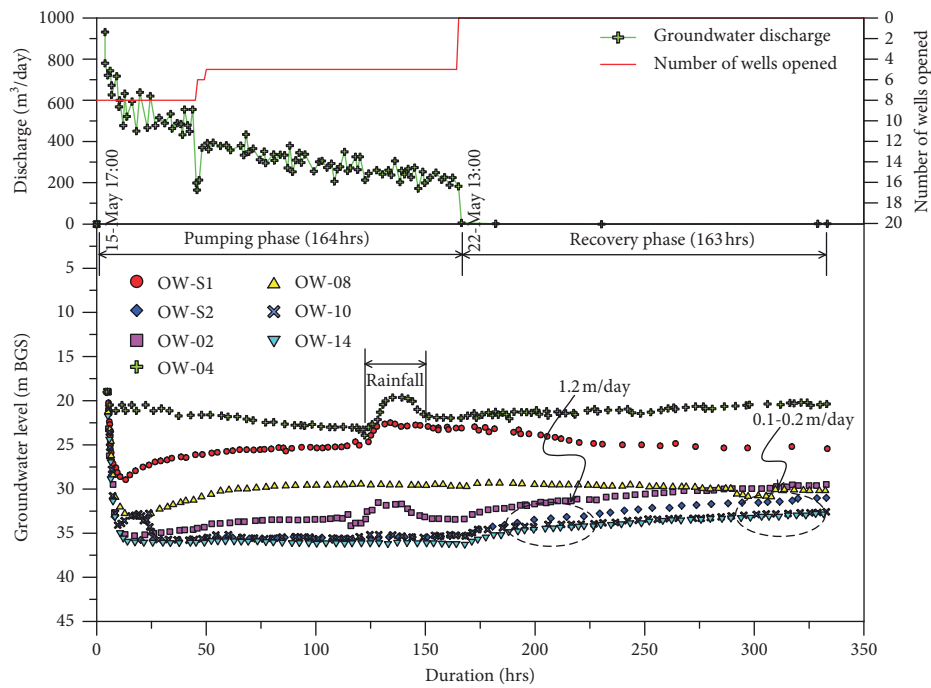


FIGURE 6: Variations of groundwater levels for verification of watertight effectiveness.

TABLE 1: Details for the monitoring instruments used in the pumping test.

Location	Well type	Instrument no.	Depth (m)
Inside the diaphragm wall	Observation well	OW-S1	40
	Observation well	OW-S2	45
	Observation well	OW-02	45
	Observation well	OW-04	45
	Observation well	OW-08	45
	Observation well	OW-10	45
Outside the diaphragm wall	Observation well	OW-14	40

the unignorable contribution from the effects of the diaphragm wall construction and the strut removal to the ground surface settlements, the associated increases were typically 4.8–9.4 mm and 5.5–7.5 mm, respectively, for SM-A to C and SM-T1 to T4 and 1–13 mm and 8.2–13.1 mm, respectively, for SM-01 to 07. While the pit excavation appeared to have minimal influence on the ground surface settlements, it is worth to mention that when the ground was unfrozen prior to the installation of new vehicle underpass, the ground surface settlements increased very quickly, especially for SM-01 to SM-07. Despite the increases in the surface settlement, the surface settlements then soon reached a steady state condition.

3. Analysis and Discussions

3.1. Triggering Mechanism. The piping phenomenon was responsible for initiating the water leak incident, with reference to the testimony of workmen. Notwithstanding that, the initiation of piping was conceived variously. The existing vehicle underpass, in fact, led to some difficulties in installing the jet-grout columns exactly in the plumb. Thus, the overlapping of jet-grout columns was estimated to be less than the design value of 60 cm, and some seepage-prone weak zones were thus developed. On the other hand, as the groundwater level was at 5–6 m depths below the ground surface, the head difference between the groundwater level and the 34 m depth where the piping initiated was 29 m. The length of the shortest path for groundwater seepage was from the bottom of the soilcrete body to the point of water ingress, that is, 2.4 m (Figure 2(b)). This came out with the hydraulic gradient i being equal to about 12.1 ($i = 29 \text{ m}/2.4 \text{ m} = 12.1$). The critical hydraulic gradient i_{cr} for triggering piping within gap-graded sand-gravel mixture could be as low as 0.2–0.3 as compared to $i_{cr} = 0.9$ –1.0 for clean sands [26]. In spite that this might not be true for the Kaohsiung soil with the finer particle-size range, the soil particles could easily be detached or washed away as subjected to such a high hydraulic gradient of 12.1. It is evident that the seepage-prone weak zones allowed the water to flow through the jet-grout columns and into the sump pit and that this high hydraulic gradient made the water inflow even greater. The combined effects of high hydraulic gradient and existence of seepage-prone weak zones were deemed as the main cause to initiate the water leak incident.

3.2. Soil Erodibility. Sherard et al. [26] described the pinhole test where water flows through a 1 mm diameter hole

punched in a specimen of compacted clay and the water emerging from dispersive clay carries a suspension of colloidal particles [27]. Sherard et al. [28] then utilised the pinhole test to investigate erosion in clay-silt mixtures in response to the problem emerging from occasional failure of low-height earth dams which occurred upon water filling in Australia and U.S. The pinhole test provides a direct qualitative measurement of the dispersibility or deflocculation and consequent erodibility of clay soils as stated in ASTM standard D4647-93 [29]. There were seven 33 mm diameter, 25 mm height specimens tested in the pinhole test for which their properties are summarised in Table 2. The average grain size D_{50} for the specimens was about 0.075 mm. A steel nipple was pushed into the specimen, and the hole was punched through the nipple as a guide hole using a 1 mm diameter steel needle. Wire screen and pea gravel were placed in the pinhole cell on either side of the specimen, as shown in Figure 8. As the pinhole cell assembled, distilled water was allowed to percolate through the specimen under constant heads of 50, 180, 380, and 1020 mm, in accordance with ASTM standard D4647-06. The principal differentiation between dispersive and non-dispersive soils, however, is given by the test results under 50 mm of head, as suggested by Sherard et al. [26], indicating that there is no necessity to carry out the test through to 1020 mm of head. The purpose to further increase the head is to classify dispersive soils, which is not within the scope of this study. The effluent turbidity and size of pinhole at the end of each test were recorded. If the effluent remains clear and the pinhole size unenlarged, then the soil is non-dispersive. Contrarily, the effluent is turbid and the pinhole size is enlarged for dispersive soil.

Table 3 summarises the results of the pinhole test. For the specimens which were categorised as D, they were dispersive soils. There was also a common characteristic. Most of the specimens primarily included silt with a fines content varying from 52 to 96% [30] and their Unified Soil Classification System (USCS) symbols were ML and SM-ML. The pinhole size enlarged in a range of 2–4 mm after the test. The specimen S-19 categorised as ND was nondispersive soil with a fines content of 94% and mainly consisted of clay. The USCS classified this specimen as CL, which was an indication of low plasticity clay. The pinhole size for the specimen S-19 remained unenlarged after the test. The test results revealed a fact indicative of the tendency of the silt from Kaohsiung, Taiwan to possess high dispersion, or very low strength, or both. The particle-size distribution analysis indicated that the Kaohsiung soil belonged neither to the gap-graded gravelly

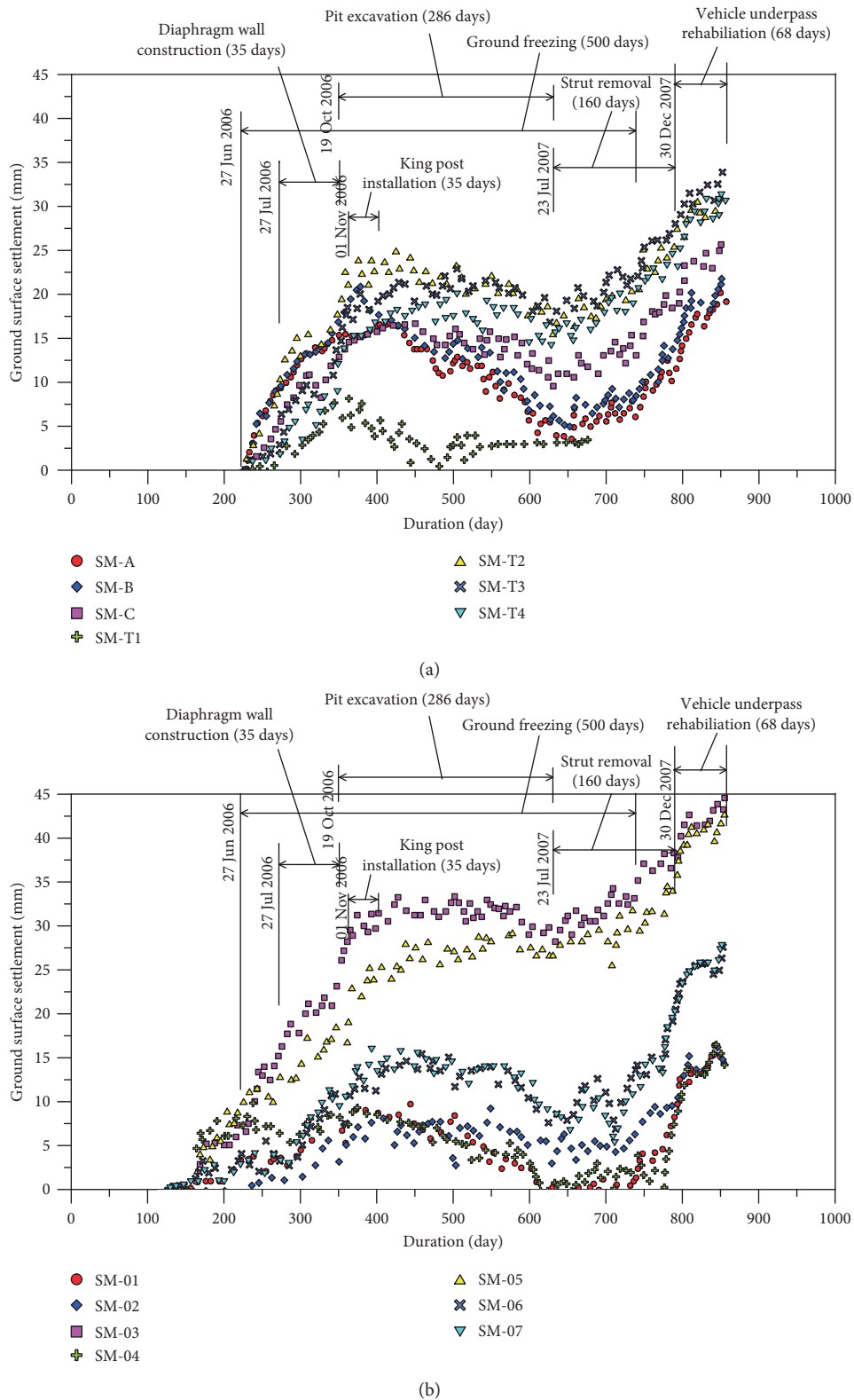


FIGURE 7: Variations of ground surface displacements for progressing the rehabilitation: (a) SM-A to C and SM-T1 to T4 and (b) SM-01 to 07.

sands susceptible for segregation piping nor to the dispersive clay prone to internal erosion. In fact, the particle size for the Kaohsiung soil lay midway in the range of silt and sand. The

pinhole tests were regarded as an effective means to identify not only the nonplastic nature of the Kaohsiung silt contained in the sand but also its high vulnerability to piping or internal

TABLE 2: Summary of soil properties in the pinhole test.

Specimen no.	Depth (m)	USCS symbol	SPT-N	Sand (%)	Silt (%)	Clay (%)	Water content ω (%)	Liquid limit LL (%)	Plastic index PI
S-14	20.55–21	ML	21	19	76	5	22.4	27	4.1
S-15	22.05–22.5	SM-ML	20	48	52	0	25.6	21.4	0.8
S-16	23.55–24	ML	17	15	82	3	24.4	27.5	1.2
S-17	25.05–25.5	ML	23	4	86	10	19.5	35.2	6.4
S-18	26.55–27	ML	24	20	74	6	21.7	26.5	3.3
S-19	28.08–28.53	CL	16	6	56	38	42.9	43.9	20
S-20	30–30.45	ML	21	15	84	1	25.1	26.1	1.2

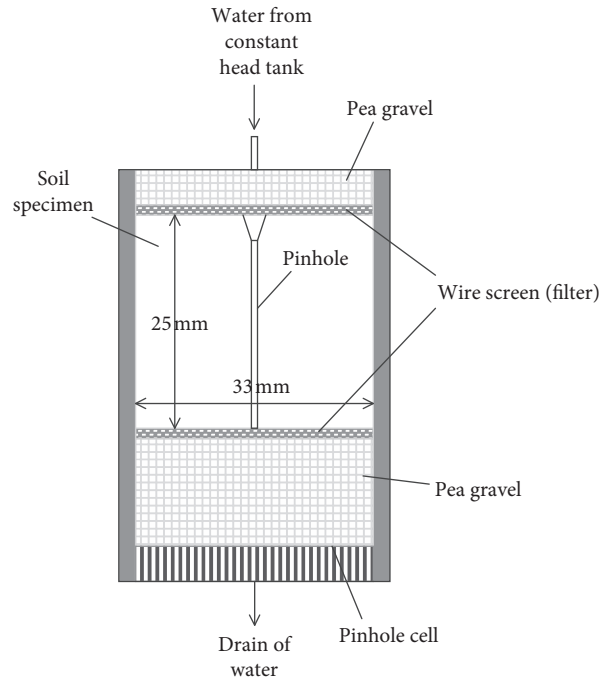


FIGURE 8: Pinhole test apparatus for assessing the dispersion and consequent erodibility of the local sandy silt.

TABLE 3: Summary of the pinhole test results.

Specimen no.	Final head (mm)	Colour cloudiness	Pinhole size after test (mm)	Specific surface area (m^2/g)	Dispersion classification
S-14	50	Moderately dark	3	3.20	D
S-15	50	Barely visible	2	3.27	D
S-16	50	Moderately dark	3	3.11	D
S-17	50	Dark	4	2.95	D
S-18	50	Dark	4	2.84	D
S-19	180	Clear	1	6.18	ND
S-20	50	Moderately dark	3	3.07	D

Note: D = dispersive soil; ND = nondispersive soil.

erosion. It may be conclusively mentioned that the seepage-prone weak zones and high hydraulic gradient initiated the water leak incident and that water from the two undermined water mains transferred the Kaohsiung silt into more flowable debris and its nonplastic nature aggravated the collapse even further. Despite an apparent inadequacy in dealing with similar incident in other sites, the local sandy silt was found to be prone to the piping at deep depths under large hydraulic gradients, and the two undermined water mains enhanced its

flowable nature, thereby enlarging the scale of the water leak incident.

3.3. Lessons Learned. Quite often subway construction failures are not explained nor published, which makes the same mistakes to be made another time with great casualties and economic losses. Some bullet points that indicate what engineers should do or avoid are learned and summed up as follows:

- (i) Quality control for grouting: since in-ground obstructions such as wastewater and electricity mains can result in some difficulty in installing jet-grout columns exactly in the plumb, a trial grouting should be performed prior to the formal one to verify the design grouting parameters.
- (ii) Seepage-prone weak zone: except for trial grouting, additional soilcrete columns, resulting from chemical grouting, should be considered during design phase and constructed next to jet-grout columns, which not only increases the length of path for the groundwater seepage but also prevents formation of the seepage-prone weak zone.
- (iii) Local soil nature: the Kaohsiung silt contained in the sand has proved to possess high dispersion, or low strength, or both. There is a necessity to investigate the nature of local soils while progressing upcoming subway construction project if they are found to exhibit peculiar behaviour differentiated from common sense in soil mechanics.

4. Concluding Remarks

The main cause to lead to the water leak incident was investigated. The pinhole tests were conducted to highlight not only the nonplastic nature of the Kaohsiung silt but also its vulnerability to piping or internal erosion. Some main concluding remarks can be drawn as follows:

- (1) The piping was responsible for initiating the water leak incident. Dumping sand bags and quick-set cement failed to ease the water leak. Mud water carried away fine particles in the ground and together flowed into the tunnels through the ripped liner joints leading to serious ground loss. Such ground loss caused two surface cave-ins. The surface cave-ins not only impeded traffic but also caused damages to adjacent properties.
- (2) The hydraulic pressure at the point of water ingress was estimated to be about 300 kPa. The length of shortest path for groundwater seepage was from the bottom of the soilcrete body to the point of water ingress, that is, 2.4 m, corresponding to the hydraulic gradient of 12.1.
- (3) The existing vehicle underpass led to some difficulties in installing the jet-grout columns exactly in the plumb, and some seepage-prone weak zones were thus developed. The seepage-prone weak zones allowed the water to flow through the jet-grout columns into the sump pit, and such high hydraulic gradient made the water inflow even greater. The combined effects were deemed as the main cause initiating the water leak incident.
- (4) The results of the pinhole test identified not only the nonplastic nature of the Kaohsiung silt but also its vulnerability to piping or internal erosion under large hydraulic gradients. Water from the two undermined water mains and the nonplastic nature

of the Kaohsiung silt aggravated the collapse even further. More detailed investigation is considered to be necessary to address the explored issue with different aspects of view.

Data Availability

The data used to support the findings of this study are included within the article.

Conflicts of Interest

The authors declare that they have no conflicts of interest.

Acknowledgments

This study would not have been possible without financial supports from the Special Fund for Basic Scientific Research of Central Colleges, Chang'an University, under Grant no. 300102269502.

References

- [1] Y.-S. Jo, S.-H. Cho, and Y.-S. Jang, "Field investigation and analysis of ground sinking development in a metropolitan city, Seoul, Korea," *Environmental Earth Sciences*, vol. 75, no. 20, p. 1353, 2016.
- [2] Y. Hou, Q. Fang, D. Zhang, and L. N. Y. Wong, "Excavation failure due to pipeline damage during shallow tunnelling in soft ground," *Tunnelling and Underground Space Technology*, vol. 46, pp. 76–84, 2015.
- [3] R. P. Chen, Z. C. Li, Y. M. Chen, C. Y. Ou, Q. Hu, and M. Rao, "Failure investigation at a collapsed deep excavation in very sensitive organic soft clay," *Journal of Performance of Constructed Facilities*, vol. 29, no. 3, Article ID 04014078, 2015.
- [4] S.-J. Feng and S.-F. Lu, "Failure of a retaining structure in a metro station excavation in Nanchang city, China," *Journal of Performance of Constructed Facilities*, vol. 30, no. 4, Article ID 04015097, 2016.
- [5] Y. Tan and Y. Lu, "Forensic diagnosis of a leaking accident during excavation," *Journal of Performance of Constructed Facilities*, vol. 31, no. 5, Article ID 04017061, 2017.
- [6] J. H. Shin, I. K. Lee, Y. H. Lee, and H. S. Shin, "Lessons from serial tunnel collapses during construction of the Seoul subway line 5," *Tunnelling and Underground Space Technology*, vol. 21, no. 3-4, pp. 296–297, 2006.
- [7] Y. Tan and B. Wei, "Performance of an overexcavated metro station and facilities nearby," *Journal of Performance of Constructed Facilities*, vol. 26, no. 3, pp. 241–254, 2012.
- [8] Y. Tan, B. Wei, X. Zhou, and Y. Diao, "Lessons learned from construction of shanghai metro stations: importance of quick excavation, prompt propping, timely casting and segmented construction," *Journal of Performance of Constructed Facilities*, vol. 29, no. 4, Article ID 04014096, 2015.
- [9] W.-C. Cheng, J. C. Ni, J. S.-L. Shen, and H.-W. Huang, "Investigation into factors affecting jacking force: a case study," *Proceedings of the Institution of Civil Engineers—Geotechnical Engineering*, vol. 170, no. 4, pp. 322–334, 2017.
- [10] W.-C. Cheng, J. C. Ni, A. Arulrajah, and H.-W. Huang, "A simple approach for characterising tunnel bore conditions based upon pipe-jacking data," *Tunnelling and Underground Space Technology*, vol. 71, pp. 494–504, 2018.

- [11] W.-C. Cheng, L. Wang, Z.-F. Xue, J. C. Ni, M. Rahman, and A. Arulrajah, "Lubrication performance of pipejacking in alluvial deposits," *Tunnelling and Underground Space Technology*, vol. 91, Article ID 102991, 2019.
- [12] Z.-F. Wang, W.-C. Cheng, and Y.-Q. Wang, "Investigation into geohazards during urbanization process of Xi'an, China," *Natural Hazards*, vol. 92, no. 3, pp. 1937–1953, 2018.
- [13] Z. Ye and H. B. Liu, "Mechanism and countermeasure of segmental lining damage induced by large water inflow from excavation face in shield tunneling," *International Journal of Geomechanics*, vol. 18, no. 12, Article ID 04018163, 2018.
- [14] Z. C. Wang, Z. Hu, J. X. Lai, H. Wang, K. Wang, and W. B. Zan, "Settlement characteristics of jacked box tunneling underneath a highway embankment," *Journal of Performance of Constructed Facilities*, vol. 33, no. 2, Article ID 04019005, 2019.
- [15] R. Spruit, F. van Tol, W. Broere, E. Slob, and E. Niederleithinger, "Detection of anomalies in diaphragm walls with crosshole sonic logging," *Canadian Geotechnical Journal*, vol. 51, no. 4, pp. 369–380, 2014.
- [16] J. Lai, J. Qiu, H. Fan et al., "Fiber Bragg grating sensors-based in situ monitoring and safety assessment of loess tunnel," *Journal of Sensors*, vol. 2016, Article ID 8658290, 10 pages, 2016.
- [17] H. F. Xing, F. Xiong, and J. M. Wu, "Effects of pit excavation on an existing subway station and preventive measures," *Journal of Performance of Constructed Facilities*, vol. 30, no. 6, Article ID 04016063, 2016.
- [18] J. Lai, S. He, J. Qiu et al., "Characteristics of seismic disasters and aseismic measures of tunnels in Wenchuan earthquake," *Environmental Earth Sciences*, vol. 76, no. 2, pp. 76–94, 2017.
- [19] S. L. Shen, Z. F. Wang, and W. C. Cheng, "Estimation of lateral displacement induced by jet grouting in clayey soils," *Géotechnique*, vol. 67, no. 7, pp. 1–10, 2017.
- [20] W.-C. Cheng, J. C. Ni, S. L. Shen, and Z.-F. Wang, "Modeling of permeation and fracturing grouting in sand: laboratory investigations," *Journal of Testing and Evaluation*, vol. 46, no. 5, pp. 2067–2082, 2018.
- [21] Z.-F. Wang, J. S. Shen, and W.-C. Cheng, "Simple method to predict ground displacements caused by installing horizontal jet-grouting columns," *Mathematical Problems in Engineering*, vol. 2018, Article ID 1897394, 11 pages, 2018.
- [22] W.-C. Cheng, J. C. Ni, H.-W. Huang, and J. S. Shen, "The use of tunnelling parameters and spoil characteristics to assess soil types: a case study from alluvial deposits at a pipejacking project site," *Bulletin of Engineering Geology and the Environment*, vol. 78, no. 4, pp. 2933–2942, 2019.
- [23] W.-Y. Xia, Y.-J. Du, F.-S. Li et al., "In-situ solidification/stabilization of heavy metals contaminated site soil using a dry jet mixing method and new hydroxyapatite based binder," *Journal of Hazardous Materials*, vol. 369, no. 5, pp. 353–361, 2019.
- [24] W. L. Wang, "A study of reconstruction for ground settlement—the LUO09 shield tunnel for the Kaohsiung MRT system CO₂ section," M.Sc. thesis, National Taipei University of Technology, Taipei, Taiwan, 2011.
- [25] A. W. Skempton and J. M. Brogan, "Experiments on piping in sandy gravels," *Geotechnique*, vol. 44, no. 3, pp. 449–460, 1994.
- [26] J. L. Sherard, E. F. Steele, R. S. Decker, and L. P. Dunnigan, "Pinhole test for identifying dispersive soils," *Journal of the Geotechnical Engineering Division ASCE*, vol. 102, no. 1, pp. 69–85, 1976.
- [27] F. G. Bell and D. J. H. Walker, "A further examination of the nature of dispersive soils in Natal, South Africa," *Quarterly Journal of Engineering Geology and Hydrogeology*, vol. 33, no. 3, pp. 187–199, 2000.
- [28] J. L. Sherard, L. P. Dunnigan, and R. S. Decker, "Some engineering problems with dispersive clays," in *Proceedings of Symposium on Dispersive Clays, Related Piping, and Erosion in Geotechnical Projects*, pp. 3–12, Chicago, IL, USA, June–July 1977.
- [29] ASTM D4647-93, *Standard Test Method for Identification and Classification of Dispersive Clay Soils by the Pinhole Test*, American Society for Testing and Materials, West Conshohocken, PA, USA, 2006.
- [30] J. Lu, T.-H. Wang, W.-C. Cheng, T. Yang, and Y. Luo, "Permeability anisotropy of loess under influence of dry density and freeze-thaw cycles," *International Journal of Geomechanics*, vol. 19, no. 9, Article ID 04019103, 2019.

Research Article

Correlation Analysis of Macroscopic and Microscopic Parameters of Coal Measure Soil Based on Discrete Element Method

Hong Zhang , Wei Liao , Junbo Lin, Bang Zhang, and Haoran Feng 

School of Civil and Architectural Engineering, Nanchang Institute of Technology, Nanchang 330099, China

Correspondence should be addressed to Hong Zhang; hongzhang@nit.edu.cn

Received 12 July 2019; Revised 29 August 2019; Accepted 3 September 2019; Published 22 September 2019

Academic Editor: Roberto Nascimbene

Copyright © 2019 Hong Zhang et al. This is an open access article distributed under the Creative Commons Attribution License, which permits unrestricted use, distribution, and reproduction in any medium, provided the original work is properly cited.

Numerical simulation of the triaxial test of coal measure expansive soil distributed along the highways in Pingxiang District, Jiangxi, was carried out by means of discrete particle flow, during which the macromechanical properties and the formation and developmental patterns of shear displacement field of the coal measure expansive soil were studied from a mesoscopic perspective. The result showed that the macroscopic stress and strain of test specimens can be significantly influenced by the interparticle friction coefficient of the coal measure expansive soil. Peak value of the deviatoric stress of test specimens increased with increasing friction coefficient, and before reaching the deviatoric stress peak value, the stress-strain relationship of the soil body basically presented a linear variation trend; the soil interparticle contact stiffness varied hyperbolically with the deviatoric stress peak value of test specimens, and the increasing contact stiffness ratio led to a gradual decrease of the deviatoric stress peak value but had only a small impact on the residual strength of test specimens; confining pressure was found to have remarkable influence on both the deviatoric stress peak value and the residual strength of test specimens; when the experimental confining pressure increased from 0.2 MPa to 1.2 MPa, the deviatoric stress peak value and the residual strength of test specimens increased by 2.14 times and 5.11 times, respectively. This paper reveals the macroinstability and failure mechanism of coal measure expansive soil from a microperspective.

1. Introduction

Coal measure soil mostly appears ash black in appearance, while the soil mass exposed is greyish with weak interlayer bonding and loose structure. Since coal measure soil is easily weathered and disintegrated with poor water stability after excavation, large gullies are likely to be caused by water and soil loss during heavy rain. Therefore, an urgent problem which should be solved currently is how to handle and utilize engineering with coal measure soil. Some researchers at home and abroad have researched problems and reinforcement measures for engineering with coal measure soil [1–3]. Nevertheless, characteristics of engineering with coal measure soil and causes of the abovementioned problems are rarely documented. Focusing on the coal measure soil along the Guangzhou-Wuzhou expressway, Hu et al. [4] determined the shear strength of coal measure soil under

different water contents and its influence law with the routine straight shear test. Zhu et al. [5] established a mathematical model regarding the stability of the slope infiltrated by rainfall and analyzed the influence of cracks and weathered layers on slope stability using the limit equilibrium method together with the shear strength theory of unsaturated soil. Zhang et al. [6] simulated and analyzed the slope stability of coal measure soil with different cracks and weathering degrees under rainfall infiltration using the transient unsaturated seepage software based on some secondary slope of Daqing-Guangzhou expressway in Jiangxi. Li and Liu [7] took the red clay and powdered coal measure soil in hilly and mountainous areas of southwestern China as the objects of study to investigate the influencing rule of different water contents on parameters such as the cohesion, internal friction angle, and shear strength using the common straight shear test. Yang and Zheng [8]

determined the soil-water characteristic curve for samples of remolded unsaturated coal measure soil with different dry densities using a soil moisture characteristic curve meter, and they fit the data measured with the VG model. Most of the abovementioned documents tend to research from the perspective of macromechanics. However, macromechanical property is a symbol of parameter changes in the micro-structure of soil mass. In that case, the slope of coal measure soil can be considered as a system comprised of soil particles in different sizes. Those soil particles in the system are discrete, and the interaction between the particles is characterized by nonlinear dissipation. To be specific, it is the micromechanical behavior of particles inside the system that determines many macromechanical properties of the slope. Hence, microscopic analysis must be performed on the composition of particle structure of the slope soil and distribution characteristics of contact force chain and movement characteristics of particles, so as to disclose the mechanism of macroscopic static and dynamic features shown by the granular system of the slope of coal measure soil [9–14].

In 1979, Cundall and Strack [15, 16] proposed the distinct element method (DEM), which has gradually become an effective tool to study the microstructures of granular systems. Many scholars modeled typical soil mechanics experiments (e.g., biaxial compression and direct shear tests) using the discrete element method [17–23]. The unloading of silos is a typical bulk flow process. After the appearance of the discrete element method, Langston et al. [24–29] used DEM to study hopper unloading. In the field of complex soil dynamics or machine-soil dynamics, some scholars use the discrete element method to simulate the excavation, drilling, shoveling, penetration, and pipeline laying processes [30–36].

A large amount of coal measure strata containing montmorillonite and illite are distributed along the Pingxiang-Lianhua expressway in Jiangxi. As a result, expansive soil can be found in coal measures. Nonetheless, few researches on mechanical properties of the expansive coal measure soil have been reported currently. In this paper, the discrete element method (DEM) is employed to have a 3D numerical simulation of the triaxial test on the expansive coal measure soil, to probe into the influencing rule of parameter changes of the micromechanic structure of the soil mass particles on macromechanical characteristics of the expansive coal measure soil, and to discuss the formation and development law of the shear displacement field of the expansive coal measure soil. The research findings can provide theoretical references for the protective slope design and construction of the expansive coal measure soil.

2. Principles of Discrete Element Method

2.1. Physical Equations. The discrete element method (DEM) is to consider objects of research as an integral whole consisting of a finite number of discrete particles, in which each particle is idealized as a rigid body and deemed as a discrete calculating unit. The particles are independent of each other with contact and friction. Assuming that the

normal contact forces F_i^n between two contact solid elements are directly proportional to the normal relative displacement U^n between them, the following algebraic relation can be obtained [37]:

$$F_i^n = K^n U^n n_i, \quad (1)$$

where K^n is the normal stiffness of the distinct element; U^n is the normal displacement of the distinct element; and n_i is the unit normal vector over the contact surface.

The tangential contact force between granular particles is defined as the shear force whose size is closely related to the movement track of the particles and their loading history. In this paper, the shear force between granular particles is expressed in the form of increment. When a contact is formed between granular particles, the total tangential contact force F_i^s between the particles is assumed to be initialized to zero. And the increment of the tangential contact force resulting from the relative displacement between the particles is accumulated in each cycle of calculating time steps. The calculating relationship can be expressed as follows:

$$\Delta F_i^s = -K^s \Delta U^s, \quad (2)$$

where ΔF_i^s is the shear stress increment between distinct elements in each calculation step; K^s is the tangential contact stiffness of the distinct element; and ΔU^s is the increment of the tangential relative displacement of the distinct element.

2.2. Equations of Motion. Based on equation (2), the resultant force and the resultant moment imposed on granular particles after the accumulation of each calculation of time steps are calculated. After that, the acceleration and the rotational angular velocity of granular particles are calculated according to Newton's second law. Thus, physical quantities such as velocity, linear displacement, and angular displacement of the granular particles in the calculation period can be known. If the resultant shearing force acting on the granular particles in the direction of x at the moment of t_0 is assumed as F_x , the motion of granular particles can be expressed by the following two equations:

$$\begin{aligned} \ddot{u}_x(t_0) &= \frac{F_x}{m}, \\ \ddot{\omega}_x(t_0) &= \frac{M_x}{I_x}, \end{aligned} \quad (3)$$

where $\ddot{u}_x(t_0)$ is the average acceleration of granular particles at the moment of t_0 in the direction of x ; $\ddot{\omega}_x(t_0)$ is the rotational acceleration of granular particles at the moment of t_0 in the direction of x ; m is the mass of granular particles; M_x is the bending moment of the resultant force acting on the granular particles; and I_x is the rotational inertia of granular particles.

2.3. Particle Contact Constitutive Model. Since many coal particles are contained in expansive coal measure soil, especially that in the weathering layer of the slope is loose, it

results in weak cohesive force between the soils. The shear strength is formed primarily by the internal friction between soil particles. Therefore, a contact sliding model can be utilized to describe the constitutive relationship between the normal force and the tangential shear force interacting between particles. The normal tension between particles is neglected in the contact sliding model. The sliding motion between particles only occurs under set conditions, that is, the shearing force actually generated between particles should be greater than the preset threshold; also, the sliding between particles must be performed within a certain range of shear strength. Assuming that the displacement overlapping between two particles is less than or equal to zero, it can be considered that the two particles have no contact or their contact force is zero. In this way, their constitutive behavior can be described as

$$F_{\max}^s = \mu |F_i^n|, \quad (4)$$

where μ is the friction coefficient between particles. If so, then the particles will slide. Meanwhile, in the next cycle step, F_i^s will be

$$F_i^s \leftarrow F_i^s \left(\frac{F_{\max}^s}{|F_i^s|} \right). \quad (5)$$

3. Numerical Simulation of Particle Flow of Expansive Coal Measure Soil

A particle flow calculation model is firstly established in this paper according to the actual particle size range of the soil mass by assuming that particles of the soil mass are rigid materials. Meanwhile, the above contact sliding model is used to indicate the particle interaction. After simulating the stress-strain relationship of test pieces in the triaxial test by changing microscopic parameters of particles, the results obtained are compared with those from the laboratory triaxial test. Finally, microscopic parameters of the soil particles that can reflect macromechanical properties of the soil mass are determined through numerous trial calculations and analyses. Furthermore, the calculation model is taken as a basic model for analyzing the influencing law of changes of particle microscopic parameters on macroscopic characteristics of the expansive coal measure soil.

3.1. Principles of Numerical Calculation of the Triaxial Test.

The key to the calculation principle of numerical simulation in the triaxial test is to calculate the stress state of the test piece in the loading process along with stress control. While the test piece is loaded by controlling the movement velocity of the bottom plate and the top plate of the model constraint boundary in the triaxial test that is simulated with the discrete particle flow program [38]. The stress of the test piece can be obtained by dividing the resultant force of all the forces acting on the test piece by the area of the corresponding test piece. The strain of the test piece in the directions of x and y can be obtained as follows:

$$\varepsilon = \frac{L - L_0}{1/2(L_0 + L)}, \quad (6)$$

where L is the current length of the test piece in the corresponding direction and L_0 is the original length of the test piece in that direction. Concerning the cylindrical test piece, the axial strain ε_H and the radial strain ε_R can be expressed as follows:

$$\varepsilon_H = \frac{H - H_0}{1/2(H_0 + H)}, \quad (7)$$

$$\varepsilon_R = \frac{R - R_0}{1/2(R_0 + R)}.$$

Servo functions can be called in the cycle of calculating the time steps to reduce the difference between the monitoring stress and the preset stress in the calculation of numerical simulation. The numerical servo functions are adopted to adjust the velocity of conducting lateral restraint against the wall of the test piece, so that the restraint stress can be inclined to a certain constant. The numerical servo functions are achieved by the following algorithms; the velocity of boundary restraint can be expressed as follows:

$$\dot{u}^{(\omega)} = G(\sigma^{\text{measured}} - \sigma^{\text{required}}) = G\Delta\sigma, \quad (8)$$

where $\dot{u}^{(\omega)}$ is the velocity of laterally restraining the wall and G is an "incremental" parameter obtained through the following method.

Assuming that the increment of the binding force generated in the movement of lateral wall restraining within a calculated step can be expressed as follows:

$$\Delta F^{(\omega)} = K^{n(\omega)} N_c \dot{u}^{(\omega)} \Delta t, \quad (9)$$

where N_c is the number of contact surfaces on the constraint boundary and $K^{n(\omega)}$ is the average stiffness of these contact surfaces. Therefore, the average increment of restraint stress is

$$\Delta\sigma^{(\omega)} = \frac{K^{n(\omega)} N_c \dot{u}^{(\omega)} \Delta t}{A}, \quad (10)$$

where A is the area of regions involved in the constraint boundary. In order to achieve stable test loading in the numerical simulation of the triaxial test, the absolute value of the variable of restraint stress must be smaller than the difference between the monitored value and the preset value. Amplification of coefficients is adopted in the simulation of actual numerical simulation. α is assumed as an amplification coefficient. To guarantee the loading stability, we may have

$$|\Delta\sigma^{(\omega)}| < \alpha |\Delta\sigma|, \quad (11)$$

which leads to

$$\left| \frac{K^{n(\omega)} N_c \dot{u}^{(\omega)} \Delta t}{A} \right| < \alpha |\Delta\sigma|, \quad (12)$$

where $K^{n(\omega)} > 0$, $N_c > 0$, $\Delta t > 0$, and $A > 0$; thus,

$$\frac{K^{n(\omega)}N_c\Delta t}{A}|G\Delta\sigma| < \alpha|\Delta\sigma|. \quad (13)$$

Eliminate $|\Delta\sigma|$ by taking $G > 0$ and $\Delta\sigma > 0$, we can obtain

$$\frac{K^{n(\omega)}N_c\Delta t}{A}G < \alpha. \quad (14)$$

The following equation can be obtained by transposing the inequation:

$$G < \frac{\alpha A}{K^{n(\omega)}N_c\Delta t}. \quad (15)$$

Therefore, the increment can be determined by the following equation:

$$G = \frac{\alpha A}{K^{n(\omega)}N_c\Delta t}. \quad (16)$$

In general, $\alpha = 0.5$ is taken in actual simulated calculations.

3.2. Test Materials and Laboratory Triaxial Test. The test soil samples source from the slope of original coal measures at K12 + 110 in A2 section of Wanzai-Yichun expressway in Jiangxi. Natural physical and mechanical indexes of the samples are as follows: the average density of soil particles is 2230 kg/m^3 ; the average natural density is 1680 kg/m^3 ; the natural porosity is 0.32; and the moisture content W of the test pieces is 18.2%. The distribution of particle contents in different particle size ranges of the expansive coal measure soil can be obtained by conducting particle grading test on the samples with the sieving method and the mixed method, as shown in Table 1. Soil particles mainly range from 0.25 to 10 mm, accounting for 85.41%; with $d_{10} = 0.129$, $d_{30} = 0.58$, and $d_{60} = 1.27$; the nonuniform coefficient C_u is 9.84; and the curvature coefficient C_c is 2.08. The SLB-1 triaxial shear permeameter manufactured by the Nanjing Soil Instrument Factory is used in the test which takes unconsolidated-undrained (UU) shearing. The test pieces are 40 mm in diameter and 80 mm in height. The triaxial shear test is conducted under the ambient pressure of 0.1 MPa, 0.3 MPa, and 0.6 MPa, respectively.

3.3. Numerical Modeling of Triaxial Test and Determination of Microscopic Parameters. Sizes of numerical modeling and particle simulation are magnified to save time for calculation and improve the efficiency of analysis. The numerical model of the triaxial test is 2 meters in height and 0.8 meters in diameter. As can be known from the results of the laboratory particle grading test for expansive coal measure soil in Table 1, the particle size ranges from 0.25 to 10 mm. The particle diameter should be set within this range in modeling. And a total of 3,058 solid particles can be generated in the form of uniform distribution. The calculation model is shown in Figure 1.

The walls on the top and at the bottom of the particle flow soil samples are driven to conduct relative movement via the numerical servo system under consolidated and

TABLE 1: Test results of particle size distribution of coal measure expansive soils.

Test material	Particle size (mm)	Content (%)
Coal measure expansive soil	>20	2.26
	10~20	7.73
	5~10	14.63
	2~5	36.31
	0.5~2	24.3
	0.25~0.5	10.17
	0.075~0.25	3.02
	>0.075	1.58

ambient pressure of 0.1 MPa, 0.3 MPa, and 0.6 MPa, so as to unload the test pieces. At the same time, the ambient pressure of the test pieces can be guaranteed unchanged through adjustment of the side wall displacement before the end of loading. Numerical calculation results are approximated to the results of the laboratory triaxial test via repeated trial calculation by changing microscopic parameters of the particles. The final calibrated results of microscopic parameters of the particles are obtained, as shown in Table 2. Three-axis simulation results calculated by DEM are compared with the laboratory test results, as shown in Figure 2. It can be seen from the figure that the peak value of the deviatoric stress calculated by numerical simulation of the triaxial test is relatively close to the laboratory triaxial test results with consistent change trends of the stress-strain curve. Thus, it indicates that the microscopic parameters calibrated finally can relatively approach the real model.

4. Correlation Analysis of Microscopic Parameters and Macroscopic Mechanics of Coal Measure Soil

4.1. Relationship between Friction Coefficients and Stress-Strain. The friction coefficient μ between particles is set as 0.1, 0.3, 0.5, 0.7, and 0.9 for numerical simulation in order to discuss the influence of friction coefficients on the macroscopic stress and strain of the expansive coal measure soil. Microscopic parameters of other particles in the calculation model can have assignment according to Table 1. The influencing relationship curve of different friction coefficients on stress-strain of expansive coal measure soil is shown in Figure 3.

According to the deviatoric stress-axial strain curve in Figure 3(b), as the friction coefficient μ between the particles grows, the peak value of the deviatoric stress of the test piece will also increase continuously. The stress-strain relationship of the soil mass tends to be in linear change before the test piece reaches the peak. The soil mass enters the strain softening stage right after that. As can be seen from Figure 3(a), strain softening of the soil is apparent. As the friction coefficient increases, a growth of the interaction force between soil particles can be observed; and the force for overcoming the sliding between particles is also improved. Thus, there is an increase of the modulus of deformation of the soil. Certain enhancement of the residual strength of the soil can be seen with the friction coefficient after the test

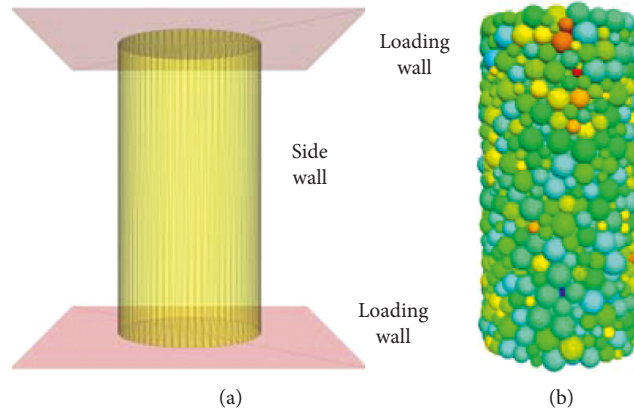


FIGURE 1: Computational model for triaxial numerical experiments. (a) Boundary wall. (b) Particle set.

TABLE 2: Microscopic parameters used in the discrete element method simulations.

Particle density	2230 kg/m ³
Porosity	0.32
Model particle diameter	20 mm~200 mm
Friction coefficient	0.3
Normal stiffness of particle contact	1 × 10 ⁹ N/m
Tangential stiffness of particle contact	1 × 10 ⁷ N/m

tangential sliding from normal compression and overlapping between particles. Consequently, the volume of the test piece becomes smaller, macroscopically resulting in shrinkage. The volumetric strain increases with the axial strain at the later stage of loading. The test piece is slid tangentially with the increase in volume, macroscopically leading to dilatancy. The volumetric strain of the test piece is enlarged with the increase of friction coefficients.

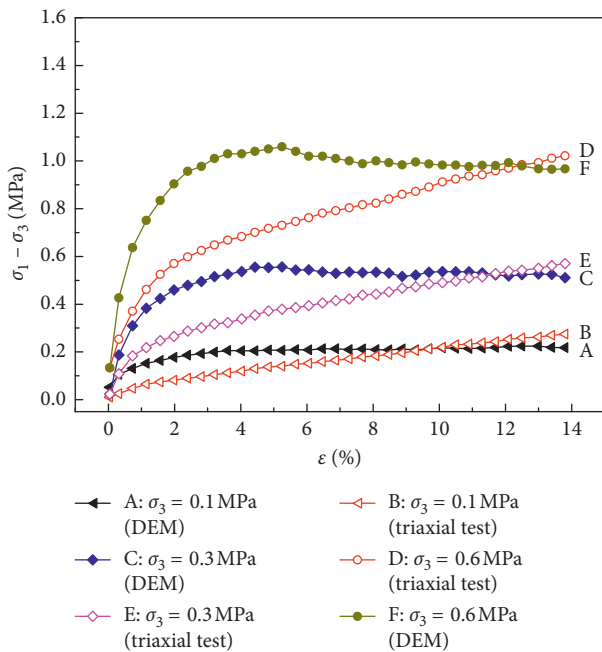


FIGURE 2: The results of deviation stress and strain of the triaxial test are compared with those of numerical simulation.

piece is loaded and unloaded, which, however, is insignificant. Moreover, the residual strength of the soil increases insignificantly when the friction coefficient is large.

Figure 4 presents the relationship curve between the volumetric strain and the axial strain of the test piece under different friction coefficients, indicating that the volumetric strain decreases with the increase of axial strain at the initial stage of loading, whereas particle deformation changes into

4.2. Relationship between Contact Stiffness and Stress-Strain of Particles. Based on the original calculation model, the ambient pressure is 0.3 MPa; and the contact stiffness K^s is 1 GPa, 3 GPa, 5 GPa, 7 GPa, 9 GPa, and 12 GPa, respectively. Other parameters are constant. Numerical simulation of the triaxial test specific to the test piece is conducted in 6 working conditions. The stress-strain relationships of the test piece with different contact stiffness are shown in Figures 5 and 6.

As can be seen from Figure 5, the deviatoric stress peak of the test piece decreases with the increase of the contact stiffness of the particles. When the contact stiffness K^s increases from 1 GPa to 3 GPa, the decline of the deviatoric stress peak of the test piece is significant; when the contact stiffness K^s increases from 5 GPa to 12 GPa, the deviatoric stress peak of the test piece is slow; when the contact stiffness K^s is large, the residual strength of the test piece tends to be the same value (as shown in Figure 5(a)). According to the test results of numerical simulation, with the increase of the contact stiffness K^s between particles of the test piece, the macroscopic initial tangential modulus of the test piece will also experience an increase, while the deviatoric stress peak and the axial strain corresponding to the strength reaching the peak value become smaller, suggesting that the contact stiffness has little influence on the residual strength of the test piece.

It can be observed from Figure 6 that the deformation of the test piece is constituted primarily by normal particle compression and overlapping as the volumetric strain decreases with the increase of the axial strain at the initial stage of loading. As a result, the test piece is shrunk. The influence of the contact stiffness of particles on the shrinkage of the

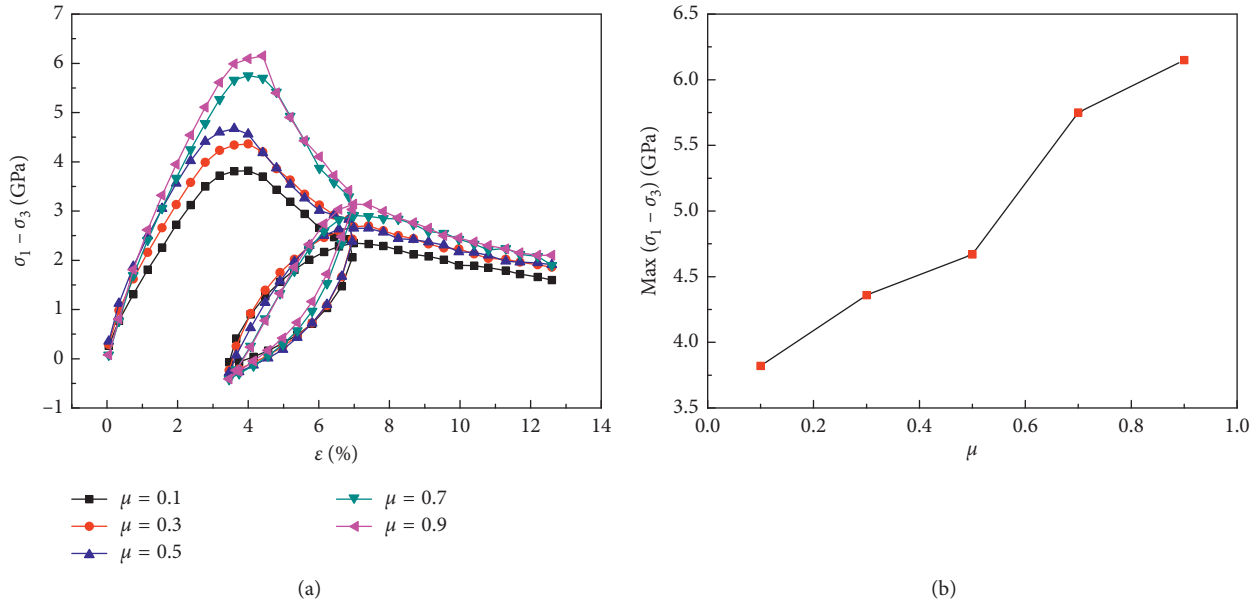


FIGURE 3: Graph showing the relationship between bias stress and axial strain with different friction coefficients: (a) bias stress and axial strain; (b) peak deviating stress and friction coefficient.

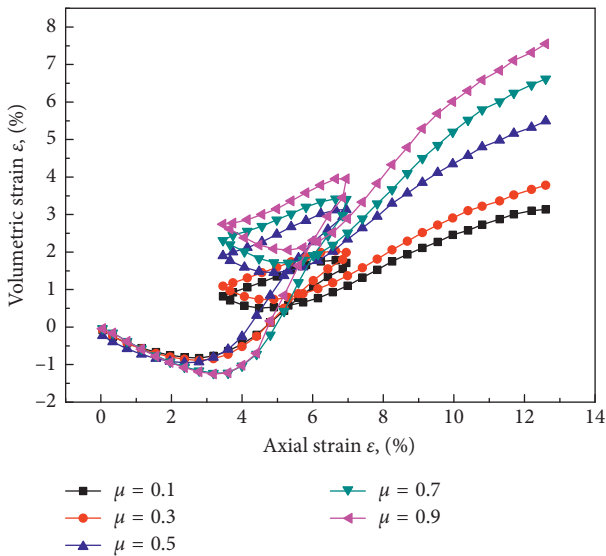


FIGURE 4: Graph showing the relationship between volumetric strain and axial strain with different friction coefficients.

test piece is not obvious at the early stage. As the test piece is further loaded, its volumetric strain becomes positive and increases with the axial strain, whereas particle deformation changes into tangential sliding from normal compression and overlapping between particles and causes volume expansion, which is macroscopically manifested as dilatancy. The volumetric strain of the test piece rises with the contact stiffness of the test piece. Such increase, however, is unapparent at the later stage.

As can be seen from Figure 7 that presents calculation results of the stiffness ratio K^n/K^s between different particles, the initial tangential modulus of the test piece at the early stage is decreased and the strength of the peak value of

the deviatoric stress gradually decreases with the increase of the particle stiffness ratio, exerting little influence on the residual strength of the test piece. Furthermore, the stiffness ratio K^n/K^s has an invisible influence on characteristics such as shrinkage and dilatancy of the test piece.

4.3. Stress-Strain Relationship under Different Ambient Pressures. The stress state around the test piece in the tri-axial test is changed to explore the changing law of deviatoric stress and axial strain under different ambient pressures. Ambient pressures calculated are valued as 0.2 MPa, 0.4 MPa, 0.6 MPa, 0.8 MPa, 1.0 MPa, and 1.2 MPa, while other microscopic parameters remain constant. The calculation results are shown in Figures 8 and 9.

From Figure 8, the initial tangential modulus of the test piece is growing (the slope of the curve increases gradually) before the softening of the curve strain with the increase of the ambient pressure. In the meantime, the deviatoric stress peak and the residual strength of the test piece are also improved constantly to realize linear change. As a result, ambient pressure has appreciable influence on the residual strength of the test piece.

The relationship curve of the volumetric strain and the axial strain under different ambient pressures of the test piece is shown in Figure 9. It can be observed that the volumetric strain of the test piece is negative at the early loading stage. As the axial strain increases, the test piece is shrunk gradually, which becomes increasingly obvious with the increase of the ambient pressure. When the ambient pressure is small, the test piece is diverted to dilatancy from shrinkage. It can also be observed that the volumetric strain of the test piece constantly decreases with the increase of the ambient pressure. When the ambient pressure is small, the declining range is significant; when the ambient pressure is

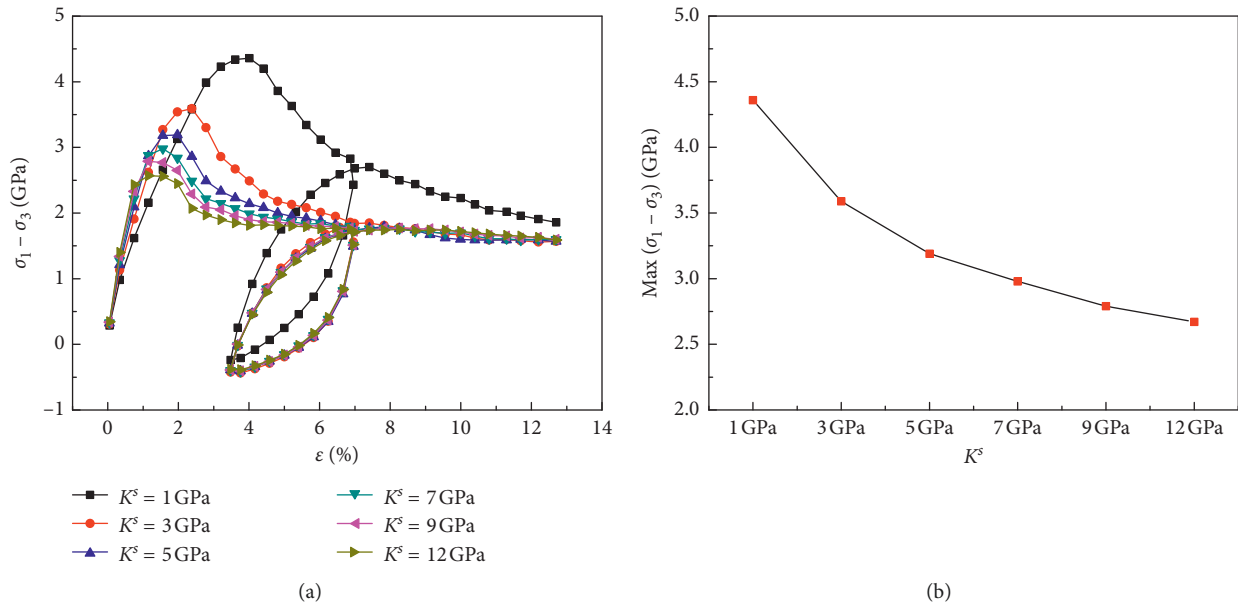


FIGURE 5: Graph showing the relationship between different tangential contact stiffness and stress-strain: (a) deviation stress and axial strain; (b) peak deviating stress and tangential contact stiffness.

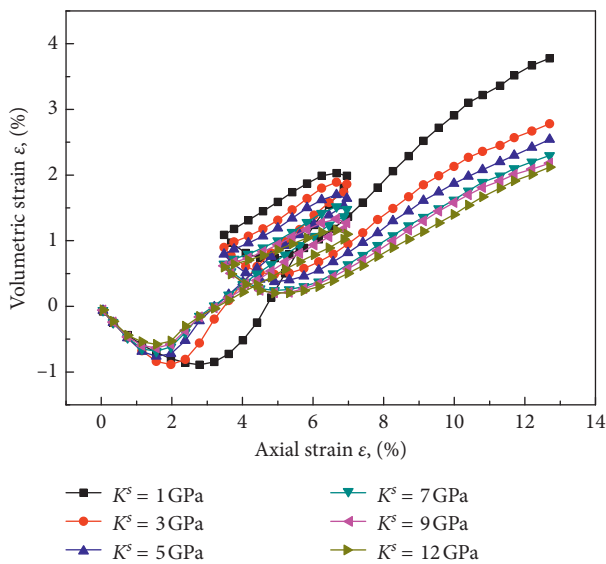


FIGURE 6: Graph showing the relationship between volumetric strain and axial strain with different tangential contact stiffness.

large, the declining range of the volumetric strain is insignificant.

4.4. Analysis of the Influence of Porosity on Shear Strength Parameters. Based on the original calculation model, the ambient pressure is set as 0.8 MPa; and the porosity of the test piece is set as 0.3, 0.35, 0.4, 0.45, and 0.5, respectively, while other parameters maintain constant, thus to analyze the stress-strain relationships of the test piece under different porosity conditions. The simulated calculation results are shown in Figure 10. As can be seen from Figure 10(a), the

porosity has certain influence on the deviatoric stress peak of the test piece. The deviatoric stress peak of the test piece is large when the porosity is small; that is, the larger the porosity is, the smaller the deviatoric stress peak of the test piece will be. Nonetheless, the porosity has an insignificant influence on the residual strength of the test piece.

The relationship curve of volumetric strain and axial strain under different porosity conditions of the test piece is shown in Figure 10(b). It can be observed when the test piece with low porosity (samples are dense) is sheared, a shrinkage will be witnessed for the test piece with the decreased volume at the early loading stage. After that, the volume of the test piece will rapidly increase, macroscopically manifesting as dilatancy in an obvious manner, as the particles in the test piece are sheared and moved. When the test piece with high porosity (samples are loose) is sheared, its volume will decrease before the subsequent rebound, mainly manifesting shrinkage. Moreover, the volume increase of the test piece gradually decreases with the increase of porosity.

4.5. Discussion on the Evolution Law of Shear Displacement Field of Expansive Coal Measure Soil.

The displacement and velocity change paths of particles in the test piece can be monitored and tracked in real time in the loading process of numerically simulating the triaxial test with the particle flow code. Moreover, the formation of the shear displacement field and the change law of the stress field of the test piece can be analyzed through elaboration of the displacement vector. Figure 11 shows the vector diagram presenting the formation and evolution of the shear displacement field of the test piece under different axial strains (calculation of time steps) when the ambient pressure is 0.6 MPa. To be specific, Figures 11(a) and 11(b) show the formation of the shear displacement vector at the initial loading stage of the test

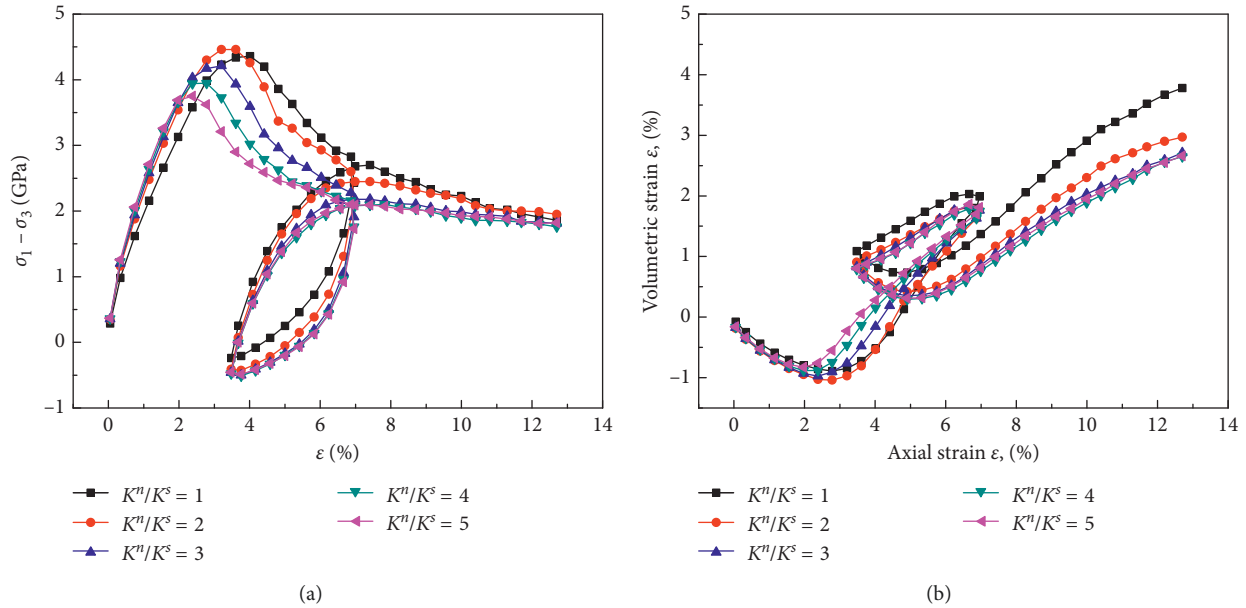


FIGURE 7: Graph showing the relationship between stress and strain with different contact stiffness ratios of particles: (a) deviation stress and axial strain; (b) volumetric strain and axial strain.

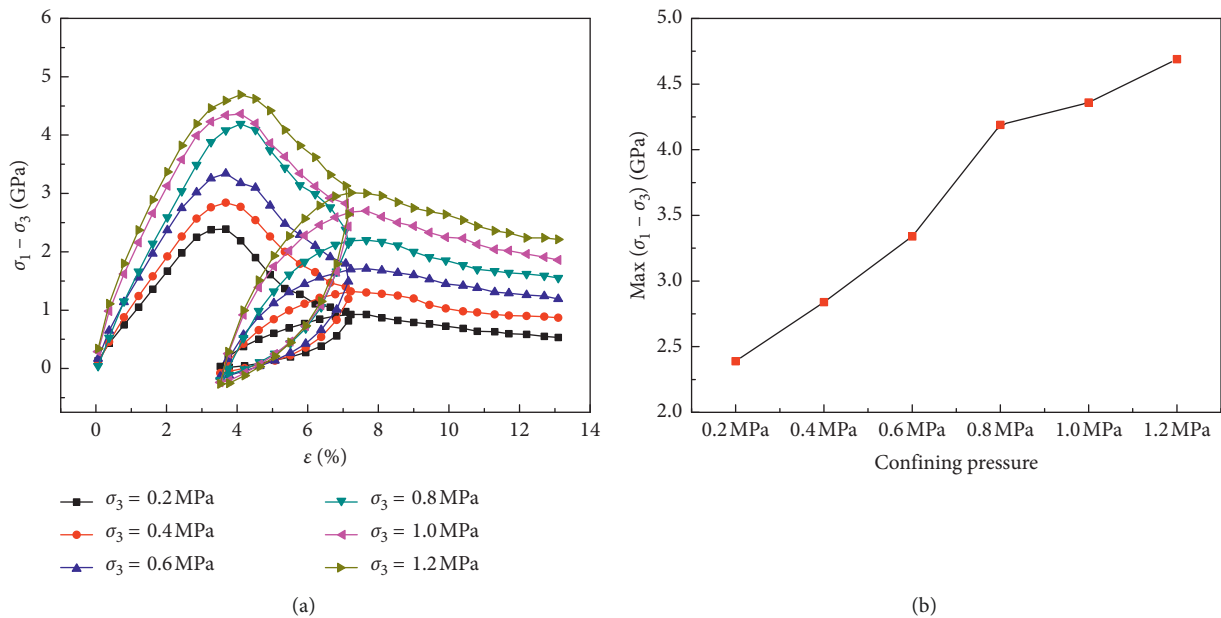


FIGURE 8: Graph showing the relationship between stress and strain with different confining pressures: (a) deviation stress and axial strain; (b) peak deviating stress and confining pressure.

piece. It can be seen from Figure 11(a) that particles in the test piece are moved towards the central section at this time with the insignificant shape of the shear zone, indicating that the test piece is at the early stage of dilatancy. It can be observed from Figure 11(b) that the shear zone of the test piece is formed initially as loading continues. At this time, the motion of particle displacement vector approaches the direction of 45°. Whereas Figures 11(c) and 11(d) show the evolution of the shear displacement vector after the deviatoric stress of the test piece reaches the peak. Since particle

motion changes from the low potential energy to the high potential energy, the directional trend of the shear displacement field becomes significant with the increase of the axial strain of the test piece. Meanwhile, the thickness of the shear zone is getting smaller in the state of instability.

Distribution of the shear displacement field of the test piece under different ambient pressures is presented in Figure 12. It can be observed that the width of the shear displacement belt of particles is gradually narrowed as the ambient pressure increases. Analyzing the microscopic

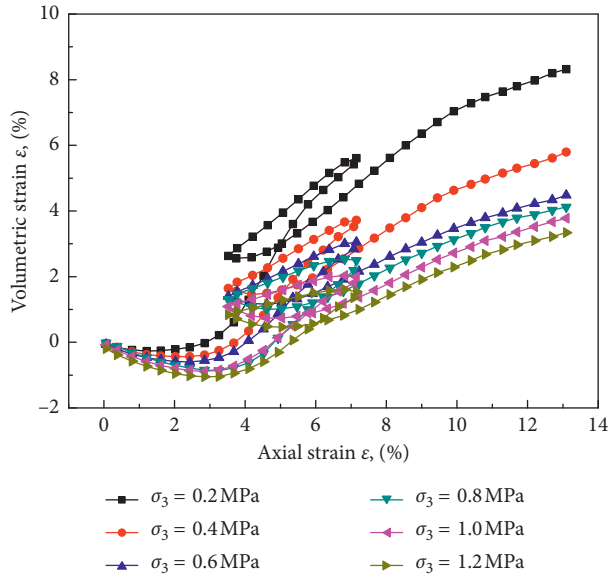


FIGURE 9: Graph showing the relationship between volumetric strain and axial strain with different confining pressures.

mechanism shows that it is mainly because the resistance of particle motion in the restrained test piece increases with the ambient pressure of the test piece. That is to say, the difficulty of displacing the relative sliding of the particle has also increased, which is further manifested by the enhanced deviatoric stress peak of the test piece from the macroperspective.

5. Macroinstability of Coal Measure Soil and Micromechanism Analysis of Shear Band Localization

Cundall and Strack [39] as well as Bardet and Proubet [40] studied the localization of shear strain with the PFC discrete element analysis software. Vardoulakis and Aifantis [41] and Chambon et al. [42] theoretically explored the mechanism of production of shear zones based on the second gradient. In this paper, the author analyzed the mesoscopic mechanism of localization of shear zones with the volume fraction of particles, coordination number, and other mesoscopic parameters. The gradation of test samples in the triaxial test originated from the undisturbed coal-bearing soil samples on the side slope at mark K12 + 110 of section A2 on the Wanzai-Yichun expressway in Yichun, Jiangxi. The gradation is shown in Table 1. The numerical model in the triaxial test was 2.0 m in height and 0.8 m in diameter; the average soil particle density was determined as $2230 \text{ kg}\cdot\text{m}^{-3}$, and the natural porosity was 0.32. The values of mesoscopic parameters of the test samples were in accordance with the calibrated values in Table 2. To track the parametric variation in the particle system, a measuring sphere (MS1) outside the shear zone and one (MS2) inside the shear zone were selected to highlight the variation of volume fraction, coordination number, and other parameters within and outside the shear zone.

5.1. Macroscopic Instability of Coal Measure Soil. The results of deviator stress and volumetric strain of the test samples simulated by the triaxial test are shown in Figure 13. Figure 13(a) shows the complete process of elastoplasticity, which the particle system underwent. When the axial strain was $\epsilon < 2.0\%$, the deviator stress and axial strain exhibited a linear change at the macrolevel, and the particle system exhibited elastic properties. When ϵ increased, the particle system entered the plastic stage. When the axial strain was $2\% \leq \epsilon \leq 3.5\%$, the deviator stress of the test samples underwent violent fluctuations and peaked at the axial strain value of 2.4%. Later, the deviator stress gradually decreased; during this process, the test samples hardened. When the axial strain was $\epsilon > 3.5\%$, the particle system entered the softening stage, where the deviator stress considerably decreased, which indicated the presence of internal damage to the system. According to Figure 13(b), when the particle system was under pressure, the volumetric strain ϵ_v decreased to a negative value; when the particle volume fraction n increased, the stress in the system increased. When the axial strain was $\epsilon < 2.0\%$, the system was in an elastic strain. When the axial strain was $\epsilon = 3.2\%$, the volumetric strain was $\epsilon_v = -1.8\%$ while the system achieved its highest density and maximum volume fraction. When the axial strain was $\epsilon > 3.2\%$, the volumetric strain ϵ_v increased and the particle system entered the plastic stage. When the axial strain was $\epsilon = 5.3\%$, the volumetric strain became $\epsilon_v = 0$, which indicated that the volumetric strain of the system returned to the initial state. When $\epsilon > 5.3\%$, the volume fraction of the particle system gradually decreased while the volumetric strain experienced slight fluctuations. At the same time, the change in slope remained constant. The system experienced a dilatative shear failure.

5.2. Mesomechanism Analysis of Shear Band Localization of Coal Measure Soil. Figure 14 illustrates the relationship curve between the axial strain and volume fraction, which were measured using the measuring spheres. Figure 14 shows that the volume fraction n of both MS1 and MS2 gradually increased at first, while the particle system remained at the elastic stage, which was represented as shrinkage. When the axial strain was $2\% \leq \epsilon \leq 3.2\%$, the volume fraction at the shear zone (MS2) remained the same at 65.38%, with the system shifting to the hardening stage. When $\epsilon = 3.2\%$, the MS2 volume fraction n exhibited a slight decrease with a small range of variation and the particle system may have internally developed small cracks. The MS2 volume fraction n exhibited only minor changes before $\epsilon < 4.5\%$. When $\epsilon = 4.5\%$, the MS2 volume fraction n progressed in a sustained decline and the system entered the critical state, which indicated the growth of the dominant shear zone. When the axial strain increased, the in-shear zone (MS2) volume fraction n exhibited an overall downward trend with occasional small upward and downward deviations, which implies that the dilatancy of the particle system was primarily caused by the loose arrangement of particles within the shear zone. The varying pattern of the outer-shear zone (MS1) volume fraction was similar to that of MS2.

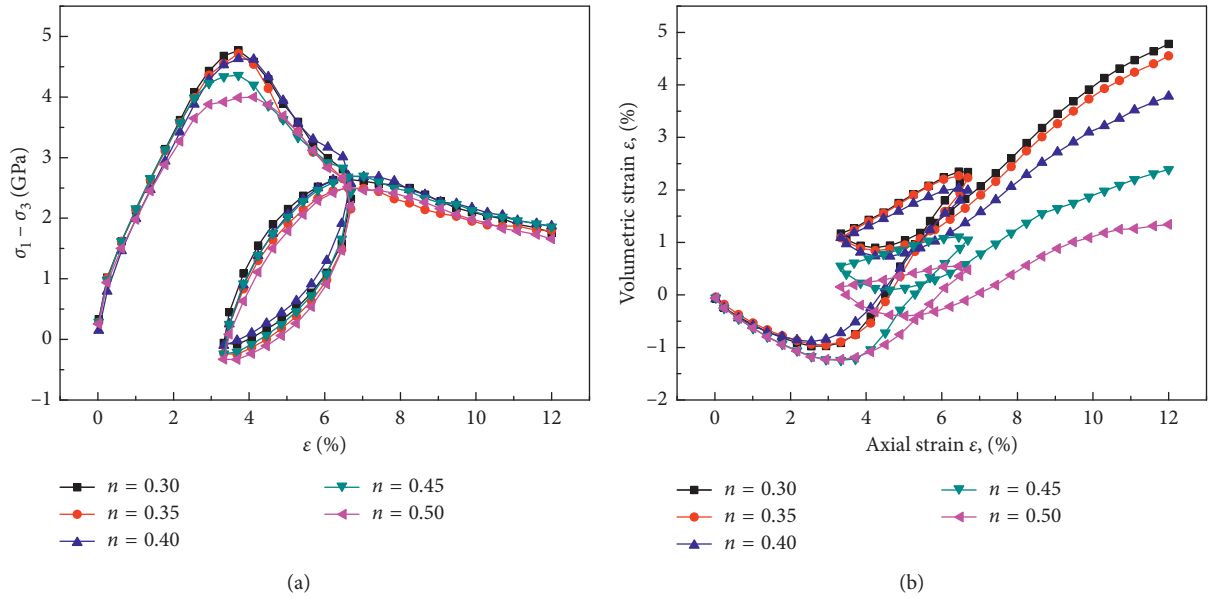


FIGURE 10: Graph showing the relationship between stress and strain with different porosity: (a) deviation stress and axial strain; (b) volumetric strain and axial strain.

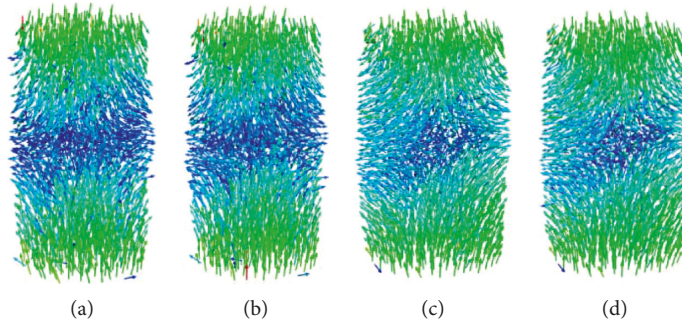


FIGURE 11: Graph showing the formation and variation of shear displacement field of specimen particles during loading (the confining pressure is 0.6 MPa): (a) $\epsilon_1 = 1.35\%$; (b) $\epsilon_1 = 2.32\%$; (c) $\epsilon_1 = 8.28\%$; (d) $\epsilon_1 = 11.15\%$.

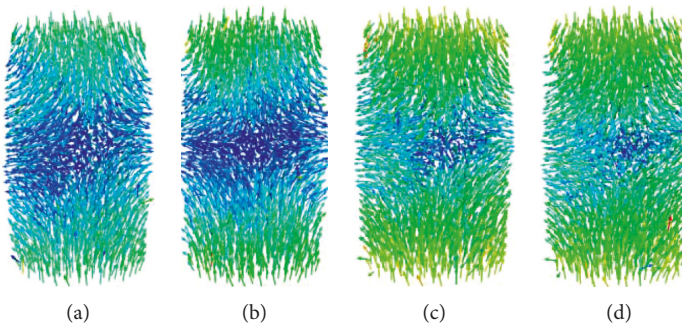


FIGURE 12: Graph showing the distribution of shear displacement field of specimens with different confining pressures: (a) $\sigma_3 = 0.1$ MPa; (b) $\sigma_3 = 0.4$ MPa; (c) $\sigma_3 = 0.8$ MPa; (d) $\sigma_3 = 1.6$ MPa.

Figure 15 shows the variation curve of the coordination number and axial strain. It is observed that when the axial strain was $\epsilon < 2\%$, as the loading process of the entire particle system continued, the coordination number Z gradually increased. When $2\% \leq \epsilon \leq 4.5\%$, the coordination number Z

of MS1 and MS2 exhibited small oscillations, and the maximum coordination number of MS1 was 5.5 and that of MS2 was 5.84. When $\epsilon = 4.5\%$, the coordination number Z of MS1 and MS2 clearly decreased, which indicates the increase in porosity in the central area of the particle system.

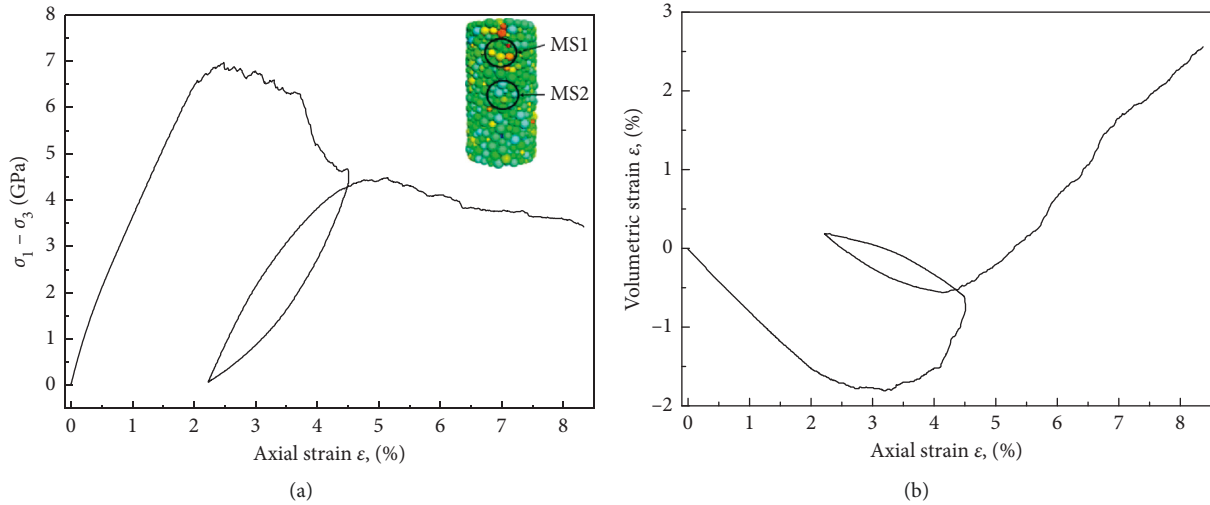
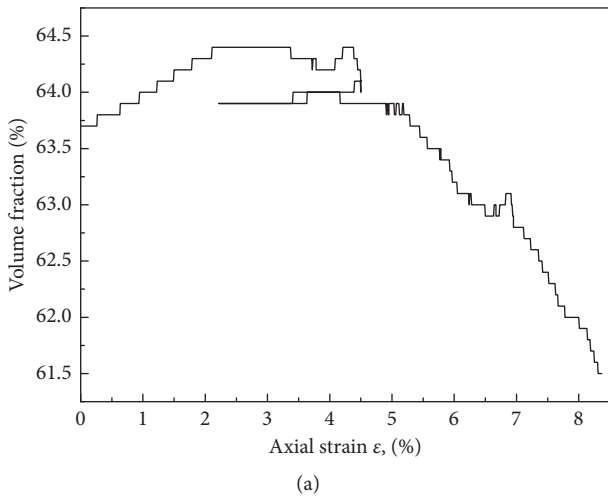
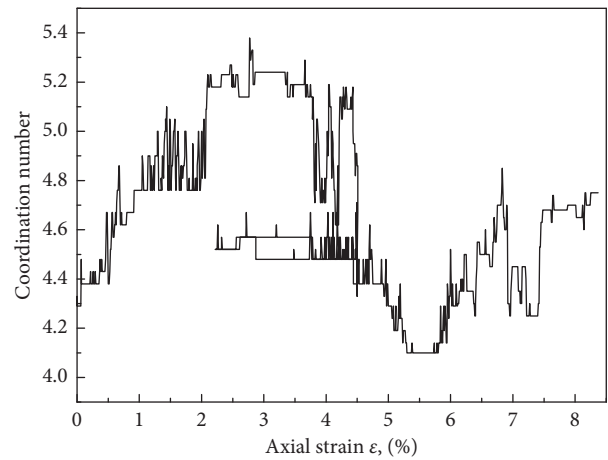


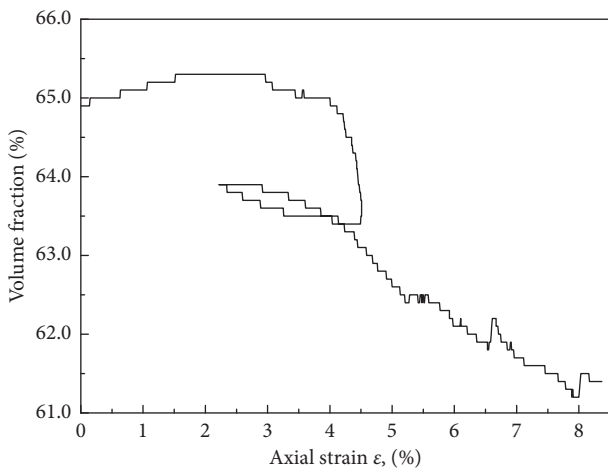
FIGURE 13: Simulated results of the triaxial test for specimens: the relation curve between (a) deviating stress and axial strain and (b) volumetric strain and axial strain.



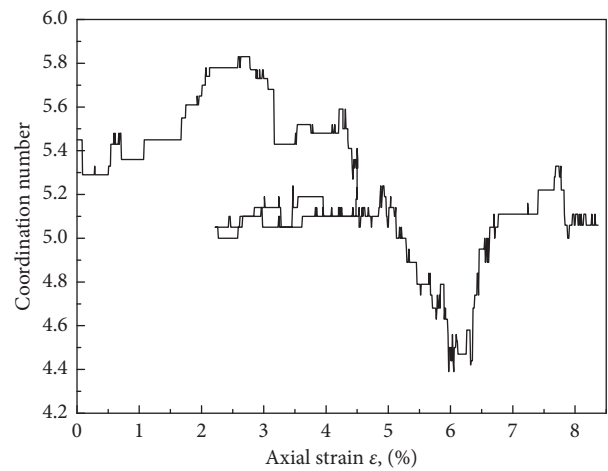
(a)



(a)



(b)



(b)

FIGURE 14: The curve of relationship between volume fraction and axial strain: (a) the relationship between volume fraction and axial strain at the measuring sphere 1 (outside shear band); (b) the relationship between volume fraction and axial strain at the measuring sphere 2 (in shear band).

FIGURE 15: Relation between coordination number and axial strain: (a) the relationship between coordination number and axial strain at the measuring sphere 1 (outside shear band); (b) the relationship between coordination number and axial strain at the measuring sphere 2 (in shear band).

Meanwhile, the volumetric strain gradually increased from the minimum, which indicates a clear dilatancy of the entire particle system during the softening stage. When the axial strain was $\varepsilon = 5.8\%$, the coordination number of the particle system increased again. Therefore, it was concluded that the dilative shear failure of the particles included slippage between the particles and angular displacement, which was generated by particle rotation. When the axial strain was 7.5%, the coordination number of the particle system remained practically unchanged and the coordination numbers of MS1 and MS2 were 4.7 and 5.1, respectively.

6. Conclusions

Based on the theory of discrete element method (DEM), this paper performed numerical calculations on the triaxial test of expansive coal measure soil as well as simulated the macromechanical properties of the coal measure soil as well as the formation and development of the shear displacement field from the perspective of particle microscopic parameters, from which, results similar to the laboratory test can be obtained. By analyzing microscopic parameters of the particles and the influencing law of the macroscopic stress-strain curve of the expansive coal measure soil, the following conclusions can be made.

- (1) The friction coefficient between soil particles exerts a significant influence on the macroscopic stress and strain of the test piece. As the friction coefficient μ between particles grows, the deviatoric stress peak of the test piece also increases continuously. The stress-strain relationship of the soil mass tends to be in linear change before the test piece reaches the peak. The soil mass enters the strain softening stage immediately after reaching the peak, whereas the increase in the residual strength of soil mass is not obvious when the friction coefficient is large.
- (2) The contact stiffness between particles increases, whereas the deviatoric stress peak of the test piece decreases, basically presenting a hyperbolic change. When the contact stiffness ratio K^n/K^s increases, the deviatoric stress peak of the test piece will decrease gradually with nearly no effect on the residual strength of the test piece. Meanwhile, the stiffness ratio K^n/K^s has insignificant effect on characteristics such as shrinkage and dilatancy of the test piece.
- (3) The deviatoric stress peak and the residual strength are significantly affected by the ambient pressure in the test. By analyzing from the microscopic mechanism, it is mainly a result of the resistance increase of particle motion in the restrained test piece with the ambient pressure of the test piece. That is to say, the difficulty of displacing the relative sliding of the particle has also increased, which is further manifested by the enhanced deviatoric stress peak of the test piece from the macroperspective.
- (4) The monitoring of volume fraction and coordination number in shear band shows that the volume fraction in shear band of coal measure soil decreased

with the increase of axial strain when the granular system was in the softening stage, which indicated that the dilatancy behavior of the granular system was basically caused by the loose distribution of particles in the shear band. At the same time, the coordination number began to decrease significantly, indicating that the porosity in the central region of the particle system began to increase, and the dilatancy failure behavior of the particles included not only the slip between the particles but also the angular displacement caused by the rotation of the particles.

Data Availability

The data used to support the findings of this study are available from the corresponding author upon request.

Conflicts of Interest

The authors declare that there are no conflicts of interest regarding the publication of this paper.

Acknowledgments

This study was supported by the National Natural Science Foundation of China (Grant no. 51609114), the Science and Technology Project of Jiangxi Education Department (Grant no. GJ161101), and the Superiority Science and Technology Innovation Team Project of Nanchang City (Grant no. 2017CXTD012).

References

- [1] J. D. Li, "Stability analysis and control of cutting high slopes in coal measure strata along Xiaotang-Gantang of Beijing-Zhuhai expressway," *Hydrogeology and Engineering Geology*, vol. 30, no. 5, pp. 86–88, 2003.
- [2] W. Liu, "Strengthening treatment of high cut slope on coal measures layer," *Technology of Highway and Transport*, vol. 5, pp. 15–18, 2004.
- [3] M. J. Jiang and Z. F. Shen, "Three-dimensional microscopic contact model for DEM analyses of bonded assembly," *Chinese Journal of Underground Space and Engineering*, vol. 12, no. 1, pp. 30–37, 2016.
- [4] X. Hu, B. N. Hong, Q. Du, and Y. M. Meng, "Influence of water contents on shear strength of coal-bearing soil," *Rock and Soil Mechanics*, vol. 30, no. 8, pp. 2291–2294, 2009.
- [5] L. Zhu, S. Y. Han, B. N. Hong, and X. J. Song, "Analysis on stability of coal measure soil slope considering fissures and weathering under rainfall infiltration," *Journal of Water Resources and Architectural Engineering*, vol. 8, no. 4, pp. 86–89, 2010.
- [6] Y. Zhang, S. Y. Han, and J. H. Zheng, "Analysis on stability of coal-bearing soil slope considering cracks under rainfall infiltration," *Highway Engineering*, vol. 39, no. 1, pp. 10–13, 2014.
- [7] H. Li and S. Q. Liu, "Comparative study on the water sensitivity of remoulded red clay and powered soil of coal measure strata," *Acta Scientiarum Naturalium Universitatis Sunyatseni*, vol. 54, no. 6, pp. 89–93, 2015.

- [8] J. K. Yang and M. X. Zheng, "Effects of density and drying-wetting cycle on soil water characteristic curve of coal soil," *Journal of East China Jiaotong University*, vol. 35, no. 3, pp. 91–95, 2018.
- [9] Y. Zeng and J. Zhou, "Influence of micro parameters of sandy soil on its macro properties," *Chinese Journal of Underground Space and Engineering*, vol. 4, no. 3, pp. 499–503, 2008.
- [10] F. Gao and D. Stead, "Discrete element modelling of cutter roof failure in coal mine roadways," *International Journal of Coal Geology*, vol. 116–117, no. 9, pp. 158–171, 2013.
- [11] R. Wen, C. Tan, Y. Wu, and C. Wang, "Grain size effect on the mechanical behavior of cohesionless coarse-grained soils with the discrete element method," *Advances in Civil Engineering*, vol. 2018, Article ID 4608930, 6 pages, 2018.
- [12] S. Yeom and K. Sjoblom, "Structural soil crust development from raindrop impacts using two-dimensional discrete element method," *Computers & Geosciences*, vol. 97, no. 12, pp. 49–57, 2016.
- [13] Y. Fu, Z. J. Wang, X. R. Liu et al., "Meso damage evolution characteristics and macro degradation of sandstone under wetting-drying cycles," *Chinese Journal of Geotechnical Engineering*, vol. 12, no. 4, pp. 1653–1661, 2017.
- [14] L. Jin and Y. W. Zeng, "Refined simulation for macro-and meso-mechanical properties and failure mechanism of soil-rock mixture by 3D DEM," *Chinese Journal of Rock Mechanics and Engineering*, vol. 37, no. 6, pp. 1540–1550, 2018.
- [15] P. A. Cundall and O. D. L. Strack, "The distinct element method as a tool for research in granular media," in *Part II Report to the National Science Foundation*, University of Minnesota, Minneapolis, MN, USA, 1979.
- [16] O. D. L. Strack and P. A. Cundall, "The distinct element method as a tool for research in granular media," in *Part I Report to the National Science Foundation*, University of Minnesota, Minneapolis, MN, USA, 1978.
- [17] O. R. Walton and R. L. Braun, "Stress calculations for assemblies of inelastic spheres in uniform shear," *Acta Mechanica*, vol. 63, no. 1–4, pp. 73–86, 1986.
- [18] J. R. Williams and N. Rege, "The development of circulation cell structures in granular materials undergoing compression," *Powder Technology*, vol. 90, no. 3, pp. 187–194, 1997.
- [19] J. R. Williams and N. Rege, "Granular vortices and shear band formation," *Mechanics of Deformation & Flow of Particulate Materials*, pp. 62–76, ASCE, Reston, VA, USA, 2010.
- [20] M. Oda and H. Kazama, "Microstructure of shear bands and its relation to the mechanisms of dilatancy and failure of dense granular soils," *Geotechnique*, vol. 48, no. 4, pp. 465–481, 1998.
- [21] K. Iwashita and M. Oda, "Micro-deformation mechanism of shear banding process based on modified distinct element method," *Powder Technology*, vol. 109, no. 1–3, pp. 192–205, 2000.
- [22] C. Thornton and S. J. Antony, "Quasi-static shear deformation of a soft particle system," *Powder Technology*, vol. 109, no. 1–3, pp. 179–191, 2000.
- [23] C. Thornton and L. Zhang, "Numerical simulations of the direct shear test," *Chemical Engineering & Technology*, vol. 26, no. 2, pp. 153–156, 2003.
- [24] P. A. Langston, U. Tuzun, and D. M. Heyes, "Discrete element simulation of granular flow in 2D and 3D hoppers: dependence of discharge rate and wall stress on particle interactions," *Chemical Engineering Science*, vol. 50, no. 6, pp. 967–987, 1995.
- [25] P. A. Langston, U. Tuzun, and D. M. Heyes, "Discrete element simulation of internal stress and flow fields in funnel flow hoppers," *Powder Technology*, vol. 85, no. 2, pp. 153–169, 1995.
- [26] K. D. Kafui and C. Thornton, "Some observations of granular flow in hoppers and silos," in *Powders & Grains 97*, R. P. Behringer and T. J. Jenkins, Eds., pp. 511–514, Balkema, Rotterdam, Netherlands, 1997.
- [27] S. Masson and J. Martinez, "Effect of particle mechanical properties on silo flow and stresses from distinct element simulations," *Powder Technology*, vol. 109, no. 1–3, pp. 164–178, 2000.
- [28] L. Q. Yu and J. B. Xing, "Discrete element method simulation of forces and flow fields during filling and discharging materials in silos," *Transactions of the Chinese Society of Agricultural Engineering*, vol. 16, no. 4, pp. 15–19, 2000.
- [29] Y. Xu, K. D. Kafui, C. Thornton, and G. Lian, "Effects of material properties on granular flow in a silo using DEM simulation," *Particulate Science and Technology*, vol. 20, no. 2, pp. 109–124, 2002.
- [30] P. W. Cleary, "DEM simulation of industrial particle flows: case studies of dragline excavators, mixing in tumblers and centrifugal mills," *Powder Technology*, vol. 109, no. 1–3, pp. 83–104, 2000.
- [31] H. Tanaka, M. Momozu, A. Oida, and M. Yamazaki, "Simulation of soil deformation and resistance at bar penetration by the distinct element method," *Journal of Terramechanics*, vol. 37, no. 1, pp. 41–56, 2000.
- [32] P. Jiang, R. Q. Li, and D. F. Kong, "Computer simulation of the dynamic compacting process on granular soil by DEM," *Rock And Soil Mechanics*, vol. 20, no. 3, pp. 29–34, 1999.
- [33] H. Nakashima and A. Oida, "Algorithm and implementation of soil-tire contact analysis code based on dynamic FE-DE method," *Journal of Terramechanics*, vol. 41, no. 2–3, pp. 127–137, 2004.
- [34] H. Nakashima, H. Fujii, A. Oida et al., "Parametric analysis of lugged wheel performance for a lunar microrover by means of DEM," *Journal of Terramechanics*, vol. 44, no. 2, pp. 153–162, 2007.
- [35] M. Momozu, A. Oida, M. Yamazaki, and A. J. Koolen, "Simulation of a soil loosening process by means of the distinct element method," *Journal of Terramechanics*, vol. 39, no. 3, pp. 207–220, 2003.
- [36] H. Tanaka, K. Inooku, M. Momazu, M. Miyazaki, and O. Sumikawa, "Numerical analysis of soil loosening in sub-surface tillage by a vibrating type subsoiler by means of distinct element method," in *Proceedings of the 13th International Conference of the ISTVS*, pp. 791–798, Munich, Germany, September 1999.
- [37] Y. Luo, X. N. Gong, and F. Lian, "Simulation of mechanical behaviors of granular materials by three-dimensional discrete element method based on particle flow code," *Chinese Journal of Geotechnical Engineering*, vol. 30, no. 2, pp. 292–297, 2008.
- [38] D. O. Potyondy and P. A. Cundall, "A bonded-particle model for rock," *International Journal of Rock Mechanics and Mining Sciences*, vol. 41, no. 8, pp. 1329–1364, 2004.
- [39] P. A. Cundall and O. D. L. Strack, "Discussion: a discrete numerical model for granular assemblies," *Géotechnique*, vol. 30, no. 3, pp. 331–336, 1980.
- [40] J. P. Bardet and J. Proubet, "Numerical simulations of shear bands in idealized granular materials," *Solid State Phenomena*, vol. 23–24, pp. 473–481, 1992.
- [41] I. Vardoulakis and E. C. Aifantis, "A gradient flow theory of plasticity for granular materials," *Acta Mechanica*, vol. 87, no. 3–4, pp. 197–217, 1991.

- [42] G. Chambon, J. Schmittbuhl, A. Corfdir, J. P. Vilotte, and S. Roux, "Shear with comminution of a granular material: microscopic deformations outside the shear band," *Physical Review E Statistical Nonlinear & Soft Matter Physics*, vol. 68, no. 1, article 011304, 2003.